

# **Holocene Sea Level Change in Northeastern Australia: A High-Resolution Record from Albatross Bay, Cape York Peninsula**

**Stacy Pei Shan Oon**

B.Soc.Sci. (Hons), 2009, National University of Singapore

M.Soc.Sci., 2012, National University of Singapore

Thesis presented for the degree of Doctor of Philosophy

Department of Environmental Sciences

Macquarie University, Sydney NSW

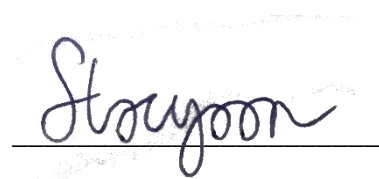
February 2018



**MACQUARIE**  
University  
SYDNEY · AUSTRALIA

# Declaration

I certify that the work in this thesis entitled *Holocene Sea level Change in Northeastern Australia: A High-Resolution Record from Albatross Bay, Cape York Peninsula* has not been submitted previously, in whole or in part, for a degree at Macquarie University or any other university. To the best of my knowledge, this thesis does not contain any material published or written by another person, except where acknowledged. I certify that this thesis is an original piece of research that is comprised of solely my own work.

A handwritten signature in dark ink, reading "Stacy Oon", is written over a horizontal line.

Stacy Oon

05/02/2018

# Acknowledgements

I have been so incredibly fortunate to be surrounded by an army of people who have given me so much support throughout this whole process – endless encouragement when I needed it, boundless enthusiasm when mine faltered and steadfast confidence in me when I lost faith in myself. Words cannot express how much gratitude I have for the following people and organisations:

Associate Professor Trish Fanning, my supervisor. None of this would have been possible without you. You took a chance on me as a student and welcomed me so warmly to Australia, going so far as to having me over my first Christmas in the country when I still did not know anyone else. Not only have you guided me through this entire academic process and spent countless hours reading my work, you even took up a shovel and helped me dig for hours to collect the samples I needed. You've gone above and beyond your obligations as a supervisor and for this and so much more, I am truly grateful.

Dr Kira Westaway, my co-supervisor and the OSL guru. Thank you for teaching me all about OSL dating, from first principles, to the methods, the results and how to make sense of it all. Your door was always open for a chat (though those human skulls on your desk made me hesitant). You were encouraging and upbeat, and always made me feel like I was a priority, even when you had so much on your plate.

Dr Craig Sloss, my supervisor up in Brisbane. Thank you for all the guidance and help. You were incredible in the field, helping me take my first steps into coastal research, showing me the ropes, and just making fieldwork so much fun. Your enthusiasm and love for science was infectious. Your guidance and feedback regarding my results and discussion were invaluable. You even cooked dinner for me and let me stay with you and your family (twice!) when I came up to Brisby.

This research arose as part of a larger project funded by an Australian Research Council Linkage Projects grant (LP110100180), awarded to a multi-institution team lead by Associate Professor Patricia Fanning from Macquarie University, with Rio Tinto Alcan (Weipa) Pty Ltd as the industry partner. This project grant provided me with a scholarship, fieldwork travel and accommodation, access to equipment, and funding for the geochronology component of my project. Additional funding was provided by Macquarie University.

Fieldwork would not have been possible without the RTA Community Relations staff who helped organise the permissions and access I needed for my fieldwork. Permission for the research to be conducted on Aboriginal land was provided by the Western Cape Communities Coexistence Agreement (WCCCA) and the Napranum Aboriginal Shire Council on behalf of the Traditional Owners of country around Weipa. I am grateful for the trust they placed in me.

The Department of Environmental Sciences admin staff – Paula, Farhana, Glenys and Darina. Administration and paperwork is never fun, and you guys always put in the extra effort to make sure things go smoothly for us students. You all were always patient and unruffled, even when I rushed down with forms that were supposed to have been submitted days ago. Russell Field, scientific officer, fieldwork officer, facilities manager... Just who are you really? All I know is that you taught me how to use all the equipment in the lab, helped me procure anything I needed that wasn't there, fixed all the stuff I broke, and were good company over hours I spent down there. The Faculty of Science HDR staff, especially Jane Yang. You all went the extra mile to help me through all my problems and, once again, this thesis would not exist without you.

My fieldwork crew! Ali Sternes and Lynda Petherick helped carry all that equipment, slogged through the bush and dug all them holes with me. The archaeologists who were on the same project as me – Kasey Allely, Eloise Hoffman, Bernie Larsen, Tim Mackrell, Justin Shiner, Simon Holdaway and Fiona Petchey. You guys taught me how to use all the various bits of high tech gear we had and the best fieldwork practices. You all were such great booze and banter company the weeks we were in the field. We even had a freaking Death Star!! Best of all, you crazy Aussies (and Kiwis) taught me the joy of the post-fieldwork shower beer!!

My Quaternary buddy, Daniela Mueller. It was a blast travelling around the same conference circuit as you and picking your brain. The OSL lab group, Lani Barnes and Zacc Larkin. Hours in a red-lit room does strange things to your mind. Lucky you guys were there to keep me sane.

My PhD gang – Eric Portenga, Amy Chen, Danielle Toase, Stuart Mead, Tetsuya Okada, Rebecca Wilson, Rory Williams, Marek Rouillon and, my work wife, Emma Singh. Thanks for all the days and nights at the Ubar, and all the coffee sessions. You guys have supported me through this journey. I'll always have fond memories of our time with Donrita. We'll always be the Frosties!

My Australian family who broke me out of this academic bubble whenever I needed an escape. Emily Kitchin, my first friend in this country. Sure, I was only hanging out with you at first



cause you could drive me to the shops for groceries. But over the years, I have grown very fond of you. Bobbie Wan, the best flatmate a girl could ask for. All those blissful nights spent on the couch watching sitcoms... I'm sorry I moved out before we could finish watching Xena: Warrior Princess. Mick and Marki, my regular weekend date. I can't wait to play more board games and video games with you guys.

Mental wellbeing is an unacknowledged, but pervasive, issue within higher degree research. I am grateful to the support system Macquarie University has implemented to care of its students. Campus Wellbeing, and Dr Richa Gupta in particular, were always friendly, sympathetic and soothing. When I got too busy to make another appointment to see Richa, she personally called to check up on me, and it was a comfort to know I always had a safety net to catch me. I believe that all final year PhD students need to be made aware of the support services available to them. We need to make mental wellbeing a priority, not something to be hidden and ashamed of.

My parents, Steven and Adeline, and brother, Shaun, have been my steadfast cheerleaders my entire life. This PhD process was no different. I've not always been the best kid, and it's especially hard to maintain a relationship when I'm in a different country and mired in PhD-land. My family was always in the background, ready and waiting to provide me any assistance I needed. I've also been lucky enough to have the support of my partner's family. Alice and Joe, thanks for all the love. You've brought me into the family and have made me feel so welcome. Thanks for all the help puppy-sitting, and for sending food my way when I was too busy to even think about feeding myself. Lana, I would say that I'm grateful you live only a few doors down from us and am always around whenever I need, but you've been more trouble than you're worth. Truthfully though, I'm so happy that Bren has such an awesome sister who even checks up on me and makes sure I'm doing ok even when she's in South Africa!

Brendon, you know what you mean to me. I look forward to every new day with you. You've made my world a happier place and have changed my life for the better. Life is so much more worthwhile when you have someone to share it with who's also your perfect other half. Let's see the world together. Last, but certainly not least, I freakin' love Pepperoni.

# Abstract

There is a lack of data from the Gulf of Carpentaria (GoC), northeastern Australia, about the timing and elevation of sea level fluctuations during and following the culmination of the Holocene marine transgression, and how the coastal environment responded. A localised sea level reconstruction is needed because of the inherent variability in relative sea level change, both globally and within northeastern Australia. The study area of Albatross Bay also has an extensive archaeological record: Aboriginal shell mounds are present across the region that have a history of formation dating back to the mid-Holocene. A high-resolution palaeoenvironmental reconstruction and, in particular, a record of Holocene sea level change, are missing components that currently limit understanding of human-environment interactions in the past in the region. The overarching aim of the research reported in this thesis is to produce a Holocene sea level curve for Albatross Bay, on the northeastern coast of the GoC, which will address these gaps in current knowledge and improve our understanding of Holocene sea level change.

The research reported in this thesis was conducted at three locations in Albatross Bay: Red Beach, Kwamter and Wathayn. At Red Beach, a sequence of thirteen beach ridges parallel to the shoreline contained a high-resolution record of sea level change and coastal progradation. At Kwamter and Wathayn, the presence of a single beach ridge at each location, formed during a period of higher relative sea level, along with extensive supratidal mudflats bordered with mangroves, provided ideal proxies for sea level reconstruction. All three field locations are also the focus of past and ongoing archaeological investigations.

To establish the sedimentary stratigraphy and quantify the depositional history of each location, pits were hand-excavated into each beach ridge crest, most swales, and across the supratidal mudflats. A soil auger and a D-section corer were used to extract additional sediment samples from beneath the pits, and from the mangrove zone at Wathayn. A trench was also excavated through the modern beach at Red Beach to aid in understanding the formation of the beach ridges and relict beach ridge plain. A total of 38 excavations were conducted: 24 at Red Beach, 8 at Kwamter and 6 at Wathayn. Sediment samples were collected from each stratigraphic section, and organic carbon content, carbonate content, and particle size parameters were analysed in the laboratory. Samples were also collected for absolute age determination using radiocarbon and Optically Stimulated Luminescence techniques.

Sandy beach and relict foredune sediments overlie intertidal or supratidal sediments in most of the beach ridges. At Red Beach, basal sediments of all but the three proximal ridges were cemented with carbonate, forming calcrete. Supratidal mudflat and intertidal mangrove deposits were uncovered at Kwamter and Wathayn. A transgressive shell lag was also discovered beneath the supratidal mudflat at Kwamter, formed during a period of higher relative sea level in the past.

A sediment facies scheme for the Albatross Bay coastal environments, developed from the field and laboratory data, was combined with the geochronological data to create a high-resolution record of Holocene coastal evolution and sea level change in Albatross Bay. At approximately 6,500 years BP, relative sea level was approximately -1.7 m below present mean sea level (PMSL). Mangroves were present at Kwamter, corresponding to the “big swamp” phase of extensive mangrove habitats reported by other researchers from across the northern coastline of Australia. Relative sea level was rising, and reached PMSL prior to approximately 5,000 years BP. Relative sea level continued to rise, reaching a mid-Holocene highstand of approximately +1 m above PMSL approximately 4,000 years ago, leading to the formation of the beach ridges at Kwamter and at Wathayn. The transgressive shell-lag was deposited at Kwamter during the same period. Relative sea level then either remained at this elevation for a further 1,000 years before falling, or began to fall very gradually after approximately 4,000 years ago. Once relative sea level began to fall, the beach ridges at Kwamter and Wathayn were isolated from active coastal processes. Infilling of the Embley River estuary led to the formation of a mangrove zone on the proximal side of the beach ridge at Kwamter. As relative sea level continued to fall, shoreline progradation resulted in the formation of the supratidal mudflat at Kwamter and Wathayn.

Relative sea level was between +0.5 to +1 m above PMSL approximately 2,200 years ago when beach ridge formation commenced at Red Beach, partially influenced by an increase in effective precipitation, and thus sediment supply into Albatross Bay, at this time. From 1,700 years ago to present, there was a change in the morphology, sedimentology and coastal progradation rates within the beach ridges at Red Beach, linked to a further increase in sediment supply into Albatross Bay, together with the re-commencement of tropical cyclone activity in the region. Relative sea level fell to approximately +0.7 m above PMSL around 500 years ago, and then to PMSL.

This sea level curve for Albatross Bay provides a new, high-resolution sea level record for the GoC, and for northern Australia. It adds to our understanding of the magnitude, patterns and drivers of local and regional coastal evolution and relative sea level change during the mid- to late-Holocene. It will also have immediate utility for ongoing archaeological research within Albatross Bay, and elsewhere in northern Australia.

# Table of Contents

<b>Declaration</b>	<b>i</b>
<b>Acknowledgements</b>	<b>ii</b>
<b>Abstract</b>	<b>v</b>
<b>List of Figures</b>	<b>xiii</b>
<b>List of Tables</b>	<b>xxiii</b>
<b>List of Abbreviations</b>	<b>xxv</b>
<b>Chapter 1 Introduction.....</b>	<b>1</b>
<b>1.1 Background .....</b>	<b>1</b>
<b>1.2 Thesis aims and objectives .....</b>	<b>4</b>
<b>1.3 Organisation of thesis .....</b>	<b>5</b>
<b>1.4 The Albatross Bay study area.....</b>	<b>6</b>
1.4.1 Climate and oceanography.....	7
1.4.2 Geological and geomorphological setting.....	11
<b>Chapter 2 Holocene Sea Level Change in Northeastern Australia: A Review .....</b>	<b>17</b>
<b>2.1 Late-Quaternary sea level change .....</b>	<b>17</b>
2.1.1 Global patterns of sea level change, LGM to present day .....	19
2.1.2 Sea level change in Australia since the LGM .....	25
<b>2.2 Sea level change in northern Australia .....</b>	<b>31</b>
<b>2.3 Sea level change in eastern Australia.....</b>	<b>39</b>
<b>2.4 Sea level change in the Gulf of Carpentaria.....</b>	<b>49</b>
<b>2.5 Summary .....</b>	<b>55</b>
<b>Chapter 3 Methods .....</b>	<b>57</b>
<b>3.1 Methods of sea level reconstruction .....</b>	<b>57</b>
3.1.1 Overview .....	57
3.1.2 Palaeo-shoreline indicators (beach ridges).....	58
3.1.3 Sedimentary stratigraphic sequences .....	60

<b>3.2 Field methods .....</b>	<b>63</b>
3.2.1 Selection of field locations.....	63
3.2.2 Surveying field features .....	67
3.2.3 Stratigraphic recording and sediment sample collection .....	70
3.2.3.1 Augering, coring and excavation .....	70
3.2.3.2 Field descriptions of sediment and stratigraphy .....	73
3.2.3.3 Sediment sampling.....	76
<b>3.3 Sediment analyses .....</b>	<b>76</b>
3.3.1 Drying and storage of sediment samples .....	76
3.3.2 Organic carbon and carbonate content.....	77
3.3.3 Particle size analysis .....	79
3.3.3.1 Mean grain size.....	80
3.3.3.2 Sediment sorting .....	80
3.3.3.3 Sediment skewness .....	81
3.3.3.4 Sediment Kurtosis.....	81
3.3.3.5 Method .....	81
<b>3.4 Geochronology .....</b>	<b>85</b>
3.4.1 Optically Stimulated Luminescence (OSL) .....	85
3.4.1.1 Field Sample collection.....	85
3.4.1.2 Laboratory sample processing procedures.....	86
3.4.1.3 Disc preparation .....	87
3.4.1.4 Sample analysis equipment.....	88
3.4.2 Radiocarbon Ages .....	88
3.4.2.1 Field sample collection .....	88
3.4.2.2 Laboratory sample processing .....	90
<b>Chapter 4 Coastal Sedimentary Environments of Albatross Bay .....</b>	<b>92</b>
<b>4.1 Red Beach.....</b>	<b>92</b>
4.1.1 Modern beach sediments.....	96
4.1.2 Beach ridge plain sediments .....	102
4.1.3 Intertidal mudflat sediments.....	110
<b>4.2 Kwamter .....</b>	<b>111</b>
4.2.1 Beach ridge and supratidal mudflat sediments.....	114
<b>4.3 Wathayn .....</b>	<b>116</b>
4.3.1 Beach ridge, supratidal mudflat and mangrove sediments.....	119

<b>4.4 Coastal sedimentary facies of Albatross Bay .....</b>	<b>121</b>
4.4.1 Facies A .....	124
4.4.2 Facies B.....	127
4.4.3 Facies C.....	134
4.4.4 Facies D .....	138
<b>4.5 Summary .....</b>	<b>139</b>
 <b>Chapter 5 A Chronology of Coastal Evolution and Sea Level Change at Albatross Bay ..</b>	<b>143</b>
 <b>5.1 Optically-stimulated luminescence (OSL) dating .....</b>	<b>143</b>
5.1.1 Principles of OSL dating.....	143
5.1.2 OSL dating of coastal sediments.....	147
5.1.2.1 Foreshore Environments .....	148
5.1.2.2 Coastal aeolian environments .....	149
5.1.2.3 Supratidal mudflat environments .....	151
5.1.2.4 Summary .....	152
5.1.3 Determining the equivalent dose ( $D_e$ ).....	153
5.1.3.1 Determining preheat temperatures .....	153
5.1.3.2 Determining dose recovery potential .....	155
5.1.3.3 Single-aliquot analysis .....	156
5.1.3.4 Single-grain analysis.....	158
5.1.3.5 Rejection criteria for single-aliquot and single-grain analysis.....	160
5.1.3.6 Calculating the $D_e$ .....	160
5.1.4 Assessing bleaching conditions at Albatross Bay.....	161
5.1.4.1 Buried environments.....	161
5.1.4.2 Modern analogue environments.....	163
5.1.5 Measuring the environmental dose rate at Albatross Bay.....	166
5.1.5.1 High-resolution gamma spectrometry (HRGS) .....	166
5.1.5.2 In-field gamma spectroscopy .....	166
5.1.5.3 Beta counting .....	167
5.1.5.4 Internal alpha dose and cosmic ray contribution .....	167
5.1.5.5 Moisture content .....	167
5.1.5.6 Dose rate calculations .....	168
5.1.6 Age determination.....	174
5.1.6.1 Single-aliquot results .....	174
5.1.6.2 Single grain results.....	179

5.1.6.3 Summary: OSL age determinations on coastal sedimentary deposits at Albatross Bay .....	184
<b>5.2 Radiocarbon dating .....</b>	<b>191</b>
5.2.1 Principles of radiocarbon dating .....	191
5.2.2 Results.....	193
<b>5.3 Summary .....</b>	<b>195</b>
<b>Chapter 6 Coastal Evolution and Sea level Change at Albatross Bay .....</b>	<b>197</b>
<b>6.1 The record from Red Beach.....</b>	<b>197</b>
6.1.1 Topography and sediment stratigraphy .....	197
6.1.2 OSL and radiocarbon chronology .....	204
6.1.3 Initiation of beach ridge plain formation .....	207
6.1.3.1 Changes in storminess.....	208
6.1.3.2 Changes in relative sea level.....	208
6.1.3.3 Changes in sediment supply.....	208
6.1.4 Changes in the tempo of beach ridge plain progradation.....	211
6.1.4.1 Change in relative sea level .....	211
6.1.4.2 Change in sediment supply .....	211
6.1.4.3 Change in storminess .....	212
6.1.5 Sea level history and shoreline evolution at Red Beach .....	214
<b>6.2 The record from Kwamter.....</b>	<b>216</b>
6.2.1 Topography and sediment stratigraphy .....	216
6.2.2 OSL and radiocarbon chronology .....	222
6.2.3 Sea level history and shoreline evolution at Kwamter .....	222
<b>6.3 The record from Wathayn .....</b>	<b>226</b>
6.3.1 Topography and sediment stratigraphy .....	226
6.3.2 OSL and radiocarbon chronology .....	230
6.3.3 Sea level history and shoreline evolution at Wathayn .....	230
<b>6.4 Constructing a Holocene sea level curve for Albatross Bay .....</b>	<b>231</b>
6.4.1 Directional sea level index points .....	232
6.4.2 Fixed sea level index points.....	233
6.4.2.1 Indicative meaning for mangrove deposit at Kwamter .....	234
6.4.2.2 Indicative meaning for beach ridge unconformity at Red Beach.....	235
6.4.2.3 Indicative meaning for relict supratidal mudflat at Kwamter .....	236
6.4.3 The sea level curve.....	238



6.4.4 Limitations of this study .....	241
<b>6.5 Synthesis: a record of Holocene sea level change in Albatross Bay .....</b>	<b>244</b>
<b>Chapter 7 Summary and Conclusions .....</b>	<b>248</b>
<b>7.1 Research objectives and outcomes .....</b>	<b>249</b>
7.1.1 Objective One: Geomorphological and sedimentological evidence of Holocene sea level change in Albatross Bay .....	251
7.1.2 Objective Two: Establishing a chronology of mid- to late-Holocene sea level change .....	251
7.1.3 Objective Three: A high-resolution record of Holocene sea level change in Albatross Bay .....	252
7.1.4 Objective Four: A Holocene sea level curve for Albatross Bay .....	253
7.1.5 Objective Five: The significance of the Albatross Bay sea level curve .....	253
<b>7.2 Suggestions for future research .....</b>	<b>254</b>
7.2.1 The geomorphological and sedimentological record .....	255
7.2.2 The chronological record .....	255
7.2.3 Additional sea level proxies .....	257
7.2.4 A record of tidal changes within the GoC over the mid to late Holocene .....	258
7.2.5 A record of late-Holocene tropical cyclone activity at Red Beach .....	258
<b>References .....</b>	<b>259</b>
<b>Appendix A: Sediment Laboratory Data .....</b>	<b>286</b>
<b>Appendix B: Sedimentary Logs .....</b>	<b>296</b>
<b>Appendix C: OSL Preheat Test Results .....</b>	<b>334</b>
<b>Appendix D: OSL Dose Recovery Results .....</b>	<b>336</b>

# List of Figures

## Chapter 1

Figure 1.1: Map of Australia and surrounding areas showing the locations of Albatross Bay and other places mentioned in the text. (Source: GoogleEarth, accessed 3 <sup>rd</sup> March 2016).....	2
Figure 1.2: Map of Albatross Bay showing the main geographical features and locations described in the text. The three study locations used for this research (Red Beach, Kwamter and Wathayn) are also indicated. (Source: GoogleEarth, accessed 6 <sup>th</sup> September 2017).....	7
Figure 1.3: Map of tropical cyclone tracks that passed within 50 km of Weipa from 1906-2006 (Source: Bureau of Meteorology (2016e)).....	9
Figure 1.4: Tidal datums for Albatross Bay (Source: data calculated from tidal data recorded by the Bureau of Meteorology (2016c) at Humbug Point, Weipa. See footnote 2).....	10
Figure 1.5: Perennial and nonperennial rivers and waterbodies around the Gulf of Carpentaria, with the locations of larger river catchments, as identified in the Department of the Environment (2007) report, indicated. (Source: modified from the State of the Environment Committee (2011), Figure 4.2).....	11
Figure 1.6: The major geomorphic regions in Weipa as defined by Smart (1977a). (Source: Cameron and Cogger (1992), Figure 3).....	12
Figure 1.7: (A) Bauxite mine face at Andoom in the Rio Tinto Aluminium mine. Note that as the bauxite deposit consists of pisoliths with little to no matrix, the mine wall collapses readily, resulting in an accumulation of loose pisoliths at the base of the mine face. (Source: Taylor <i>et al.</i> (2008b), Figure 1A). (B) Sample of pisoliths collected from Red Beach, Cape York, Australia. ....	13
Figure 1.8: Examples of the environments found within the Mapoon Plain in Albatross Bay – (A) beach ridge located behind the mangroves at Red Beach, (B) intertidal mudflat exposed at low tide at Red Beach, (C) mangroves located at Wathayn and (D) supratidal mudflat at Kwamter with desiccation cracks seen on the surface. ....	14
Figure 1.9: Geomorphology of the eastern coast of the Gulf of Carpentaria, with the southeastern coastline dominated by mudflats and chenier plains, in contrast to the northeastern coastline that is dominated by beach ridges. (Source: modified from Hopley (1985), Figure 124-1). ....	15

## Chapter 2

Figure 2.1: The Australasian region 20,000 years ago during the LGM, when lower sea levels connected Australia to Papua New Guinea and the major islands of the Indonesian Archipelago with Indochina (Source: modified from Reeves <i>et al.</i> (2013b), Figure 9). ...	20
Figure 2.2: Major variations in relative sea level change during the Holocene (Source: Bird (2008), Figure 3.6).....	21
Figure 2.3: Map of Australia and surrounding areas showing the locations of Quaternary sea level change and palaeo-environmental studies, along with other locations referred to in text. (Source: modified from GoogleEarth, accessed 3 <sup>rd</sup> March 2016).....	27
Figure 2.4: Australian continent and continental shelf (at elevations greater than -200 m) with the thick arrowed line showing the approximate tilt axis described in the text. The thin dashed line shows the inferred position of the mid-Miocene shorelines, demonstrating onshore marine Miocene records to the south and southwest, and offshore records to the north and northeast (Source: Sandiford (2007), Figure 3). ....	28
Figure 2.5: Map of Australia showing the three coastal regions reviewed in the text (A, B, C). (Source: modified from GoogleEarth, accessed 3 <sup>rd</sup> March 2016; approximate axis tilt line derived from Sandiford (2007)). ....	31
Figure 2.6: (A) Australia's climatic zones, based on a modified Köppen classification system and derived from climate data (1961-1990) on mean rainfall, mean maximum temperature and mean minimum temperature (Source: modified from the Bureau of Meteorology (2014)). (B) Australia's spring tide range based on data from the National Tidal Centre (Source: modified from Short and Woodroffe (2009), Figure 2.13).....	32
Figure 2.7: Distribution of mangroves around Australia (Source: Short and Woodroffe (2009), Figure 3.4).....	33
Figure 2.8: Map of key sea level study sites along the northern margin of Australia (Source: modified from GoogleEarth, accessed 3 <sup>rd</sup> March 2016). ....	34
Figure 2.9: Compilation of sea level index points from studies around the northern Australian margin across Region A. Sea level envelopes are also included for the Northern Territory (NT) and Western Australia (WA) (data from Figures 3 and 7 in Lewis <i>et al.</i> , 2013) and King Sound in WA (data from Figure 18 in Jennings, 1975). Note that the data from Engel <i>et al.</i> (2014) are referenced to mean high water (MHW) while all the other index points and sea level envelopes are referenced to mean sea level, Australian Height Datum (AHD). ....	38
Figure 2.10: Distribution of coral reefs around Australia (Source: Short and Woodroffe (2009), Figure 3.4).....	41

Figure 2.11: Map of key sea level study sites along the eastern margin of Australia that utilise sedimentary deposits and microfossils as sea level indicators (Source: modified from GoogleEarth, accessed 3 <sup>rd</sup> March 2016). .....	43
Figure 2.12: Map of key sea level study sites along the eastern margin of Australia that utilise corals and coral microatolls as sea level indicators. These study sites show no indication of a mid-Holocene sea level stillstand (Source: modified from GoogleEarth, accessed 3 <sup>rd</sup> March 2016).....	44
Figure 2.13: Map of key sea level study sites along the eastern margin of Australia that utilise corals and coral microatolls as sea level indicators. These study sites indicate that mid-Holocene sea level remained at a stillstand prior to falling to PMSL (Source: modified from GoogleEarth, accessed 3 <sup>rd</sup> March 2016).....	46
Figure 2.14: Compilation of sea level index points around the eastern Queensland coast (Region B). Sea level envelopes are drawn from data in Lewis <i>et al.</i> (2013) Figure 4, Larcombe <i>et al.</i> (1995) Figure 9, and Beaman <i>et al.</i> (1994) Figure 4.....	47
Figure 2.15: Map of key sea level study sites within the Gulf of Carpentaria (Source: modified from GoogleEarth, accessed 3 <sup>rd</sup> March 2016). .....	50
Figure 2.16: Compilation of sea level index points from the GoC (Region C). The chenier sea level envelope is drawn from data from Figure 6.3 in Rhodes (1980), while the beach ridge sea level envelope is drawn from data from Figure 6.6 in Rhodes (1980). Note that the elevation data on the y-axis does not refer to the Australian Height Datum, but rather an approximation of Indian Spring Low Water as defined by Rhodes (1980). Relative sea level fall is therefore measured by comparing the elevation of the highest sea level index point of each sea level proxy (either chenier or beach ridge) to that of the lowest sea level index point for the same proxy.....	54

### Chapter 3

Figure 3.1: The Weipa region with the location of study locations highlighted in yellow (Source: modified from GoogleEarth, accessed 17 <sup>th</sup> Jan 2016). .....	64
Figure 3.2: Leica Viva GNSS set-up to collect positional information in the field. Images illustrate the base station unit (left), the base station set-up (centre), and collecting position data with the rover (right).....	67
Figure 3.3: Map of the Albatross Bay study region showing the location of transects and D-section cores at Red Beach, Kwamter and Wathayn. In some locations, D-section cores were collected relatively close to each other, therefore some location points have been superimposed. (Source: GoogleEarth, accessed 17 <sup>th</sup> Jan 2016).....	69

Figure 3.4: Stratigraphic recording and sediment sample collection. (A) Pit excavation at Red Beach. (B) Sediment stratigraphy and sediment sample collection sites spaced 10 cm apart within a typical pit at Red Beach. OSL sample tubes can also be seen. (C) Recording and collecting sediment samples using an auger. (D) Recording in-field observations. ....	71
Figure 3.5: D-section coring. (A) Collecting D-section core from the base of a pit on the intertidal mudflat at Kwamter (B) describing a D-section core from within the mangrove fringe at Wathayn, (C) close-up of D-section core collected from the base of a pit at Red Beach showing the transition from sandy beach ridge sediments to the intertidal muds below, (D) close-up of D-section core collected at within the mangrove fringe at Wathayn.....	71
Figure 3.6: Coarse fragments found within sediments at the Albatross Bay study locations. (A) Pisoliths, (B) Quartz granules, (C) Subrounded to subangular rock fragments, (D) Whole shell, (E) Shell fragments and shell hash. ....	75
Figure 3.7: D-section cores sampling strategy.....	77
Figure 3.8: (A) OSL tube inserted into pit wall. (B) Hammering OSL tube into pit wall. (C) OSL sample collected. The ends of each tube were protected by black plastic caps and duct tape.....	86
Figure 3.9: Samples sent for radiocarbon dating. (A) Arcidae ( <i>T. granosa</i> ) shell from Red Beach RS5 (sample RB09 103). (B) Ostreidae shell from Red Beach RR5 (sample RB10 113). (C) Bulk sediment samples (marked with red box) from Red Beach RR3 (sample RB06 166 and RB06 167). ....	89

## Chapter 4

Figure 4.1: Modern beach at Red Beach, showing sand and pisoliths mixed with shells, shell hash and organic detritus abutting an intertidal mudflat exposed at low tide. ....	93
Figure 4.2: (A) Satellite image of the Red Beach study location, showing the extent of vegetation cover. Clearing inland for bauxite mining can be clearly seen on the northwestern edge of the image (Source: GoogleEarth, accessed 27 <sup>th</sup> Dec 2017). (B) A digital elevation model of the Red Beach study location, showing detail of the topography of the beach ridge plain. A wetland separating the inland beach ridge set from the seaward beach ridge set can be seen in blue. The location of the topographic profile surveyed across the beach ridge plain is indicated by the line of red dots, each of which marks the location of excavated pits (Source of elevation data: LiDAR 0.25 m grid survey data flown in 2010 and provided by Riotinto Pty Ltd). ....	94
Figure 4.3: Topographic profile of Red Beach showing major land units and vegetation cover.....	94

Figure 4.4: Red Beach transect location looking east towards the shoreline. Pink flags mark the locations of each ridge crest and swale which are of low relief. Vegetation includes <i>Eucalyptus tetradonta</i> and <i>Pandanus</i> spp. with a tall grass understorey that had been recently burnt when this image was taken. ....	95
Figure 4.5: Vegetation map of the Red Beach study location (Source: Queensland Herbarium, <a href="https://environment.ehp.qld.gov.au/map-request/re-broad-veg-group/">https://environment.ehp.qld.gov.au/map-request/re-broad-veg-group/</a> , accessed 13 <sup>th</sup> Jan 2018). ....	96
Figure 4.6: Cross-section through the modern beach at Red Beach. (A) Composite image of sediments exposed in the trench (scale divisions each 10 cm). (B) Stratigraphic profile showing positions of logged sections (Figures 4.7-4.9).....	97
Figure 4.7: Sedimentary log of section RBMT DFO1 through the modern trench at Red Beach (see Section 4.4 for facies descriptions). ....	98
Figure 4.8: Sedimentary log of section RBMT DFO3 through the modern beach at Red Beach (see Section 4.4 for facies descriptions). ....	99
Figure 4.9: Sedimentary log of section RBMT DFO5 through the modern beach at Red Beach (see Section 4.4 for facies descriptions). ....	100
Figure 4.10: Comparison between shell fragments and shell hash. (A) Abundant shell fragments in a clast-supported sedimentary unit in a beach ridge at Red Beach. (B) Many shell hash in a sand-dominated sedimentary unit in a beach ridge at Red Beach. ....	101
Figure 4.11: Stratigraphic profile across the beach ridge plain at Red Beach (see Section 4.4 for facies descriptions). Detailed sedimentary logs of each pit can be found in Appendix B. ....	103
Figure 4.12: Broad swale between RR9 and RR10 at Red Beach. ....	104
Figure 4.13: D-section core collected from the base of RR3 showing the transition from the sandy beach ridge deposits on the left to the intertidal muds on the right. ....	104
Figure 4.14: (A) Articulated <i>T. granosa</i> shells collected from an anthropogenic shell mound at Wathayn. These shells are likely to have been discarded and buried relatively quickly after harvesting. (B) Disarticulated <i>T. granosa</i> shells collected from within a beach ridge at Red Beach. (C) Gastropods collected from within the shell deposits at Kwamter showing increasing signs of wear. ....	106
Figure 4.15: (A) Calcrete occurrence in coastal beach ridges. Hardpan calcrete forms near the water table and hardpan/tubular calcrete also forms within the beach ridges. Hardpan calcrete forms as an indurated sheet-like layer, while tubular calcrete formed from roots casts/tubules. More layers of calcrete often form in older beach ridges that are located further inland (Chen <i>et al.</i> , 2002). Image modified from Figure 7.2.20 in Chen <i>et al.</i> (2002). (B) Section through RR12. This beach ridge has two separate layers of hardpan calcrete, with the upper layer forming above the lower calcrete deposit in a “... perched moisture zone...” (Chen <i>et al.</i> , 2002, p. 127). (C) Section through RR8. This beach ridge	

has a well-developed calcrete layer. (D) Section through RR8. While not as distinct as the calcrete layer in the inland ridges, this calcrete unit was too cemented for an OSL sample to be collected from. The OSL sample tube can be seen above the calcrete unit.	
(E) Section through RR4. The calcrete is patchy and cementation weak. ....	107
Figure 4.16: Sedimentary log for RR3 (see Section 4.4 for facies descriptions). ....	109
Figure 4.17: Sedimentary log for RR11 (see Section 4.4 for facies descriptions). ....	110
Figure 4.18: (A) Red Beach at low tide, showing the exposed mudflat seaward of the sandy foreshore. (B) An intertidal mud sample (photo taken from the D-section core collected from the base of a pit dug into the proximal flank of RR3 at Red Beach), showing shell fragments and shell hash in a sandy silt matrix. ....	111
Figure 4.19: (A) Satellite image of the Kwamter study location, showing extent of vegetation cover. Clearing associated with bauxite mining can be seen on the eastern edge of the image (Source: GoogleEarth, accessed 27 <sup>th</sup> Dec 2017). (B) A digital elevation model of the Kwamter study location, showing detail of the topography of the estuarine floodplain. The location of the topographic profile surveyed across the single beach ridge and onto the distal margin of the floodplain is indicated by the line of red dots, each of which marks the location of the excavated pits (source of elevation data: LiDAR 0.25 m grid survey data flown in 2010 and provided by Riotinto Pty Ltd). ....	112
Figure 4.20: Topographic profile of Kwamter showing major land units and vegetation cover. ....	113
Figure 4.21: Vegetation map of the Kwamter study location (Source: Queensland Herbarium, <a href="https://environment.ehp.qld.gov.au/map-request/re-broad-veg-group/">https://environment.ehp.qld.gov.au/map-request/re-broad-veg-group/</a> , accessed 13 <sup>th</sup> Jan 2018). ....	114
Figure 4.22: Stratigraphic profile across the beach ridge and estuarine floodplain at Kwamter (see Section 4.4 for facies descriptions). Detailed sedimentary logs of each pit can be found in Appendix B. ....	115
Figure 4.23: (A) Satellite image of the Wathayn study location showing extent of vegetation cover (Source: modified from GoogleEarth, accessed 27 <sup>th</sup> Dec 2017). (B) A digital elevation model of the Wathayn study location, showing detail of the topography of the hillslope, beach ridge and supratidal mudflat. The location of the topographic profile surveyed across the single beach ridge and onto the distal margin of the floodplain is indicated by the line of red dots, each of which marks the location of the excavated pit. (Source: the elevation data is derived from a LiDAR 0.25 m grid survey data flown in 2010 and provided by Riotinto Pty Ltd). ....	117
Figure 4.24: Topographic profile of Wathayn showing major land units and vegetation cover. ....	118
Figure 4.25: Vegetation map of the Wathayn study location (Source: Queensland Herbarium, <a href="https://environment.ehp.qld.gov.au/map-request/re-broad-veg-group/">https://environment.ehp.qld.gov.au/map-request/re-broad-veg-group/</a> , accessed 13 <sup>th</sup> Jan 2018). ....	119

Figure 4.26: Stratigraphic profile across the beach ridge and supratidal mudflat at Wathayn (see Section 4.4 for facies descriptions). Detailed sedimentary logs of each pit can be found in Appendix B. ....	120
Figure 4.27: Alternating units of Facies A (pisoliths-dominated) and Facies B (sand-dominated) at the (A) modern beach at Red Beach and (B) relict beach ridge RR2 at Red Beach. ....	124
Figure 4.28: (A) Sub-facies A1, from the top of the pit at ridge 2, Red Beach, showing the abundant pisoliths, common whole shell, and abundant shell fragments and shell hash present in this unit. (B) Sub-facies A2, from the middle of the pit at ridge 7, Red Beach, showing the abundant pisoliths, few whole shells and abundant shell fragments and shell hash present in this unit. ....	125
Figure 4.29: Particle size distribution of sample RB01_10cm from Red Beach, classified as sub-facies A1, showing how the distribution is very fine skewed, most likely due to the predominance of pisoliths in the sample. ....	127
Figure 4.30: Sample of calcrete collected from the base of ridge 8 at Red Beach. It consists of sand, pisoliths, shell fragments and shell hash cemented together by calcium carbonate. ....	128
Figure 4.31: (A) Sub-facies B1, from the top of the pit at ridge 10, Red Beach, showing few pisoliths in a sandy matrix. (B) Sub-facies B2, from the middle of the pit at ridge 9, Red Beach, showing many pisoliths in a sandy matrix. (C) Sub-facies B3, from the middle of the pit at the flank of ridge 3, Red Beach, showing many pisoliths, many shell fragments and shell hash, along with very few to few whole shells in a sandy matrix. (D) Sub-facies B4, from the top of the pit at ridge 3, Red Beach, showing many pisoliths, common to many whole shells and many shell fragments and shell hash in a sandy matrix. (E) Sub-facies B5, from the middle of the pit within the ridge crest at Kwamter, showing very few to few quartz granules in a sandy matrix. (F) Sub-facies B6, from the base of the pit within the ridge flank at Wathayn, showing common to many sub-rounded to sub-angular gravel clasts in a silty sand matrix. ....	129
Figure 4.32: Modern foredune at Red Beach showing a sand unit at the surface with pisoliths present. ....	130
Figure 4.33: Particle size distribution of sample WHA02_70cm from Wathayn showing the trimodal distribution of sub-facies B6. ....	134
Figure 4.34: (A) Sub-facies C1, from the D-section core collected within the mangroves at Wathayn, showing significant organic matter (roots and leaves) in a sandy silt matrix. (B) Sub-facies C2, from the D-section core collected from the base of a pit dug into the proximal flank of ridge 3 at Red Beach, showing few shell fragments and shell hash in a sandy silt matrix. (C) Sub-facies C3, from the middle of a pit within the supratidal mudflat at Kwamter, showing the shell layer comprising very abundant whole and fragmented shell in a silty sand matrix. (D) Sub-facies C4, from the top of a pit within the supratidal	



mudflat at Wathayn, showing very few quartz granules in a sandy silt matrix. (E) Sub-facies C5, from the base of pit within the supratidal mudflat at Wathayn, showing few sub-rounded to sub-angular gravel clasts in a sandy silt matrix. ....	135
Figure 4.35: (A) Sub-facies D1, from the top of a pit dug into the swale between ridge 8 and ridge 9 (RS9) at Red Beach, showing few pisoliths in a sandy silt matrix. (B) Sub-facies D2, from the middle of a pit dug into the swale between ridge 8 and ridge 9 (RS9) at Red Beach, showing many pisoliths in a sandy silt matrix. ....	138
Figure 4.36: Simplified sedimentary facies model for (A) Red Beach and (B) Wathayn and Kwamter showing the stratigraphic relationships between the facies and where they are located within the modern environment .....	141

## Chapter 5

Figure 5.1: Preheat plot (with associated measurement errors) for R9, WHA01_1 and KW07. The blue box identifies the chosen preheat temperatures for each sample. ....	155
Figure 5.2: Dose recovery results on 8 aliquots of samples R9, WHA01_01 and KW07. The mean $D_e$ value (in Gy) and associated error (blue shading) are plotted as a dotted line. ....	156
Figure 5.3: OSL bleaching tests conducted at Macquarie University (A) set-up of bleaching tests where samples are exposed to direct sunlight. (B) close-up of disc holder containing samples being bleached.....	162
Figure 5.4: Bleaching test data for beach ridge crest (R8) and swale (Rswale) samples from Red Beach. ....	163
Figure 5.5: Total SA dose rate (Gy/ka) plotted for all Red Beach samples arranged according to distance from the modern shore. ....	174
Figure 5.6: Decay curves (A) (C) (E) and dose response curves (B) (D) (F) from an OSL single-aliquot disc for a sample from Red Beach (RB01), Kwamter (KW06) and Wathayn (WHA01_1). ....	176
Figure 5.7: Decay curves (A) (C) (E) and dose response curves (B) (D) (F) for an OSL single-grain with a bright luminescence signal from samples RB02, KW06 and WHA01_1. ....	181
Figure 5.8: Graphical comparison of single-aliquot (SA) and single-grain (SG) ages from Red Beach and Kwamter. Ages are in years before sample collection. ....	185
Figure 5.9: $D_e$ values displayed in radial plots for samples from Red Beach (RB02, RB01, RB17, RB08, RB10 and RB12). ....	186
Figure 5.10: $D_e$ values displayed in radial plots for samples from Red Beach (RB03, RB21, RB25, RB18, RB20, RB19). ....	187

Figure 5.11: $D_e$ values displayed in radial plots for sample RB27 from Red Beach, samples KW05, KW06 and KW07 from Kwamter and samples WHA01_1 and WHA01_2 from Wathayn. ....	188
---	-----

## Chapter 6

Figure 6.1: Sedimentary log for RR2, a type 1 beach ridge with alternating units of facies A and facies B. ....	199
Figure 6.2: Sedimentary log for RR11, a type 2 beach ridge composed entirely of facies B deposits .....	200
Figure 6.3: Chrono-stratigraphic profile across the beach ridge plain at Red Beach. Type 1 and Type 2 beach ridges are indicated (see text). Detailed sedimentary logs of each pit can be found in Appendix B.....	201
Figure 6.4: Coastal progradation over the mid to late Holocene at Red Beach based on the data contained in Table 6.1.....	203
Figure 6.5: OSL and radiocarbon ages from the beach ridge plain at Red Beach plotted against the distance from the shoreline. Standard errors are indicated with vertical black bars. Radiocarbon ages from RR3 (RB06 166 and RB06 167) were excluded as these samples were collected from the intertidal sediments below the beach ridge plain and would not be comparable with the beach ridge OSL burial ages. Radiocarbon ages have been calibrated using OxCal v4.2.4, IntCal13 and Marine 13, using a $\Delta R$ of $-103 \pm -16$ (see Section 3.4.2.2). ....	205
Figure 6.6: Chrono-stratigraphic profile across the beach ridge at Kwamter. Detailed sedimentary logs of each pit can be found in Appendix B.....	217
Figure 6.7: Sedimentary log for KMF2, representative of the sedimentary deposits found within the supratidal mudflat at Kwamter.....	218
Figure 6.8: Sedimentary log for KMF3. The transgressive shell lag unit (facies C3) is laterally discontinuous across the pit face.....	219
Figure 6.9: Sedimentary log for KR1, the Kwamter beach ridge. ....	221
Figure 6.10: Chrono-stratigraphic profile across the beach ridge at Wathayn. Detailed sedimentary logs of each pit can be found in Appendix B.....	227
Figure 6.11: Sedimentary log for WMF2, located in the centre of the supratidal mudflat at Wathayn. The profile here contains the entire record of formation of the supratidal mudflat. ....	228
Figure 6.12: Sedimentary log for WR1, excavated into the crest of the beach ridge at the Wathayn study location. ....	229
Figure 6.13: Example of how the directional sea level index points are illustrated on the sea level curve.....	233

Figure 6.14: The calculation of the indicative meaning and range of the mangrove deposit at Kwamter.....	234
Figure 6.15: Example of how the fixed sea level index points (mangrove deposits and the unconformity between the beach ridge and intertidal mudflat) are illustrated on the sea level curve.....	235
Figure 6.16: The calculation of the indicative meaning and range of the beach ridge unconformity at Red Beach. ....	236
Figure 6.17: The calculation of the indicative meaning and range of the relict supratidal mudflat at Kwamter.....	237
Figure 6.18: Example of how the sea level envelope for the relict supratidal mudflat is illustrated on the sea level curve.....	238
Figure 6.19: Holocene sea level index points (SLIPS) from Albatross Bay.....	239
Figure 6.20: Comparison of Holocene sea level data from Albatross Bay and SLIPs from previous studies around the eastern Queensland coast. Sea level envelopes compiled by various authors are also included, as indicated in the key. ....	240
Figure 6.21: Comparison of Holocene sea level data from Albatross Bay with SLIPs from previous studies from northern Australia. Sea level envelopes compiled by various authors are also included, as indicated in the key. Note that a few data points are referenced to MHW (to the right of the graph), while most of the SLIPs, including those from this study, are referenced to m AHD (to the left of the graph). For exact details on which SLIPs are referenced to MHW, see Figure 2.16.....	241

# List of Tables

## Chapter 3

Table 3.1: Summary of sediment stratigraphy excavations for the Albatross Bay study area.....	72
Table 3.2: Statistical formulae used in GRADISTAT to calculate grain size parameters and the associated descriptive terminology for the grain size data ( $P_{\chi}$ is the grain diameter in metric units, at the cumulative percentile value of $\chi$ ) (Source: Blott <i>et al.</i> (2001), Table II). .....	85
Table 3.3: Radiocarbon dating strategy for shell and bulk sediment samples collected from Red Beach, Kwamter and Wathayn.....	89

## Chapter 4

Table 4.1: Summary of the sedimentary characteristics of facies identified from Red Beach, Wathayn and Kwamter. Values are means unless otherwise stated.....	123
---	-----

## Chapter 5

Table 5.1: SAR protocols used for Albatross Bay samples in this study.....	158
Table 5.2: Results from the SAR procedure on the modern analogue samples. ....	164
Table 5.3: Single-aliquot OSL ages for the modern analogue samples. ....	164
Table 5.4: Comparison of dose rates measured by HRGS and in-situ gamma spectroscopy from Red Beach. ....	169
Table 5.5: HRGS results for samples from Albatross Bay. Samples highlighted in red have a deficiency of that radionuclide within the decay chain while samples highlighted in blue have an excess of that radionuclide within the decay chain. Samples with no highlights have negligible variations within the decay chain and are therefore in secular equilibrium. ....	171
Table 5.6: Summary of total dose rates of samples from Albatross Bay. ....	173
Table 5.7: Summary of the OSL results from the SAR procedure on single-aliquot discs from Albatross Bay.....	175
Table 5.8: Single-aliquot OSL ages for samples from Red Beach and Kwamter with the associated dose rate and equivalent dose data. All samples were in the 90-125 $\mu\text{m}$ size range. Equivalent dose rates and ages were calculated using the CAM. Ages reported at a 1 $\sigma$ confidence interval.....	178

Table 5.9: Summary of OSL results from the SAR procedure on single-grain discs from Albatross Bay. ....	179
Table 5.10: Summary of single-grain rejections based on the detailed rejection criteria for samples from Albatross Bay. ....	180
Table 5.11: Single-grain OSL ages for samples from Red Beach, Kwamter and Wathayn with the associated dose rate and equivalent dose data. All samples were in the 180-212 $\mu\text{m}$ size range. Ages reported at a 1 $\sigma$ confidence interval. ....	183
Table 5.12: Comparison of single-aliquot (SA) and single-grain (SG) burial ages. Ages reported at a 1 $\sigma$ confidence interval. ....	184
Table 5.13: Compiled OSL ages from Albatross Bay combining the single-aliquot and single-grain data selected for each sample. All single-aliquot (SA) samples were in the 90-125 $\mu\text{m}$ size range, all single-grain (SG) samples were in the 180-212 $\mu\text{m}$ size range. Ages reported at a 1 $\sigma$ confidence interval. ....	190
Table 5.14: Conventional radiocarbon age determinations, calibrated mean age $\pm 2 \sigma$ and corresponding age range for samples from Red Beach, Kwamter and Wathayn. ....	194

## Chapter 6

Table 6.1: Coastal progradation rates at Red Beach. Beach ridges are grouped together when the OSL ages overlap (see Section 6.1.2). ....	203
Table 6.2: Comparison of OSL burial ages from beach ridges at Red Beach (this study) and conventional radiocarbon ages from beach ridges at Botchet Beach (Hayne, 1992, in Stone, 1995, Figure 3.5). ....	206
Table 6.3: Sedimentation rates at Big Willum Swamp, on the Weipa Plateau. (Source: data modified from Stevenson <i>et al.</i> , 2015, Table 2). ....	209

## Chapter 7

Table 7.1: Summary of research objectives, key outcomes and associated chapters. ....	250
---	-----

# List of Abbreviations

## Places

GBR	Great Barrier Reef
GoC	Gulf of Carpentaria
KW	Kwamter
NSW	New South Wales
NT	Northern Territory
RB	Red Beach
WHA	Wathayn
WA	Western Australia

## Organisations

BoM	Bureau of Meteorology
ERISS	Environmental Research Institute of the Supervising Scientist
IUGS	International Union of Geological Sciences
UNESCO	United Nations Educations, Scientific and Cultural Organisation

## Sea level terms

AHD	Australian Height Datum
FBI	Fixed Biological Indicators
HAT	Highest Astronomical Tide
LAT	Lowest Astronomical Tide
LGM	Last Glacial Maximum
MHW	Mean High Water
MHWN	Mean High Water Neaps
MHWS	Mean High Water Springs

MLW	Mean Low Water
MLWN	Mean Low Water Neap
MLWS	Mean Low Water Spring
MSL	Mean Sea Level
PMSL	Present Mean Sea Level

### **Chronology terms**

AMS	Accelerator Mass Spectrometry
BP	Before Present, where “present” is defined as AD 1950
Bq/kg	Becquerel/kilogram (a measure of radionuclide activity)
Gy	Grays (unit of absorbed dose)
HRGS	High resolution gamma spectrometry
IR	Infrared
ka	thousand years
OSL	Optically Stimulated Luminescence
SA	Single-aliquot
SAR	Single-aliquot regenerative-dose
SG	Single-grain
TL	Thermoluminescence

### **Equipment**

GPR	Ground Penetrating Radar
HPGe	High purity germanium detector

### **Chemical formulas and elements**

CaCO <sub>3</sub>	Calcium carbonate
CO <sub>2</sub>	Carbon dioxide

H <sub>2</sub> O <sub>2</sub>	Hydrogen peroxide
HCl	Hydrochloric acid
K	Potassium
NaOH	Sodium hydroxide
MgO	Magnesium oxide
Pb	Lead
Ra	Radium
Th	Thorium
U	Uranium

### **Measurements**

±	Plus and minus, an error margin
km	kilometre
m	metre
mm	millimetre
µm	microns
yr	year

### **Other terms**

DW	Dry Weight
E	East
ENSO	El Niño-Southern Oscillation
N	North
S	South



# Chapter 1

## Introduction

### 1.1 Background

The period of Earth history from the peak of the Last Glacial Maximum (LGM, 22-20 ka BP) to the present day was a time of dramatic changes in glacio-eustatic sea level, with global sea level rising from approximately 120-125 m below present mean sea level to present mean sea level (PMSL) due to the melting of extensive continental ice sheets (Fleming *et al.*, 1998; Lambeck *et al.*, 2000; Lambeck *et al.*, 2002; Cutler *et al.*, 2003; Murray-Wallace, 2007a). Attempts have been made to construct a post-LGM global eustatic sea level curve. During the early 1980s, it became apparent that such attempts were futile: sea level trends were not universal due to regional variability in tectonic, isostatic, climatic, tidal regime and oceanographic processes that influence sea level histories (Kidson, 1982; Walling and Jacovides, 1983; Pirazzoli, 1991b). The focus of sea level research shifted to local and regional sea level reconstructions that would, in turn, contribute to constructing a general picture of global sea level change. The research reported in this thesis is one such project: it documents coastal evolution over the mid- to late-Holocene around Albatross Bay, located within the Gulf of Carpentaria (GoC), northern Australia (Figure 1.1), and considers how such changes reflect relative sea level change over the same period.

Within Australia, there have been several attempts to accurately reconstruct and synthesise Holocene sea level histories, particularly along the northeastern coast of Australia (e.g. McLean *et al.*, 1978; Chappell *et al.*, 1983; Hopley, 1983, 1987; Larcombe *et al.*, 1995; Lewis *et al.*, 2008; Lewis *et al.*, 2013). Larcombe *et al.* (1995) produced a Holocene sea level curve for the central Great Barrier Reef (GBR), in northeastern Australia (Figure 1.1). This sea level curve was based on an extensive database of 364 radiocarbon dates from a wide variety of sea level indicators such as mangrove muds, fossil mangroves, shell beds, fixed biological indicators, coral and coral micro-atolls. The data indicated that relative sea level was approximately -35 m below present at 11,000 years BP and rising, reaching PMSL before 6,000 years BP. Sea level then continued to rise above PMSL, culminating in a mid-Holocene highstand of +1.7 m at approximately 5,500 years BP. Sea level remained at this level until approximately 3,500 years BP before falling to PMSL (Larcombe *et al.*, 1995). Larcombe *et*

*al.* (1995) were not able to pinpoint when sea level reached PMSL along the central GBR, nor the nature of the sea level fall to PMSL (i.e., smooth versus oscillating) due to the low precision of the sea level indicators available. Larcombe *et al.* (1995) compared their sea level curve with similar reconstructions from the Huon Peninsula in Papua New Guinea (Chappell and Polach, 1991) and New South Wales (NSW) in south-eastern Australia (Figure 1.1) (Thom and Roy, 1983). While all the datasets were consistent, the vertical spread of the sea level data was large, both within the sea level curve of Larcombe *et al.* (1995) and across the three sea level curves. This spread in data is a result of the wide variety of sea level indicators used, the varied depositional environments these sea level proxies were associated with, the large geographic regions the sea level curves encompassed and the errors associated with radiocarbon dating each sea level proxy (see Section 2.1.1).

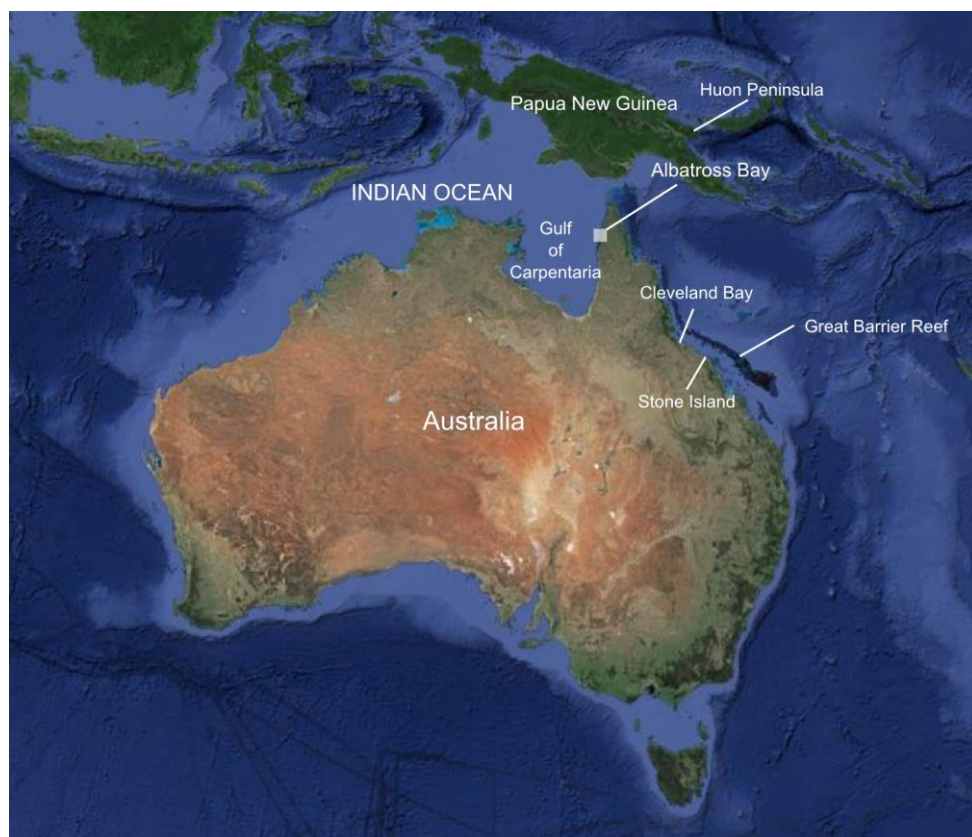


**Figure 1.1:** Map of Australia and surrounding areas showing the locations of Albatross Bay and other places mentioned in the text. (Source: GoogleEarth, accessed 3<sup>rd</sup> March 2016).

Research into Holocene sea level histories along the northeastern coast of Australia have also shown significant local and regional variability. There are differences in the timing of attainment of PMSL following the post-LGM sea level rise, whether (and when) sea level

continued to rise above PMSL to reach a mid-Holocene highstand, the elevation of sea level during the mid-Holocene highstand, the geographical extent of such a highstand, whether sea level remained at this highstand for a period of time before falling to PMSL, and whether this sea level fall was smooth or oscillating (Chappell *et al.*, 1982; Nakada and Lambeck, 1989; Lambeck and Nakada, 1990; Lambeck *et al.*, 2010; Lewis *et al.*, 2013). For example, the mid-Holocene highstand was recorded to be +3.3 m above PMSL at Cleveland Bay, GBR (Woodroffe, 2009b), but only around +0.5 m above PMSL across several island sites within the inner zone of the northern GBR (Chappell *et al.*, 1983; Grindrod and Rhodes, 1984) (Figure 1.1). The time at which the mid-Holocene highstand maximum first occurred was estimated to be 6,800 years BP at Stone Island in the GBR (Chappell *et al.*, 1983) and 3,600 years BP at Cleveland Bay (Woodroffe, 2009b). There are also differences reported in the time at which sea level first reached PMSL, before rising to a mid-Holocene highstand (Nakada and Lambeck, 1989), with some studies failing to find evidence for a Holocene highstand at all (Thom *et al.*, 1975; Woodroffe *et al.*, 1986; Chappell, 1993; Wolanski and Chappell, 1996). Some sea level studies support the Fairbridge (1961) model of Holocene sea level oscillations (Larcombe *et al.*, 1995; Lewis *et al.*, 2008) or suggest the matter is unresolved (Lewis *et al.*, 2015), while most other studies indicate that sea level fall was smooth (Chappell, 1983; Horton *et al.*, 2007a).

These studies have provided local and regional sea level histories, furthering the knowledge of the use of sea level proxies and how relative sea level has changed in northeastern Australia during the Holocene. They also highlight how much regional variability exists when reconstructing sea level change, and the need for more local records to refine the sea level history of northeastern Australia. The research described in this thesis provides an additional local sea level history and adds to the growing understanding of the sea level history of Australia by providing a high-resolution record of Holocene sea level change from estuarine and coastal environments in Albatross Bay, GoC.

Within the GoC, sea level has changed dramatically over the Quaternary. At the LGM, relative sea level was -120 m to -125 m below PMSL and the Gulf was reduced to a large fresh-to-brackish waterbody called “Lake Carpentaria”. Approximately 12,000 years BP, sea level rose enough to breach the Arafura Sill that separated the GoC from the Indian Ocean to the west (Figure 1.1) (McCulloch *et al.*, 1989; Nott, 1996; Chivas *et al.*, 2001). The GoC became fully marine by approximately 10,500 years BP (McCulloch *et al.*, 1989; Reeves *et al.*, 2008). Studies indicate that sea level within the GoC reached PMSL in the early to mid-Holocene and

continued to rise above PMSL, reaching different highstand elevations for different lengths of time at different locations within the GoC over the mid-Holocene before falling smoothly to PMSL (Rhodes, 1980; Chappell *et al.*, 1982; Lambeck and Nakada, 1990). However, there are still few published studies of sea level change within the GoC, and knowledge about Holocene sea level change within the GoC is limited (see Section 2.4 for a more extensive review of sea level studies from the GoC).

Albatross Bay is of interest to archaeologists due to the presence of more than 500 Aboriginal shell mounds in the area that designates it a region of high cultural importance, placed on the Register of the National Estate of the Australian Heritage Commission since 1980 (Bailey *et al.*, 1994; Morrison, 2003, 2010). While there has been almost 50 years of archaeological research in this region, there is still a limited understanding of these shell mounds and the insights they provide about how humans have interacted with this landscape in the past (Morrison, 2010). Archaeologists have stated that a comprehensive environmental reconstruction of the region is a vital component for furthering such understanding (Morrison, 2010, 2013; Shiner *et al.*, 2013). To this end, a reconstruction of sea level change and its influence on coastal landscape evolution around Albatross Bay will not only contribute a new sea level record where data is currently lacking but will also address a pressing need in current archaeological research within the region.

## **1.2 Thesis aims and objectives**

The overarching aim of this thesis is to produce a Holocene sea level curve for Albatross Bay, which will contribute a new sea level record within Australia that will not only fill a gap in current knowledge, but will also have immediate applications to ongoing archaeological research.

This aim is addressed through the following objectives:

1. Investigate the coastal environment around Albatross Bay in far north Queensland, Australia, and document the geomorphological and sedimentological evidence for Holocene sea level change (sea level proxies) that is present in the area;
2. Establish a chronology for the response of the coastal environment to Holocene sea level change;
3. Combine the geomorphological, sedimentological and chronological evidence to create a high-resolution record of Holocene sea level change in Albatross Bay;

4. Convert this record of Holocene sea level change in Albatross Bay into sea level index points to construct a Holocene sea level curve;
5. Place this new sea level curve within the context of existing knowledge of Holocene sea level change in northeastern Australia.

### **1.3 Organisation of thesis**

This thesis comprises seven chapters. In the first chapter, I introduce the subject of sea level change and need for local and regional sea level reconstructions due to the variability in tectonic, climatic, tidal regime and oceanographic processes that influence sea level histories. Gaps in our knowledge of sea level change across northeastern Australia and within the GoC are highlighted, with the lack of a local sea level record limiting current archaeological research in Albatross Bay. The aims of the thesis are then presented. The chapter ends with a description of the Albatross Bay study area.

Chapter 2 reviews relevant published literature on coastal evolution and sea level change. It begins by summarising the causes and global patterns of late Quaternary sea level change. The regional and local variability of sea level change is highlighted and the reasons for this variability are discussed. A broad overview of sea level change around Australia is provided, examining why Australia is an ideal location to study glacio-eustatic and hydro-isostatic sea level change. The remainder of the chapter reviews existing knowledge on sea level change across three regions relevant to my study location of Albatross Bay – (1) northern Australia, (2) eastern Australia, and (3) the GoC. The lack of sea level data within the GoC is highlighted, emphasising the significance of my study.

Chapter 3 outlines the methods used in this study, beginning with an overview of methods of sea level reconstruction, focussing on the sea level proxies chosen for this study – palaeoshoreline indicators (beach ridges) and sedimentary stratigraphic sequences. Field methods are described, including the choice of study site, the surveying and recording of field features, and the collection of sediment samples for laboratory analysis. The second part of the chapter focusses on the methods chosen for sediment sample analysis and for geochronology, describing how samples were prepared and analysed in the lab.

Chapter 4 presents the results of the sedimentary stratigraphic analysis of the three field locations. Field descriptions are combined with the results of laboratory sediment analyses to develop a sedimentary facies scheme for Albatross Bay. The facies scheme links the sediments

to their environment of deposition which subsequently allows evaluation of how the coastal environment of Albatross Bay changed in response to environmental change.

The results of the geochronology analysis are presented in Chapter 5. The principles of each chosen technique – Optically Stimulated Luminescence (OSL) dating and radiocarbon dating - are explained, together with their limitations. Chronologies for sediment deposition at the three study locations around Albatross Bay are presented.

In Chapter 6, the facies scheme from Chapter 4 is combined with the chronology developed in Chapter 5 to present a narrative of mid- to late-Holocene sea level and environmental change and the accompanying response of the coastal environment at each study location. The sea level records for the three field locations are then combined to construct a mid- to late-Holocene sea level curve for Albatross Bay, which is then compared with records from previous research across northern Australia.

In Chapter 7, I synthesise the findings of my research, discuss their significance in the context of Australian sea level change research, and conclude with recommendations for future research.

#### **1.4 The Albatross Bay study area**

Albatross Bay (12.41°S, 141.41°E) is a large coastal embayment located on the northeastern coast of the Gulf of Carpentaria (GoC), approximately 250 km south-west of the northern tip of Cape York (Figure 1.2). Four rivers drain into the embayment – the Pine, Mission, Embley and Hey Rivers – depositing predominantly sandy to muddy sediments into Albatross Bay (Jones, 1987). This investigation focuses on the Andoom Peninsula, between the Pine and Mission Rivers, and the Weipa Peninsula, between the Mission and Embley Rivers, with both areas having been the focus of past and current archaeological studies that identify sea level reconstruction as crucial to furthering understanding of past human-environment interactions in the area (Bailey, 1991; Bailey *et al.*, 1994; Morrison, 2003, 2010, 2013; Shiner *et al.*, 2013; Morrison, 2014). The Weipa and Andoom Peninsulas also contain palaeo-sea level indicators suitable for such a reconstruction.

The Weipa Peninsula rises gently in elevation from west to east, from sea level to approximately 80 m above PMSL (Specht *et al.*, 1977; Taylor and Eggleton, 2004; Barkley *et al.*, 2008), while the Andoom Peninsula rises gently northwards from sea level to



approximately 60 m above PMSL (Geoscience Australia, 2017). Both peninsulas are relatively broad, flat surfaces with little local variation in relief (Laffan, 2001), most likely due to structural control of the underlying bauxite bedrock.

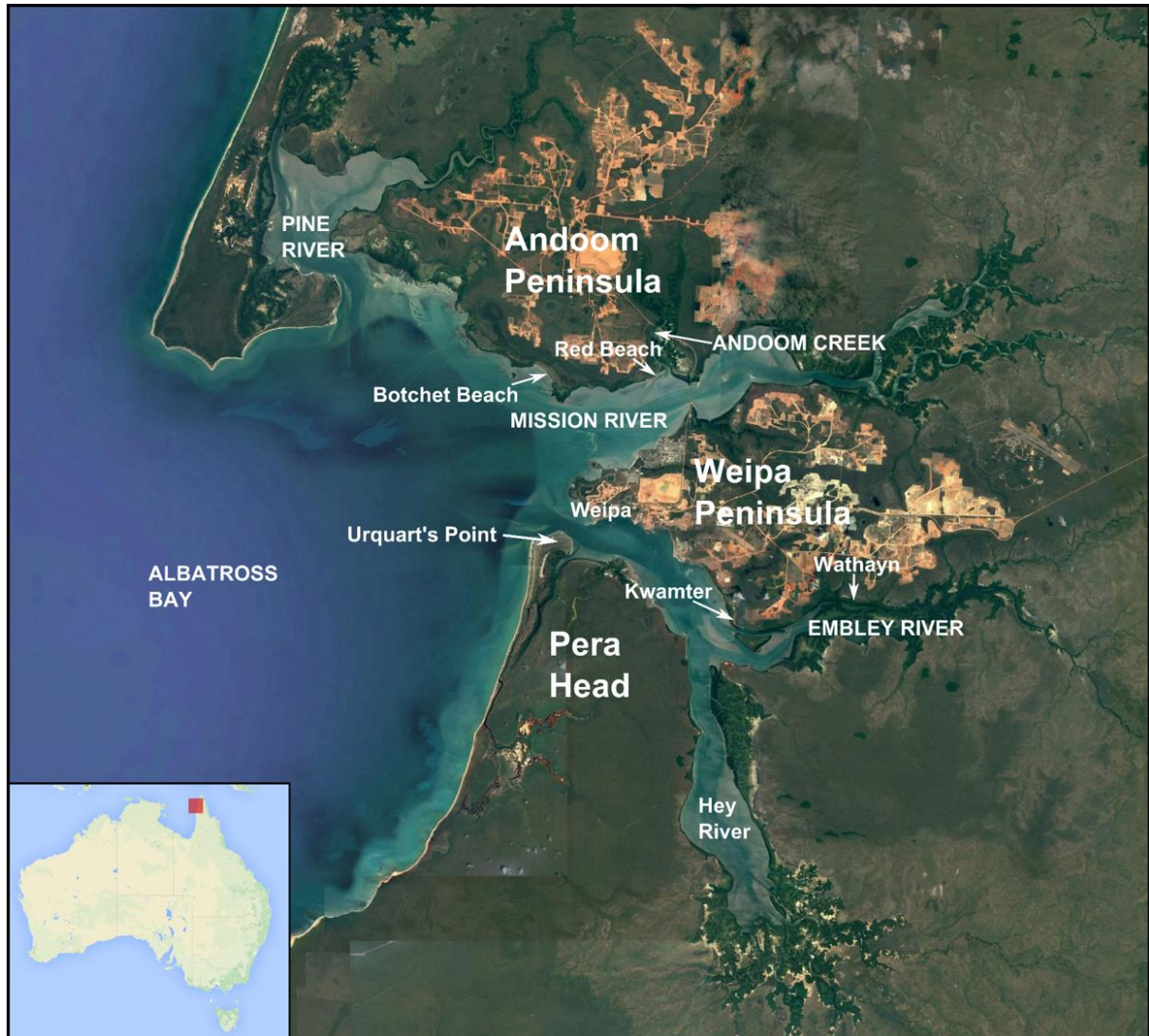


**Figure 1.2: Map of Albatross Bay showing the main geographical features and locations described in the text. The three study locations used for this research (Red Beach, Kwamter and Wathayn) are also indicated. (Source: GoogleEarth, accessed 6<sup>th</sup> September 2017).**

#### 1.4.1 Climate and oceanography

Albatross Bay experiences a tropical monsoonal climate, with distinct wet and dry seasons that are most pronounced from December to March and May to September respectively (Bureau of Meteorology, 2016a). Average annual rainfall is 1785 mm, with more than 95% of this rainfall occurring between November and April, and the heaviest rains, totalling

approximately 1250 mm, occurring between January and March (see Bureau of Meteorology, 2016b, for climate statistics). On the other hand, an average of only 14.5 mm of rain falls between June and September (Bureau of Meteorology, 2016b). This high seasonal variability in rainfall, along with high evaporation throughout the year, leads to large seasonal fluctuations in the water table, with near total saturation of the regolith profile during the wet season, and a water table up to 10 m below the ground surface, contributing to a marked moisture deficit, during the dry season (Lees *et al.*, 1993; Laffan, 2001). During the wet season, winds are light to moderate and from the northwest, while light to moderate southeast trade winds persist during the dry season (Lees *et al.*, 1993; Bureau of Meteorology, 2016a). Daily maximum temperatures are relatively uniform throughout the year, ranging from 31°C in July to 35°C in November (Bureau of Meteorology, 2016a).

Albatross Bay lies within Australia's cyclone belt, and cyclones regularly affect the area between December and April (Bureau of Meteorology, 2016a). In the hundred years from 1906 to 2006, the Australian Government Bureau of Meteorology recorded 15 cyclones that crossed the coast within 50 km of the town of Weipa (Figure 1.3), 26 that crossed within 100 km, 52 cyclones that crossed within 200 km, and 109 that crossed within 400km (Bureau of Meteorology, 2016e). Since the radius of cyclone-generated gale force winds recorded in Australia ranges from 70 km (Cyclone Rosita in 2000) to 350-400 km (Cyclone Orson in 1989) (Bureau of Meteorology, 2016d), the impacts of these cyclones on Weipa can be significant. On 23rd January 2013, Tropical Cyclone Oswald passed approximately 145 km to the south of Weipa, which experienced its highest daily rainfall on record (353.2 mm) (Bureau of Meteorology, 2016b). The previous major cyclone to pass directly over Weipa was Tropical Cyclone Mark, on the 10th of January 1992. This cyclone had maximum sustained wind speeds of 28 m/s which caused widespread minor damage across the town of Weipa, with falling trees damaging houses and powerlines and wave action resulting in approximately AUD\$3.5 million worth of damage at the Weipa Port (Bureau of Meteorology, 2016f).

No major ocean currents are present within the Gulf of Carpentaria and Albatross Bay, but tidal currents are an important factor to the movement of water and transport of sediments within Albatross Bay (Department of the Environment, 2007). Albatross Bay is micro-tidal, with tides that vary from semi-diurnal to diurnal. Mean spring and neap tidal ranges are 1.7 m



and 0.2 m respectively<sup>1</sup>, with the highest spring tidal range being approximately 2.4 m and the lowest neap tide range being less than 0.05 m (Bureau of Meteorology, 2016c). The high degree of variability in tidal levels within Albatross Bay mean that hydrodynamic processes and, consequently, coastal sediment deposition act over a wide range, moving further inland during spring tides compared to neap tides.

Figure 1.4 shows the elevation in meters above or below the Australian Height Datum (m AHD) of common tidal datums around Albatross Bay<sup>2</sup>. Australian Height Datum (AHD) is the official national vertical datum for Australia that was established by Geoscience Australia, and adopted by the National Mapping Council of Australia, in 1971 (Geoscience Australia, 2015b). Mean sea level was assigned a value of 0.000 m on the AHD across 30 tide gauges around the Australian coast, including at Weipa (Geoscience Australia, 2015b). Therefore, in this study, mean sea level (MSL) is assumed to be 0 m AHD.

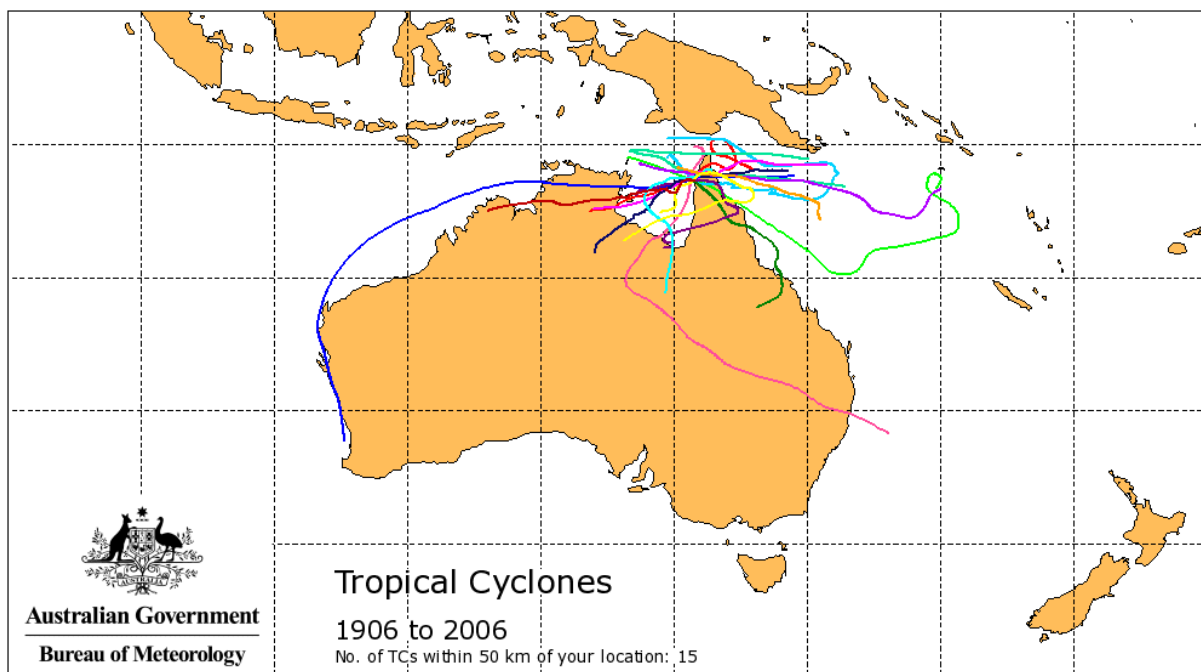


**Figure 1.3: Map of tropical cyclone tracks that passed within 50 km of Weipa from 1906-2006 (Source: Bureau of Meteorology (2016e)).**

<sup>1</sup> The mean spring and neap tide ranges at Weipa were calculated by taking the average of the tidal ranges at Weipa during a new moon and full moon (spring tide) and first quarter and last quarter moon (neap tide) over 2016 as recorded by the Australian Government Bureau of Meteorology (BoM, Bureau of Meteorology, 2016c)

<sup>2</sup> The elevations of these tidal datums were calculated using tidal data recorded by the Australian Government BoM over 2016 (Bureau of Meteorology, 2016c). This data was collected at Humbug Point, Weipa, Lat 12° 40' S, Long 141° 52' E. Note that the BoM tidal data uses the Lowest Astronomical Tide (LAT) as the datum of prediction. The tidal data was converted from LAT to m AHD using the Maritime Safety Queensland Tidal datum information for 2016, which states that AHD is 1.729 m above LAT (Queensland Government, 2017).

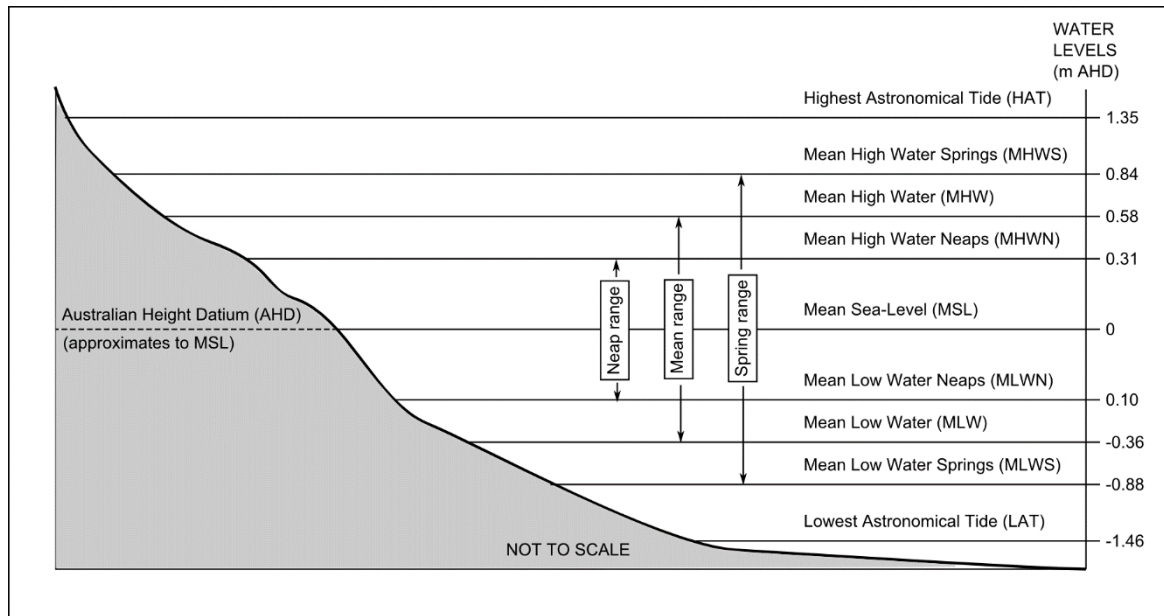


**Figure 1.4: Tidal datums for Albatross Bay (Source: data calculated from tidal data recorded by the Bureau of Meteorology (2016c) at Humbug Point, Weipa. See footnote 2).**

High tidal velocities within Albatross Bay create a dynamic nearshore environment, with a sandy seabed that is mobile and often disturbed (Queensland Government, 2015). Significant wave height in Albatross Bay is relatively low<sup>3</sup>, at approximately 0.41 m (Queensland Government, 2015), although wave energy is higher than elsewhere in the GoC, especially during the wet season when the northwest monsoon winds drive a long fetch across the northern part of the Gulf (Department of the Environment, 2007). The catchment areas of the rivers draining into Albatross Bay are relatively small compared with the other perennial river catchments around Australia and within the Gulf of Carpentaria, such as the Mitchell River catchment which is the largest river within Cape York (Figure 1.5) (Department of the Environment, 2007). Rainfall is also lower within Albatross Bay than in other parts of the GoC, leading to limited sediment, nutrient and freshwater inflow into the bay (Department of the Environment, 2007).

<sup>3</sup> The average significant wave height around Albatross Bay was calculated using wave data from 2008 – 2015 collected by the Queensland Government (Queensland Government, 2015)

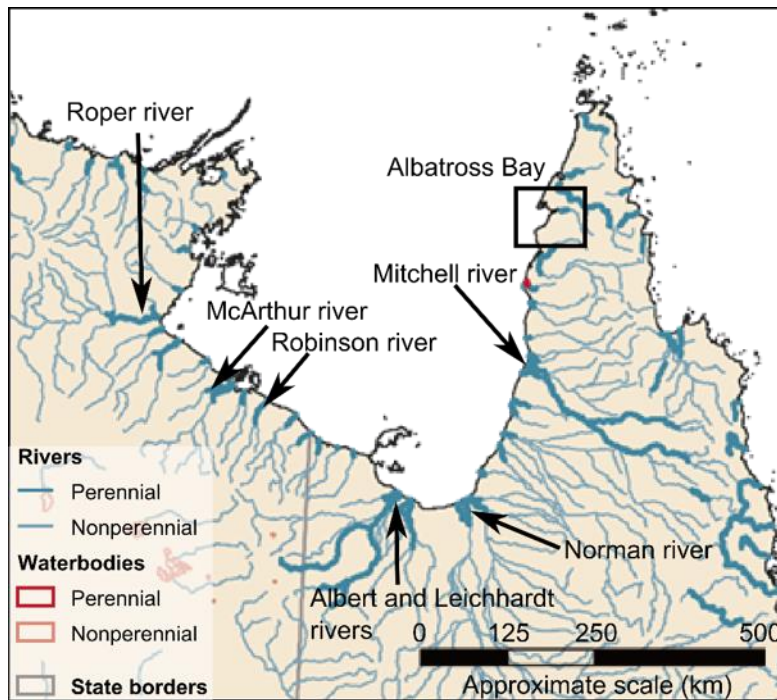


**Figure 1.5: Perennial and nonperennial rivers and waterbodies around the Gulf of Carpentaria, with the locations of larger river catchments, as identified in the Department of the Environment (2007) report, indicated. (Source: modified from the State of the Environment Committee (2011), Figure 4.2).**

#### 1.4.2 Geological and geomorphological setting

Cape York Peninsula comprises of a series of sedimentary basins overlying Proterozoic and Palaeozoic rocks including Paleoproterozoic to Cambrian metamorphic rocks, Silurian to Devonian granites, Upper Devonian to Permian sedimentary volcanic rocks and Permian granites (Taylor *et al.*, 2008a). On the Weipa Peninsula, Cretaceous sandstones and siltstones of the Carpentaria basin, known as the Rolling Downs group, overlie these older rocks and in turn are overlain in parts by the Bulimba Formation, a marginal fluvial to open-marine quartzose sandstone with minor siltstone and peat beds that was formed by marine transgression during the Tertiary (Laffan, 2001; Taylor *et al.*, 2008a). The Bulimba Formation does not extend north onto the Andoom Peninsula where, instead, modern sediments are deposited directly upon the Rolling Downs group (Laffan, 2001).

The present-day landscapes of the Weipa and Andoom Peninsulas have been divided into three geomorphic regions by Smart (1977b): (i) the Merluna Plain; (ii) the Weipa Plateau and (iii) the Mapoon Plain coastal lowlands (Figure 1.6). These landscape divisions persist across subsequent studies of the geology and geomorphology of Cape York (see, for example, Cameron and Cogger, 1992; Laffan, 2001; Taylor *et al.*, 2008a; Pain *et al.*, 2011). The Merluna Plain is an eroded undulating inland plain developed on the Rolling Downs group and lies to

the east of the Weipa Plateau (Laffan, 2001). Acidic loamy yellow earth soil profiles overlie the sandstones and siltstones of the Rolling Downs group, and support the growth of eucalypt woodlands that experience water logging during the wet season (Cameron and Cogger, 1992).

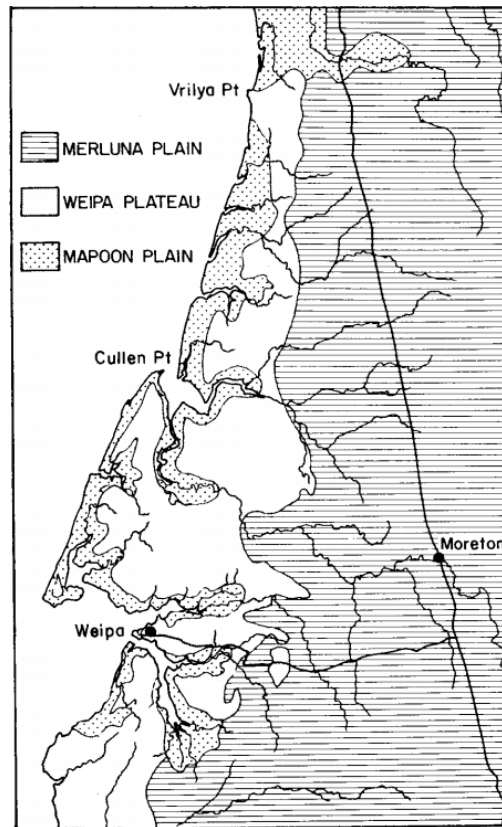


**Figure 1.6: The major geomorphic regions in Weipa as defined by Smart (1977a). (Source: Cameron and Cogger (1992), Figure 3).**

The Weipa Plateau lies between the Merluna and Mapoon Plain, running parallel to the coast and extending up to 60 km inland (Laffan, 2001). In this region, the Rolling Downs Group and Bulimba Formation are overlain by an aluminous laterite, which is the source of a large bauxite deposit that is currently being mined commercially (Cameron and Cogger, 1992). This bauxite deposit is extensive, spread over an area of roughly 10,000 km<sup>2</sup> and extending to a depth of between 1 m to 6 m (Taylor *et al.*, 2008b). The Weipa Bauxite deposit is primarily made up of pisoliths with little or no matrix present (Figure 1.7A) (Taylor *et al.*, 2008a). Pisoliths are small, approximately spherical, mineral particles approximately 0.2 cm to 2 cm in diameter, with a median size of approximately 0.5 cm (Figure 1.7B) (Rintoul and Fredericks, 1995; Taylor and Eggleton, 2004; Taylor *et al.*, 2008a). The Weipa pisoliths “...are composed of gibbsite, boehmite, nano-particulate anhydrous aluminium minerals, kaolinite, quartz,

hematite and/or goethite in widely varying proportions and about 2% anatase...” (Taylor *et al.*, 2008b, p. S45). The bauxite is a duricrust that has formed from the *in situ* weathering of the Rolling Downs group and Bulimba formation and is therefore chemically related to its substrate (Taylor and Eggleton, 2008). Formation of the bauxite may have begun as early as the mid-Cretaceous, and may still be forming today (Taylor and Eggleton, 2008).

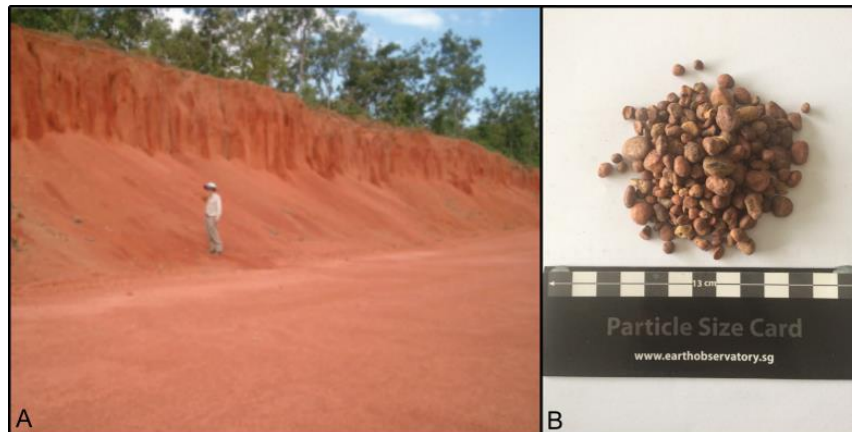


**Figure 1.7: (A) Bauxite mine face at Andoom in the Rio Tinto Aluminium mine. Note that as the bauxite deposit consists of pisoliths with little to no matrix, the mine wall collapses readily, resulting in an accumulation of loose pisoliths at the base of the mine face. (Source: Taylor *et al.* (2008b), Figure 1A). (B) Sample of pisoliths collected from Red Beach, Cape York, Australia.**

The Mapoon Plain is an irregular coastal plain between 2.5 and 5 km wide, formed from the deposition of materials eroded from the Merluna Plain and Weipa Plateau (pisoliths, sand, silt and clay) and located between the Weipa Plateau and the sea (Cameron and Cogger, 1992; Burne and Graham, 1995). Along the coastline of Albatross Bay, the seafloor has a relatively steep profile that experiences effective wave processes, leading to the transport of the fine sediment offshore, leaving sand and pisoliths to be reworked into a beach ridge or a series of beach ridges that occupy parts of the narrow coastal plain (Figure 1.8A) (Burne and Graham, 1995). By contrast, the southern part of the GoC, from Karumba to Cape Keer Weer, has a low-gradient seafloor, with lower effective offshore sediment transport resulting in the formation of expansive mudflats and chenier plains rather than beach ridge plain development (Figure 1.9) (Burne and Graham, 1995).

The sandy coastal and beach ridge plains around Albatross Bay are predominantly comprised of siliceous sands, with occasional areas of calcareous sands. The sedimentary profiles developed within them are generally deep and excessively drained (Newman, 1996).



Shell material may be present within the sediment (Newman, 1996). Being excessively drained means that water is readily drained following rainfall, and may also move laterally from the beach ridges to the swales during heavy rainfall. Within the swales, the water table can rise close to the surface during the wet season (Newman, 1996).

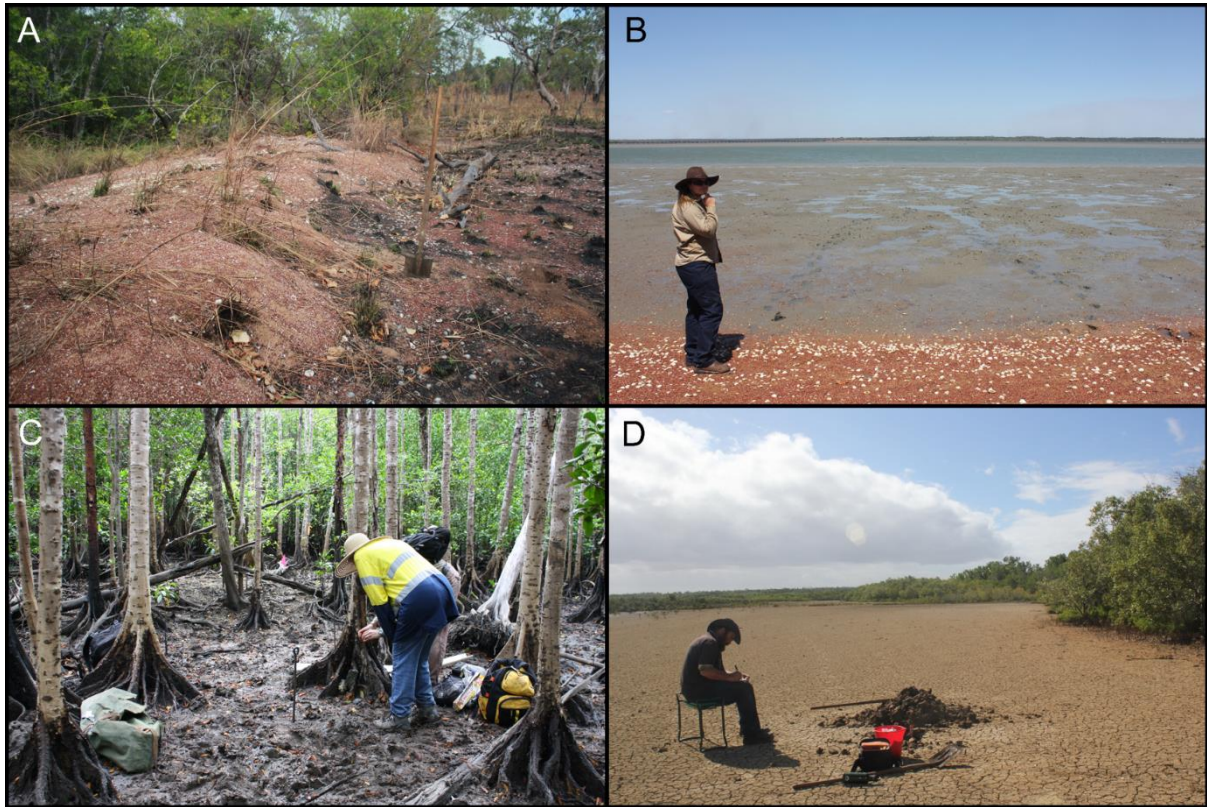


**Figure 1.8: Examples of the environments found within the Mapoon Plain in Albatross Bay – (A) beach ridge located behind the mangroves at Red Beach, (B) intertidal mudflat exposed at low tide at Red Beach, (C) mangroves located at Wathayn and (D) supratidal mudflat at Kwamter with desiccation cracks seen on the surface.**

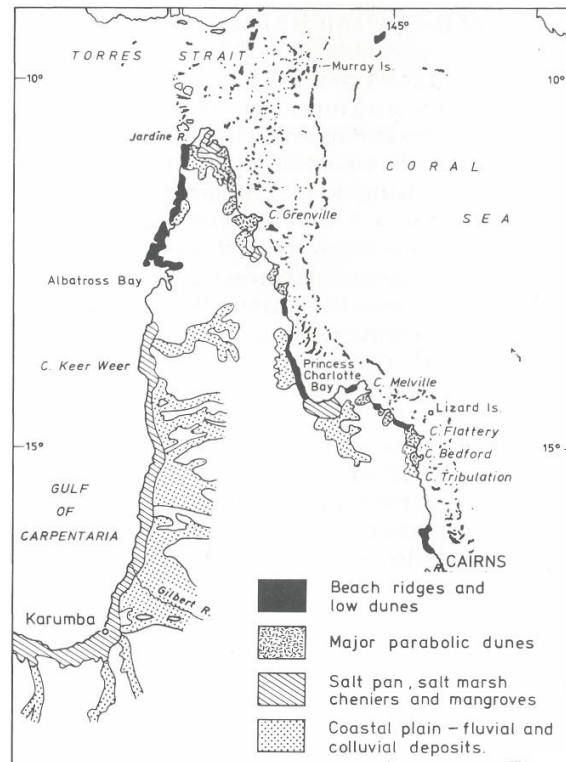


**Figure 1.9: Geomorphology of the eastern coast of the Gulf of Carpentaria, with the southeastern coastline dominated by mudflats and chenier plains, in contrast to the northeastern coastline that is dominated by beach ridges. (Source: modified from Hopley (1985), Figure 124-1).**

As well as beach ridges and beach ridge plains around the coast, intertidal and subtidal mudflats, mangroves and supratidal mudflats are also present along the estuaries draining into Albatross Bay (Cameron and Cogger, 1992; Newman, 1996; Laffan, 2001). Among these three environment types, intertidal and subtidal mudflats are found at the lowest elevations, with subtidal mudflats occurring below mean low water spring (MLWS) and intertidal mudflats present between MLWS to mean high water spring (MHWS) elevations (Figure 1.8B) (Dyer *et al.*, 2000). Intertidal and subtidal mudflats are unvegetated, have a low gradient and are generally made up of poorly to moderately sorted sandy muds and muddy sands (Geoscience Australia, 2015c). Within intertidal and subtidal mudflats, carbonate concentrations are moderate due to the presence of shells, and organic carbon content is variable and location dependent (Geoscience Australia, 2015c).

Mangroves are a taxonomically diverse group of trees and shrubs that grow in tropical and subtropical regions and have adapted to, and are the dominant species in, low energy, muddy intertidal environments (Blasco *et al.*, 1996; Edyvane, 2005; Zong, 2007). Mangrove communities are well developed in Albatross Bay and are generally found growing along estuaries at an elevation between mean sea level to MHWS (Figure 1.8C) (Cameron and

Cogger, 1992; Newman, 1996; Geoscience Australia, 2015c). Mangrove roots act as an effective trap for sediments (Breitfuss *et al.*, 2015). Sediments that accumulate in mangrove environments are generally poorly to moderately sorted muds with a low carbonate content and high organic matter content (Geoscience Australia, 2015c).

Supratidal mudflats, also known as saltflats or salt marshes, are hypersaline coastal environments characterised by a lack of trees and tall shrubs, leaving the ground bare, with only the occasional salt-tolerant grass present (Figure 1.8D) (Jaensch, 2005; Geoscience Australia, 2015d). Supratidal mudflats normally occur “...on shorelines where mangrove establishment is precluded or development is limited...” (Saintilan *et al.*, 2009, p. 858). However, supratidal mudflats can also be found co-existing with mangroves in some locations, including Australia, in dry evaporative environments (Newman, 1996; Jaensch, 2005; Saintilan *et al.*, 2009; Dale *et al.*, 2015). Where supratidal mudflats and mangroves co-exist, supratidal mudflats will be found on low gradient estuarine floodplains, landward of mangroves (Jaensch, 2005; Saintilan *et al.*, 2009; Dale *et al.*, 2015). Supratidal mudflats are rarely inundated, only becoming waterlogged when king tides occur, leading to desiccation cracks forming on the surface (Dale *et al.*, 2015; Geoscience Australia, 2015d). Sediments within supratidal mudflats generally comprise poorly sorted sandy muds with a low carbonate concentration and high organic carbon content (Dale *et al.*, 2015). Supratidal mudflats are present along all of the estuaries draining into Albatross Bay, behind the mangroves.



## **Chapter 2**

# **Holocene Sea level Change in Northeastern Australia: A Review**

Australia is distant from major ice-sheet accumulation ('far field') and largely unaffected by neo-tectonics. Therefore, Australia is an ideal location to examine glacio-eustatic and hydro-isostatic sea level change. This chapter reviews previous research on how sea level has changed globally, and across Australia, following the Last Glacial Maximum (LGM). The review demonstrates that there is a consensus that, in Australia, sea level began to rise following the LGM, reaching a highstand of at least +1 m above present day sea level during the mid-Holocene, before falling to PMSL, but that the timing and rate of this sea level change is variable across the country. This review focuses on three regions in northern Australia that are proximal to, and therefore the most relevant to sea level reconstruction at the study area of Albatross Bay; the northern coast of Australia (Figure 2.5, region A), the northeastern (Queensland) coast of Australia (Figure 2.5, region B), and within the Gulf of Carpentaria (Figure 2.5, region C). I review sea level research in these regions, and the sea level curves that have been constructed as a result. This review will then serve as the framework from which my sea level reconstruction fills in, builds upon and/or contrasts with previous research on sea level change in Australia.

### **2.1 Late-Quaternary sea level change**

The Quaternary is the most recent geological period of Earth's history, beginning approximately 2.6 million years ago and extending to the present day. The Tertiary to Quaternary transition is marked by the start of an "Ice Age" and the Quaternary was a time of highly unstable climate, with cold glacial periods interspersed with warmer interglacials (Lowe and Walker, 2015). Approximately 20 to 30 glacial-interglacial cycles occurred over the Quaternary (Benn and Evans, 1998; Ehlers and Gibbard, 2007; Marshall, 2009). It is now accepted that these glacial-interglacial cycles were primarily caused by variations in the Earth's orbit – its eccentricity, obliquity and precession – as described by Milutin Milanković (Hays *et al.*, 1976; Williams *et al.*, 1998). As the Earth's orbital path, tilt and orientation changed at

intervals of approximately 100,000, 42,000 and 22,000 years respectively, the duration and intensity of the climatic seasons along with the distribution of solar radiation on the Earth's surface also changed, causing temperature fluctuations of as much as 15°C and the growth or decline of ice sheets and glaciers (Flannery, 2005; Lowe and Walker, 2015). Changes in ice sheet and glacier volume, in turn, had a direct impact on sea level through a process termed “glacio-eustatic sea level change” (Stright, 2005). During cold glacial periods, water evaporated from the ocean basins was stored in glaciers and ice sheets, leading to a decrease in ocean volume and a fall in sea level. During warmer interglacial periods, water from glaciers and ice sheets was released back into the ocean, leading to an increase in ocean volume and thus a rise in sea level (Lambeck and Chappell, 2001; Carlson, 2011). Eustatic sea level changes are uniform across the globe – they result in either an absolute net increase or an absolute net decrease in the overall volume or mass of the ocean (Rovere *et al.*, 2016). Eustasy has been the dominant factor controlling sea level change over the late-Quaternary (Murray-Wallace, 2007a).

Sea level has, over the Quaternary, also been influenced by isostasy, steric changes, geoidal changes and human impacts, all resulting in variable relative sea level changes across the globe. Isostasy is the movement of the Earth's crust caused by changes in weight from loading and unloading on the surface by glaciers (glacio-isostasy), water in the ocean basins (hydro-isostasy) or sediments (Stright, 2005). Both glacio-isostasy and hydro-isostasy were significant over the Quaternary due to the growth and melting of glaciers, with isostatic impacts superimposed on those caused by glacio-eustasy. The late-Quaternary sea level rise following the LGM led to a marine transgression over continental shelves that were previously exposed when sea level was lower during the LGM, with the marine transgression then causing the continental crust, and thus shorelines, to subside to varying degrees depending on the width and slope of the continental shelf which, in turn, altered the volume and weight of water load. Shallow continental shelves, exposed during the sea level lowstands and subsequently drowned, were particularly affected, and adjacent shorelines tilted upwards by at least one metre (Bird, 2008; Short and Woodroffe, 2009).

Steric changes are changes to the volume of sea water due to temperature (the higher the temperature, the greater the volume) and salinity (higher salinity, lower volume) (Milne, 2008). Geoidal sea level changes are a consequence of oceans having an undulating surface, with domes and troughs caused by gravitational, hydrological and meteorological forces. Sea levels change as the configuration of these domes and troughs change (Bird, 2008). In more

recent times, there is evidence to show that human activities, such as groundwater, oil and natural gas extraction, the loading of coastal land with human structures, the building of artificial structures such as tidal barrages, land reclamation and dredging, and anthropogenically-induced climate change, also impact sea level (Bird, 2008; Church *et al.*, 2013).

#### 2.1.1 Global patterns of sea level change, LGM to present day

Variations in sea level were once assumed to be similar across the globe due to the interconnectedness of the oceans (Kidson, 1982). Therefore, until the 1970s and 1980s, a primary goal of sea level research was to develop a universal eustatic sea level curve (Pirazzoli, 1991b). To achieve this goal, in 1974, the United Nations Educational, Scientific and Cultural Organisation (UNESCO) and the International Union of Geological Sciences (IUGS) launched Project 61 “Sea level changes during the last hemicycle (about 15,000 years)”, scheduled to run till 1982 and whose primary aim “... was to establish a graph of the trend of mean sea level during the period of deglaciation and continuing to the present day, based on compilations of sea level index points from all over the world...” (Tooley, 1982, p. 3). However, by the end of Project 61, data indicated that sea level was more variable and complex than predicted. Three conclusions were drawn from Project 61 which then became the foundation for the direction of future sea level research. Firstly, Kidson (1982, p. 144) stated definitively that “... the search for a universal eustatic curve must be regarded as over...”. Following from this first conclusion, the second conclusion reached was that sea level curves only had regional validity and the third conclusion was that no part of the Earth’s crust is completely stable (Kidson, 1982).

Project 200, titled “Late Quaternary Sea Level Changes: Measurement, Correlation and Future Applications”, was then launched by the United Nations Educational, Scientific and Cultural Organisation (UNESCO) and the International Union of Geological Sciences (IUGS) and ran from 1983 to 1987. Project 200 recognised sea level variability, aiming to quantify local sea level change and understand the tectonic, climatic, tidal and oceanographic processes driving these changes along with the global, regional and local scales in which these processes operate. The ultimate goal was then to allow the prediction of future sea level change and its impacts on low lying coastal areas (Walling and Jacobides, 1983; Pirazzoli, 1991b). This paradigm shift in sea level research, from the notion of a universal sea level change to regional and local sea level variability, means that there is no record of “absolute” sea level change; rather, any sea level change described, including in this study, is always “relative”, i.e. change relative to the present mean sea level (PMSL) in each location studied (Shennan, 2007).

It is now clear that there are regional differences in the rate and elevation of sea level change during and following the LGM. During the LGM, ice sheets covered an estimated additional 13% of the Earth's surface (Murray-Wallace, 2007b), with ice sheet thickness modelled at a maximum of around 3800 m over North America (Marshall *et al.*, 2002), and a maximum of 2700 m over northern Europe (Siegert and Dowdeswell, 2004). With a significant amount of ocean water stored in these ice sheets and glaciers, sea level during the LGM was approximately 120-125 m below PMSL (Lambeck *et al.*, 2002; Murray-Wallace, 2007a) and coastlines advanced seawards (Bird, 2008). For example, in Southeast Asia, the drop in sea level caused the emergence of the Sunda Shelf connecting the Indonesian islands of Sumatra, Java and Borneo with Indochina (Voris, 2000), while a land bridge was established between Australia and Papua New Guinea (Figure 2.1) (Reeves *et al.*, 2013b). In addition to the storage of ocean water, continental ice sheets in the higher latitudes, known as the “near field” area because of their proximity to the ice sheets, also loaded vast amounts of weight onto the crust, causing the downward deformation of the crust under the centre of the ice sheets and uplift of the crust (and seafloor) at the edges, creating a forebulge on the periphery of the ice sheets, and causing relative sea level to fall further in these regions (Mitrovica and Peltier, 1991).

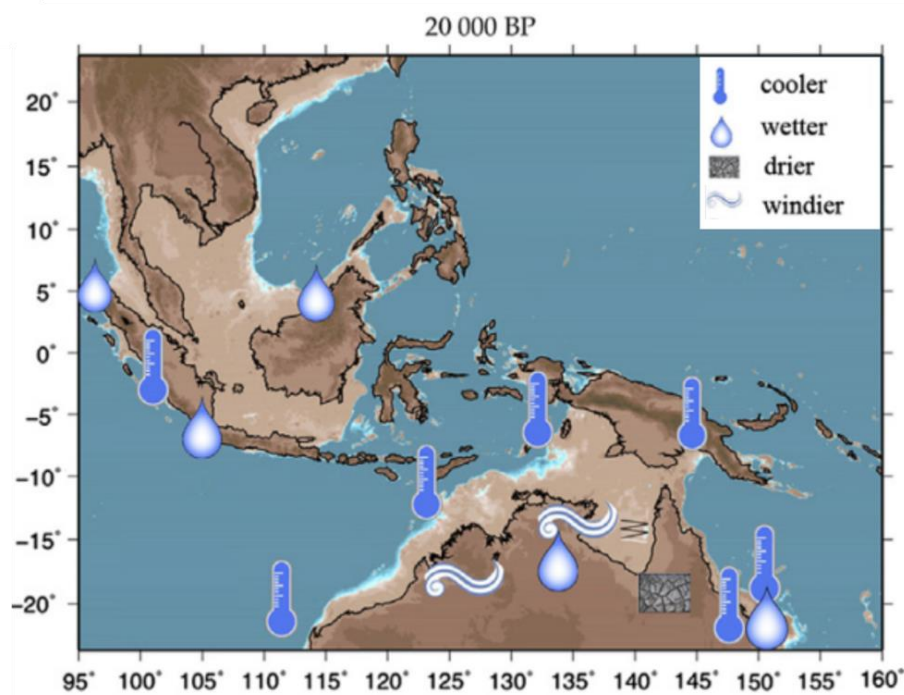


**Figure 2.1:** The Australasian region 20,000 years ago during the LGM, when lower sea levels connected Australia to Papua New Guinea and the major islands of the Indonesian Archipelago with Indochina (Source: modified from Reeves *et al.* (2013b), Figure 9).

At the start of the Holocene (approximately 11,700 years ago) the Earth's climate became warmer and ice sheets and glaciers melted, returning water to the oceans which, in turn, resulted in the Holocene marine transgression where sea levels rose from their previous low point of approximately -125 m below PMSL. As the previously exposed continental shelves became submerged, the differential impacts of isostasy, climatic and oceanographic processes lead to regional differences in the patterns of relative sea level change (Figure 2.2).

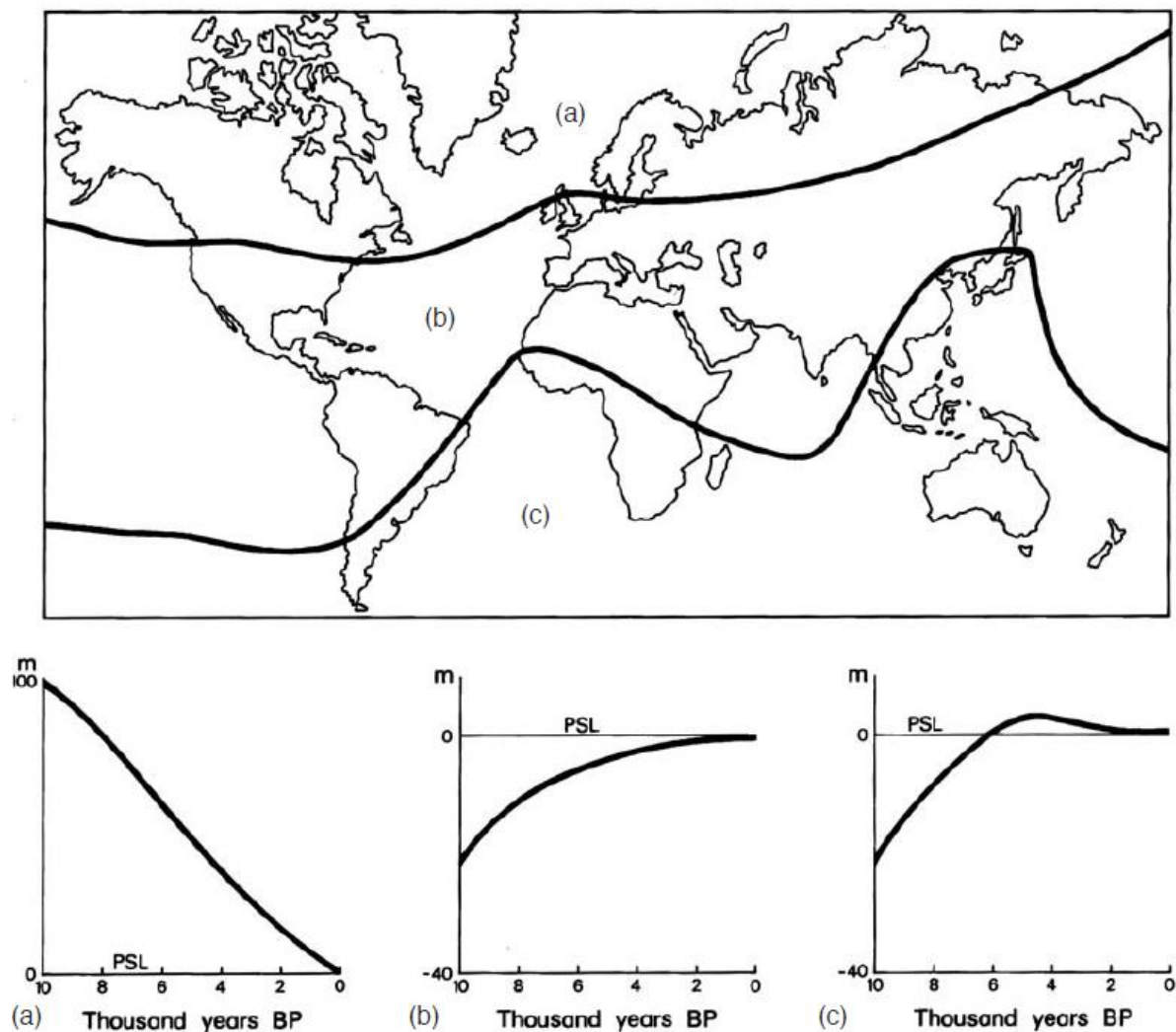


Figure 2.2: Major variations in relative sea level change during the Holocene (Source: Bird (2008), Figure 3.6).

Broadly speaking, over the Holocene, relative sea level has fallen in the high northern latitude near field areas because, as the ice sheets melted and their weight was removed, the central continental crust was uplifted (Mitrovica and Peltier, 1991). Even though Holocene sea level was also rising concurrent to land uplift due to meltwater input, the rate of crustal uplift

exceeded that of rising sea level, producing a relative sea level fall (Lambeck and Chappell, 2001; ÓCofaigh and Bentley, 2007). In the middle latitude “intermediate” field sites, relative sea level has risen, at a decreasing rate, to PMSL, as melting ice sheets increased the volume of water in the ocean (Horton, 2007; Bird, 2008). In contrast, much of the Southern Hemisphere and Southeast Asia, which are known as “far field” sites (approximately 30°N and 30°S), recorded a relative sea level rise to above present levels, creating a mid-Holocene highstand between 3,000 and 7,000 years ago (Horton *et al.*, 2005; Woodroffe and Horton, 2005; Horton, 2007; Zong, 2007). The height and duration of the mid-Holocene highstand varied from region to region, before sea level subsequently fell to PMSL (Bird, 2008).

The mid-Holocene highstand was caused by geoidal changes, in a process coined “equatorial ocean syphoning” (Mitrovica and Peltier, 1991; Woodroffe and Horton, 2005). As the LGM ice sheet-induced peripheral forebulge subsided in the higher northern latitudes, ocean water flowed into these near field regions from far field sites. This movement of water resulted in a relative sea level fall in far field locations during the mid- to late-Holocene (Mitrovica and Peltier, 1991). Hydro-isostatic loading along the coastal margins of near field regions also contributed to the syphoning effect (Mitrovica and Milne, 2002). Deglaciation adds a significant amount of meltwater load onto the ocean floor, causing it to subside and the adjacent land to uplift slightly, through a levering effect, as viscous mantle material migrates landward (Mitrovica and Peltier, 1991; Woodroffe and Horton, 2005; Murray-Wallace, 2007a). There is then a flux of water from far field ocean basins into these areas of near field ocean floor subsidence. Mitrovica and Milne (2002) estimate that ocean syphoning through the collapse of the peripheral forebulge, accounts for approximately 60% of the amplitude of the mid-Holocene highstand. A significant portion of the remaining 40% is then associated with hydro-isostatic loading and continental levering in near field locations.

Local variations in the amplitude and timing of the mid-Holocene highstand in far field sites are due to their distance from, and the distribution of, glacial meltwater (Lambeck and Chappell, 2001), localised continental levering (differences in the width of the continental shelves along these coastlines causing varying hydro-isostatic adjustments) (Lambeck, 2002; Murray-Wallace, 2002; Woodroffe and Horton, 2005; Murray-Wallace, 2007a), and the geological and geomorphological configuration of the locations themselves, such as available sediment accommodation space (Lambeck and Nakada, 1990; Cooper, 2007). While these processes of continental readjustment were ongoing since the commencement of glacial melting following the LGM, the effect of the redistributed flow was masked by the

overwhelming volume of water introduced back into the ocean following glacial melting (glacioeustasy), hence the initial relative sea level rise. Once the majority of ice sheet melting in the northern hemisphere ceased between 6,000 and 4,000 years BP (Lambeck, 2002), the equatorial ocean syphoning and hydro-isostatic adjustments then had a notable impact in far field locations, including Australia, in the mid- to late-Holocene, causing relative sea level to fall (Mitrovica and Peltier, 1991; Khan *et al.*, 2015).

A recurring point of dispute in Holocene sea level reconstruction studies is the nature of this sea level movement – whether the sea level fall was smooth over time, or if there were oscillations in sea level that ranged in scale from decimetres to metres (Murray-Wallace, 2007a; Shennan, 2007; Bird, 2008; Lewis *et al.*, 2008; Woodroffe, 2009b; Lewis *et al.*, 2013). The debate between smooth versus oscillating sea level change has been described as “...the most contentious issue remaining to be resolved...” (Lewis *et al.*, 2013, p. 17). Rhodes Fairbridge (1961) was one of the first researchers to propose an oscillating sea level change when he compiled sea level data, creating a record of global sea level changes over the Quaternary that contained vertical oscillations in sea level through the Pleistocene and Holocene to present day. One of the regions that Fairbridge (1961) examined was western Australia, where he identified four relative sea level highstands from 6000 to 4600 years BP, 4000 to 3400 years BP, 2600 to 2100 years BP and 1600 to 1000 years BP. In contrast, Shepard (1963, 1964) argued that sea level change was continuous, with relative sea levels rising at a diminishing rate until the present day. There followed a series of sea level change papers from around the world that demonstrated a broad division into either the Fairbridge or the Shepard schools of thought (see Kidson, 1982 and references therein). This debate continued past IUGS project 61, with Searle and Woods (1986) disputing the oscillating sea level curve proposed by Fairbridge (1961), finding no evidence of eustatic fluctuations from western Australia but, rather, that relative sea level reached a highstand of +2.5 m above PMSL at 6,400 years BP before falling smoothly to PMSL. According to Pirazzoli (1991a), new data was then published by Playford and Leech (1988) to support the original interpretation of sea level oscillations in western Australia.

Since those early studies, the nature of the Holocene sea level change is still being hotly debated. Returning to the western Australian study region of Fairbridge, Searle and Woods, Baker *et al.* (2005) argued for an oscillating relative sea level fall from a mid-Holocene highstand to present day based on studies of fixed biological indicators around Rottnest Island. In contrast, Collins *et al.* (2006) proposed a smooth relative sea level fall from the mid-

Holocene highstand to present day based on coral pavements around the Houtman Abrolhos Islands, just north of Rottnest Island.

Angulo and Lessa (1997) reviewed data from southeast Brazil, concluding that multiple studies proposing two oscillations in sea level, as relative sea level fell from the mid-Holocene highstand to present, were inaccurate and that relative sea level fell smoothly to the present. According to Angulo and Lessa (1997), oscillating sea level curves from Brazil were predominantly based on samples from shell middens, with the assumption that human settlements would be established above the high tide level, therefore sea level would be lower than the depth of the shell sampled. However, these studies failed to account for post-depositional changes within the shell middens, such as compaction or slumping, and it is unreliable to use anthropogenic shell middens to reconstruct sea level, which assumes a cultural behaviour, when other sea level proxies in the region indicate no such oscillations (Angulo and Lessa, 1997). The studies that Angulo and Lessa (1997) refuted included work done by Suguio *et al.* (1976, 1985, 1988) and Martin *et al.* (1979, 1986), prompting these authors to publish a comment in the same journal defending their conclusions (see Martin *et al.*, 1998 and subsequent reply from Lessa and Angula, 1998). Martin *et al.* (2003) and Angulo *et al.* (2006) subsequently published further reviews of sea level fluctuations in eastern and south-eastern Brazil, once again debating a smooth or oscillating sea level decline in the mid- to late-Holocene.

In Australia, much of the evidence for an oscillating Holocene sea level curve comes from the study of fixed biological indicators (FBIs) (Baker and Haworth, 2000a; b; Baker *et al.*, 2001, 2005; and Lewis *et al.*, 2008). FBIs such as coral microatolls and intertidal organisms (e.g., oysters, tubeworms, cyanobacteria, limpets, vermetids) grow in narrow, distinct and predictable vertical zones, controlled by the amount of exposure to sea spray, waves and tides each elevation receives (Baker and Haworth, 2000b). FBIs that live near the mean sea level are particularly useful for sea level reconstruction (Laborel and Laborel-Deguen, 1996). As sea level changes, FBIs that are unable to keep up with the pace of sea level change will die, leaving behind fossils that are fixed in their growth positions and are potentially preserved for millennia, making them useful proxies to investigate the smooth or oscillating Holocene sea level change debate (Baker and Haworth, 2000b).

Around Australia, fossilised tubeworms, barnacles and oyster beds, studied from as far north as Magnetic Island in Queensland (Lewis *et al.*, 2008), south through the New South



Wales coastline (Baker and Haworth, 2000b; Baker *et al.*, 2001) and across to Rottnest Island in Western Australia (Baker *et al.*, 2005), indicate that relative sea level reached a maximum elevation of approximately +1.7 m above PMSL by approximately 7,000 years BP. Sea level was stable until approximately 4,800 years BP, when two sea level oscillations with magnitudes of between 0.3 and 1 m occurred – relative sea level fell between 4,800 to 4,500 years BP, rose again before experiencing another fall from 3,000 to 2,700 years BP, then rose a second time before falling to present day levels after 2,000 years BP (Baker *et al.*, 2005; Lewis *et al.*, 2008). However, sea level reconstructions based on intertidal FBIs assume that the wave climate and tidal range in a region has not altered over the period of study because these factors would affect the growth elevation range of the FBI. As there is a lack of data on wave climate and tidal range changes over the Holocene in Australia, it is difficult to then assess the precision of these sea level oscillations (Sloss *et al.*, 2007).

Thus, while many researchers favour a model of smooth relative sea level change from the mid-Holocene highstand to present (Lambeck and Chappell, 2001; Woodroffe and Horton, 2005; Woodroffe, 2009b), there is reported evidence of Holocene sea level oscillations in far field locations showing this issue is far from resolved. In addition to the evidence from Brazil and Australia described above, sea level oscillations have also been recorded from South Africa (Compton, 2001), China (Zhao and Yu, 2002), India (Banerjee, 2000) and Japan (Sawai *et al.*, 2002; Kato *et al.*, 2003). Such oscillations, should they exist, cannot be attributed to hydro-isostasy, but instead may be a response to climatic fluctuations, such as the dynamics of the Antarctic ice sheet (Goodwin, 1998; Baker and Haworth, 2000a), multi-decadal and centennial-scale climatic forcing such as the El-Nino Southern Oscillation (ENSO) and changing ocean temperatures (Lewis *et al.*, 2008).

### 2.1.2 Sea level change in Australia since the LGM

Located in the middle of the Indo-Australian plate, Australia is regarded as tectonically stable, free from neo-tectonics and the impacts of glacio-isostasy (Chappell, 1987; Chivas *et al.*, 2001; Yokoyama *et al.*, 2001; Murray-Wallace, 2002; Woodroffe and Horton, 2005; Sloss *et al.*, 2007; Switzer *et al.*, 2010; Lewis *et al.*, 2013). Late Pleistocene glaciation in Australia was brief and restricted to the highlands of Tasmania and parts of the Snowy Mountains on the mainland (Figure 2.3) (Galloway, 1965; Barrows *et al.*, 2002). Australia was deglaciated well before the Holocene, with the last glacial advance (known as the Mount Twynam Advance)

commencing approximately  $16,800 \pm 1,400$  years ago and terminating approximately  $15,900 \pm 1,400$  years ago (Barrows *et al.*, 2001). Due to the limited extent and localised nature of glaciation in Australia, along with being far afield of any major ice-sheet accumulation and disintegration over the Quaternary, glacio-isostasy had a marginal impact on relative sea level change and the coastal evolution of Australia at a continental scale (Murray-Wallace, 2007a).

The extent of tectonic stability in Australia, however, is more complicated than first thought (Twidale, 2011). By the early 1960s, C.V.G. Phipps had already postulated that the eastern coast of Australia was subsiding (Gill and Hopley, 1972). While the impact of tectonic movement on Australia's shoreline is often neglected in sea level studies, the possibility of coastal warping during the Holocene influencing sea levels should not be dismissed (Hopley, 1987; Bird, 2005). By examining the geological and stratigraphic records along the coastline of Australia, Sandiford (2007) observed that the southern coastal margin of Australia was uplifted. Mid-Eocene sediments can be found up to approximately 400 km inland of the present day southern shoreline of Australia, at a maximum elevation around 300 m above present day sea level. In contrast, along the northern and eastern margin of Australia, equivalent-age sediments are almost entirely absent from the continental record, with any sedimentary evidence being found either less than 10 m above present day sea level or offshore (Sandiford, 2007). Furthermore, evidence indicated that the south-western part of the continent has risen significantly higher than the south-east, leading Sandiford (2007) to propose a continental-scale tilting – north-downwards, south-south-west-upwards – occurring since the mid-Miocene at a rate of approximately  $15\text{--}20 \text{ m Myr}^{-1}$  (Figure 2.4). This continental-scale tilting is linked to the northward movement and subduction of the Indo-Australian Plate beneath the Pacific Plate at a rate of  $6\text{--}7 \text{ cm yr}^{-1}$  (Murray-Wallace, 2002; Sandiford *et al.*, 2004; Hillis *et al.*, 2008; Quigley *et al.*, 2010). Evidence from Pleistocene and Holocene shoreline elevations, with palaeo-shorelines along the southern continental margin higher than the northern continental margin by several metres, indicates that tilting may have continued to the present day (Sandiford, 2007; Clarke *et al.*, 2011).

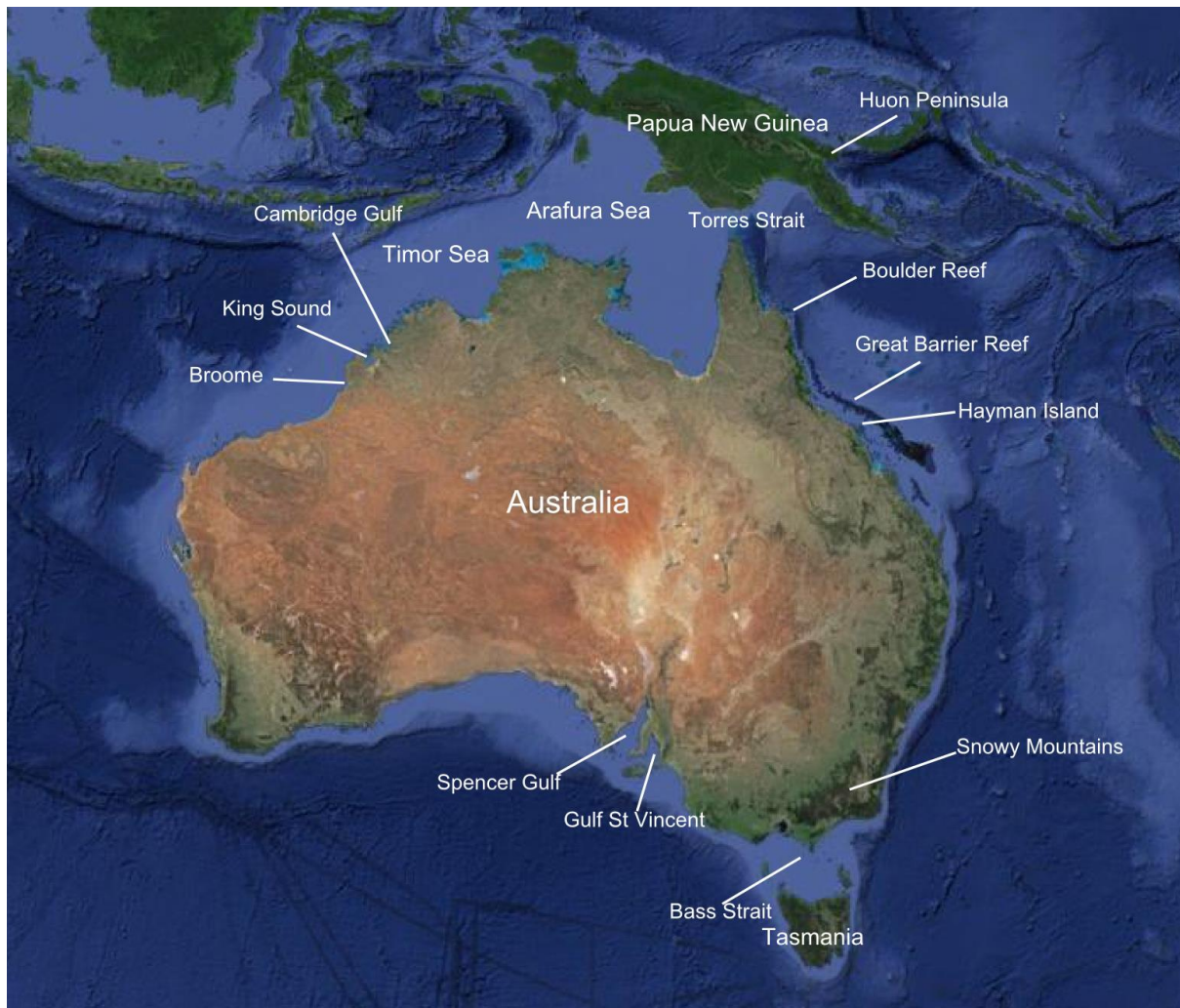


**Figure 2.3: Map of Australia and surrounding areas showing the locations of Quaternary sea level change and palaeo-environmental studies, along with other locations referred to in text. (Source: modified from GoogleEarth, accessed 3<sup>rd</sup> March 2016).**

According to Gill and Hopley (1972), it is important to account for continental tilting in sea level reconstruction because, depending on the study area, this movement may negate any Holocene submergence or emergence. That being said, Bryant (1992) employed trend surface analysis to examine the distributions of sea level maxima around Australia during three time periods: the last interglacial (approximately 125,000 years ago), the Holocene maximum marine transgressions (approximately 6,000–5,000 years ago) and the last 20 years. Results indicated that, during the last interglacial, tilting of the Australian continent can account for 77.3% of the variance in maximum sea levels observed around the continental margin ( $p \leq 0.05$ ). However, while Bryant (1992) argues that the distributions of sea level maxima around the Australian coastline still supported the influence of continental tilting, tectonic deformation during the Holocene only accounts for 9.4% of the variance ( $p \leq 0.14$ ) because the pattern of

Holocene sea level change was dominated by local variations from hydro-isostatic loading of the continental shelf. Bryant (1992) further calculated that, from the time of the mid-Holocene transgression to present, continental tilting would only cause approximately 0.23 m of maximum sinking along the northern margin of the Australian continent, an amount that would be difficult to detect above the eustatic and hydro-isostatic signal of sea level change. By contrast, tectonically active areas have experienced uplift of up to 3.3 m/100 yr (e.g. Huon Peninsula, Figure 2.3) (Chappell, 1987; Ota *et al.*, 1993) over the Holocene, significantly dwarfing uplift and submergence rates from continental tilting in Australia.

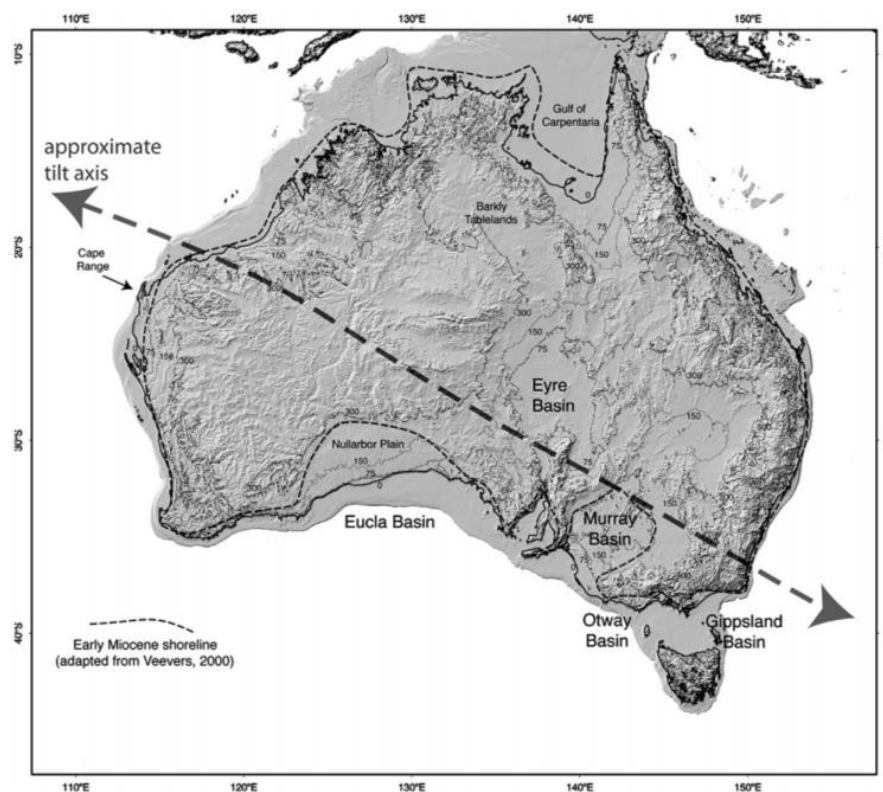


**Figure 2.4:** Australian continent and continental shelf (at elevations greater than -200 m) with the thick arrowed line showing the approximate tilt axis described in the text. The thin dashed line shows the inferred position of the mid-Miocene shorelines, demonstrating onshore marine Miocene records to the south and southwest, and offshore records to the north and northeast (Source: Sandiford (2007), Figure 3).

Hopley (1987), Chappell (1987), Murray-Wallace (2002, 2007) and Yokoyama *et al.* (2001) all reach similar conclusions to Bryant (1992) – even though tectonism was a factor in sea level change around Australia over the Pleistocene and Holocene, the rates of change are small, slow, and significantly overshadowed by the glacio-eustatic and hydro-isostatic signal following the LGM. The Australian coast is therefore still considered to be an ideal location to

study glacio-eustatic and hydro-isostatic sea level change and is extensively studied for the reconstruction of post-glacial (i.e., late-Pleistocene and Holocene) sea level fluctuations (Nakada and Lambeck, 1989; Bryant, 1992).

During the LGM, sea level was approximately 120–130 m below modern Australian Height Datum (AHD) in the Australasian region (Chappell, 1987; Lambeck and Nakada, 1990; Yokoyama *et al.*, 2001), in line with global observations (see Section 2.1.1). During this time, Australia's land area was approximately 25% larger than present, and land bridges joined mainland Australia to Papua New Guinea in the north and to Tasmania in the south (Figure 2.4) (Murray-Wallace, 2007a). Following the LGM, sea level rose gradually between 19,000 and 16,000 years BP, and more rapidly between 16,000 and 12,500 years BP (Lambeck *et al.*, 2002). After a pause in sea level rise between 12,500 and 11,500 years BP, possibly in response to the colder Younger Dryas<sup>4</sup> period (~12,800–11,600 years BP), sea level resumed rising rapidly, with oceans approaching their present-day volumes approximately 7,000 years ago (Lambeck *et al.*, 2002). While there has been little change in ocean volume since then, ongoing isostatic adjustments caused relative sea level to continue changing (Woodroffe, 1993).

It is generally agreed that sea levels around Australia reached present day levels before 6,000 years BP (Lambeck and Nakada, 1990). Although there is considerable variation around Australia in the precise timing, this event occurred earlier in Australia than northern Europe and North America (Lambeck and Nakada, 1990). As hydro-isostatic adjustment and equatorial ocean syphoning began to have a significant impact on relative sea level changes around Australia, a mid-Holocene highstand was created around parts of the Australian coastline (Mitrovica and Peltier, 1991; Khan *et al.*, 2015). At this time, sea level was between +1 m and +3 m higher than PMSL in many parts of the Australian coastline, with ample evidence from Queensland (northern coast of Australia - see Sections 2.3 and 2.4), to New South Wales (eastern coast of Australia - Sloss *et al.*, 2007; Switzer *et al.*, 2010), South Australia (southern coast of Australia - Belperio *et al.*, 2002) and Western Australia (western coast of Australia -

---

<sup>4</sup> The Younger Dryas is a distinct cold event that occurred during the late-glacial period, estimated to have started approximately 12,800 years BP, and lasted until approximately 11,600 years BP (Rasmussen *et al.*, 2006; Björck, 2007; Tibby, 2012). The Younger Dryas was preceded by a warmer stage, known as the Allerød oscillation, and followed by the present interglacial period (Björck, 2007). During the Younger Dryas, an abrupt decrease in annual temperature in the Northern Hemisphere resulted in glacial advances and the expansion of cold-tolerant vegetation at the expense of the previously spreading forest vegetation which, in turn, caused a distinct lithologic change in the sedimentary records of the Northern Hemisphere (Björck, 2007). While the significant extent of the Younger Dryas in the Northern Hemisphere ought to have an effect on the climate system in the Southern Hemisphere, evidence of a Younger Dryas in the Southern Hemisphere is inconclusive (Björck, 2007; Tibby, 2012), and an alternative mechanism may be the cause of the pause in sea level rise noted by Lambeck *et al.* (2002).

Wyrwoll *et al.*, 1995; Lessa and Masselink, 2006; Engel *et al.*, 2014), with reconstructions based on multiple sea level proxies including mangroves, cheniers, coral microatolls and sedimentary stratigraphic sequences (Chappell, 1987; Lambeck and Nakada, 1990; Lewis *et al.*, 2013). However, there are also locations around Australia that have no evidence of a mid-Holocene highstand, such as within the van Diemen Gulf (Woodroffe *et al.*, 1993) and the Joseph Bonaparte Gulf (Thom *et al.*, 1975), both in the Northern Territory. There is also no record of a mid-Holocene sea level highstand in Tasmania where, instead, sea level reached and stabilised at present day levels approximately 6,000 years ago (Lambeck and Nakada, 1990; Gehrels *et al.*, 2012). Following this mid-Holocene highstand, where evidence for one is present, relative sea level then fell to present day levels, with consensus amongst researchers that this fall was steady rather than oscillating (Lambeck and Nakada, 1990; Murray-Wallace, 2007a; Yu and Zhao, 2010).

In the remainder of this chapter, I review the current state of knowledge on relative sea level change in Australia in more detail. Due to the variable nature of the timing and magnitude of post-glacial sea level change, focus is restricted to the northern and eastern coasts of Australia because these are most pertinent to my study area, described in Section 1.4. The radiocarbon ages discussed in this review have been re-calibrated, where required, using the IntCal13 and Marine13 database (Reimer *et al.*, 2013) in the OxCal program (version 4.2) (Ramsey, 2009). The Marine13 calibration curve employs a hypothetical “global” marine reservoir calculated by Reimer *et al.* (2013), upon which a further regional oceanic correction ( $\Delta R$ ) needs to be applied due to regional variations in the marine reservoir effect from factors such as terrestrial water input, upwelling and variations in inter-hemispheric atmospheric  $^{14}\text{C}$  (see Section 5.2.1) (Petchey *et al.*, 2004; Ulm, 2006). More information on the calculation of  $\Delta R$  values can be found in Ulm (2002). For study sites along the eastern coast of Queensland (region B, Figure 2.5), a  $\Delta R$  of  $12 \pm 10$  years was chosen based on the guide to Australian  $\Delta R$  values by Ulm (2006). For study sites within the Gulf of Carpentaria (GoC) (region C, Figure 2.5), a  $\Delta R$  of  $-103 \pm -16$  years was used, based on unpublished calculations by Ulm (Dr F. Petchey, Waikato Radiocarbon Laboratory, pers. comm., 15 March 2016). All radiocarbon dates reported in this thesis are calibrated ages, unless stated otherwise, and are reported as (calendar) years before present (BP), where “present” is defined as AD 1950. All optically stimulated luminescence (OSL) dates are reported as “years ago”, referenced from the time of sample collection.



## 2.2 Sea level change in northern Australia

Evidence for sea level change along the northern margin of the Australian continent, extending from west of the GoC in the Northern Territory to Port Hedland in Western Australia (region A, Figure 2.5), is reviewed here. To minimise any complications from the north-downwards (submergence)/south-south-west-upwards (emergence) relative sea level change previously described, however marginal the impact of this tilt on sea level changes over the Holocene may have been, the western-most sites examined in this study are bounded by the continental tilt axis identified by Sandiford (2007).

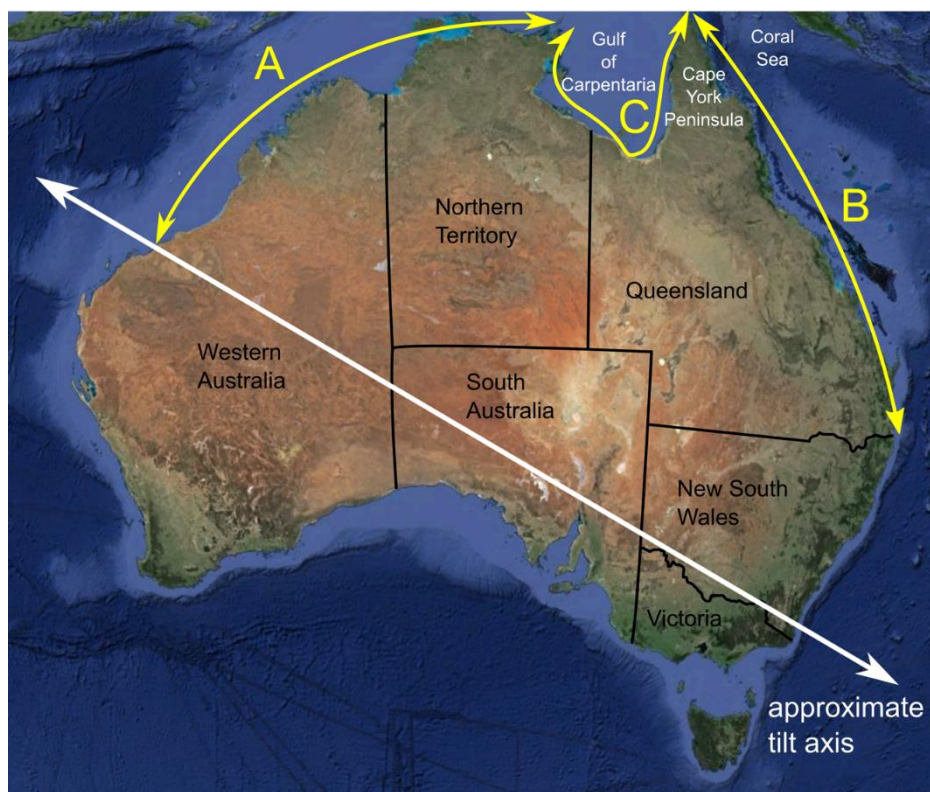


**Figure 2.5:** Map of Australia showing the three coastal regions reviewed in the text (A, B, C). (Source: modified from GoogleEarth, accessed 3<sup>rd</sup> March 2016; approximate axis tilt line derived from Sandiford (2007)).

The northern coast of Australia encompasses a range of climate zones, from arid and semi-arid in the northwest to tropical in the northeast (Figure 2.6A) (Bureau of Meteorology, 2014). The northern third of the continent, north of the Tropic of Capricorn, experiences relatively high mean annual temperatures due to its latitude, and high precipitation generated by both the northwest monsoon and tropical cyclones (Short and Woodroffe, 2009). The northern Australian coastline also has a wide and shallow continental shelf (see Figure 2.4 and

Figure 2.5), which contributes to tidal ranges in excess of 2 m (Figure 2.6B), with the majority of coastlines in the region being macrotidal (between 4 and 6 m) (Flemming, 2002; Short and Woodroffe, 2009). Australia's highest tides have been recorded within this region including Derby in King Sound (12 m), Broome (9 m), and Wyndham in Cambridge Gulf (8m) (Figures 2.3 and 2.6B) (Short and Woodroffe, 2009). By contrast, spring tides in the southern half of the continent are all less than 2 m (i.e. the coastlines are microtidal), aside from a few locations, such as Spencer Gulf and Gulf St Vincent in South Australia and within Bass Strait (Figures 2.3 and 2.6B).

These large tidal ranges have the potential to displace the shoreline by hundreds of meters during each tidal cycle (Short and Woodroffe, 2009), complicating any sea level reconstructions as any sea level proxies employed would have a large indicative meaning. The indicative meaning is the relationship of a sea level proxy to tidal range (Shennan, 2007). Defining this relationship enables researchers to use a sea level proxy to reconstruct sea level change relative to PMSL. An indicative meaning comprises a reference water level and an indicative range where the proxy could occur (see Section 3.1 for further details). If a sea level proxy can be deposited over a tidal range of between 4 and 6 m, any relative sea level change smaller than this tidal range is likely to be obscured.

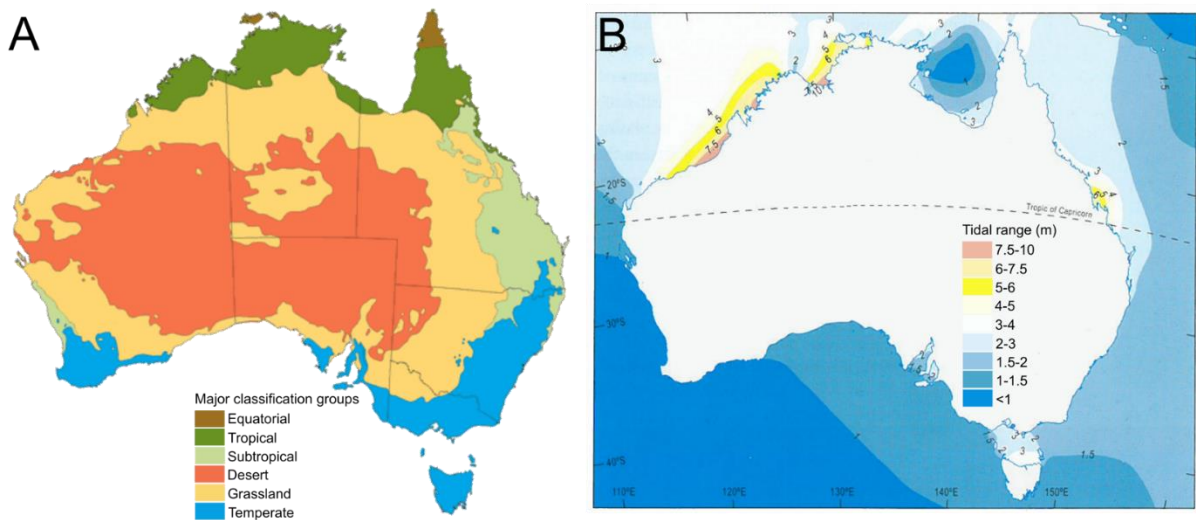


**Figure 2.6: (A) Australia's climatic zones, based on a modified Köppen classification system and derived from climate data (1961-1990) on mean rainfall, mean maximum temperature and mean minimum temperature (Source: modified from the Bureau of Meteorology (2014)). (B) Australia's spring tide range based on data from the National Tidal Centre (Source: modified from Short and Woodroffe (2009), Figure 2.13).**



The climate and tidal regimes around Australia influence the ecosystems and landforms found around the coast which, in turn, dictates the sea level proxies that are present at each location. Mangroves, for example, thrive in sheltered, macrotidal, tropical shorelines (Short and Woodroffe, 2009) and therefore are particularly prolific in the monsoonal tropical northern coast of Australia (Figure 2.7). Eighty eight percent of Australia's mangrove communities are found across the Kimberly region of northwestern Australia, the Northern Territory and Queensland (Flemming, 2002; Short and Woodroffe, 2009). Mangrove species diversity and height increase in a northerly direction, making mangrove communities along the northern shoreline highly diverse, tall, and spread over a wide area as a function of tidal range (Short and Woodroffe, 2009). Furthermore, the diverse mangrove species along the northern coast are zoned within tidal ranges (Short and Woodroffe, 2009), aiding in sea level reconstruction. It is unsurprising, then, that a large proportion of Holocene sea level studies along Australia's northern coastal margin (Figure 2.8) are in, or involve, mangrove environments.



**Figure 2.7: Distribution of mangroves around Australia (Source: Short and Woodroffe (2009), Figure 3.4).**

Mangrove fragments and wood collected from the Cambridge Gulf-Ord River that drains into Joseph Bonaparte Gulf (Jennings, 1975; Thom *et al.*, 1975), the Fitzroy River that drains into King Sound (Jennings, 1975), the Mary, Adelaide and South Alligator rivers that drain into the van Diemen Gulf (Woodroffe *et al.*, 1985, 1986, 1989, 1993; Wolanski and Chappell, 1996), and the Daly River (Chappell, 1993), have been used to reconstruct sea level along the northern margin of Australia (Figure 2.8). Along the South Alligator River, basal

mangrove sediments deposited above the valley floor returned radiocarbon dates of between  $8,267 \pm 247$  years BP to  $9,242 \pm 883$  years BP (Woodroffe *et al.*, 1986, p. 183), indicating that relative sea level was between 10 m and 12 m below PMSL prior to 9,200 years BP and rising, causing a marine transgression across the valley floor and the development of mangroves (Woodroffe *et al.*, 1986; Wolanski and Chappell, 1996). As relative sea level continued to rise, mangroves flourished as sedimentation was able to keep pace with rising sea levels, leading to an extensive mangrove forest being established by 7,400–7,850 years BP (Woodroffe *et al.*, 1985, 1986, 1989).

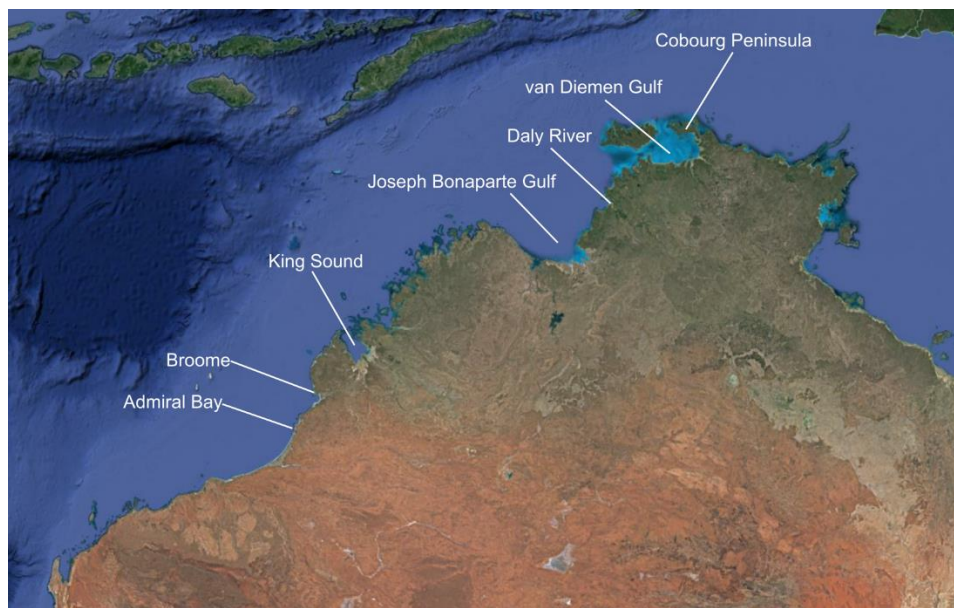


**Figure 2.8: Map of key sea level study sites along the northern margin of Australia (Source: modified from GoogleEarth, accessed 3<sup>rd</sup> March 2016).**

Similar records have been found at the Cambridge Gulf and the Fitzroy River where the oldest mangrove fragments, deposited on top of early-Holocene sand dunes, indicate that relative sea level was between 0.7 m and 4.5 m below PMSL between  $8,206 \pm 197$  years BP and  $7,036 \pm 537$  years BP (Jennings, 1975, p. 238; Thom *et al.*, 1975, p. 227). At the Daly River, mangrove swamp sediments were also deposited between  $6,015 \pm 280$  years BP and  $8,115 \pm 265$  years BP at depths from 1.5 m to 15 m below PMSL (Chappell, 1993, p. 346). Along the Adelaide River and the Mary River, mangrove sediments were deposited between 2 m and 4 m beneath the estuarine plain and were dated within the same range ( $6,957 \pm 283$  years BP,  $6,866 \pm 299$  years BP and  $6,400 \pm 480$  years BP (Adelaide River), and between  $7,621 \pm 824$  years BP and  $6,100 \pm 455$  years BP (Mary River; Woodroffe *et al.*, 1993, p. 265). As there

were no spatial trends in the radiocarbon ages spread across the entire mangrove unit, the mangroves appear to have been widespread throughout northern Australia at this time, rather than growing and shifting location as relative sea level changed (Chappell, 1993). Woodroffe *et al.* (1989, p. 737) describes this period in the Holocene sea level record of northern Australia as the “big swamp” phase.

All but one study of the mangrove sea level record in northern Australia conclude that relative sea level reached PMSL sometime between 5,500 and 6,800 years BP, where it stabilized, with no indication of a mid-Holocene highstand occurring (Thom *et al.*, 1975; Woodroffe *et al.*, 1985, 1986, 1989, 1993; Chappell, 1993; Wolanski and Chappell, 1996). As sea level stabilized and sedimentation continued, mangroves persisted for a time until increased sedimentary input into the catchment led to coastal progradation and vertical accretion of the tidal flat, with alluvial clay being deposited above the palaeo-mangrove deposits, causing a shift in the intertidal environment necessary for mangrove growth and the decline of mangroves, with mangroves then only present along active fluvial channels (Thom *et al.*, 1975; Woodroffe *et al.*, 1985, 1986; Chappell, 1993). At the South Alligator River, mangroves began declining from approximately 6,300 years BP and were replaced by sedges and grasses by 4,500 years BP (Woodroffe *et al.*, 1986). Similarly, mangroves began to decline along the Daly River over the last 5,700 years (Chappell, 1993), while at the Cambridge Gulf, Thom *et al.* (1975, p. 227) found that mangroves reached their maximum extent at approximately  $5,564 \pm 597$  years BP before declining. Mangroves along the Adelaide and Mary River persisted for a longer period of time, up to  $4,687 \pm 758$  years BP and  $4,450 \pm 813$  years BP, respectively (Woodroffe *et al.*, 1993, p. 265).

While there is a lack of evidence for a mid-Holocene sea level highstand from the palaeo-mangrove deposits described above, this may be due to sediment compaction. Post-deposition compaction of mangrove sediments may occur as new sediments are deposited due to the highly organic nature of the sediments, which will in turn affect the accuracy of sea level reconstruction by lowering the reconstructed sea level elevation (Bird *et al.*, 2004; Murray-Wallace and Woodroffe, 2014). Both Thom *et al.* (1975) and Woodroffe *et al.* (1986) downplay this possibility, with Thom *et al.* (1975, p. 226) writing that “...sediment compaction and tectonic movement of the land relative to the sea have not significantly affected depositional processes over the past 8000 years or so...” and Woodroffe *et al.* (1986, p. 125) stating that “...one source of error which is known to affect mangrove sediments is compaction of muds and consequent downward displacement of material. This does not appear to have had a major

effect, as there is good agreement in terms of age and depth between basal samples, which cannot have been compacted, and those from above large unconsolidated sediment...”.

The large tidal ranges along the northern Australian coastline (Figure 2.6) may have also obscured the evidence of a highstand, had there been one. Mangroves form between MSL and MHWS (Cohen *et al.*, 2005; Zong, 2007; Ellison, 2008; Geoscience Australia, 2015c; Waller, 2015). As such, in locations where the tidal range, and therefore the elevation difference between MSL and MHWS, is small, mangrove sediments can accurately constrain past relative sea levels at elevation changes of less than 1 m (see Section 6.4.2.1 for a comprehensive example of the use of mangrove sediments as a sea level proxy). However, along the northern Australian coastline, where tidal ranges often exceed 5 m, mangrove sediments can be deposited over a much larger elevation range, and any relative sea level highstand is likely to be obscured.

Geophysical modelling predicted a mid-Holocene highstand higher than present day sea levels in the van Diemen Gulf (Lambeck and Nakada, 1990). Lambeck and Nakada (1990) suggested that the lack of observed evidence of a highstand may be due to local subsidence from continental tilting (see Section 2.1.2) and that more studies are required. Even in the 21<sup>st</sup> century, according to Lessa and Masselink (2006, p. 101), “...the northwest of Australia is the only sector of the Australian coastline lacking sound evidence of higher sea level during the mid- to late-Holocene...”.

Evidence does exist that suggests a mid-Holocene relative sea level highstand along the northern margin of Australia. Contrary to the study by Thom *et al.* (1975), a study by Jennings (1975) indicates that there is evidence for sea levels higher than PMSL during the mid-Holocene in the Cambridge Gulf and Fitzroy River. By examining mangrove and shore facies that overlie, and are also bordered by, Quaternary red sand dunes, Jennings (1975) concluded that, as relative sea level rose and transgressed the shoreline, mangroves became widespread along the coast, depositing sediments above and around the sand dunes. By radiocarbon dating wood fragments within the mangrove clay, Jennings (1975, p. 238) concluded that relative sea level was between +1 m and +2 m above PMSL sometime between  $6,840 \pm 431$  years BP and  $1,120 \pm 158$  years BP, before falling to PMSL.

More recent studies along Buckley’s Plain in Broome (Lessa and Masselink, 2006) and at Admiral Bay, 110 km southwest of Broome (Engel *et al.*, 2014) also support a mid-Holocene sea level highstand in northern Australia (Figure 2.8). At Admiral Bay, a mangrove unit

deposited 2–5 m below present mean high water (MHW), above Pleistocene sandstone, was radiocarbon dated to 8,203–8,326 years BP (Engel *et al.*, 2014). By around 7,000 years BP, relative sea level was between -2.5 m and +0.5 m relative to present MHW, and intertidal coarse sand was deposited above the mangrove muds, changes in line with the mangrove evidence presented above (Engel *et al.*, 2014). While the ongoing sea level rise over the mid-Holocene period is missing from the Admiral Bay sea level record (there is a gap in the data between 6,900 and 2,100 years BP), a backshore deposit found +1.5 m above present MHW and radiocarbon dated between  $2,095 \pm 58$  years BP and  $824 \pm 47$  years BP indicates a mid-Holocene highstand that persisted until approximately 800 years BP before falling rapidly to present (Engel *et al.*, 2014, p. 730). Similarly, an upper mud flat deposit at Buckley's Plain, found +1 m above present MHW and radiocarbon dated to  $2,836 \pm 83$  years BP, led Lessa and Masselink (2006, p. 104) to conclude that relative sea level was at least +1 m above PMSL during the mid-Holocene highstand and fell to PMSL within the last 2,000 years. At Smith Point on the Cobourg Peninsula (Figure 2.8), Woodroffe *et al.* (1992) found a notch in exposed bedrock, located behind a mid-Holocene sequence of beach ridges, and concluded that relative sea level was zero to +1 m above PMSL between 5,000 and 6,000 years ago. Unfortunately, the studies by Woodroffe *et al.* (1992), Lessa and Masselink (2006) and Engel *et al.* (2014) were unable to provide more details on a possible mid-Holocene highstand in northern Australia due to a lack of data.

Figure 2.9 summarizes all the information available on relative sea level change across northern Australia. Note that the sea level envelope of Western Australia compiled by Lewis *et al.* (2013) includes sites outside of Region A, across the western and southern margins of Western Australia, that have experienced a higher mid-Holocene highstand than that recorded for the northern coastline. This accounts for the higher mid-Holocene sea level envelope from Western Australia that contains no sea level index points. Because the Western Australia sea level envelope also contains evidence from the Joseph Bonaparte Gulf and King Sound, it has been included in this graph. Along the northern margin of Australia, relative sea level was approximately 10–14 m below PMSL prior to 9,000 years BP and rising. Sea level reached PMSL approximately 5,500–6,800 years BP and continued to rise, resulting in a mid-Holocene highstand between 0 m and +1 m (potentially as high as +2 m) above PMSL. Sea level likely remained at this highstand until at least 1,000–2,000 years BP, before falling to PMSL.

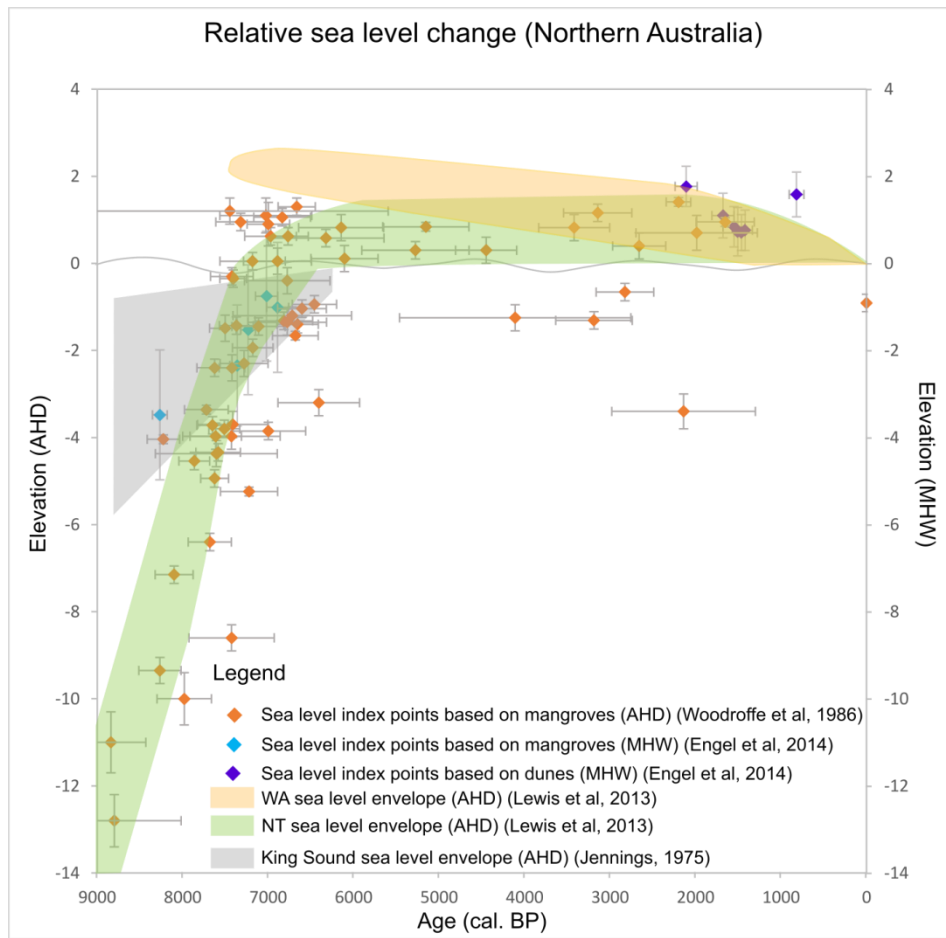


**Figure 2.9: Compilation of sea level index points from studies around the northern Australian margin across Region A.** Sea level envelopes are also included for the Northern Territory (NT) and Western Australia (WA) (data from Figures 3 and 7 in Lewis *et al.*, 2013) and King Sound in WA (data from Figure 18 in Jennings, 1975). Note that the data from Engel *et al.* (2014) are referenced to mean high water (MHW) while all the other index points and sea level envelopes are referenced to mean sea level, Australian Height Datum (AHD).

While there appear to be numerous sea level index points on the graph in Figure 2.9, most of these are derived from just two studies, those of Woodroffe *et al.* (1986) and Engel *et al.* (2014). Furthermore, most of these sea level index points have been derived from mangrove sediments which is complicated by potential sediment compaction and the large tidal ranges experienced in northern Australia. Future research should investigate whether alternate sea level proxies are present around the northern Australian coastline which can then be compared with this mangrove evidence. In general, the northern Australian coastline is still understudied, particularly the arid regions of northwestern Australia which are especially remote (Semeniuk, 1995; Lessa and Masselink, 2006; Engel *et al.*, 2014). More research is required to fine-tune the sea level envelope for northern Australia.

### 2.3 Sea level change in eastern Australia

The eastern coast of Australia, from the tip of Cape York Peninsula down to the border of Queensland and NSW (Figure 2.5), is characterised by equatorial, tropical and subtropical environments (Figure 2.6A). Unlike the arid western and northwestern coast of Australia, the northwest monsoons and the southeast trade winds bring precipitation to the Queensland coast, and mangroves and salt marshes thrive (Figure 2.7) (Short and Woodroffe, 2009). The entire east coast of Australia is influenced by the southwest Pacific tidal system, with the tides increasing in height towards the north, where shoaling across the wide and shallow continental shelf, along with a convergence and resonance, results in all tides exceeding 2 m along the eastern Queensland coast, and reaching 8 m in the Broad Sound region (Figure 2.6B) (Short and Woodroffe, 2009). Similarly to the northern coastline of Australia, these large tidal ranges would complicate any sea level reconstruction due to the large indicative meaning and range any sea level proxies would have (see Section 2.2).

The eastern coastline of Australia has a wide and variable continental shelf, with shelf widths of over 200km (Figure 2.4) (Hopley *et al.*, 2007), making the impact of post-glacial hydro-isostatic loading particularly significant and complicating the construction of a regional sea level curve. This region also includes the eastern coastline of Cape York Peninsula, which is intimately connected to sea level change on the western coastline of Cape York Peninsula, where the study area of Albatross Bay is located. Because the eastern coastline of Cape York Peninsula fringes the Coral Sea, which is almost entirely open ocean (Figure 2.5), while the western coastline of Cape York Peninsula is within the smaller semi-enclosed GoC, a larger water load was imposed on the eastern margin of Cape York Peninsula during the post-LGM sea level rise. This hydroisostatic loading caused the eastern coast of Cape York Peninsula to deform and submerge downwards relative to the western coastline. Relative sea level during the mid-Holocene highstand thus attained higher elevations around the coastline of the GoC, than along the coastline fringing the Coral Sea (Chappell *et al.*, 1982; Woodroffe *et al.*, 1989).

The most prominent coastal feature along the eastern Queensland coast is the Great Barrier Reef (GBR). While coral reefs are present across the entire northern margin of Australia (Figure 2.10), the GBR is the largest expanse of reef in Australia. Spreading across the broad continental shelf of eastern Queensland and stretching up to 250 km wide in places, the GBR is the largest coral reef system in the world (Short and Woodroffe, 2009), forming as the post-LGM marine transgression flooded the continental shelf (Hopley *et al.*, 2007). Coral reefs and microatolls are potentially one of the best sea level proxies available in far field sites where sea

surface temperatures remain above 20°C throughout the year (Zong, 2007; Montaggioni and Braithwaite, 2009). As coral reefs cannot survive more than a brief exposure to air, they will only grow to around the mean low water level (MLW) (Woodroffe, 2007; Montaggioni and Braithwaite, 2009). Corals therefore have a narrow vertical depth range, which, combined with being able to date them using radiocarbon and/or uranium-thorium methods, makes them valuable sea level proxies (Zong, 2007). When coral reef colonies reach the maximum elevation of their growth beneath MLW, they begin to grow outwards forming a flat discoidal surface termed a “microatoll” (Woodroffe, 2007). When found in growth position, fossil microatolls provide a precise indicator of relative sea level and sea level variations, with water level fluctuations recorded on the upper surface of a microatoll as a series of concentric undulations, while more permanent relative sea level falls will form a series of terraces with fossil terraces at the highest elevations and a living coral terrace continuing to form laterally beneath the water surface (Woodroffe, 2007; Montaggioni and Braithwaite, 2009; Yu *et al.*, 2009; Mann *et al.*, 2016).

Coral reefs and microatolls are therefore one of the common sea level proxies employed in the reconstruction of LGM and Holocene sea level change along the Queensland coast. However, there is little data available on relative sea level rise during the post-LGM to early Holocene period within the coral record because the substrate upon which the coral reefs grow is relatively shallow and thus was only inundated late in the post-glacial marine transgression period (Hopley *et al.*, 2007). According to Hopley *et al.* (2007), the earliest radiocarbon dates obtained from the GBR complex, from Boulder Reef and Hayman Island (Figure 2.3), date to approximately 9,500 years ago, indicating that the GBR complex started forming only after approximately 10,000 years ago, when sea level was 15–20 m below PMSL and rising – an age with which Chappell *et al.* (1983) concur. While fringing reefs grew at lower levels through the post-glacial marine transgression, their depths make sampling difficult, and thus, little Pleistocene and early-Holocene sea level data has been obtained (Hopley *et al.*, 2007) and the coral microatolls of the GBR have been used to reconstruct sea level change mainly from the mid-Holocene to present.





**Figure 2.10: Distribution of coral reefs around Australia (Source: Short and Woodroffe (2009), Figure 3.4).**

Pleistocene and Holocene sea level reconstructions along the Queensland coastline are also complicated by the variable width of the continental shelf (Figure 2.4) which causes differential hydro-isostatic warping and thus relative sea level change through time (Hopley, 1978; Woodroffe, 2009a; Lambeck *et al.*, 2010). These variable local sea level histories have contributed to controversy in reconstructing sea level change in eastern Australia, with debates once again surrounding, firstly, the existence of a mid-Holocene highstand (Thom *et al.*, 1969; Gill and Hopley, 1972; Thom *et al.*, 1972; Cook and Polach, 1973; Hopley, 1978; Belperio, 1979; Lambeck *et al.*, 2010), secondly, the timing and magnitude of the mid-Holocene highstand and, thirdly, whether relative sea level fall following the highstand was smooth or oscillating (Lambeck *et al.*, 2010). Sea level studies along the eastern coast of Queensland (Region B, Figure 2.5) are more comprehensive than along the northern margin of Australian (Region A, Figure 2.5), but detailed Holocene sea level reconstructions are still lacking in large portions of the GBR. Such data is required to deepen the understanding of the sea level history of the GBR and the eastern coast of Queensland (Hopley *et al.*, 2007; Lewis *et al.*, 2013).

Sea level indicators in coastal and marine sediments have been used to create a sea level envelope for the area. At Cleveland Bay, mangrove deposits indicate that relative sea level was between 24 m to 30 m below PMSL between  $10,025 \pm 475$  years BP and  $10,800 \pm 1,150$  years BP (Figure 2.11) (Ohlenbusch, 1991; Tye, 1992; both cited in Woodroffe, 2009b, p. 2478, 2479). By 8,500–9,500 years BP, relative sea level had risen to approximately 10–15 m below PMSL (Belperio, 1979; Carter *et al.*, 1993), with a subtidal foraminifera sea level transfer function by Horton *et al.* (2007a, p. 50) indicating that sea level was -8.9 m below PMSL by

approximately  $8,964 \pm 366$  years BP and was within -1 m of PMSL by approximately 7,000 years BP. Further north, mangrove sediments collected from Innisfail and Hinchinbrook Island corroborate this sea level record (Figure 2.11), with the Innisfail record indicating that relative sea level was 23 m below PMSL approximately 10,000 years BP (Gagan, 1990) and the oldest mangrove sediments dated at Hinchinbrook Island indicating that relative sea level was between 14 m and 18 m below PMSL by approximately 9,000–10,000 years BP (Grindrod and Rhodes, 1984). However, at Hinchinbrook Island, sea level reached PMSL later than at Cleveland Bay and was 5.8 m below PMSL by approximately 8,000 years BP and 1.4 m below PMSL at approximately 5,500 years BP (Bloom, 1980). Sea level was only within 1 m below PMSL at approximately 4,500 years BP, reaching PMSL prior to 3,000 years BP (Grindrod and Rhodes, 1984). Other mangrove records from Deerel (Crowley *et al.*, 1990), along with a dune barrier at Hinchinbrook Island (Pye and Rhodes, 1985) agree well with data from Grindrod and Rhodes (1984) (Figure 2.11).

Subtidal and intertidal foraminifera transfer functions indicate that a mid-Holocene relative sea level highstand occurred at Cleveland Bay, and relative sea level reached a height of +1.7 m above PMSL, at approximately 7,200 years BP (Horton *et al.*, 2007a), and a maximum of approximately +2.8 m above PMSL about 6,200 years BP (Woodroffe, 2009b). Relative sea level then fell to between +1.3 m and +2.1 m of PMSL by approximately 3,700 years BP, remained at this elevation until 2,300 years BP and at +1 m above PMSL until at least approximately 1,500 years BP before falling slowly to present within the last 1,000 years (Woodroffe, 2009b). At Alva Beach, Townsville, Halifax Bay and the Burdekin delta (Figure 2.11), sea level data compiled by Larcombe *et al.* (1995) indicate that relative sea level reached 0.67 m below PMSL at  $7,572 \pm 133$  years BP (Carter, unpub; cited in Larcombe *et al.*, 1995, p. 10, 11) where it remained relatively stable, between 1.5 m below PMSL to +1.8 m above PMSL with large error margins that cross PMSL. However, mangroves within Princess Charlotte Bay (Figure 2.11) were found at near-uniform depth from  $7185 \pm 233$  years BP to  $580 \pm 192$  years BP, which may indicate that, similar to the northern Australia sea level record (Section 2.2), sea level remained constant over the mid-Holocene to present (Chappell and Grindrod, 1984, p. 205). However, Chappell and Grindrod (1984) suspect that, in this case, sediment compaction has eliminated the evidence of a mid-Holocene highstand because the bulk density of the mangrove sediments increases towards the rear of the swamp, indicating that compaction has occurred.

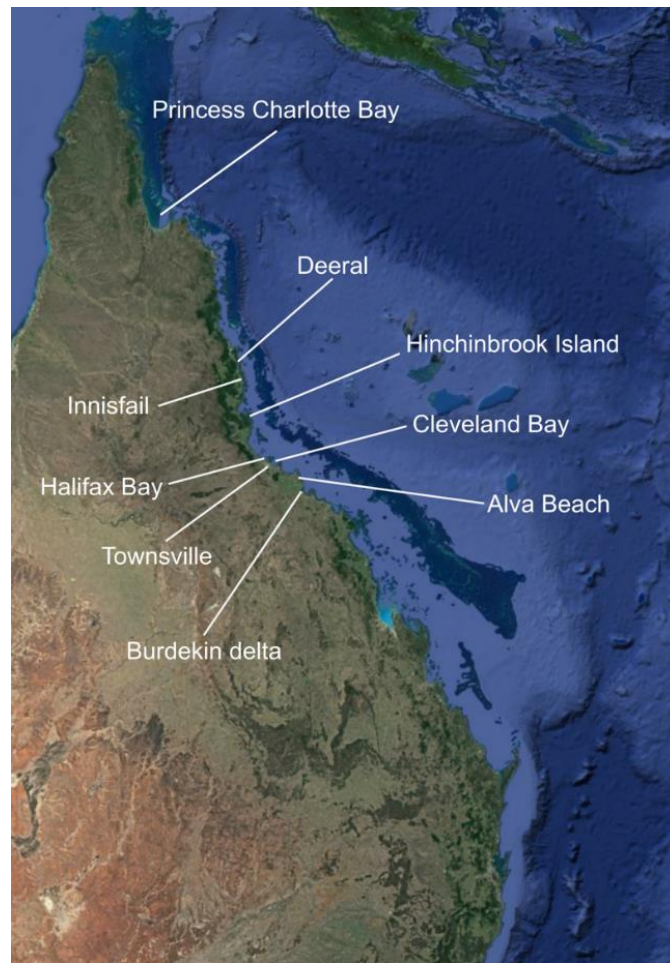


**Figure 2.11: Map of key sea level study sites along the eastern margin of Australia that utilise sedimentary deposits and microfossils as sea level indicators (Source: modified from GoogleEarth, accessed 3<sup>rd</sup> March 2016).**

Coral microatoll sea level records and other FBIs studied from around the GBR are in general agreement with the sedimentary record, though the maximum heights of the mid-Holocene sea level highstand deduced from the data is generally between +1 m to +1.3 m above PMSL (Hopley, 1978, 1983; Hopley *et al.*, 2007). However, while some coral-based sea level reconstructions state that sea level fell smoothly to PMSL following the mid-Holocene highstand, others postulate the existence of an extended mid-Holocene highstand, where sea level remained at a “stillstand” for a period, before falling to PMSL. Coral microatolls studies span the GBR, from as far north as King Island down south to Moreton Bay (Figure 2.12). At Flinders Island, King Island, Dunk Island, Fantome Island, Goold Island, the Palm Islands, Orpheus Island, Camp Island and Stone Island (Figure 2.12), extensive studies by Chappell (1983) and Chappell *et al.* (1983) found that relative sea level reached a maximum of approximately +1 m above PMSL at around 6,500 years BP, then relative sea level fell smoothly to present, with no evidence of a stillstand or any secondary oscillations. The earliest

date that sea level reached the mid-Holocene highstand was recorded at Stone Island, where relative sea level was approximately +1 m above PMSL at  $6865 \pm 275$  years BP, while the latest date was recorded at the Palm Islands where relative sea level was +0.85 m above PMSL at  $5820 \pm 245$  years BP (Chappell *et al.*, 1983, p. 226).

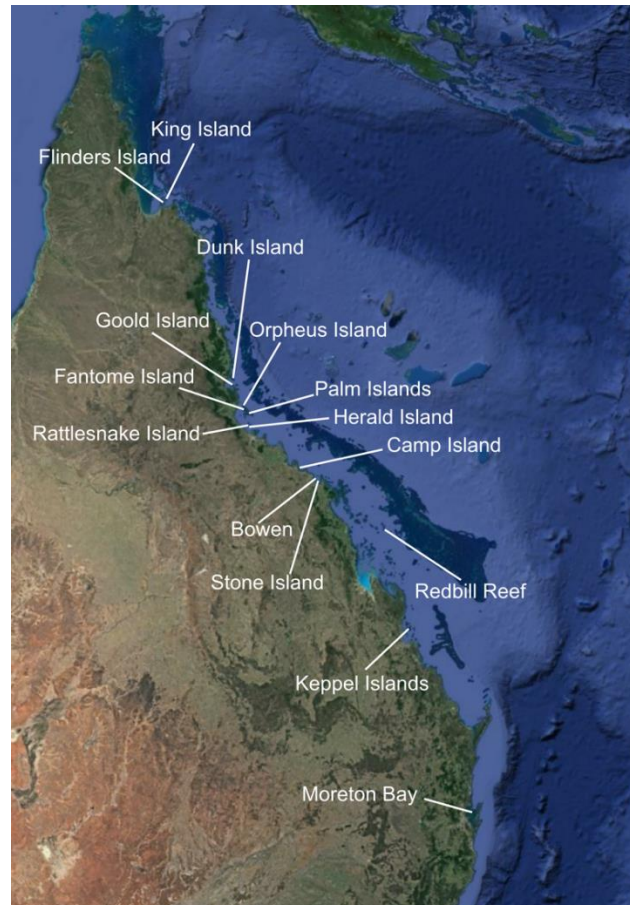


**Figure 2.12: Map of key sea level study sites along the eastern margin of Australia that utilise corals and coral microatolls as sea level indicators. These study sites show no indication of a mid-Holocene sea level stillstand (Source: modified from GoogleEarth, accessed 3<sup>rd</sup> March 2016).**

At Bowen and Rattlesnake Island, Hopley (1983, p. 96, 98) recorded coral microatolls +1.25 m above PMSL at  $5,633 \pm 278$  years BP and  $5,906 \pm 290$  years BP respectively, and found coral microatolls at a similar elevation (but undated) at Herald Island (Figure 2.12). At the Keppel Islands (Figure 2.12), coral microatolls indicated that relative sea level was approximately +0.5 m to +0.8 m above PMSL at around 6,500 years BP, falling to approximately +0.3 m above PMSL at 2,800 years BP and +0.2 m above PMSL by 970 years BP (Leonard *et al.*, 2015). In Moreton Bay (Figure 2.12), coral microatoll evidence pointed to a relative sea level at least +1.1 m above the MLW between 6,600 and 5,700 years BP, after

which relative sea level either fell rapidly or climatic and/or environmental changes caused the termination of reef growth, with no corals found after this date (Leonard *et al.*, 2013). This reconstructed +1 m mid-Holocene highstand agrees well with geophysical models of the area (Chappell *et al.*, 1982). At Redbill Reef (Figure 2.12), the mid-Holocene highstand occurred later than the other coral microatoll records indicate, with relative sea level reconstructed at +1.4 m above PMSL between 4,800 and 4,000 years BP (Hopley, 1983).

Rather than an immediate fall to PMSL following the mid-Holocene sea level highstand, other evidence from corals and intertidal FBIs indicate that relative sea level remained at a mid-Holocene stillstand before falling to PMSL. At Yule Point (Figure 2.13), Chappell *et al.* (1983, p.266) recorded the mid-Holocene highstand at +1.2 m above PMSL at  $5,145 \pm 266$  years BP. Bird (1971, p. 113) obtained a radiocarbon date of  $4,225 \pm 253$  years BP for the same fossil reef at +1.2 m PMSL at Yule Point, indicating that rather than an immediate sea level fall, relative sea level may have remained at this highstand for at least 1,000 years. McLean *et al.* (1978) did an extensive survey of emergent fossil corals along the northern GBR and obtained radiocarbon dates and elevation data for selected coral microatolls within their dataset, including microatolls at Petherbridge Island, Houghton Island, Leggatt Island, Low Wooded Isle, Nymph Island and Three Isles (Figure 2.13). Instead of a smooth sea level fall, McLean *et al.* (1978) proposed an extended sea level stillstand, suggesting that relative sea level reached PMSL approximately 6,500 years BP and continued to rise, reaching at least +1 m above PMSL by 6,200 years BP and remaining there until approximately 3,700 years BP whereupon it began to fall, but was still at a higher elevation of approximately +0.6m above present at  $1,988 \pm 183$  years BP (McLean *et al.*, 1978, p. 174).



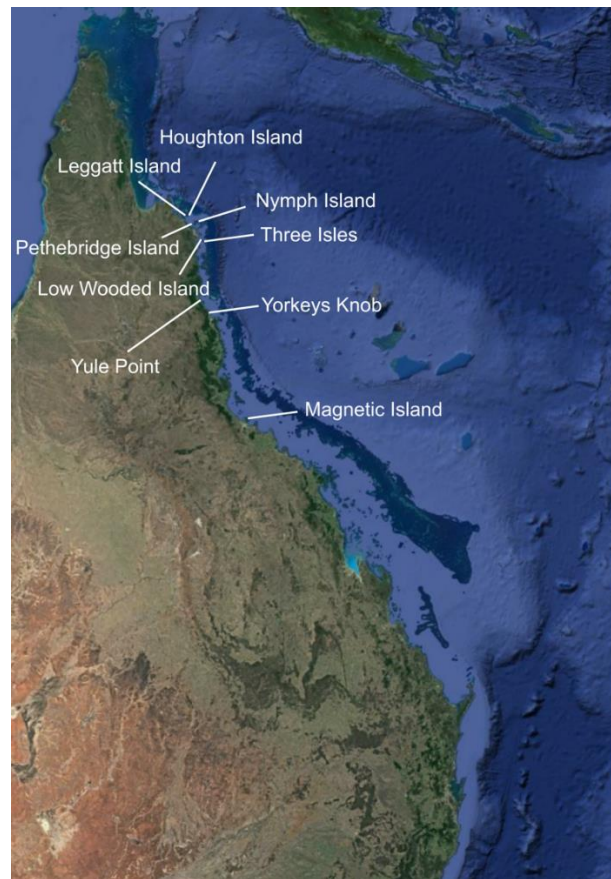


**Figure 2.13: Map of key sea level study sites along the eastern margin of Australia that utilise corals and coral microatolls as sea level indicators. These study sites indicate that mid-Holocene sea level remained at a stillstand prior to falling to PMSL (Source: modified from GoogleEarth, accessed 3<sup>rd</sup> March 2016).**

At Magnetic Island (Figure 2.13), uranium-thorium dating of coral microatolls indicate that relative sea level was a minimum of +0.7 m higher than present by approximately 7,000 years ago (Yu and Zhao, 2010). Relative sea level continued to rise and reached a mid-Holocene highstand of between +1 m and +1.6 m PMSL sometime between 6,700 and 5,000 years ago, where it remained until approximately 2,200 years ago before falling to PMSL (Yu and Zhao, 2010). Chappell *et al.* (1983) found that relative sea level at Magnetic Island was at an elevation of +0.15 m above PMSL by approximately 400 years BP. Intertidal FBIIs at Magnetic Island (fossil oyster beds and barnacles) have been studied by Beaman *et al.* (1994), Higley (2000), Lewis *et al.* (2008) and Lewis *et al.* (2015). The fossil oyster beds on Magnetic Island agree with the coral microatoll record, indicating that relative sea level was approximately +1.65 m above PMSL around 6,300 to 4,000 years BP, with no fossil oysters found above this elevation and scattered fossil barnacles only extending decimetres above it (Beaman *et al.*, 1994). Sea level remained at this highstand before falling smoothly to present day after  $4,052 \pm 159$  years BP (Beaman *et al.*, 1994, p. 883). Lewis *et al.* (2015, p. 25) recorded

relative sea level still being +1 m above present before  $1,225 \pm 75$  years BP before reaching present day levels by  $760 \pm 120$  years BP. Further north, fossil oyster beds at Yorkeys Knob, near Cairns (Figure 2.13), agree well with the FBI record at Magnetic Island, indicating that relative sea level was +0.8 to +0.9 m higher than present between 800 and 900 years BP before falling to PSML (Wright, 2011).

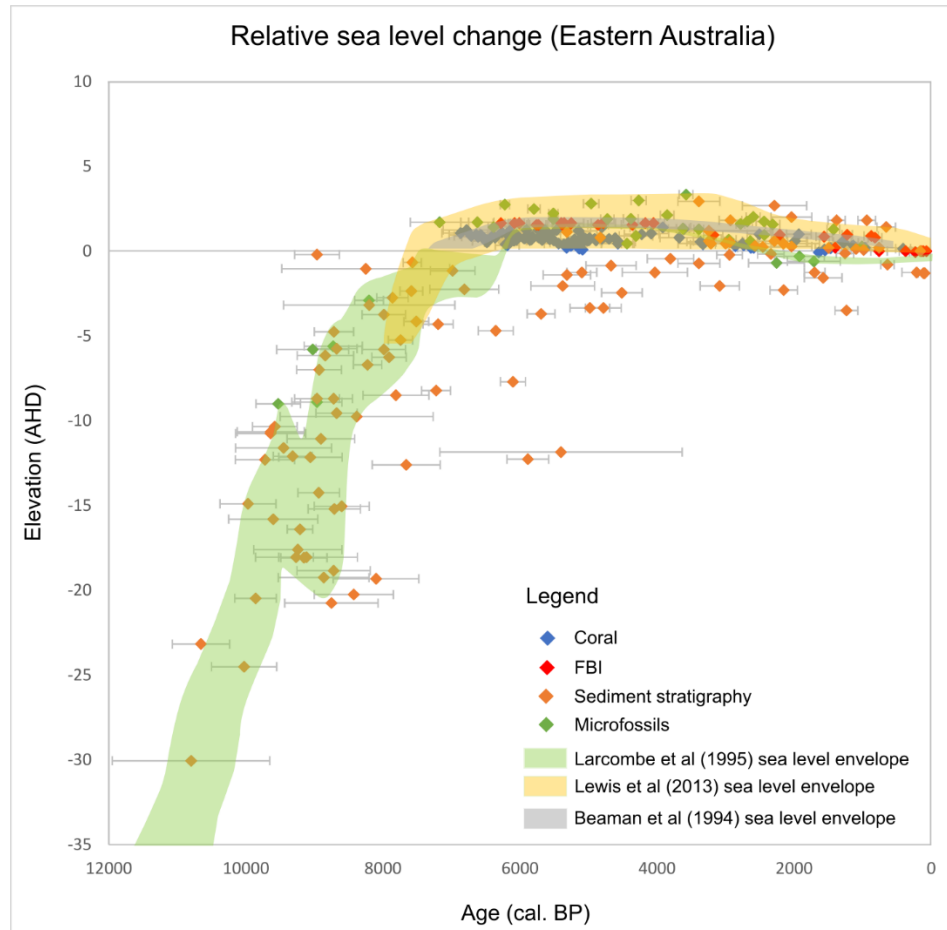


**Figure 2.14: Compilation of sea level index points around the eastern Queensland coast (Region B). Sea level envelopes are drawn from data in Lewis *et al.* (2013) Figure 4, Larcombe *et al.* (1995) Figure 9, and Beaman *et al.* (1994) Figure 4.**

Figure 2.14 illustrates all the available sea level index points from eastern Queensland and includes sea level envelopes compiled by various researchers. Sea level index points based on sediment stratigraphy, including mangrove muds, have the largest potential elevation errors, and index points that are lower than the other indicators, in part due to sediment compaction and uncertainties associated with the large tidal range along some areas of the eastern coast of Australia. For instance, Beaman *et al.* (1994) argue that sea level reconstructions from

Queensland that are based on buried Holocene mangrove muds may require between 1 m and 5 m of upward correction. However, sedimentary and microfossil evidence is also able to extend the sea level record past the Holocene sea level highstand where FBI and coral evidence is lacking. Thus, while FBI and coral evidence is often considered more reliable sea level indicators (Lewis *et al.*, 2013), the sedimentary evidence should not be dismissed. However, the sea level reconstruction envelopes do favour coral, microfossil and FBI evidence where they are available (Figure 2.14).

As indicated by Figure 2.14, evidence points to a rapidly rising sea level over the early Holocene, with modern day levels reached along the eastern coast of Queensland as early as 8,000 years BP. All lines of evidence point to sea level continuing to rise, reaching a mid-Holocene highstand after approximately 6,000 BP, though the timing and magnitude of this highstand differs from +3.34 m above PMSL at  $3,577 \pm 100$  years BP (based on foraminifera; Woodroffe, 2009b, p. 2482) to +0.5 m above PMSL at  $5927 \pm 292$  years BP indicated by some coral microatoll evidence (Chappell *et al.*, 1983, p. 226). While Chappell *et al.* (1983) argue that sea level then fell smoothly to present day, more recent sea level evidence and compilations indicate a sustained highstand followed by a fall after 2,000 BP (Larcombe *et al.*, 1995; Lewis *et al.*, 2008).

The published sea level envelope of Larcombe *et al.* (1995) also includes a sea level oscillation between approximately 9,500 and 9,000 years BP, fuelling debate about a smooth versus oscillating sea level change within the sea level records from the eastern coast of Queensland (see Section 2.1.2). Larcombe *et al.* (1995) stated that an episodic sea level rise with sea level oscillations fits best with the evidence they had obtained. Other studies also proposed sea level oscillations, this time over the mid- to late-Holocene. Lewis *et al.* (2008) suggested that FBI evidence compiled across eastern Australia indicate two potential periods of sea level fall of between 0.3 m and 1 m, occurring around 4,600 and around 2,800 years BP, before sea level rose again to a highstand. At the Keppel Islands, Leonard *et al.* (2015) also suggested sea level oscillations with sea level falling by at least 0.4m between 5,500 and 5,300 years BP before returning to higher levels. Such oscillations remain contentious and more study is necessary to understand the nature of Holocene sea level change along the eastern coast of Queensland.



## 2.4 Sea level change in the Gulf of Carpentaria

The GoC is a semi-enclosed, shallow, epicontinental sea located between Australia and New Guinea (Figures 2.5 and 2.15). It currently has a maximum depth of 70 m, although the nearshore zone is often less than 20 m deep (Woodroffe and Chappell, 1993). It is bordered to the east by the Torres Strait, which is 12 m deep, and to the west by the Arafura Sill that is 53 m deep (Figure 2.3) (Chivas *et al.*, 2001). The eastern Arafura tidal system rotates clockwise around the GoC, with shorelines within the GoC generally experiencing low tidal ranges that average between 1 m and 2 m, increasing near and across the Torres Strait to more than 2 m (Figure 2.6B) (Reeves *et al.*, 2008; Short and Woodroffe, 2009). Tides within the GoC vary from semi-diurnal to fully diurnal, and are strongly affected by changing meteorological conditions, such as monsoonal winds that can cause annual positive and negative surges of up to  $\pm 1$  m (Davies, 1977; Rhodes, 1982). Wave energies within the GoC are low to moderate, although the occasional tropical cyclone during the wet season results in high wave energy and causes storm surges that have a significant impact on the coastal plain (Davies, 1977; Rhodes, 1982; Bird, 2005). These storm surges are the result of a combination of the low-pressure weather system caused by the tropical cyclone, the onshore winds pushing sea water to the coast, along with increased fluvial discharge (Rhodes, 1982; Bureau of Meteorology, 2018). As the majority of the GoC coast is low-lying, such changes in sea level can have a significant geomorphic impact on coastal features (Davies, 1977).



**Figure 2.15: Map of key sea level study sites within the Gulf of Carpentaria (Source: modified from GoogleEarth, accessed 3<sup>rd</sup> March 2016).**

While coral reefs are present within the GoC, particularly around the Wellesley Islands in the south and Groote Eylandt in the west (Figure 2.10), they are largely found between depths of 14–30 m below PMSL (Harris *et al.*, 2004; Harris *et al.*, 2008). Near-surface coral reefs, such as those found within the GBR, are absent. The coral reefs within the GoC started growing at around 10,500–9,500 years BP but stopped growing by approximately 7,000 years BP (Harris *et al.*, 2008). Possible reasons for the cessation of reef growth in the GoC include the slow rate of reef growth relative to sea level rise, changes in water turbidity, and changes in ocean circulation around the GoC leading to poor dispersal of coral larvae (Harris *et al.*, 2008). Coral records therefore have not been utilised in sea level studies within the GoC. Instead, the western and southern coastline of the GoC is fringed by a wide belt of mangrove swamps, supratidal mudflats, salt marshes and salt pans (Figures 1.8 and 2.7), while the eastern coastline is dominated by beach ridge and chenier systems (Figure 1.9) (Flemming, 2002). Sea level studies from the GoC rely on these sea level proxies in their reconstruction.

Relative sea level has changed dramatically over the Quaternary within the GoC. During glacial periods, when sea levels fell below the height of the Arafura Sill and Torres Strait, the Gulf became separated from the Indian Ocean to the west and the Pacific Ocean to

the east, forming a large fresh-to-brackish waterbody called “Lake Carpentaria” (Torgersen *et al.*, 1988; Woodroffe, 1993; Woodroffe and Chappell, 1993; Yokoyama *et al.*, 2001). Between 80,000 years BP and 40,000 years BP, sea levels repeatedly entered and receded from the GoC, with the GoC last becoming a freshwater lake during the last glacial period, from approximately 40,000–12,000 years BP (Nott, 1996; Chivas *et al.*, 2001). The timing of the most recent marine inundation into the GoC is recorded in its sedimentary facies, ostracod assemblages, and their shell chemistry, all of which indicate a marine transgression commencing approximately 12,000 years ago as sea level rose above -53 m relative to PMSL and breached the Arafura Sill (McCulloch *et al.*, 1989). A fully marine environment was present by approximately 10,500 years BP and, by approximately 8,000–7,000 years BP, sea level rose above -12 m relative to PMSL and crossed the Torres Strait Sill, linking the GoC to the Coral Sea (McCulloch *et al.*, 1989; Reeves *et al.*, 2008).

As relative sea level rose within the GoC, from the shallower Lake Carpentaria to the present deeper levels, this would cause significant changes in the tidal regime within the Gulf. Tidal currents would be stronger in shallow water depths, weakening as relative sea level continued to rise (Kantha and Clayson, 2000). Furthermore, tidal ranges would be more spatially variable, and likely higher, in a shallower GoC, leading to complications in determining the indicative meaning of sea level proxies. The relative sea level rise will also alter the configuration of coastal features and the evolution of the coastline. Paleotidal modelling is required to account for changes in the tidal regime over the course of the period of sea level reconstruction (see, for example, Khan *et al.*, 2017). However, such models are unavailable within the GoC and the construction of such a model is beyond the scope of this research.

Sea level reconstructions are often inherently based on the assumption that wave climate and tidal ranges have not changed significantly throughout the period of reconstruction (e.g. Baker *et al.*, 2001). While such an assumption is likely false, they are a necessary evil in palaeoenvironmental research – one needs to hold some factors constant in order to reconstruct others since it is impossible to directly observe and measure these changes. Sloss *et al.* (2007, p. 1011) notes this in a review of sea level change in southeastern Australia, stating that there is a “... lack of data relating to changes in tidal range, wave climate and the configuration of the nearshore zone during the mid Holocene...”. Larcombe *et al.* (1995, p. 39) also writes that “... reconstruction of ancient sea levels necessarily assume that tidal range has been similar for the duration of inundation of the GBR shelf. However, this is unlikely as increasing water depth

and changing coastal and bathymetric configurations will have significantly changed tidal characteristics...”. Therefore, the effect of these changes on sea level proxies remain unaccounted for in any sea level studies from the GoC. However, the GoC was fully marine by approximately 10,500 years BP (McCulloch *et al.*, 1989; Reeves *et al.*, 2008). Therefore, tidal changes would be less significant when reconstructing relative sea level change over the mid- to late-Holocene in the GoC as opposed to during the early- to mid- Holocene when the GoC was transitioning from Lake Carpentaria to a shallow GoC to its current extent.

Studies indicate that relative sea level within the GoC reached present levels in the early to mid-Holocene, before continuing to rise to above PMSL. Relative sea level attained different highstand elevations at various locations around the GoC for different lengths of time (Rhodes, 1980; Chappell *et al.*, 1982; Nakada and Lambeck, 1989; Lambeck and Nakada, 1990; Nott, 1996). While these variations are most likely caused by differential hydroisostasy, there are still few published studies of relative sea level change in the GoC, and knowledge about Holocene sea level change within the GoC is relatively limited, especially when compared with studies of the eastern Australian coast (Section 2.3).

Progradational sequences of chenier ridges, separated by broad supratidal mud flats, or more closely spaced beach ridges, line the shoreline of the eastern and southern GoC (Figure 1.9) (Smart, 1976b; Davies, 1977; Woodroffe and Chappell, 1993), with the base of both ridge types comprising fine-grained intertidal sediments (Chappell *et al.*, 1982). These chenier and beach ridges were studied intensively by Eugene Rhodes in the 1980s for Holocene sea level reconstruction. At Karumba (Figure 2.15), Rhodes (1980) used the detailed sedimentary stratigraphy of a chenier ridge plain to investigate the sea level history of the area. As cheniers are a storm-built landform, their crest elevations may not be a reliable indicator of relative sea level. However, chenier ridges form near the top of the intertidal zone, within or behind mangrove swamps (Chappell, 1987). Thus, Rhodes (1980) used the facies boundary between the shelly chenier sand and underlying estuarine mud as a sea level indicator. Relative sea level at Karumba reached its present elevation prior to 7,000 years BP, continuing to rise to a maximum of about +2.4 m above PMSL 6,517 ± 207 years BP (Rhodes, 1980, p. 224). A stillstand of approximately 1,500 years duration then occurred, before relative sea level fell smoothly to its present position from about 4,000 years BP (Figure 2.16) (Rhodes, 1980).

Of the three other sites around the GoC studied by Rhodes (1980) – Christmas Creek, Edward River and Pandanus Yard (Figure 2.15) - Pandanus Yard had a composite beach ridge

and chenier ridge plain and was chosen to examine composite coastal progradation. However, due to the complex landforms present, Rhodes (1980) did not attempt to reconstruct a sea level curve for this location. Christmas Creek and Edward River have relict beach ridge plains that, due to their proximity, have experienced a similar sea level history (Figure 2.16) – relative sea level appears to have reached its present position prior to 7,000 years BP, continuing to rise to a maximum elevation of between +0.8 m to +1.5 m above present at approximately  $6,607 \pm 217$  years BP (Rhodes, 1980, p. 224). At Edward River, this was followed by a 500-year sea level stillstand then a fall to present day levels. No high sea level stillstand was recorded at Christmas Creek. Instead, relative sea level fell rapidly between  $6,607 \pm 217$  years BP and  $5,837 \pm 152$  years BP, before continuing to fall at a slower rate until reaching present day levels (Figure 2.16) (Rhodes, 1980, p. 224). At Karumba, Christmas Creek and Edward River, relative sea level reached its present position by approximately 300 years BP.

Rhodes (1980) attributed the differences in relative sea level change between Edward River and Christmas Creek on the one hand, and Karumba on the other, to a differential hydroisostatic response to post LGM water loading between the southern and eastern GoC. However, the differences in the reconstructed relative sea level curve between Edward River, Christmas Creek and Karumba may instead be due to the different proxies employed at both sites – i.e. the use of beach ridges at Christmas Creek and Edward River and the use of cheniers at Karumba. Beach ridges are generally formed from swash action and have a direct relationship to mean sea level and tidal range during the time of formation (Bird, 2008; see Section 3.1.2). Cheniers, on the other hand, are formed during storm events and therefore are potentially deposited over a wide elevation range dependent on the strength of the storm, making them potentially unsuitable for sea level reconstruction (Clifton and Hunter, 1982; Otvos, 2005).

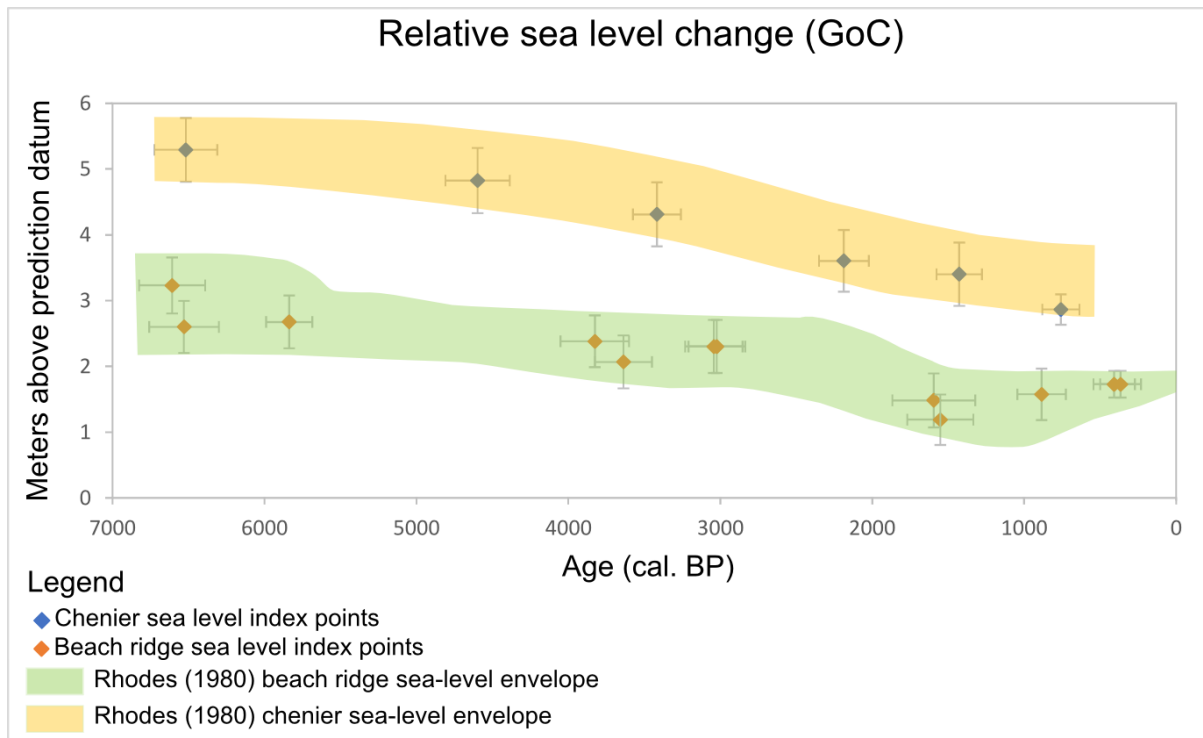


**Figure 2.16: Compilation of sea level index points from the GoC (Region C). The chenier sea level envelope is drawn from data from Figure 6.3 in Rhodes (1980), while the beach ridge sea level envelope is drawn from data from Figure 6.6 in Rhodes (1980). Note that the elevation data on the y-axis does not refer to the Australian Height Datum, but rather an approximation of Indian Spring Low Water as defined by Rhodes (1980). Relative sea level fall is therefore measured by comparing the elevation of the highest sea level index point of each sea level proxy (either chenier or beach ridge) to that of the lowest sea level index point for the same proxy.**

While the only sea level index points available for the GoC are from the Rhodes (1980) study (Figure 2.16), other sea level information from other locations around the GoC is in general agreement with Rhodes (1980). Woodroffe and Chappell (1993) examined mangrove sediments and *in situ* shell beds at the McArthur River delta (Figure 2.15), concluding that relative sea level was similar to present day levels by  $7,023 \pm 239$  years BP. Relative sea level continued to rise and was  $+1.5 \pm 0.5$  m above present at  $4,059 \pm 211$  years BP, before receding to present day levels. As the relationship between modern shell beds and sea level at the McArthur River delta is not well understood, Woodroffe and Chappell (1993) were unable to provide a more detailed reconstruction of Holocene sea level at the site.

On the Sir Edward Pellew Group of islands, in close proximity to the McArthur River delta (Figure 2.15), a relict beach ridge indicated that relative sea level was approximately +1.6 m above present around 5,500 years BP (Chappell *et al.*, 1982). Nanson *et al.* (2013) described coastal progradation of over 17 km at the Mitchell River delta (Figure 2.15), commencing approximately 5,700 years BP in response to a relative sea level fall of 1.5 m, while at the Gilbert River delta (Figure 2.15), Jones *et al.* (1993) report progradation of approximately 13

km over the past 6,000 years due to a (unquantified) decrease in relative sea level. Pollen records from the South Wellesley Islands (Figure 2.15), reported by Moss *et al.* (2015, p. 139) indicate a change from a near-shore beach environment to a mangrove environment between approximately 2,430 years BP and 500 years BP, most likely due to falling sea levels.

Finally, at my study area of Albatross Bay, in the northeast of the GoC (Figure 1.2, Figure 2.15), limited radiocarbon dating by Bailey *et al.* (1994) at Botchet Beach, along the Hey River, and at Urquarts Point (Figure 1.2) point to coastal progradation associated with a relative sea level fall within Albatross Bay occurring during the last 3,000 years, though this record lacks any detail.

## 2.5 Summary

Sea level changes are not uniform across the globe, with regional and local variations in sea level history caused by a combination of eustatic sea level change, isostatic effects, geoidal changes, human impact and tectonics among other factors. Located in the middle of the Indo-Australia plate, Australia is generally regarded as tectonically stable, free from neo-tectonics and the impacts of glacio-isostasy and therefore the ideal location to study glacio-eustatic and hydro-isostatic sea level change. However, evidence of raised mid-Eocene shorelines along the southern coastal margin of Australia, along with a lack of equivalent-age sediments from the continental record across the northern and eastern margin of Australia, led Sandiford (2007) to propose a continental-scale tilting of Australia (north-downwards, south-south-west-upwards), occurring since the mid-Miocene. This sea level review is restricted to the northern and eastern coasts of Australia to minimise complications from the continental tilt axis identified by (Sandiford, 2007).

This review demonstrates that sea level change across the northern and eastern coasts of Australia has undergone broadly similar trends from the LGM to present day. As glaciers and ice sheets began to melt in the higher latitude near field regions following the LGM, sea level began to rise. This post-LGM sea level rise may not have been continuous; rather, rates of sea level rise varied over time and the sea level rise was marked by minor oscillations and stillstands, potentially due to climatic fluctuations such as the Younger Dryas (Larcombe *et al.*, 1995; Lambeck *et al.*, 2002). Sea level reached present-day levels sometime prior to 6,000 years BP, where it may have continued to rise, resulting in a mid-Holocene highstand of between approximately +1 m to +3 m above PMSL. Following the mid-Holocene highstand,

sea level may have remained at a stillstand for a several thousand years before falling (smoothly or marked by oscillations) to PMSL.

While sea level change along the northern and eastern coasts of Australia follow this general trend, there are local variations in the elevation of the mid-Holocene highstand, along with differences in the time that sea level first reached PMSL before rising to the highstand, whether sea level remained at a mid-Holocene stillstand, and the nature (smooth or oscillating) of the sea level fall to PMSL. A main point of difference between the northern and eastern coasts of Australia is that mangrove evidence along the northern coast of Australia indicates that the Holocene marine transgression may have culminated in a “big swamp” phase, with no evidence of a mid-Holocene sea level highstand. Some of this variability may be due to limitations associated with various techniques of sea level reconstruction, such as sediment compaction, large tidal ranges leading to large indicative ranges and the accuracy of storm-built proxies including cheniers.

Within the GoC, there is a lack of data regarding Holocene sea level change. While there are a few sea level studies from locations along the present-day coastline of the GoC, the only sea level curve for the region is by Rhodes *et al.* (1980) and shows a significantly different sea level history between the southern and eastern GoC, with the elevation of the mid-Holocene highstand differing by up to 1 m. Archaeologists have also identified a need for a high-resolution sea level reconstruction to further understand the history of human-environment interactions in the area (Morrison, 2010, 2013; Shiner *et al.*, 2013). Therefore, a sea level curve from Albatross Bay will help to fill the gap in sea level records within the GoC. This new sea level curve can help address issues associated with hydro-isostatic influences on sea level change and inform on human response to sea level change in the area.



## **Chapter 3**

### **Methods**

Having established in Chapters 1 and 2 that there is a significant gap in our knowledge of Holocene sea level change for northern Australia, particularly for the northeastern shoreline of the Gulf of Carpentaria, this chapter describes the methods used to reconstruct the record of shoreline evolution and sea level change for Albatross Bay. The chapter is divided into four sections. First, methods for sea level reconstruction are reviewed, with particular focus on the sea level proxies present within Albatross Bay, namely palaeoshoreline indicators (beach ridges) and sedimentary stratigraphic sequences. Second, the selection of field locations is described, the primary goal of which is to maximise the potential of meeting the thesis aims outlined in Chapter 1. Field survey and sample collection methods are then described. In the third section, laboratory methods employed to analyse sediment samples are described. In the final section, sample collection and initial laboratory preparation of samples collected for Optically Stimulated Luminescence (OSL) and radiocarbon age estimation are explained and described.

#### **3.1 Methods of sea level reconstruction**

##### **3.1.1 Overview**

Any vertical movement in sea level will cause a corresponding horizontal shift in coastal environments. These shifts leave behind traces that, if preserved, act as proxies of past sea level position. A variety of proxies can be utilised for the reconstruction of past sea level. A reliable sea level proxy should fulfil three criteria: (1) accuracy, with a discernible relationship to sea level, (2) good preservation potential, and (3) ability to be dated (Rashid, 2014, p. 14). To reconstruct sea level accurately, each proxy needs to provide four pieces of information: (1) geographic location, (2) age, (3) elevation of the proxy relative to its modern equivalent, and (4) tendency (i.e., records a rise (positive tendency) or a fall (negative tendency) in sea level) (Shennan, 2015, p. 8).

The elevation of a sea level proxy is the most crucial, but also the most complicated, to ascertain. It is not common for proxies to form directly at mean sea level, or at some other

specified elevation. Rather, sea level proxies are often formed over a range of elevations within a specific tidal zone. Therefore, each sea level “index point” cannot provide an absolute elevation with regard to their contemporary sea level and relative to PMSL. Instead, the index points have an “indicative meaning”, comprising a reference water level, such as mean sea level or mean high water spring tide (MHWS), and an indicative range which is the vertical range where the sea level indicator could occur during formation (Shennan, 2007). The preservation and dating potential is dependent on the sea level proxy in question and depositional environment.

For a comprehensive review of the common proxies used in sea level reconstruction, see Sloss *et al.* (2007), Lewis *et al.* (2013) and Shennan *et al.* (2015). The remainder of this section will focus on the sea level proxies present around Albatross Bay that were used in this study – palaeoshoreline indicators (i.e., beach ridges) and sediment stratigraphic sequences including mangrove deposits (see Sections 1.4.2 and 2.4).

### 3.1.2 Palaeo-shoreline indicators (beach ridges)

Beach ridges are stabilised coastal deposits comprising a mixture of siliciclastic, calcareous or mixed carbonate and siliciclastic sediments (Otvos, 2000). Beach ridges form at, or above, the MHWS and are parallel or sub-parallel to the shore (Scheffers *et al.*, 2012). As new beach ridges form in front of older ones, a ridge plain is created, separated by narrow swales composed of similar sediment to the ridges (Otvos, 2000). This feature contrasts with chenier ridges that are composed of relatively coarse sand, gravel and shell built over fine-textured intertidal muds or silts and separated from each other by upper-intertidal mud flats (Otvos, 2005). Sequences of beach ridges mark the changing position of the shoreline in the past.

Many divergent views exist on the process of beach ridge construction. Beach ridges can have different origins, such as wave-built berm ridges with or without additional aeolian input, aeolian-built sand dunes, sandbars that form offshore but have now shifted landwards, or the welding of a coastal spit to the beach or by storm waves (Otvos, 2005; Bird, 2008; FitzGerald and Buynevich, 2009; Nott, 2010; Scheffers *et al.*, 2012). With berm ridges, deposition from swash action (the turbulent rush of water that moves up the beachface after an incoming wave breaks) leads to the build-up of a subdued wedge-shaped terrace (i.e., a berm) that forms parallel to the shoreline at the limit of wave swash during high tide (Bird, 2008). The berm is bounded by the steeper upper foreshore slope of the beachface, and the adjacent

gently landward-dipping sub-horizontal backbeach (Otvos, 2000). Swash action, along with occasional wash-over during higher-energy events that raise tide levels, results in sediment continuing to accrete on the top, and landward, of the berm, raising the berm above the adjacent backbeach (Otvos, 2000; Bendixen *et al.*, 2013). Over time, the berm ridge may become isolated from wave action (except during the highest tides and high-energy storm events) due to sea level fall, coastal progradation, a change in sediment supply to the coast, or a combination of these factors. Sediments may still be deposited on berm ridges, transported by aeolian rather than wave processes (Otvos, 2000; Bird, 2008). Furthermore, plants growing on the berms “...from rhizomes, seedlings, storm-buried roots, and germinating seeds in the protection of beach debris...” will trap sediments, causing these berm ridges to increase in size (Otvos, 2000, p. 97). As the coast progrades, a new berm will form seaward, separated from the original one by an inter-ridge swale, and beginning the ridge-forming process again (Tamura, 2012; Bendixen *et al.*, 2013).

Beach ridges can also be formed by storm waves that transport coarse detritus onshore (Nott, 2010). These storm-built sandy beach ridges form in areas that experience tropical cyclones which then generate storm surges (Nott *et al.*, 2009). While tropical cyclone-generated winds themselves have the energy to transport coarse-grained sediments, any wind-blown sands could be transported hundreds of metres inland and may be widely dispersed, rather than accumulate at the back of a beach or onto ridges. Storm surges associated with tropical cyclones often inundate the beach, restricting aeolian sediment entrainment. These ridges are thus formed from the tropical cyclone-induced inundation itself and comprise coarser sand grains and/or coral reef rubble, gravels and boulders (Nott, 2010). An entire ridge can be deposited during a single storm event (Nott *et al.*, 2009), or can be formed over time by storm events alternating with fair weather phases (Tamura *et al.*, 2018). As storm-built beach ridges can be deposited over a wide elevation range dependent on the strength of the storm, they may be unsuitable for sea level reconstruction (Clifton and Hunter, 1982; Otvos, 2005). Rather than being constructive, due to the increase in the sediment carrying capacity of waves, which then leads to the formation of storm-built beach ridges, tropical cyclones may instead be destructive, leading to coastal erosion due to the increase in wave energy (Oliver, 2016).

The height (or thickness) of beach ridges is dependent on many factors, including sediment availability, grain size and shape, wave height and, if formed by storm events, the energy level and duration of the storm, along with the approaching angle of the storm surge (Scheffers *et al.*, 2012). Beach ridges and their subsurface deposits therefore contain a record

of the sedimentary environments and processes (be it over one event or many), including past shoreline position, relative sea level change, sediment supply changes, and palaeostorm activity (Scheffers *et al.*, 2012; Tamura, 2012).

While the elevation of a beach ridge can be an approximate indicator of past sea level, for sea level reconstruction it is more accurate to look for a recognisable boundary between the wave-built foreshore and the overlying aeolian deposit (Otvos, 2000; Tamura *et al.*, 2012). Under stable sea level, aeolian accumulation can result in varying heights in neighbouring ridges. Thus, if the absolute elevation of a beach ridge is to be used as a sea level indicator, a beach ridge set needs to be measured and averaged to account for the potential irregularity of elevation (Tamura, 2012). The boundary between aeolian sediment and the underlying beach facies forms at the landward swash limit of constructive waves, and thus is the most frequently used indicator of mean sea level (Tamura, 2012). However, while aeolian sediments characteristically consist of fine-grained sands and marine sediments are coarse-grained (Nott *et al.*, 2009), particle size and sedimentary structures may not always be sufficient to make this distinction (Otvos, 2000; Tamura *et al.*, 2012). Particle size and content analysis of sediments comprising the modern beach and foredune will provide direct comparisons with sediments in the beach ridges, aiding in palaeo-environmental reconstruction (Nott, 1996; Tamura, 2012).

### 3.1.3 Sedimentary stratigraphic sequences

The sedimentology, facies analysis and facies associations of coastal deposits can provide insight into the geomorphic evolution of the coastal landscapes. According to Sloss (2005, p. 53), a sedimentary facies is “...a body of rock, or a package of sedimentary material, characterised by particular combination of lithology, sedimentary characteristics, physical and biological features which is distinguishable from other sedimentary units...”. As explained by Walker (1992, p.3), “...the key to the interpretation of facies is to combine observations made on their spatial relations and internal characteristics (lithology and sedimentary structures) with comparative information from other well-studied stratigraphic units, and particularly from studies of modern sedimentary environments...”. Sedimentary facies may range from a few millimetres to tens or hundreds of meters thick (López, 2015). Each distinctive sedimentary facies is a product of the sediment provenance, transporting mechanism and pathways, and depositional process associated with the depositional environment. Depositional environments also have specific physical, chemical and biological processes (such as salinity, temperature, water depth, tides, waves and currents) that act on the sediments (Thomas and Goudie, 2000; López, 2015). Sedimentary facies are also modified by post-depositional diagenesis, for

example groundwater movement, the formation of a soil profile and/or bioturbation by plants or animals, all of which will impact the original depositional properties (Sloss, 2005).

Walther's Law states that a vertical progression of sedimentary facies can only be formed through the interactions of depositional environments that are laterally adjacent with each other (Middleton, 1973). For example, as sea level shifts, the relative position of the shoreline moves, altering the depositional environments associated with the coastal environment. This significantly influences geomorphological features due to vertical and lateral changes in sedimentary facies associated with changes in depositional environments. Once a sedimentary facies has been identified and described, and the present day depositional environment examined, the vertical sedimentary record and its relation to longer-term environmental change can be established (Hesselbo, 2008; López, 2015).

Coastal sediments originate from multiple sources such as cliff erosion, rivers, glaciers, volcanic ash and lava, coral reefs, seashells, skeletons of marine organisms, wind transport, and the continental shelf itself. On a regional scale, the sediment source, strength and type of erosional, transportational and depositional processes that occur, and the chemical and biological processes in the area, will dictate the sedimentary composition and characteristics in a coastal zone (Clifton, 2005; Trenhaile, 2005). On a local scale, across a beach for example, sedimentary characteristics such as grain size and organic matter content are not uniform; rather, they are vertically zoned in relation to tide level and the gradual transition from a marine to a terrestrial environment (Edwards, 2007b). Vertical coastal depositional sequences are formed from the interaction between the abovementioned sedimentary processes (i.e. the nature and rate of sedimentation) and isostatic and eustatic processes (i.e. relative sea level change) (Clifton, 2005; Abbott and Carter, 2007). The majority of sea level studies have employed coastal sediment stratigraphy as one of their techniques for sea level reconstruction (Nelson, 2015) because sediments can be found anywhere, unlike other proxies such as fossils which are restricted by habitat requirements.

Particularly distinctive sedimentary facies changes in coastal settings occur when a coastline shifts landwards (also termed "coastal retrogradation" or a "marine transgression") or advances seawards (also termed "coastal progradation" or a "marine regression") (Bokuniewicz, 2005, p 565). During a coastal retrogradation, there will be a landward shift in sediment facies. For example, deeper-water marine deposits will overlie shallow-water marine deposits, with terrestrial sediment at the base. When a coastline progrades, sediment facies will

shift seawards and terrestrial sediment will be deposited above shallow-water marine deposits, with deep-water marine deposits at the base (Clifton, 2005; Cooper, 2007; Edwards, 2007a). Coastal retrogradation and progradation are caused by any combination of eustatic sea level change, coastal subsidence or uplift and/or sedimentation or erosion (Bokuniewicz, 2005). Coastal retrogradation that occurs as sea level rises will cause a change in sedimentary facies over a regional scale. Retrograding contacts that arise when sediment shortages occur, leading to coastal erosion and the landward migration of the shoreline, would lead to more local changes in sedimentary facies (Cooper, 2007). Conversely, prograding contacts may reflect a regional fall in sea level, a high sedimentary input, or a combination of the two which results in the seaward migration of the coast (Cooper, 2007). Even with relative sea level rise, a prograding contact may still occur if the sediment influx is high, outpacing sea level rise and leading to the coastline shifting seaward. Thus, to use sediment stratigraphy in sea level studies, it is important to identify both regional and local patterns in sedimentary stratigraphic sequences, along with available data on a location's climate and oceanography, to understand the driving forces of these observed changes (Cooper, 2007).

Mangrove mud deposits are a particularly useful sedimentary stratigraphic unit in sea level research. The composition of a mangrove community is determined by many factors, including sediment type, temperature, duration and frequency of inundation, tidal and wave energies, sedimentation rate and the incidence of cyclones and floods (Blasco *et al.*, 1996). Mangroves are sensitive environmental proxies, with minor alterations in the hydrological (including sea level change) and/or sedimentological regimes of an area causing shifts in mangrove species or even causing the mangroves to disappear altogether (Blasco *et al.*, 1996; Woodroffe *et al.*, 2015). During marine transgressions, mangrove communities often develop and expand, aiding the deposition of organic muds over the top of terrestrial sediments (Grindrod *et al.*, 1999). During marine regressions, mangrove communities retreat as sea level falls and terrestrial sediments are deposited above the mangrove sediments (Grindrod *et al.*, 1999; Zong, 2007).

Mangrove muds can be radiocarbon dated to provide a record of sea level inundation (Cohen *et al.*, 2005; Zong, 2007). Any radiocarbon dates derived from mangrove deposits need to be carefully interpreted as these deposits may be mixed with younger carbon from root penetration and younger or older carbon from bioturbation caused by burrowing animals (Woodroffe, 1990; Sloss *et al.*, 2013; Woodroffe *et al.*, 2015). As root penetration and burrowing activity may extend up to approximately 2 m in depth (Saenger, 2002), they can

have a significant impact on radiocarbon dates obtained. Care should be taken in the preparation of mangrove sediment samples for radiocarbon dating to reduce the possibility of sample contamination. For example, roots and rootlets should be removed from a sample prior to dating (see Section 3.4.2.2 and Section 5.2.1 for more information on radiocarbon dating). Not only can mangrove fossils provide an estimate of the chronology of marine transgressions or regressions, but because mangrove species are intertidal and grow within a known and narrow elevation range close to the local mean high water (MHW) levels, they can also provide estimates of relative sea level elevation (Cohen *et al.*, 2005; Zong, 2007).

## **3.2 Field methods**

### **3.2.1 Selection of field locations**

The following factors played a significant part in the choice of locations for fieldwork in the Albatross Bay study area (Figure 3.1):

- 1) The availability of the palaeo-sea level indicators described above;
- 2) Accessibility to potential fieldwork locations, given current mining activity in the area and the need to obtain permission from Aboriginal Traditional Owners to carry out research on their land. Some locations were entirely closed due to these restrictions, and others were temporarily closed or access to them had to be rerouted.
- 3) Proximity to accommodation and other essential facilities provided by Rio Tinto Pty Ltd at Weipa.

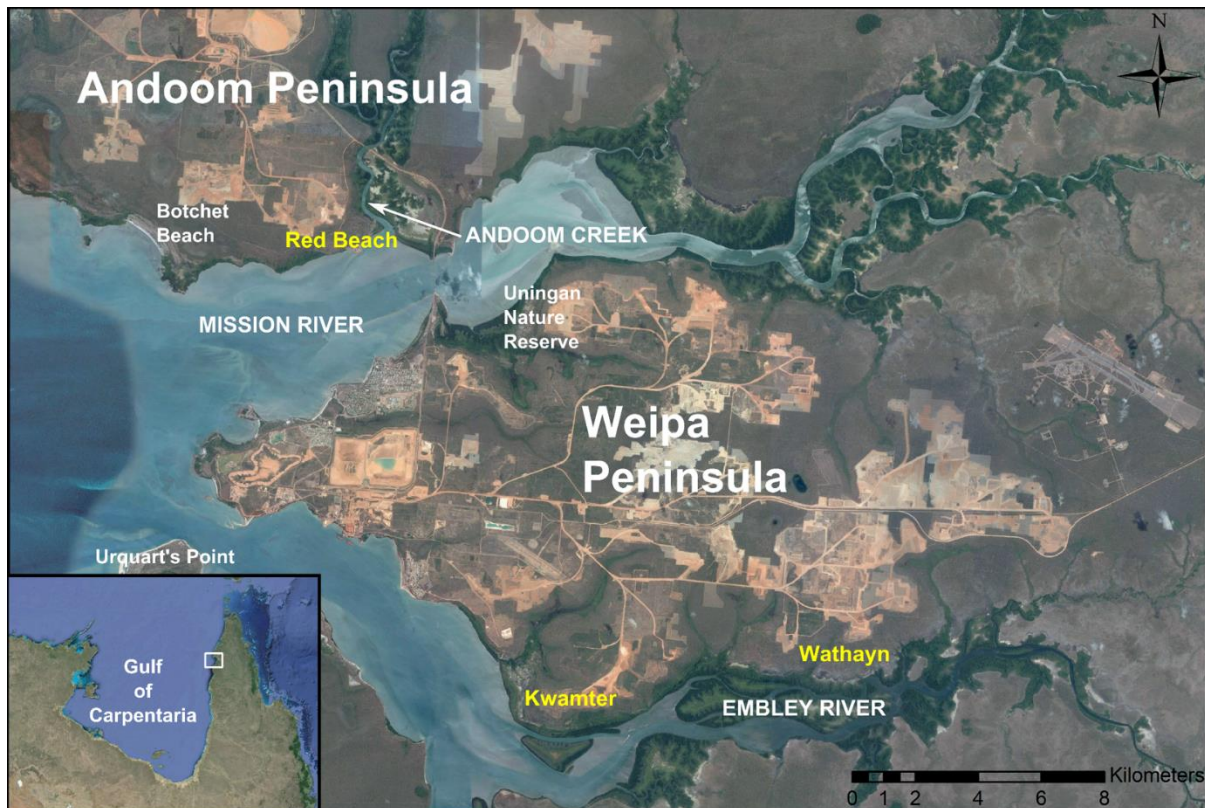


Figure 3.1: The Weipa region with the location of study locations highlighted in yellow (Source: modified from GoogleEarth, accessed 17<sup>th</sup> Jan 2016).

Locations around Albatross Bay with beach ridge plains include Red Beach, Botchet Beach, Urquart's Point and within Uningan Nature Reserve (Figure 3.1). Red Beach (12°35'16.67"S, 141°52'26.53"E), on the northern shore of Albatross Bay 9 km northeast of the Weipa township, has been the focus of several geographical and archaeological investigations in the past (see, for example, Bailey *et al.*, 1994; Stone, 1995; Morrison, 2015). Bailey *et al.* (1994) noted that a beach ridge plain runs parallel to the shoreline, allowing for the building of a detailed, high-resolution record of coastal evolution in response to sea level change at this location. While Bailey *et al.* (1994, p. 74) dated modern *Tegillarca granosa* (syn. *Anadara granosa*) at Red Beach, along with a fossil specimen collected from the base of an anthropogenic shell mound ( $790 \pm 110$  years BP), the beach ridges themselves were not dated.

Stone (1995) and Morrison (2015) also examined the shell mounds at Red Beach. Eight uncalibrated radiocarbon dates were collected across four beach ridges by Stone (1995, p. 85), who was proposing a natural origin for the shell mounds. They suggest coastal progradation at Red Beach occurred from  $4530 \pm 80$  radiocarbon years BP, at the rear of the sequence, to  $800 \pm 40$  radiocarbon years BP, at the front of the sequence. Stone (1995) advises caution using



these radiocarbon dates due to the possibility of shell reworking and uncertainty in the application of the marine correction factor. In contrast, investigations into the age, stratigraphy and composition of shells within the shell mounds led Morrison (2015) to conclude that the shells mounds are a human construct, built since approximately 800 years BP when shellfish species were established in the intertidal mudflats around Red Beach.

Red Beach is located adjacent to Botchet Beach (Figure 3.1), which also exhibits a beach ridge plain that was the focus of research for an Honours thesis by Hayne (1992). Hayne (1992, cited in Stone, 1992, p. 94) obtained 16 conventional radiocarbon dates from across the beach ridge plain, ranging in age from  $2440 \pm 60$  years BP at the rear of the sequence to  $220 \pm 50$  years BP from the youngest beach ridge. Bailey *et al.* (1994, p. 74) also obtained two radiocarbon age determinations at Botchet Beach, one date from the middle of the sequence of seven beach ridges ( $1120 \pm 90$  radiocarbon years BP), and one from the distal margin ( $2230 \pm 80$  radiocarbon years BP). Both radiocarbon dates came from whole shell collected at 1 m depth. These radiocarbon dates indicate that coastal progradation at Botchet Beach may have commenced later than at Red Beach. This could be related to a number of factors, such as differences in sediment supply, offshore geometry, and wind and wave regime. Red Beach is situated at the mouth of Andoom Creek, and opposite the mouth of the Mission River, both of which are likely to have been the major sources of sediment into Albatross Bay. Botchet Beach, on the other hand, has no proximal sediment source and is closer to the mouth of Albatross Bay, most likely resulting in differences in wave regime and offshore geometry leading to differences in onshore sedimentation.

Red Beach was therefore selected for detailed study in this thesis because of the presence of a beach ridge plain and extensive coastal sedimentary sequences extending into the subtidal zone, both of which would allow the construction of a record of sea level change for at least the mid- to late-Holocene. Previous research there had also given rise to several important unanswered questions relating to Holocene sea level change and coastal evolution in the northeast GoC, such as, for example, differences in the timing of commencement of coastal progradation at Red Beach (approximately 4500 years ago based on work by Stone (1995)) compared to Botchet Beach (approximately 2,500 years ago based on work by Hayne (1992) and Bailey *et al.* (1994)). It was expected that the application of modern survey, sediment analysis and dating techniques would enable a deeper understanding of the coastal sedimentary environments and sea level history of the local area.

Reconnaissance for my research also identified the presence of beach ridges and extensive supratidal mudflats, bordered with mangroves, along the northern shoreline of the lower Embley River, at Kwamter and Wathayn (Figure 3.1). Both of these locations are sites of previous and ongoing archaeological research. Bailey *et al.* (1994) describe anthropogenic shell mounds from two locations at Kwamter (12°43'14.90"S, 141°55'0.86"E), situated approximately 11 km southeast of Weipa, along the lower estuary of the Embley River. First reported by Wright in 1963, the Kwamter shell mounds are located on a single beach ridge running parallel to the shoreline between the edge of an open forest and the mangrove fringe. Valentin (1959; cited in Bailey *et al.*, 1994) related this beach ridge to higher sea levels during the mid-Holocene. The Kwamter location has also been the subject of intensive archaeological debate about the origin of the Weipa shell mounds (Bailey, 1977; Stone, 1989; Bailey, 1991; Cribb, 1991; Stone, 1991; Bailey, 1993; Bailey *et al.*, 1994; Stone, 1995). These previous studies did not, however, adequately discuss the sea level history of the area due to the lack of data (Bailey, 1977). Thus, despite the absence of a beach ridge plain, Kwamter was chosen as a suitable field area for my research because of its accessibility, the presence of coastal sediment sequences extending from the distal beach ridge to the proximal supratidal mudflat, and the previous published research.

The third fieldwork site of Wathayn (12°42'34.42"S, 141°59'30.26"E) is located ca. 9 km upstream of Kwamter on the Embley River (Figure 3.1). It is the location of extensive archaeological investigations of the Aboriginal cultural heritage of the Weipa region (Shiner *et al.*, 2013; Stevenson *et al.*, 2015a; Brockwell *et al.*, 2017; Holdaway *et al.*, 2017; Larsen *et al.*, 2017; Fanning *et al.*, 2018). There are many shell mounds at Wathayn, along with other archaeological features including shell scatters, earth mounds, stone artefacts and scar trees (Shiner and Morrison, 2009; Shiner *et al.*, 2013). The shell mounds are located on a variety of substrates including bedrock, sandy and gravelly beach ridges, intertidal mudflats and mangroves deposits (Shiner and Morrison, 2009; Shiner *et al.*, 2013). The presence of a single beach ridge and extensive coastal sediment sequences at Wathayn therefore offered another opportunity to attempt to reconstruct Holocene sea level change in a setting with an extensive and well-documented mid-to late Holocene archaeological record (Holdaway *et al.*, 2017), but where a record of sea level change was lacking.

Fieldwork was carried out during four field trips between 2012 and 2014, during the dry season (August 2012, July 2013, September 2013 and September 2014). A reconnaissance trip was initially undertaken in August 2012 to investigate the field locations and confirm their

suitability for Holocene sea level reconstruction. The Wathayn and Kwamter field areas were surveyed and sampled and work commenced at Red Beach during the July 2013 field season. Surveying and sampling of beach ridge plain at Red Beach was completed over two field seasons in September 2013 and September 2014.

### 3.2.2 Surveying field features

A Leica Viva GS10 global navigation satellite system (GNSS) real-time kinematic (RTK) differential global positioning system (DGPS) was used to collect accurate position (latitude and longitude) and elevation data (Figure 3.2) with horizontal and vertical accuracies of approximately  $\pm 10$  mm and  $\pm 20$  mm respectively (Leica Geosystems AG, 2012).

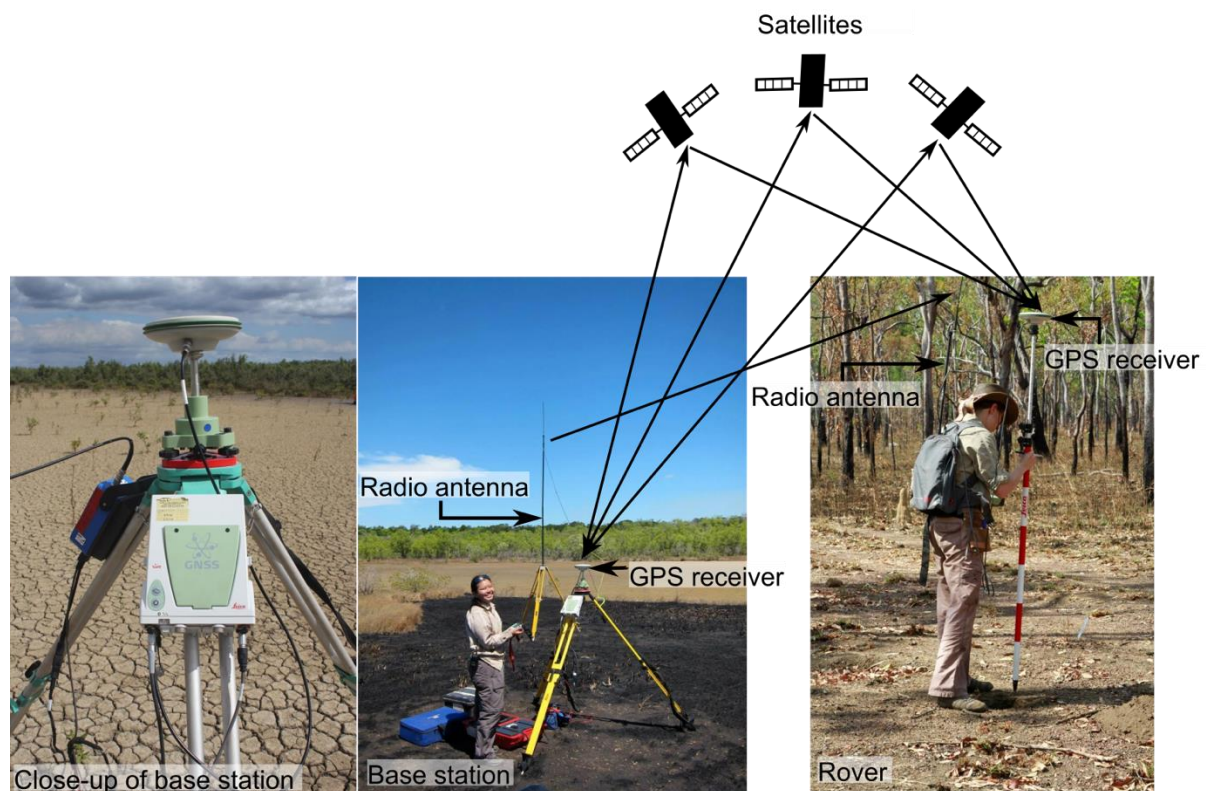


**Figure 3.2: Leica Viva GNSS set-up to collect positional information in the field. Images illustrate the base station unit (left), the base station set-up (centre), and collecting position data with the rover (right).**

The Leica Viva GS10 base station consists of a GPS receiver which obtains positional data from satellites, and a radio antenna that transmits the positional data to the rover. The base station was set up for a minimum of 12 hours before surveying commenced to obtain accurate positional data. The GPS data was uploaded onto the AUSPOS (Australia Positioning) website which processed the data and determined the Geocentric Datum of Australia 1994 (GDA94)

coordinates and elevation of the base station (Geoscience Australia, 2015a). AUSPOS computes the elevation of the base station benchmarked against the AHD using the AUSGeoid2020 model (for further information see Geoscience Australia (2018) and Section 1.4.1). Once these corrected coordinates are loaded into the base station, the base station continuously transmits its corrected location via the radio antenna. The RTK rover GPS receiver (Figure 3.2) collected positional data for each specific site from overhead satellites relative to the base station. Through a process of triangulation between the base station, satellites and the RTK rover, millimetre-accurate positional and elevational data are obtained in real time.

Topographic data for the beach ridge plain at Red Beach and the beach ridge and supratidal mudflat at Kwamter and Wathayn were collected along transect lines perpendicular to the shoreline (Figure 3.3A). Transect locations were chosen where the full variability of the coastal features present could be recorded. At Red Beach, the transect was located where the beach ridge crests were most distinct. It extended approximately 800 m east to west across the beach ridge plain, from just west of a narrow mangroves fringe growing along the modern shoreline, inland to the base of an aluminous laterite bedrock outcrop (Figure 3.3B).



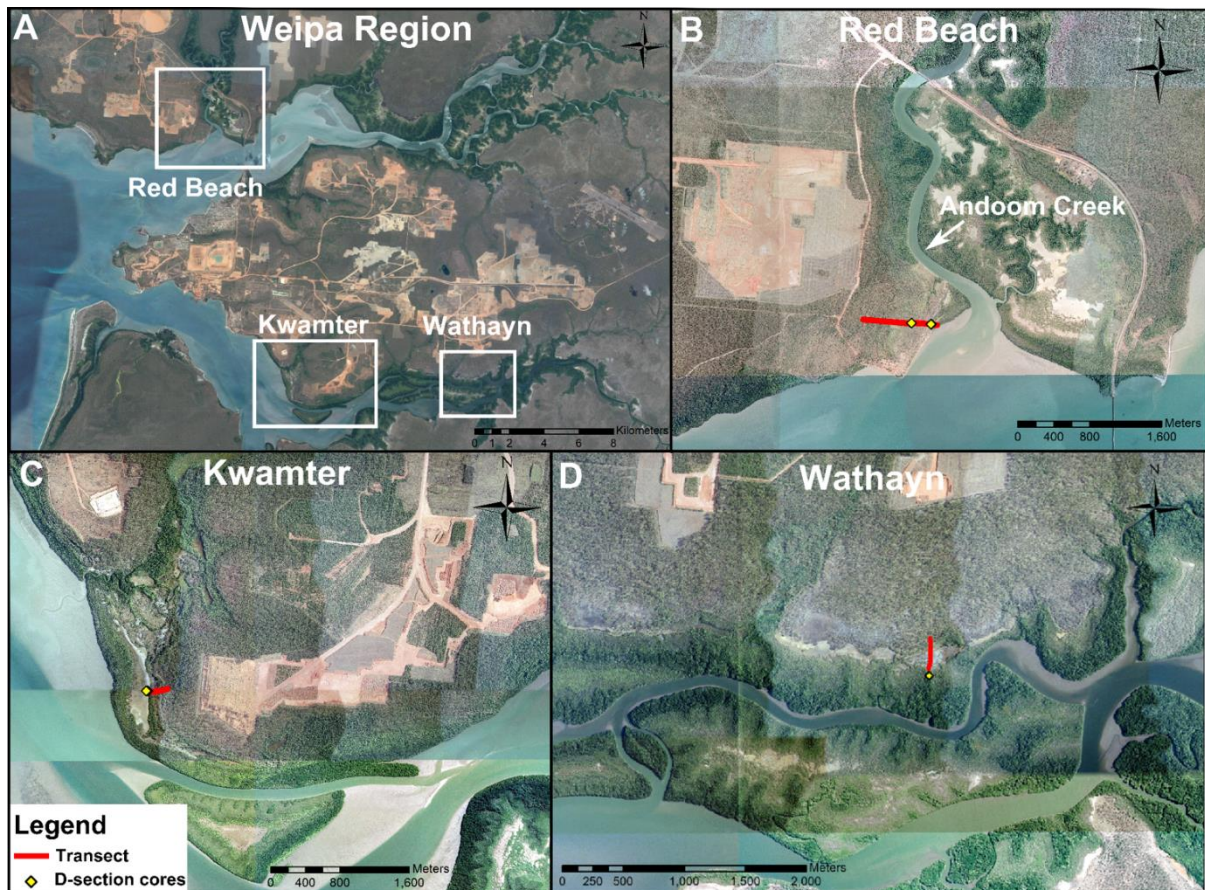


Figure 3.3: Map of the Albatross Bay study region showing the location of transects and D-section cores at Red Beach, Kwamter and Wathayn. In some locations, D-section cores were collected relatively close to each other, therefore some location points have been superimposed. (Source: GoogleEarth, accessed 17<sup>th</sup> Jan 2016).

At Kwamter and Wathayn, the transects were located where the beach ridge formed a prominent topographic feature parallel to the modern shoreline. At Kwamter, the transect extended from east to west for approximately 260 m, starting in a swale inland of the single beach ridge and continuing across the supratidal mudflat to the modern high-water mark (Figure 3.3C). At Wathayn, the transect extended from north to south for approximately 300 m, from the base of the hillslope behind the single beach ridge across the supratidal mudflat to the distal edge of the mangrove fringe (Figure 3.3D).

The variable interval method of transect surveying was employed. Static GPS point measurements at all three sites were collected approximately every 10 m, with the distance between points adjusted according to the terrain. If the change in elevation was gradual, the distance between points were increased to approximately 40 m apart, and if the change in elevation was significant, such as at the beach ridges, points were collected every 1 to 2 m. The

elevation data was then cross-referenced with aerial LiDAR<sup>5</sup> data, obtained from a 0.25 m grid survey flown in 2010 and provided by Rio Tinto Alcan (Weipa) Pty Ltd, to ensure the accuracy of the transects.

### 3.2.3 Stratigraphic recording and sediment sample collection

#### 3.2.3.1 Augering, coring and excavation

Sediment stratigraphy recording and sample collection were facilitated by hand excavation of pits, soil augering, and coring using a D-section (or “Russian”) corer (Figures 3.4 and 3.5). Pits approximately 1 m x 1 m square and up to 1.54 m deep were excavated using a mattock to loosen the earth and shovels, buckets and trowels to remove it to the side of the pit, where it was stockpiled and later used to backfill the excavation. Once the maximum safe dig depth was reached, a soil auger was sometimes used to extract sediments beneath the floor of the pit. The soil auger was also used to investigate the sediment stratigraphy in between some of the pits. The D-section corer was used to extract intact cores of sediment beneath some of the pits in the Red Beach plain transect, beneath the supratidal mudflat at Kwamter, and within the mangrove zone at Wathayn. The D-section (“Russian”) corer is a closed chamber semi-cylindrical corer that is employed in sampling soft unconsolidated sediments such as mangrove, intertidal or peat deposits (Aaby and Digerfeldt, 1986; Glew *et al.*, 2001; Woodward and Sloss, 2013). Once the pits were dug or the D-section cores were retrieved, the sediments were described and recorded in a field notebook (Figures 3.4D and 3.5B) before being sampled for further analysis (see Section 3.2.3.3).

---

<sup>5</sup> Locational and elevation data was estimated using a Digital Elevation Model (DEM) developed from LiDAR data, with the DEM provided courtesy of Rio Tinto Alcan (Weipa) Pty Ltd



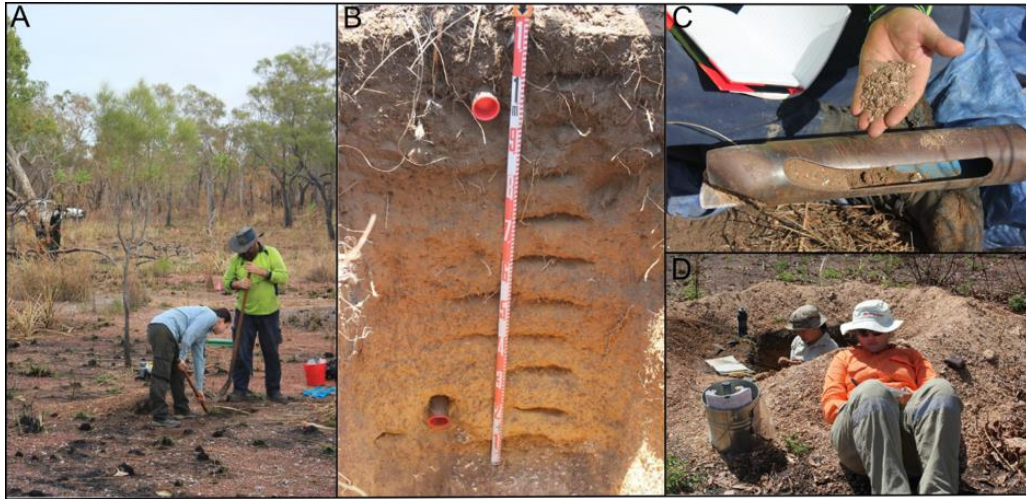


**Figure 3.4: Stratigraphic recording and sediment sample collection. (A) Pit excavation at Red Beach. (B) Sediment stratigraphy and sediment sample collection sites spaced 10 cm apart within a typical pit at Red Beach. OSL sample tubes can also be seen. (C) Recording and collecting sediment samples using an auger. (D) Recording in-field observations.**



**Figure 3.5: D-section coring. (A) Collecting D-section core from the base of a pit on the intertidal mudflat at Kwamter (B) describing a D-section core from within the mangrove fringe at Wathayn, (C) close-up of D-section core collected from the base of a pit at Red Beach showing the transition from sandy beach ridge sediments to the intertidal muds below, (D) close-up of D-section core collected at within the mangrove fringe at Wathayn.**

The sedimentary archive of beach ridges, and the beach ridge plain at Red Beach in particular, is integral to building a high-resolution chronology of sea level change and coastal progradation in Albatross Bay. However, the formation of beach ridges and their relation to sea level can be complicated (see Section 3.1.2). To better understand the various depositional sedimentary environments that may have contributed to the formation of beach ridges in

Albatross Bay, a trench was dug by hand through the modern beach at Red Beach during low tide to expose the sediment stratigraphy of the beachface, berm and backbeach. Comparison of this modern analogue with the sediment stratigraphy found within the relict beach ridges, combined with knowledge of present day environmental conditions that constructed the modern beach (climatic seasonality, tides and the occurrence of storms), was expected to improve understanding of the formation of the beach ridges and relict beach ridge plain (see Section 4.4).

Table 3.1 summarises the excavation data for all three study locations. A total of 38 excavations were conducted, 24 at Red Beach, 8 at Kwamter and 6 at Wathayn.

**Table 3.1: Summary of sediment stratigraphy excavations for the Albatross Bay study area.**

Location	Field Code	Location (UTM coordinates)	Landform	Surface elevation (m AHD)	Total depth (m)	Excavation method
Red Beach	RBMT DFO1-DFO5	E 595122.2776 N 8608416.537	Modern beach	0.65 - 0.79	0.40 - 0.54	Trench
Red Beach	RB01	E 595171.1147 N 8608563.894	Beach ridge crest (RR2)	1.99	1.25	Pit
Red Beach	RB02	E 595194.3321 N 8608559.992	Beach ridge crest (RR1)	2.37	1.54	Pit
Red Beach	RB03	E 594943.4154 N 8608578.979	Beach ridge crest (RR8)	2.42	1.07	Pit
Red Beach	RB04	E 595174.9934 N 8608563.137	Beach ridge swale (RS1)	1.80	0.88	Pit
Red Beach	RB05	E 595153.1557 N 8608566.034	Beach ridge swale (RS2)	1.53	1.40	Pit
Red Beach	RB06	E 595145.0251 N 8608567.358	Beach ridge crest (RR3)	2.21	1.80	Pit + Auger + D-section
Red Beach	RB07	E 595138.7368 N 8608568.088	Beach ridge swale (RS4)	2.04	1.32	Pit + Auger
Red Beach	RB08	E 595131.7323 N 8608568.384	Beach ridge crest (RR4)	2.33	1.26	Pit
Red Beach	RB09	E 595123.4966 N 8608568.818	Beach ridge swale (RS5)	2.27	1.03	Pit
Red Beach	RB10	E 595093.0226 N 8608571.045	Beach ridge crest (RR5)	2.73	1.48	Pit
Red Beach	RB11	E 595084.7887 N 8608572.398	Beach ridge swale (RS6)	2.50	0.97	Pit
Red Beach	RB12	E 595026.337 N 8608578.91	Beach ridge crest (RR7)	2.77	1.17	Pit
Red Beach	RB13	E 5950647754 N 8608574.318	Beach ridge crest (RR6)	2.68	1.06	Pit
Red Beach	RB14	E 595042.6492 N 8608577.16	Beach ridge swale (RS7)	2.11	0.70	Auger
Red Beach	RB15	E 594911.061 N 8608582.558	Beach ridge swale (RS8)	2.12	0.90	Auger
Red Beach	RB16	E 594916.6305 N 8608576.047	Beach ridge swale (RS9)	2.01	1.20	Pit
Red Beach	RB17	E 595148.8877 N 8608566.476	Beach ridge proximal flank (RS3)	1.96	2.13	Pit + D-section
Red Beach	RB18	E 594587.2971 N 8608605.277	Beach ridge crest (RR11)	2.81	1.15	Pit
Red Beach	RB19	E 594491.3462 N 8608613.654	Beach ridge crest (RR13)	2.81	1.36	Pit
Red Beach	RB20	E 593540.3258 N 8608607.882	Beach ridge crest (RR12)	2.56	1.23	Pit
Red Beach	RB21	E 594861.5084 N 8608580.512	Beach ridge crest (RR9)	2.06	1.26	Pit
Red Beach	RB25	E 594674.145 N 8608597.795	Beach ridge crest (RR10)	2.59	1.20	Pit
Red Beach	RB27	E 594398.2002 N 8608621.533	Beach ridge swale (RS10)	2.24	1.55	Pit + Auger
Kwamter	KW03	E 599800.7976 N 8593802.064	Supratidal mudflat (KMF2)	0.49	1.30	Pit + D-section
Kwamter	KW04	E 599837.8668 N 8593796.209	Mangrove zone (KI1)	0.71	0.60	Pit
Kwamter	KW05	E 599814.8826 N 8593799.688	Supratidal mudflat (KMF4)	0.56	0.50	Pit
Kwamter	KW06	E 599782.7033 N 8593804.1	Supratidal mudflat (KMF1)	0.46	1.80	Pit + D-section
Kwamter	KW07	E 599931.8501 N 8593803.581	Beach ridge crest (KR1)	2.49	1.22	Pit
Kwamter	KW08	E 599974.357 N 8593809.751	Beach ridge swale (KS2)	1.81	0.26	Pit
Kwamter	KW09	E 599894.1555 N 8593797.588	Beach ridge proximal flank (KS1)	1.46	0.55	Pit
Kwamter	KW10	E 599808.2071 N 8593800.397	Supratidal mudflat (KMF3)	0.52	0.60	Pit
Wathayn	WHA01	E 610040.1333 N 8594548.235	Beach ridge crest (WR1)	3.79	0.95	Pit
Wathayn	WHA02	E 610040.9064 N 8594524.652	Beach ridge proximal flank (WS1)	2.45	0.71	Pit
Wathayn	WHA03	E 610040.1138 N 8594493.636	Supratidal mudflat (WMF3)	1.47	0.35	Pit
Wathayn	WHA04	E 610039.6669 N 8594446.151	Supratidal mudflat (WMF2)	1.18	0.50	Pit
Wathayn	WHA05	E 610034.0107 N 8594369.229	Supratidal mudflat (WMF1)	1.16	0.88	Pit
Wathayn	WHAD06	E 610027.1809 N 8594274.447	Mangrove zone (W1)	1.05	0.50	D-section



### 3.2.3.2 Field descriptions of sediment and stratigraphy

Sediments and stratigraphy for each excavation were described in the field following recommendations in Dackombe and Gardiner (1983) and the National Committee on Soil and Terrain (2009). Individual sediment layers were distinguished primarily based on sediment lithology, grain size, sorting, roundness, and macro-faunal elements, by comparison with charts and tables from Dackombe and Gardiner (1983).

Sediment colour was described using the revised standard soil colour charts which is based on the Munsell system of soil colours (Oyama and Takehara, 1967). If mottling was present, the abundance, size, contrast and distinctness of boundaries of the mottles with the surrounding sediment were recorded using the following guide (McDonald and Isbell, 2009, p114-115):

<b>Abundance of mottles</b>	<b>Percentage of unit</b>
None	0
Very few	< 2%
Few	2% - 10%
Common	10% - 20%
Many	20% - 50%

<b>Size of mottles</b>	
Fine	< 5 mm
Medium	5 mm – 15 mm
Coarse	15 mm – 30 mm
Very coarse	> 30 mm

<b>Contrast of mottles</b>	
Faint	Indistinct; evident only on close examination
Distinct	Readily evident although not striking
Prominent	Striking and conspicuous

<b>Distinctness of boundaries</b>	
Sharp	Knife-edge boundary between colours
Clear	Colour transition over less than 2 mm
Diffuse	Colour transition over 2 mm or more

The abundance and characteristics of coarse fragments present in the sediments were also recorded in the field. The term “coarse fragments” is defined by McDonald *et al.* (2009, p. 97) as “... particles coarser than 2 mm. They include unattached rock fragments and other fragments such as charcoal and shells ... they are not, or not considered to be, of pedogenic origin...”. Four classes of coarse fragments were recognised from the Albatross Bay study locations (Figure 3.6): (1) pisolithic bauxite (abbreviated to pisoliths); (2) quartz granules; (3) subrounded to angular rock fragments; and (4) macrofossils (primarily whole and fragmented shell). Their abundance was recorded using the following guide from (McDonald *et al.*, 2009, p. 97-98):

<b>Abundance of coarse fragments</b>	<b>Percentage of unit</b>
None	0%
Very few	<2%
Few	2% - 10%
Common	10% - 20%
Many	20% - 50%
Abundant	50% - 90%
Very abundant	> 90%

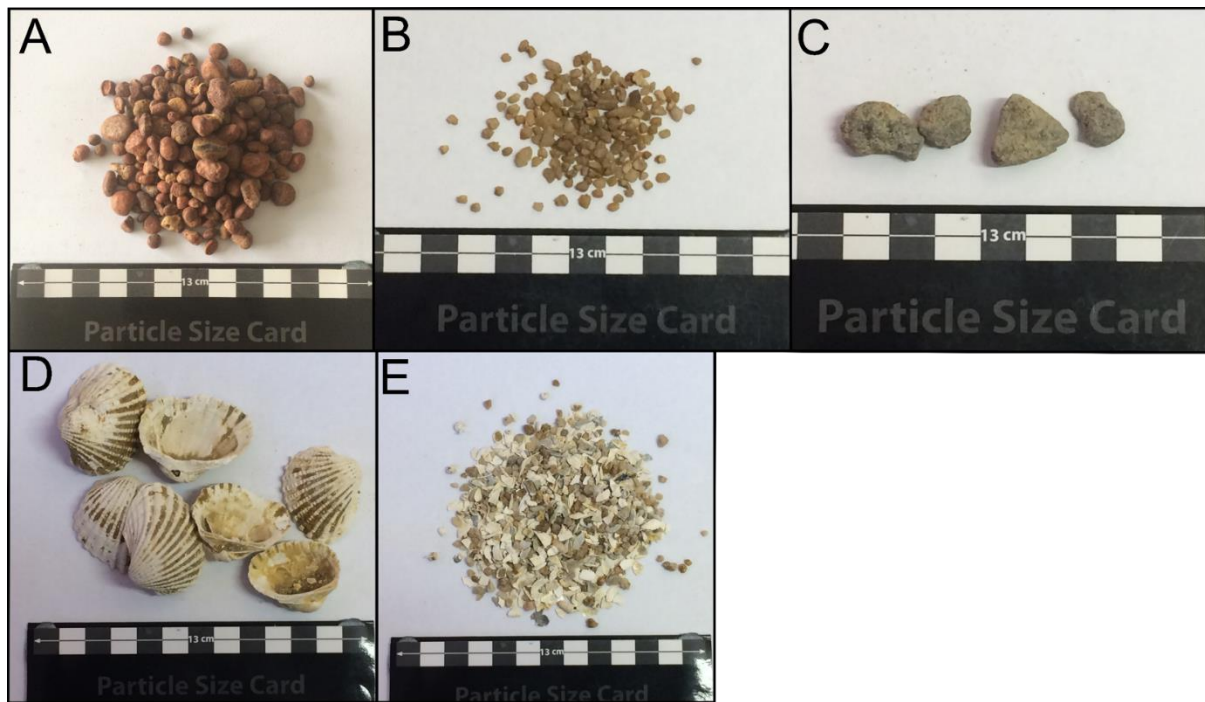


**Figure 3.6:** Coarse fragments found within sediments at the Albatross Bay study locations. (A) Pisoliths, (B) Quartz granules, (C) Subrounded to subangular rock fragments, (D) Whole shell, (E) Shell fragments and shell hash.

The presence of roots and other plant macrofossils within the sediments were described as follows (McDonald and Isbell, 2009, p. 148):

Root size	Diameter
Very fine	< 1 mm
Fine	1 mm – 2 mm
Medium	2 mm – 5 mm
Coarse	> 5 mm

Root abundance	Number of roots per 0.01 m <sup>2</sup> (100 mm x 100 mm)	
	Very fine and fine roots	Medium and coarse roots
None	0	0
Few	1 – 10	1 or 2
Common	10 – 25	2 - 5
Many	25 – 200	> 5
Abundant	> 200	> 5

Finally, the nature of the lower boundary of each sediment layer was recorded using the following guide from McDonald and Isbell (2009, p. 149):

<b>Boundary distinctness</b>	<b>Width of boundary</b>
Sharp	< 5 mm
Abrupt	5 mm – 20 mm
Clear	20 mm – 50 mm
Gradual	50 mm – 100 mm
Diffuse	> 100 mm

### 3.2.3.3 Sediment sampling

Sediment samples for laboratory analyses were collected from each excavation and auger hole at 10 cm intervals. Additional samples were collected where there were marked changes in the stratigraphy. The sampling interval of 10 cm was based on the overall thickness of the sedimentary units observed within each pit while in the field. This sampling interval enabled a high-resolution record of depositional environmental change to be delineated. Samples of approximately 100 g field weight were transferred to plastic Ziploc bags, with details of the sample recorded on the bag with a permanent marker as well as in a field notebook. Location and sample data was transferred to an Excel spreadsheet each evening. The samples were double-bagged prior to transport to the laboratory. The D-section cores were extruded into rigid polyvinyl cradles. The cradles were then wrapped with plastic film and the ends of each tube were sealed with adhesive tape to protect them from damage and compaction during transport back to the laboratory.

## 3.3 Sediment analyses

### 3.3.1 Drying and storage of sediment samples

All the sediment samples and cores were transferred from the field to the soils and sediments analysis facility at Macquarie University. D-section cores were stored in their field state in a refrigerator prior to analysis to reduce the rate of microbial metabolism and to prevent the shrinkage of the D-section cores from moisture loss (Gale and Hoare, 1991). Each D-section core was sampled according to the strategy illustrated in Figure 3.7. A quarter of each

core was allocated to measuring particle size, organic carbon content and carbonate content. This quarter was sampled at 1 cm intervals, with the outer edges of each subsample removed to prevent sample contamination. All sediment samples from this quarter of the D-section core, along with samples from the pits and auger holes, were oven dried at 60°C for 65 hours to remove moisture (Lewis and McConchie, 1994). This drying temperature was chosen to minimise the alteration of clay particles (Lewis and McConchie, 1994) and is consistent with other studies from within the GoC and along the eastern coast of Australia (e.g. Couapel, 2005; Petherick *et al.*, 2008). The second quarter of each D-section core was allocated for future biological analysis, while the remaining two quarters were preserved for collecting samples from for radiocarbon dating, and for any future analyses.

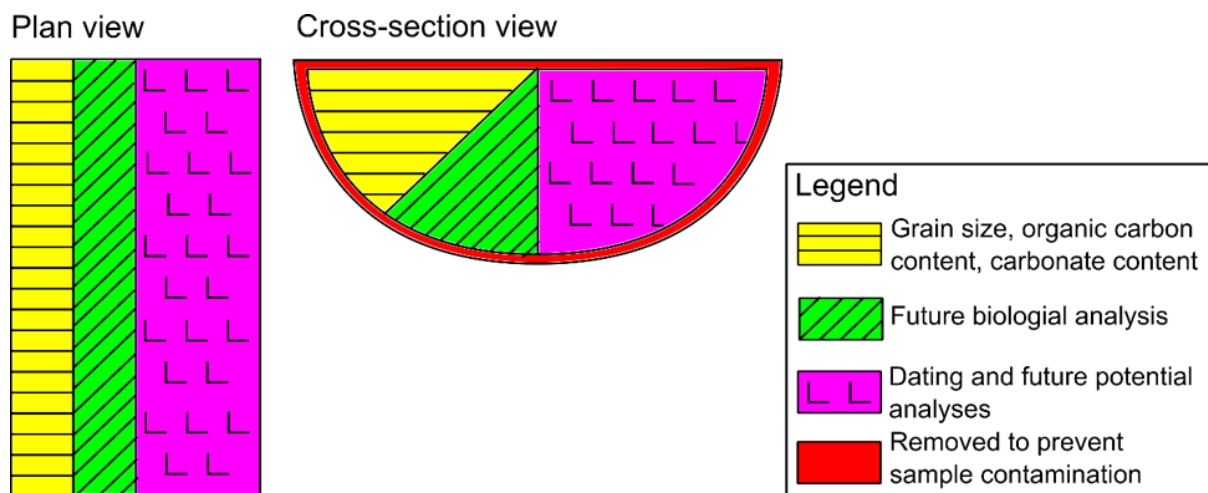


**Figure 3.7: D-section cores sampling strategy.**

Once dry, sediment samples were stored in plastic zip lock bags or cleaned plastic containers prior to analysis.

### 3.3.2 Organic carbon and carbonate content

Measuring the organic carbon content and carbonate content within sediments is a fundamental and routine technique in geomorphological research (Kennedy and Woods, 2013). Organic carbon within sediments comes from the decomposition of plants and animals, and, “... a wide variety of organic carbon forms are present and range from freshly deposited litter (e.g. leaves, twigs, branches) to highly decomposed forms such as humus...” (Schumacher, 2002, p. 2). Carbonates (inorganic carbon) within sediments originate from geological sources (e.g. carbonate sedimentary rocks; Schumacher, 2002) or, as is more likely in coastal sediments,

from biogenic sources such as coral, shell fragments and foraminifera (Short, 2005). Trends in the organic carbon content and carbonate content of sediments are therefore correlated to changes in the depositional environment (environmental, climatic and/or biological changes) (Santisteban *et al.*, 2004). These changes in the depositional environment may be drastic and observable in the stratigraphic record. However, fluctuations in organic carbon content and carbonate content may also be “... evidence of subtle or temporary changes that do not necessarily lead to any large-scale environmental change that is expressed in the litho- or biostratigraphy...” (Plater *et al.*, 2015, p. 312-313), hence the importance of this analysis.

Coastal sedimentary characteristics such as organic carbon content and carbonate content vary across various coastal environments as the ecosystem shifts from a marine-dominated to a freshwater-dominated one, allowing environments to be identified based partly on these characteristics (Plater *et al.*, 2015). For example, because intertidal and subtidal mudflats are generally un-vegetated, organic carbon content may be low compared to mangrove environments. Similarly, a high proportion of shells and shell fragments within intertidal and subtidal mudflats leads to such environments having a higher carbonate content than mangrove environments (see Section 1.4.2) (Geoscience Australia, 2015c).

There are numerous methods to determine organic carbon and carbonate content in sediments. These methods measure carbon content by determining either the amount of carbon dioxide released from a sample by wet or dry combustion, or the loss in mass of a sample from the removal of carbon by ignition or oxidation with hydrogen peroxide (Gale and Hoare, 1991). Each method has its own advantages and disadvantages in terms of convenience, cost and accuracy (for review see Nelson and Sommers, 1982; Gale and Hoare, 1991). Percentage loss on ignition (%LOI) was used in this study because it is widely employed and is the most practical and straightforward method available (Gale and Hoare, 1991; Heiri *et al.*, 2001; Rayment and Lyons, 2010).

Opinions vary on the optimum ignition temperature for measuring %LOI<sub>organics</sub>, with recommendations ranging from 360°C to 550°C (Ball, 1964; Davies, 1974; Bengtsson and Enell, 1986; Gale and Hoare, 1991; Heiri *et al.*, 2001; Boyle, 2004; Santisteban *et al.*, 2004; Rayment and Lyons, 2010; Salehi *et al.*, 2011; ASTM, 2014). While lower ignition temperatures of around 360°C reduce the loss in the mass of a sample from factors other than the combustion of organic carbon, such as mineral dewatering, which in turn reduces inaccurate measurements, low ignition temperatures also lead to partial (and variable) combustion of

organic matter, which in turn increases measurement inaccuracy (Boyle, 2004). Selecting an ignition temperature is therefore a compromise, with selection based on the sample material and the questions being investigated. Boyle (2004) recommends low ignition temperatures for organic-poor, clay-rich sediments. The bulk of sediment samples from this study were neither clay-rich nor organic-poor. Accordingly, an ignition temperature of 500°C for 4 hours was selected, as recommended by Heiri *et al.* (2001), Rayment and Lyons (2010) and Engel *et al.* (2014). The ignition temperature to measure %LOI<sub>carbonates</sub> is less controversial, with an ignition temperature of 950°C for 2 hours used in this study, following the work of Heiri *et al.* (2001) and Rayment and Lyons (2010).

Porcelain crucibles used for %LOI analysis were weighed and recorded (M<sub>1</sub>). To ensure that samples were at a constant dry weight prior to ignition, a minimum of 1g of the clay to sand-size fraction (<2 mm) of each sample was placed in the pre-weighed crucibles and left in an oven at 60°C for a minimum of 65 hours, a temperature consistent with the drying method described in Section 3.3.1. The crucibles were moved into a desiccator and cooled to room temperature before being reweighed (M<sub>2</sub>). Care was taken to minimise the time the crucible contents were exposed to air to minimise any increase in mass as the sample equilibrates with laboratory humidity. The crucibles were then carefully placed in a muffle furnace and burnt at 500°C for 4 hours before being removed once more to the desiccator to cool to room temperature. The crucibles were then weighed a third time (M<sub>3</sub>), and %LOI<sub>organics</sub> calculated using the following formula:

$$\%LOI_{organics} = 100[(M_2 - M_1) - (M_3 - M_1)] / (M_2 - M_1)$$

Next, the porcelain crucibles containing the burnt samples were ignited in the muffle furnace at 950°C for 2 hours, cooled to room temperature in a desiccator, and weighed a fourth time (M<sub>4</sub>). %LOI<sub>carbonates</sub> was then calculated using the following formula:

$$\%LOI_{carbonates} = 100[(M_3 - M_1) - (M_4 - M_1)] / (M_2 - M_1)$$

Prior to each sample run, all the empty crucibles were put through the same process (500°C for 4 hours, followed by 950°C for 2 hours) to remove any contaminants.

### 3.3.3 Particle size analysis

Particle size analysis is regarded as an essential tool for interpreting sedimentary stratigraphy and depositional environments (Briggs, 1977; Poppe *et al.*, 2000; Switzer and Pile, 2015). The particle size distribution of a sedimentary facies is controlled by the source material

of the sediments, the transportation mechanisms involved, and the physical and chemical processes operating at the specific depositional environment (Blott and Pye, 2001; Reeves, 2004; Switzer, 2013). Particle size, and particle size parameters, are commonly measured and described using the Udden-Wentworth scale that is based on a logarithmic ( $\phi$ ) scale developed by Krumbein (1934). With the increasing use of laser-based technology to measure particle size, there has been a shift from using the Udden-Wentworth scale to metric units (microns ( $\mu\text{m}$ )) (Switzer, 2013; Switzer and Pile, 2015). Four parameters are used to describe the particle size distribution of a sediment sample: mean grain size, sorting, skewness and kurtosis. These parameters are calculated via either mathematical (method of moments) or graphical methods (see Section 3.3.3.5) (Blott and Pye, 2001).

#### 3.3.3.1 Mean grain size

Mean grain size refers to the average diameter of the particles within a sediment sample, and is the most commonly used parameter to describe sediments, for example as fine-, medium- or coarse-grained sand (Switzer, 2013). Within a beach environment, the grain size of a sediment sample is dependent on the sediment source, the offshore gradient, wave energy, tidal regime, and coastal currents, all influencing the erosion, transportation, selective sorting and deposition of the sediments. Coarser deposits are usually found in environments that experience higher wave energy and/or steeper offshore gradients, while finer deposits are found where wave energy is low or non-existent and/or offshore gradients are flat (Gale and Hoare, 1991; Lewis and McConchie, 1994; Switzer and Pile, 2015).

#### 3.3.3.2 Sediment sorting

Grain sorting describes the range of particle diameters within a sediment sample, measured as the standard deviation around the mean grain size. Well-sorted samples exhibit a smaller range of particle diameters while poorly-sorted samples exhibit a larger range (Blott and Pye, 2001; Switzer, 2013). Similar to mean grain size, how well a sediment sample is sorted depends on the energy levels of the transportation and deposition processes acting within an environment (Lewis, 1984). For example, beach sediments are better sorted on coasts that have a higher wave energy and are swash-dominated, compared with those on low-wave energy coastlines. Aeolian sediments are commonly well-sorted, while glacial sediments are often poorly sorted (Goldsmith, 1985; Trenhaile, 2005; Bird, 2008; Switzer, 2013). However, this pattern is not always linear. For example, during high-energy events in a coastal environment, such as storms, the competency and carrying capacity of waves increase, allowing the coarsest grains being transported as well as finer particles. If the competency and carrying capacity



rapidly decreases at the end of the storm, all the grain sizes being transported will be deposited together, resulting in a poorly sorted deposit (Lewis, 1984).

#### 3.3.3.3 Sediment skewness

Skewness is a particle size distribution descriptor that refers to whether the distribution of particle diameters in the sample is symmetrical about the mean, or whether it is asymmetrical. If there is an excess of fine-grained material in the sample, the particle size distribution will be fine-skewed (positively-skewed). If there is an excess of coarse-grained material, the distribution will be coarse-skewed (negatively-skewed) (Lewis, 1984; Blott and Pye, 2001; Sloss, 2005; Switzer, 2013). Skewness can help identify the environment of deposition of the sediment. For example, beach sediments are commonly coarse-skewed because fine particles are often removed by wind or wave action, and/or coarse sediments are added to the deposit by higher-energy events (Gale and Hoare, 1991; Trenhaile, 2005; Bird, 2008). In contrast, aeolian sediments are commonly fine-skewed due to the transport of fine-grained sediment in suspension by the wind (Friedman, 1961; Goldsmith, 1985). However, the particle size distribution of beach sediments may also be fine-skewed, with fine-skewed distributions occurring more often in coarse-grained sand rather than very fine- to medium-grained sands (Friedman, 1961; Trenhaile, 2005)

#### 3.3.3.4 Sediment Kurtosis

Kurtosis refers to the “peakedness” of a particle size distribution, with a flatter distribution curve being classified as “platykurtic”, a highly-peaked distribution curve considered “leptokurtic”, and those in between referred to as “mesokurtic” (for information on the precise calculation and classification of kurtosis, see Lewis, 1984). Kurtosis can be a secondary indicator of sorting, with platykurtic curves indicating poorly-sorted sediments, and leptokurtic curves indicating well-sorted sediments (Switzer, 2013). For example, aeolian sediments are often leptokurtic, while beach sediments are mesokurtic or platykurtic (Goldsmith, 1985).

#### 3.3.3.5 Method

Particle size analysis was carried out on all the sediment samples collected at 10 cm intervals from the excavated pits, and at 10 cm intervals from selected D-section cores ( $n = 487$  samples). Physical sediment analysis was conducted using a Malvern Mastersizer 2000 laser diffraction particle size analyser with an attached Hydro 2000G sample dispersion unit. The Malvern Mastersizer 2000 is capable of measuring the particle size distribution of samples

from 0.02 to 2000  $\mu\text{m}$  (Malvern Instruments, 2007). Where necessary, particles that were larger than 2000  $\mu\text{m}$  (2 mm) were analysed by manual sieving.

Samples were dry-sieved through a 2 mm mesh sieve, and all grains  $>2$  mm were set aside for further sieve analysis. For the  $<2$  mm grains, any visible roots and large shells were removed by hand and the samples pre-treated with hydrochloric acid (HCl, 10%) and hydrogen peroxide ( $\text{H}_2\text{O}_2$ , 10%) to remove all other carbonates and organic matter until reactions were complete (Switzer and Pile, 2015). Organic matter is removed because it may bind the mineral particles together, affecting sample dispersion and median grain size and therefore particle size measurements (Murray, 2002). Carbonate also acts as a cement that binds particles together and, along with the presence of shell fragments, will affect particle size data (Murray, 2002). Following pre-treatment, samples were dried in an oven at  $60^\circ\text{C}$ , gently crushed, and dry-sieved at a 2 mm mesh size a second time to ensure that the maximum size fraction that can be passed through the Hydro 2000G pump was not exceeded.

The refractive index (RI) and its absorption (ABS) along with the dispersant used (water) and its RI, need to be entered for the Malvern Mastersizer software to apply the Mie theory to the particle size data. The optical properties of natural sediments are highly variable (Sperazza *et al.*, 2004). A standard method of measurement therefore has not been established, and it is common for published literature to lack information on measurement details of laser diffraction particle size analysis, including the RI and ABS used (Ryżak and Bieganski, 2011). A RI of 1.544 (the RI of silicon dioxide/natural quartz) and ABS of 1 was used based on the recommendations of Sperazza *et al.* (2004). The dispersant used for this study was water, which has a RI of 1.33.

A riffle splitter was used to obtain a representative subsample of approximately 1 g to 3 g from each sample. The quantity of sediment that can be added to the Malvern Mastersizer is constrained by the “obscuration” measured by the Malvern Mastersizer, which is the percentage of light that is obscured from the laser beam as the suspended particles pass in front of it. If the obscuration level is too low, the number of particles present is too small to obtain reliable results; if too high, the laser beam may undergo secondary refraction, affecting particle size measurements (Ryżak and Bieganski, 2011). The manufacturer recommends an obscuration range between 3% and 20%, depending on the sample and dispersion units used, with lower obscuration values recommended for finer sediments and higher obscuration values for coarser sediment (Malvern Instruments, 2007). Accordingly, for the finer samples such as

sediments from the D-section cores, an obscuration value of between 5% and 10% was chosen. For the coarser samples, such as the sediments from the beach ridges, an obscuration value of between 10% and 20% was chosen.

Samples introduced into the Malvern Mastersizer are automatically dispersed using ultra-sonication set at 50% power. Without sonication, the mean grain size of the sample might be overestimated because of natural grain aggregation, and the measurement result may lack reproducibility. Ultrasonic dispersion was continued until a stable particle size distribution was observed and the obscuration level was stable. The Malvern Mastersizer 2000 Hydro 2000G sample dispersion unit also contains a stirrer that prevents the settlement of particles in the dispersion unit, and a pump to move the sediment suspension through the measuring flow cell. For the samples analysed here, it was observed that all particles were circulating through the system, and stable results were recorded, when the stirrer speed was set at 500 rpm and the pump speed at 1250 rpm.

Three successive laser diffraction runs of 45 seconds each were run per sample. Prior to each laser diffraction measurement, background measurements of the dispersant of 30 seconds duration each were recorded. The suitability of the parameters chosen (obscuration, ultra-sonic power, pump speed and stirrer speed) was examined for all samples by looking at any change, or lack thereof, in the median grain size measured, known as  $d(0.5)$ , during the consecutive measurements. If the  $d(0.5)$  remains stable across the three measurements, it indicates that all aggregates were broken up and the sample was stable throughout the measurement, giving confidence in the results (Ryżak and Bieganski, 2011). The residual value for each measurement was also under 1%, as recommended by Malvern Instruments (2007). Measurement data was compiled and analysed with Malvern's Mastersizer software version 5.6.

Particle size analysis on the  $>2$  mm portion of each sample was done using the dry-sieving technique commonly used for sand-sized and coarser sediments. Macro-organic matter, shells and shell fragments were first removed by hand before the samples were dry-sieved at  $1\phi$  intervals from  $-1\phi$  to  $-5\phi$  (2 mm – 32 mm) following procedures detailed in Lewis and McConchie (1994). Sieves were cleaned before each use by inverting and tapping out any remaining sediments and gently brushing the mesh screens with a soft brush. Each sample was then added to the top sieve within the sieve stack, with care taken not to overload the sieves. Samples were sieved for 10 minutes using an Endecotts Octagon 200CL sieve shaker set to an

amplitude of 1.5 mm, and the portion of sediment from each sieve was weighed to four decimal places to obtain a particle size distribution.

There are difficulties in merging particle size data that was measured using different techniques because each technique measures particle size slightly differently. In this case, laser diffraction measures the size of a particle by “... providing a diameter of the sphere that yields an equivalent light scattering pattern to the particle being measured...” (Switzer, 2013, p. 225). On the other hand, sieving measures the size of a particle by its two shortest dimensions (Mason, 2016). However, there is no single technique that can measure the entire spectrum of particle sizes (for example, sieving is not suitable for silt- or clay-sized particles while laser analysis cannot measure particle larger than 2 mm) (Switzer and Pile, 2015). Merging of particle size data sets to obtain the particle size distribution of a sample is routine in geomorphological studies (see, for example, Cheetham *et al.*, 2008; Forsyth *et al.*, 2010; Nott *et al.*, 2013).

Merging of the laser diffraction and dry-sieving particle size results was carried out using recommendations of the North East Atlantic Marine Biological Analytical Quality Control Scheme (NMBAQC), Best Practice Guidance for particle size analysis (Mason, 2016). Because the Malvern Mastersizer software calculates the percentage of grains at set micron intervals, the laser diffraction data was first transferred into a Microsoft Excel spreadsheet and converted into the Udden-Wentworth scale (Wentworth, 1922), to produce a particle size distribution in terms of % sand, % silt and % clay and their finer subdivisions (i.e. % very fine silt, % fine silt, % medium silt, and so on). The laser diffraction volume data (%) was then converted into weight (g), using the total weight of the sediment portion that was < 2 mm, and merged together with the sieve weights for sediment > 2 mm to produce a merged particle size percentage distribution. The particle size parameters described above (mean, median, sorting, skewness and kurtosis) were then calculated by geometric graphical methods, according to the formulas of Folk (1954) and Folk and Ward (1957) using GRADISTAT, a grain size distribution and statistics package created by Blott and Pye (2001) (Table 3.2). Particle size results from this study are reported in metric units.

**Table 3.2: Statistical formulae used in GRADISTAT to calculate grain size parameters and the associated descriptive terminology for the grain size data ( $P_\chi$  is the grain diameter in metric units, at the cumulative percentile value of  $\chi$ )**  
(Source: Blott *et al.* (2001), Table II).

Geometric (modified) Folk and Ward (1957) graphical measures

Mean		Standard deviation	
$M_G = \exp \frac{\ln P_{16} + \ln P_{50} + \ln P_{84}}{3}$		$\sigma_G = \exp \left( \frac{\ln P_{16} - \ln P_{84}}{4} + \frac{\ln P_5 - \ln P_{95}}{6.6} \right)$	
Skewness		Kurtosis	
$Sk_G = \frac{\ln P_{16} + \ln P_{84} - 2(\ln P_{50})}{2(\ln P_{84} - \ln P_{16})} + \frac{\ln P_5 + \ln P_{95} - 2(\ln P_{50})}{2(\ln P_{25} - \ln P_5)}$		$K_G = \frac{\ln P_5 - \ln P_{95}}{2.44(\ln P_{25} - \ln P_{75})}$	
Sorting ( $\sigma_G$ )		Skewness ( $Sk_G$ )	
Very well sorted		Very fine skewed	
Well sorted		Fine skewed	
Moderately well sorted		Symmetrical	
Moderately sorted		Coarse skewed	
Poorly sorted		Very coarse skewed	
Very poorly sorted			
Extremely poorly sorted			
		Kurtosis ( $K_G$ )	
		Very platykurtic	
		Platykurtic	
		Mesokurtic	
		Leptokurtic	
		Very leptokurtic	
		Extremely leptokurtic	

### 3.4 Geochronology

#### 3.4.1 Optically Stimulated Luminescence (OSL)

##### 3.4.1.1 Field Sample collection

Eighteen samples for OSL dating were collected in stainless steel tubes, 20 cm in length and 5 cm in diameter, to ensure that samples were not exposed to any light prior to analysis in the laboratory. Seventeen tubes were hammered horizontally into the walls of the pits dug into the beach ridge crests, swales and supratidal mudflats at Red Beach, Kwamter and Wathayn (Figure 3.8). An additional sample was retrieved from below the water table at Kwamter by attaching the sampling tube to the end of a soil auger and augering vertically into the floor of the pit.

When sampling from a pit wall, a metal cap was attached to one end of the stainless-steel tube, and the other end was placed flush against the pit wall and hammered in until the outer end of the tube was flush with the section (Figure 3.8). The tube was then removed from the pit wall, and both ends were packed with paper before being re-capped and sealed tightly with duct tape to avoid the shifting and mixing of exposed bleached grains and unbleached grains within the tubes during transport. Because most of the samples were from beach ridges rich in quartz grains, only one tube was collected from each location. While most of the samples were collected at least 30 cm from stratigraphic unconformities to minimise any changes in the

gamma ray contribution to the sediment dose rate from changing sediment compositions (Bateman, 2015; Duller, 2015), it was not always possible to do this due to the sediment stratigraphy within the pits, the difficulty of sampling within the narrow confines of pits and uncertainties about the depth of penetration of the auger. The location of each sample with respect to stratigraphic boundaries is shown in the sedimentary log diagrams in Appendix C.



**Figure 3.8: (A) OSL tube inserted into pit wall. (B) Hammering OSL tube into pit wall. (C) OSL sample collected. The ends of each tube were protected by black plastic caps and duct tape.**

#### 3.4.1.2 Laboratory sample processing procedures

All OSL samples were processed and analysed at “Traps”, Macquarie University’s luminescence dating facility (<https://www.mq.edu.au/research/research-centres-groups-and-facilities/secure-planet/facilities/osl-laboratory>). Processing and analysis was carried out under subdued red-light conditions to preserve the light-sensitive luminescence signal. Once opened, approximately 5 cm of sediment from the ends of each tube were removed as the material was potentially exposed to light during sample collection. These sediments were used to measure the water content of the sample, then crushed to a fine powder using a ball mill for dosimetry analysis.

The remaining undisturbed inner portion of the sample was sieved using tap water to separate the grains into <90  $\mu\text{m}$ , 90-212  $\mu\text{m}$  and >212  $\mu\text{m}$  fractions. Once separated, the various fractions were each rinsed with distilled water and the >212  $\mu\text{m}$  fraction was transferred to a

beaker, dried in an oven at a temperature not exceeding 50°C, and bagged and stored in a light-tight container. The <90 µm fraction that still contained the distilled water washings was double-bagged and stored in a light-tight container. The 90-212 µm size fraction to be used for luminescence dating was treated with 10% HCl for a minimum of 24 hours, then 10% H<sub>2</sub>O<sub>2</sub> for a minimum of 24 hours, to remove carbonates and organics respectively. The 90-212 µm size fraction samples were rinsed with distilled water before being dried in the oven prior to mineral separation.

The 90-212 µm size fraction was next separated into quartz, feldspar and heavy mineral components using sodium polytungstate density separation solution. The quartz and feldspars were first separated from the heavy minerals using a density of 2.7 cm<sup>3</sup>. The sample was added to the sodium polytungstate and the resultant mixture was centrifuged for 7 mins, whereupon the quartz and feldspar grains floated to the top and the heavy minerals sank to the bottom of the centrifuge tube. The grains were then separated from the sodium polytungstate by decanting the solution through filter paper and drying in an oven. The process was repeated with the quartz and feldspar grains where, at a density of 2.62 cm<sup>3</sup>, the feldspar grains float to the top and the quartz grains sink to the bottom of the centrifuge tube. The feldspar grains were washed with distilled water, dried and stored in light-tight containers.

The separated quartz grains were also washed with distilled water and dried. The quartz grains were then etched in 40% hydrofluoric acid (HF) for 45 minutes to remove the alpha-irradiated outer layer of the quartz grains and remove any potential feldspar contamination. Finally, after being washed in distilled water and dried, the quartz grains were sieved and separated into their <90 µm, 90-125 µm, 125-180 µm and 180-212 µm size fractions, with the 90-125 µm grains used in single-aliquot analysis, the 180-212 µm grains used in single-grain analysis, and the remaining size fractions stored in light-tight containers.

#### 3.4.1.3 Disc preparation

For single-aliquot analysis, the 90-125 µm quartz fraction was mounted onto 10 mm stainless steel discs using silicone oil spray (silkospray). The discs were loaded onto a disc carrier, covered using a selected mask size and lightly sprayed with silkospray. Because the sediment samples from Albatross Bay were found to have a bright luminescence signal during preliminary investigations, a 1 mm mask was used for most samples, with a 7 mm mask used only when preparing samples for bleaching experiments. A small mask size was chosen to increase the accuracy of the D<sub>e</sub> measurement as there would be less averaging of grains and

any issues with sediment mixing or partial bleaching becomes more apparent (Duller, 2008). After silkospray was applied, the discs were individually inverted, dipped into a pile of loose grains, and tapped to ensure that only a monolayer of grains remained. Stray grains along the sides and bottom of each disc were wiped away, and the prepared discs were stored in a disc holder and wrapped in black plastic to guard against any potential light exposure prior to measurement.

For single-grain analysis, the 180-212  $\mu\text{m}$  quartz fraction was loaded onto 10 mm aluminium discs that had 100 precision-drilled holes (with depth and diameter of 300  $\mu\text{m}$ ) arranged in a ten-by-ten grid. The single-grained discs were prepared one at a time under a microscope, with loose grains being lightly brushed onto the disc with a small paintbrush.

#### 3.4.1.4 Sample analysis equipment

For all samples analysed, luminescence emissions were detected by an Electron Tubes Ltd 9235QA photomultiplier tube fitted with a 7.5 mm Hoya U-340 filter mounted onto a Risø TL/OSL reader, model TL-DA-20. For single-aliquot measurements of the natural, regenerative and test doses, the discs were stimulated at 125°C for 100 seconds using an array of blue diodes at 50% optical power. For single-grain measurements of the natural, regenerative and test doses, the each grain was stimulated at 125°C for 2 seconds using a 10 mW 532 nm Nd:YVO<sub>4</sub> solid-state diode pumped single-grain green laser at 90% optical power.

#### 3.4.2 Radiocarbon Ages

##### 3.4.2.1 Field sample collection

Whole shell samples for radiocarbon dating were collected from the pits dug into the beach ridge crests, swales and intertidal mudflats at Red Beach, Kwamter and Wathayn (Figure 3.9). At Red Beach, the radiocarbon shell samples were selected to address one of two goals (Table 3.3). Firstly, radiocarbon samples were collected to expand the Red Beach chronology established through OSL dating. Shell samples were therefore collected from the base of pits excavated into two separate swales on the beach ridge plain (RS2 and RS5). Most of the samples for OSL were collected from the beach ridge crests, with only one swale (RS10) dated using OSL techniques. Secondly, radiocarbon samples were collected from the bases of pits excavated into five beach ridge crests (RR2, RR4, RR5, RR9 and RR11) to provide a direct comparison with OSL ages from the same environments of deposition.

At Kwamter, a shell sample from a shelly deposit within the supratidal mudflat (KI2) was collected for radiocarbon age determination to expand the chronology obtained through



OSL dating (Table 3.3). This shell sample was expected to provide an estimated age for the deposition of the transgressive shell lag. A total of 8 shell samples were collected for radiocarbon dating.

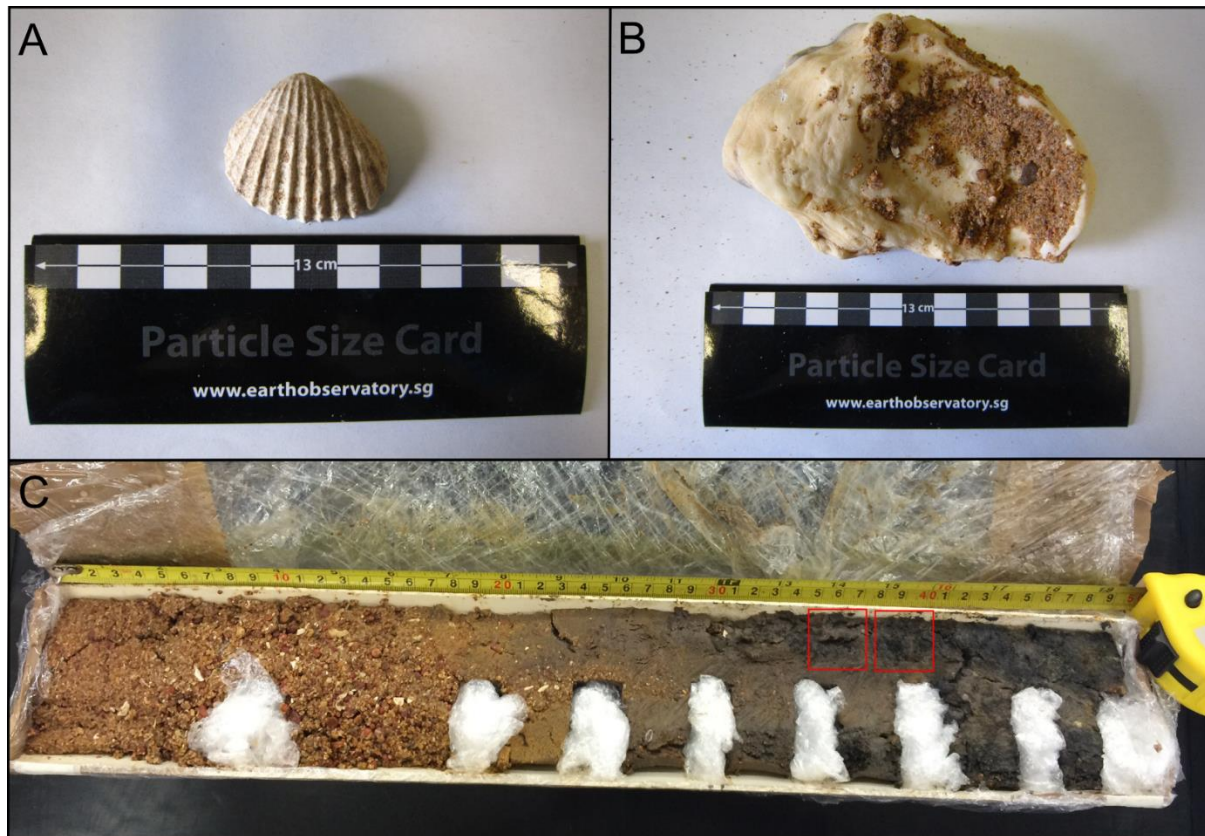


**Figure 3.9: Samples sent for radiocarbon dating. (A) Arcidae (*T. granosa*) shell from Red Beach RS5 (sample RB09 103). (B) Ostreidae shell from Red Beach RR5 (sample RB10 113). (C) Bulk sediment samples (marked with red box) from Red Beach RR3 (sample RB06 166 and RB06 167).**

**Table 3.3: Radiocarbon dating strategy for shell and bulk sediment samples collected from Red Beach, Kwamter and Wathayn.**

Location	Field Code	Sample material	Reason for Radiocarbon dating
Red Beach - RS2	RB05 140	Shell	Expand Red Beach chronology - dating beach swale
Red Beach - RS5	RB09 103	Shell	
Red Beach - RR2	RB01 104-109	Shell	Compare with burial ages obtained through OSL techniques
Red Beach - RR4	RB08 100	Shell	
Red Beach - RR5	RB10 113	Shell	
Red Beach - RR9	RB21 91	Shell	
Red Beach - RR11	RB18 115	Shell	
Kwamter - KMF2	KW03	Shell	Expand Kwamter chronology - dating transgressive shell lag
Red Beach - RR3	RB06 166	Sediment	Expand Red Beach chronology - dating intertidal deposit below beach ridge
Red Beach - RR3	RB06 167	Sediment	
Kwamter - KMF1	KW06 178	Sediment	Expand Kwamter chronology - dating intertidal deposit below supratidal mudflat
Wathayn - W11	WHA D06 48	Sediment	Expand Wathayn chronology - dating intertidal deposit at the end of Wathayn transect

In addition to the shell samples, bulk sediment samples collected from within the D-section cores at Red Beach, Kwamter and Wathayn were also sent for radiocarbon analysis (Figure 3.9). At Red Beach, ages were obtained for two radiocarbon bulk sediment samples from the intertidal mudflat sediments deposited beneath the beach ridge RR3 (RB06 166 and RB06 167). A bulk sediment sample from the base of a D-section core (KW06 178) collected at Kwamter was also analysed to obtain an estimated age for the commencement of sediment accumulation within the core (Table 3.3). A bulk sediment sample from the base of the D-section core collected in the mangrove fringe at the proximal end of the Wathayn beach ridge transect (WHA D06 48) was analysed to provide an estimated age for the colonisation by mangroves after formation of the beach ridge (WR1) (Table 3.3). A total of four bulk sediment samples were sent to the lab for radiocarbon age determination.

#### 3.4.2.2 Laboratory sample processing

All samples for radiocarbon age determination were sent to the University of Waikato Radiocarbon Dating Laboratory in New Zealand. Shells were identified to species level prior to being sent for analysis. Difficulties in identification led to two Ostreidae shells being identified only to family level. The selected shells were all from species that are suspension feeders because the dating of deposit feeders is known to be unreliable. Radiocarbon age determination from deposit feeders are often contaminated by ‘old’ carbon introduced through ingested sediments (Ulm, 2006). All shells accepted for analysis were tested in the Waikato lab for evidence of recrystallization and shells showing signs of recrystallization were rejected.

Six of the shell samples were large enough to be analysed using standard radiometric dating, while the Accelerator Mass Spectrometry (AMS) technique was used for the other four shells. The same pretreatment process was applied to all the shell samples (Dr F. Petchey, Waikato Radiocarbon Laboratory, pers. comm.). The shell surfaces were cleaned, and shells were washed with distilled water in an ultrasonic bath. Samples were then acid washed using dilute HCl (2M) for 120 seconds to minimise the possibility of contamination through isotopic exchange between the sample and its environment. Shells were then rinsed again and dried prior to being analysed.

The AMS technique was used for all the bulk sediment samples and all samples were subject to the same pretreatment process (Dr F. Petchey, Waikato Radiocarbon Laboratory, pers. comm.). The samples were examined under a microscope, and all visible contaminants including roots and rootlets were removed. Samples were then washed in hot HCl to remove

the inorganic carbon and absorbed CO<sub>2</sub>, rinsed, and treated with multiple hot sodium hydroxide (NaOH) washes. The NaOH insoluble fraction was treated with hot HCl, filtered, rinsed and dried prior to analysis.

All radiocarbon ages obtained for this research were calibrated using OxCal version 4.2.4 using the IntCal13 and Marine13 calibration curves of Reimer *et al.* (2013). A  $\Delta R$  of  $-103 \pm -16$  years was used, based on unpublished calculations by Ulm (see Section 2.1.2) (Dr F. Petchey, Waikato Radiocarbon Laboratory, pers. comm., 15 March 2016).

## **Chapter 4**

### **Coastal Sedimentary Environments of Albatross Bay**

Chapter 4 presents the results obtained from the field surveys of the topography and sedimentary stratigraphy at the three study locations in Albatross Bay, and the laboratory-based sedimentary analyses described in Section 3.3. The chapter begins with descriptions of the landscapes and sediments at the three field locations identified in Section 3.2.1. The field descriptions and laboratory data are then combined to develop a facies scheme for Albatross Bay. The facies scheme described in Section 4.4 is essentially a summary of the characteristics of the coastal sediment stratigraphy around the shoreline of Albatross Bay; the complete laboratory dataset and sedimentary logs can be found in Appendix A and B respectively. This facies scheme, when combined with a chronological framework (Chapter 5), will facilitate determination of the geomorphic evolution of these coastal landscapes in response to palaeo-environmental and sea level change, as discussed in Chapter 6.

#### **4.1 Red Beach**

As previously described (Section 3.2.1), Red Beach is located on the northern shore of Albatross Bay 9 km northeast of Weipa township (Figure 3.1). The shoreline is approximately 650 m long and faces southeast towards the mouth of the Mission River where it flows into Albatross Bay. The modern beach at Red Beach consists of a gently sloping beachface, a narrow flat berm and a backbeach of variable width abutting the foredune. It is predominantly composed of mineral sands and pisoliths, along with shell, shell hash and organic detritus, overlying an intertidal mudflat that is exposed at low tide (Figure 4.1). Behind the beach, a beach ridge plain comprising a sequence of 13 beach ridges and intervening swales extends approximately 1 km inland (Figure 4.2, Figure 4.3). Note that this is a beach ridge plain, formed from fair-weather swash processes alternating with low frequency, higher magnitude storm events (see Section 6.1.1), as opposed to the chenier plains found along the southern and eastern shoreline of the GoC that were studied by Rhodes (1980) (see Section 2.4). This difference in beach ridge and chenier development is a result of the geomorphology of the coastal zone (see Section 1.4.2).

The Red Beach beach ridges are most distinct towards the northeast, near Andoom Creek, where they are protected from erosion by a fringe of mangroves between the foredune and the open water (Figure 4.2A). The ridges have a relatively low relief, with an average height difference between ridge crest and swale of 0.52 m, and a maximum height difference between ridge crest and swale of 1.26 m (Figures 4.3 and 4.4). A wetland that is inundated during the wet season is located near the middle of the beach ridge plain (Figures 4.2B and 4.3). Inland of the beach ridge plain, the land rises to elevations of approximately 10 m above sea level at the top of the bauxite plateau that is currently being mined commercially (Figure 4.2B).



**Figure 4.1: Modern beach at Red Beach, showing sand and pisoliths mixed with shells, shell hash and organic detritus abutting an intertidal mudflat exposed at low tide.**



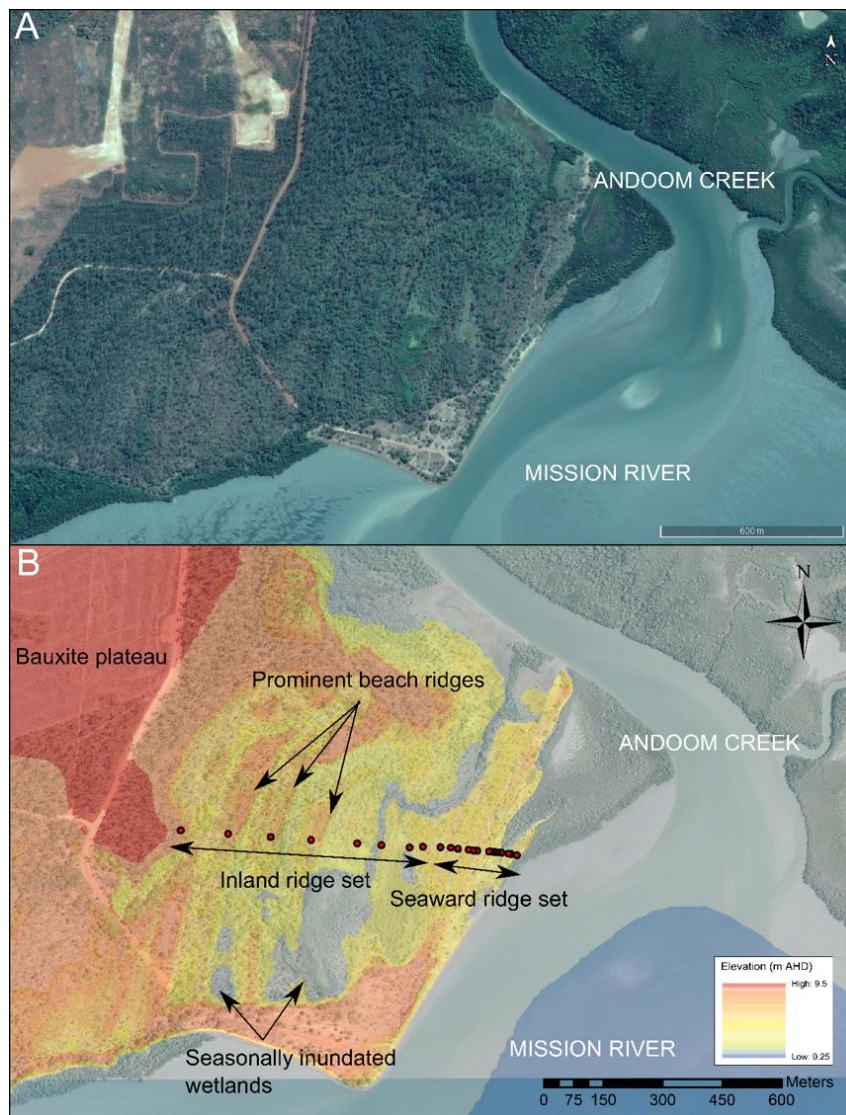


**Figure 4.2:** (A) Satellite image of the Red Beach study location, showing the extent of vegetation cover. Clearing inland for bauxite mining can be clearly seen on the northwestern edge of the image (Source: GoogleEarth, accessed 27<sup>th</sup> Dec 2017). (B) A digital elevation model of the Red Beach study location, showing detail of the topography of the beach ridge plain. A wetland separating the inland beach ridge set from the seaward beach ridge set can be seen in blue. The location of the topographic profile surveyed across the beach ridge plain is indicated by the line of red dots, each of which marks the location of excavated pits (Source of elevation data: LiDAR 0.25 m grid survey data flown in 2010 and provided by Riotinto Pty Ltd).

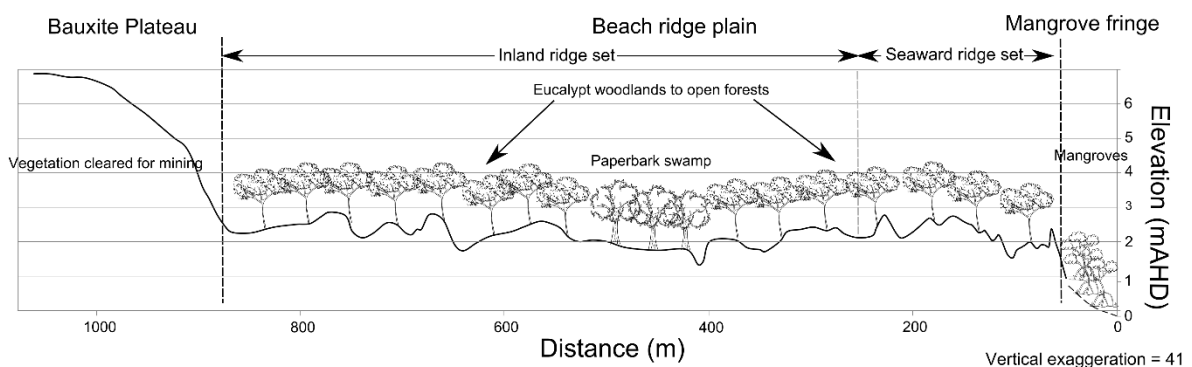


**Figure 4.3:** Topographic profile of Red Beach showing major land units and vegetation cover.



**Figure 4.4:** Red Beach transect location looking east towards the shoreline. Pink flags mark the locations of each ridge crest and swale which are of low relief. Vegetation includes *Eucalyptus tetradonta* and *Pandanus* spp. with a tall grass understorey that had been recently burnt when this image was taken.

Data obtained from the Queensland Herbarium (<https://environment.ehp.qld.gov.au/map-request/re-broad-veg-group/>, accessed 13<sup>th</sup> Jan 2018) indicates that the Red Beach study area supports two broad vegetation types – mangroves and saltmarshes, and eucalypt woodlands and open forests (Figures 4.3 and 4.5) (Queensland Herbarium, 2016). Mangrove species include *Rhizophora stylosa*, *Bruguiera gymnorhiza*, *Bruguiera cylindrica* and *Avicennia marina* in a closed to low closed forest, representing a mid to low intertidal mangrove assemblage. The vegetation on the beach ridge plain is predominantly *Eucalyptus tetradonta* (Darwin stringybark) woodland and includes *Corymbia clarksoniana* (Clarkson’s bloodwood) and *Eucalyptus brassiana*. *Pandanus* spp. are present in the sparse sub-canopy tree/shrub layer and the ground layer is dominated by tall grasses (Queensland Herbarium, 2016). Further inland, in seasonally inundated sections of the beach ridge plain, the vegetation comprises low open woodland, dominated by *Melaleuca viridiflora* (Paperbark), a species associated with wetland conditions (Townsend, 2016). *Corymbia* spp. and *Eucalyptus* spp. are also present, together with tall grasses and sedges.

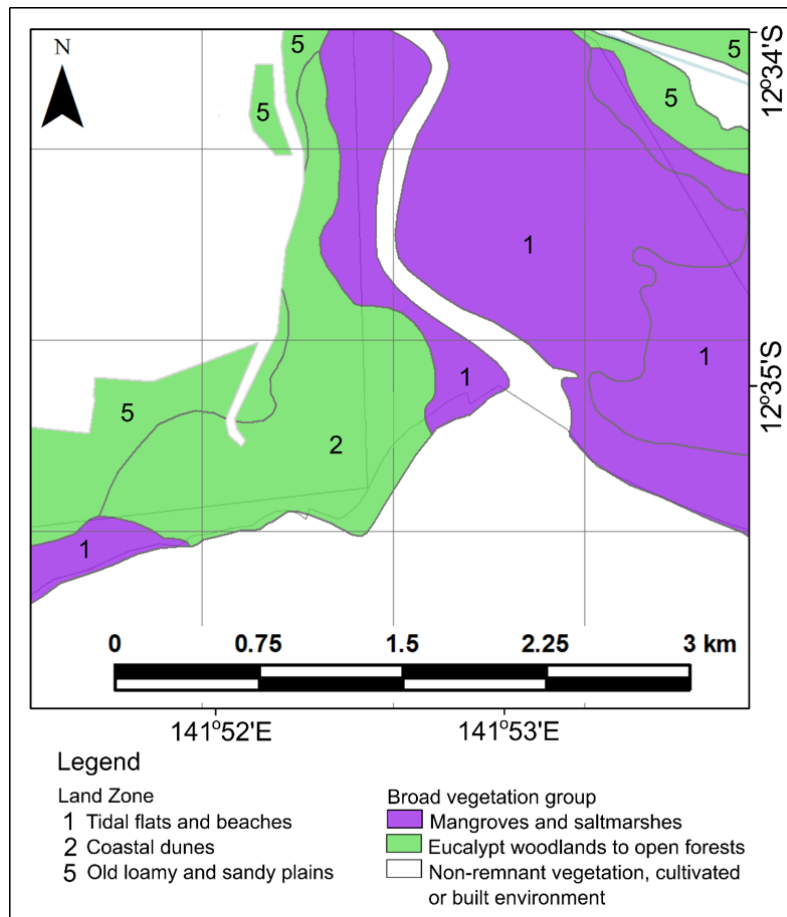


**Figure 4.5: Vegetation map of the Red Beach study location** (Source: Queensland Herbarium, <https://environment.ehp.qld.gov.au/map-request/re-broad-veg-group/>, accessed 13<sup>th</sup> Jan 2018).

#### 4.1.1 Modern beach sediments

As described in Chapter 3 (Section 3.2.3.1), a trench was excavated by hand perpendicular to the shoreline at Red Beach, to expose the sediments and stratigraphy underlying the beachface, berm and backbeach (Figure 4.6). The trench extended down to between 40 to 55 cm below the surface, until the water table was reached. Three vertical profiles through the sediments were described and sampled, with the sampled sediments then analysed in the laboratory, as described in Chapter 3 (Section 3.3). The field descriptions and the results of the laboratory analyses (Appendix A) were then combined to produce sedimentary logs of the three profiles (RBMT DF01, DF03 and DF05 – Figures 4.7, 4.8, and 4.9).



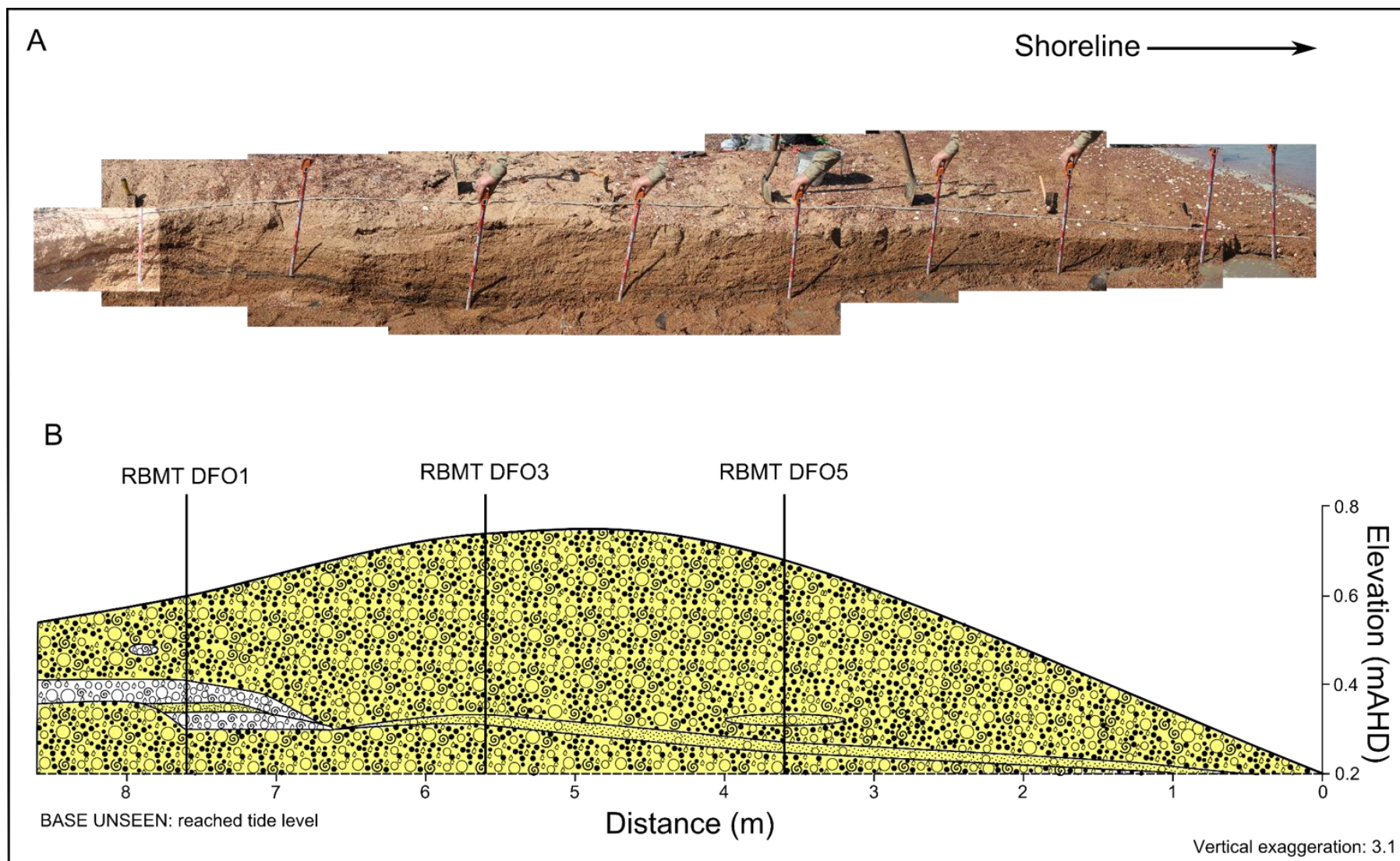


**Figure 4.6: Cross-section through the modern beach at Red Beach. (A) Composite image of sediments exposed in the trench (scale divisions each 10 cm). (B) Stratigraphic profile showing positions of logged sections (Figures 4.7-4.9).**

The sediments largely comprise coarse to very coarse sand with many pisoliths, many shell fragments and shell hash, but few whole shells. A thin (2 cm) layer of medium sand with few pisoliths extends across the entire section, at approximately 0.25 – 0.35 m AHD at the proximal end of the trench, rising to approximately 0.4 m AHD at the distal end of the trench (Figure 4.6B). At the distal end of the trench, this layer is sandwiched between thin (max. 5 cm) clast-supported units of abundant pisoliths with abundant shell fragments (Figures 4.6B and 4.7).

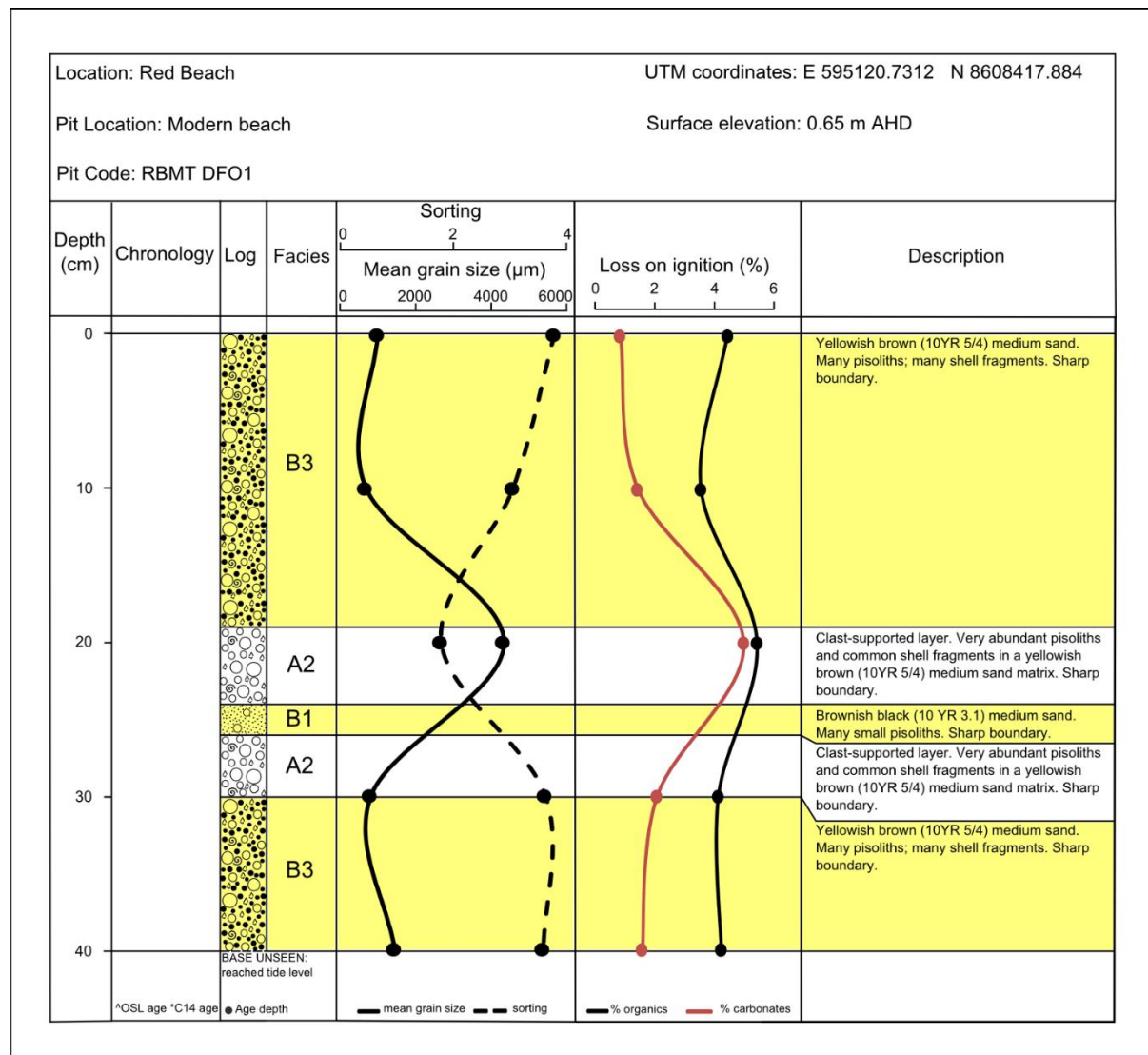
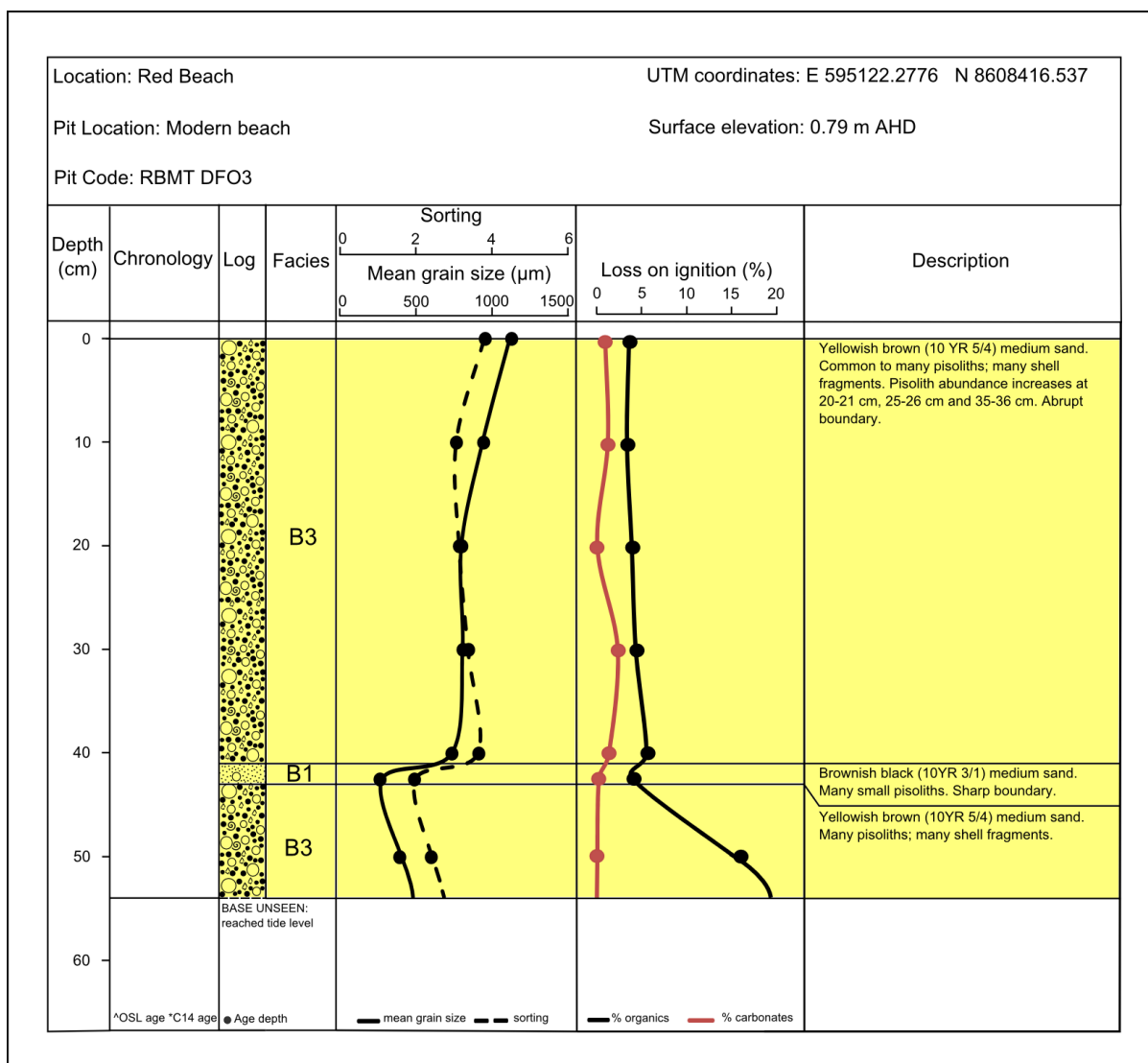
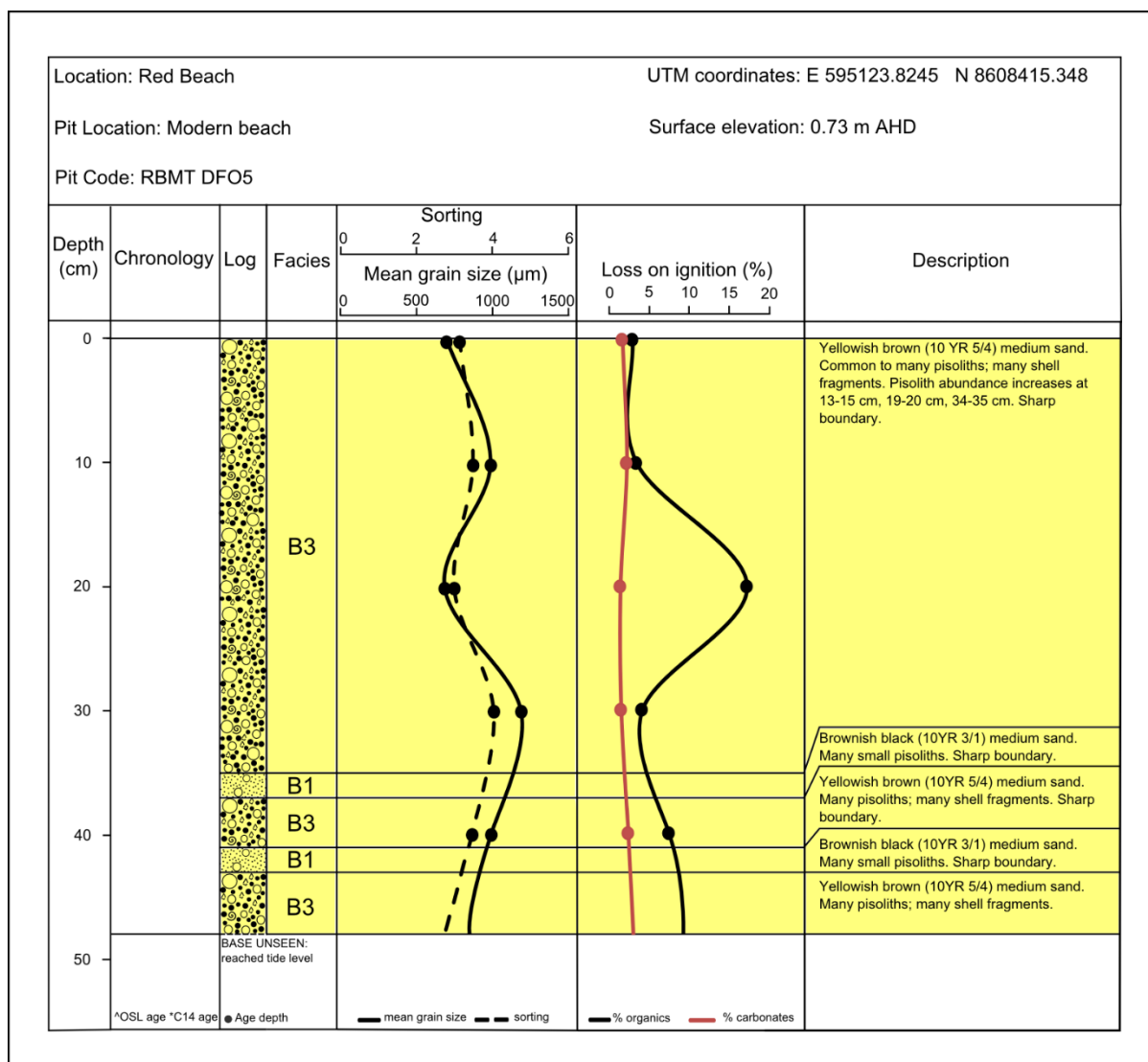


Figure 4.7: Sedimentary log of section RBMT DFO1 through the modern trench at Red Beach (see Section 4.4 for facies descriptions).



**Figure 4.8: Sedimentary log of section RBMT DFO3 through the modern beach at Red Beach (see Section 4.4 for facies descriptions).**



**Figure 4.9: Sedimentary log of section RBMT DFO5 through the modern beach at Red Beach (see Section 4.4 for facies descriptions).**

The pisoliths observed at Red Beach (illustrated in Figure 3.6) range in size from 2 mm to 15 mm, with a mean particle size of 4.2 mm. These values are similar to those reported by Taylor *et al.* (2008b) for the Weipa Plateau pisolithic bauxite deposit, which has a size range of 2 mm to 10 mm and a mean particle size of 5 mm. It is likely therefore that the pisoliths found at Red Beach originated on the Weipa Plateau, where they comprise a significant component of the aluminous laterite (i.e. bauxite) bedrock. Once released by weathering, they were most likely transported down the rivers and estuaries by fluvial and estuarine processes, then reworked and redeposited by coastal processes along the shorelines around Albatross Bay (see Section 1.4.2).



The whole shell, shell fragments and shell hash found within the Red Beach modern beach (illustrated in Figure 3.6) are allochthonous – they have been transported away from their original living habitat and deposited in a different location (Kidwell *et al.*, 1986). The difference between shell fragments and shell hash in this study is purely qualitative: shell hash has a greater degree of fragmentation, and therefore comprises shell particles that are smaller than shell fragments (Figure 4.10). It is useful to have this distinction between shell fragments and shell hash because the degree of shell fragmentation is indicative of energy levels in the original environment of deposition. Higher shell fragmentation occurs in environments with high water turbulence and/or a coarser substrate, where shells become impacted by other shells, mineral sediments, and waves (Gordillo *et al.*, 2014). Shell fragmentation, however, can also be caused by other factors such as the duration of transport prior to deposition, post-depositional compaction, predation, bioturbation, and/or chemical dissolution (Zuschin *et al.*, 2003). Further discussion on the significance of macrofossils for environmental reconstruction at Red Beach can be found in Section 4.1.2 below.

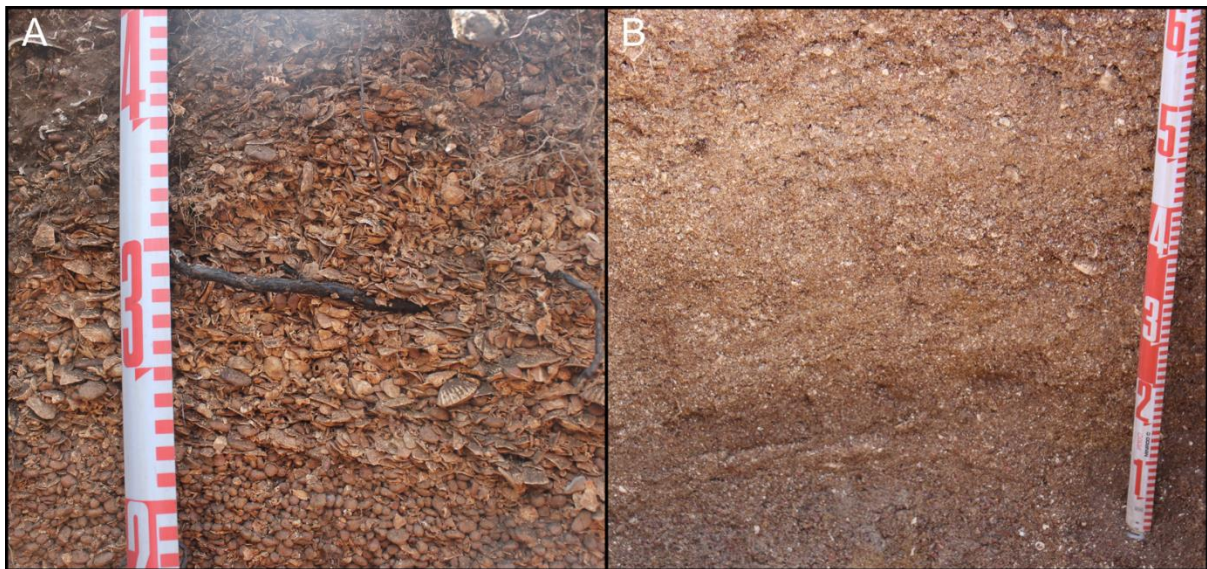


**Figure 4.10: Comparison between shell fragments and shell hash. (A) Abundant shell fragments in a clast-supported sedimentary unit in a beach ridge at Red Beach. (B) Many shell hash in a sand-dominated sedimentary unit in a beach ridge at Red Beach.**

The sediments of the modern beach at Red Beach were classified into facies, and their environments of deposition interpreted based on a combination of sedimentary characteristics, stratigraphic relationships, and the coastal environmental context of Albatross Bay. These facies are presented and discussed in detail in Section 4.4 below.

#### 4.1.2 Beach ridge plain sediments

As described in Chapter 3 (Section 3.2), a transect of pits was excavated across the beach ridge plain at Red Beach to expose the underlying sediments and stratigraphy. Pits were sunk into every ridge crest and swale, extending from the surface down to either the maximum safe limit for hand excavation or to where the material was too hard to dig. The sediments were described and sampled, with the sampled sediments analysed in the laboratory as described in Chapter 3 (Section 3.3). The field descriptions were combined with the results of the laboratory-based sediment analyses (Appendix A) to construct sediment stratigraphy logs for each of the pits (Appendix B). These logs were then added to the transect survey data (Figure 4.3) to produce a stratigraphic profile of the surveyed transect (Figure 4.11).

As illustrated in Figure 4.11, the 13 beach ridge crests comprising the beach ridge plain have a mean elevation of 2.49 m above AHD. The highest elevations are the crests of ridges RR11 and RR13, at 2.81 m AHD. Ridge RR2 has the lowest elevation along the surveyed transect, at 1.99 m AHD. The swales have a mean elevation of 2.00 m AHD. The lowest point in the beach ridge plain is the swale between RR9 and RR10, at 1.33 m AHD. This swale divides the beach ridge plain into two parts and is inundated during the wet season (Figure 4.2B). Ridge to swale amplitudes range from 0.06 m (between RR4 and RS5) to 1.26 m (between RR10 and the broad swale between RR9 and RR10) and average 0.5 m (Figure 4.11).

It is clear from the surveyed transect (Figure 4.11) that there is a change in the morphology of the ridges with distance inland from the modern beach. The inland beach ridge set (ridges RR8 to RR13) is at a slightly higher elevation (between approximately +2.5 m and +3 m AHD), are wider and are more distinct than the seaward beach ridge set (ridges RR1 to RR7). The seaward ridges are narrower, more closely spaced and are less prominent in the landscape (Figures 4.2B and 4.3).

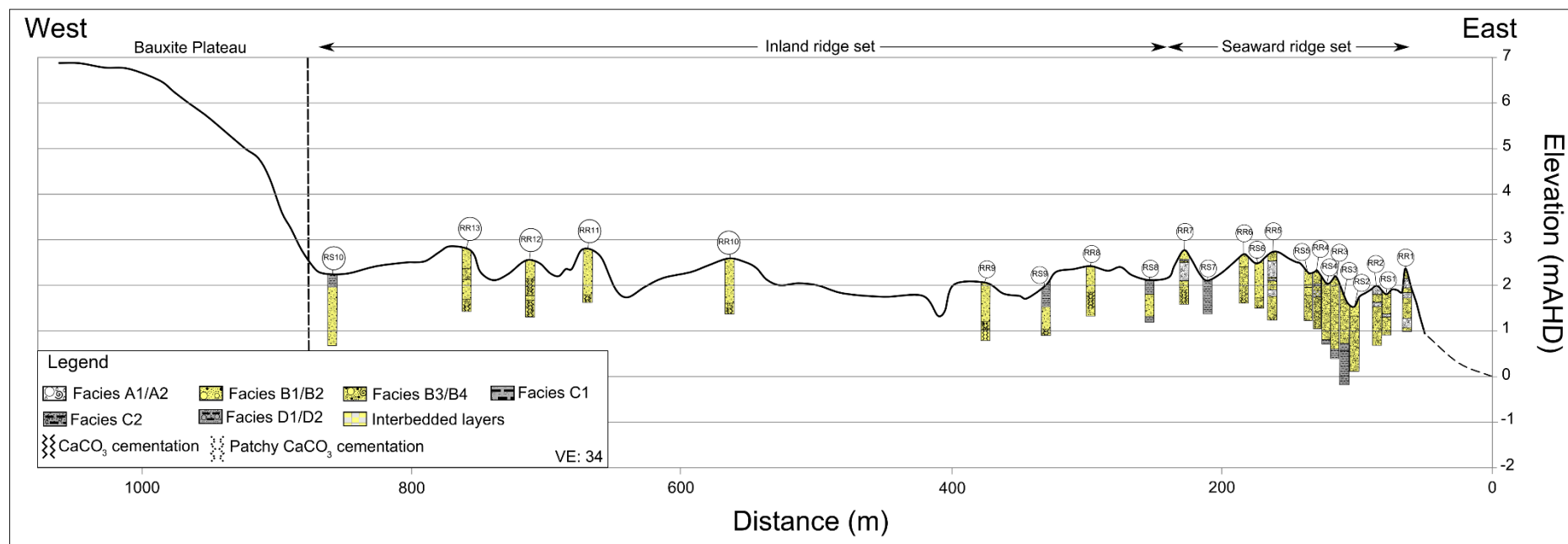


Figure 4.11: Stratigraphic profile across the beach ridge plain at Red Beach (see Section 4.4 for facies descriptions). Detailed sedimentary logs of each pit can be found in Appendix B.

As shown in the sedimentary logs (Figure 4.11 and Appendix B), the beach ridges are dominated by sand-sized sediments. Sandy deposits are also found in the inter-ridge swales between RR1 and RR6, replaced by mud from RR6 onwards. Between RR9 and RR10 lies a broad swale that is seasonally inundated (Figures 4.2B, 4.11 and 4.12). The ground within the swale comprises dense mud, and a pit could not be dug into it with the tools available. All the other swales inland of this broad swale are of a similar texture. While they are not as low in elevation as the broad swale behind RR9, these inland swales are also likely seasonally inundated (Figures 4.2B and 4.11). The Red Beach beach ridges overlie intertidal muds, as indicated by the sedimentary logs (Appendix B, Figures 4.11 and 4.13).



**Figure 4.12: Broad swale between RR9 and RR10 at Red Beach.**



**Figure 4.13: D-section core collected from the base of RR3 showing the transition from the sandy beach ridge deposits on the left to the intertidal muds on the right.**



Macrofossils, comprising whole shell, shell fragments and shell hash, were found throughout the beach ridges at Red Beach (see, for example, Facies B3/B4 in Figure 4.11; see Section 4.4 for facies descriptions). Barnacles were observed attached to some of the shells, and rare coral fragments and tube worm tubes were also found. As previously described, fossil assemblages can either be autochthonous, parautochthonous or allochthonous. Autochthonous assemblages are fossils that have been preserved in their life positions. Parautochthonous assemblages are autochthonous assemblages that have been reworked to some extent, but have still been preserved in their original living habitat. Allochthonous assemblages are fossil deposits that have been transported away from their original living habitat and subsequently deposited in a separate location (Kidwell *et al.*, 1986).

Fossil assemblages can be distinguished by the proportion of articulated and disarticulated shells (e.g., Figure 4.14A-B), the degree of shell fragmentation, signs of wear on the shells (e.g., Figure 4.14C), and whether shells are found in their life position (Martin, 1999). Shells become disarticulated post-death due to “...the decay of the organic ligament that joins the valves together...” followed by “...exhumation or exposure [of the shells] by currents and bioturbators...” (Pilarczyk and Barber, 2015, p. 261). While the ease of shell disarticulation is partly dependent on the shell species (Brenchley and Harper, 1998; Pilarczyk and Barber, 2015), as a general rule, a high shell articulation ratio indicates a fossil assemblage that has not undergone much transport prior to deposition (Brenchley and Harper, 1998). Thus, an autochthonous marine macrofossil deposit can be identified by a high proportion of shells being articulated, with a low proportion of shell fragmentation, shell surfaces which show little signs of wear (such as abrasions that occur when shells knock other shells or sediments during transport), and some shells being in life position (Martin, 1999). On the other hand, an allochthonous fossil assemblage can be characterised by a low proportion of articulated shell, a high proportion of fragmented shells, shell surfaces that show signs of wear, and a majority of shells being rotated from their original life positions (Martin, 1999).



**Figure 4.14:** (A) Articulated *T. granosa* shells collected from an anthropogenic shell mound at Wathayn. These shells are likely to have been discarded and buried relatively quickly after harvesting. (B) Disarticulated *T. granosa* shells collected from within a beach ridge at Red Beach. (C) Gastropods collected from within the shell deposits at Kwamter showing increasing signs of wear.

The macrofossils observed at Red Beach are all randomly oriented, predominantly non-articulated, and contain a significant portion of fragmented shell with shell surfaces showing signs of wear. They are therefore interpreted as allochthonous. The shells have no appearance of sorting either by size or shape, indicating that there have been little or no hydrodynamic effects at play during deposition. Because the macrofossils are allochthonous, they may either be approximately contemporaneous in age with the containing mineral sediment, or they may be older, especially if they were transported for an extended period of time prior to deposition. If they were introduced into the older sediment via burrows or fissures, they may even be younger than the containing sediment (Kidwell *et al.*, 1986).

As indicated in the stratigraphic profile (Figure 4.11) and the stratigraphy logs (Appendix B), some sedimentary units from the relict beach ridge plain are cemented with calcium carbonate, forming hardpan calcrete. Hardpan calcrete is a form of calcrete that comprises a continuous indurated sheet-like layer, with a sharp upper surface, a gradational lower boundary and an internal structure that can range from massive and structureless to complex, containing recemented nodules, carbonate pisoliths, and breccias (Chen *et al.*, 2002). In Holocene coastal areas, hardpan calcretes have a relatively simple structure and the thickness can vary from several centimetres to about 50 cm (Chen *et al.*, 2002).

Hardpan calcrete is found at the base of all but the first three beach ridges at Red Beach. The calcrete cementation is only patchy (i.e., weakly cemented) at the base of RR4, then increases with distance inland and, by RR7, the calcrete is a well-developed layer (Figure 4.15). The thickness of the calcrete unit also increases inland, most likely a function of time and density of vegetation (after Semeniuk, 1986; Semeniuk, 1995; Chen *et al.*, 2002).

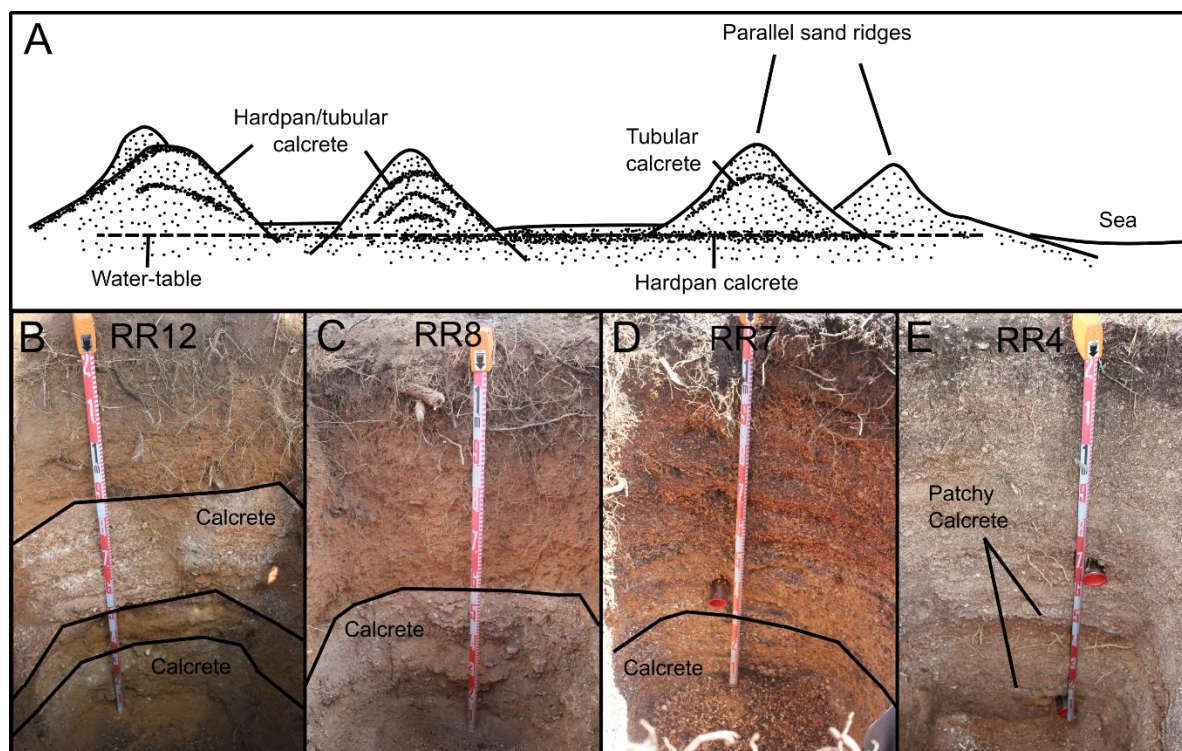


**Figure 4.15:** (A) Calcrete occurrence in coastal beach ridges. Hardpan calcrete forms near the water table and hardpan/tubular calcrete also forms within the beach ridges. Hardpan calcrete forms as an indurated sheet-like layer, while tubular calcrete formed from roots casts/tubules. More layers of calcrete often form in older beach ridges that are located further inland (Chen *et al.*, 2002). Image modified from Figure 7.2.20 in Chen *et al.* (2002). (B) Section through RR12. This beach ridge has two separate layers of hardpan calcrete, with the upper layer forming above the lower calcrete deposit in a “... perched moisture zone...” (Chen *et al.*, 2002, p. 127). (C) Section through RR8. This beach ridge has a well-developed calcrete layer. (D) Section through RR8. While not as distinct as the calcrete layer in the inland ridges, this calcrete unit was too cemented for an OSL sample to be collected from. The OSL sample tube can be seen above the calcrete unit. (E) Section through RR4. The calcrete is patchy and cementation weak.

Hardpan calcretes generally form at the mean water table depth, as saturation point is reached and calcium carbonate is reprecipitated as a result of two concurrent processes – the downward drainage of rainwater through calcareous beach ridge sediments, and the upward movement of water via evapotranspiration (Figure 4.15) (Semeniuk and Searle, 1985; Semeniuk, 1986; Chen *et al.*, 2002; Carson and Peterson, 2011). Chen *et al.* (2002, p. 124) reports the distribution of calcretes within the coastal dunes of Australia as “...only along the drier coasts of western Victoria (including Bass Strait, e.g. Flinders Island (Dimmock, 1957), South Australia and southern Western Australia...” and that calcrete is very rarely found along Cape York Peninsula (see Figure 7.2.1 in Chen *et al.* (2002, p. 114)). However, cemented sediments have been found at the base of Holocene beach ridges examined along the eastern GoC coastline, south of Albatross Bay (Smart, 1976a; b). The carbonates in these beach ridges were leached before being reprecipitated at the dry-season water table. There was a decline in carbonate content within these beach ridges with distance inland and an increasing depth of

leaching, which may, in turn, reduce the volume of the beach ridges (Smart, 1976b). Smart (1976a, p. 12) states that “...if the process continues, the final profile would be a leached zone devoid of carbonate, over a hard pan of carbonate-cemented sand and shells...”.

This “final profile” discussed by Smart (1976a) was observed in the relict beach ridges at Red Beach. The carbonate profile of the seaward ridge RR3 varies from a low of 0.5% to a maximum of 15%, and declines at approximately 80 cm depth to 2% at the bottom of the profile (Figure 4.16). In contrast, the inland ridge RR11 (Figure 4.17) has a carbonate content of less than 0.5% from the top of the pit section down to a depth to 100 cm, where it increases to 3% in the carbonate-cemented basal unit. Unlike the beach ridges observed by Smart (1976b), however, the depth of leaching and reprecipitation of calcium carbonate does not increase with distance inland at Red Beach (Figure 4.11). Rather than forming at the depth of the water table *per se*, calcrete in the Red Beach beach ridges reflects the changing stratigraphy, forming at the depth of transition from the highly permeable sandy beach ridge sediments to the more impermeable intertidal muds beneath (see Section 4.1.3).

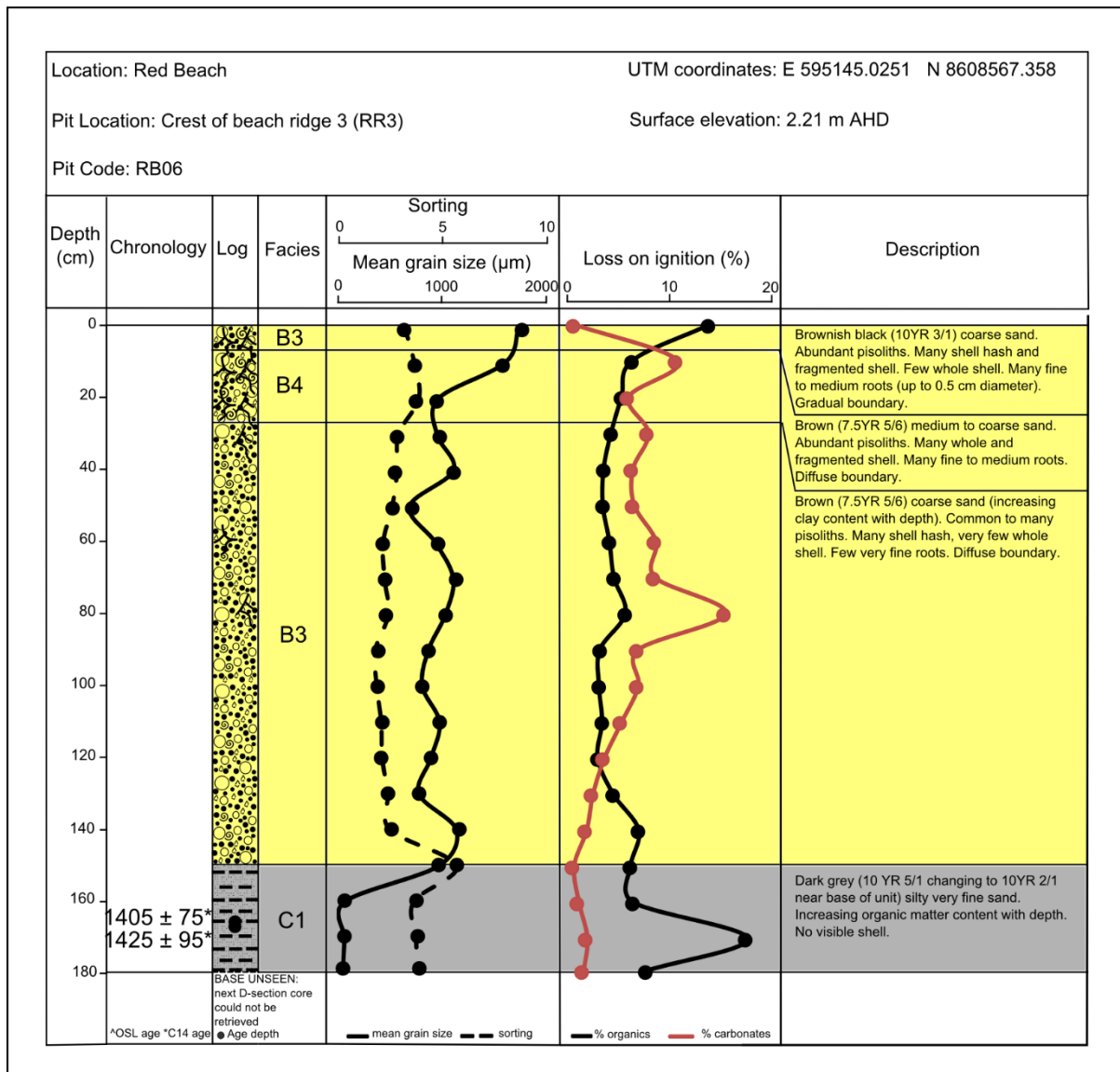


Figure 4.16: Sedimentary log for RR3 (see Section 4.4 for facies descriptions).







**Figure 4.18: (A) Red Beach at low tide, showing the exposed mudflat seaward of the sandy foreshore. (B) An intertidal mud sample (photo taken from the D-section core collected from the base of a pit dug into the proximal flank of RR3 at Red Beach), showing shell fragments and shell hash in a sandy silt matrix.**

## **4.2 Kwamter**

As described in Section 3.2.1, Kwamter is located approximately 11 km southeast of Weipa, along the lower estuary of the Embley River (Figure 3.1). A zone of mangroves separates the open water of the estuary from the unvegetated supratidal mudflat (Blaber *et al.*, 1990). A second, narrower zone of mangroves at the distal edge of the mudflat appears to be located above the dry season water table, with the ground surface consisting of hardened and cracked mud. It is most likely sustained by water inundation during the wet season (Figures 4.19 and 4.20). A single beach ridge oriented parallel to the modern shoreline is located inland of the inner zone of mangroves. It is visible on the LiDAR-derived elevation map and is separated by a swale from the bauxite plateau that is currently being mined commercially (Figures 4.19B and 4.20).

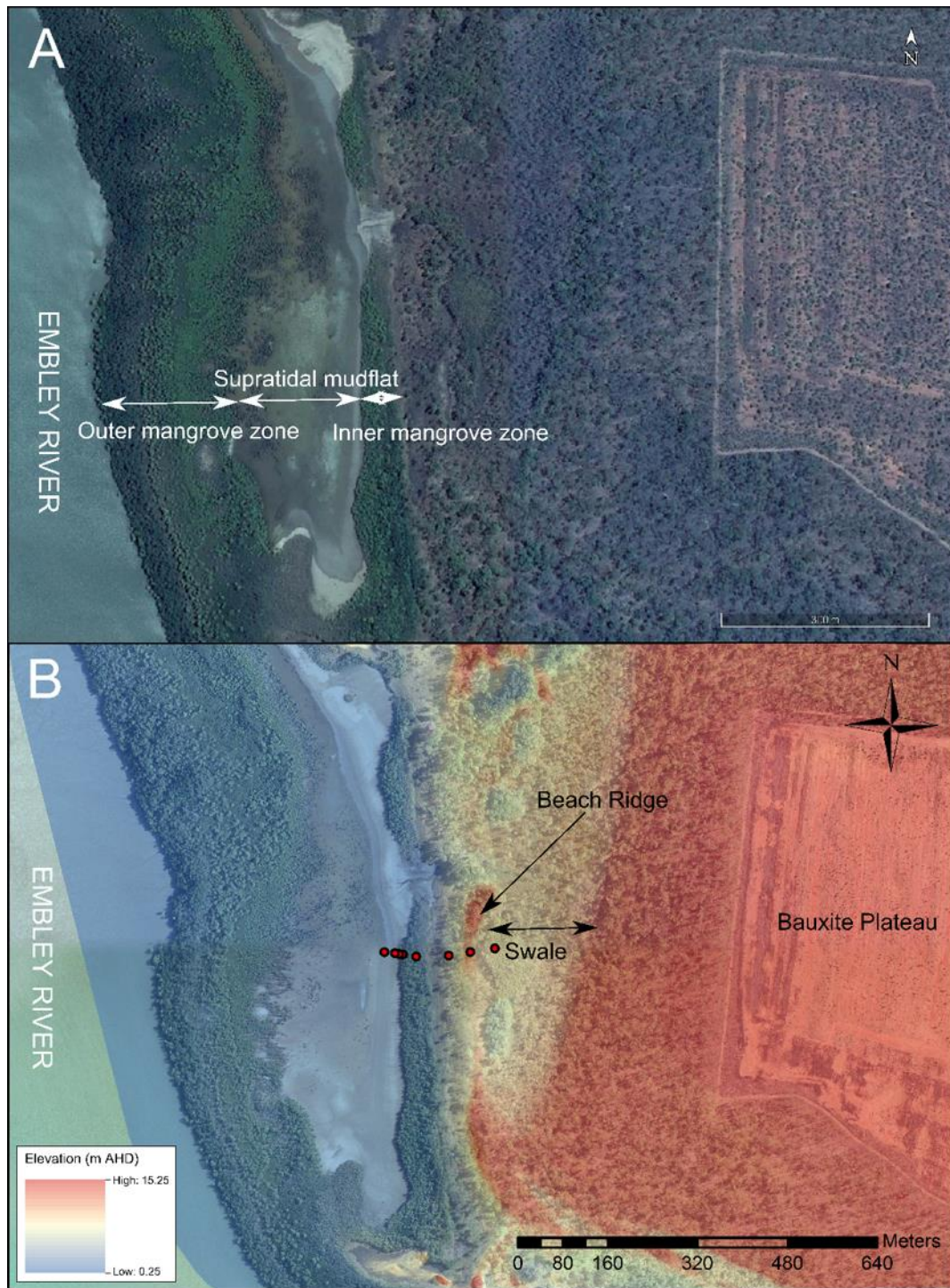


**Figure 4.19: (A) Satellite image of the Kwamter study location, showing extent of vegetation cover. Clearing associated with bauxite mining can be seen on the eastern edge of the image (Source: GoogleEarth, accessed 27<sup>th</sup> Dec 2017). (B) A digital elevation model of the Kwamter study location, showing detail of the topography of the estuarine floodplain. The location of the topographic profile surveyed across the single beach ridge and onto the distal margin of the floodplain is indicated by the line of red dots, each of which marks the location of the excavated pits (source of elevation data: LiDAR 0.25 m grid survey data flown in 2010 and provided by Riotinto Pty Ltd).**



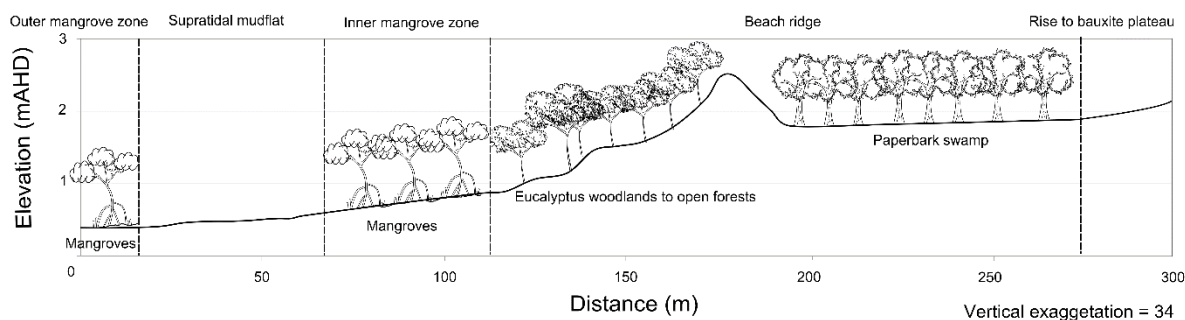


**Figure 4.20: Topographic profile of Kwamter showing major land units and vegetation cover.**

Data obtained from the Queensland Herbarium (<https://environment.ehp.qld.gov.au/map-request/re-broad-veg-group/>, accessed 13<sup>th</sup> Jan 2018) indicates that the Kwamter study area supports two broad vegetation types – mangroves and saltmarshes, and eucalypt woodlands and open forests (Figures 4.20 and 4.21). The mangrove species present include mid- to low-intertidal species such as *Rhizophora stylosa*, *Bruguiera gymnorhiza*, *Bruguiera cylindrica* and *Avicennia marina* in a closed to low closed forest. Also present are mangrove species from the upper tidal limit, including *Ceriops tagal* and *Excoecaria agallocha*. Grasses, sedges and halophytic forbs such as *Sporobolus virginicus* and *Tecticornia* spp. (samphire) are scattered across the supratidal mudflat, while grasses such as *Sarga plumosum* and *Perotis rara* and the occasional shrub and tree, including *Grevillea parallela* (silver oak), are present near the beach ridge. The beach ridge at Kwamter supports *Eucalyptus tetradonta* (Darwin stringybark) woodland. Other species present include *Corymbia nesophila* and *Corymbia stockeri*. The groundcover comprises grasses including *Heteropogon triticeus*, *Aristida* spp. and *Sarga plumosum*. Within the swale behind the beach ridge (Figure 4.19B), the vegetation shifts to low open woodland, dominated by *Melaleuca viridiflora* (Paperbark) with few grasses or shrubs present.

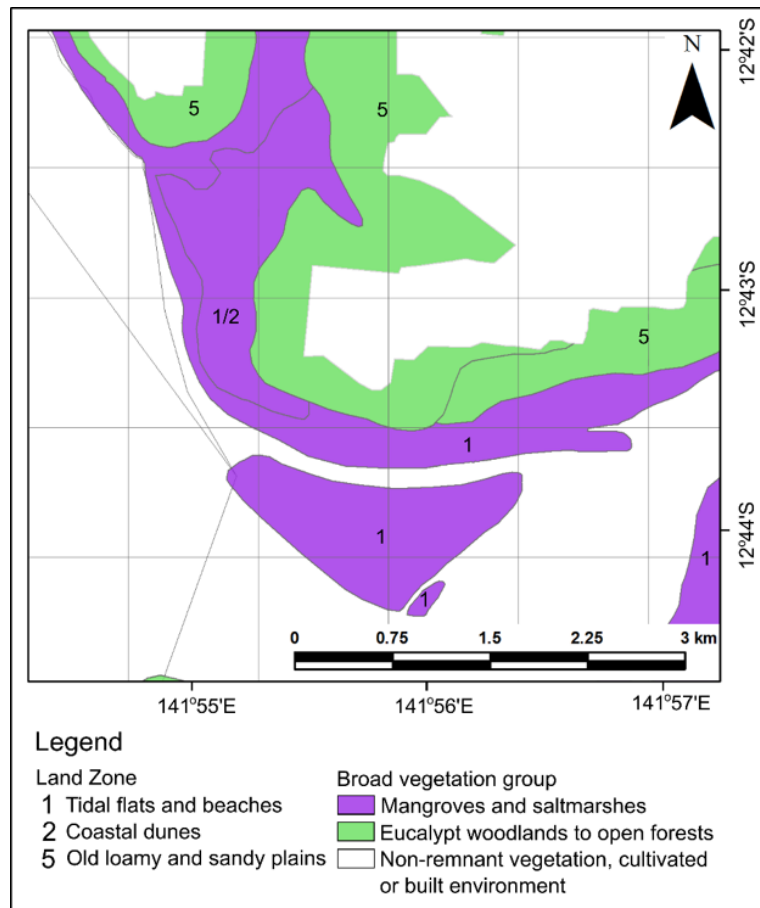


**Figure 4.21: Vegetation map of the Kwamter study location (Source: Queensland Herbarium, <https://environment.ehp.qld.gov.au/map-request/re-broad-veg-group/>, accessed 13<sup>th</sup> Jan 2018).**

#### 4.2.1 Beach ridge and supratidal mudflat sediments

As described in Chapter 3 (Section 3.2), a transect was surveyed across the beach ridge and onto the supratidal mudflat at Kwamter. The underlying sediments were exposed by sinking pits, auger holes and cores at each of the locations indicated on the location map (Figure 4.19B). The sediments were described in the field and sampled for laboratory analysis. The field descriptions and results of the laboratory analyses (Appendix A) were then combined to generate sedimentary logs of each of the excavations (Appendix B). These logs were then added to the transect survey data (Figure 4.20) to produce a stratigraphic profile of the surveyed transect (Figure 4.22).

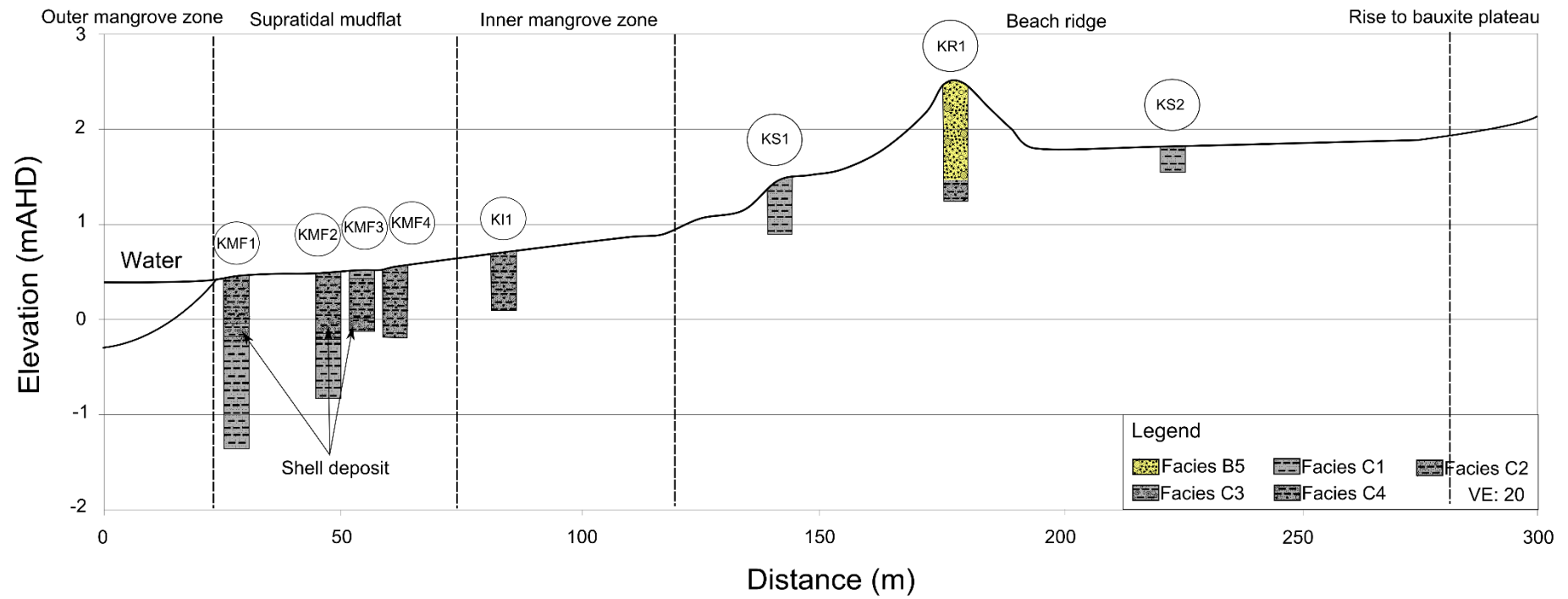


**Figure 4.22: Stratigraphic profile across the beach ridge and estuarine floodplain at Kwamter (see Section 4.4 for facies descriptions). Detailed sedimentary logs of each pit can be found in Appendix B.**

The supratidal mudflat at the Kwamter study location rises gradually from an elevation of 0.46 m AHD at its proximal edge to 0.56 m AHD at its distal edge (Figure 4.22). The landsurface then rises more steeply to an elevation of 0.71 m AHD in the middle of the distal mangrove zone, 1.46 m AHD on the proximal flank of the beach ridge and to a maximum elevation of 2.49 m AHD at the crest of the beach ridge. The ground then slopes down to an elevation of 1.82 m AHD within the distal swale before rising to approximately 15.25 m AHD at the top of the bauxite plateau (Figures 4.19B and 4.22).

The sediments at the surface of the supratidal mudflat largely comprise sandy silt with few quartz granules present (Figure 4.22 and Appendix B). The quartz granules (illustrated in Figure 3.6), also found within the beach ridge sediments, most likely originate from fluvial sediments transported along the Embley River and subsequently deposited on the estuarine shoreline. A shell layer is also present at depth within the supratidal mudflat, comprising very abundant whole and fragmented shell, with few shell hash in a sandy silt matrix (Figure 4.22 and the sedimentary logs for KMF1-KMF3 in Appendix B). The shells within the layer are all randomly oriented and predominantly non-articulated, indicating that this shell deposit is allochthonous (Section 4.1.2).

The sediments within the distal mangrove zone are similar to the supratidal mudflat sediments, comprising sandy silt with few quartz granules (Figure 4.22). The beach ridge is dominated by sand-sized sediments, with few quartz granules present (Figure 4.22 and Appendix B). Unlike at Red Beach, there were no macrofossils observed in the beach ridge sediments at Kwamter. The beach ridge overlies silty sand with common quartz granules. Sandy silt sediments line the distal swale, behind the beach ridge (Figure 4.22 and Appendix B).

The sediments of the beach ridge and estuarine floodplain at Kwamter were classified into facies, and their environments of deposition determined based on a combination of sedimentary characteristics, stratigraphic relationships, and the coastal environmental context of Albatross Bay. These results are presented and discussed in detail in Section 4.4 below.

### **4.3 Wathayn**

The Wathayn study area is located approximately 19.5 km southeast of Weipa, and 10 km east of Kwamter, along the northern shore of the Embley River (Figure 3.1). A zone of mangroves approximately 200 m to 500 m wide forms the proximal margin of the floodplain

at this location (Blaber *et al.*, 1990). A supratidal mudflat, up to approximately 200 m wide, is located inland of the mangroves (Figures 4.23 and 4.24). The landsurface then rises gradually to a single beach ridge, oriented east to west and parallel to the modern shoreline (Figure 4.23B and 4.24). The ground elevation dips slightly inland of the beach ridge, forming a subtle swale, prior to rising up to the bauxite plateau that has a maximum elevation of approximately +30.5 m AHD (Figures 4.23B and 4.24).

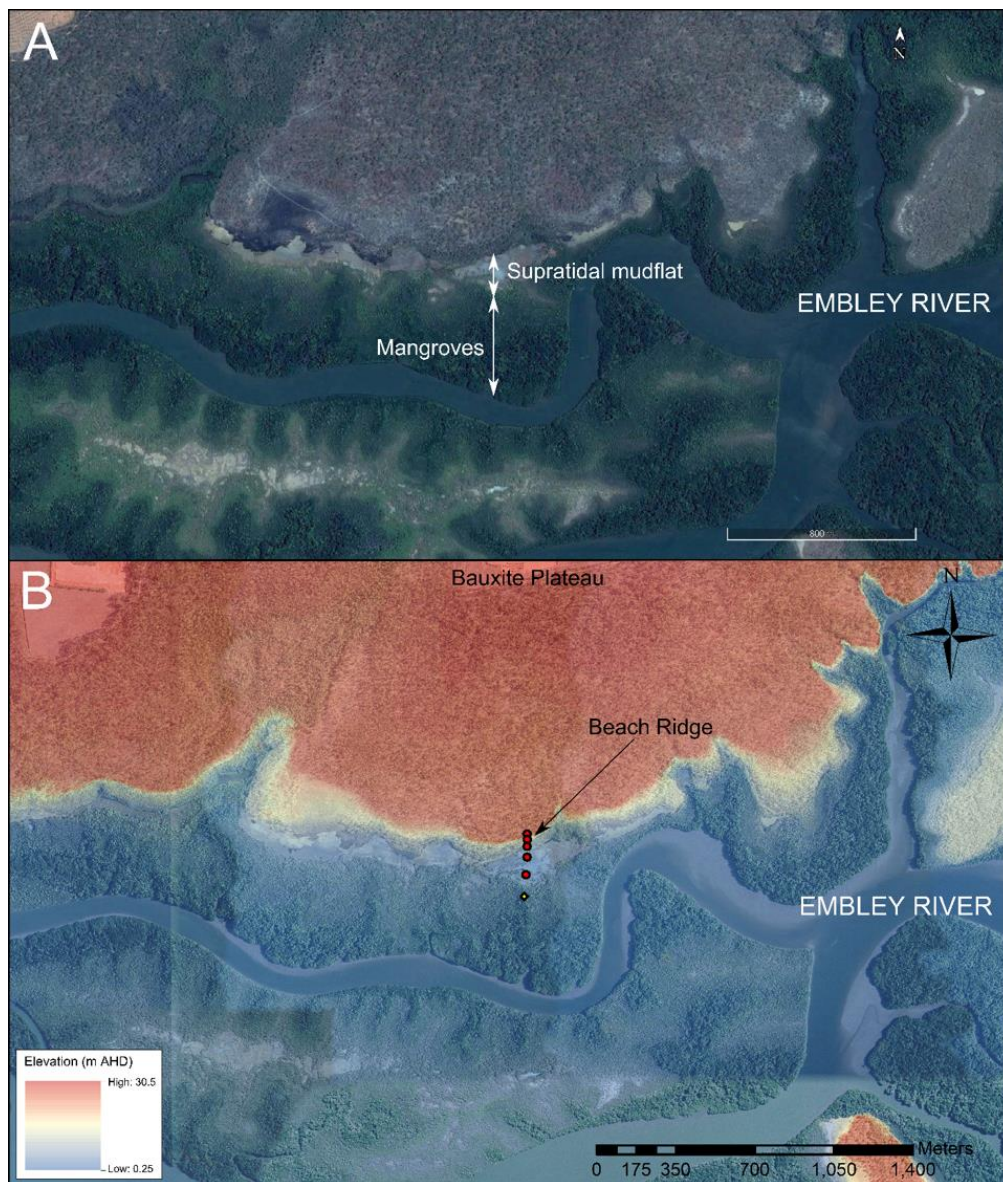


**Figure 4.23:** (A) Satellite image of the Wathayn study location showing extent of vegetation cover (Source: modified from GoogleEarth, accessed 27<sup>th</sup> Dec 2017). (B) A digital elevation model of the Wathayn study location, showing detail of the topography of the hillslope, beach ridge and supratidal mudflat. The location of the topographic profile surveyed across the single beach ridge and onto the distal margin of the floodplain is indicated by the line of red dots, each of which marks the location of the excavated pit. (Source: the elevation data is derived from a LiDAR 0.25 m grid survey data flown in 2010 and provided by Riotinto Pty Ltd).

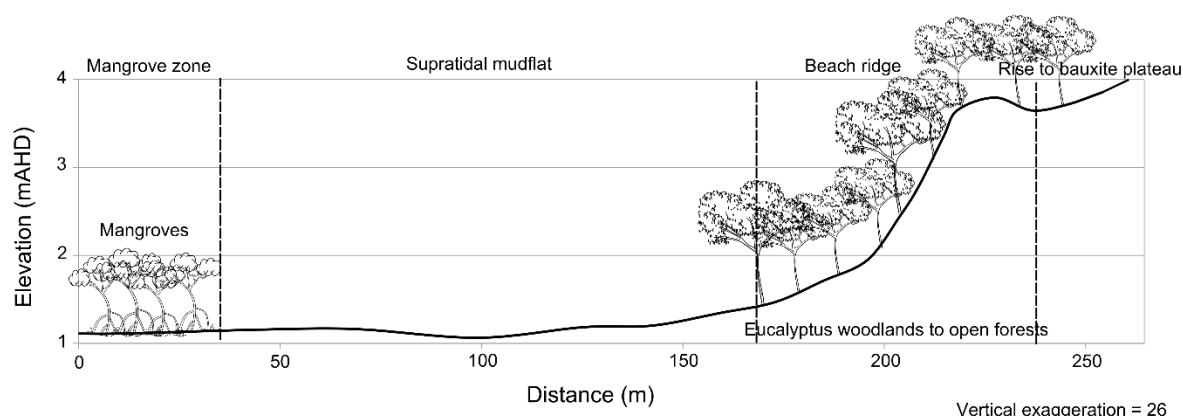


**Figure 4.24: Topographic profile of Wathayn showing major land units and vegetation cover.**

Data obtained from the Queensland Herbarium (<https://environment.ehp.qld.gov.au/map-request/re-broad-veg-group/>, accessed 13<sup>th</sup> Jan 2018) indicates that the Wathayn study area supports two broad vegetation types – mangroves and saltmarshes, and eucalypt woodlands and open forests (Figures 4.24 and 4.25). The mangrove species at Wathayn are the same as those at Kwamter, comprising high to mid intertidal zone species such as *Ceriops tagal* and *Excoecaria agallocha* and mid to low intertidal zone species such as *Rhizophora stylosa*, *Bruguiera gymnorhiza*, *Bruguiera cylindrica* and *Avicennia marina*. Grasses, sedges and halophytic forbs, including *Sporobolus virginicus* and *Tecticornia* spp. (samphire) are scattered across the supratidal mudflat. Across the beach ridge at Wathayn, *Corymbia clarksoniana* (Clarkson’s bloodwood) is dominant. Other species present include *Lophostemon suaveolens*, *Melaleuca viridiflora* and *Alphitonia pomaderroides*. Grasses and sedges, including *Fimbristylis* spp., *Heteropogon triticeus* and *Aristida* spp. form a dense groundcover.



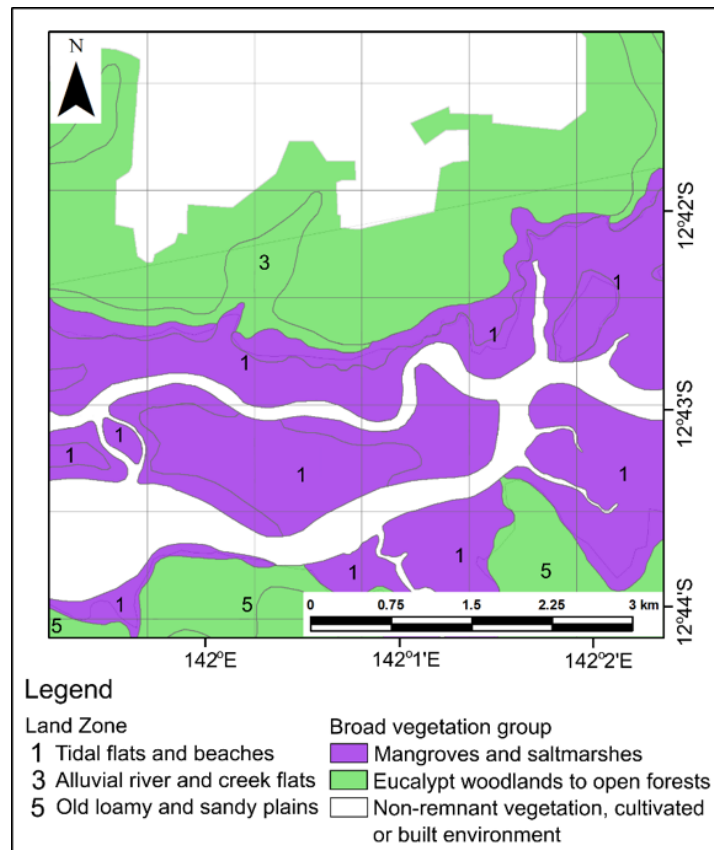


**Figure 4.25: Vegetation map of the Wathayn study location** (Source: Queensland Herbarium, <https://environment.ehp.qld.gov.au/map-request/re-broad-veg-group/>, accessed 13<sup>th</sup> Jan 2018).

#### 4.3.1 Beach ridge, supratidal mudflat and mangrove sediments

As described in Chapter 3 (Section 3.2), a transect was surveyed across the beach ridge and onto the estuarine floodplain at Wathayn. The underlying sediments were exposed by sinking pits at each of the locations indicated on the location map (Figure 4.23B). The pits extended down to the maximum safe depth for excavation by hand in unconsolidated sediments, or to the level where the sediments were too hard to dig. The sediments were described in the field and sampled for laboratory analysis. The field descriptions and results of the laboratory analyses (Appendix A) were then combined to generate sedimentary logs of each of the excavations (Appendix B). These logs were then added to the transect survey data (Figure 4.24) to produce a stratigraphic profile of the surveyed transect (Figure 4.26).



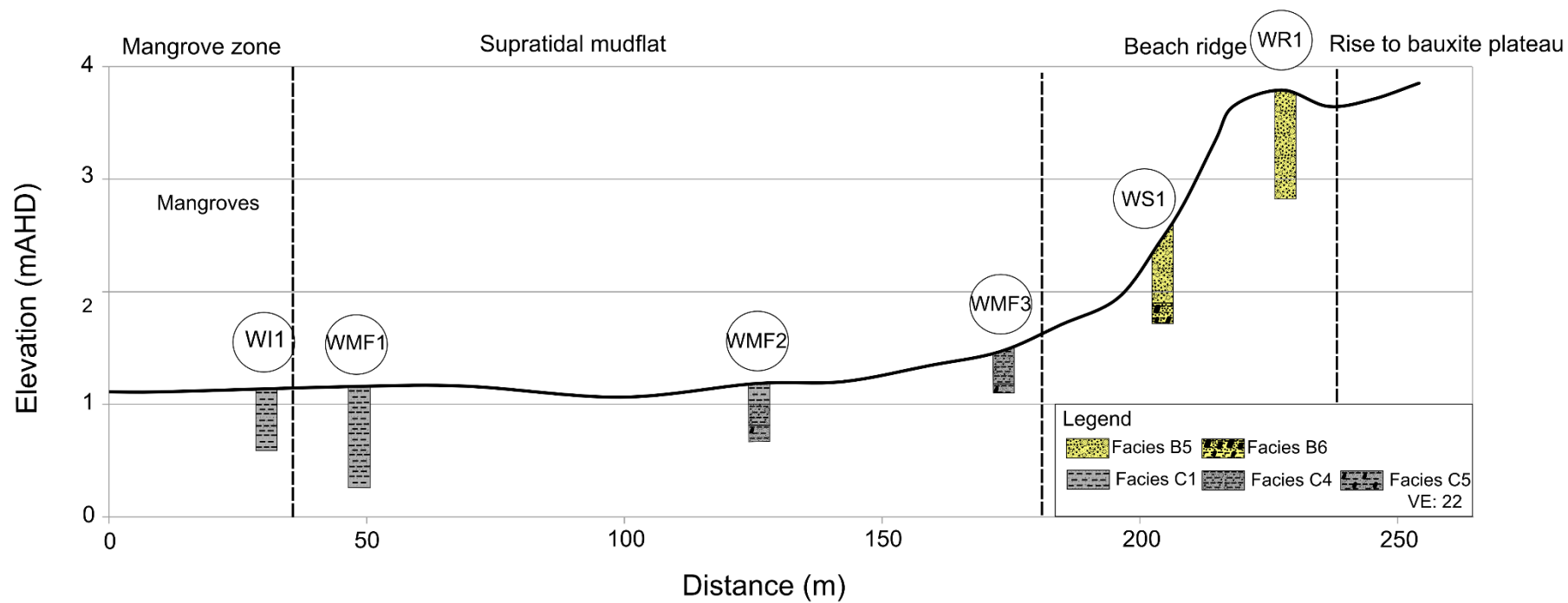


**Figure 4.26: Stratigraphic profile across the beach ridge and supratidal mudflat at Wathayn (see Section 4.4 for facies descriptions). Detailed sedimentary logs of each pit can be found in Appendix B.**

The supratidal mudflat at Wathayn rises gradually from an elevation of +1.05 m AHD at its proximal boundary with the outer mangrove zone to +1.47 m AHD at its distal boundary with the flank of the single beach ridge (Figure 4.26). The landsurface rises to a maximum elevation of +3.79 m AHD at the crest of the beach ridge, falls slightly in the swale then rises gradually to the top of the bauxite plateau.

The sediments beneath the transect at Wathayn are largely similar to those at Kwamter, not surprising given that both are located along the Embley River. Within the mangrove fringe, the sediments comprise sandy silt, with common fine to very fine roots. No quartz granules are present (Figure 4.26 and Appendix B). Sandy silt with few to common quartz granules were observed on the surface of the supratidal mudflat, with the quartz granules declining in frequency towards the mangrove zone at the proximal end of the transect. The beach ridge at Wathayn is dominated by sand-sized sediments, with few quartz granules and no macrofossils present, similar to the beach ridge at Kwamter (Figure 4.26 and Appendix B).

Subrounded to angular rock fragments (illustrated in Figure 3.6) are present at the base of the pit within the flank of the beach ridge (WS1), and also in the pits in the middle (WMF2) and distal end (WMF3) of the supratidal mudflat. The rock fragments are composed of a mixture of quartzose sandstone and bauxite, likely derived from the Bulimba Formation and the aluminous laterite deposited within the Weipa Plateau (see Section 1.4.2). The subrounded to angular rock fragments have either been transported along the Embley River during periods of relatively high-energy fluvial transport or are derived from the weathering of bedrock beneath the beach ridge and estuarine floodplain at Wathayn. These rock fragments were not observed at Red Beach or Kwamter.

The sediments of the beach ridge and estuarine floodplain at Wathayn were classified into facies, and their environments of deposition determined based on a combination of sedimentary characteristics, stratigraphic relationships, and the coastal environmental context of Albatross Bay. These results are presented and discussed in detail in Section 4.4 below.

#### **4.4 Coastal sedimentary facies of Albatross Bay**

The sediments recorded and sampled at the Red Beach, Kwamter and Wathayn study locations were classified into distinct sedimentary facies based on a combination of field observations and the results of the laboratory analyses described above. Four primary sedimentary facies, and a variable number of sub-facies, were identified on the basis of

sediment composition and characteristics and biological structures present. The field and laboratory data is summarised for each facies in Table 4.1. A summary of all the laboratory data for each excavation can be found in Appendix A. This data, combined with the field descriptions, forms the basis for the interpretation below. Facies A and D are only found at Red Beach, while facies B and C are found at all three field sites. Facies A is a clast-supported, pisolith-dominated facies. Facies B is matrix-supported, sand-dominated facies. Facies C and D are both dominated by fine-grained sediment (silt and clay). However, Facies C comprise sediments that are deposited in nearshore, intertidal and supratidal environments, while Facies D comprises sediments that are deposited in swales of the beach ridge plain.

**Table 4.1: Summary of the sedimentary characteristics of facies identified from Red Beach, Wathayn and Kwamter. Values are means unless otherwise stated.**

Summary of the sedimentary characteristics of facies identified from Red Beach, Wathayn and Kwamter. Values are the means unless otherwise stated.																
Facies Code	Textural Group <sup>1</sup>	Coarse Fragments <sup>2</sup>		Grain size statistics <sup>3</sup>						Sediment components				%Organic Matter	%Carbonates	
				Mean Grain size (µm)	Sorting		Skewness		Kurtosis		%Clay	%Silt	%Sand			%Gravel
A1	Sandy gravel to gravel	Pisoliths	Abundant	2677.43	3.05	Poorly sorted	-0.462	Very fine skewed	1.371	Leptokurtic	0.13	2.12	28.28	69.47	6.21	11.76
		Quartz granules	None													
		Subangular to subrounded clasts	None													
		Shell fragments and shell hash	Abundant													
		Whole shell	Common													
A2	Muddy sandy gravel to gravel	Pisoliths	Abundant	2863.01	4.63	Very poorly sorted	-0.542	Very fine skewed	2.255	Very leptokurtic	0.72	8.61	10.25	80.43	7.14	14.56
		Quartz granules	None													
		Subangular to subrounded clasts	None													
		Shell fragments and shell hash	Abundant													
		Whole shell	Few													
B1	Slightly gravelly sand to gravelly sand	Pisoliths	Few	320.88	2.22	Poorly sorted	-0.041	Symmetrical	1.514	Very leptokurtic	0.31	4.95	91.21	3.53	3.96	0.41
		Quartz granules	None													
		Subangular to subrounded clasts	None													
		Shell fragments and shell hash	None													
		Whole shell	None													
B2	Gravelly sand to sandy gravel	Pisoliths	Many	877.62	4.77	Very poorly sorted	0.104	Coarse skewed	1.015	Mesokurtic	0.47	5.04	58.78	35.71	4.00	0.72
		Quartz granules	None													
		Subangular to subrounded clasts	None													
		Shell fragments and shell hash	None													
		Whole shell	None													
B3	Gravelly sand to sandy gravel	Pisoliths	Many	954.67	3.52	Poorly sorted	0.167	Coarse skewed	1.019	Mesokurtic	0.13	2.65	66.32	30.91	4.50	5.53
		Quartz granules	None													
		Subangular to subrounded clasts	None													
		Shell fragments and shell hash	Many													
		Whole shell	Very few to few													
B4	Gravelly sand to sandy gravel	Pisoliths	Many	1029.71	3.50	Poorly sorted	0.138	Coarse skewed	0.786	Platykurtic	0.01	1.55	63.19	35.24	4.53	4.42
		Quartz granules	None													
		Subangular to subrounded clasts	None													
		Shell fragments and shell hash	Many													
		Whole shell	Common to many													
B5	Gravelly muddy sand to gravelly sand	Pisoliths	None	461.24	3.05	Poorly sorted	-0.237	Fine skewed	1.398	Leptokurtic	0.98	8.82	86.25	3.95	2.58	0.20
		Quartz granules	Very few to few													
		Subangular to subrounded clasts	None													
		Shell fragments and shell hash	None													
		Whole shell	None													
B6	Gravelly muddy sand to muddy sandy gravel	Pisoliths	None	423.22	14.56	Very poorly sorted	-0.255	Fine skewed	1.058	Mesokurtic	3.95	18.66	46.83	30.56	4.59	0.76
		Quartz granules	None													
		Subangular to subrounded clasts	Common to many													
		Shell fragments and shell hash	None													
		Whole shell	None													
C1	Mud to muddy sand	Pisoliths	None	30.87	4.88	Very poorly sorted	-0.041	Symmetrical	0.840	Platykurtic	9.85	56.37	33.78	0.00	10.49	1.98
		Quartz granules	None													
		Subangular to subrounded clasts	None													
		Shell fragments and shell hash	None													
		Whole shell	None													
C2	Sandy mud to muddy sand	Pisoliths	None	52.13	4.59	Very poorly sorted	-0.318	Very fine skewed	1.037	Mesokurtic	6.20	43.59	50.05	0.16	5.99	4.51
		Quartz granules	None													
		Subangular to subrounded clasts	None													
		Shell fragments and shell hash	Few													
		Whole shell	None													
C3	Gravelly mud to slightly gravelly sandy mud	Pisoliths	None	50.49	8.60	Very poorly sorted	-0.167	Fine skewed	0.662	Very platykurtic	7.78	40.06	48.24	3.92	5.23	1.80
		Quartz granules	Few													
		Subangular to subrounded clasts	None													
		Shell fragments and shell hash	Many													
		Whole shell	Abundant													
C4	Slightly gravelly sandy mud to gravelly mud	Pisoliths	None	18.69	5.78	Very poorly sorted	0.321	Very coarse skewed	0.819	Platykurtic	14.09	61.75	21.73	2.43	9.51	1.89
		Quartz granules	Very few to few													
		Subangular to subrounded clasts	None													
		Shell fragments and shell hash	None													
		Whole shell	None													
C5	Slightly gravelly sandy mud to gravelly mud	Pisoliths	None	30.77	9.75	Very poorly sorted	0.297	Coarse skewed	0.804	Platykurtic	9.90	54.79	30.06	5.26	7.67	1.81
		Quartz granules	None													
		Subangular to subrounded clasts	Few													
		Shell fragments and shell hash	None													
		Whole shell	None													
D1	Slightly gravelly mud to slightly gravelly muddy sand	Pisoliths	Few	51.96	6.87	Very poorly sorted	0.092	Symmetrical	1.160	Leptokurtic	9.16	54.40	31.58	4.86	7.45	1.23
		Quartz granules	None													
		Subangular to subrounded clasts	None													
		Shell fragments and shell hash	None													
		Whole shell	None													
D2	Gravelly mud to muddy sandy gravel	Pisoliths	Common to many	179.58	11.47	Very poorly sorted	-0.061	Symmetrical	1.035	Mesokurtic	4.97	34.36	38.60	22.08	7.02	1.43
		Quartz granules	None													
		Subangular to subrounded clasts	None													
		Shell fragments and shell hash	None													
		Whole shell	None													

#### 4.4.1 Facies A

Facies A is an unconsolidated (clast-supported) pisolith-rich sand unit, comprising approximately 70% to 80% pisoliths and 20% to 30% sand, silt and clay (primarily sand). Macrofossils are present in this unit as whole shell, shell fragments and shell hash, along with rare coral clasts and tubeworm fragments. The shells present in Facies A are a mixed assemblage of predominantly bivalves and gastropods, including specimens of *T. granosa*, *Marcia hiantina*, *Telescopium telescopium*, *Ostres* sp., *Trochus* sp., *Circe* sp., and *Paphies* sp. The shells are randomly oriented and have no evidence of size sorting. Facies A is present at Red Beach, within the first seven seaward ridges and the modern beach and is commonly found in alternating units with Facies B (Figures 4.6, 4.7, 4.11 and 4.27).

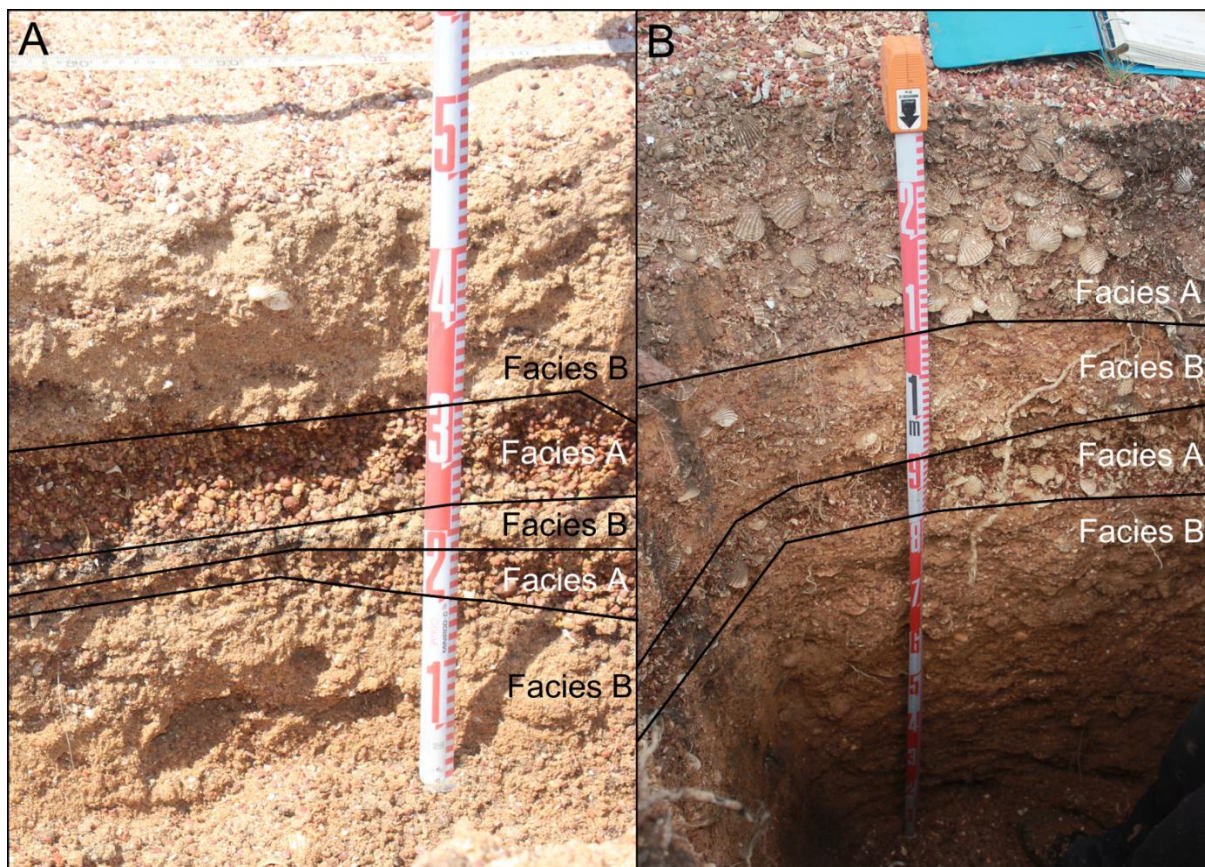


**Figure 4.27: Alternating units of Facies A (pisoliths-dominated) and Facies B (sand-dominated) at the (A) modern beach at Red Beach and (B) relict beach ridge RR2 at Red Beach.**

Sediment samples from Facies A have the highest carbonate content compared to the other facies (between 12% to 15%) due to the larger number of macrofossils present compared to the other facies (Table 4.1). Furthermore, at approximately 7% dry weight (DW), Facies A



has a higher organic carbon content than Facies B (Table 4.1), most likely because the larger void spaces between the pisoliths in this clast-supported sediment allows the accumulation of a greater abundance of roots and other organic matter compared to Facies B. The alternative explanation for the higher organic content of Facies A is that it is composed primarily of gibbsitic pisoliths (see Section 1.4.2 for background on the pisolithic deposit). Gibbsite-rich materials undergo substantial moisture losses when ignited in a furnace, even at low temperatures, which is a common limitation of using loss on ignition to estimate organic carbon content (Gale and Hoare, 1991). While loss on ignition in this study was carried out on the < 2 mm portion of each sample, minimising the proportion of pisoliths in each sample because the majority of pisoliths are > 2 mm, the moisture loss from any gibbsitic pisoliths in each loss on ignition sample would artificially increase the measured loss in weight from each sample from the ignition of organic matter, increasing the % organic matter value for these samples. Facies A is very fine skewed and leptokurtic (see Section 3.3.3).

Facies A has been subdivided into two sub-facies. Sub-facies A1 (Figure 4.28A, Table 4.1) comprises abundant rounded to sub-rounded pisoliths that are approximately 0.3 cm to 0.5 cm in diameter (very few to 1.5 cm). There is common whole shell in the unit, along with abundant shell fragments and shell hash, in a poorly sorted medium to coarse sandy matrix. Depending on the proportion of sand and pisoliths, sediment samples from this facies show either a unimodal or a bimodal grain size distribution. Sub-facies A1 has an average carbonate content of approximately 12% and an organic carbon content of approximately 6%.



**Figure 4.28: (A) Sub-facies A1, from the top of the pit at ridge 2, Red Beach, showing the abundant pisoliths, common whole shell, and abundant shell fragments and shell hash present in this unit. (B) Sub-facies A2, from the middle of the pit at ridge 7, Red Beach, showing the abundant pisoliths, few whole shells and abundant shell fragments and shell hash present in this unit.**

Sub-facies A2 (Figure 4.28B, Table 4.1) is like Sub-facies A1, in that it is comprised of abundant sub-rounded to sub-angular pisoliths that are approximately 0.3 cm to 0.5 cm in diameter (very few to 2 cm). However, in contrast with Sub-facies A1, there are few whole shells and abundant shell fragments and shell hash in a very poorly sorted silty medium sand matrix. While the majority of sediment samples included in this sub-facies show a unimodal grain size distribution, some samples have a bimodal or a trimodal grain size distribution due to the mixture of pisoliths, sand, and silt and clay. Sub-facies A2 has a carbonate content of approximately 15% and an organic carbon content of approximately 7%.

Sub-facies A1 and A2 are interpreted as indicative of deposition in a high-energy coastal setting where the wave energy would be sufficient to be able to transport and deposit the relatively large quantities of pisoliths and whole shell that make up the facies. Tropical cyclone-related storm surges that have high flow velocities are one example of a high-energy setting suitable for the deposition of Facies A, particularly given the location of Albatross Bay within Australia's cyclone belt (see Section 1.4.1).

Coastal deposits from high-energy events, such as tropical cyclones and tsunamis, are sometimes coarse-skewed, reflecting the deposition of coarse-grained sediments while the fine-grained sediments are transported away (Moore *et al.*, 2007; Nott *et al.*, 2013; Wassmer *et al.*, 2015). However, Facies A is very fine skewed (Figure 4.29). The very fine skewness of this facies is likely due to two factors. Firstly, the calculation of "coarse" or "fine" skewness is not directly linked to grain size but, instead, whether the particle size distribution is preferentially spread to one side of the average (Blott and Pye, 2001). As Facies A is dominated by pisoliths (70% to 80% of the unit), the 20 to 30% of sand and mud that is present in Facies A is finer than the pisoliths and therefore makes Facies A "fine skewed". Secondly, the larger void spaces present between the pisoliths within this facies are subject to secondary infilling with sand and mud, once again resulting in an increased proportion of finer material in this unit (Dashtgard *et al.*, 2006).



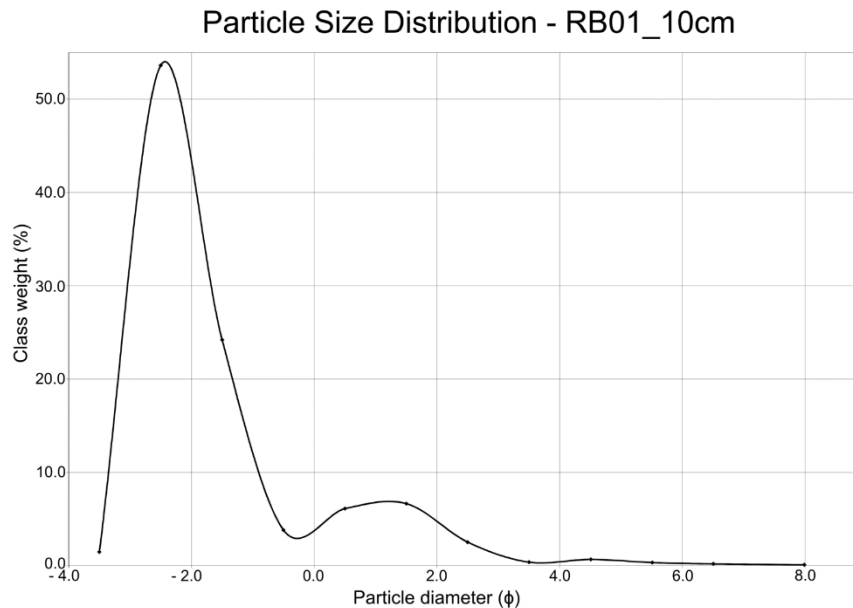


**Figure 4.29: Particle size distribution of sample RB01\_10cm from Red Beach, classified as sub-facies A1, showing how the distribution is very fine skewed, most likely due to the predominance of pisoliths in the sample.**

Morton *et al.* (2007) report that, like Facies A at Albatross Bay, tropical cyclone-related storm surge deposits often contain a high concentration of reworked (disarticulated) whole shells and shell fragments in a well- to poorly-sorted sandy matrix with rare mud present (because mud has been transported away from the beach due to high velocity transport during the storm) and an abrupt basal contact.

#### 4.4.2 Facies B

Facies B is a matrix-supported unit dominated by sand. Most sub-facies in Facies B contain 60% to 90% sand and less than 5% silt and/or clay, with the remainder consisting of coarse fragments (Table 4.1). Facies B is found within the beach ridge and swale landforms and within the modern beach trench at Red Beach, and within the beach ridge at Wathayn and at Kwamter (Figures 4.11, 4.22 and 4.26). Facies B has the lowest organic carbon content of all facies, approximately 2.5% to 4.5%, while the carbonate content varies between the different sub-facies, ranging from as low as 0.2% to as high as 6% (Table 4.1).

Facies B has been divided into six sub-facies, though not all of them are present at all sampling locations. Sub-facies B1 to B4 are found only at Red Beach. Due to the relatively large number of pisoliths present in these units, sub-facies B2 to B4 exhibit a bimodal grain size distribution. Sub-facies B5 is present at both Wathayn and Kwamter, while Sub-facies B6 is present only at Wathayn.

As described in Section 4.1.2 above, some units of Facies B at Red Beach are cemented with calcium carbonate, forming hardpan calcrete (Figure 4.30). Calcrete is not a separate and distinctive sedimentary facies at Red Beach. Rather, the calcrete forms from carbonate cementation of the host stratigraphic unit, which may comprise any of the sub-facies of Facies B present at Red Beach. Calcrete is present at the base of Ridge 4 (RR4 in Figure 4.11) and thereafter in every ridge and some of the swales from RR4 to RS10. The calcrete layers generally increase in hardness and thickness with distance inland.



**Figure 4.30:** Sample of calcrete collected from the base of ridge 8 at Red Beach. It consists of sand, pisoliths, shell fragments and shell hash cemented together by calcium carbonate.

Sub-facies B1 (Figure 4.31A, Table 4.1) is composed of approximately 90% medium quartz sand, with few (av. 4%) rounded to sub-rounded pisoliths. The pisoliths are predominantly between 0.3 cm and 0.4 cm in diameter, with very few up to 1.3 cm in diameter. The pisoliths in Sub-facies B1 have the smallest mean grain size (approx. 0.35 cm) compared to the pisoliths found in the other facies. Nevertheless, because of their presence, sub-facies B1 is classified as poorly sorted, with a unimodal grain size distribution that is symmetrical and very leptokurtic. Sub-facies B1 contains approximately 5% silt and/or clay-sized particles, and has an organic carbon content of approximately 4% and a carbonate content of 0.5%.

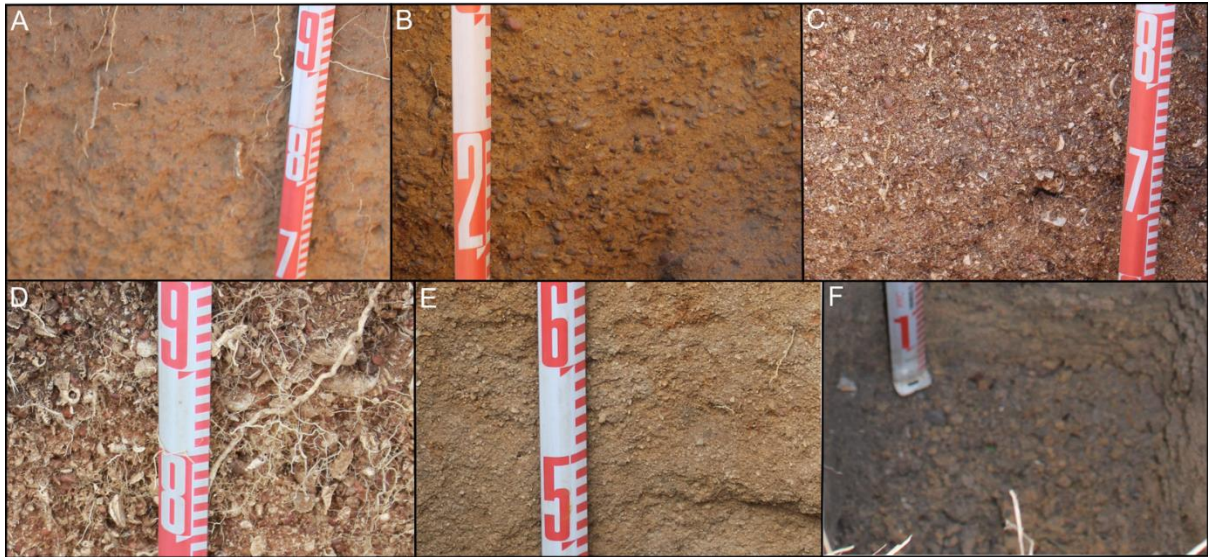


**Figure 4.31:** (A) Sub-facies B1, from the top of the pit at ridge 10, Red Beach, showing few pisoliths in a sandy matrix. (B) Sub-facies B2, from the middle of the pit at ridge 9, Red Beach, showing many pisoliths in a sandy matrix. (C) Sub-facies B3, from the middle of the pit at the flank of ridge 3, Red Beach, showing many pisoliths, many shell fragments and shell hash, along with very few to few whole shells in a sandy matrix. (D) Sub-facies B4, from the top of the pit at ridge 3, Red Beach, showing many pisoliths, common to many whole shells and many shell fragments and shell hash in a sandy matrix. (E) Sub-facies B5, from the middle of the pit within the ridge crest at Kwamter, showing very few to few quartz granules in a sandy matrix. (F) Sub-facies B6, from the base of the pit within the ridge flank at Wathayn, showing common to many sub-rounded to sub-angular gravel clasts in a silty sand matrix.

Sub-facies B2 (Figure 4.31B, Table 4.1) is composed of approximately 60% coarse to very coarse quartz sand with many (av. 36%) rounded to sub-rounded, occasionally sub-angular, pisoliths; i.e. it is coarser overall than sub-facies B1. The pisoliths are predominantly between 0.3 cm and 0.6 cm in diameter, with very few pisoliths up to 1.7cm. Sub-facies B2 is thus classified as very poorly sorted, with a bimodal grain size distribution that is coarse skewed and mesokurtic. Similar to sub-facies B1, sub-facies B2 contains approximately 5% silt and/or clay-sized particles and has an organic carbon content of approximately 4% and a carbonate content of 0.7%.

As shown in Figure 4.11, sub-facies B1 and B2 are found at the top of the Red Beach beach ridge and swale sedimentary sequences. Sub-facies B1 is also present in the sediments of the modern beach (Figure 4.6), but as a layer of only 2 cm thickness. Sub-facies B1 and B2 have the smallest mean grain sizes of all the facies at Red Beach (with sub-facies B1 containing smaller pisoliths than all the other facies present). The low carbonate contents of Sub-facies B1 and B2 (the lowest carbonate contents of all the sub-facies within Facies B) reflects the lack of whole shell and shell fragments in these sediments. Thus, sub-facies B1 is interpreted as aeolian in origin, most likely formed by wind transport of relatively fine grained sediments off the beach and onto the primary beach ridge or foredune. This process may have been aided by



the presence of vegetation on the foredune (Figure 4.32) which could trap sand grains and coarser particles saltating across the surface. While it may seem counterintuitive that pisoliths, with an average mean diameter of at least 3 mm (data from Facies B1), can be transported by aeolian processes, there is evidence in the literature that such transport is possible. Newell and Boyd (1955), for example, describe aeolian ripples that were composed of very coarse sand and granules in the Inca Desert along the Peruvian coast, where the modal diameter was approximately 3 mm and the coarsest grains were 6 mm to 7 mm in diameter. Twaddle *et al.* (2017) also describe an aeolian unit that contains common to present pisoliths and well-sorted quartz sand within the beach ridges at Bentinck Island in the Gulf of Carpentaria.



**Figure 4.32: Modern foredune at Red Beach showing a sand unit at the surface with pisoliths present.**

To transport grains that are larger than 2 mm, either extremely strong winds are required, or the sediment in question needs to be relatively porous, with a low density (Pye and Tsoar, 2009; Douillet *et al.*, 2014). Gibbsite pisoliths from the Weipa bauxite deposit have a specific gravity of between 1.95 and 2.76 and a porosity of between 21% and 30% (Taylor *et al.*, 2008b). In contrast, quartz has a specific gravity of 2.65, and calcareous sand has a specific gravity of between 2.64 and 2.71 (Carter and Bentley, 2016). Pisoliths therefore should be easier to transport than sand grains of a similar size. The modern foredune at Red Beach (Figure

4.32) is capped by a fine sand unit containing pisoliths, supporting the hypothesis that pisoliths can be transported by wind.

Sub-facies B3 (Figure 4.31C, Table 4.1) is composed of poorly sorted coarse to very coarse quartz sand, which makes up approximately 65% of the unit. There are many rounded to sub-rounded gibbsitic pisoliths (approximately 30% of unit) that are predominantly between 0.3 cm and 0.6 cm in diameter, with very few pisoliths up to 2 cm in diameter. This sub-facies has an organic carbon content of approximately 5%, similar to sub-facies B1 and B2, and has a bimodal grain size distribution, is coarse skewed and mesokurtic. Sub-facies B3 contains many shell fragments and shell hash, along with very few to few whole shells of similar species to those found in Facies A. The whole shells are randomly oriented. Sub-facies B3 also has a higher carbonate content than sub-facies B1 or B2, at approximately 6%, reflective of the higher shell content of this sub-facies.

Sub-facies B3 is the main sedimentary facies present on the modern beach at Red Beach, where it comprises the beachface (Figures 4.6 and 4.27A). Within the modern beach, sub-facies B3 contains many pisoliths and many shell fragments and shell hash but few whole shells, reflective of the relatively high wave energy in which it would be transported and deposited. Sub-facies B3 is also the dominant facies present within the beach ridges at Red Beach, is commonly encountered beneath sub-facies B1 and/or B2, and is found alternating with Facies A when Facies A is present within the beach ridges (Figures 4.11 and 4.27B). It is therefore interpreted as a beachface deposit that was subsequently buried beneath aeolian sediments as the shoreline at Red Beach prograded seaward.

Sub-facies B4 (Figure 4.31D, Table 4.1) is composed of poorly sorted coarse to very coarse quartz sand, which makes up approximately 65% of the unit. There are also many (approximately 35% by volume) rounded to sub-rounded gibbsitic pisoliths which have a diameter of between approximately 0.35 cm and 0.45 cm, with very few pisoliths up to 1.8 cm in diameter. This facies has a bimodal grain size distribution, is coarse skewed and platykurtic. There are many shell fragments and shell hash, along with common to many whole shells that are randomly oriented. Sub-facies B4 has a similar organic carbon content and carbonate content to sub-facies B3, at 5% and 4% respectively.

Sub-facies B4 is like sub-facies B3 except that, rather than having very few to few whole shells present, sub-facies B4 has common to many whole shells. Sub-facies B4 is encountered less frequently than the other sub-facies at Red Beach: it is located at various

depths within the first 5 seaward beach ridges (RR1 to RR5 in Figure 4.11) but is not encountered again until beach ridge RR11, near the distal margin of the beach ridge sequence. In ridge RR11, sub-facies B4 is found at the base of the pit, below sub-facies B1 and sub-facies B2. Because of its relatively coarse mean particle diameter and relatively high proportion of pisoliths, whole shell and shell fragments content, sub-facies B4 is more likely to be a beach deposit than an aeolian deposit. It was not encountered in the trench across the modern beach at Red Beach. Nevertheless, the presence of common to many whole shells in this sub-facies indicates that it was transported and subsequently deposited in a higher energy environment than sub-facies B3. The maximum thickness of a sub-facies B4 unit within the Red Beach beach ridges is 20 cm (RR3 in Figure 4.11), compared to sub-facies B3, the beachface deposit, where units can be up to 124 cm thick (RS4 in Figure 4.11). This difference in the maximum thickness of the deposit implies that sub-facies B4 was not deposited by daily processes such as wind or wave action, but rather by irregular deposition events. Therefore, sub-facies B4 is interpreted as possibly representing a backbeach deposit, an area reached only during the highest tides and storm events which would have the energy to transport and subsequently deposit the whole shell characteristic of this sub-facies (Ellis, 1978; Brenninkmeyer, 1982; Clifton, 2005).

Sub-Facies B5 (Figure 4.31E, Table 4.1) is composed of poorly sorted medium to coarse quartz sand, making up approximately 85% of this unit. There are also very few to few sub-rounded quartz granules (approx. 4%) that have a diameter between approximately 0.3 cm and 0.4 cm. Sub-facies B5 has a unimodal grain size distribution, is fine skewed and leptokurtic. It has the lowest carbonate content of all the sub-facies (0.2%), reflective of the lack of shell in this sub-facies. Sub-facies B5 also has the lowest organic carbon content among all the sub-facies, at 2.6%. Sub-facies B5 is found within the beach ridge and ridge flank at Kwamter and Wathayn, but is not present at Red Beach. Apart from sub-facies B1, sub-facies B5 has a significantly lower mean grain size (461  $\mu\text{m}$ ) compared with the sub-facies found at Red Beach (av. 960  $\mu\text{m}$ ); it also has a greater proportion of silt and clay (approx. 10%).

With a smaller mean grain size and a higher proportion of silt and clay, sub-facies B5 was most likely deposited in a lower energy environment than sub-facies B2, B3 and B4. This may be due to the locations of Kwamter and of Wathayn in the lower and middle reaches of the Embley river estuary respectively, rather than in the more open marine coastal setting of Red Beach (Figure 3.1). Under this scenario, the larger mean grain size of sub-facies B5 at

Kwamter than at Wathayn (726  $\mu\text{m}$  cf. 267  $\mu\text{m}$ ), may be reflective of an even lower energy environment of deposition in the more upstream location (i.e., Wathayn).

However, in addition to the relatively fine particle size of the B5 samples, the lack of marine macrofossils, the fine-skewed particle size distribution (see Section 3.3.3.3), and its position within the beach ridges at Kwamter and Wathayn (Figures 4.22 and 4.26) indicate that sub-facies B5 is most likely the product of aeolian deposition. It should be noted, however, that the absence of marine macrofossils does not necessarily mean that they were not present when the unit was initially deposited because, over time, any macrofossils present may have been dissolved and the carbonate leached by downward percolating rainwater (Stephens *et al.*, 1973).

Sub-Facies B6 (Figure 4.31F, Table 4.1) is composed of very poorly sorted silty coarse quartz sand (22% silt and/or clay, 47% sand) with common to many (31%) sub-rounded to sub-angular gravel up to 5 cm max diameter. Due to the significant proportions of silt and/or clay, sand and gravel, sub-facies B6 has a trimodal grain size distribution (Figure 4.33), and is fine skewed and mesokurtic. Sub-facies B6 has an organic carbon content of approximately 4.6% and a relatively low carbonate content of 0.8%. It is only found at the base of the ridge flank at Wathayn, and the sample was moist, indicating that the water table was in close proximity to the base of the pit.

Sub-facies B6 is interpreted as a transitional facies between the aeolian beach ridge facies of sub-facies B5 and the substrate below the beach ridge. Unlike Red Beach and Kwamter, where the beach ridges are underlain by intertidal or supratidal mudflat deposits respectively, the presence of the sub-angular to sub-rounded clasts indicates that the beach ridge at Wathayn may have been deposited over a different substrate, such as alluvium or weathering bedrock.



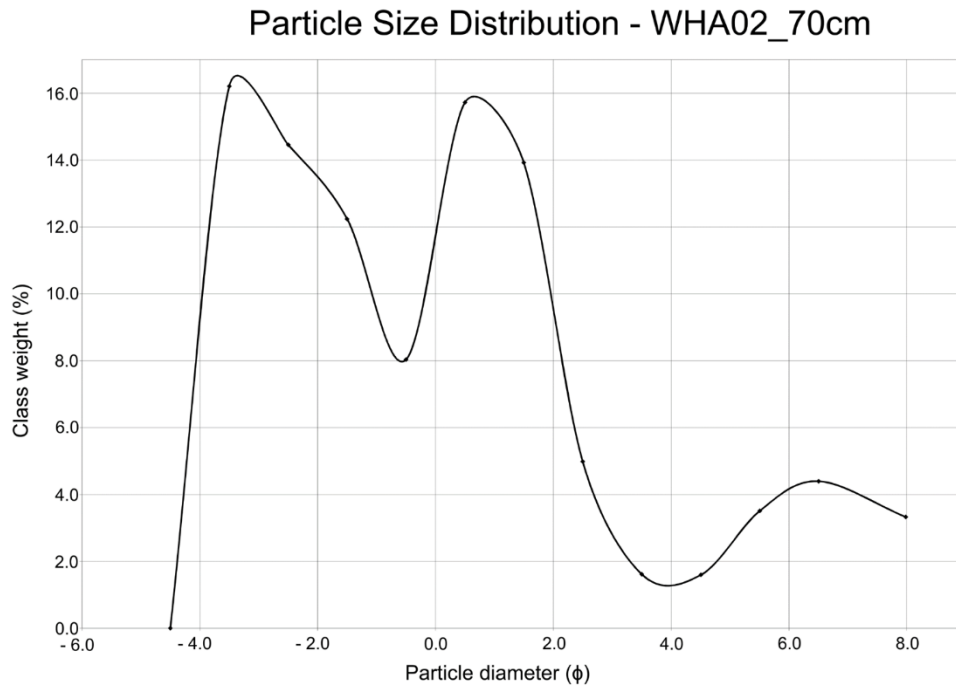


**Figure 4.33: Particle size distribution of sample WHA02\_70cm from Wathayn showing the trimodal distribution of sub-facies B6.**

#### 4.4.3 Facies C

Facies C is a matrix-supported unit that is composed of between 45% and 75% mud, with varying portions of sand (between 22% and 50%) and coarse fragments. At Red Beach, Facies C is encountered beneath the beach ridges where it underlies Facies B (Figure 4.11). At Kwamter and Wathayn, Facies C is present within the flank of the beach ridge and in the supratidal mudflats and mangroves (Figures 4.22 and 4.26). Facies C has been divided into five subfacies.

Sub-Facies C1 (Figure 4.34A, Table 4.1) is composed of very poorly sorted sandy silt to silty fine quartz sand. It is approximately 66% mud and 34% sand, with no coarse fragments. C1 has either a unimodal or bimodal grain size distribution, depending on the proportion of mud and sand in each sample. The grain size distribution is also symmetrical and platykurtic. C1 has the highest organic carbon content amongst all the facies identified in this study, at approximately 10%, and a carbonate content of approximately 2%. Sub-facies C1 is encountered mainly at Wathayn and at Kwamter where it is the primary sedimentary unit found in the D-section cores collected from within the mangroves.



**Figure 4.34:** (A) Sub-facies C1, from the D-section core collected within the mangroves at Wathayn, showing significant organic matter (roots and leaves) in a sandy silt matrix. (B) Sub-facies C2, from the D-section core collected from the base of a pit dug into the proximal flank of ridge 3 at Red Beach, showing few shell fragments and shell hash in a sandy silt matrix. (C) Sub-facies C3, from the middle of a pit within the supratidal mudflat at Kwamter, showing the shell layer comprising very abundant whole and fragmented shell in a silty sand matrix. (D) Sub-facies C4, from the top of a pit within the supratidal mudflat at Wathayn, showing very few quartz granules in a sandy silt matrix. (E) Sub-facies C5, from the base of pit within the supratidal mudflat at Wathayn, showing few sub-rounded to sub-angular gravel clasts in a sandy silt matrix.

A sample of C1 sediment from one of these cores (WHAD06; Figure 4.26) returned a radiocarbon date of Modern (see Table 5.13 in Chapter 5). Therefore, sub-facies C1 is interpreted as a fine-grained intertidal sediment deposited in a mangrove environment. The high organic carbon content of sub-facies C1 further supports this conclusion (see Section 1.4.2). At Red Beach, it is only found at the base of the pit beneath one beach ridge (ridge RR3; Figure 4.11). The mean grain size of sub-facies C1 at Red Beach is larger than at Kwamter and Wathayn ( $73.08\ \mu\text{m}$  compared to  $27.67\ \mu\text{m}$  and  $23.40\ \mu\text{m}$  respectively), possibly reflecting the higher energy environment of deposition present at Red Beach. Nevertheless, it is likely to

have been deposited in an intertidal mudflat environment that was progressively buried beneath the beach ridges on a prograding shoreline.

Sub-facies C2 (Figure 4.34B, Table 4.1) is composed of very poorly sorted sandy silt to silty fine to medium quartz sand (approximately 50% silt and clay and 50% sand). Sub-facies C2 has the highest carbonate content of Facies C, at approximately 4.5%, most likely due to the presence of some shell hash, along with an organic carbon content of approximately 6%. Sub-facies C2 also has a unimodal grain size distribution that is very fine skewed and mesokurtic. Sub-facies C2 is found within the mangroves at Wathayn (Figure 4.26), within the supratidal mudflat at Kwamter (Figure 4.22), and at the base of the flank of one ridge (RS3) and base of a swale (RS9) at Red Beach (Figure 4.11).

Sub-facies C2 is interpreted as an intertidal mudflat facies due to the fine-grained (silt and clay) nature of the sediment along with the presence of shell hash and a lower organic carbon content than sub-facies C1 (see Section 1.4.2). Furthermore, the higher proportion of sand in this sub-facies compared to sub-facies C1 indicates a direct interaction with the beachface that would then introduce sand into this sub-facies. Similar to Facies B and sub-facies C1, the mean grain size of sub-facies C2 at Red Beach is coarser than that from Kwamter and Wathayn (78.3  $\mu\text{m}$  compared to 42.35  $\mu\text{m}$  and 30.11  $\mu\text{m}$  respectively). It can be observed at the modern beach at Red Beach, where the intertidal mudflat is exposed during low tide (see Section 4.1.3).

Sub-Facies C3 (Figure 4.34C, Table 4.1) is a shell layer comprising very abundant whole and fragmented shell, with few shell hash, in a silty sand matrix with few quartz granules present. The shells present in sub-facies C3 are similar to those recorded for Facies A – *T. granosa*, *M. hiantina*, *T. telescopium*, *Ostres* sp., *Trochus* sp., *Circe* sp., and *Paphies* sp. The shells are randomly oriented with no evidence of size sorting. The matrix in sub-facies C3 comprises approximately 48% mud, 48% sand and 4% quartz granules that are approximately 0.2 cm to 0.4 cm in diameter. C3 is very poorly sorted, fine skewed and very platykurtic, with an organic matter content of approximately 5%. It has a low carbonate content of approximately 1.8% even though it is a shell lens, which is likely due to the loss on ignition analyses being conducted on only the < 2mm portion of each sample. While sub-facies C3 has abundant whole and fragmented shell, there are few shell hash present, and the whole shell and shell fragments were greater than 2 mm in diameter and were thus excluded from the analysis. Sub-Facies C3 is only found beneath the supratidal mudflat at Kwamter (Figure 4.22).

The whole shell within sub-facies C3 is randomly oriented, with shells predominantly disarticulated, a significant proportion of shell fragmentation, and shells showing signs of degradation. There are four ways in which these shell concentrations form – event concentration, composite concentration, hiatal concentration and lag concentration (see Kidwell, 1991, for a detailed review of shell bed formation). The Kwamter shell bed is most likely a transgressive lag concentration, formed nearshore as sea level rose (see Section 3.1.3), eroding the seafloor sediment and transporting these sediments towards the new higher elevation beachface, leaving behind a lag of shell material (Flessa and Kowalewski, 1994; Pilarczyk and Barber, 2015). Identifying features of a transgressive lag concentration include evidence of the reworking and transport of sediments away from the shell concentration, poorly sorted shells that are randomly oriented, shells with encrustations and signs of corrosion, and few articulated shells (Pilarczyk and Barber, 2015). These features are all observed within the Kwamter shell bed (sub-facies C3).

Sub-facies C4 (Figure 4.34D, Table 4.1) is composed of very poorly sorted sandy silt to silty fine to medium quartz sand, containing approximately 76% silt and clay (the highest silt and clay content of all facies present) and 22% sand. There are very few to few (approx. 2%) quartz granules, with approximate diameters between 0.2 cm and 0.4 cm. Consequently, C4 has the smallest mean grain size of all facies present, at approximately 18.7  $\mu\text{m}$ . Sub-facies C4 has a unimodal or bimodal grain size distribution, depending on the proportion of sand and quartz granules in each sample, and is very coarse skewed and platykurtic. It has an organic matter content of approximately 10% and a carbonate content of approximately 2%. It is present only at Wathayn and Kwamter, predominantly as the surface unit of the supratidal mudflat, but is also present below intertidal mudflat deposits (sub-facies C1 and C2), and transgressive shell lag deposits (sub-facies C3) (Figures 4.22 and 4.26). Sub-facies C4 is commonly found at the surface of the modern supratidal mudflats. The high organic carbon content and low carbonate concentration of sub-facies C4, along with the very poorly sorted sandy mud texture, are all characteristics of sediments deposited in this environment (Geoscience Australia, 2015d).

Sub-facies C5 (Figure 4.34E, Table 4.1) is composed of very poorly sorted sandy silt (65% silt and clay, 30% sand) with few (approx. 5%) sub-rounded to sub-angular gravel clasts up to 5 cm max diameter. The proportions of sand, silt and clay, together with the presence of gravel, means that sub-facies C5 has a trimodal grain size distribution, similar to sub-facies B6, which is coarse skewed and platykurtic. The organic matter content of this sub-facies is



relatively high, at approximately 8%, and the carbonate content is approximately 2%. Sub-facies C5 is only found at Wathayn, beneath the supratidal mudflat (below sub-facies C4. Figure 4.26). Sub-facies C5 is like sub-facies B6, in that it is only found at Wathayn, at the base of the pit, and, due to the presence of sub-rounded to sub-angular gravel clasts, has a trimodal grain size distribution. Sub-facies C5 is interpreted as a transitional facies between the supratidal mudflat facies (sub-facies C4) and the substrate beneath.

#### 4.4.4 Facies D

Facies D is a matrix-supported sediment unit that comprises at least 40% mud and 30% to 40% sand, with the remaining portion being gibbsitic pisoliths (Table 4.1). It is only found beneath the swales at Red Beach, mainly as the surface unit of the more inland swales (RS7 to RS10, Figure 4.11), although it is also present at depth beneath two of the more seaward swales (RS4 and RS8). Facies D has been subdivided into two subfacies.

Sub-facies D1 (Figure 4.35A, Table 4.1) is composed of very poorly sorted sandy silt to silty fine quartz sand with few rounded to sub-rounded gibbsitic pisoliths (occasionally angular). It contains approximately 64% mud, 31% sand and 5% pisoliths. The pisolith diameters range from approximately 0.3 cm to 0.75 cm, with very few up to 1.5 cm in didepositameter. This sub-facies has either a unimodal, bimodal or trimodal grain size distribution, depending on the proportions of sand, silt and pisoliths in the samples. The grain size distribution is symmetrical and leptokurtic. Sub-facies D1 has an organic carbon content of approximately 7%, and a carbonate content of approximately 1%.

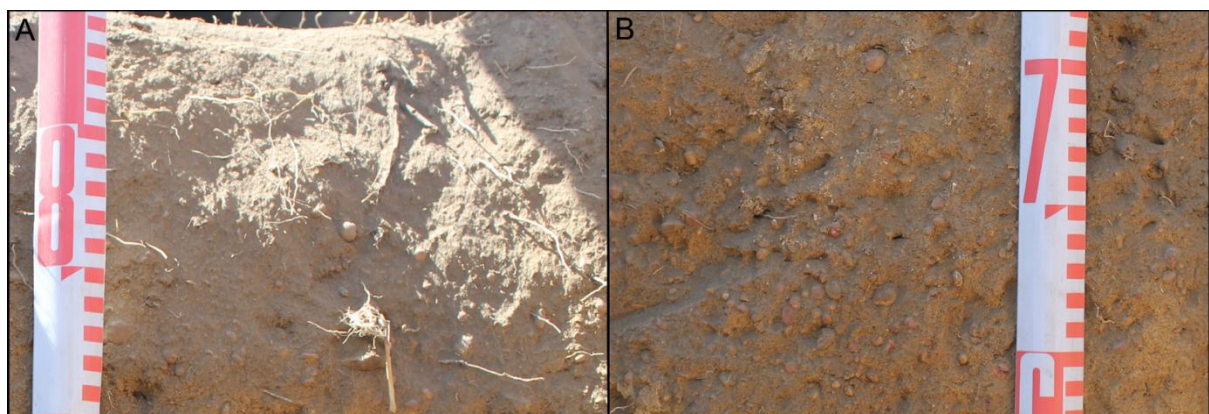


**Figure 4.35: (A) Sub-facies D1, from the top of a pit dug into the swale between ridge 8 and ridge 9 (RS9) at Red Beach, showing few pisoliths in a sandy silt matrix. (B) Sub-facies D2, from the middle of a pit dug into the swale between ridge 8 and ridge 9 (RS9) at Red Beach, showing many pisoliths in a sandy silt matrix.**

Sub-facies D2 (Figure 4.35B, Table 4.1) is like sub-facies D1, in that it is composed of very poorly sorted sandy silt to silty medium quartz sand with common to many rounded to sub-rounded gibbsitic pisoliths. However the proportion of silt and clay is lower and that of pisoliths is higher, at approximately 39% silt and clay, 39% sand and 22% pisoliths. The pisolith mean diameters range from 0.5 cm to 0.8 cm, with very few up to 1.5 cm in diameter. The high proportion of silt and clay, sand and pisoliths in sub-facies D2 gives this facies a trimodal grain size distribution that is symmetrical and mesokurtic. Sub-Facies D2 has an organic carbon content of approximately 7%, and a carbonate content of approximately 1%.

Sub-facies D1 and D2 are both interpreted as swale deposits from the beach ridge plain. In a beach ridge system, the water table lies closer to the surface of the lower elevation swales than the higher elevation beach ridge crests. During wet seasons, the water table rises and may intercept the swale surface, creating a pool of standing water (Oertel, 2005). These standing water pools tend to be ephemeral, drying out during the dry season or during periods of low precipitation (Oertel, 2005). Morrison (2015) noted that similar seasonal inundation occurs on the beach ridge plain at Red Beach (Figure 4.2B). Although he only refers to the largest swamp within the beach ridge plain, it is probable that standing water is also present in the other swales. During the periods of time that standing water is present in the swales, fine grained sediments settle out of suspension, depositing a layer of less permeable mud on the surface (Anthony, 2009). Furthermore, over time, as the density of plants in a swale increases, organic matter becomes concentrated there, adding to the reduction in permeability (Healy, 2005; Oertel, 2005; Anthony, 2009). A positive feedback loop ensures that the layer of mud on the surface of swales makes the land surface more impermeable, increasing the frequency of inundation and, hence, the deposition of fines. The fine grain size and the relatively high organic matter contents of the samples from sub-facies D1 and sub-facies D2 are reflective of this kind of environment of deposition. The pisoliths present within the samples are most likely residual material derived from the bauxite bedrock.

#### **4.5 Summary**

The presence of a beach ridge plain at Red Beach enables a detailed, high-resolution record of coastal evolution to be constructed, with Tamura (2012) even likening the study of beach ridges and its accompanying swales for palaeoenvironmental reconstruction to the study of tree rings or sedimentary stratigraphic sequences. This record is supplemented with data

from the single beach ridge, and pits and D-section cores excavated into the supratidal mudflats, at Kwamter and Wathayn.

As described above, four sedimentary facies were identified based on their sedimentary composition and characteristics and the biological structures they contain. Figure 4.36 shows a simplified sedimentary facies model for Red Beach, Kwamter and Wathayn. Facies A is a clast-supported, pisoliths-dominated facies found only at Red Beach, and interpreted as indicative of deposition in a high-energy coastal setting, most likely a tropical cyclone induced storm surge deposit. Facies B is a matrix-supported, sand-dominated facies, indicative of deposition within the beach zone. Sub-facies B1, B2 and B5 are aeolian sand units deposited on top of beach ridges. Sub-facies B3 is a beachface deposit, while Sub-facies B4 is a backbeach deposit. Sub-facies B6 from Wathayn is likely a transition facies between the beach ridge deposit and the substrate below. It contains common to many sub-rounded to sub-angular gravel clasts, possibly derived from weathering of the local bedrock. Facies C and D are both dominated by fine-grained sediment (silt and clay). Sediments from Facies C have been deposited in nearshore, subtidal, intertidal and supratidal environments. Sub-facies C1 contains sediments deposited within an intertidal mangrove environment, while Sub-facies C2 contains sediments deposited within an intertidal and subtidal mudflat. Sub-facies C3 is a transgressive shell lag concentration formed in the nearshore environment. Sub-facies C4 is a supratidal mudflat facies. Sub-facies C5, like Sub-facies B6, is likely a transition facies between the supratidal mudflat deposit at Wathayn and the substrate beneath. Finally, Facies D is composed of sediments that have been deposited within the beach swales at Red Beach.



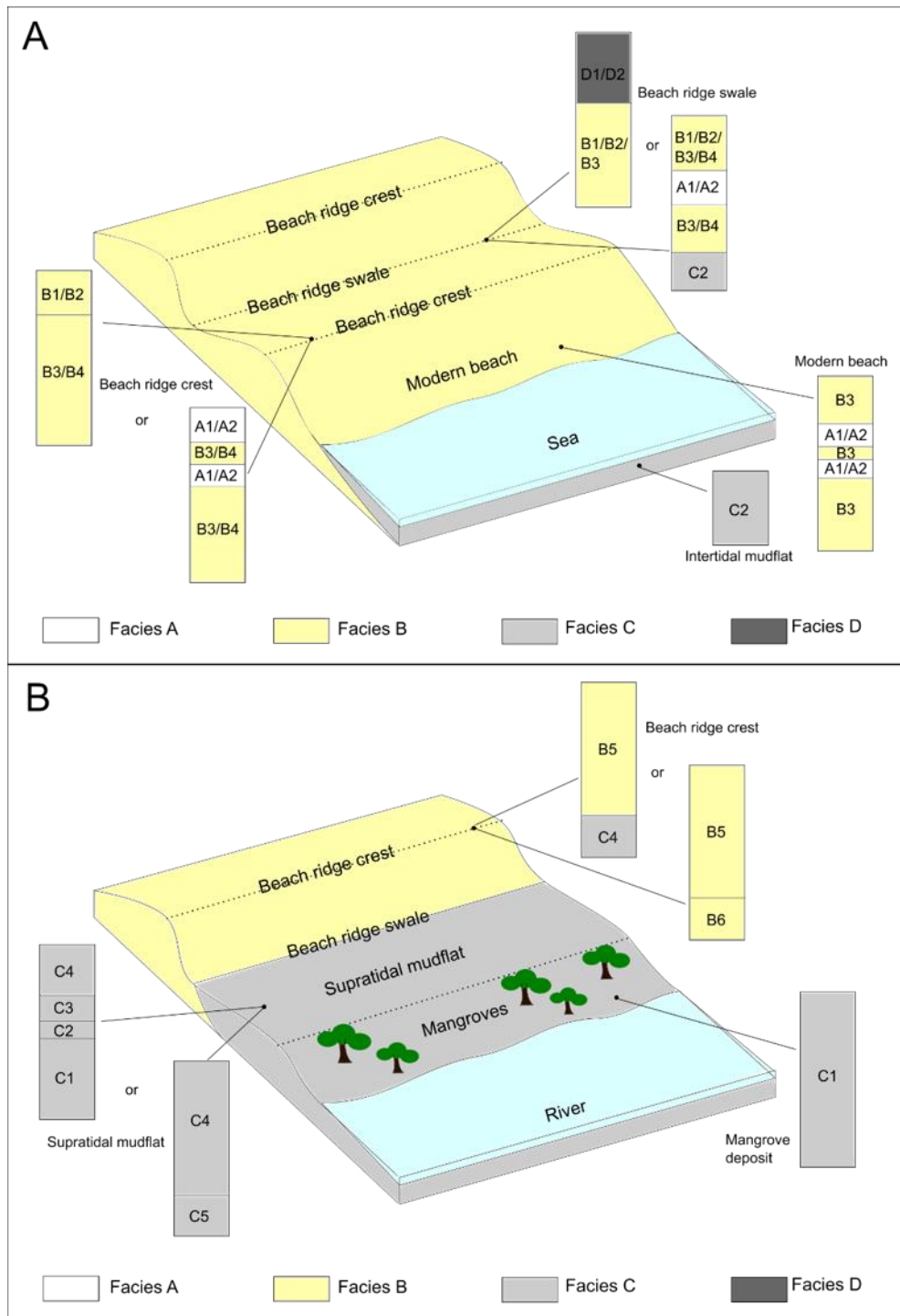


**Figure 4.36: Simplified sedimentary facies model for (A) Red Beach and (B) Wathayn and Kwamter showing the stratigraphic relationships between the facies and where they are located within the modern environment**

With the identification and characterisation of the sedimentary facies within the shoreline environments of Albatross Bay, an understanding of the coastal environment and its response to relative sea level change during the Holocene can now be constructed. The next

step in reconstructing relative sea level change in Albatross Bay is to establish a chronology for these observed sedimentological changes, the focus of the next chapter.

## **Chapter 5**

# **A Chronology of Coastal Evolution and Sea level Change at Albatross Bay**

Having identified and characterised the coastal sedimentary environments and chosen sea level proxies around Albatross Bay in the previous chapter, the next step in developing a Holocene sea level curve is to establish an accurate chronology for the changes in those environments and proxies. Following a brief introduction to the principles of absolute dating of environmental events using Optically Stimulated Luminescence (OSL) and radiocarbon techniques, this chapter presents the results of these techniques applied to samples collected from the three field locations at Albatross Bay. These results provide a chronological framework for the reconstruction of the evolution of coastal environments and Holocene sea level change in Albatross Bay (Chapter 6).

### **5.1 Optically-stimulated luminescence (OSL) dating**

#### **5.1.1 Principles of OSL dating**

Since being proposed by Huntley *et al.* (1985), OSL dating has become a well-established method of developing a chronology for coastal environmental change, both globally (see, for example, Roberts and Plater, 2007; Bjørnsen *et al.*, 2008; López and Rink, 2008; Carr *et al.*, 2010; Burdette *et al.*, 2012; Dörschner *et al.*, 2012; Fuchs *et al.*, 2012; Tamura *et al.*, 2012; Choi *et al.*, 2014; Alappat *et al.*, 2015; Bateman, 2015; Gao *et al.*, 2016) and within Australia (see, for example, Murray-Wallace *et al.*, 2002; Brooke *et al.*, 2008; Lewis *et al.*, 2013; Brooke *et al.*, 2015; Jankowski *et al.*, 2015; Oliver *et al.*, 2015; Oliver, 2016; Tamura *et al.*, 2018). Luminescence dating was developed on the basis that defects are present in the crystal lattice structure of many minerals, including quartz and feldspar grains. These defects trap electrons that are energised by the decay of naturally occurring radiation, accumulating a signal within the mineral grain over time (Aitken, 1998; Bateman, 2015). Four types of environmental radiation are present - alpha, beta, gamma and cosmic – all of which contribute to the radiation dose a sample receives. Cosmic rays originate from high-energy sources in the universe, including supernovas, while alpha particles, beta particles and gamma rays originate

from the decay of radioactive isotopes present in rocks and sediments, the most significant of which are the radioactive isotopes of uranium (U), thorium (Th) and potassium (K) (Duller, 2008, 2015; Guérin, 2015).

The accumulated signal is evicted when the sediment, and thus the quartz grain, is stimulated by either light or heat, effectively removing the signal in a process known as “zeroing” or “bleaching” (Lian and Roberts, 2006; Duller, 2008; Rhodes, 2011; Sloss *et al.*, 2013). Therefore, as sediment is being eroded, transported, and eventually deposited, the signal trapped within the quartz grains may be exposed to sufficient light such that the signal within is zeroed (Duller, 2015; Mauz, 2015). A quartz grain can be fully bleached in less than 30 seconds when exposed to full sunlight (Bateman, 2015), with the time required increasing when sunlight is obscured, such as by cloud cover or turbid water (Godfrey-Smith *et al.*, 1988; Olley *et al.*, 2004; Mauz, 2015). Once the sediment is deposited and buried and consequently blocked from further light exposure, the quartz grains will begin to accumulate a signal (Bateman, 2015). It is this signal that is measured during the luminescence dating procedure, with the age obtained representing the last time the quartz grains were exposed to light prior to their most recent burial, assumed to be contemporaneous to the time of deposition (Duller, 2015).

The signal is measured in the laboratory after stimulation with light (Optically-Stimulated Luminescence; OSL) or heat (Thermoluminescence; TL) to evict the electrons from the traps to recombine in luminescence centres and produce a luminescence signal. First, the “natural” signal in the quartz grains is measured. The quartz grains are then artificially irradiated with known doses of radiation to construct a dose response curve to test the sensitivity of the sample to dose (Duller, 2008; Bateman, 2015; Duller, 2015). The “equivalent dose” ( $D_e$ ) is obtained by interpolation of the natural signal (in luminescence counts) onto this dose response curve. The equivalent dose is a radiation dose value (in Grays, Gy) that is equivalent to the amount of radiation received by the sample for the duration of its burial period (Aitken, 1998; Bateman, 2015; Duller, 2015). Because the amount of natural radiation the grains receive differs from location to location, this environmental dose is also measured in the form of an annual dose rate, measured in Grays per thousand years (Gy/ka) (Duller, 2008; Rhodes, 2011; Bateman, 2015). By measuring both the accumulated signal in the quartz grains and the environmental dose rate, the time since the sediment was last exposed to sunlight can be calculated using the following formula:

$$Age \text{ (years)} = \frac{Equivalent \text{ dose } (D_e)(Gy)}{Dose \text{ rate } (Gy/ka)}$$

Unlike other dating techniques commonly used in coastal studies, primarily radiocarbon dating, U-series dating and amino acid racemisation, OSL dating results in a direct age determination of the sediments themselves, rather than their associated material such as shells or corals. OSL dating can thus provide an estimated age for the actual deposition of the coastal sediments, and the formation of landform features, rather than relying on biological indicators which, following the death of the organism, can be transported and reworked for a period of time prior to final deposition, leading to misleadingly older estimated ages (Bateman, 2015; Hendricks and Hodson, 2015). Australian quartz is well suited for OSL dating because the quartz grains usually have a high luminescence intensity and sensitivity and are able to store large doses (~200 Gy) before reaching saturation, maximising the dating range of the technique (Fitzsimmons *et al.*, 2010; Bateman, 2015).

A significant issue when measuring the equivalent dose of a sample is the potential for incomplete (partial) bleaching of sediment grains prior to deposition and burial. In ideal conditions, the quartz OSL signal can be rapidly bleached, with early experiments by Godfrey-Smith *et al.* (1988) demonstrating that an optical signal of  $10^6$  luminescence counts per milligram (cps/mg), emanating from unbleached quartz grains, can decay to 1% of its original value after 10 seconds of sunlight exposure and to negligible amounts of less than 150 cps/mg after 30 minutes of sunlight exposure. However, bleaching conditions are often not ideal, leading to the partial bleaching of the OSL signal within the grains. As some quartz grains are fully bleached and some are bleached more than others prior to burial, the  $D_e$  measured will be the dose acquired since deposition, plus an inherited signal that could be tens of Gy, causing inaccurate burial age calculations (Duller, 2015).

Partial bleaching concerns are compounded when multiple quartz grains are measured at once to obtain a  $D_e$ , as is the case when employing the single-aliquot regenerative-dose (SAR) protocol for  $D_e$  determination. The SAR protocol is a common dating protocol in studies of coastal and marine sediments (Jacobs, 2008; Zöller and Wagner, 2015). Duller (2004) estimates that when dating quartz with a diameter of 200  $\mu\text{m}$ , a single-aliquot may contain as many as 500 to 1000 grains (a number controlled by mask size, with standard mask sizes of 1 mm, 3 mm and 7 mm). Should a smaller mask size be used, this number could be reduced to tens of grains (Duller, 2008). When grains are partially bleached, a single-aliquot measurement would therefore be an average of the luminescence signals of the well-bleached and poorly bleached grains. This leads to an inaccurate  $D_e$  measurement and therefore, an inaccurate OSL age determination. Different  $D_e$  values within a sample can also be caused by the introduction

of younger or older grains to the sample from mixing of the sedimentary layers, either from past human or animal action such as trampling or bioturbation or sampling error (Jacobs *et al.*, 2006a). In general, the smaller the mask size used, the more accurate the  $D_e$  measurement, as less averaging of grains occurs and issues of partial bleaching and/or sediment mixing become more apparent in the spread of  $D_e$  measurements from the same sample (Duller, 2008).

The spread of  $D_e$  values from a sample, “... over and above that due to the estimation error associated with each observation...”, is termed the “overdispersion” (OD) (Galbraith and Roberts, 2012; p. 25). A high OD value can be an indicator of sediments being partially bleached, or of grain mixing in a sample (Rhodes, 2011). An OD value of less than 20% is commonly cited in the literature as an indicator of a well-bleached sample, based on work by Olley *et al.* (2004) in the study of well-bleached fluvial samples (see, for example, Couapel, 2005; Galbraith *et al.*, 2005; Brooke *et al.*, 2006; Jacobs *et al.*, 2006b; Lian and Roberts, 2006; Jacobs and Roberts, 2007; Galbraith and Roberts, 2012; Roberts and Jacobs, 2015).

Single-aliquot OSL measurements can therefore provide accurate  $D_e$  measurements when certain conditions are met. Most importantly, samples need to be well bleached, a possibility in a coastal environment where sand is repeatedly washed up and down the shoreline, receiving substantial sunlight exposure (Murray and Olley, 2002). Typically as much as 95% of the luminescence signal for a sample may be attributed to less than 5% of grains measured, with many grains not luminescing at all (Duller, 2008). Thus, in a well bleached sample that has a strong luminescence signal (enabling a small mask size to be used), a single-aliquot with tens of grains, with the OSL signal originating from 5% of those grains, can mean that  $D_e$  measurements may be as accurate as measuring each grain individually (Duller, 2008).

There also are two main points to consider when determining the dose rate for a sample – the water content of a sample and whether the dose rate was constant (i.e. in secular equilibrium) over the time the dose was accumulating in a sample. Within a sedimentary unit, interstices between grains may be wholly or partially filled by air or water. If filled by water, the water will absorb a portion of the radiation energy, lowering the dose rate received by the grains (Duller, 2015). Therefore, it is vital to estimate the average water content in a sample over the time period being dated to calculate the dose rate of a sample (see Section 5.1.5.5). Disequilibrium in the radioactive decay chain in a sedimentary environment will cause a change in dose rate over time, complicating the determination of a dose rate for luminescence

age calculations (Duller, 2008). High-resolution gamma spectrometry can be used to check for radioactive disequilibrium in an environment (see Section 5.1.5.6).

Within carbonate-rich environments such as coastal environments, sediments may become cemented with carbonate, forming calcrete (see Section 4.1.2). This carbonate cementation will also affect OSL dose rate measurements as it not only has a different dose rate to that of the host sediments, but will also attenuate the dose rate received by sediment grains as pore spaces are filled. Nathan and Mauz (2008) concluded that dose rates due to progressive carbonate cementation may be altered by up to 30%, affecting their OSL age determination by up to 15%.

The following section discusses the use of OSL techniques for obtaining ages of coastal sediments, including the bleaching potential in coastal environments and potential issues that may arise with this technique.

#### 5.1.2 OSL dating of coastal sediments

OSL dating has been successfully utilised in studies from a variety of coastal and marine environments, from beach ridges to estuarine sediments, intertidal flats and offshore marine cores (Couapel, 2005; Madsen *et al.*, 2007b; Brooke *et al.*, 2008; Jacobs, 2008; Mauz *et al.*, 2010; Bateman, 2015; Rémillard *et al.*, 2015; Nian *et al.*, 2018). Coastal sediments, in particular, are commonly exposed to sunlight for an extended time prior to deposition, increasing the potential for the sediments to be fully bleached prior to burial and making these sediments well suited for OSL dating (Duller, 2015; Mauz, 2015). Coastal deposits were therefore integral in both the development and validation of both TL and OSL dating methods (Jacobs, 2008).

While the OSL signal from sediments that have been exposed to daylight is often bleached within seconds (Godfrey-Smith *et al.*, 1988), bleaching efficiency can drop significantly depending on the specific depositional setting, which then leads to the potential for partial bleaching (Jacobs, 2008). For instance, bleaching is slower during overcast conditions (Godfrey-Smith *et al.*, 1988). Grains may also be transported at night, thus receiving no light exposure, and therefore no bleaching, prior to deposition (Rhodes, 2011). The effects of partial bleaching on dose estimates are more significant when dating younger sediments, such as the Holocene-aged samples characteristic of this study, because “...the effects of incomplete bleaching at burial will be exacerbated by the comparative small dose absorbed after deposition...” (Jacobs, 2008, p. 527).



Thus, while coastal sediments are generally well bleached, different coastal settings undergo different transport processes that can affect the extent of sediment bleaching (Mauz *et al.*, 2010; Bateman, 2015). The remainder of this section focusses on the use of OSL dating within foreshore environments, coastal aeolian environments and mudflat environments, the three environments where OSL samples were collected for this study.

#### 5.1.2.1 Foreshore Environments

Foreshore sediments deposited in the intertidal zone are frequently reworked by wave action and subjected to repeated exposure to sunlight over multiple tidal cycles, increasing the potential for these sediments to be fully bleached prior to final deposition and burial (Murray and Olley, 2002; Ballarini *et al.*, 2003; Rhodes, 2011; Bateman, 2015; Mauz, 2015). However, samples that are deposited within a water column will bleach more slowly due to reduced light levels from water turbidity, and the attenuation and scattering of light by the water (Richardson, 2001; Murray and Olley, 2002; Olley *et al.*, 2004; Mauz, 2015). Rendell *et al.* (1994) and Sanderson *et al.* (2007) conducted underwater bleaching experiments to test the strength of the optical luminescence signal remaining in sediments samples after exposure to light while submerged at various water depths. Rendell *et al.* (1994) exposed sediment samples to 3 hours of daylight at water depths between 4 m and 14 m in the English Channel where there was good underwater visibility to 15 m. At all water depths, the samples were effectively zeroed, with the OSL signal at 2.3% of the initial signal after 3 hours of exposure. This research demonstrates that, even at substantial water depths, there is still good potential for bleaching. The bleaching potential should increase in shallow water.

Sanderson *et al.* (2007) exposed sediment samples to 1 day and 10 days of daylight at water depths of 0-5 cm to 150 cm in the East Baray, Angkor Borei, Cambodia, where underwater visibility is poor, and the intensity of daylight is reduced to 5% of surface levels at 150 cm depth. While the levels of sediment bleaching were poor at the lower depths, samples from 0-5 cm were bleached to less than 0.1 Gy from an initial dose of 40 Gy after being exposed for 1 day, and to approximately 0.01 Gy after 10 days of exposure. These underwater bleaching experiments show that grains transported in the intertidal zone can be bleached relatively quickly, and that foreshore sediments are therefore ideal for OSL dating. OSL dating has been widely utilised to establish a chronology for foreshore sediments globally (López and Rink, 2007; Carr *et al.*, 2010; Burdette *et al.*, 2012; Tamura *et al.*, 2012).

In Australia, Brooke *et al.* (2006) used quartz SAR OSL dating to develop a chronology for sediments collected from relict beach ridges at Keppel Bay, Queensland. The sample  $D_e$  overdispersion (OD) was low, between 0% and 9%, indicating that the foreshore samples were well-bleached prior to deposition (see Section 5.1.1 on sample overdispersion). Brooke *et al.* (2006) were then able to construct a record of coastal sediment accumulation over the past 1,500 years at Keppel Bay, with data indicating periods of rapid beach ridge formation approximately every 200 to 500 years alternating with periods of quiescence.

Gao *et al.* (2016) applied SAR OSL dating to a coastal sediment core collected from the Yangtze River delta. The OSL results, and the sample OD values in particular, led Gao *et al.* (2016) to conclude that samples were well bleached prior to deposition and burial. Gao *et al.* (2016) were able to construct a depositional history of the Yangtze River delta from their sediment core, noting a depositional hiatus during the LGM as sediments were transported further out to the outer shelf of the East China Sea during lower sea levels, and delta formation initiating around 8,000 years ago after Holocene sea level rose and reached its maximum transgression.

Gao *et al.* (2016) noted three potential issues in the OSL dating of coastal sediments. Firstly, potential disequilibria of the uranium decay series due to the presence of organic matter and precipitated carbonates can impact dose rate calculations. Secondly, there may be difficulties in estimating the cosmic ray contribution due to changing water column depths and changing thicknesses of the sediment overburden as sediments accumulate above the sample. Thirdly, it is difficult to estimate the water content of samples from coastal environments, required in dose rate calculations, due to shifts in the water table caused by sea level change, and the dewatering and compaction of sediment after deposition.

Thus, while it is generally accepted that sediments deposited within the coastal foreshore are well-bleached and are therefore ideal samples for OSL dating, other factors that affect dose rate calculations need to be considered. For example, as the level of bleaching in sediments is influenced by tidal and wave action, spatial and temporal variability in the degree of sediment bleaching exists along the foreshore (Mauz, 2015). The potential for partial bleaching needs to be investigated in every study.

#### 5.1.2.2 Coastal aeolian environments

Sediments transported by aeolian processes have a high probability of sunlight exposure prior to deposition and burial (Bateman, 2015). The process of saltation, whereby

individual sediment grains are lifted and “bounced” along a surface by the wind, is particularly effective in this regard. Aeolian sediments thus have a high potential of being well-bleached and are one of the sediment types most commonly dated by luminescence techniques (Aitken, 1998; Bateman, 2015). Olley *et al.* (1998), for example, dated sediments collected from a modern aeolian dune at Cooloola, Queensland. Out of 96 aliquots of dune sand tested, 93% had an apparent dose of 0 Gy, with arithmetic mean of  $0.020 \pm 0.006$  Gy, implying that they had been completely bleached. While Olley *et al.* (1998) did not report an estimated age of their modern aeolian dune sample, a subsequent paper estimated that this  $D_e$  represents an age of approximately 20 years using “...typical dose rates...” (Murray and Olley, 2002, p. 5). Bailey *et al.* (2001) dated an aeolian sample collected from the crest of a dune at Aberffraw, Anglesey, North Wales, using the OSL SAR protocol and determined that it had a  $D_e$  of  $0.03 \pm 0.02$  Gy, resulting in an age of approximately  $20 \pm 10$  years. Thomas *et al.* (2008) collected five modern analogue samples from coastal dunes at Torreira and Sao Jacinto in Portugal. The  $D_e$  values from the modern dune samples range from  $0.02 \pm 0.01$  Gy to  $0.06 \pm 0.02$  Gy, resulting in ages between  $10 \pm 4$  years to  $45 \pm 15$  years. Similar results have been obtained from the dating of modern dune sands from the Netherlands (Ballarini *et al.*, 2003), Denmark (Nielsen *et al.*, 2006; Madsen *et al.*, 2007a), North America (Forman *et al.*, 2006) and Namibia (Bristow *et al.*, 2007). While all the samples collected from modern dunes in these studies still carried a minor residual signal, such a signal was considered insignificant when dating Quaternary sediments and all studies concluded that the aeolian sediments were well-bleached at time of deposition and burial.

Murray-Wallace *et al.* (2002) was one of the first studies to apply OSL dating to Holocene coastal dunes. Working at Guichen Bay, Australia, Murray-Wallace *et al.* (2002) collected samples exclusively from the aeolian facies of the beach ridges and found that dune formation commenced approximately  $5400 \pm 230$  years ago, after the end of the last post-glacial marine transgression. Coastal progradation was initially rapid, with the coastline prograding 1600 m over a 1,000 years, before slowing down and prograding a similar distance over the next 4000 years (Murray-Wallace *et al.*, 2002). Numerous studies have since employed OSL dating techniques to establish a chronology for aeolian sediments (see, for example, Ballarini *et al.*, 2003; Rink and Forrest, 2005; Nielsen *et al.*, 2006; Clemmensen *et al.*, 2007; Giannini *et al.*, 2007; Porat and Botha, 2008; Thomas *et al.*, 2008; Carr *et al.*, 2010; Rink and López, 2010; Reimann *et al.*, 2011; Tamura *et al.*, 2011; Forsyth *et al.*, 2012).

Oliver (2016) dated aeolian sands collected from beach ridges at Moruya, Wonboyn and Callala Beach in NSW, Australia, to construct a chronology of Holocene coastal progradation. The sample  $D_e$  OD was generally low (between 2% and 23%), leading Oliver (2016) to conclude that the samples are not affected by incomplete bleaching or post-depositional mixing. With the OSL ages obtained, Oliver (2016) concluded that coastal progradation commenced approximately 7500 years ago, following the end of the last post-glacial marine transgression, and proceeded at a linear rate. Roberts *et al.* (2009) utilised OSL dating to establish a chronology of coastal dunes at False Bay and Duinefontyn, South Africa. The  $D_e$  OD of aeolian sediment samples from both sites was between 4% and 12%, indicating that the sediment was fully bleached prior to deposition and burial. Roberts *et al.* (2009) concluded there were three phases of dune formation at False Bay, during marine isotope stage 7 (MIS 7), MIS 5 and the Holocene, while there were only two phases of dune formation at Duinefontyn (MIS 5 and the Holocene). These phases of dune formation were primarily controlled by sea level, which in turn affected the proximity of the dune fields to a sediment source (a sandy beach).

While aeolian sediments have an ideal depositional environment for OSL dating, there are potential issues with the technique. Due to the rapidity of bleaching of the luminescence signal when exposed to sunlight, any reworking or movement of coastal dunes by subsequent aeolian transport will reset the luminescence signal. The event being dated therefore may not be the initial formation of a landform following deposition and burial of sediment, but rather when the sediment was subsequently reworked, leading to burial ages that could be younger than initial deposition by a few centuries (van Heteren *et al.*, 2000). Furthermore, coastal dunes can accrete vertically over time, resulting in changing thickness of the sediment overburden, impacting the estimation of the cosmic ray contribution to the dose rate (Bateman, 2015). Aeolian dunes can also be subjected to carbonate cementation, forming aeolianite. This carbonate cementation will affect OSL measurements and need to be considered in any OSL age determinations (see Section 5.1.1).

#### 5.1.2.3 Supratidal mudflat environments

Sediments deposited within supratidal mudflats are more prone to partial bleaching than those deposited within a foreshore or an aeolian environment. Sediment deposition in supratidal mudflats commonly occurs only when the area is waterlogged during king tides (see Section 1.4.2). Sediments deposited within this environment comprise poorly sorted sandy mud, with the fine grains being suspended while the supratidal mudflat is waterlogged, before being

deposited *en masse* (Bateman, 2015). The suspension of fine sediments reduces light penetration within the water column and, along with the light scattering and attenuation that occurs within a water column, sediments may not be exposed to sufficient sunlight to fully bleach them prior to deposition (Richardson, 2001; Bateman, 2015).

There are few published studies on the optical dating of supratidal mudflat sediments. However, in a study of the optical dating of intertidal and subtidal sediments along the North Sea coast, across Germany, Belgium and France, Mauz *et al.* (2010) found variable bleaching of these sediments, with the tidal reworking of sediments crucial to resetting the luminescence signal. The variability in bleaching levels is attributed to the transport and depositional processes in the tidal environment – fine grained muds are transported by suspension, with the proportion of sediments in suspension higher at the sediment-water interface and decreasing moving upwards, which in turn affects the amount of sunlight exposure sediments receive (Mauz *et al.*, 2010). Mauz *et al.* (2010) therefore found it necessary to factor in partial bleaching when calculating ages for some of their samples.

An example of the successful employment of OSL dating in a supratidal mudflat environment can be found in a study by Madsen *et al.* (2007b) who collected a 13.5 cm sediment core from a supratidal mudflat at Skallingen, Denmark. While Madsen *et al.* (2007b) did not report their sample  $D_e$  overdispersion values, their surface sample returned an age of  $7 \pm 4$  years, and their basal samples reflected an age of  $68 \pm 6$  years. The basal estimated age of the initiation of the supratidal mudflat deposit was consistent with estimates based on historical mapping. Madsen *et al.* (2007b) therefore concluded that in this environment there was complete bleaching of the supratidal mudflat sediment prior to sample deposition and burial.

#### 5.1.2.4 Summary

Coastal sediments from foreshore and coastal aeolian environments are suitable for luminescence dating because wind and wave transport processes have a high potential to fully zero the optical luminescence signal within the grains prior to deposition and burial. However, greater caution is required when examining sediments deposited by tidal processes, such as within mudflat environments, due to a higher potential for the incomplete bleaching of sediments. In any study, it is still “...good practice to study the suitability of a coastal environment for luminescence dating by examining the residual dose in modern samples...” (Mauz, 2015, p. 447). In addition to sufficient resetting of the OSL signal, other factors that may affect age determinations based on this technique are mostly associated with dose rate

calculations – cementation of sediments, changing cosmic ray contribution due to changing sediment overburden, and difficulties in the estimation of sediment moisture content due to repeated wetting and drying of sediments in a coastal environment due to shifting water tables (Mauz *et al.*, 2010; Mauz, 2015). The majority of OSL samples collected for this research were from non-cemented units, except for two samples from Red Beach (see Section 5.1.5.6). With regard to changing sediment overburden, within Albatross Bay, the beach ridges are subtle, particularly at Red Beach, indicating that there was limited vertical accretion of the ridges by aeolian deposition over time and thus, changing sediment overburden is unlikely to be an issue. Finally, with respect to changing sediment moisture content, beach ridges are generally free-draining and “...unless there is clear sedimentological or other evidence to suggest past changes in moisture, values as measured at the present-day are generally used...” (Bateman, 2015, p. 410). Similarly, while sediments collected from intertidal and subtidal mudflats are subjected to changing moisture content through time, the supratidal mudflat is only occasionally inundated and would be less impacted by repeated wetting and drying.

### 5.1.3 Determining the equivalent dose ( $D_e$ )

Following sample collection and disc preparation (see Section 3.4.1), the  $D_e$  was determined on the single-aliquot and single-grain discs via the single-aliquot regenerative-dose (SAR) protocol of Murray and Roberts (1998) and Murray and Wintle (2000). The SAR protocol is a well-established OSL dating protocol that is routinely employed in coastal studies (Murray and Olley, 2002; Jacobs, 2008; Bateman, 2015; Zöller and Wagner, 2015). Prior to the application of the SAR protocol, the appropriate preheat temperature should be determined and a dose recovery test performed to ensure that accurate OSL ages can be obtained for this study site.

#### 5.1.3.1 Determining preheat temperatures

During luminescence procedures, the artificial radiation used to construct the dose response curve populates the thermally unstable shallow traps as well as the thermally stable deeper traps. A ‘preheat’ procedure is employed to remove the radiation signal from the unstable shallow traps (Duller, 2015), which involves heating the samples up to a predetermined temperature (between 200-260°C) and holding them there for 10 seconds prior to each OSL stimulation measurement (for the natural dose and each regenerative dose used). This process ensures that the luminescence signal recorded in the laboratory originates only from the most stable electron traps, like those traps that contribute to the natural signal (Duller, 1995, 2008, 2015).

To determine the appropriate preheat temperatures for each sample, preheat plateau tests were carried out on nine out of the 18 samples from Albatross Bay, encompassing all three field sites and the various depositional environments within. Six samples from Red Beach were tested, five from across the beach ridge plain and one from the only swale landform sampled. One sample each from the beach ridge at Kwamter and at Wathayn were tested, as well as a sample from the supratidal mudflat at Kwamter.

Four aliquots of each sample were prepared as described in Section 3.4.1.3. The natural signal was removed from each aliquot by stimulating them with blue light-emitting diodes (LEDs) for 100 seconds at room temperature to most closely mimic the bleaching process in nature. A dose of 10 Gy was then administered to the aliquots to act as a surrogate natural dose. Four different preheat temperatures – 220°C, 240°C, 250°C and 260°C – were applied to the sample using the SAR protocol (see Section 5.1.3.3 below), thus, for each sample, each preheat temperature was tested on one aliquot. The resulting  $D_e$  values were plotted against preheat temperature to determine the presence of a preheat plateau and thus the most stable signal for measurement.

The preheat test results of three samples, one from each field location, are shown in Figure 5.1 (the complete dataset can be found in Appendix C). Most of the samples, except for R4, do not have a significant change in  $D_e$  with increasing temperatures. The recycling ratios range between 0.9 and 1.1. The temperature that best recovered a dose closest to the surrogate natural of 10 Gy while also having a recycling ratio close to 1 was identified as the most suitable pre-heat temperature. Thus, a preheat temperature of 240°C was chosen for R4 and KW07, and a preheat temperature of 250°C was chosen for WHA01\_1. For most samples, a preheat temperature of 240°C or 250°C was the most acceptable, with only one sample, RSwale, requiring a preheat temperature of 260°C.



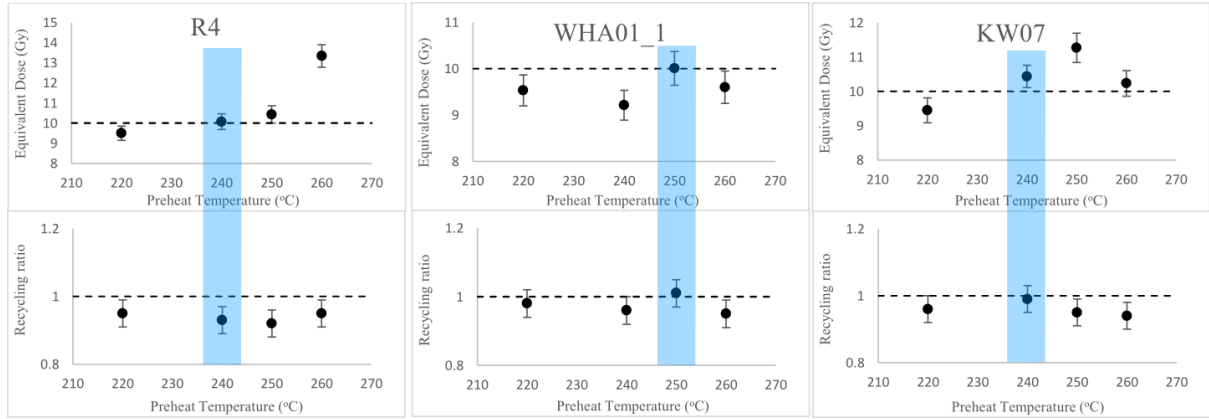


**Figure 5.1: Preheat plot (with associated measurement errors) for R9, WHA01\_1 and KW07. The blue box identifies the chosen preheat temperatures for each sample.**

### 5.1.3.2 Determining dose recovery potential

The dose recovery experiment tests the reliability of the SAR protocol to deliver an accurate and precise age at the preheat temperatures chosen (Ballarini *et al.*, 2003; Murray and Wintle, 2003). The dose recovery test is particularly important when samples have no independent age control (Murray and Wintle, 2003).

Six samples were chosen for dose recovery tests, one from each of the depositional environments across the three field locations. Eight aliquots of each sample were prepared, and each aliquot was bleached under blue LEDs for 200 seconds at room temperature to remove the natural signal prior to being artificially irradiated with the equivalent of 50 Gy. This dose was chosen because the SAR runs conducted for the preheat tests revealed it to be below the saturation threshold of the grains (i.e. no higher than  $2 \times D_0$ ) while providing good counting statistics. The luminescence signals of the samples were then measured using the SAR protocol (see below) to check that the samples recover the administered dose of 50 Gy at the previously selected preheat temperatures.

The dose recovery results of three samples, one from each field location, are shown in Figure 5.2 (the complete dataset can be found in Appendix D). All samples had good dose recovery and were able to recover the administered dose of 50 Gy with recycling ratios of between 0.9 and 1. Furthermore, all samples display low recuperation rates, and thermal transfer does not appear to be a problem for these samples. The OSL samples in this study could therefore be reliably measured using the SAR protocol with the chosen preheat temperatures.

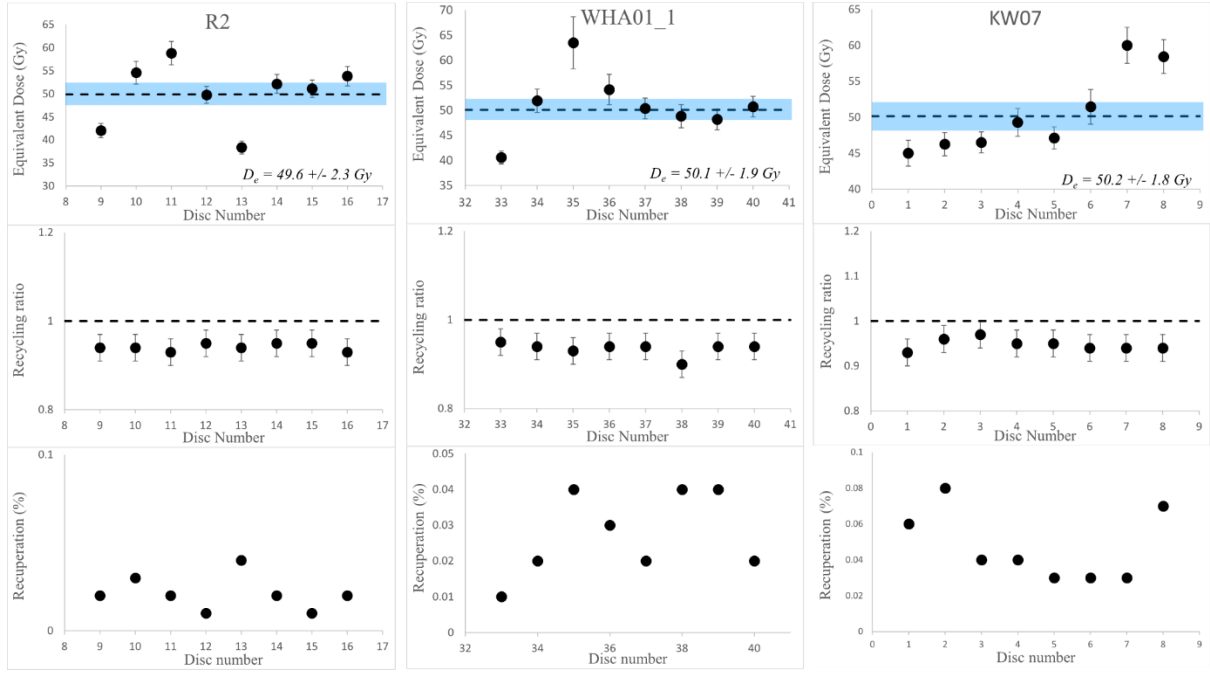


**Figure 5.2:** Dose recovery results on 8 aliquots of samples R9, WHA01\_01 and KW07. The mean  $D_e$  value (in Gy) and associated error (blue shading) are plotted as a dotted line.

### 5.1.3.3 Single-aliquot analysis

There are two main techniques for measuring the  $D_e$  of a sample – the additive dose method and the regenerative dose method (Murray and Roberts, 1998; Duller, 2015). Of these techniques, the SAR protocol is commonly employed in coastal OSL dating studies (Murray and Olley, 2002; Jacobs, 2008; Bateman, 2015; Zöller and Wagner, 2015). The SAR protocol involves calibrating the natural luminescence signal accumulated in a sample aliquot against a dose response curve, constructed by introducing the same aliquot to known doses of radiation and measuring the regenerated signal, with the aliquot bleached after each regenerative cycle (Murray and Roberts, 1998; Murray and Wintle, 2000; Duller, 2015). The SAR protocol is devised to overcome the problem of sensitivity changes that occur when regenerating doses in a sample by dividing each regenerative measurement by a smaller test dose measurement. This test dose is used to quantify any changes in luminescence sensitivity between each measurement caused by time, temperature and past radiation exposure (Roberts and Plater, 2007).

The SAR protocol also contains a regenerative dose that is repeated (a “double regen”) so that the first and the last regenerative cycles contain the same dose. A comparison can then be made to ensure that there is no machine sway and that the test dose is reliably correcting for any sensitivity changes, enabling a measurement of a dose at the start of the regenerative cycles

to be replicated by the end. The ratio between the two measurements of the same dose is known as the “recycling ratio”, with a recycling ratio of between 0.9 and 1.1 being acceptable for OSL measurements (Duller, 2008).

Finally, the SAR protocol includes one regenerative cycle as a zero-dose luminescence measurement, taken when the sample has not been irradiated (a “zero-dose” OSL measurement). The use of this zero-dose regenerative cycle enables the accumulation of signal to be monitored because any signal that has not been fully removed between each regenerative cycle will contribute to the next measurement in a process known as “recuperation”. Recuperation occurs when the luminescence signal emptying from traps during bleaching or preheating transfers into other traps rather than being removed from the sample. This process is known as “thermal transfer” and causes a sample to retain a luminescence signal between measurements, leading to an overestimation in regenerative dose values and an underestimation in the calculated age. Recuperation is expressed as a percentage of the natural signal and an aliquot is rejected when it exceeds 5% (Murray and Wintle, 2000; Murray and Olley, 2002; Wintle and Murray, 2006).

As described in Section 3.4.1.3, single-aliquot analysis was carried out on all 18 of the samples using a 1 mm mask. Twenty four aliquots were prepared for each sample, and a modified SAR protocol of Murray and Wintle (2000; 2003) and Olley *et al.* (2004) was used to measure the equivalent dose of each sample (Table 5.1).

**Table 5.1: SAR protocols used for Albatross Bay samples in this study.**

Step	Sample treatment
1	Give dose <sup>a</sup> , $D_i$
2	Preheat at $X^\circ\text{C}$ for 10 seconds ( $X$ = temperature selected during preheat tests)
3	IRSL wash at $50^\circ\text{C}$ for 100 seconds <sup>b</sup>
4	Measure OSL signal (Stimulation by blue LEDs for 100 seconds at $125^\circ\text{C}$ )
5	Irradiate with selected test dose
6	Cut-heat to $160^\circ\text{C}$
7	IRSL wash at $50^\circ\text{C}$ for 100 seconds
8	Measure OSL signal (Stimulation by blue LEDs for 100 seconds at $125^\circ\text{C}$ )
9	Give first regeneration dose and repeat steps 2-8 <sup>c</sup>
10	Give second regeneration dose and repeat steps 2-8
11	Give third regeneration dose and repeat steps 2-8
12	Give fourth regeneration dose and repeat steps 2-8 <sup>d</sup>
13	Give fifth regeneration dose and repeat steps 2-8 <sup>e</sup>

- For the natural signal,  $D_i = 0$
- A infrared stimulated luminescence (IRSL) was done prior to each OSL measurement to remove any possible contamination from IR-sensitive grains (Olley *et al.*, 2004)
- The regenerative doses are chosen to bracket the approximate natural signal anticipated within a sample (Murray and Olley, 2002)
- The fourth regeneration dose = 0 and is the zero-dose applied to monitor any recuperation of signal from thermal transfer
- The fifth and final dose is the same as the first regeneration dose and is used to calculate the recycling ratio which indicates the ability of the SAR protocol to correct for any sensitivity changes between dose measurements and reproduce the same signal for the same dose

The luminescence results were processed with the Risø Luminescence Analyst program, version 4.14.6. The measured OSL signal (step 4) was recorded over 250 channels, with the integration of the first five channels (corresponding to the first 2 seconds of measurement) used to calculate the luminescence signal, following the recommendations of Murray and Wintle (2000; 2003). Murray and Wintle (2000; 2003) recommend that only the initial part of the luminescence signal be used in measurements to ensure that only the rapidly bleachable component is used in the  $D_e$  calculations and to maximise the signal-to-noise ratio. The integration of the last 50 channels (corresponding to the last 20 seconds of measurement) was used to calculate the background noise. The dose response curve was fitted exponentially.

#### 5.1.3.4 Single-grain analysis

Results from the single-aliquot analysis indicated that the Kwamter and Wathayn samples were only partially bleached prior to deposition and burial (see Section 5.1.6.1). In partially bleached samples, the accuracy of OSL age determinations can be improved by measuring the  $D_e$  from each individual grain, rather than an average from a single aliquot. By

measuring the  $D_e$  of single grains in a sample, the well bleached grains can be distinguished from the partially bleached ones, allowing ages to be calculated based on only the well bleached grains (Roberts *et al.*, 1998; Olley *et al.*, 1999). The grains with poor luminescence characteristics can be rejected. Single-grain OSL techniques were therefore employed on all the Kwamter and Wathayn samples. While the single-aliquot results from the Red Beach samples indicated that the samples were well bleached prior to deposition and burial, Jacobs (2008) still recommends measuring single-grains for some samples in each study, even if well bleached, to strengthen OSL age determinations. Therefore, single-grain analysis was also carried out on seven of the thirteen samples from Red Beach to obtain more information on the luminescence characteristics of the grains from this field site.

For single-grain analysis, 10 discs were prepared for each sample, as detailed in Section 3.4.1.3, leading to a total of 1000 grains measured per sample. The discs were run using the modified SAR protocol outlined above, with minor modifications for single-grain measurements. At step 4 and step 8 (Table 5.1), the OSL signal was measured by stimulating each individual grain with a green laser for two seconds. In addition to the five regeneration doses (and thus six measurement cycles including the first natural dose measurement cycle) in the single-aliquot SAR protocol outline above, a sixth regeneration dose (seventh cycle) was added to the single-grain SAR protocol to check for feldspar contamination. For this sixth regeneration, the same dose was administered to the sample as the first and fifth regeneration cycle, but instead of being after the preheat step as with the single-aliquot processing, the infrared emissions (and therefore any feldspar contamination) was first removed by infrared light stimulation at room temperature for 100 seconds before the sample was preheated and measured (swapping steps 2 and 3). The ratio between the sixth and fifth regeneration is known as the IR depletion ratio. If there was any potential feldspar contamination, the sixth dose measured would be significantly (more than two standard deviations) lower than the fifth (Duller, 2003; Jacobs *et al.*, 2003).

The measured OSL signal was recorded over 100 channels, with the first five and last five channels collecting dark counts (the laser was not switched on). The integration of the channels 6 to 15 (corresponding to the signal from 0.1 seconds to 0.28 seconds) was therefore used to calculate the luminescence signal and the integration of the channels 81 to 95 (corresponding to the signal from 1.6 seconds to 1.88 seconds) was used to calculate the background noise. The dose response curve was exponentially fitted.

#### 5.1.3.5 Rejection criteria for single-aliquot and single-grain analysis

Single-aliquot and single-grain data was analysed and grains were rejected based on criteria described in Jacobs *et al.* (2003) and Jacobs *et al.* (2006a). These criteria included:

- a test dose signal that was less than 3 times the background;
- aliquots or grains that were super saturated; and/or
- aliquot or grains that did not produce a measurable OSL signal (i.e., there was no evidence of decay on the shine down signal)

If the single-aliquot or single-grain sample was affected by any of the above three criteria, no  $D_e$  measurement was obtained. If any samples provided a  $D_e$  measurement, the samples were evaluated to assess the robustness of the measurement obtained. Aliquots or grains were rejected if there was:

- a poor recycling ratio (RR) of  $<0.9$  or  $>1.1$ ;
- any signals that showed significant IR depletion (IR depletion ratio  $<0.9$  or  $>1.1$ );
- recuperation of the luminescence signal greater than 5 %; and/or
- large changes in sensitivity during measurements as seen by the Tn/Tx plots.

While not a rejection criteria of Jacobs *et al.* (2003; 2006a), single-aliquots or single-grains were also only accepted if the decay curve had a steep slope to background levels within the selected integration limits. A steep slope would ensure that only the rapidly bleachable fast component is factored into the  $D_e$  calculations and maximises the signal-to-noise ratio, as recommended by Murray and Wintle (2003). This additional criterion has been adopted in various studies (Olley *et al.*, 2004; Brooke *et al.*, 2006; Bickel *et al.*, 2015).

#### 5.1.3.6 Calculating the $D_e$

Once measured, "...the large number of  $D_e$  values obtained for each sample need to be displayed, interpreted and combined in some way to obtain a single value of  $D_e$  that can be used in the final age calculation to obtain a true depositional age for the sediment..." (Jacobs *et al.*, 2006a, p. 265). There are several methods of analysing luminescence data to obtain a  $D_e$  value (e.g. Olley *et al.*, 1998; Stokes *et al.*, 2001; Lepper and McKeever, 2002). The central age model (CAM) and the minimum age model (MAM) (Galbraith *et al.*, 1999) were both used in this study. The choice of age model used is largely based on an interpretation of the sedimentary environment. Understanding the depositional context of a sample allows inferences to be made on whether a sample would be well bleached or partially bleached and whether there is potential for the introduction of older or younger grains (grain mixing) in a

sample (Jacobs *et al.*, 2006a; Roberts and Jacobs, 2015). Roberts and Jacobs (2015, p. 438) also state that “...statistical models should not be applied without first taking into account the archaeological or geologic context of a sample, stratigraphic considerations, and other relevant information, such as independent age control...”.

The CAM is appropriate for well-bleached samples that have the same environmental dose rate following burial and are unaffected by post-depositional sediment mixing (Roberts and Jacobs, 2015). The CAM calculates the weighted mean of all the  $D_e$  values from a sample, the errors associated with that weighted mean, and gives a measure of the overdispersion of individual  $D_e$  values (Lian and Roberts, 2006; Rhodes, 2011). An overdispersion value of less than 20% is generally indicative of a well bleached sample (see Section 5.1.1).

When the overdispersion of  $D_e$  values is high (greater than 20%), and partial bleaching is suspected, the MAM is preferred over the CAM. This model calculates a  $D_e$  by estimating the central age from the lower-dose population of aliquots or grains (Lian and Roberts, 2006). When a sample is incompletely bleached prior to burial, some grains will already have a luminescence signal prior to burial and deposition, resulting in higher  $D_e$  measurements, causing the OSL age to be overestimated if the CAM is used. The MAM estimates a  $D_e$  that is “...specific to the population of well bleached grains...” (Galbraith and Roberts, 2012, p. 16), reflective of the true time of sediment deposition and burial.

In coastal environments, sediments are generally well bleached and therefore have low overdispersion values (see Section 5.1.2). Therefore, the CAM is used to calculate a  $D_e$  for most of the samples in this study. However, samples from the supratidal mudflat at Kwamter and beach ridge at Wathayn had a higher overdispersion value (>20%) and partial bleaching was suspected. Sediments deposited within supratidal mudflats are more likely to be partially bleached than those within foreshore or aeolian environments (see Section 5.1.2.3). Bleaching tests also indicated that partial bleaching may be an issue within some beach ridges (see section 5.1.4). For these samples,  $D_e$  was recalculated using the MAM. Further discussion on the application of the models can be found below in Section 5.1.6.

#### 5.1.4 Assessing bleaching conditions at Albatross Bay

##### 5.1.4.1 Buried environments

Bleaching tests were carried out on two of the buried samples collected from within the beach ridges at Red Beach. Thirty-six aliquots of 90-125  $\mu\text{m}$  quartz grains from the R8 beach ridge crest and RSwale were prepared using a 7 mm mask, following the protocol outlined in



Section 3.4.1.3, resulting in a total of 72 discs. The  $D_e$  of these samples was first measured using the SAR protocol to obtain data on the effect that choice of mask size (1 mm compared to 7 mm) has on the OSL age determination<sup>6</sup>. All 72 aliquots were then dosed with 200 Gy to introduce a large known dose and provide good counting statistics for measurement. Comprehensive resetting of this OSL signal by exposure to natural light, conditions comparable to modern beach ridge formation processes at Red Beach, would provide confidence for the use of the CAM as a means of estimating the time since the quartz grains were last exposed to sunlight.

Four aliquots of each sample were exposed to direct sunlight at Macquarie University in Sydney, using eight bleaching durations – 10 seconds, 60 seconds, 15 minutes, 30 minutes, 1 hour, 3 hours, 6 hours and 12 hours, during December 2014 (R8) and July 2015 (RSwale) (Figure 5.3). The aliquots were then measured in the lab following the SAR protocol, and the CAM used to calculate a  $D_e$  for each bleaching time.

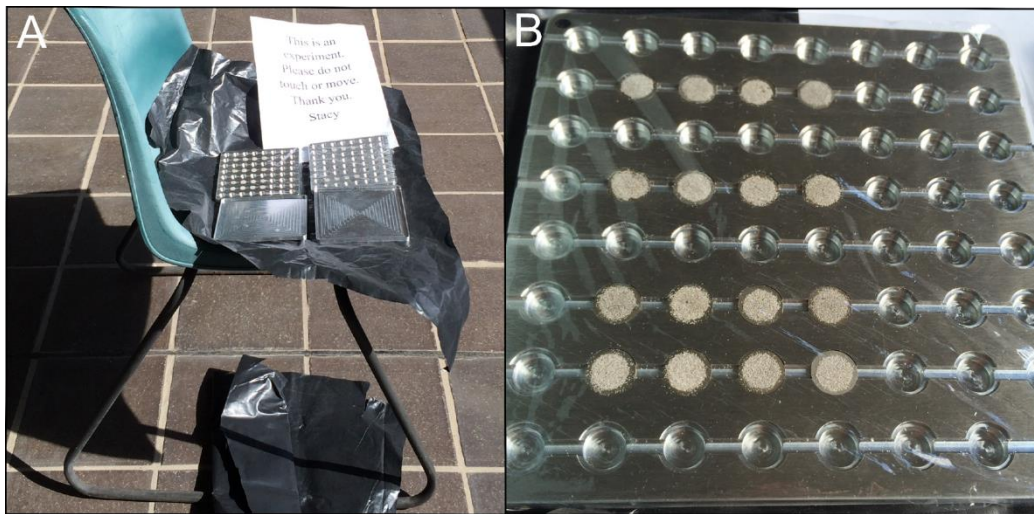


**Figure 5.3: OSL bleaching tests conducted at Macquarie University (A) set-up of bleaching tests where samples are exposed to direct sunlight. (B) close-up of disc holder containing samples being bleached.**

Results of the bleaching tests on the buried samples from Red Beach are shown in Figure 5.4. Grains from the beach ridge crest (R8) bleached rapidly, with the signal dropping to approximately 1% of the original value of 200 Gy after 1 minute and to negligible amounts

<sup>6</sup> The OSL ages for R8 and RSwale using a 1 mm and a 7 mm mask are similar within the margin of error. The age determined for R8 was  $1,685 \pm 92$  years (1 mm mask) or  $1,759 \pm 89$  years (7 mm mask), while the age determined for RSwale was  $2,326 \pm 136$  years (1 mm mask) or  $2,504 \pm 139$  years (7 mm mask)

after 10 minutes of exposure to sunlight. These rapid bleaching times are consistent with those measured by Godfrey-Smith *et al.* (1988). Grains from the swale sample (Rswale) also bleached quickly, though slower than the crest sample, with the signal dropping below 1% of the original value after 15 minutes of sunlight exposure and to 0.6% after 30 minutes of sunlight exposure. These bleaching times are compatible with the processes of beach ridge formation (see Section 5.1.2), thus there is a good likelihood that the quartz grains from the samples at Red Beach were well-bleached prior to burial.

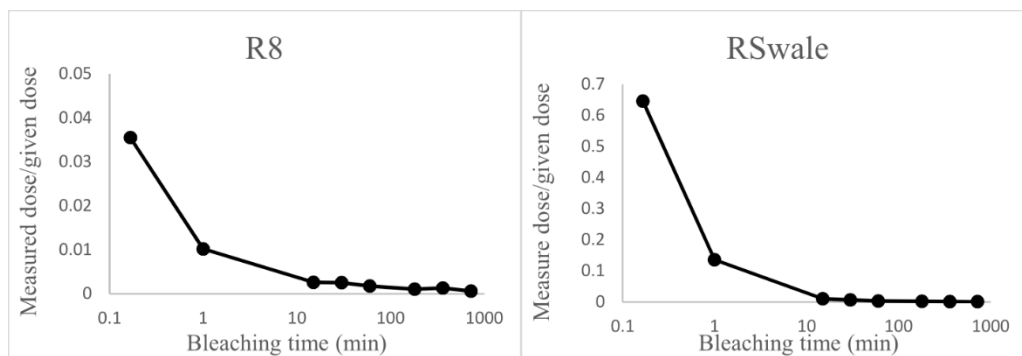


**Figure 5.4:** Bleaching test data for beach ridge crest (R8) and swale (Rswale) samples from Red Beach.

#### 5.1.4.2 Modern analogue environments

To complement the buried environments bleaching test data and examine the efficiency of grain bleaching at Albatross Bay, three OSL samples of surface sediment were collected from the modern beach at Red Beach. One sample was collected from the intertidal zone, one from the middle of the backshore and one from the surface of the modern beach ridge crest (Figure 4.1). All samples were collected within a 30-minute period in the afternoon, in September 2014. Clear sky conditions persisted for the entire day. At each location, the top 5 mm of sediment was scraped up with a trowel and transferred to a Ziploc bag. While care was taken to collect only the surface layer, it is possible that some deeper grains may have been collected due to mixing with the trowel. Sediments from the intertidal zone were damp and clung to each other, while vegetation roots held sediments together on the surface of the modern ridge crest. Sample contamination was likely to be lowest in the backshore environment where sediments were dry and unaffected by vegetation.

The sediments were wrapped in thick black plastic sheets to prevent further light exposure, transferred to the OSL lab, and processed according to the procedures outlined in

Chapter 3 (see Section 3.4.1.2). The  $D_e$  for each sample was measured using the SAR protocol and a 1 mm mask (see Section 5.1.3.3), with 24 single-aliquot discs analysed for the intertidal and ridge crest samples. However, there were only 17 single-aliquot discs analysed for the backshore sample due to a lack of quartz grains.

Tables 5.2 and 5.3 summarise the results of the bleaching tests of the modern beach sediment samples. All samples had an overdispersion above 100%, which is significantly greater than the OD values of between 10% and 20% for the buried beach ridge samples at Red Beach (see Table 5.7). These high overdispersion values are typical when examining the residual dose in modern samples (Mauz, 2015).

**Table 5.2: Results from the SAR procedure on the modern analogue samples.**

Location	Sample code	Single-aliquots processed	Single-aliquots rejected	Reason for rejection	Overdispersion (%)	Statistical model
Red Beach - modern intertidal zone	RB mod inter	24	0		107.1	CAM/MAM
Red Beach - modern backshore	RB mod shore	17	1	RR	118.4	CAM/MAM
Red Beach - modern beach ridge crest	RB mod crest	24	1	Saturated	172.1	CAM/MAM

**Table 5.3: Single-aliquot OSL ages for the modern analogue samples.**

Location	Sample code	Meters AHD (m)	Single Aliquot (SA) / Single Grain (SG)	Grain size ( $\mu\text{m}$ )	Mask Size (mm)	Gamma dose rate (Gy/ka)	Beta dose rate (Gy/ka)	Cosmic-ray dose rate (Gy/ka)	Water content (%)	Total dose rate (Gy/ka)	Statistical model	Equivalent dose (Gy)	Age
Red Beach	RB mod inter	1	SA	90 - 125	1	0.728	1.315662	0.189	9.2 $\pm$ 2.3	2.001 $\pm$ 0.077	CAM	0.248 $\pm$ 0.055	124 $\pm$ 28
Red Beach	RB mod shore	1.25	SA	90 - 125	1	0.548	1.325064	0.189	1 $\pm$ 0.3	1.954 $\pm$ 0.112		0.188 $\pm$ 0.057	96 $\pm$ 30
Red Beach	RB mod crest	1.5	SA	90 - 125	1	0.309	0.75521	0.189	0.7 $\pm$ 0.2	1.207 $\pm$ 0.058		0.778 $\pm$ 0.280	644 $\pm$ 234
Red Beach	RB mod inter	1	SA	90 - 125	1	0.728	1.315662	0.189	9.2 $\pm$ 2.3	2.001 $\pm$ 0.077	MAM	0.037 $\pm$ 0.007	18 $\pm$ 3
Red Beach	RB mod shore	1.25	SA	90 - 125	1	0.548	1.325064	0.189	1 $\pm$ 0.3	1.954 $\pm$ 0.112		0.033 $\pm$ 0.011	16 $\pm$ 5
Red Beach	RB mod crest	1.5	SA	90 - 125	1	0.309	0.75521	0.189	0.7 $\pm$ 0.2	1.207 $\pm$ 0.058		0.056 $\pm$ 0.019	46 $\pm$ 27

All the 24 intertidal zone aliquots were accepted for further age calculations. Twenty-one of these had a  $D_e$  of less than 1 Gy (between 0.03 Gy and 0.77 Gy). The remaining three aliquots, however, had equivalent doses of 1.07 Gy, 2.21 Gy and 4.04 Gy. Using the CAM resulted in a  $D_e$  of  $0.248 \pm 0.055$  Gy. When calculated with the intertidal dose rate data, a burial age of  $124 \pm 28$  years was obtained. When recalculated using the MAM, a  $D_e$  of  $0.037 \pm 0.007$  Gy and a burial age of  $18 \pm 3$  years were obtained.

Only 17 aliquots from the modern backshore sample were processed due to a lack of quartz grains in the required size range of 90-125  $\mu\text{m}$ . Of these, one disc was rejected due to a poor recycling ratio of 0.38. The other 16 samples had a  $D_e$  of less than 1 Gy (0.03 Gy to 0.90

Gy). Using the CAM to calculate the  $D_e$  of the modern backshore gives a  $D_e$  of  $0.188 \pm 0.057$  Gy. Combining this with the backshore dose rate data resulted in a burial age of  $96 \pm 30$  years. Recalculation using the MAM resulted in a  $D_e$  of  $0.033 \pm 0.011$  Gy, and a burial age of  $16 \pm 5$  years.

Of the 24 aliquots processed from the modern beach ridge crest sample, one was rejected because the sample was saturated and no  $D_e$  could be calculated. The modern beach aliquots had the largest spread of  $D_e$  values of all the modern analogue samples, with an overdispersion of 172%. It is possible that the effect of sediment binding by roots caused more sample contamination than anticipated. A higher  $D_e$  of  $0.778 \pm 0.280$  Gy was calculated using the CAM, resulting in a burial age of  $644 \pm 234$  years. When recalculated using the MAM, the  $D_e$  decreased to  $0.056 \pm 0.019$  Gy, resulting in a burial age of  $49 \pm 27$  years.

With regard to the bleaching characteristics of sediments from Red Beach, the modern samples had higher burial ages than would be expected in well bleached samples, particularly those collected from the surface of the modern beach ridge crest (interpreted as an aeolian deposit, sub-facies B1 – see Section 4.4). The wide spread of  $D_e$  values could be attributed to partial bleaching. It is also possible that the higher  $D_e$  within the modern analogue samples is due to sediment mixing. The effect of sediment binding by roots on the modern beach ridge crest may cause older grains with an accumulated dose to mix with more modern grains. In the intertidal zone sample, grains were moist and stuck to each other, also possibly leading to the mixing of older with younger sediments. Issues of post-depositional sedimentary mixing or partial bleaching are more pronounced in young and modern samples because the intrusion of grains from older sediments or older sedimentary layers can be relatively large compared to the small or negligible doses in modern or young grains with short burial periods (Arnold *et al.*, 2009). When the MAM is used to calculate a  $D_e$  for the modern analogue samples, effectively modern burial ages of less than 50 years (after Jacobs, 2008) are obtained.

Thus, the buried environments bleaching test indicated that, overall, sediments from Red Beach were likely to have been well-bleached prior to deposition, and therefore the CAM is appropriate for most samples in this study. However, when overdispersion values indicate that a sample may only be partially bleached, the MAM is used to provide accurate ages for those samples.

### 5.1.5 Measuring the environmental dose rate at Albatross Bay

The concentrations of U, Th and K in the environment were measured for all eighteen of the samples in this study via high-resolution gamma spectrometry (HRGS) and these concentrations were then used to calculate an annual dose rate. In addition, the environmental radiation emissions for five samples were counted directly by combining in-situ gamma spectroscopy with beta counting (Duller, 2008). In-situ gamma spectroscopy was also used to calculate the environmental dose rate for all three modern analogue samples.

#### 5.1.5.1 High-resolution gamma spectrometry (HRGS)

Sediment samples collected from the ends of each of the 18 OSL tubes (see Section 3.4.1.2) were ground to a fine powder using a ball mill and sent to the Environmental Research Institute of the Supervising Scientist (ERISS) laboratory in Darwin, Australia, for analysis. At the ERISS lab, high purity germanium (HPGe) detectors were used to measure the activity of gamma ray emitting radionuclides, with results presented in becquerel (Bq)/kg at the date of measurement. A benefit of using high-resolution gamma spectrometry is that it provides data on the equilibrium status of the U and Th decay chains (Duller, 2015). Any disequilibrium will affect the dose rate a sample receives and thus has an impact on the OSL age determined.

#### 5.1.5.2 In-field gamma spectroscopy

Gamma dose rates were also measured in the field at five beach ridges at Red Beach, using a Ludlum 732 portable gamma spectroscopy system with a 5 x 5 cm Thallium doped Sodium Iodide NaI(Tl) scintillator. In-situ gamma measurements were also taken for the modern analogue samples. In-situ gamma measurements measure the contribution of the gamma rays within a 30 cm sphere around the sample to account for any heterogeneity in the sediment column or a significant change in stratigraphical boundary. Dose rates calculated from in-situ gamma spectrometry data were compared to the dose rates derived from the HRGS data to ensure that they were similar and therefore that the samples were not affected by variable gamma radioactivity caused, for example, by unseen variations in sediment stratigraphy.

After extraction of OSL sampling tubes at each sample location, the holes in each pit wall were widened and deepened with a trowel until the 18-cm long NaI(Tl) scintillator could be fully inserted. The space around the inserted scintillator was then plugged with the original sediment. The concentrations of U, Th and K were then counted for 25 minutes.

#### 5.1.5.3 Beta counting

Beta counting was conducted on all samples with in-situ gamma spectrometry data. Beta dose rates were counted using a Risø GM-25-5A Geiger-Muller Beta Multi-counter system housed in a lead brick stack. Three small sample pots, packed with powdered sediment, were prepared for each sample and measured simultaneously along with two calibration standards, magnesium oxide (MgO) and SHAP with a known beta dose rate (5.77 Gy/ka). The beta dose rate is then calculated with reference to the known standard (SHAP) and background value (MgO) (Sanderson, 1988).

#### 5.1.5.4 Internal alpha dose and cosmic ray contribution

An effective internal quartz dose rate of  $0.030 \pm 0.011$  Gy/ka was assumed for 90-125  $\mu\text{m}$  grains and  $0.031 \pm 0.011$  Gy/ka was assumed for the 180-212  $\mu\text{m}$  grains (Feathers and Migliorini, 2001). Cosmic ray contributions to each sample were calculated from the sediment depth, altitude and geomagnetic latitude and longitude of each sample (Prescott and Hutton (1994). The long-term burial history of the samples was assumed to be equal to the present-day burial depths, with no change in depth of overburden through time. The beach ridges at Albatross Bay, being of relatively low relief and mostly devoid of thick aeolian surface deposits, therefore do not show any evidence of additional vertical accretion over time. They have not been active for a long period of time, as evidenced by their dense vegetation cover. Short phases of construction followed by long periods of stability are common in beach ridges (Bateman, 2015).

#### 5.1.5.5 Moisture content

Water attenuates the luminescence dose rate by absorbing radioactive energy (Wintle, 1981; Guérin, 2015). A 1% decrease in water content can lead to about a 1% increase in dose rate and a 1% decrease in age for quartz sediments (Jacobs *et al.*, 2006a; Duller, 2015). Water content for each sample was therefore measured from the light exposed portion of sediments within each sampling tube (Section 3.4.1.2). To calculate the water content, a clean glass beaker was weighed ( $W_1$ ) and the sediments placed within to obtain a wet weight ( $W_2$ ). The sample was then placed in a drying oven at 70°C for seven days and reweighed to obtain a dry weight ( $W_3$ ). Moisture content was then calculated using the following equation:

$$\text{Moisture content} = 100 \times \frac{[(W_2 - W_1) - (W_3 - W_1)]}{(W_2 - W_1)}$$

As sediment moisture content has likely fluctuated over the burial period, a 25% error was applied to each sample measurement following the correction factor used by Jankowski *et al.* (2015) for a similar deposition environment (coastal dunes in Australia) and a similar time period (over the Holocene).

Environmental dose rates were then calculated from either

- (1) the HRGS data combined with the internal alpha contribution, cosmic ray contribution and water content data, or
- (2) the in-situ gamma spectroscopy data, combined with the beta counting data, the internal alpha contribution, cosmic ray contribution and water content data.

#### 5.1.5.6 Dose rate calculations

Environmental dose rates were determined by combining the internal, alpha, beta, gamma and cosmic ray dose rate, modified by the water content. The dose rate was calculated using the dose correction factors of Adamiec and Aitken (1998), the beta-dose attenuation factors calculated by Mejdahl (1979) and adjusting for water content following Aitken (1985) and Readhead (1987). Results from the comparison of the total dose rate calculations based on HRGS measurements and in-field gamma spectroscopy measurements are presented in Table 5.4. Most samples have similar total dose rates indicating that the total dose rates calculated using the HRGS data are accurate. However, the total dose rate between the HRGS data and in-field gamma differed significantly at Red Beach RR10, sample code RB25 (2.983 Gy/ka and 1.994 Gy/ka respectively, a difference of approximately 33%). Two OSL samples, RB21 (RR9) and RB25 (RR10) were collected from within calcrete cemented units (see sedimentary logs for RR9 and RR10 in Appendix B). The total environmental dose rate for sample RB21 does not appear to be significantly affected by the calcrete cementation. However, the cementation in ridge RR9 was not as solid, and almost 40 cm of calcrete was excavated before digging ceased. In ridge RR10, the cementation was more solid and only 20 cm of calcrete was excavated before digging ceased. Calcrete cementation affects the dose rate as the calcrete attenuates the dose rate received by sediment grains as the pore spaces are filled (see Section 5.1.1).



**Table 5.4: Comparison of dose rates measured by HRGS and in-situ gamma spectroscopy from Red Beach.**

Location	Sample code	Total dose rate calculation based on HRGS data (Gy/ka)	Total dose rate error based on HRGS data (se)	Total dose rate calculation based on in-situ gamma spectroscopy data (Gy/ka)	Total dose rate error based on in-situ gamma spectroscopy data (se)
Red Beach - RR9	RB21	2.112	0.081	1.988	0.063
Red Beach - RR10	RB25	2.983	0.130	1.994	0.071
Red Beach - RR11	RB18	2.253	0.081	2.599	0.062
Red Beach - RR12	RB20	2.409	0.109	2.549	0.075
Red Beach - RR13	RB19	2.97	0.133	2.845	0.101

Modelling work by Nathan and Mauz (2008) suggests that the difference in dose rates from time of deposition, to the final dose rate after cementation could differ by 30%. The calcrete cementation in RR10 (RB25) may be the cause for the discrepancy between the HRGS dose rate calculations and in-field gamma spectroscopy calculations. The HRGS measurements were carried out on uncemented sediments, collected from within the OSL tube (see Section 5.1.5.1), whereas the in-field gamma spectroscopy measurements were measured 30 cm around the sample (see Section 5.1.5.2), thereby attenuating the dose rate more than the HRGS sample. While the timing of calcrete formation in RR10 is unknown, the in-field gamma spectroscopy measurements are likely to be more indicative of the environmental dose rate in this sample. For all other samples, the HRGS data is used for age calculations.

Table 5.5 shows the HRGS data obtained for the Albatross Bay samples. The HRGS data allows an assessment of the state of equilibrium (or disequilibrium) in these sedimentary environments by providing information on the  $^{238}\text{U}$  and  $^{232}\text{Th}$  decay chains and therefore the concentrations of the daughter and parent nuclides. In typical sand deposits, the  $^{238}\text{U}$  decay chain contributes to approximately 27% of the total dose rate a sample receives, while  $^{232}\text{Th}$  contributes approximately 26% (Olley *et al.*, 1996). Disequilibrium in one or both decay chains will impact the measured dose rate and, consequently, the calculated age. It is therefore crucial to assess the state of equilibrium at each sedimentary environment when using OSL techniques to develop a chronology of environmental change.

Across the three field locations, the  $^{232}\text{Th}$  decay chain appears to be in or close to secular equilibrium, with negligible excess or depletion in the  $^{238}\text{Ra}$  and  $^{228}\text{Th}$  radionuclides (Table 5.5). Thorium is generally immobile in sediments and the daughter nuclides of Thorium have a short half-life ( $^{228}\text{Ra}$  has a half-life of 5.7 years and  $^{228}\text{Th}$  has a half-life of 1.91 years)

(Demeter *et al.*, 2012). Therefore, the thorium decay chain is usually in secular equilibrium in most natural sedimentary deposits older than 20 years (Olley *et al.*, 1996; Demeter *et al.*, 2012).

Disequilibrium in the  $^{238}\text{U}$  decay was present across all three field locations. In these sedimentary environments, four potential disequilibrium states in the  $^{238}\text{U}$  decay chain have been identified (Table 5.5):

- a. A deficiency in  $^{226}\text{Ra}$  compared to  $^{238}\text{U}$  (samples highlighted in red in the  $^{226}\text{Ra}$  column in Table 5.5) of
  - i. between 15-82% at Kwamter
  - ii. 22% at Wathayn and
  - iii. between 8-26% at Red Beach
- b. An excess in  $^{226}\text{Ra}$  compared to  $^{238}\text{U}$  (samples highlighted in blue in the  $^{226}\text{Ra}$  column in Table 5.5) of
  - i. between 8-20% at Red Beach
- c. A deficiency in  $^{210}\text{Pb}$  compared to  $^{226}\text{Ra}$  (samples highlighted in red in the  $^{210}\text{Pb}$  column in Table 5.5) of
  - i. between 7-19% at Kwamter
  - ii. 24% at Wathayn and
  - iii. between 4-25% at Red Beach
- d. An excess in  $^{210}\text{Pb}$  compared to  $^{226}\text{Ra}$  (samples highlighted in blue in the  $^{210}\text{Pb}$  column in Table 5.5) of
  - i. 60% at Kwamter
  - ii. 3% at Red Beach

**Table 5.5: HRGS results for samples from Albatross Bay. Samples highlighted in red have a deficiency of that radionuclide within the decay chain while samples highlighted in blue have an excess of that radionuclide within the decay chain. Samples with no highlights have negligible variations within the decay chain and are therefore in secular equilibrium.**

Location	Sample Code	Sample elevation (mAHD)	Radionuclide activities (Bq kg <sup>-1</sup> )					
			<sup>238</sup> U	<sup>226</sup> Ra	<sup>210</sup> Pb	<sup>228</sup> Ra	<sup>228</sup> Th	<sup>40</sup> K
Red Beach - RR1	RB02	1.37	98 ± 6	72.4 ± 1.4	65 ± 5	89 ± 2.9	90.7 ± 2.2	16 ± 4.7
Red Beach - RR2	RB01	0.93	90 ± 6	74.7 ± 1.5	62 ± 5	95.6 ± 3.1	96.6 ± 2.5	22 ± 9.0
Red Beach - RS3	RB17	0.89	100 ± 6	78.5 ± 1.5	63 ± 5	87 ± 2.9	93.4 ± 2.3	26 ± 7.6
Red Beach - RR4	RB08	1.12	43 ± 4	37.6 ± 1.1	28 ± 4	41.1 ± 2.1	43.7 ± 1.4	29 ± 8.0
Red Beach - RR5	RB10	1.45	64 ± 5	64.3 ± 1.4	64 ± 5	73.4 ± 2.6	73.7 ± 1.9	17 ± 7.0
Red Beach - RR7	RB12	1.98	62 ± 6	61 ± 1.4	54 ± 5	67.2 ± 2.8	67.4 ± 2.0	31 ± 9.1
Red Beach - RR8	RB03	1.44	73 ± 5	66.9 ± 1.4	58 ± 5	76.6 ± 2.6	79.7 ± 2.0	22 ± 6.4
Red Beach - RR9	RB21	0.97	57 ± 3	51 ± 1	47 ± 3	54 ± 2	56 ± 1.0	18 ± 5.3
Red Beach - RR10	RB25	1.58	68 ± 6	85 ± 2	73 ± 5	75 ± 3	79 ± 2.0	28 ± 8.2
Red Beach - RR11	RB18	1.84	52 ± 3	63 ± 1	60 ± 3	52 ± 1	55 ± 1.0	8 ± 2.3
Red Beach - RR12	RB20	1.72	61 ± 5	58 ± 1	58 ± 4	59 ± 2	61 ± 2.0	21 ± 6.1
Red Beach - RR13	RB19	1.58	74 ± 6	67 ± 1	69 ± 5	80 ± 3	84 ± 2.0	16 ± 8.0
Red Beach - RS 10	RB27	1	92 ± 7	101 ± 2	91 ± 6	106 ± 3	109 ± 3.0	17 ± 5.0
Kwamter - KMF4	KW05	-0.15	137 ± 6	24.8 ± 1.1	20 ± 4	34.7 ± 2.3	36.2 ± 1.3	176 ± 14
Kwamter - KMF1	KW06	0.01	37 ± 4	31.4 ± 1	29 ± 4	33.6 ± 2	35 ± 1.2	141 ± 11
Kwamter - KR1	KW07	1.52	8 ± 3	4 ± 0.7	10 ± 1	4.3 ± 1.4	5.5 ± 0.6	20 ± 5.8
Wathayn - WR1	WHA01_1	2.96	27 ± 4	21.1 ± 0.9	16 ± 3	16.1 ± 1.7	14.2 ± 0.8	23 ± 6.7
Wathayn - WR1	WHA01_2	3.19	12 ± 3	13.9 ± 0.8	12 ± 3	10.6 ± 1.5	10.6 ± 0.7	15 ± 4.4

In the <sup>238</sup>U decay chain, disequilibrium is common in the surficial environment (Olley *et al.*, 1996; Olley *et al.*, 1997). The daughter nuclides of Uranium also have a longer half-life than that of Thorium (<sup>226</sup>Ra has a half-life of 1602 years and <sup>210</sup>Pb has a half-life of 22 years) (Demeter *et al.*, 2012). Therefore, any disequilibrium present in the surficial environment may persist for millennia in sedimentary deposits, affecting the dose rate a sample receives (Olley *et al.*, 1996). An excess of <sup>210</sup>Pb over <sup>226</sup>Ra is commonly attributed to the fallout of <sup>210</sup>Pb on surface sediments (Olley *et al.*, 1996). The cause of the deficiency or excess in <sup>210</sup>Pb over <sup>226</sup>Ra in the older sediments at Kwamter and Red Beach is unknown. However, as <sup>210</sup>Pb has a half-life of 22 years, any excess <sup>210</sup>Pb should decay in < 100 years, younger than the samples from these two field locations. Furthermore, the decay of <sup>210</sup>Pb to <sup>206</sup>Pb (the end member in this decay chain) only contributes to a small proportion (2.9%) of the total dose rate (Olley *et al.*, 1996). Therefore, any excess or deficiency of <sup>210</sup>Pb at Red Beach or Kwamter is likely to have a negligible impact on the total sample dose rate.

The disequilibrium in the decay series between <sup>238</sup>U and <sup>226</sup>Ra has a greater impact on the total sample dose rate and needs to be examined further. The deficiency in <sup>226</sup>Ra within the majority of the Albatross Bay samples indicates that radium redistribution is occurring in these coastal environments, likely due to the effects of leaching (see Section 4.1.2). Rather than a

deficiency, excess  $^{226}\text{Ra}$  is accumulating in samples from the older beach ridges at Red Beach, likely due to the hydrological conditions at this location (Table 5.5). Further investigation of the hydrology at Red Beach would aid in understanding this accumulation of  $^{226}\text{Ra}$ , but this is outside the scope of this study.

Olley *et al.* (1996) modelled the effects that a 50% disequilibrium in  $^{226}\text{Ra}$  in a closed environment would have on the environmental dose rate (apart from one sample, KW05, all other samples from Albatross Bay had a decay chain disequilibrium of  $\leq 50\%$ ). Assuming that the environmental dose rate has remained constant throughout the sample burial period, this difference of 50% would lead to a  $<3\%$  change in the true dose rate. As the  $^{238}\text{U}$  decay chain contributes to approximately 27% of the total dose rate, a  $<3\%$  change in the dose rate equates to  $<0.81\%$  of the total dose rate (Demeter *et al.*, 2012). However, this value of  $<3\%$  assumes that the sediments are buried in a closed environment. The coastal environments of Albatross Bay are likely to be open systems, increasing the dose rate error margin to  $\sim 6\%$  (Olley *et al.*, 1997). Therefore, to accommodate the potential errors in the environmental dose rate from the identified disequilibrium in these decay chain, the error margins on all the dose rates have been increased by 6% for each sample, following the findings of Olley *et al.* (1997) and methods of Demeter *et al.* (2012).

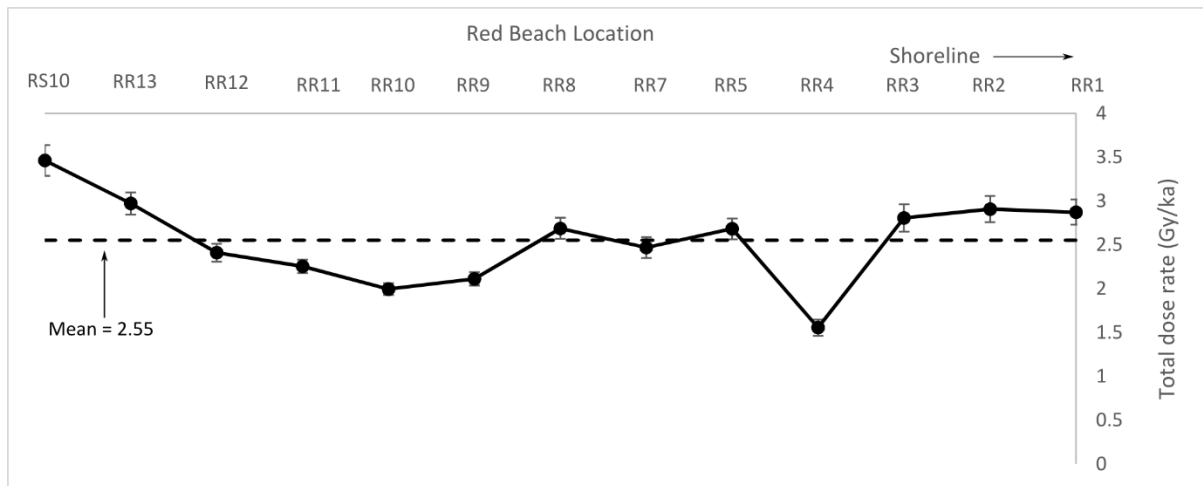
One sample from Albatross Bay has a  $^{238}\text{U}$  decay disequilibrium of  $>50\%$  (82% for sample KW05, collected from the supratidal mudflat). This disequilibrium of 82% is less than the “large disequilibria” of  $>100\%$  that Olley *et al.* (1996, p. 758) states will have a significant effect on dose rate. However, the OSL age obtained from sample KW05 should still be treated with caution. A second sample, KW06, was collected at a similar depth within the same supratidal mudflat at Kwamter. KW06 has a smaller decay chain disequilibrium of 15% and will provide a comparison for the OSL age of sample KW05.

Table 5.6 shows the total dose rates of all 18 samples from Albatross Bay. Because different quartz grain sizes are used for single-aliquot and single-grain analysis (90 to 125  $\mu\text{m}$  and 180 to 212  $\mu\text{m}$  respectively), the internal alpha contribution to total dose rates are different. Therefore, the total dose rate used for the single-aliquot and single-grain data differs slightly. Further information on the individual components of the total dose rate - the radionuclide activity, cosmic dose rate and water content - can be found in Section 5.1.6 below (Table 5.8, Table 5.11 and Table 5.13). At Red Beach, all beach ridge samples (RR1 to RR10) had similar environmental dose rates (weighted mean of  $2.55 \pm 0.11$  Gy/ka) with no discernible trend with

distance inland (Figure 5.5). The distal swale at Red Beach (RS10) has a slightly higher environmental dose rate of 3.46 Gy/ka. At Kwamter, the environmental dose rate within the supratidal mudflat, at approximately 1.5 Gy/ka, was higher when compared with the beach ridge which had an environmental dose rate of approximately 0.55 Gy/ka. The beach ridge at Wathayn has an environmental dose rate of between 0.65 and 0.88 Gy/ka, slightly higher than that for the beach ridge at Kwamter, but lower than the environmental dose rates found at Red Beach.

**Table 5.6: Summary of total dose rates of samples from Albatross Bay.**

Location	Sample code	Total SA dose rate (Gy/ka)	Total SA dose rate error	Total SG dose rate (Gy/ka)	Total SG dose rate error
Red Beach - RR1	RB02	2.872	0.153	2.799	0.148
Red Beach - RR2	RB01	2.907	0.157		
Red Beach - RS3	RB17	2.806	0.167		
Red Beach - RR4	RB08	1.555	0.098	1.518	0.095
Red Beach - RR5	RB10	2.681	0.126		
Red Beach RR7	RB12	2.467	0.126		
Red Beach - RR8	RB03	2.687	0.128	2.620	0.124
Red Beach - RR9	RB21	2.112	0.081	2.061	0.079
Red Beach - RR10	RB25	1.994	0.071		
Red Beach - RR11	RB18	2.253	0.081	2.199	0.079
Red Beach - RR12	RB20	2.409	0.109		
Red Beach - RR13	RB19	2.970	0.133	2.896	0.129
Red Beach - RS 10	RB27	3.462	0.186	3.375	0.181
Kwamter - KMF4	KW05	1.506	0.166	1.463	0.161
Kwamter - KMF1	KW06	1.361	0.128	1.330	0.124
Kwamter - KR1	KW07	0.549	0.041	0.541	0.040
Wathayn - WR1	WHA01_1	0.875	0.074	0.858	0.071
Wathayn - WR1	WHA02_2	0.667	0.068	0.656	0.066



**Figure 5.5: Total SA dose rate (Gy/ka) plotted for all Red Beach samples arranged according to distance from the modern shore.**

#### 5.1.6 Age determination

The burial age of each sample was obtained by dividing the  $D_e$  value of the sample with the dose rate (see Section 5.1.1). This age is equivalent to the time elapsed since the quartz grain was last exposed to sunlight.

##### 5.1.6.1 Single-aliquot results

The Albatross Bay samples generally had good luminescence properties. Most samples had all aliquots accepted for dose estimation (Table 5.7). The only rejection criterion was poor recycling ratios (RR) of  $<0.9$  or  $>1.1$ . An example of a typical decay curve and dose response curve for the samples from Red Beach, Kwamter and Wathayn is shown in Figure 5.6. These samples were dominated by the “fast” decay component, with the luminescence signal reduced to background levels within the first 2 seconds of measurement. The regenerative doses produced dose response curves that had an ideal shape, growing with increased doses, and the single-aliquot samples had good RR of between 0.95 and 1.

**Table 5.7: Summary of the OSL results from the SAR procedure on single-aliquot discs from Albatross Bay.**

Location	Sample code	Single-aliquots processed	Single-aliquots rejected	Reason for rejection	Overdispersion (%)
Red Beach - RR1	RB02	24	1	RR	11.2
Red Beach - RR2	RB01	24	0		10.2
Red Beach - RS3	RB17	24	0		7.0
Red Beach - RR4	RB08	24	0		10.5
Red Beach - RR5	RB10	24	0		17.3
Red Beach - RR7	RB12	24	0		18.2
Red Beach - RR8	RB03	24	0		10.9
Red Beach - RR9	RB21	24	0		13.6
Red Beach - RR10	RB25	24	0		11.0
Red Beach - RR11	RB18	24	0		10.9
Red Beach - RR12	RB20	24	3	RR	11.2
Red Beach - RR13	RB19	24	0		9.7
Red Beach - RS 10	RB27	24	0		10.0
Kwamter - KMF4	KW05	24	0		26.3
Kwamter - KMF1	KW06	24	0		18.6
Kwamter - KR1	KW07	24	1	RR	12.9
Wathayn - WR1	WHA01_1	24	0		21.4
Wathayn - WR1	WHA01_2	24	2	RR	36.6

While generally used in single-grain rather than single-aliquot OSL data analysis, the statistical overdispersion obtained when applying the CAM to single-aliquot  $D_e$  results still gives an indication of how well bleached the samples were prior to deposition and burial (see, for example, Oliver, 2016) especially when small aliquots are used. An overdispersion of <20% is generally regarded as well bleached and >20% generally as partially bleached (see Section 5.1.1). Overdispersion was below 20% for all samples from Red Beach, and two samples from Kwamter. Overdispersion was above 20% for one sample from Kwamter (from the supratidal mudflat) and all samples from Wathayn (from the aeolian beach ridge) (Table 5.7). Partial bleaching was not unexpected in the sample collected from the supratidal mudflat at Kwamter (see Section 5.1.2.3). While beach ridges are generally well-bleached, partial bleaching was also observed in the modern analogue sample from the beach ridge crest at Red Beach (see Section 5.1.4.2).

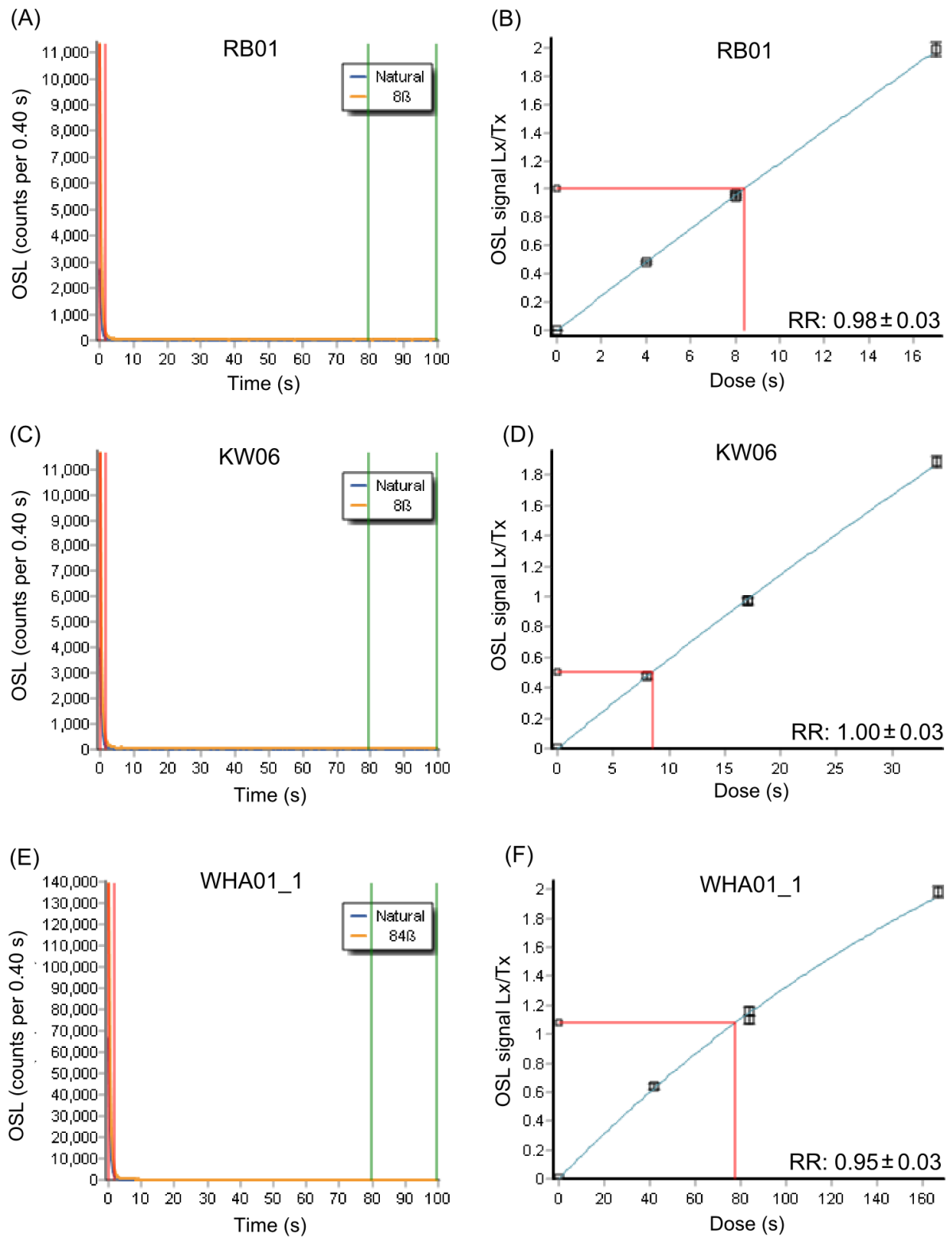


**Figure 5.6: Decay curves (A) (C) (E) and dose response curves (B) (D) (F) from an OSL single-aliquot disc for a sample from Red Beach (RB01), Kwamter (KW06) and Wathayn (WHA01\_1).**

The sedimentological context (coastal sediments from the foreshore or aeolian deposits) indicates that the Albatross Bay samples are likely to be well-bleached (see Section 5.1.2) and



the CAM would be the appropriate age model used for  $D_e$  calculations. The statistical overdispersion is in general agreement with the CAM as the choice of age model. In the few samples where sample overdispersion was >20%, the CAM was not appropriate to calculate a sample equivalent dose. As such, no  $D_e$  values and burial ages are presented for these samples (KW05, WHA01\_1 and WHA01\_2). The single-aliquot burial ages for samples with a statistical overdispersion of <20% are presented in Table 5.8.

**Table 5.8: Single-aliquot OSL ages for samples from Red Beach and Kwamter with the associated dose rate and equivalent dose data. All samples were in the 90-125  $\mu\text{m}$  size range. Equivalent dose rates and ages were calculated using the CAM. Ages reported at a 1  $\sigma$  confidence interval.**

Location	Sample code	Facies code	Meters AHD (m)	Radionuclide activities (Bq Kg <sup>-1</sup> )						Cosmic-ray dose rate (Gy/ka)	Water content (%)	Total dose rate (Gy/ka)	Equivalent dose (Gy)	Age estimate (years)
				<sup>238</sup> U	<sup>226</sup> Ra	<sup>210</sup> Pb	<sup>228</sup> Ra	<sup>228</sup> Th	<sup>40</sup> K					
Red Beach - RR1	RB02	B3	1.37	98 ± 6	72.4 ± 1.4	65 ± 5	89 ± 2.9	90.7 ± 2.2	16 ± 4.7	0.177	11.9 ± 3	2.872 ± 0.153	0.822 ± 0.024	286 ± 18
Red Beach - RR2	RB01	B3	0.93	90 ± 6	74.7 ± 1.5	62 ± 5	95.6 ± 3.1	96.6 ± 2.5	22 ± 9.0	0.176	11.9 ± 3	2.907 ± 0.157	1.071 ± 0.024	368 ± 22
Red Beach - RS3	RB17	B3	0.89	100 ± 6	78.5 ± 1.5	63 ± 5	87 ± 2.9	93.4 ± 2.3	26 ± 7.6	0.176	15.9 ± 4	2.806 ± 0.167	1.398 ± 0.022	498 ± 31
Red Beach - RR4	RB08	B3	1.12	43 ± 4	37.6 ± 1.1	28 ± 4	41.1 ± 2.1	43.7 ± 1.4	29 ± 8.0	0.174	6.9 ± 1.7	1.555 ± 0.098	1.253 ± 0.029	806 ± 54
Red Beach - RR5	RB10	B3	1.45	64 ± 5	64.3 ± 1.4	64 ± 5	73.4 ± 2.6	73.7 ± 1.9	17 ± 7.0	0.173	4.1 ± 1	2.681 ± 0.126	3.694 ± 0.136	1378 ± 84
Red Beach RR7	RB12	B3	1.98	62 ± 6	61 ± 1.4	54 ± 5	67.2 ± 2.8	67.4 ± 2.0	31 ± 9.1	0.179	4.2 ± 1.1	2.467 ± 0.126	3.910 ± 0.151	1585 ± 103
Red Beach - RR8	RB03	B3	1.44	73 ± 5	66.9 ± 1.4	58 ± 5	76.6 ± 2.6	79.7 ± 2.0	22 ± 6.4	0.177	6.2 ± 1.6	2.687 ± 0.128	4.528 ± 0.107	1685 ± 92
Red Beach - RR9	RB21	B2	0.97	57 ± 3	51 ± 1	47 ± 3	54 ± 2	56 ± 1.0	18 ± 5.3	0.176	4.2 ± 1.1	2.112 ± 0.081	4.241 ± 0.122	2008 ± 101
Red Beach - RR10	RB25	B3	1.58	68 ± 6	85 ± 2	73 ± 5	75 ± 3	79 ± 2.0	28 ± 8.2	0.177	3.3 ± 0.8	1.994 ± 0.071	3.463 ± 0.086	1740 ± 80
Red Beach - RR11	RB18	B2	1.84	52 ± 3	63 ± 1	60 ± 3	52 ± 1	55 ± 1.0	8 ± 2.3	0.177	3.5 ± 0.9	2.253 ± 0.081	3.908 ± 0.091	1734 ± 80
Red Beach - RR12	RB20	B2	1.72	61 ± 5	58 ± 1	58 ± 4	59 ± 2	61 ± 2.0	21 ± 6.1	0.179	3.3 ± 0.8	2.409 ± 0.109	5.058 ± 0.128	2100 ± 112
Red Beach - RR13	RB19	B3	1.58	74 ± 6	67 ± 1	69 ± 5	80 ± 3	84 ± 2.0	16 ± 8.0	0.174	4 ± 1	2.97 ± 0.133	6.635 ± 0.137	2234 ± 114
Red Beach - RS 10	RB27	B2	1.00	92 ± 7	101 ± 2	91 ± 6	106 ± 3	109 ± 3.0	17 ± 5.0	0.174	12.4 ± 3.1	3.462 ± 0.186	8.053 ± 0.171	2326 ± 136
Kwamter - KMF1	KW06	C4	0.01	37 ± 4	31.4 ± 1	29 ± 4	33.6 ± 2	35 ± 1.2	141 ± 11	0.183	32.6 ± 8.2	1.361 ± 0.128	1.327 ± 0.052	975 ± 96
Kwamter - KR1	KW07	B5	1.52	8 ± 3	4 ± 0.7	10 ± 1	4.3 ± 1.4	5.5 ± 0.6	20 ± 5.8	0.177	1.1 ± 0.3	0.549 ± 0.041	1.599 ± 0.045	2914 ± 186

The OSL burial ages of the beach ridges at Red Beach generally increase with distance from the modern shore. The one inconsistency is the age obtained for RR9, which is older than those for RR10 and RR11. Burial ages at Kwamter also increase with distance inland, with the beach ridge sediments (KR1, sample KW07) deposited prior to the supratidal mudflat sediments (KMF1, sample KW06).

#### 5.1.6.2 Single grain results

As discussed in Section 5.1.6.1, some samples from Wathayn and Kwamter had high overdispersion values of >20%. Therefore, all samples from these two field locations were analysed using single-grain OSL techniques. Seven samples from Red Beach, selected from across the entire beach ridge plain, were also analysed using single-grain OSL techniques. Results from the single-grain OSL measurements are shown in Table 5.9. Grains were rejected based on the criteria outlined in Section 5.1.3.5 and as shown in Table 5.10. A target of 1000 grains measured per sample was set (see Section 5.1.3.4) but some samples had insufficient grains for analysis (Table 5.9). It was particularly important to obtain data for samples KW05, WHA01\_1 and WHA01\_2 as single-aliquot analysis indicated that these samples were partially bleached, and no accurate burial age could be obtained for them. Therefore, to ensure that there were sufficient grains accepted for OSL analysis, 400 more grains were processed for sample WHA01\_1.

**Table 5.9: Summary of OSL results from the SAR procedure on single-grain discs from Albatross Bay.**

Location	Sample code	Single grains processed	Single grains accepted	Single grains rejected	Proportion of luminescence emitting grains (%)	Rejection rate (%)	Overdispersion (%)	Statistical model
Red Beach - RR1	RB02	900	33	867	3.67	96.33	16.4	CAM
Red Beach - RR4	RB08	1000	36	964	3.60	96.40	4.7	CAM
Red Beach - RR8	RB03	1000	66	934	6.60	93.40	20.7	MAM
Red Beach - RR9	RB21	1000	86	914	8.60	91.40	14	CAM
Red Beach - RR11	RB18	800	67	733	8.38	91.63	24.5	MAM
Red Beach - RR13	RB19	600	59	541	9.83	90.17	19.6	CAM
Red Beach - RS 10	RB27	800	80	720	10.00	90.00	14.6	CAM
Kwamter - KMF4	KW05	1000	80	920	8.00	92.00	45.7	MAM
Kwamter - KMF1	KW06	900	58	842	6.44	93.56	25.2	MAM
Kwamter - KR1	KW07	900	57	843	6.33	93.67	18.2	CAM
Wathayn - WR1	WHA01_1	1400	157	1243	11.21	88.79	36.9	MAM
Wathayn - WR1	WHA01_2	1000	142	858	14.20	85.80	29.2	MAM

**Table 5.10: Summary of single-grain rejections based on the detailed rejection criteria for samples from Albatross Bay.**

Location/ Criteria for rejection	Signal <3 BG	Recycling ratio > 10% unity	IR ratio IR > 2 sigma signal	Supersaturating grains	Recuperation >5%	No Decay	Large changes in sensitivity	Dominance of medium component	Total number of grains rejected
RB02	495	88	28	5	3	219	19	10	867
RB08	512	123	35	7	2	232	30	23	964
RB03	425	45	37	1	3	340	35	48	934
RB21	340	101	30	5	1	334	37	66	914
RB18	313	130	26	7	0	214	11	32	733
RB19	341	15	7	9	0	98	31	40	541
RB27	236	93	32	2	4	188	49	116	720
KW05	545	82	29	12	1	209	5	37	920
KW06	542	68	19	15	1	157	21	19	842
KW07	540	66	23	0	2	156	14	42	843
WHA01_1	377	132	48	6	5	471	29	175	1243
WHA01_2	269	108	23	12	3	312	16	115	858

All samples had a high single-grain rejection rate of between 85% and 96% (Table 5.9). Most grains for all samples were rejected because of a low signal to background ratio or because they had no measurable OSL signal (no decay) (Table 5.10). The high single-grain rejection rate indicates that the OSL signals measured from the single-aliquot discs were produced by a few bright grains rather than from most of the grains on each disc. The high single-grain rejection rate in these samples are not unusual. Duller (2008) notes how, with quartz grains, as much as 95% of the luminescence signal for a sample may be attributed to less than 5% of grains measured, with many grains not luminescing at all.

An example of a typical decay curve and dose response curve for an accepted bright grain for a sample from Red Beach, Kwamter and Wathayn is shown in Figure 5.7. Like the single-aliquot results, these samples were dominated by the “fast” decay component, with the luminescence signal reduced to background levels between channels 6 to 15 (between 0.1 and 0.28 seconds). The regenerative doses produced dose response curves that had an ideal shape, growing with increased doses. These samples had good recycling ratios of between 0.97 and 1.03.

Statistical overdispersion in samples will typically increase when measuring single-grains versus single-aliquots due to an increase in the amount of data points (24 vs hundreds). An increase in overdispersion % can thus be observed in all the single-grain OSL samples except for RB08. However, while sample overdispersion has increased, samples from Red Beach were still generally well-bleached (overdispersion <20%), with only 2 out of 7 samples with an overdispersion now >20% (RB03, 20.7%; RB18, 24.5%). Only one sample from Kwamter had an overdispersion <20%, with all samples from Wathayn once again having an overdispersion of >20%. Like the single-aliquot  $D_e$  calculations, the samples with an

overdispersion of <20% were calculated using the CAM, while samples with an overdispersion >20% were calculated using the MAM (Table 5.9).

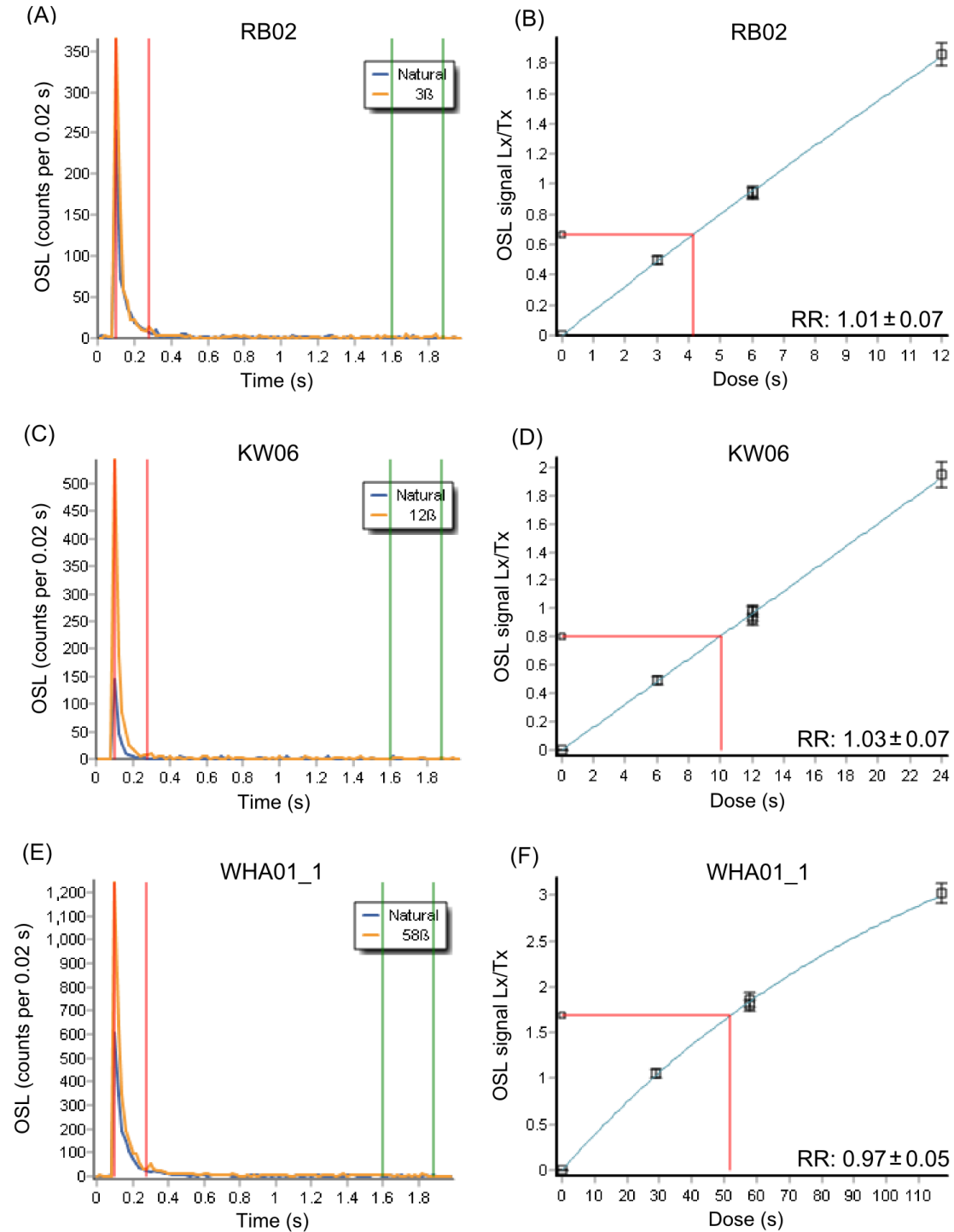


**Figure 5.7: Decay curves (A) (C) (E) and dose response curves (B) (D) (F) for an OSL single-grain with a bright luminescence signal from samples RB02, KW06 and WHA01\_1.**

The single-grain burial ages for all samples analysed are presented in Table 5.11. The single-grain burial ages for the beach ridge samples at Red Beach increase with distance from the modern shore. Again, the only inconsistency is the age obtained for RR9 which is older than that for RR11. The distal swale at Red Beach (RS10, sample RB27) also has an estimated age younger than the oldest ridge, RR13. At Kwamter, the supratidal mudflat sediments, KMF4 (sample KW05) and KMF1 (sample KW06), both have similar burial ages of between 800 and 900 years old. Both are younger than the age obtained for the single beach ridge (KR1, sample KW07). Age determinations for the beach ridge at Wathayn (WR1, samples WHA01\_1 and WHA01\_2), at  $4,000 \pm 324$  years old and  $3,153 \pm 319$  years old respectively, are like that for the beach ridge at Kwamter, at  $3,392 \pm 263$  years old.

**Table 5.11: Single-grain OSL ages for samples from Red Beach, Kwamter and Wathayn with the associated dose rate and equivalent dose data. All samples were in the 180-212  $\mu\text{m}$  size range. Ages reported at a 1  $\sigma$  confidence interval.**

Location	Sample code	Facies code	Meters AHD (m)	Radionuclide activities (Bq Kg <sup>-1</sup> )						Cosmic-ray dose rate (Gy/ka)	Water content (%)	Total dose rate (Gy/ka)	Statistical model	Equivalent dose (Gy)	Age estimate (years)
				<sup>238</sup> U	<sup>226</sup> Ra	<sup>210</sup> Pb	<sup>228</sup> Ra	<sup>228</sup> Th	<sup>40</sup> K						
Red Beach - RR1	RB02	B3	1.37	98 ± 6	72.4 ± 1.4	65 ± 5	89 ± 2.9	90.7 ± 2.2	16 ± 4.7	0.177	11.9 ± 3	2.799 ± 0.148	CAM	0.861 ± 0.032	307 ± 30
Red Beach - RR4	RB08	B3	1.12	43 ± 4	37.6 ± 1.1	28 ± 4	41.1 ± 2.1	43.7 ± 1.4	29 ± 8.0	0.174	6.9 ± 1.7	1.518 ± 0.095	CAM	1.325 ± 0.028	872 ± 57
Red Beach - RR8	RB03	B3	1.44	73 ± 5	66.9 ± 1.4	58 ± 5	76.6 ± 2.6	79.7 ± 2.0	22 ± 6.4	0.177	6.2 ± 1.6	2.62 ± 0.124	MAM	4.228 ± 0.301	1632 ± 140
Red Beach - RR9	RB21	B2	0.97	57 ± 3	51 ± 1	47 ± 3	54 ± 2	56 ± 1.0	18 ± 5.3	0.176	4.2 ± 1.1	2.061 ± 0.079	CAM	4.613 ± 0.087	2239 ± 116
Red Beach - RR11	RB18	B2	1.84	52 ± 3	63 ± 1	60 ± 3	52 ± 1	55 ± 1.0	8 ± 2.3	0.177	3.5 ± 0.9	2.199 ± 0.079	MAM	3.829 ± 0.091	1740 ± 80
Red Beach - RR13	RB19	B3	1.58	74 ± 6	67 ± 1	69 ± 5	80 ± 3	84 ± 2.0	16 ± 8.0	0.174	4 ± 1	2.896 ± 0.129	CAM	7.218 ± 0.203	2493 ± 136
Red Beach - RS 10	RB27	B2	1.00	92 ± 7	101 ± 2	91 ± 6	106 ± 3	109 ± 3.0	17 ± 5.0	0.174	12.4 ± 3.1	3.375 ± 0.181	CAM	9.239 ± 0.173	2138 ± 131
Kwamter - KMF4	KW05	C4	-0.15	137 ± 6	24.8 ± 1.1	20 ± 4	34.7 ± 2.3	36.2 ± 1.3	176 ± 14	0.181	45.3 ± 11.3	1.463 ± 0.161	MAM	1.294 ± 0.070	884 ± 104
Kwamter - KMF1	KW06	C4	0.01	37 ± 4	31.4 ± 1	29 ± 4	33.6 ± 2	35 ± 1.2	141 ± 11	0.183	32.6 ± 8.2	1.33 ± 0.124	MAM	1.084 ± .036	815 ± 78
Kwamter - KR1	KW07	B5	1.52	8 ± 3	4 ± 0.7	10 ± 1	4.3 ± 1.4	5.5 ± 0.6	20 ± 5.8	0.177	1.1 ± 0.3	0.541 ± 0.040	CAM	1.835 ± 0.053	3392 ± 263
Wathayn - WR1	WHA01_1	B5	2.96	27 ± 4	21.1 ± 0.9	16 ± 3	16.1 ± 1.7	14.2 ± 0.8	23 ± 6.7	0.179	2 ± 0.5	0.858 ± 0.071	MAM	3.436 ± 0.108	4000 ± 324
Wathayn - WR1	WHA02_2	B5	3.19	12 ± 3	13.9 ± 0.8	12 ± 3	10.6 ± 1.5	10.6 ± 0.7	15 ± 4.4	0.182	2 ± 0.5	0.656 ± 0.066	MAM	2.072 ± 0.062	3153 ± 319

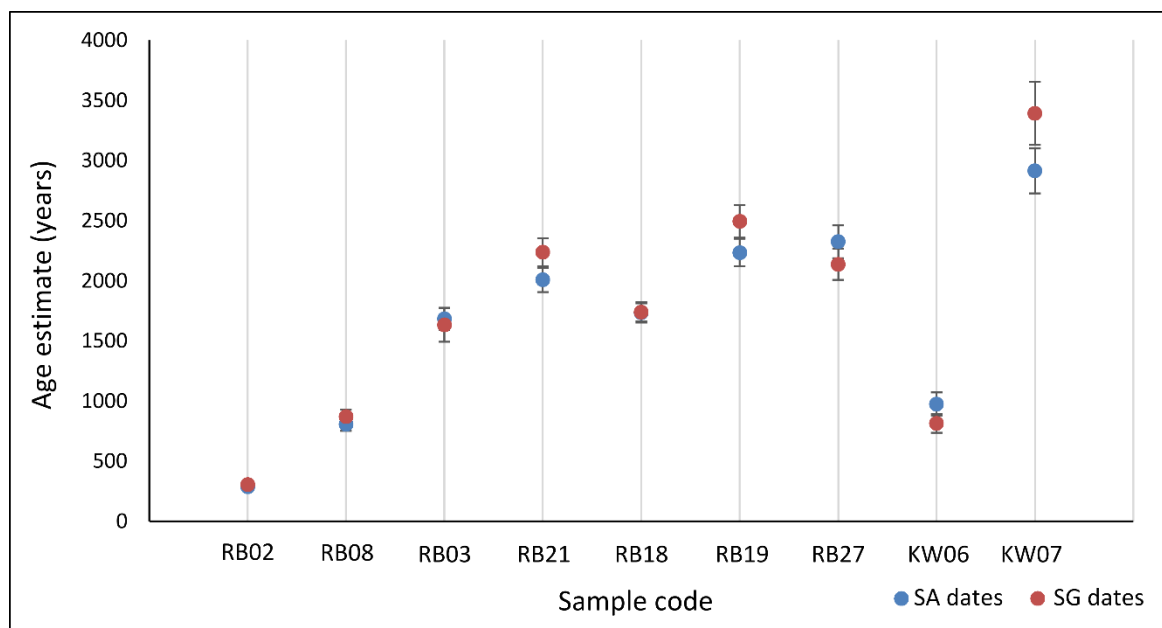
### 5.1.6.3 Summary: OSL age determinations on coastal sedimentary deposits at Albatross Bay

Table 5.12 and Figure 5.8 compare single-aliquot and single-grain burial age determination for samples where both were able to be measured. Samples KW05, WHA01\_1 and WHA01\_2 were excluded from this comparison because no single-aliquot ages were calculated due to high sample overdispersion. The single-aliquot and single-grain age determinations are similar within error margins, even though some single-grain ages (RB03, RB18 and KW06) were calculated using the MAM due to a >20% sample overdispersion while all single-aliquot ages were calculated using the CAM. Only the beach ridge at Kwamter, KR1 (sample code KW07) has a single-grain age higher (outside the margin of error) than the single-aliquot age, though the difference is slight (Figure 5.8). As the single-aliquot and single-grain burial ages are largely similar, for consistency, the single-aliquot data is adopted for all the Red Beach OSL burial ages, while the single-grain data is adopted for all the Kwamter and Wathayn OSL burial ages.

**Table 5.12: Comparison of single-aliquot (SA) and single-grain (SG) burial ages. Ages reported at a 1  $\sigma$  confidence interval.**

Location	Sample code	SA Age (years)	SG Age (years)
Red Beach - RR1	RB02	286 $\pm$ 18	307 $\pm$ 30
Red Beach - RR4	RB08	806 $\pm$ 54	872 $\pm$ 57
Red Beach - RR8	RB03	1685 $\pm$ 92	1632 $\pm$ 140
Red Beach - RR9	RB21	2008 $\pm$ 101	2239 $\pm$ 116
Red Beach - RR11	RB18	1734 $\pm$ 80	1740 $\pm$ 80
Red Beach - RR13	RB19	2234 $\pm$ 114	2493 $\pm$ 136
Red Beach - RS 10	RB27	2326 $\pm$ 136	2138 $\pm$ 131
Kwamter - KMF1	KW06	975 $\pm$ 96	815 $\pm$ 78
Kwamter - KR1	KW07	2914 $\pm$ 186	3392 $\pm$ 263





**Figure 5.8: Graphical comparison of single-aliquot (SA) and single-grain (SG) ages from Red Beach and Kwamter. Ages are in years before sample collection.**

Radial plots for each of these samples are shown in Figures 5.9 to 5.11. Radial plots are a way to display OSL equivalent dose data whereby each individual aliquot/grain is plotted (each closed circle) along with their associated relative error and precision, enabling a visual evaluation of whether a sample is dominated by one population of  $D_e$  values or if the dose distribution is more complicated (Jacobs *et al.*, 2006a). The  $D_e$  of each aliquot/grain is read by drawing a line from the origin of the “standard estimate” axis on the left, through the dose point, to the “Dose (Gy)” axis on the right and reading off the value. The measurement uncertainty for each aliquot/grain is shown by the x-axis, with data points closer to the left having a larger relative error and being less precise, while data points closer to the right have a smaller relative error and are more precise (Roberts and Jacobs, 2015). The shaded region within each graph represents two standard deviations away from the weighted mean value (calculated using the CAM). Well-bleached samples should have the most of the data points within this shaded region (e.g. Figure 5.9). When samples are partially bleached, a significant number of data points plot outside the shaded region. For these samples (KW05, KW06, WHA01\_1 and WHA01\_2), a straight line is drawn on each radial plot from the origin of the “standard estimate” axis to the “Dose (Gy)” axis representing the  $D_e$  calculated through the MAM.

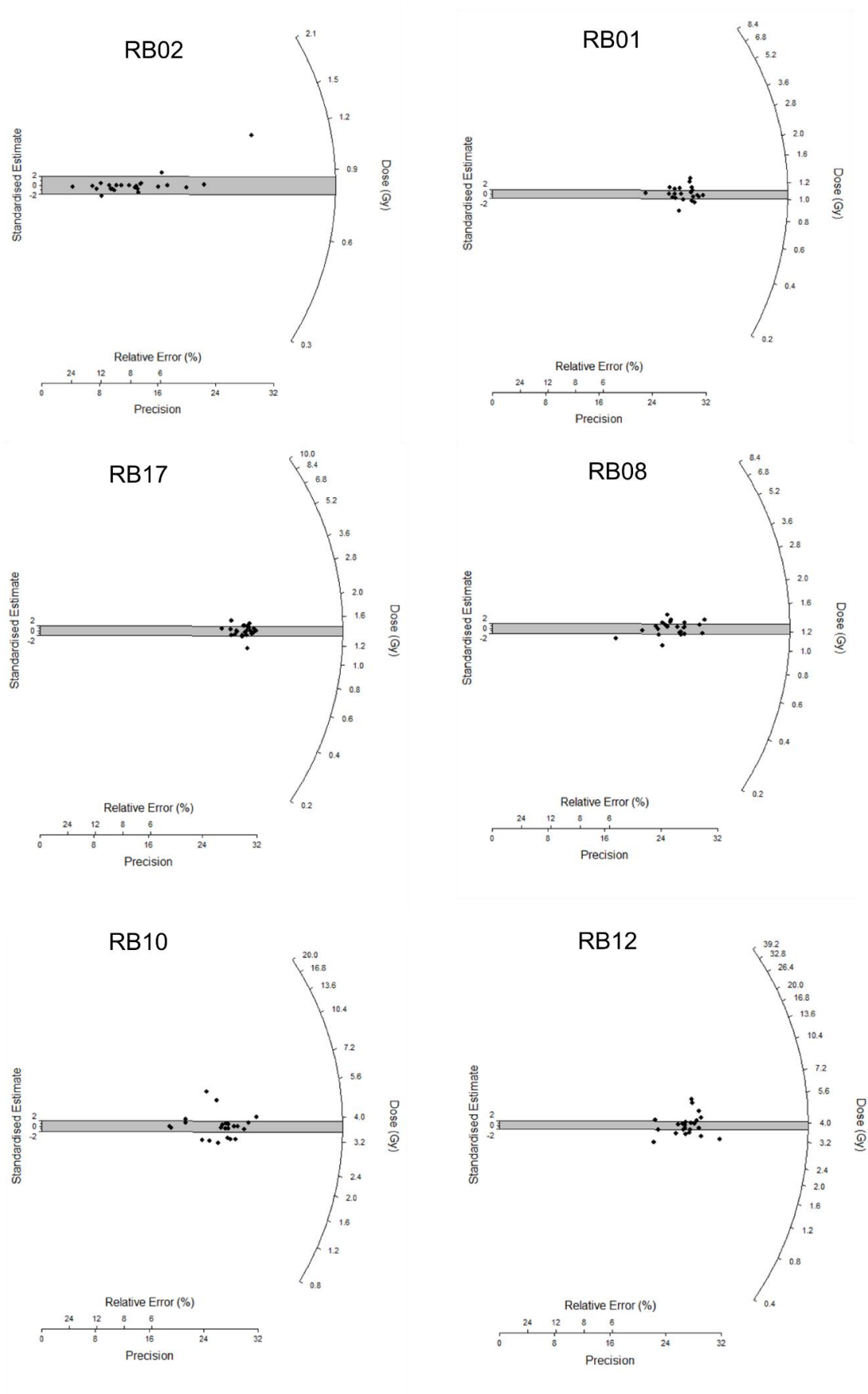


**Figure 5.9:  $D_e$  values displayed in radial plots for samples from Red Beach (RB02, RB01, RB17, RB08, RB10 and RB12).**

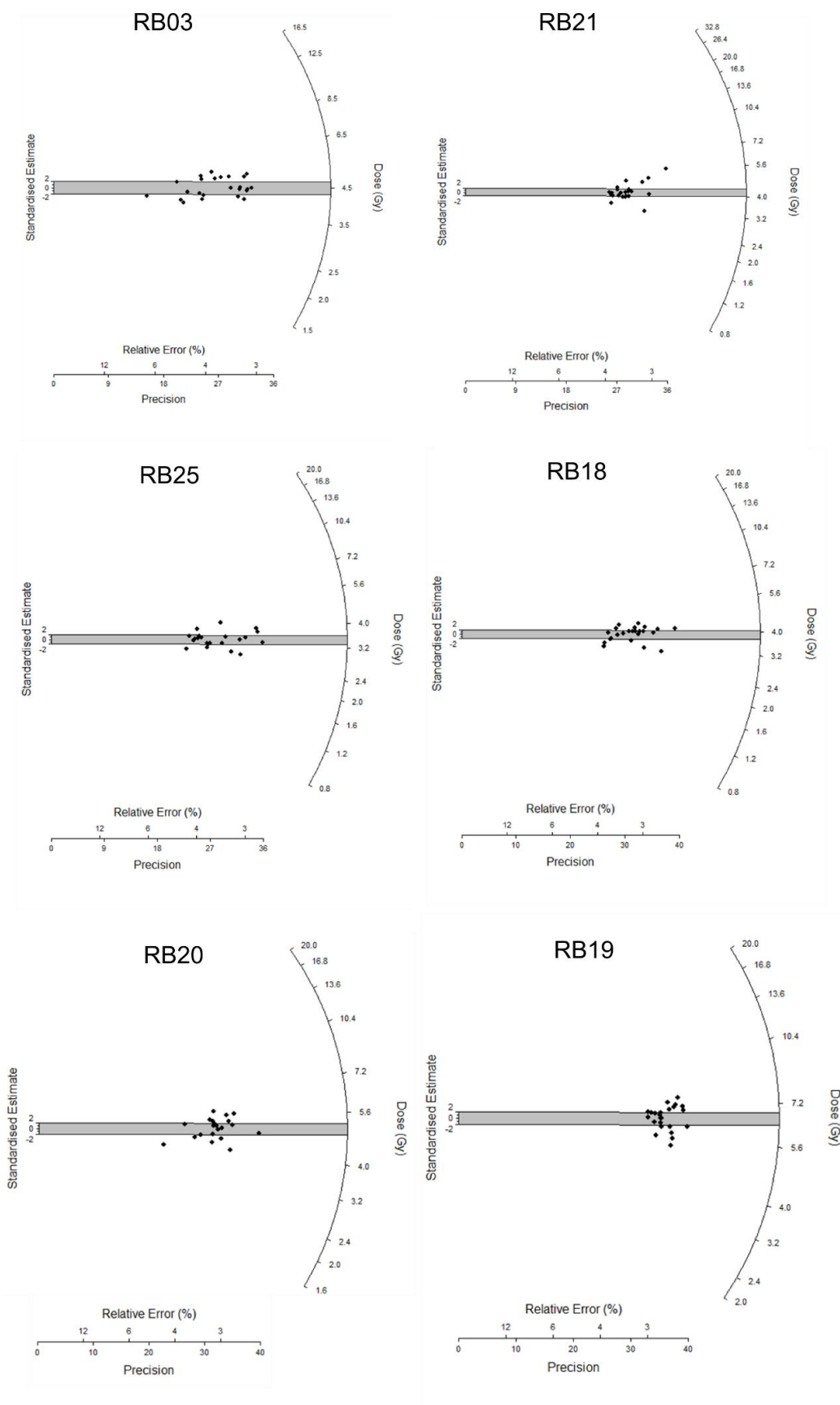


**Figure 5.10:  $D_e$  values displayed in radial plots for samples from Red Beach (RB03, RB21, RB25, RB18, RB20, RB19).**

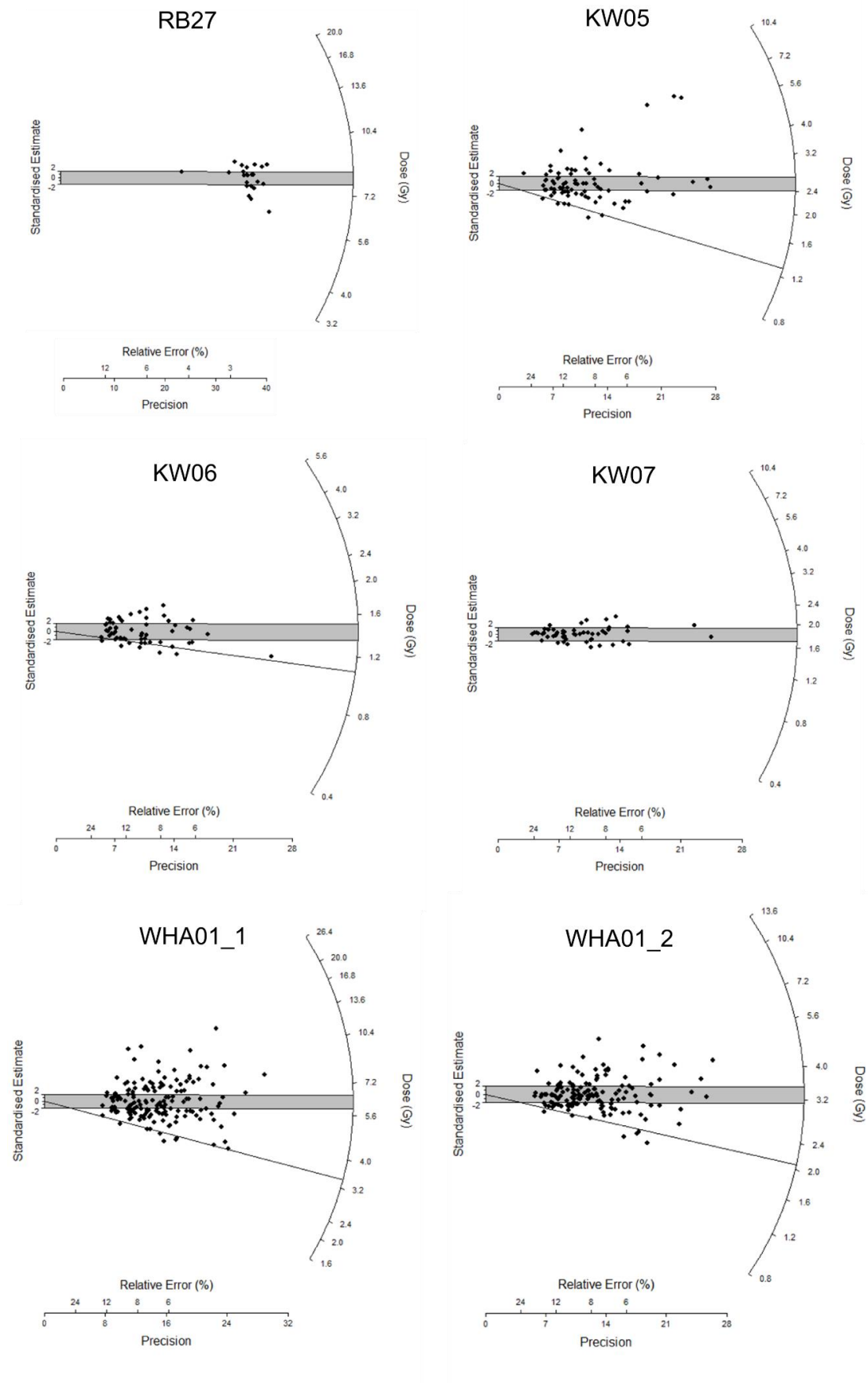


**Figure 5.11:  $D_e$  values displayed in radial plots for sample RB27 from Red Beach, samples KW05, KW06 and KW07 from Kwamter and samples WHA01\_1 and WHA01\_2 from Wathayn.**

Table 5.13 is a compilation of the selected OSL burial age data for all the Red Beach, Kwamter and Wathayn samples. These results show that the Red Beach beach ridge plain accumulated over the last 2,300 years. The single beach ridges at Kwamter and at Wathayn are older, at approximately 3,500 years and 4,000 years old respectively. The supratidal mudflat deposits at Kwamter are much younger, with age determinations between 800 and 900 years old. These results, together with those from the radiocarbon dating described in the following section, will contribute to the construction a chronology of coastal evolution and sea level change, discussed in Chapter 6.

**Table 5.13: Compiled OSL ages from Albatross Bay combining the single-aliquot and single-grain data selected for each sample. All single-aliquot (SA) samples were in the 90-125  $\mu\text{m}$  size range, all single-grain (SG) samples were in the 180-212  $\mu\text{m}$  size range. Ages reported at a 1  $\sigma$  confidence interval.**

Location	Sample code	Facies code	Meters AHD (m)	Radionuclide activities (Bq Kg <sup>-1</sup> )						Cosmic-ray dose rate (Gy/ka)	Water content (%)	Total dose rate (Gy/ka)	SA/SG - Statistical model	Equivalent dose (Gy)	Age estimate (years)
				<sup>238</sup> U	<sup>226</sup> Ra	<sup>210</sup> Pb	<sup>228</sup> Ra	<sup>228</sup> Th	<sup>40</sup> K						
Red Beach - RR1	RB02	B3	1.37	98 ± 6	72.4 ± 1.4	65 ± 5	89 ± 2.9	90.7 ± 2.2	16 ± 4.7	0.177	11.9 ± 3	2.872 ± 0.153	SA - CAM	0.822 ± 0.024	286 ± 18
Red Beach - RR2	RB01	B3	0.93	90 ± 6	74.7 ± 1.5	62 ± 5	95.6 ± 3.1	96.6 ± 2.5	22 ± 9.0	0.176	11.9 ± 3	2.907 ± 0.157	SA - CAM	1.071 ± 0.024	368 ± 22
Red Beach - RS3	RB17	B3	0.89	100 ± 6	78.5 ± 1.5	63 ± 5	87 ± 2.9	93.4 ± 2.3	26 ± 7.6	0.176	15.9 ± 4	2.806 ± 0.167	SA - CAM	1.398 ± 0.022	498 ± 31
Red Beach - RR4	RB08	B3	1.12	43 ± 4	37.6 ± 1.1	28 ± 4	41.1 ± 2.1	43.7 ± 1.4	29 ± 8.0	0.174	6.9 ± 1.7	1.555 ± 0.098	SA - CAM	1.253 ± 0.029	806 ± 54
Red Beach - RR5	RB10	B3	1.45	64 ± 5	64.3 ± 1.4	64 ± 5	73.4 ± 2.6	73.7 ± 1.9	17 ± 7.0	0.173	4.1 ± 1	2.681 ± 0.126	SA - CAM	3.694 ± 0.136	1378 ± 84
Red Beach RR7	RB12	B3	1.98	62 ± 6	61 ± 1.4	54 ± 5	67.2 ± 2.8	67.4 ± 2.0	31 ± 9.1	0.179	4.2 ± 1.1	2.467 ± 0.126	SA - CAM	3.910 ± 0.151	1585 ± 103
Red Beach - RR8	RB03	B3	1.44	73 ± 5	66.9 ± 1.4	58 ± 5	76.6 ± 2.6	79.7 ± 2.0	22 ± 6.4	0.177	6.2 ± 1.6	2.687 ± 0.128	SA - CAM	4.528 ± 0.107	1685 ± 92
Red Beach - RR9	RB21	B2	0.97	57 ± 3	51 ± 1	47 ± 3	54 ± 2	56 ± 1.0	18 ± 5.3	0.176	4.2 ± 1.1	2.112 ± 0.081	SA - CAM	4.241 ± 0.122	2008 ± 101
Red Beach - RR10	RB25	B3	1.58	68 ± 6	85 ± 2	73 ± 5	75 ± 3	79 ± 2.0	28 ± 8.2	0.177	3.3 ± 0.8	1.994 ± 0.071	SA - CAM	3.463 ± 0.086	1740 ± 80
Red Beach - RR11	RB18	B2	1.84	52 ± 3	63 ± 1	60 ± 3	52 ± 1	55 ± 1.0	8 ± 2.3	0.177	3.5 ± 0.9	2.253 ± 0.081	SA - CAM	3.908 ± 0.091	1734 ± 80
Red Beach - RR12	RB20	B2	1.72	61 ± 5	58 ± 1	58 ± 4	59 ± 2	61 ± 2.0	21 ± 6.1	0.179	3.3 ± 0.8	2.409 ± 0.109	SA - CAM	5.058 ± 0.128	2100 ± 112
Red Beach - RR13	RB19	B3	1.58	74 ± 6	67 ± 1	69 ± 5	80 ± 3	84 ± 2.0	16 ± 8.0	0.174	4 ± 1	2.97 ± 0.133	SA - CAM	6.635 ± 0.137	2234 ± 114
Red Beach - RS 10	RB27	B2	1.00	92 ± 7	101 ± 2	91 ± 6	106 ± 3	109 ± 3.0	17 ± 5.0	0.174	12.4 ± 3.1	3.462 ± 0.186	SA - CAM	8.053 ± 0.171	2326 ± 136
Kwamter - KMF4	KW05	C4	-0.15	137 ± 6	24.8 ± 1.1	20 ± 4	34.7 ± 2.3	36.2 ± 1.3	176 ± 14	0.181	45.3 ± 11.3	1.463 ± 0.161	SG - MAM	1.294 ± 0.070	884 ± 104
Kwamter - KMF1	KW06	C4	0.01	37 ± 4	31.4 ± 1	29 ± 4	33.6 ± 2	35 ± 1.2	141 ± 11	0.183	32.6 ± 8.2	1.33 ± 0.124	SG - MAM	1.084 ± .036	815 ± 78
Kwamter - KR1	KW07	B5	1.52	8 ± 3	4 ± 0.7	10 ± 1	4.3 ± 1.4	5.5 ± 0.6	20 ± 5.8	0.177	1.1 ± 0.3	0.541 ± 0.040	SG - CAM	1.835 ± 0.053	3392 ± 263
Wathayn - WR1	WHA01_1	B5	2.96	27 ± 4	21.1 ± 0.9	16 ± 3	16.1 ± 1.7	14.2 ± 0.8	23 ± 6.7	0.179	2 ± 0.5	0.858 ± 0.071	SG - MAM	3.436 ± 0.108	4000 ± 324
Wathayn - WR1	WHA02_2	B5	3.19	12 ± 3	13.9 ± 0.8	12 ± 3	10.6 ± 1.5	10.6 ± 0.7	15 ± 4.4	0.182	2 ± 0.5	0.656 ± 0.066	SG - MAM	2.072 ± 0.062	3153 ± 319

## 5.2 Radiocarbon dating

### 5.2.1 Principles of radiocarbon dating

Radiocarbon dating is a well-established method for obtaining ages of samples from the Holocene into the Late Pleistocene (Hua, 2009; Sloss *et al.*, 2013). Carbon-14 ( $^{14}\text{C}$ ) is a naturally occurring isotope of carbon that is continuously produced in the upper atmosphere, where it oxidises to form  $^{14}\text{CO}_2$ .  $^{14}\text{CO}_2$  then mixes relatively rapidly with stable  $^{12}\text{CO}_2$  and  $^{13}\text{CO}_2$  before being dispersed throughout the atmosphere, biosphere and ocean (Schellmann and Bruckner, 2005; Hua, 2009).  $^{14}\text{C}$  is present in every living organism due to the processes of photosynthesis, the consumption of plants and animals and metabolic processes (Sloss *et al.*, 2013). While the organism is alive, these processes will replace  $^{14}\text{C}$  that is lost from radioactive decay. Therefore, the concentration of  $^{14}\text{C}$  in an organism will be in equilibrium with the concentration of  $^{14}\text{C}$  in its environment (atmosphere, freshwater or saltwater) (Hua, 2009). Once an organism is dead, however, there is no more intake of  $^{14}\text{C}$ , and the  $^{14}\text{C}$  present in the organism will begin to decrease via radioactive decay. Decay occurs at a known rate called the radioactive half-life which, for  $^{14}\text{C}$ , is the Libby half-life of 5568 years (Sloss *et al.*, 2013). By measuring the concentration of  $^{14}\text{C}$  present in a dead organism and knowing the original concentration of  $^{14}\text{C}$  present in the atmosphere in combination with the  $^{14}\text{C}$  half-life, the time elapsed since the organism died can be calculated. Radiocarbon ages are expressed in years before present (BP), with “present” defined as AD 1950, the period when the radiocarbon technique was first developed (Burr, 2007).

While it was originally assumed that atmospheric  $^{14}\text{C}$  concentrations were constant, by the late 1950s, it was discovered that they have varied through space and time, therefore radiocarbon results need to be calibrated to account for this variation in concentration (de Vries, 1958; Stuiver, 1961; Reimer and Reimer, 2007). The variability in  $^{14}\text{C}$  concentration is caused by variation in the rate of radiocarbon production in the atmosphere, which is in turn linked to changes in the intensity of the Earth’s geomagnetic field, variable solar activity or changes in the carbon cycle (Burr, 2007; Hua, 2009; Sloss *et al.*, 2013). Radiocarbon ages are converted into calendar ages using calibration curves. Calibration curves describe past atmospheric  $^{14}\text{C}$  concentrations and are created by comparing  $^{14}\text{C}$  dates with dates obtained from an alternative dating technique with high-resolution and precision, such as dendrochronology (tree ring analysis). Trees absorb carbon dioxide as they grow, with certain species producing distinctive annual rings that can be dated very accurately. Radiocarbon ages for each individual tree ring are then obtained and the radiocarbon timescale is corrected using the dendrochronological

timescale, producing a calibration curve (Burr, 2007; van der Plicht, 2007). Once past the limit of dendrochronology, the calibration curves are extended using other geological archives which have a lower resolution and less precision than dendrochronology, including varved lake and marine sediments, corals and speleothems (Burr, 2007; Reimer and Reimer, 2007). The most recent calibration curves are IntCal13 (Reimer *et al.*, 2013) and SHCal13 (Hogg *et al.*, 2013).

Along with the need to calibrate radiocarbon dates due to atmospheric  $^{14}\text{C}$  variations, dates on samples obtained from marine environments also need correction for the marine reservoir effect (Hua, 2009; Sloss *et al.*, 2013). Surface ocean waters are in contact with, and exchanging  $^{14}\text{C}$  with, both the atmosphere above and deeper waters below. These deeper waters have  $^{14}\text{C}$  that is already undergoing radioactive decay through long residence times before resurfacing through upwelling (Ulm, 2006). The ocean surface therefore has a  $^{14}\text{C}$  level that is somewhere between the atmosphere and the “older” deeper ocean, leading to marine samples having seemingly older radiocarbon ages than contemporaneous terrestrial samples (Sloss *et al.*, 2013). While this marine reservoir effect results in radiocarbon age determinations up to 400 years older than the true age, this correction also varies depending on local and regional factors such as terrestrial water input, upwelling and variations in inter-hemispheric atmospheric  $^{14}\text{C}$  (Petchey *et al.*, 2004; Ulm, 2006). These regional variations in the marine reservoir effect have been modelled and the results incorporated into the Marine13 calibration curve, with the assumption that the marine reservoir correction in an area has remained constant through time (Reimer *et al.*, 2013; Sloss *et al.*, 2013).

Two different methods can be used to measure  $^{14}\text{C}$  activity and obtain radiocarbon dates – standard radiometric dating and Accelerator Mass Spectrometry (AMS) dating. In standard radiometric dating, beta rays from the decay of  $^{14}\text{C}$  are measured using gas proportional or liquid scintillation counters (Sloss *et al.*, 2013). AMS dating counts carbon atoms directly, determining the ratio between the unstable radioactive  $^{14}\text{C}$  atoms and stable  $^{13}\text{C}$  (or  $^{12}\text{C}$ ) atoms (Schellmann and Bruckner, 2005; Cook and van der Plicht, 2007). AMS dating can be used for very small samples, between 0.1 and 2 mg of carbon instead of the 0.5 – 2 g of carbon that standard radiometric dating requires, and has a shorter measurement time but is more expensive than standard radiometric dating (Sloss *et al.*, 2013).

Whichever measurement technique is selected, care must be taken to remove all sample contamination prior to analysis, because samples contaminated with other carbon-containing material will lead to incorrect dates. For instance, younger roots and rootlets that penetrate a



sediment sample will result in age determinations younger than the true age of the sediment (Sloss et al., 2013). The recrystallization of shell carbonate from chemical exchange between the shell and the surrounding environment will alter the  $^{14}\text{C}$  and  $^{12}\text{C}$  ratio, also affecting the measured age (Mathews, 1982). Contaminants are removed from a sample via physical and chemical pretreatment, with pretreatments tailored to each individual sample and environment. Pretreatments applied to the samples from Albatross Bay are described in Section 3.4.2.

### 5.2.2 Results

Radiocarbon ages for all samples analysed at the Waikato Radiocarbon Laboratory are presented in Table 5.14. At Red Beach, the radiocarbon ages within the seaward beach ridges (from beach ridge 2, RR2, to swale RS5) increase with distance from the modern shoreline from a minimum age of 520 years BP at RR2 to a maximum of 1,680 years BP at RR5. Thereafter, the radiocarbon ages are significantly older, from approximately 3,000 to 5,000 years old, and there are age reversals within the sequence. These results will be discussed in the next chapter. At Kwamter, the age determinations are stratigraphically consistent and increase in age moving inland, with the shell deposit (KW03) estimated to between 2,870 and 3,170 years BP while the intertidal mangrove sediments below it are estimated to be between 6,400 and 6,490 years BP (KW06 178). At Wathayn, sediments from the mangrove fringe at the proximal end of the Wathayn beach ridge transect (WHA D06 48) are modern.

**Table 5.14: Conventional radiocarbon age determinations, calibrated mean age  $\pm 2 \sigma$  and corresponding age range for samples from Red Beach, Kwamter and Wathayn.**

Location	Sample Code		Facies code	Technique (AMS/standard)	Sample material	Species	Metres AHD (m)	Radiocarbon age $^{14}\text{C}$ yr BP (uncorrected)	Radiocarbon median age (cal. yr BP)	Radiocarbon age range (cal. yr BP)
	Field Code	Laboratory Code								
Red Beach - RR2	RB01 104-109	Wk42466	B3	Standard	Shell	Ostreidae	0.95	925 $\pm$ 42	595 $\pm$ 75	520 - 670
Red Beach - RS2	RB05 140	Wk42469	B3	AMS	Shell	Arcidae ( <i>Tegillarca granosa</i> )	0.13	1270 $\pm$ 20	910 $\pm$ 80	830 - 990
Red Beach - RR3	RB06 166	Wk42707	C1	AMS	Sediment	Organics	0.55	1502 $\pm$ 20	1405 $\pm$ 75	1330 - 1480
Red Beach - RR3	RB06 167	Wk47108	C1	AMS	Sediment	Organics	0.55	1506 $\pm$ 20	1425 $\pm$ 95	1330 - 1520
Red Beach - RR4	RB08 100	Wk42771	B3	Standard	Shell	Arcidae ( <i>Tegillarca granosa</i> )	1.33	1798 $\pm$ 26	1445 $\pm$ 85	1359 - 1530
Red Beach - RS5	RB09 103	Wk42470	B3	AMS	Shell	Arcidae ( <i>Tegillarca granosa</i> )	1.24	1922 $\pm$ 20	1595 $\pm$ 85	1510 - 1680
Red Beach - RR5	RB10 113	Wk42772	B3	Standard	Shell	Ostreidae	1.60	4672 $\pm$ 36	4978 $\pm$ 141	4837 - 5119
Red Beach - RR9	RB21 91	Wk42477	B3	Standard	Shell	Arcidae ( <i>Tegillarca granosa</i> )	1.15	4255 $\pm$ 44	4525 $\pm$ 155	4370 - 4680
Red Beach - RR11	RB18 115	Wk42475	B4	AMS	Shell	Cardiidae ( <i>Vasticarbiium verbratum</i> )	1.66	3238 $\pm$ 20	3210 $\pm$ 110	3100 - 3320
Kwamter - KMF2	KW03	Wk42465	C3	Standard	Shell	Arcidae ( <i>Tegillarca granosa</i> )	-0.08	3112 $\pm$ 46	3020 $\pm$ 150	2870 - 3170
Kwamter - KMF1	KW06 178	Wk42954	C1	AMS	Sediment	Organics	-1.32	5659 $\pm$ 20	6445 $\pm$ 45	6400 - 6490
Wathayn - W11	WHA D06 48	Wk42950	C1	AMS	Sediment	Organics	0.61	106.5 $\pm$ 0.3	Modern	Modern

### 5.3 Summary

OSL techniques have been widely employed in coastal research to establish chronologies of coastal evolution and sea level change. They are preferable to radiocarbon ages when dating coastal landforms because the event for which an estimated age is required is the sedimentary formation of each coastal feature rather than the radiocarbon age of shells that can be transported for a significant period prior to deposition, leading to misleadingly older dates. In this study, the coastal sediments being dated via OSL techniques are from foreshore environments, aeolian deposition on beach ridges, and supratidal mudflat environments. The OSL results from Red Beach indicate that these samples were well bleached prior to deposition, and the  $D_e$  for these samples were thus calculated using the CAM on single-aliquot discs. However, OSL results from the supratidal mudflat at Kwamter and the beach ridge at Wathayn indicate that these samples were only partially bleached. Therefore, the  $D_e$  for these samples and the beach ridge at Kwamter were calculated using single-grain analysis, with the CAM used when sample overdispersion was  $<20\%$  and the MAM used when sample overdispersion was  $>20\%$ .

OSL ages for the samples from Albatross Bay are summarised in Table 5.13. The beach ridge plain at Red Beach was built over the last approximately 2,300 years, with the oldest ridge forming approximately 2,250 years ago and the youngest ridge forming approximately 300 years ago. Apart from one anomalous result between ridge 8 (RR8) and ridge 11 (RR11), the burial ages obtained from Red Beach increase in age with distance from the modern beach. Generally, the ridges were formed between 100 to 300 years apart, with the largest age gap between ridges being approximately 570 years (from RR4 to RR5). The beach ridges at Kwamter and Wathayn are older than the beach ridges at Red Beach, having formed between approximately 3,000 to 4,000 years ago. The supratidal mudflat at Kwamter is younger than the Kwamter beach ridge, having been deposited approximately 800 years ago.

The radiocarbon ages from Albatross Bay (Table 5.14) present a slightly different picture. At Red Beach, the radiocarbon ages increase with distance inland within the seaward beach ridge set, but the radiocarbon ages from ridge 5 (RR5) to ridge 11 (RR11) are significantly older and an age reversal occurs between RR5, RR9 and RR11. The radiocarbon ages from Red Beach are also consistently older than OSL burial ages from the same pits (between approximately 227 years and 3,600 years older; see Section 6.1.2 for further discussion). At Kwamter the radiocarbon ages are stratigraphically consistent, with the deeper intertidal mangrove sediment deposit dating to approximately 6,400 years ago, and the

transgressive shell lag above it dating to approximately 3,000 years ago. The transgressive shell lag was deposited during the same period as accumulation of the beach ridge. At Wathayn East, the mangrove fringe seaward of the single beach ridge is modern.

In Chapter 6, the results presented here will be combined with the sediment analysis from Chapter 4 to construct a narrative of sea level change in Albatross Bay.

## **Chapter 6**

### **Coastal Evolution and Sea level Change at Albatross Bay**

In this chapter, the sediment analyses data (Chapter 4) and chronological data (Chapter 5) are combined to construct a record of coastal evolution and relative sea level change over the mid- to late- Holocene at Albatross Bay. Across Red Beach, Kwamter and Wathayn, four sedimentary facies, deposited over the past 6,500 years, were identified. Facies A is a clast-supported, pisoliths-dominated facies indicative of deposition in a high-energy coastal setting, most likely a tropical cyclone induced storm surge deposit. Facies B is a matrix-supported, sand-dominated facies, indicative of deposition within the beach zone. Facies C is a matrix-supported, silt- and clay-dominated facies indicative of deposition within nearshore, subtidal, intertidal and supratidal environments. Facies D is a matrix-supported, silt- and clay-dominated facies deposited within beach swales. These sea level proxies, illustrated in chrono-stratigraphic profiles constructed for each of the three field locations of Red Beach, Kwamter and Wathayn, are converted into sea level index points (SLIPs), from which a mid- to late-Holocene sea level curve for Albatross Bay is constructed. By comparing this sea level curve with the previous record of relative sea level change across the region, a narrative of mid- to late-Holocene relative sea level change in Albatross Bay is developed and presented at the end of the chapter.

#### **6.1 The record from Red Beach**

##### **6.1.1 Topography and sediment stratigraphy**

The topography and sedimentary stratigraphy of the modern beach and relict beach ridge plain at Red Beach have been described and illustrated in Chapter 4 (Figures 4.6 and 4.11). The source of the sediments deposited at Red Beach are terrestrial, as indicated by the presence of pisoliths originating in the Weipa and Andoom Plateaux. These are transported by the Embley, Pine and Mission Rivers and eventually deposited into Albatross Bay from where the coarser sediments (sand and pisoliths) are reworked into beach and beach ridge deposits (see Section 1.4.2). Therefore, the sedimentary facies at this location are largely composed of quartz sand, with variable amounts of gibbsitic pisoliths, whole and fragmented shell and shell hash (Section 4.4). Calcium carbonate cementation of the beach ridge deposits occurs at depth

within some of the beach ridges, inland of ridge RR4, forming a calcrete displaying increasing hardness with distance inland. Finer grained sediments (silts and clays) line the swales between the beach ridges inland of RR6 (Figure 6.3). Intertidal mudflat deposits underlie the beach ridge plain and are exposed seaward of the beachface at low tide (Figures 4.1, 4.18 and 6.3).

The beach ridges at Red Beach are grouped into two types, based on their facies composition. In Type 1 ridges, exemplified by RR2 (Figure 6.1), facies A alternates with facies B. Type 1 ridges are therefore built from a mixture of fair-weather swash deposits alternating with low frequency, high magnitude storm surge deposits. This alternating sedimentary record is also seen in the modern beach at Red Beach (see Section 4.1.1). In contrast, Type 2 ridges are composed solely of the sand-dominated facies B (Figure 6.2).

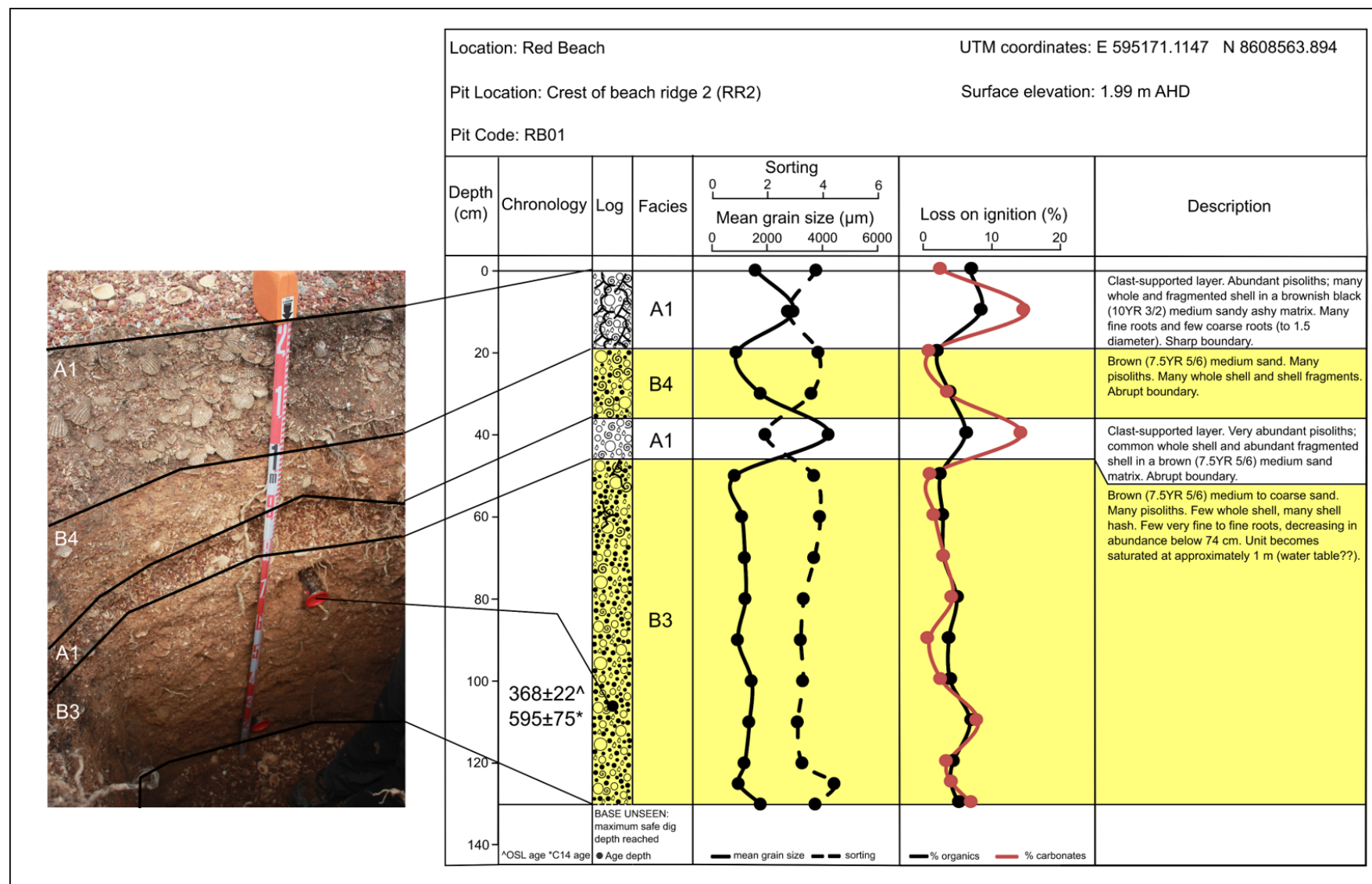


Figure 6.1: Sedimentary log for RR2, a type 1 beach ridge with alternating units of facies A and facies B.

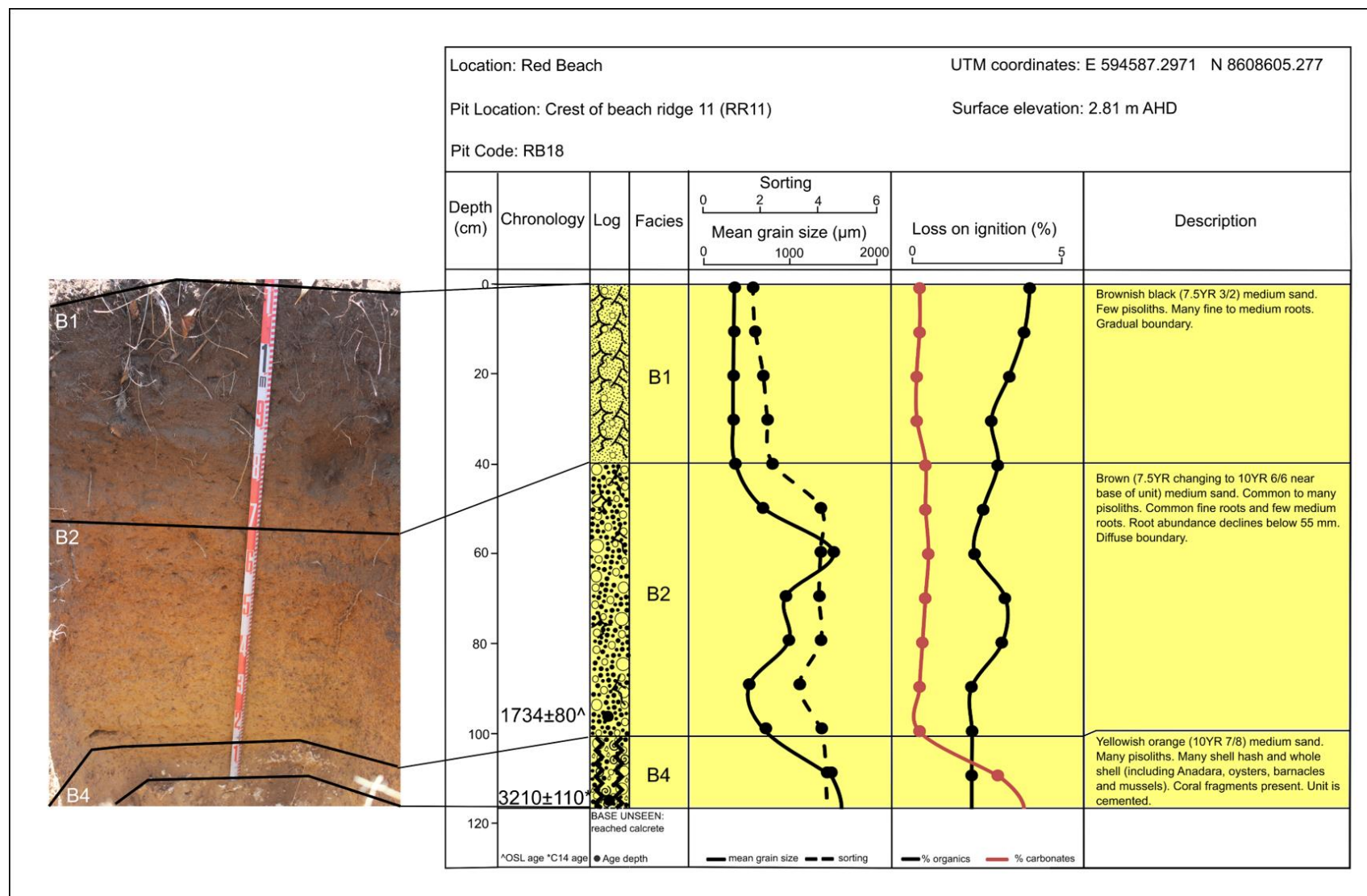


Figure 6.2: Sedimentary log for RR11, a type 2 beach ridge composed entirely of facies B deposits



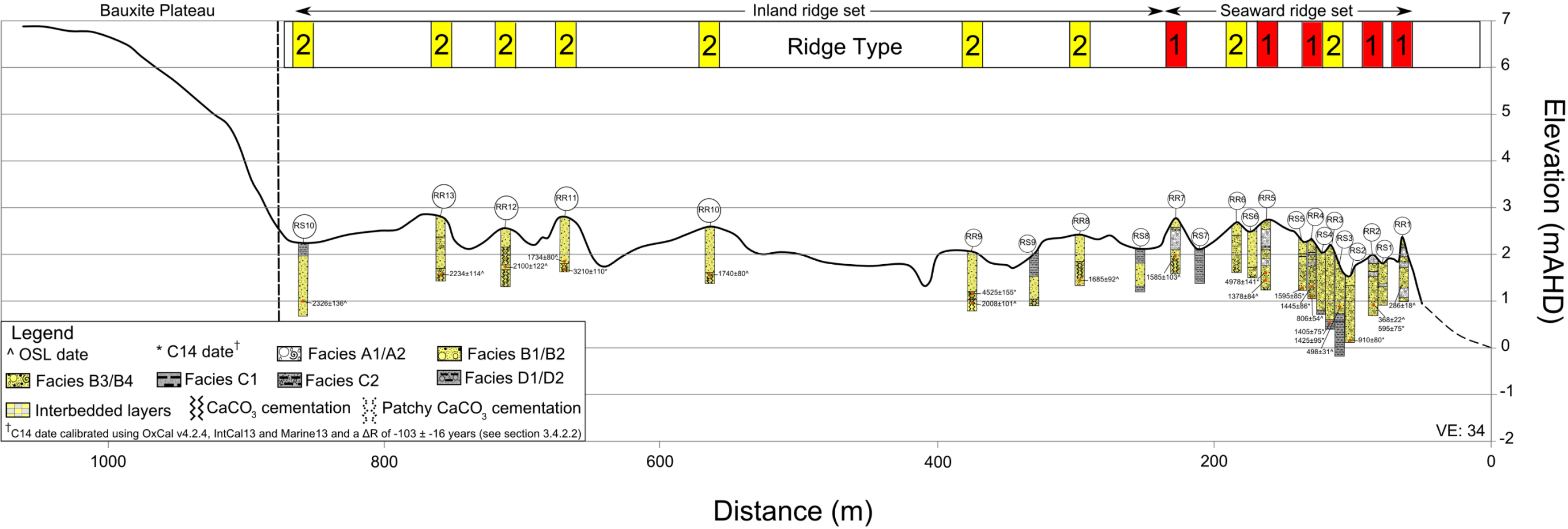


Figure 6.3: Chrono-stratigraphic profile across the beach ridge plain at Red Beach. Type 1 and Type 2 beach ridges are indicated (see text). Detailed sedimentary logs of each pit can be found in Appendix B

There is a marked change in the sediment stratigraphy of the beach ridges with distance inland, which coincides with a change in morphology described in Section 4.1.2. The seaward ridge set (from RR1 to RR7), where the ridges are lower in elevation, narrow and more closely spaced, is dominated by Type 1 ridges while the inland ridge set (from RR8 to RR13), where the ridges are at a higher elevation, wider and spaced further apart, comprises Type 2 ridges (Figure 6.3). In addition, the first five beach ridges in the seaward ridge set, those closest to the shoreline, have no aeolian capping. The remaining eight beach ridges are all capped by aeolian deposition.

The change in morphology and sediment stratigraphy is matched by a change in the rate of coastal progradation between the inland ridge set and the seaward ridge set (Table 6.1 and Figure 6.4). Within the inland ridge set, approximately 460 m of progradation (the distance from the RR8 ridge crest and RR13 ridge crest - Figure 6.3 and Figure 6.4) occurred between 1685 and 2234 years ago – a coastal progradation rate of 0.85 m/yr. Within the seaward ridge set, approximately 165 m of progradation (the distance from the RR1 ridge crest and the RR7 ridge crest – Figure 6.3 and Figure 6.4) occurred between 286 and 1585 years ago – a coastal progradation rate of 0.13 m/yr. Note that there is a decline in the rate of coastal progradation between RR12 and RR11 (Table 6.1 and Figure 6.4). There is an overlap in ages between RR7 and RR11, with these ridges forming between approximately 1,600 to 2000 years ago, possibly due to either a period of rapid coastal progradation or the analytical uncertainty associated with OSL dating (see Section 6.12 below). Accordingly, RR11 may have been deposited prior to  $1734 \pm 80$  years ago, which would increase the rate of coastal progradation. In any case, this period of lower coastal progradation is sandwiched between two phases of higher progradation from approximately 1,600 years ago to 2,300 years ago. These marked changes in morphology, sediment stratigraphy and coastal progradation rates between the inland ridge set and the seaward ridge set indicate significant changes in the drivers of coastal evolution at Red Beach, discussed in more detail in Section 6.1.4.

**Table 6.1: Coastal progradation rates at Red Beach. Beach ridges are grouped together when the OSL ages overlap (see Section 6.1.2).**

Ridges	R510 to R12 (Ages overlap, maximum and minimum ages in this ridge set selected)	RR12 to RR11	RR11 to RR7 (Ages overlap, max and min ages in this ridge set selected)	RR7 to RR5	RR5 to RR4	RR4 to R53	R53 to RR2	RR2 to RR1	RR1 to present	RR13 to RR8 (Inland ridge set)	RR7 to RR1 (Seaward ridge set)
Age from	2326 ± 136	2100 ± 112	2008 ± 101	1585 ± 103	1378 ± 84	806 ± 54	498 ± 31	368 ± 22	286 ± 18	2234 ± 114	1585 ± 103
Age to	2100 ± 112	1734 ± 80	1585 ± 103	1378 ± 84	806 ± 54	498 ± 31	368 ± 22	286 ± 18	0	1687 ± 92	286 ± 18
Duration (years)	226	366	423	207	572	308	130	82	286	547	1299
Distance prograded	146.36	42.43	441.56	65.51	33.17	17.74	26.95	20.74	64.40	462.26	164.11
Progradation rate (m/yr)	0.65	0.12	1.04	0.32	0.06	0.06	0.21	0.25	0.23	0.85	0.13

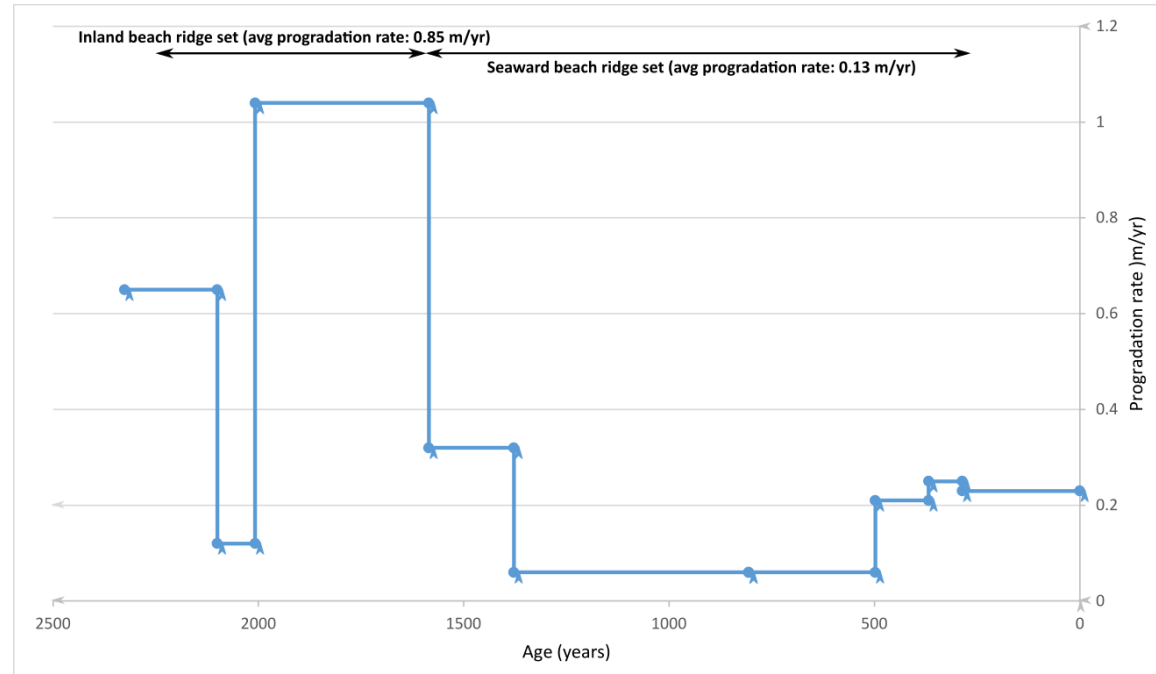


**Figure 6.4: Coastal progradation over the mid to late Holocene at Red Beach based on the data contained in Table 6.1.**

### 6.1.2 OSL and radiocarbon chronology

The OSL and radiocarbon age determinations described in Chapter 5 are used here to build a chronology for beach ridge plain development at Red Beach. The OSL burial ages at Red Beach show that the beach ridge plain increases in age progressively landwards with the youngest ridge returning an age of  $286 \pm 18$  years ago and the most inland ridge returning an age of  $2234 \pm 114$  years ago. There does not appear to be any significant age gaps in the record, with the largest age gap, between ridges RR4 and RR5, of approximately 570 years. Generally, the ridges were formed between 100 to 300 years apart (Table 5.13).

As indicated in Figure 6.5, there is an OSL age reversal between ridges RR8 and RR11. While the error margins in these ages do not overlap, the OSL ages for these ridges are still close, with the lower OSL age for RR9 (1907 years ago) differing from the upper age of RR10 (1820 years ago) by less than 100 years (Table 5.13). The ridges on either side of RR9 and RR10 (from RR7 to RR11) have OSL ages that overlap within error margins. There is another age overlap between RR12, RR13 and the most inland swale (RS10) (Figure 6.5). These overlapping ages could be reflective of either a period of rapid coastal progradation or the analytical uncertainty associated with OSL age estimation (Nott *et al.*, 2009; Tooth, 2015). Even with these overlapping OSL ages, however, there is a clear trend of increasing age with distance from the shoreline within the beach ridge sequence at Red Beach.

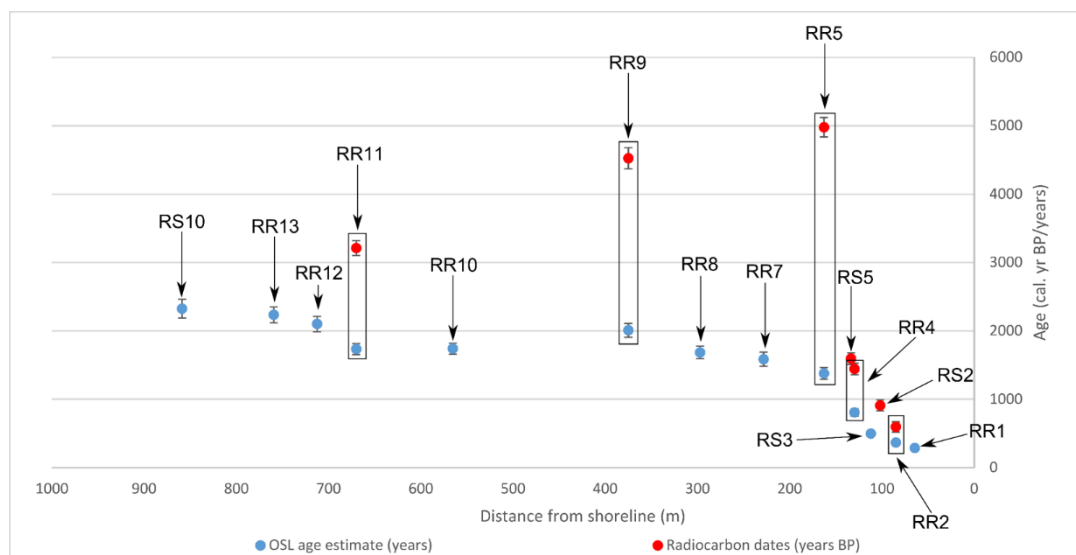


**Figure 6.5:** OSL and radiocarbon ages from the beach ridge plain at Red Beach plotted against the distance from the shoreline. Standard errors are indicated with vertical black bars. Radiocarbon ages from RR3 (RB06 166 and RB06 167) were excluded as these samples were collected from the intertidal sediments below the beach ridge plain and would not be comparable with the beach ridge OSL burial ages. Radiocarbon ages have been calibrated using OxCal v4.2.4, IntCal13 and Marine 13, using a  $\Delta R$  of  $-103 \pm 16$  (see Section 3.4.2.2).

Radiocarbon ages for shell samples collected from the beach ridge plain are also shown in Figure 6.5. The radiocarbon ages are all older than the OSL burial ages from the same ridge, even where the radiocarbon samples were from higher in the profile than the OSL samples (Tables 5.13 and 5.14, Figures 6.3 and 6.5). The largest difference between the radiocarbon and OSL ages is approximately 3600 years within RR5. Other studies have found similar discrepancies between OSL burial ages and radiocarbon ages within coastal environments, with the radiocarbon dates being consistently older than the OSL ages (Stapor Jr *et al.*, 1991; Murray-Wallace *et al.*, 2002; Rink and Forrest, 2005; Gao, 2013; Oliver *et al.*, 2015). For instance, in their study of the relict foredunes at Guichen Bay, South Australia, Murray-Wallace *et al.* (2002) found that radiocarbon ages obtained from the analysis of shell hash were older than the OSL burial ages by up to 2,710 years. Similarly, at Cape Canaveral in North America, Rink and Forrest (2005) found that radiocarbon dating of shells may have resulted in an overestimation of beach ridge formation by several thousand years.

As discussed in Section 5.1.1, this discrepancy occurs because the event being dated with radiocarbon is the time of death of the organism, whereas the event being dated with OSL techniques is the time of the last exposure to sunlight (i.e., the burial event). Shells in coastal environments are subject to reworking, leading to the introduction of older shell into younger sedimentary deposits and therefore an overestimation in age of the depositional event when using radiocarbon techniques (Smart, 1976b; Murray-Wallace *et al.*, 2002; Rink and Forrest,

2005; Hendricks and Hodson, 2015; Hart *et al.*, 2017). Such overestimation in radiocarbon ages can be seen in studies of modern shell deposits, where radiocarbon ages vary from modern to hundreds or even several thousand years old (Flessa *et al.*, 1993; Carroll *et al.*, 2003; Hendricks and Hodson, 2015). Therefore, the chronology of beach ridge plain formation at Red Beach discussed in the subsequence sections is based on the OSL age determinations.

The OSL ages from the beach ridge plain at Red Beach are in general agreement with radiocarbon ages obtained by Hayne (1992, in Stone, 1995) from the beach ridge plain at Botchet Beach, to the west of Red Beach (Figure 3.1). As shown in Table 6.2, the earliest estimated age for beach ridge formation at Botchet Beach obtained by Hayne (1992, in Stone, 1995) was  $2440 \pm 60$  radiocarbon years BP. This age is similar to the OSL burial ages obtained in this study for the distal ridge RR13 and the distal swale RS10 at Red Beach, especially considering that the radiocarbon ages for Botchet Beach were on shells which may overestimate the timing of the depositional event. Other similarities exist between the Botchet Beach and Red Beach age determinations (Table 6.2), although caution should be exercised in using Hayne's data. While the two beach ridge plains are geographically close, there are different numbers of beach ridges at the two locations (approximately seven or eight beach ridges at Botchet beach compared with thirteen at Red Beach). The Botchet Beach ages are also from shells collected from variable depths within the beach ridge crests, and not all ridge crests were dated (see Figure 3.5 in Stone, 1992).

**Table 6.2: Comparison of OSL burial ages from beach ridges at Red Beach (this study) and conventional radiocarbon ages from beach ridges at Botchet Beach (Hayne, 1992, in Stone, 1995, Figure 3.5).**

Location (this study)	Burial Age (years)	Location (Hayne, 1992)	Age (radiocarbon years BP)
Red Beach - RR1	$286 \pm 18$	Botchet Beach - front	$220 \pm 50$
Red Beach - RR2	$368 \pm 22$	Botchet Beach - front	$340 \pm 85$
Red Beach - RS3	$498 \pm 31$		
Red Beach - RR4	$806 \pm 54$	Botchet Beach - middle	$710 \pm 95$ and $1010 \pm 85$
Red Beach - RR5	$1378 \pm 84$		
Red Beach RR7	$1585 \pm 103$	Botchet Beach - middle	$1420 \pm 70$
Red Beach - RR8	$1685 \pm 92$		
Red Beach - RR9	$2008 \pm 101$	Bochet Beach - middle	$1920 \pm 60$
Red Beach - RR10	$1740 \pm 80$		
Red Beach - RR11	$1734 \pm 80$		
Red Beach - RR12	$2100 \pm 112$		
Red Beach - RR13	$2234 \pm 114$	Botchet Beach - rear	$2070 \pm 70$
		Botchet Beach - rear	$2440 \pm 60$
Red Beach - RS 10	$2326 \pm 136$		

Bailey *et al.* (1994, p. 74) obtained similar ages on shell from Botchet Beach ( $2230 \pm 80$  radiocarbon years BP from the rear of ridge plain and  $1120 \pm 90$  radiocarbon years BP from the middle of ridge plain) and from Urquart's Point ( $2510 \pm 90$  radiocarbon years BP from the rear of the beach ridge plain,  $2190 \pm 80$  radiocarbon years BP from the middle of the beach ridge plain and  $950 \pm 80$  radiocarbon years BP from the front of beach ridge plain). The radiocarbon date from the rear and middle of the beach ridge plain at Urquart's Point is similar to the age obtained from the rear of the Red Beach beach ridge plain. However, the radiocarbon date from the front of the beach ridge plain at Urquart's point is older than that at Red Beach, indicating that coastal progradation may have ceased earlier at Urquart's Point than at Red Beach, possibly a result of a lack of sediment accommodation space due to the configuration of the current coastline. Notwithstanding the common greater age determinations for shells compared with their containing sediment deposits (see Section 6.1.2), the similarity of these ages indicates a similar history of sea level change and coastal progradation at Red Beach, Botchet Beach and Urquart's Point.

Not all beach ridge plain radiocarbon age records from around Albatross Bay match well with the Red Beach record. At Red Beach itself, Stone (1995) obtained eight radiocarbon age determinations on shells from the seaward beach ridge sequence (RR1 to RR9). The conventional radiocarbon dates of  $4530 \pm 80$  and  $2850 \pm 70$  years BP from the two inland ridges (Stone, 1995, p. 85) are significantly older than the OSL burial dates for Red Beach from this study. A conventional radiocarbon age from shell from the youngest beach ridge is also older than the dates obtained from Red Beach and Botchet Beach, at  $790 \pm 220$  years BP. However, the radiocarbon ages obtained for this study are also significantly older than the OSL burial ages, most likely due to prolonged transport and reworking of shells prior to final deposition (see Section 6.1.2). The radiocarbon dates on shell obtained by Stone (1995) are therefore unlikely to be representative of beach ridge formation and progradation at Red Beach. Stone (1995, p. 92) himself states that the radiocarbon ages obtained from Red Beach "... must be interpreted with caution..." due to the possibility of reworking.

### 6.1.3 Initiation of beach ridge plain formation

Sediment deposition at Red Beach, leading to the commencement of beach ridge formation, was initiated approximately 2,300 years ago (Table 6.2). As discussed in Chapter 3 (Section 3.1.2), the formation of beach ridges and beach ridge plains is influenced by (1)

changes in storminess in an area, (2) changes in relative sea level and (3) changes in sediment supply (Taylor and Stone, 1996; Engel *et al.*, 2014; Kelsey, 2015; Oliver *et al.*, 2016).

#### 6.1.3.1 Changes in storminess

The inland beach ridge set is composed of only Type 2 beach ridges (Figure 6.3), constructed by a combination of fair-weather swash processes and aeolian deposition (Facies B – Section 4.4). The absence of Facies A (high energy storm surge deposits) within the inland beach ridge set does not eliminate the possible occurrence of tropical cyclone induced storm surge events over this period (between approximately 2,300 and 1,700 years ago) but any such events may have either not resulted in any detectable sediment deposition at Red Beach, or subsequent erosion of any sediment that was deposited. However, it is unlikely that tropical cyclone events, and thus a change in storminess, were a significant contributor to the formation of the inland beach ridge set. In contrast, the seaward beach ridge set, a mixture of Type 1 and Type 2 beach ridges (Figure 6.3), were built by a combination of fair-weather swash processes, low frequency, high magnitude tropical cyclone-induced storm surge events, and aeolian deposition (see Section 6.1.1). Environmental changes that may have driven such changes in the processes of formation of the beach ridges are discussed in more detail below.

#### 6.1.3.2 Changes in relative sea level

Relative sea level was already changing prior to the commencement of coastal progradation at Red Beach. Previous studies around the GoC suggest that relative sea level reached a mid-Holocene highstand of between approximately +1 to + 2 m above PMSL by about 6,600 years BP and may have remained at this highstand for around 1,500 years before falling gradually to its present position (see Section 2.4). However, ridge formation did not occur at Red Beach for several thousand years following the mid-Holocene sea level highstand. This may be because beach ridge formation may have occurred, but these ridges were subsequently eroded prior to 2,300 years ago. Alternatively, following the mid-Holocene highstand, the mouth of the Mission River, where Red Beach is located, could have been characterised by deep water with little sediment. It may have taken several thousand years for sediment to accumulate at the mouth of the Mission River resulting in the coastal zone at Red Beach being shallow enough with enough sediment to commence beach ridge formation.

#### 6.1.3.3 Changes in sediment supply

Palaeoenvironmental studies from the Weipa region suggest that a change in climate, from a drier to a wetter regime, occurred at the time of commencement of coastal progradation



at Red Beach. This change in climate to a wetter regime may have led to an increase in sediment supply to Red Beach. Pollen, diatom and sedimentological analysis of cores from Big Willum swamp on the Weipa plateau (Stevenson *et al.*, 2015a; Proske *et al.*, 2017) indicate that wetlands on the bauxite plateau were ephemeral between approximately 5,700 and 2,200 years BP and sedimentation into Big Willum swamp was very low, at approximately 0.01 mm/year (Table 6.3) (Proske *et al.*, 2017). The sedimentation rate in Big Willum swamp then increased to approximately 0.03 mm/year after 2,200 years BP, and to approximately 0.20 mm/year around 1340 years BP, indicating that the environment became wetter over this time period leading to Big Willum swamp transitioning from an ephemeral to a permanent water body (Table 6.3) (Stevenson *et al.*, 2015a; Proske *et al.*, 2017). Brockwell *et al.* (2017) report that wetland expansion in the headwaters of Bellevue Creek and Running Creek, located near Big Willum swamp, also began after 2,200 years BP, further evidence for a transition to a wetter environment.

**Table 6.3: Sedimentation rates at Big Willum Swamp, on the Weipa Plateau. (Source: data modified from Stevenson *et al.*, 2015, Table 2).**

Location	Core code	Laboratory number	Sample Depth (mm)	Calibrated Age (years BP)	Sedimentation rate (mm/year)	Environmental interpretation
Big Willum Swamp	BW01	Wk 34027	110	930	0.12	Wetter
Big Willum Swamp	BW01	Wk 34028	190	1340	0.20	Wetter
Big Willum Swamp	BW01	Wk 35162	220	2240	0.03	Wet
Big Willum Swamp	BW01	Wk 35163	260	5660	0.01	Dry

Other palaeoenvironmental records around the Albatross Bay region also support a transition from drier to wetter conditions during the late Holocene. Palynological evidence from the islands of Torres Strait indicate that freshwater swamps became established or expanded in the interior of the islands over the last 2,600 years, linked to an increase in freshwater supply (Rowe, 2007). Further north, Steinke *et al.* (2014) examined an offshore sediment core collected from the eastern Lombok Basin in Indonesia and, based on bulk sediment element analysis, concluded that terrigenous input, and therefore rainfall, increased after 2,800 years BP, with a further increase in rainfall after approximately 1,200 years BP. Mohtadi *et al.* (2011) also noted an increase in effective precipitation in the region over the past 2,500 years, based on a sediment core collected off South Java.

The increase in effective precipitation at Big Willum Swamp and other locations to the north of Australia appears, however, to contradict other terrestrial records from northern Australia. Climatic reconstructions show that the initiation of El Niño-Southern Oscillation (ENSO) cycles within the Australasian region occurred at approximately 4000 years BP (Shulmeister and Lees, 1995; Shulmeister, 1999; Markgraf and Diaz, 2000; Gagan *et al.*, 2004; Reeves *et al.*, 2013a). When El Niño conditions are in place, there is generally a reduction in effective precipitation in northern Australia, while La Niña conditions lead to an increase in effective precipitation (Shulmeister and Lees, 1995; Donders *et al.*, 2007; Reeves *et al.*, 2013a). Synthesis of climatic records across northern Australia indicate that El Niño conditions, more extreme than present day, were in place between approximately 2,500 and 1,700 years ago (Reeves *et al.*, 2013b), with accompanying decreased rainfall and a hiatus in coastal progradation across northern Australian. At Bentick Island in southwestern GoC, Twaddle *et al.* (2017) noted a possible hiatus in coastal progradation between 3,000 and 1,900 years BP due to a decline in precipitation during this time period. At Groote Eylandt in the western GoC, pollen records examined by Shulmeister (1992) indicate that effective precipitation declined after 3,800 years BP and only increased again after approximately 1,000 years BP. Other records that infer decreased precipitation in northern Australia during this time period include a stalagmite record from the Kimberley region of WA (Denniston *et al.*, 2013), chenier plain and coastal dune records across northern Australia (Lees and Clements, 1987; Lees *et al.*, 1990) and pollen records across eastern Australia (Donders *et al.*, 2007). The initiation of the ENSO cycles within the Australasian region has also been associated with increased climatic variability (Shulmeister and Lees, 1995; Shulmeister, 1999; Markgraf and Diaz, 2000; Gagan *et al.*, 2004; Donders *et al.*, 2007; Reeves *et al.*, 2013a; Reeves *et al.*, 2013b; Proske *et al.*, 2017). At Groote Eylandt, for example, while pollen records indicate an increase in effective precipitation only after 1,000 years BP, aeolian dunes may have stabilised as early as 2,300 years BP due to an increase in effective precipitation (Shulmeister and Lees, 1992).

The cause of the increase in rainfall at Big Willum swamp is therefore unclear, with either increasing climatic variability associated with the initiation of ENSO cycles (Proske *et al.*, 2017), or a process that counteracts the strengthened ENSO signal, leading to an increase in effective rainfall. For instance, Shulmeister and Lees (1995, p. 14) state that an apparent increase in effective precipitation over the last 1,000 to 2,000 years from various records from across northern Australia may be because “... increasing summer insolation in the Southern Hemisphere is strengthening the monsoon...”. The fact remains that sedimentation increased

in Big Willum swamp after 2,200 years BP, most likely due to increased effective precipitation. This increased wetness would have also resulted in increased sediment discharge from the rivers in the area, leading to a greater sediment supply into Albatross Bay and hence the commencement of ridge building at Red Beach.

#### 6.1.4 Changes in the tempo of beach ridge plain progradation

As the beach ridge plain at Red Beach continued prograding, , there was a change in the morphology and sedimentology of the sequence from the inland ridge set to the seaward ridge set, with the inland ridge set (from RR8 to RR13) being at a higher elevation, wider, spaced further apart and comprising Type 2 ridges, while the seaward ridge set (from RR1 to RR7) has ridges that are lower in elevation, narrower, more closely spaced and dominated by Type 1 ridges (see Section 6.1.1). This change in the beach ridge sequence at Red Beach appears to have taken place around  $1685 \pm 92$  to  $1585 \pm 103$  years ago (Figure 6.3), implying a change in ridge formation processes (relative sea level, sediment supply and/or storminess) during and after this period.

##### 6.1.4.1 Change in relative sea level

Within the GoC, previous studies indicate that relative sea level was falling smoothly from a maximum of approximately +2.4 m above PMSL about 6,000 to 4,000 years ago to PMSL (see Section 2.4). Therefore, it is likely that the entire Red Beach beach ridge plain formed in response to falling sea levels along with an increase in sediment supply. However, current literature does not mention any abrupt changes in relative sea level within the GoC, northern or eastern Australia around 1,700 years ago (see Chapter 2). Thus, the change in the morphology and sedimentology of the beach ridge sequences at Red Beach is probably due to a combination of changes in sediment supply and/or storminess during this time period, rather than a change in relative sea level.

##### 6.1.4.2 Change in sediment supply

A change in sedimentation rates occurred during this time at Big Willum Swamp, where rates increased from 0.03 mm/year to 0.20 mm/ year after 1,340 years BP (Table 6.3). Stevenson *et al.* (2015a) and Proske *et al.* (2017) did not, however, comment on this increase in sedimentation rate. Elsewhere across northern Australia, evidence indicates that strong La Niña conditions persisted between approximately 1,500 to 1,000 years ago (Markgraf and Diaz, 2000; Rein *et al.*, 2004; Mann *et al.*, 2009; Williams *et al.*, 2010; Moss *et al.*, 2015). A period of strengthened La Niña conditions would intensify moist monsoonal winds, increasing

precipitation to affected areas (Donders *et al.*, 2007; Engel *et al.*, 2014) such as Albatross Bay, which in turn may explain the increase in sedimentation rate at Big Willum Swamp after 1,340 years BP. This purported increase in effective precipitation, and hence sediment supply, is not, however, reflected in the rate of coastal progradation at Red Beach, which instead decreased from an average of 0.85 m/yr to 0.13 m/yr after approximately 1,600 years BP (see Section 6.1.1). A change in sediment supply is therefore unlikely to be the primary cause of the observed change in morphology and sedimentology of the Red Beach beach ridge sequence from the inland ridge set to the seaward ridge set.

#### 6.1.4.3 Change in storminess

The developing La Niña conditions between 1,500 to 1,000 years ago most likely resulted in an increase in the frequency of tropical cyclones that made landfall in the area. Flay and Nott (2007) present a model of tropical cyclone landfalls in Queensland driven by ENSO cycles, stating that during La Niña periods there is an increase in tropical cyclone activity, with a concomitant increase in tropical cyclones making landfall. At Red Beach, tropical cyclone storm surge deposits (the origin of Facies A – Section 4.4) begin to appear within the seaward ridge set around 1,600 years ago (Figure 6.3). The increase in tropical cyclones making landfall at Red Beach would lead to “... more frequent storm cut and less persistent fill in the intervening swell-dominated periods...” (Oliver, 2016, p. 12). Therefore, while there was most likely an increased sediment supply at Red Beach derived from increased precipitation and hence increased runoff and erosion from the catchments, coastal progradation slowed most likely due to erosion of the shoreline during tropical cyclone events. At the same time as the shoreline was being eroded, however, the tropical cyclone-induced storm surges transported and deposited coarse-grained sediments on the beach, resulting in the sediment stratigraphy observed at Red Beach (see Section 4.1 and 4.4). In his study of the cheniers and beach ridges within the southeastern GoC, Rhodes (1980, p. 283) also notes how “...storms may cause deposition as well as erosion depending on their timing...”.

A similar process of composite beach ridge formation has been observed at Cowley Beach along the northeastern coast of Australia, just south of Innisfail (Figure 2.11). The beach ridges in this location originate from fair-weather swash deposition, occasionally punctuated by erosion of the beach face or berm during tropical cyclone events, leading to the formation of a beach scarp. At higher elevations, the tropical cyclone induced storm surge deposits overwash layers onto the beach ridge (Tamura *et al.*, 2018). While beach scarps were not observed within the pits dug along the Red Beach transect, application of Ground Penetrating

Radar (GPR) techniques may provide more detail on the internal structure of the beach ridge plain.

Records of tropical cyclone incidence in north Queensland, Australia, have generally been interpreted as reflective of constant cyclone frequency over the past 5,000 years, rather than increasing approximately 1,500 years ago (Chappell *et al.*, 1983; Chivas *et al.*, 1986; Hayne and Chappell, 2001). However, some records of tropical cyclone activity from Australia do reflect an increase in cyclone activity at this time. Nott and Forsyth (2012) compiled sedimentary records of tropical cyclones across Australia to examine hiatuses in global tropical cyclone activity over the mid- to late-Holocene, including data from the chenier ridge plain at Karumba, within the GoC, investigated by Rhodes (1980). Rhodes (1980) focused on reconstructing sea level history and coastal progradation, stating that there was insufficient data at the time of his study to examine the relationship between the Karumba chenier ridge plain record and tropical cyclone activity. Therefore, the conclusions from Nott and Forsyth (2012) are discussed here rather than referring to the original source material of Rhodes (1980).

As the tropical cyclone record of Nott and Forsyth (2012) was derived from either sand or shell beach ridges, there may be biases in the data, with only stronger tropical cyclones resulting in the formation of these storm-built beach ridges rather than all tropical cyclone activity. Furthermore, the storm-built beach ridges will only record tropical cyclones that make landfall. The erosion of existing beach ridges or a decrease in sediment supply will also impact ridge development. However, Nott and Forsyth (2012) compiled this data from five fieldsites across northeastern, northern and Western Australia, and observed similarities across the northern and Western Australia tropical cyclone record, strengthening this reconstruction.

According to Nott and Forsyth (2012), there were four phases of active tropical cyclone activity within the GoC over the last 7,500 years BP – between 7,500 and 5,500 years BP, between 3,500 and 2,700 years BP, between 1,800 and 1,000 years BP and from 500 years BP to the present. This record of tropical cyclone activity matches well with the sedimentary record at Red Beach. Only Type 2 ridges, constructed by a combination of fair-weather swash processes and aeolian deposition (see Section 6.1.1), are present between 2,300 years ago, when the coastline began prograding, and 1,700 years ago (the inland beach ridge set) (Figure 6.3). Beginning  $1,585 \pm 103$  years ago (RR7), Type 1 ridges, built by a combination of fair-weather swash processes, low-frequency high-magnitude tropical cyclone-induced storm surge events, and aeolian deposition, began to appear in the beach ridge plain (see Section 6.1.1).

Nott and Forsyth (2012) report a period of tropical cyclone inactivity between 1,000 and 500 years BP. At Red Beach during this period, only one beach ridge (RR4) was deposited (Figure 6.3). This age gap between the deposition of RR5 ( $1,378 \pm 84$  years ago) and the deposition of RR4 ( $806 \pm 54$  years ago) may be reflective of this period of tropical cyclone inactivity reported by (Nott and Forsyth, 2012). RR4 is a Type 1 ridge, implying that there were tropical cyclones occurring at the time of its formation. However, the facies A deposits within this ridge are the thinnest within the Red Beach record, indicating that tropical cyclones may have been lower in strength or shorter in duration at this time (Figure 6.3, Appendix B). The next beach ridge, RR3, was deposited approximately  $498 \pm 31$  years ago, coinciding with the renewal of tropical cyclone activity within the GoC from 500 years to present.

#### 6.1.5 Sea level history and shoreline evolution at Red Beach

The unconformity between the beach ridges and underlying intertidal mud, described in Sections 4.1 and 6.1.1, marks the elevation of sea level at the time of formation of the beach ridges and is used here to reconstruct past sea level at Red Beach (see Section 6.4 below for a more detailed explanation of the use of sedimentary unconformities as sea level index points, or SLIPs). The beach ridge – intertidal mudflat boundary was exposed in the pits excavated into ridge RR3 and swales RS3 and RS4 (Figure 6.3). Inland from RR4, most of the pits terminated at the top of the calcrete unit, due to difficulty of excavating by hand through this material. The precise thickness of the calcrete within each pit therefore cannot be determined. However, it is likely that the calcrete immediately overlies the intertidal mudflat, having formed where changing hydrological conditions from more permeable beach ridge sands to less permeable intertidal mudflat deposits lead to reprecipitation of  $\text{CaCO}_3$  (see Section 4.1.2). Mean sea level over the late Holocene at Red Beach is therefore assumed to be below the beach ridges RR1 and RR2, at the elevation of the beach ridge-intertidal mudflat boundary below RR3, and is then extrapolated to below the  $\text{CaCO}_3$ -cemented sediments across the remainder of the beach ridge plain (see Figure 6.19 and discussion in Section 6.4).

The evidence described above indicates that, at the commencement of coastal progradation at Red Beach approximately 2,200 years ago, sea level was approximately +0.5 to +1 m AHD. Relative sea level was either stationary or, if it did change, sea level fell gradually between 2,200 and 1,700 years ago, across the inland beach ridge set, with the coastal progradation signal dominated by the increase in sediment supply described above. A gradual change in sea level after 2,200 years ago is indicated by two observations. Firstly, the bases of the pits dug into ridges RR13 to RR8 are all around the same elevation. While these pits do not

contain the entire sedimentary record at Red Beach because they only penetrated as far as the calcrete unit, and the thickness of the calcrete is unknown, the base of the inland ridge set is still less variable than the seaward ridge set (Figure 6.3). Secondly, as discussed in Section 6.1.2 above, several of the OSL burial ages, from RR12 to RR13 and RR7 to RR11, overlap, possibly reflective of periods of rapid coastal progradation at a relatively stable sea level.

Between approximately 1,700 and 1,600 years ago (i.e., between the formation of RR8 and RR7; Figure 6.3), while relative sea level was still stationary or falling gradually towards PMSL, the paleoenvironment at Red Beach most likely shifted from an El Niño to a La Niña-dominant phase, resulting in an increase in the frequency of tropical cyclones and an increase in sediment supply, as indicated by the sedimentary record at Big Willum swamp, previously described. Increased erosion associated with the increase in tropical cyclone frequency may have resulted in the beach ridges becoming more closely-spaced, narrower, and dominated by Type 1 ridges.

The sea level record from Red Beach matches well with regional sea level records. Within the GoC, sea level reconstructions indicate that, by 2,300 years ago, relative sea level was already falling from a highstand of +1 to +2 m above PMSL that was reached at approximately 6,500 years BP (Rhodes, 1980). Moss *et al.* (2015) state that at Bentick Island in the southwestern GoC, sea level fall from approximately 2,400 years ago led to the development of a prograding beach ridge system. Studies from the McArthur River delta (Woodroffe and Chappell, 1993), the Mitchell River delta (Nanson *et al.*, 2013) and the Gilbert River delta (Jones *et al.*, 1993) all point towards coastal progradation commencing approximately 4000 to 6000 years ago in response to sea level fall, although high-resolution reconstructions of the nature of this sea level fall were not provided (see Section 2.4).

In reviewing sea level data across eastern Australia, Larcombe *et al.* (1995) and Lewis *et al.* (2008) found that, rather than sea level falling smoothly to PMSL after reaching a maximum prior to approximately 6,000 years ago, relative sea level remained at the maximum height before falling to PMSL after 2000 years BP. Similarly, at Cleveland Bay in North Queensland, Woodroffe (2009b) found that, after reaching a maximum of approximately +2.8 m above PMSL about 6,200 years BP, relative sea level fell to between +1.3 m to +2.1 m above PMSL by approximately 3,700 years BP. Sea level remained at this elevation until 2,300 years BP, before falling to +1 m above present prior to 1,500 BP and then subsequently falling to PMSL. At Magnetic Island, relative sea level remained at a mid-Holocene highstand of

between +1 m and + 1.6 m above PMSL until approximately 2,200 years ago before falling to PMSL (Yu and Zhao, 2010) (see Section 2.3).

Across northern Australia evidence for a mid-Holocene sea level highstand and subsequent sea level fall is sparse (see Section 2.2). At Buckley's Plain in Broome, upper intertidal mudflat sediments, deposited +1 m above present MHW and radiocarbon dated to  $2,836 \pm 83$  years BP, led Lessa and Masselink (2006) to conclude that relative sea level was at least +1 m above PMSL during the mid-Holocene, falling to PMSL within the last 2,000 years. Other studies by Woodroffe *et al.* (1992) and Engel *et al.* (2014) also indicate sea level falling from a mid-Holocene highstand of at least +1 m above PMSL, though the timing of this sea level fall is unclear (see Section 2.2).

## **6.2 The record from Kwamter**

### **6.2.1 Topography and sediment stratigraphy**

The topography and sedimentary stratigraphy of the estuarine floodplain and beach ridge at the Kwamter study location have been described and illustrated in Chapter 4 (Figure 4.22). The sedimentary facies here range from quartz sand with few quartz granules within the beach ridge crest, to silty sand within the beach ridge swale and across the supratidal mudflat (Section 4.4).

The deepest deposit reached beneath the supratidal mudflat (in pits KMF1 and KMF2) is sub-facies C1, an intertidal sediment deposited in a mangrove environment (Figure 6.6 and Figure 6.7; Section 4.4.3). The intertidal mangrove sediments were then overlain by a thin unit (approximately 5 cm thick) of intertidal mudflat sediments (sub-facies C2). These were overlain, in turn, by sub-facies C3, interpreted as a transgressive shell lag (see Section 4.4.3.6). The shell lag deposit is approximately 14 cm thick at the proximal edge of the supratidal mudflat, in pits KMF1 and KMF2, but by KMF3, while still 10 cm thick, the deposit is laterally discontinuous across the pit wall, indicating that the distal edge of the shell lag deposit is nearby (Figure 6.6, Figure 6.7 and Figure 6.8). Supratidal mudflat sediments (sub-facies C4) are found at the surface in most of the pits within the supratidal mudflat zone (see sedimentary logs for KMF1 to KMF4 in Appendix B; Figure 6.6).



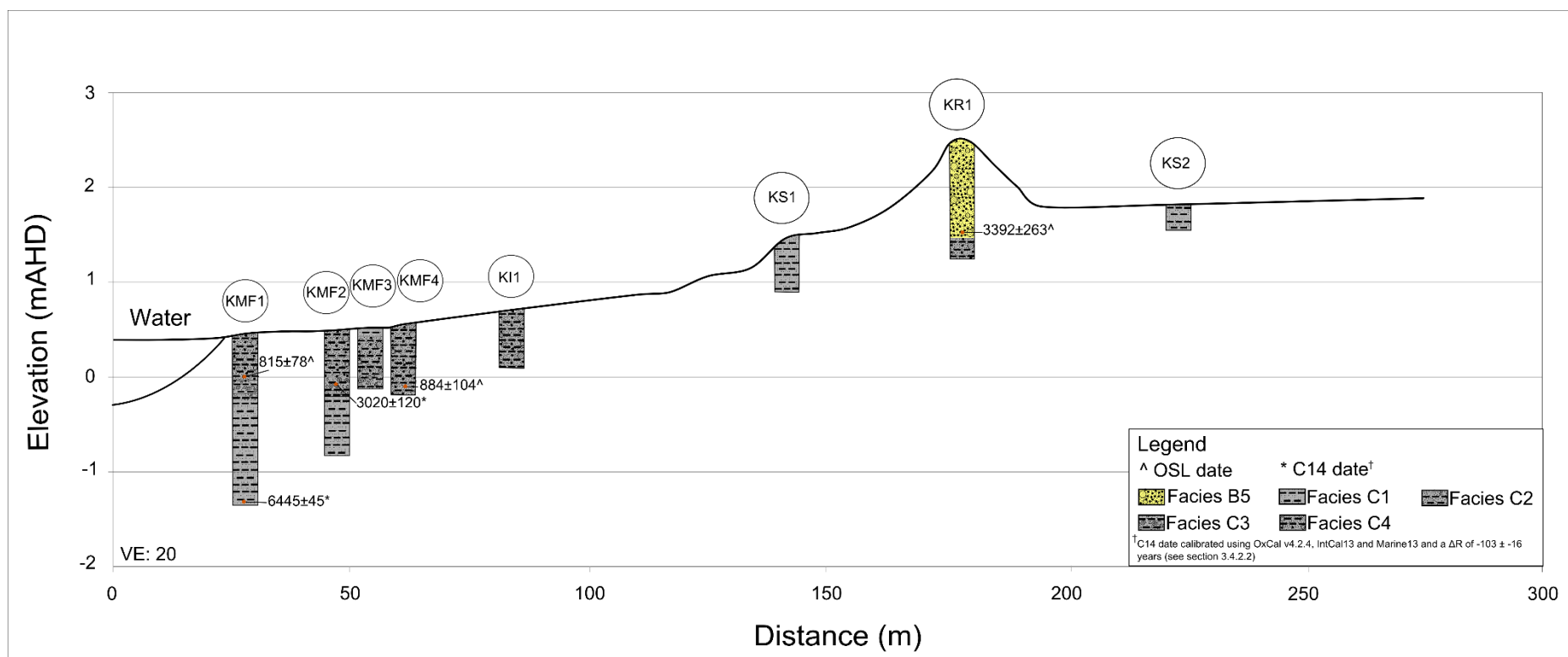


**Figure 6.6: Chrono-stratigraphic profile across the beach ridge at Kwamter. Detailed sedimentary logs of each pit can be found in Appendix B.**

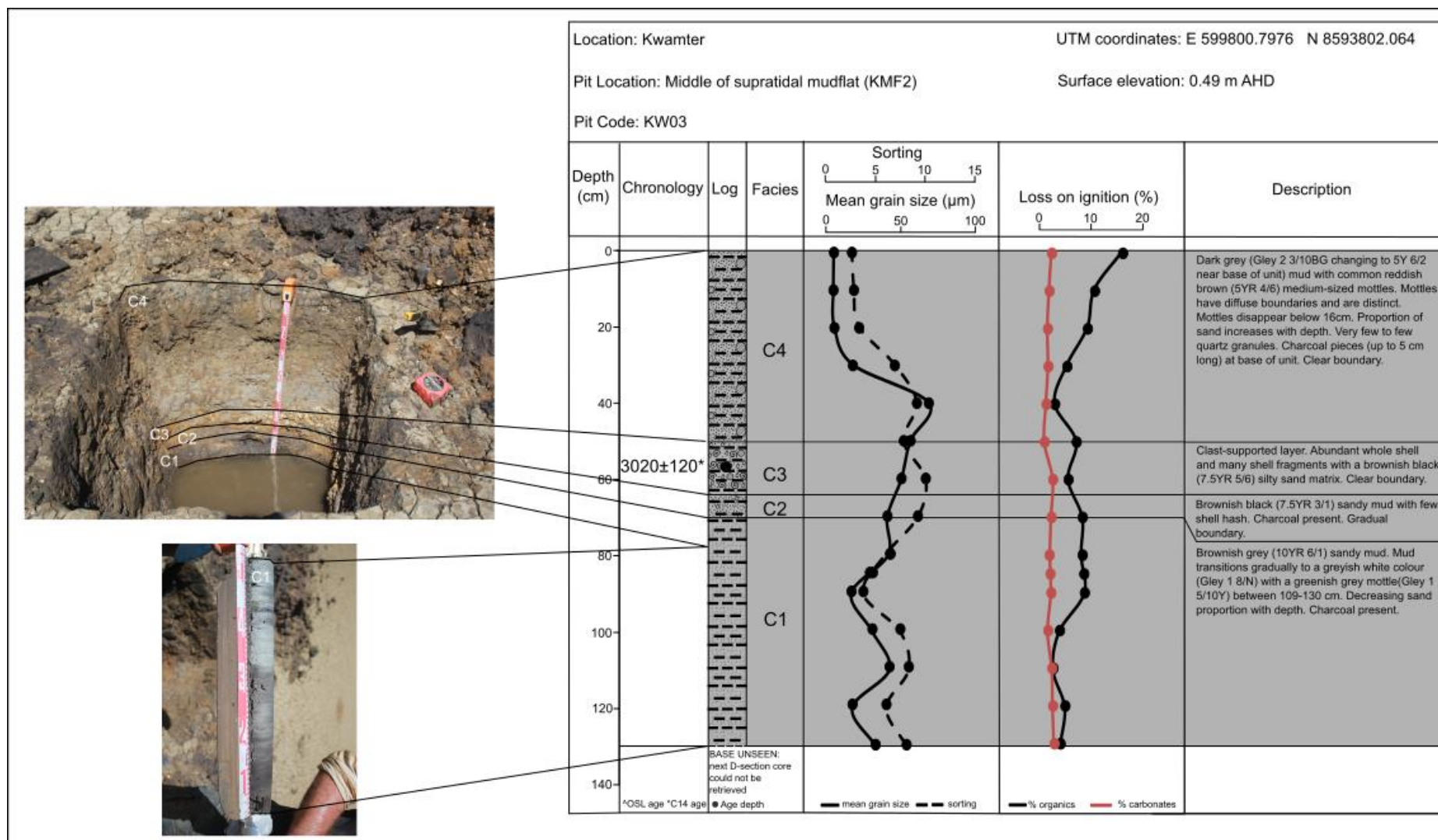


Figure 6.7: Sedimentary log for KMF2, representative of the sedimentary deposits found within the supratidal mudflat at Kwamter.

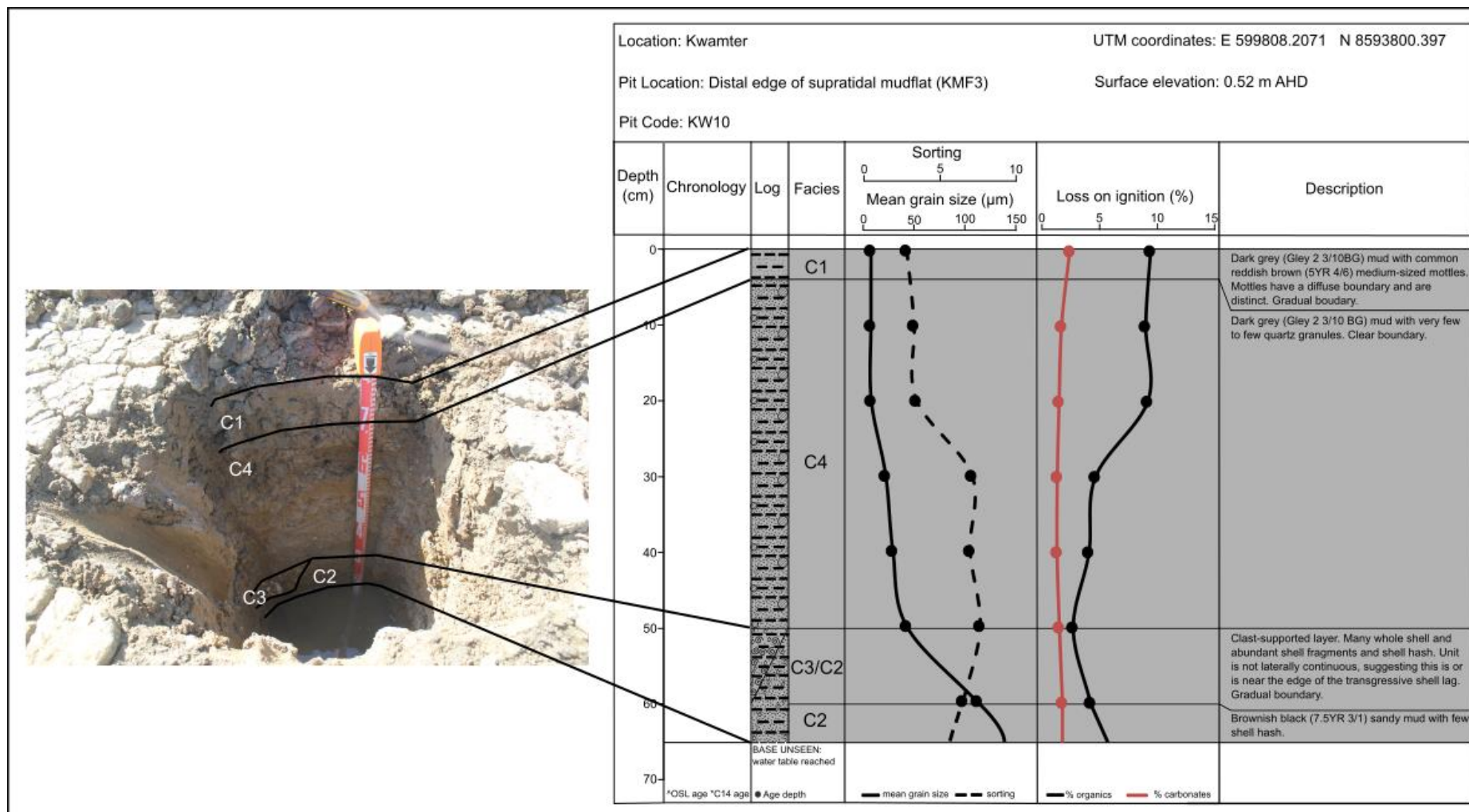


Figure 6.8: Sedimentary log for KMF3. The transgressive shell lag unit (facies C3) is laterally discontinuous across the pit face.

Supratidal mudflat deposits also underlie the distal mangrove zone. This zone is only occasionally inundated during the wet season, with insufficient time for any significant accumulation of sediment deposits characteristic of mangroves, such as sub-facies C1. Sub-facies C1 is present, however, in pit KS1 on the proximal flank of the beach ridge. The top of this deposit is at a significantly higher elevation than the equivalent unit in KMF1 and KMF2 (Figure 6.6). It is also present at a higher elevation still in pit KS2 in the swale inland of the beach ridge. These deposits may be the remnants of a laterally extensive intertidal mangrove environment that existed during a period of higher sea level in the past. Unfortunately, no dating samples were collected from either of pits KS1 and KS2, therefore the timing of deposition of these sediments is unknown.

The beach ridge at Kwamter has a relatively simple stratigraphy, with aeolian beach ridge deposits (sub-facies B5) overlying supratidal mudflat deposits (Figure 6.6 and Figure 6.9). The presence of mottling indicates intermittent saturation, most likely due to the change in hydrological conditions at the unconformity between the sandy beach ridge sediments above the unconformity and the fine-grained mudflat sediments below. Unlike the inland beach ridges at Red Beach, no calcium carbonate cementation of the basal beach ridge sediments was detected, most likely because of the lack of macrofossils (see Section 4.2.1).

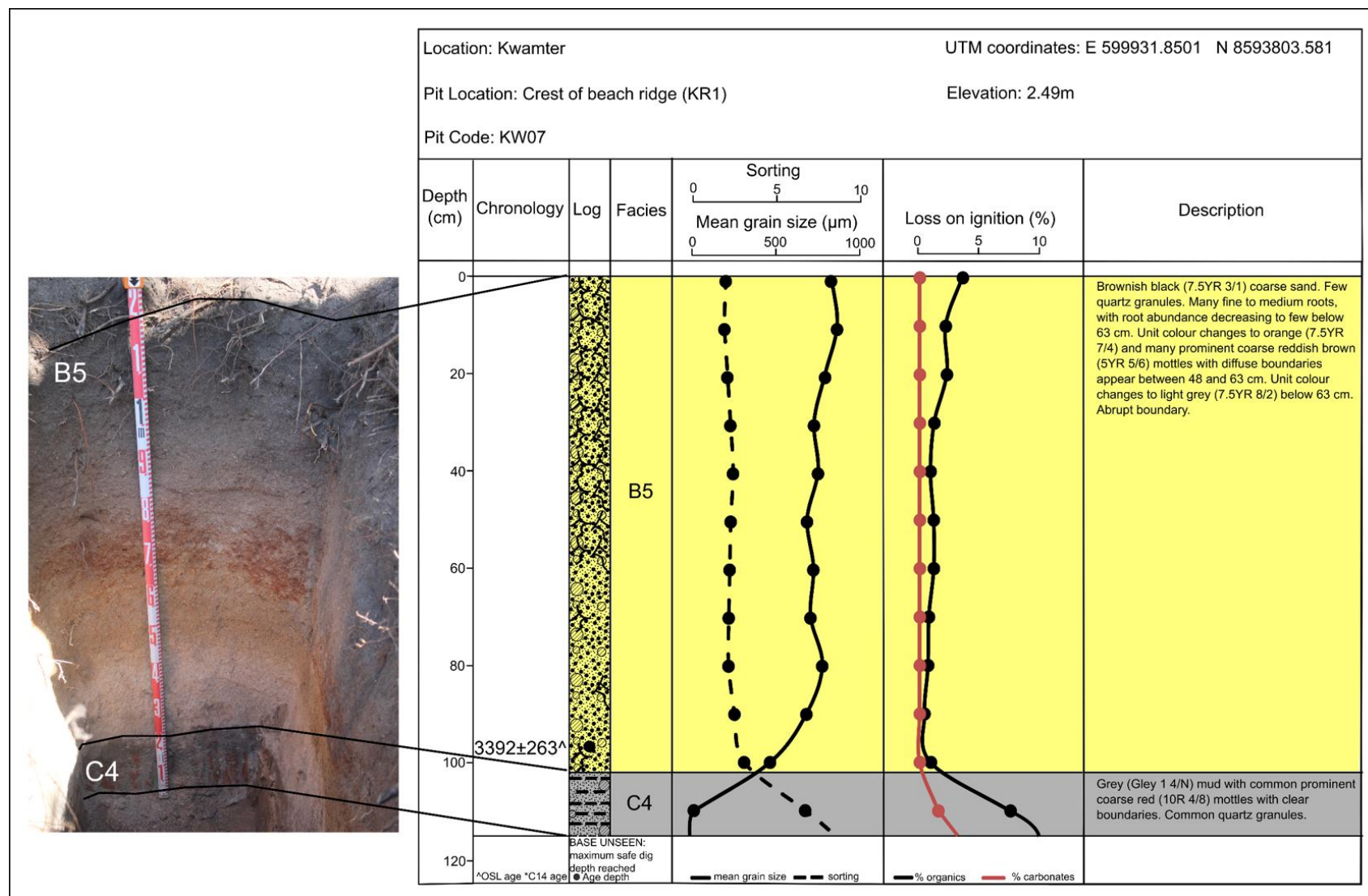


Figure 6.9: Sedimentary log for KR1, the Kwamter beach ridge.

### 6.2.2 OSL and radiocarbon chronology

The OSL and radiocarbon age determinations described in Chapter 5 are used to build a chronology for relative sea level change and its impacts on the coastal environment at Kwamter. The sedimentary record uncovered here formed from approximately 6,450 years to 800 years ago and contains a record of mid-Holocene relative sea level rise as well as the late-Holocene relative sea level fall to PMSL recorded at Red Beach.

An age of  $6445 \pm 45$  years BP was obtained from the intertidal mangrove sediments deposited at the base of the supratidal mudflat (Figure 6.6), making it the oldest sedimentary unit uncovered at any of the Albatross Bay study locations. Similar mangrove deposits from around Northern Australia have been dated to the mid-Holocene (see Section 6.2.3 below).

An age of  $3020 \pm 150$  cal. years BP (Figure 6.6) was obtained from whole shell within the transgressive shell lag deposit exposed in pit KMF2. As previously discussed (Section 6.1.2), the shell may have been extensively reworked prior to deposition and therefore the measured age may be older than the actual depositional event. However, a similar age was obtained for the burial of sediments at the base of the beach ridge ( $3392 \pm 263$  years ago), indicating that these sedimentary units were deposited concurrently, most likely in response to a rise in sea level (see Section 6.2.3 below).

Two samples of the supratidal mudflat sediments (sub-facies C4), from KMF1 and KMF4 (Figure 6.6), returned similar ages with overlapping error margins ( $815 \pm 78$  years ago and  $884 \pm 104$  years ago, respectively). The modern-day supratidal mudflat environment was most likely established at Kwamter by this time.

### 6.2.3 Sea level history and shoreline evolution at Kwamter

The sedimentary sequence from Kwamter examined for this study was deposited over the last  $6,445 \pm 45$  years BP, based on the radiocarbon age obtained from buried intertidal mangrove sediments from the proximal margin of the supratidal mudflat (Figure 6.6). The depth of this mangrove deposit beneath the supratidal mudflat (-1.32 m AHD) indicates that relative sea level was approximately between -2.16 to -1.32 m below PMSL at  $6445 \pm 45$  cal. years BP (see detailed discussion on sea level reconstruction in Albatross Bay below, Sections 6.4.2.1 and 6.4.3). Other sea level records from across the northern region of Australia indicate that mangroves were flourishing within these estuaries at a similar time (between



approximately 6,800 and 5,300 years BP), a period referred to the “big swamp” phase by Woodroffe *et al.* (1989, p. 737) (see Section 2.2).

Sea level records from within the Gulf of Carpentaria do not match the data from Kwamter, however, with Rhodes (1980), for example, suggesting that, by 6,400 years BP, relative sea level was already approximately +1 m to +1.5 m above PMSL (see Section 2.4). However, the chronology of the sea level reconstruction conducted at Karumba, Christmas Creek and Edward River by Rhodes (1980) was based on the radiocarbon dating of shells, with all of the problems associated with shell reworking previously discussed. Rhodes (1980, p. 232) himself states that “... it must be assumed that the age of the shell indicates the age of the depositional facies. Although, it is apparent from discussion in Chapter 3, that shell material is reworked on both the chenier and beach-ridge plains...”. These inaccuracies would be particularly pronounced at Karumba, where the dates were obtained from a chenier ridge plain, formed during tropical cyclone events.

The mangrove environment at Kwamter likely persisted for an extended period. It was most likely still present when relative sea level rose to PMSL, as evidenced by the top of the intertidal mangrove unit being encountered at -0.23 m AHD in pit KMF1 and -0.20 m AHD in pit KMF2 (Figure 6.6). However, no dating samples were obtained from the top of the intertidal mangrove unit, therefore the precise timing of attainment of the PMSL at Kwamter is unknown.

The rise in relative sea level above PMSL led to the decline of the mangroves, and the deposition of intertidal mudflat sediments over the top (Figure 6.6). The transgressive shell lag dating to  $3,020 \pm 120$  years BP indicates that, at this time, relative sea level was above PMSL and the area that is currently a supratidal mudflat, between KMF1 and KMF4, was a nearshore coastal environment, with coarser sandy sediments accumulating onshore to form a beach ridge. The supratidal mudflat sediments beneath the beach ridge indicate that relative sea level was between approximately 0 to +1 m above PMSL sometime between 6,500 and 3,400 years ago (see Section 6.4.2.3 below for more detailed discussion of the sea level reconstruction).

This account of shoreline evolution and sea level change at Kwamter fits well with sea level records elsewhere in the region (Section 2.4). At the McArthur river delta within the GoC, sea level was  $+1.5 \pm 0.5$  m above PMSL at  $4,059 \pm 211$  years BP (Woodroffe and Chappell, 1993). At the Sir Edward Pellew group of islands, sea level was approximately +1.6 m above present around 5,500 years BP (Chappell *et al.*, 1982) and at the Mitchell River delta, sea level was approximately + 1.5 m above PMSL approximately 5,700 years BP (Nanson *et al.*, 2013).

As discussed above, the sea level reconstruction by Rhodes (1980) at Karumba, Christmas Creek and Edward River does not match with the record at Kwamter. However, this is most likely due to errors with the radiocarbon ages measured, with the dates being older than the actual formation of the palaeoshoreline features. If the palaeoshoreline features are younger than the radiocarbon dates indicate, the maximum sea level elevations at Christmas Creek and Edward River of between +0.8 m to + 1.5 m above PMSL once again correspond well with the Kwamter sea level reconstruction.

Outside the GoC (Section 2.2), at the Cambridge Gulf and Fitzroy River, sea level was estimated by Jennings (1975) to have been between +1 m and +2 m above PMSL sometime between approximately 6,800 and 1,100 years BP. At Buckley's Plain, sea level was at least +1 m above PMSL during the mid-Holocene (Lessa and Masselink, 2006), while at Admiral Bay, sea level was +1.5 m above present MHW between  $2,095 \pm 58$  years BP and  $824 \pm 47$  years BP (Engel *et al.*, 2014). Along the eastern margin of Australia (Section 2.3), coral microatoll sea level records and other FBIs indicate that sea level was between +1 m and +3 m above PMSL during the mid-Holocene highstand (Hopley, 1978, 1983; Hopley *et al.*, 2007).

The palaeoenvironmental reconstruction at Big Willum Swamp (Stevenson *et al.*, 2015a; Proske *et al.*, 2017), discussed in Section 6.1.3, indicates that, as sea level was rising between approximately 6,000 to 3,000 years ago at Kwamter, dry conditions with low effective precipitation prevailed, possibly leading to restriction of sediment supply into Albatross Bay via the rivers. Generally, when sediment supply is high, beach ridges rapidly prograde outwards and have relatively low heights and narrow widths. In contrast, when sediment supply is low, beach ridges tend to build upwards, rather than prograde outwards, leading to higher, wider ridges (Wright, 1970; Taylor and Stone, 1996; Oliver *et al.*, 2016). Therefore, at Kwamter, a low sediment supply in the period between 6000 and 3000 years ago may have resulted in a single beach ridge which built upwards, rather than a beach ridge plain like that at Red Beach.

Once sea level began to fall, sometime after  $3392 \pm 263$  years ago, the Kwamter beach ridge became isolated from active coastal processes and construction ceased. It is likely, however, that sea level either remained at the mid-Holocene highstand of approximately +1 m above PMSL for an extended period, or sea level fall was initially gradual, only accelerating within the 500 years. Such a scenario is supported by the Red Beach sea level record, where relative sea level was still approximately +0.5 to +1 m AHD 2,200 years ago. The Wathayn sea level record, discussed in Section 6.3 below, also indicates that the beach ridge there was



active for an extended period prior to isolation from the nearshore zone due to relative sea level fall and coastal progradation.

As relative sea level remained stationary or gradually fell after 2,200 years ago, sediment supply to Albatross Bay increased due to an increase in effective precipitation (see Section 6.1.3) (Stevenson *et al.*, 2015a; Proske *et al.*, 2017). The presence of mangrove sediments within KS1 indicates that a mangrove environment developed on the proximal side of the beach ridge (Figure 6.6). The mangroves are unlikely to have formed concurrently with the beach ridge because it is constructed by aeolian accretion of sediments blowing off a sandy shoreline and any mangroves present would have inhibited aeolian transport processes (see Section 4.4.2). This hypothesis of a sea level stillstand/gradual fall in sea level followed by mangrove formation can be tested in the future by obtaining two additional OSL burial ages, one from the top of the Kwamter beach ridge to determine how long the ridge was active prior to isolation from the source of the sandy sediments, and one from within the distal mangrove zone to determine when the intertidal mangrove sediments were deposited.

The evidence discussed above indicates that, unlike Red Beach which had enough sediment supply and accommodation space for a beach ridge plain to develop, the shoreline at Kwamter rapidly transitioned from a nearshore zone open to relatively high energy coastal processes, allowing formation of a single beach ridge, to a low energy intertidal mangrove environment. The modern-day supratidal mudflat at Kwamter was already established sometime between  $815 \pm 78$  and  $884 \pm 104$  years ago (Figure 6.6). At this time, sea level was still above PMSL, as reflected in the Red Beach record (see Section 6.1.5). Despite the potential increase in sediment supply to the Embley River around 2,000 years ago (see Section 6.1.3), a beach ridge plain could not develop at Kwamter due to a lack of marine accommodation space. Accommodation space is defined by Jerve (1988, p. 47) as "... the space made available for potential sediment accumulation..." and is controlled by sea level change along with tectonic subsidence or uplift and the configuration of the coastline (Jerve, 1988; Coe *et al.*, 2003). The Embley River at the Kwamter location is a relatively narrow river channel, with a small accommodation space, whereas Red Beach is located at the mouth of the Mission River, opening into Albatross Bay, and is subject to the full range of coastal processes (Figure 1.2). As sea level remained stationary or gradually fell over the last 2,000 years, the hypothesised increased sediment supply into Albatross Bay would have rapidly filled up the available accommodation space within the lower reaches of the Embley River, causing the river channel to infill. Once there was no more accommodation space within the Embley River estuary, the

sediment was transported further out into Albatross Bay, where it became available for transport and deposition in locations with more accommodation space, such as at Red Beach and Botchet Beach.

### **6.3 The record from Wathayn**

#### **6.3.1 Topography and sediment stratigraphy**

The topography and sedimentary stratigraphy of the estuarine floodplain and beach ridge at the Wathayn study location have been described and illustrated in Chapter 4 (Figure 4.26). The sedimentary facies here range from quartz sand with few quartz granules within the beach ridge crest and proximal beach ridge flank, to silty sand across the supratidal mudflat and within the mangrove zone (Section 4.4).

The D-section core collected from within the mangrove zone (WI1) is composed entirely of intertidal mangrove sediments (sub-facies C1). This facies continues across the supratidal mudflat, forming the entire record in pit WMF1 at the proximal edge and overlying supratidal mudflat sediments in the centre (pit WMF2; Figure 6.10 and Figure 6.11). Supratidal mudflat sediments (sub-facies C4) make up the entire sedimentary record at the distal edge of the supratidal mudflat (pit WMF3; Figure 6.10). At the base of pit WMF2, sub-facies C5 represents the transition between the supratidal mudflat facies (sub-facies C4) and the substrate beneath (Figure 6.11; Section 4.4.3).

The single beach ridge at Wathayn is composed of aeolian deposits (sub-facies B5; Figure 6.10 and Figure 6.12). In pit WS1 on the proximal flank of the beach ridge, sub-facies B5 overlies sub-facies B6 (Figure 6.10). Sub-facies B6 is interpreted as a transitional facies between the aeolian beach ridge sediments and the substrate below (see Section 4.4.2), indicating that the base of pit WS1 may be close to the bottom of the Wathayn beach ridge deposits. Unfortunately, deeper excavation of pit WR1 to try to intersect this unconformity was prevented by the instability of the sides of the pit. However, extrapolation of the boundary between sub-facies B5 and the underlying B6 in pit WS1 across to pit WR1 suggests there may be as much as 0.8 m of beach ridge sediments below the base of this pit.

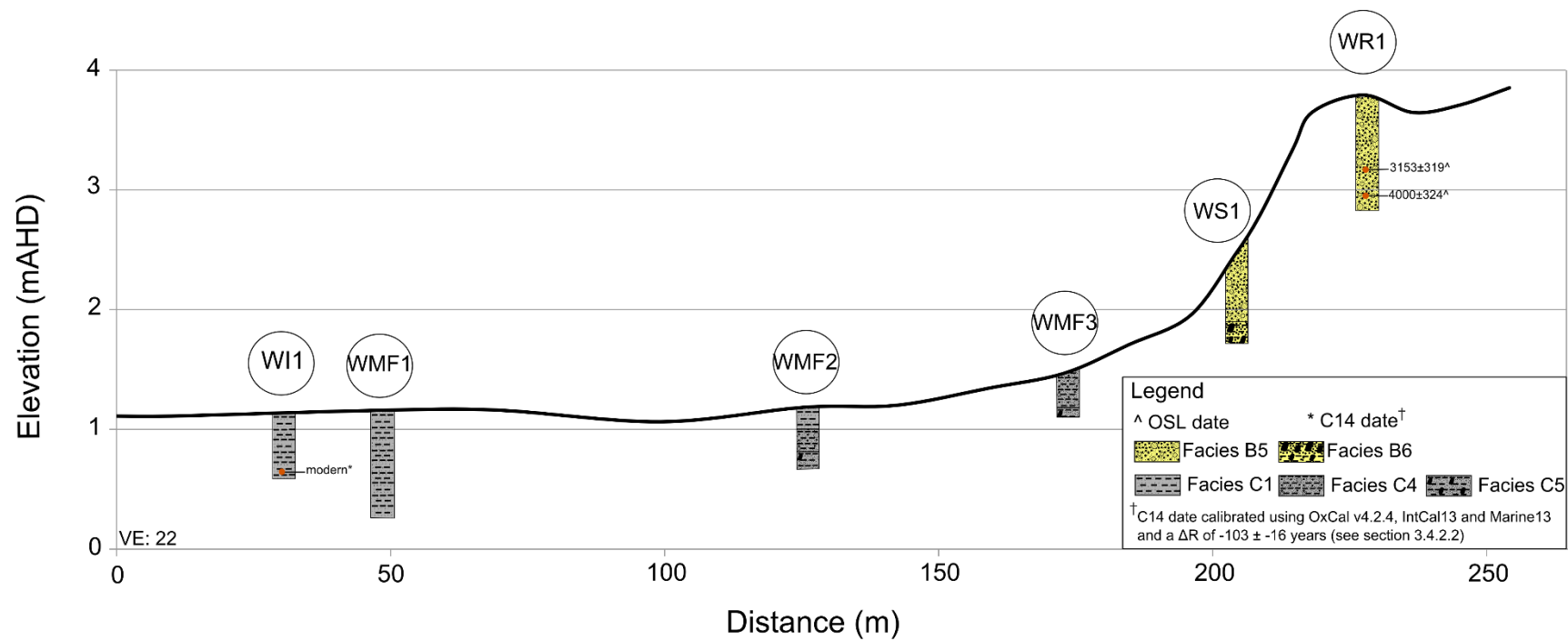


**Figure 6.10: Chrono-stratigraphic profile across the beach ridge at Wathayn. Detailed sedimentary logs of each pit can be found in Appendix B.**

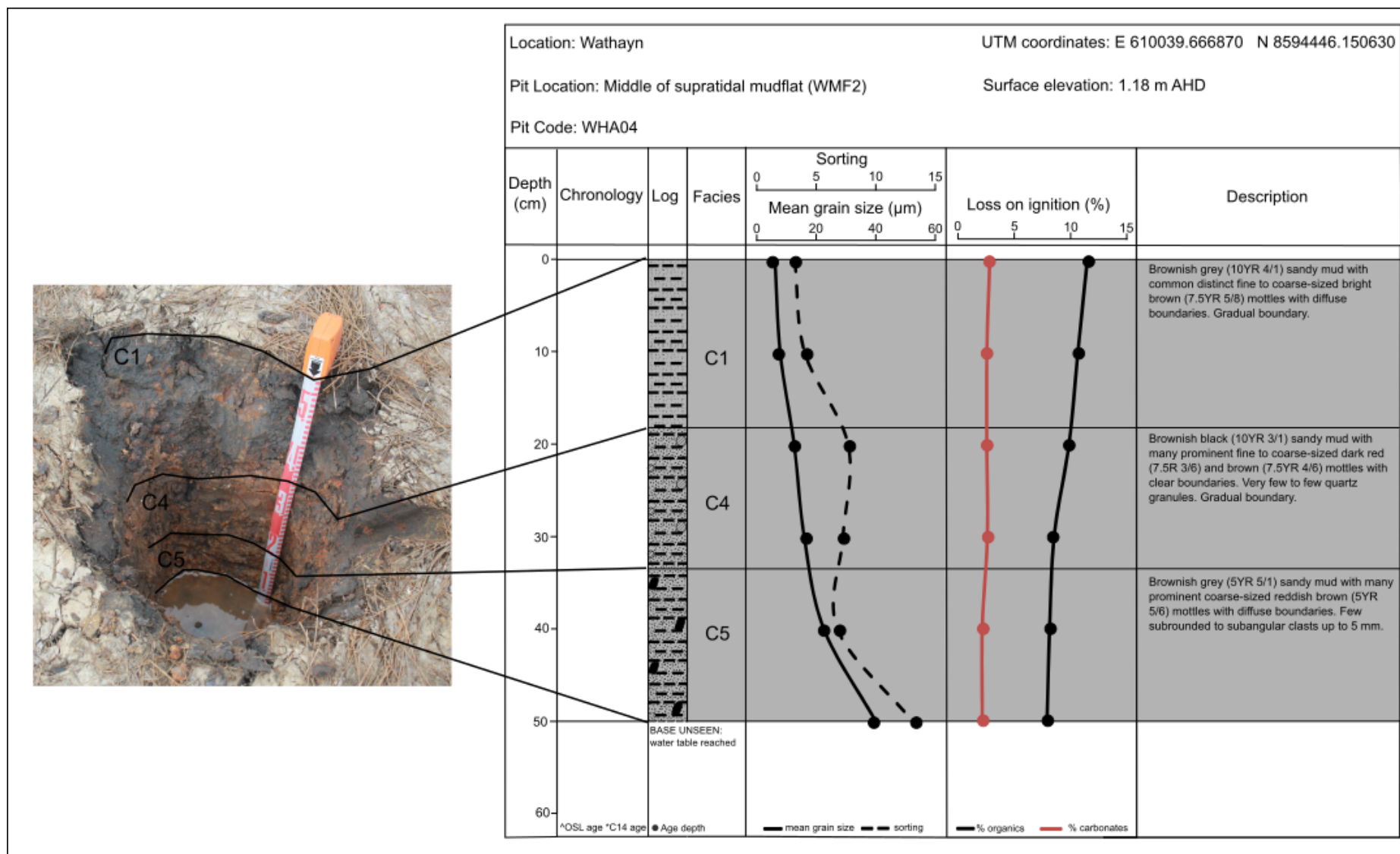


Figure 6.11: Sedimentary log for WMF2, located in the centre of the supratidal mudflat at Wathayn. The profile here contains the entire record of formation of the supratidal mudflat.

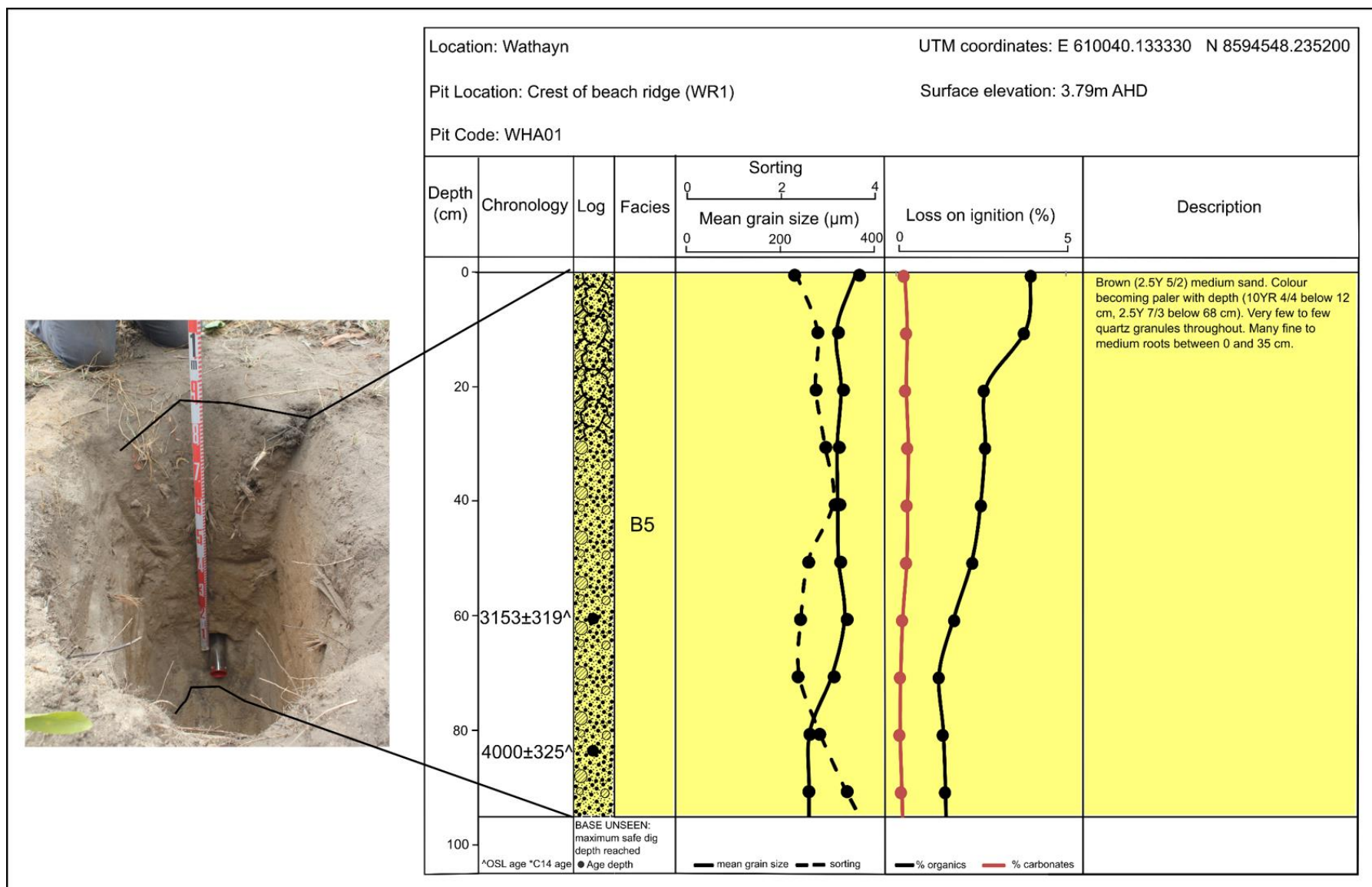


Figure 6.12: Sedimentary log for WR1, excavated into the crest of the beach ridge at the Wathayn study location.

### 6.3.2 OSL and radiocarbon chronology

The OSL and radiocarbon age determinations described in Chapter 5 are used here to build a chronology for sea level change and its impacts on the coastal environment at Wathayn. The radiocarbon age for sediments at the base of the D-section core (WI1) from within the mangrove zone at Wathayn is Modern (Figure 6.10). Two OSL samples collected from pit WR1 in the Wathayn beach ridge, at 2.96 m AHD and 3.19 m AHD, returned burial ages of  $3153 \pm 319$  years ago and  $4000 \pm 324$  years ago respectively. Since these samples were collected as much as 0.8 m above the unconformity with the substrate, accumulation of the beach ridge at Wathayn must have commenced earlier than 4,000 years ago.

### 6.3.3 Sea level history and shoreline evolution at Wathayn

The record of shoreline evolution and sea level change at Wathayn and at Kwamter are similar. While a precise date for the commencement of beach ridge formation at Wathayn is unknown, the OSL burial ages obtained for the Wathayn beach ridge are similar to that obtained from the Kwamter beach ridge ( $3392 \pm 263$  years ago; Section 6.2.2), making it likely that formation of a single beach ridge took place along the Embley River when sea level rose flooding the estuary and forming a nearshore marine environment sometime between 6,400 and 3,000 years ago.

Like Kwamter, a single beach ridge is present at Wathayn, rather than a beach ridge plain like the one at Red Beach. As discussed above, one of the contributing factors is likely to have been reduced sediment supply from the Embley River catchment due to lower effective precipitation at that time (Stevenson *et al.*, 2015a; Proske *et al.*, 2017). This limited sediment supply led to the Wathayn beach ridge building upwards rather than outwards. Support for this hypothesis is provided by the two OSL burial ages obtained from the Wathayn beach ridge. The uppermost burial age is approximately 1,000 years younger than the lower one, yet they are only 23 cm apart, implying that the Wathayn beach ridge accumulated vertically relatively rapidly. There may have been pauses in accumulation during this time, though there was no visible evidence of erosion or hiatuses in deposition within the described and sampled sediment section. In contrast, over a similar timespan of 1,000 years between 1,600 and 300 years ago (the seaward beach ridge set), seven beach ridges formed at Red Beach, each between 100 to 300 years apart, with the largest age gap between beach ridges being approximately 570 years (see Section 6.1.2). A second contributing factor is likely to have been lack of accommodation space for sediment deposition. Accommodation space at the more upstream location of

Wathayn was likely to be as restricted as Kwamter (described in Section 6.2.3), preventing the formation of anything more than a single beach ridge at both locations.

Sometime after  $3,153 \pm 319$  years ago, relative sea level began to fall towards PMSL, isolating the beach ridge at Wathayn from nearshore coastal processes. A supratidal mudflat formed on the proximal side of the beach ridge, and mangroves became established along the estuary, preventing any further accumulation of sandy sediments. Precise dates for formation of the supratidal mudflat and establishment of the mangroves are not available (the Modern date for sediments from the mangrove zone was obtained from a depth of only 50 cm – see Figure 6.10). Radiocarbon ages obtained from basal shell deposits from two anthropogenic shell mounds at Wathayn West ( $1,276 \pm 31$  y BP for SM122 and  $1234 \pm 33$  y BP for SM123; Holdaway *et al.*, 2017, Table 2) shows that the intertidal mudflat at Wathayn West was already established at least 1,200 years ago.

#### **6.4 Constructing a Holocene sea level Curve for Albatross Bay**

Methods of sea level reconstruction were reviewed in Chapter 3 (Section 3.1). A variety of proxies can be used for the reconstruction of past sea level. Those utilised from the Albatross Bay study locations were palaeoshoreline indicators (specifically, the beach ridges) and sedimentary stratigraphic sequences, including mangrove zone sediments (Section 3.1.2 and 3.1.3). In this section, the method used to construct a mid- to late-Holocene sea level curve for Albatross Bay, by converting the sea level proxies into sea level index points (SLIPs) and then plotting them against elevation, is described.

SLIPs can be broadly divided into two groups – fixed (indicative) indicators and directional (relational) indicators (Chappell, 1987; Murray-Wallace and Woodroffe, 2014). Fixed indicators are sea level proxies that form within a well-defined elevation relative to a tidal datum and include biological organisms whose habitat is constrained by specific tide levels (Chappell, 1987; Murray-Wallace and Woodroffe, 2014). Examples of fixed sea level indicators include intertidal mangrove environments, coral microatolls, and FBIs. Directional indicators do not form within a well-defined elevation range but, rather, provide an indication of whether sea level was above or below a specific tidal datum (Chappell, 1987; Lewis *et al.*, 2013; Murray-Wallace and Woodroffe, 2014). Examples of directional indicators that form above the tidal datum include beach ridges, chenier plains and freshwater peats, while directional indicators that form below the tidal datum include nearshore sediments. To convert

sea level proxies into SLIPs, four pieces of information are needed (Section 3.1.1): (1) location (geographical coordinates), (2) age, (3) elevation, and (4) tendency (whether the indicator is associated with a rise or a fall in sea level) (Shennan, 2007; Murray-Wallace and Woodroffe, 2014; Shennan, 2015).

#### 6.4.1 Directional sea level index points

Two types of directional sea level indicators are present at Albatross Bay – the beach ridges at Red Beach, Kwamter and Wathayn, and the transgressive shell lag at Kwamter (see Sections 6.1, 6.2 and 6.3 above). The only beach ridge SLIPs from Albatross Bay that are directional are those where the elevation of the unconformity between the beach ridge and the underlying intertidal mudflat was not recorded. Beach ridges where the unconformity between beach ridge sediments and the intertidal mudflat was recorded are used as fixed SLIPs, as described below (Section 6.4.2). The geographical coordinates of the SLIPs were obtained by field surveying (Section 3.2.2 and Chapter 4), and ages were obtained using either OSL or radiocarbon techniques (Chapter 5).

Beach ridges generally form at, or above, the MHWS (Section 3.1.2). Furthermore, along the modern beach at Red Beach, these sandy beach ridge sediments overlie intertidal mudflat sediment, exposed at low tide (Section 4.1). Therefore MSL must have been below the elevation of the beach ridge at their time of formation. The beach-ridge SLIPs have two elevation reference points, one where the OSL dating sample was collected, and another at the base of the pit that was dug into the beach ridge in question (Figure 6.13). Because most of the pits could not be excavated to the unconformity between the beach ridge and the underlying substrate, it follows that, at the time of formation of the beach ridge, sea level would have had to have been below the base of the pit.



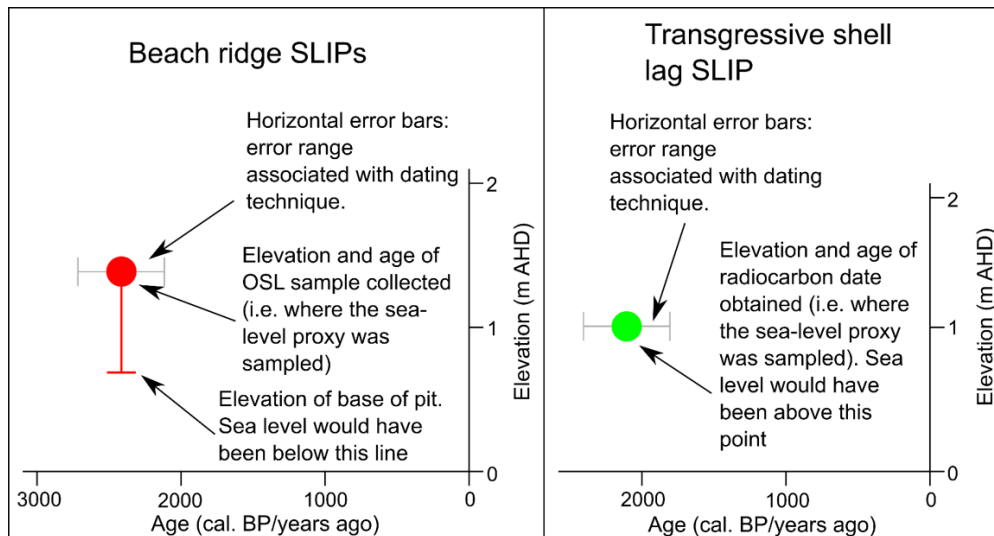


**Figure 6.13:** Example of how the directional sea level index points are illustrated on the sea level curve.

The transgressive shell lag at Kwamter (sub-facies C3) was formed in a nearshore environment as sea level rose, transporting marine sediments towards the new higher-elevation foreshore and leaving behind a lag of shell material (see Sections 4.4.3 and 6.2.3). While the precise depth at which the transgressive shell lag formed underwater cannot be quantified, sea level would have had to have been above the elevation of the transgressive shell lag at the time of its formation. The SLIP of this transgressive shell lag is represented by one reference point (Figure 6.13) and is associated with a rising sea level.

#### 6.4.2 Fixed sea level index points

Three types of fixed sea level indicators are present in Albatross Bay – the mangrove deposit beneath the modern supratidal mudflat at Kwamter, the unconformity between the beach ridges and intertidal mudflat at Red Beach, and the relict supratidal mudflat beneath the beach ridge at Kwamter (see Sections 6.1 and 6.2 above). Like the directional SLIPs, their geographical coordinates were obtained by field surveying, and ages have been obtained by either OSL or radiocarbon techniques. The elevation of a fixed sea level proxy is more complicated to ascertain than for a directional one, with each proxy needing an “indicative meaning”, comprising a reference water level (such as MSL or MHWS), and an indicative range (i.e., the vertical elevation range where the sea level indicator could occur during formation) (see Section 3.1) (Woodroffe and Horton, 2005; Murray-Wallace and Woodroffe, 2014; Rashid, 2014). This indicative meaning will vary depending on the sea level proxy and its location, with local variations in climate and oceanography most commonly affecting the indicative range (Horton, 1997; Murray-Wallace and Woodroffe, 2014). When calculating the

indicative meaning of a sea level proxy at its respective location, it has to be assumed that the tidal range has remained constant through time (Murray-Wallace and Woodroffe, 2014; Shennan, 2015). See Section 2.4 for further discussion on this assumption of a constant tidal range.

#### 6.4.2.1 Indicative meaning for mangrove deposit at Kwamter

Mangrove vegetation species (and therefore the sedimentary deposits associated with this environment) are intertidal and grow within a quantifiable and narrow elevation range (see Section 3.1.3). Mangrove ecosystems are found primarily between MSL and the MHW level (Cohen *et al.*, 2005; Zong, 2007; Ellison, 2008; Waller, 2015), and Geoscience Australia (2015c) state that, within Australia, surfaces beneath mangrove forests form between MSL and MHWS. At Albatross Bay, MSL is approximated to 0 m AHD, MHW is 0.58 m AHD and MHWS is at 0.84 m AHD (see Section 1.4.1).

The mangrove sedimentary deposit at Kwamter was collected -1.32 m below PMSL. To be conservative, this mangrove sedimentary deposit could have been deposited anywhere between MSL and MHWS. Therefore, if the Kwamter mangrove sedimentary deposit was deposited at MSL, relative sea level would have been -1.32 m below PMSL at the time of deposition (the upper limit of the indicative range of this sea level proxy). However, if the Kwamter mangrove sedimentary deposit was deposited at MHWS, +0.84 m above MSL, relative sea level would have been -2.16 m below PMSL at the time of deposition (the lower limit of the indicative range of this sea level proxy; Figure 6.14). Accordingly, the indicative range of the mangrove deposit at Kwamter is  $-1.74 \pm 0.42$  m.

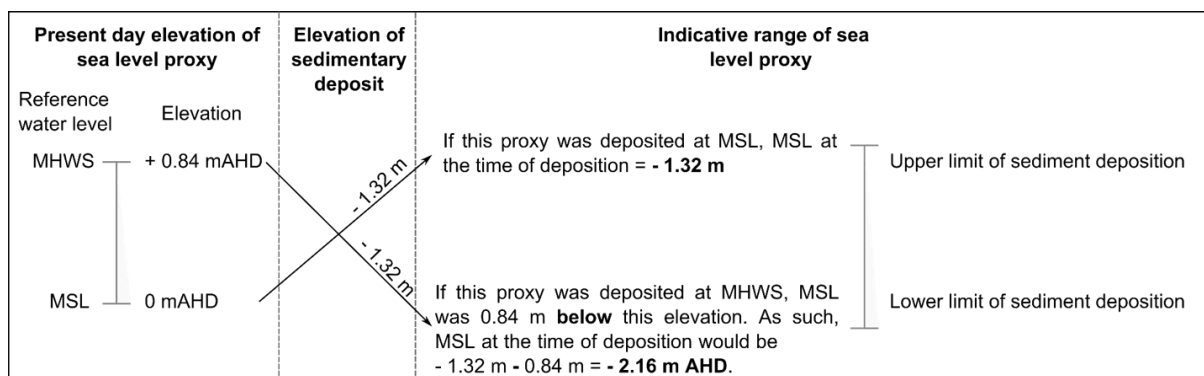
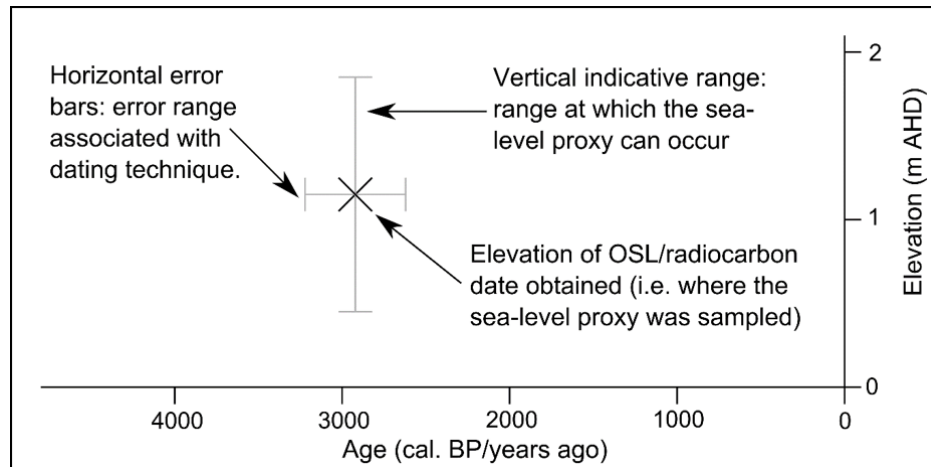


Figure 6.14: The calculation of the indicative meaning and range of the mangrove deposit at Kwamter.

The mangrove deposit SLIP is represented by one reference point, with horizontal error bars representing the error range associated with the radiocarbon date obtained, and the vertical error bars representing the indicative range of the sample (Figure 6.15).



**Figure 6.15:** Example of how the fixed sea level index points (mangrove deposits and the unconformity between the beach ridge and intertidal mudflat) are illustrated on the sea level curve.

#### 6.4.2.2 Indicative meaning for beach ridge unconformity at Red Beach

The height of a beach ridge is affected by factors other than sea level (e.g. post-formational erosion). Therefore, ridge crest elevation is not an ideal fixed sea level indicator. Instead, the boundary between the aeolian beach ridge facies and either the underlying backbeach facies, which forms at the landward swash limit of constructive waves, or intertidal mudflat facies in lower energy environments, are often used as indicators of mean sea level at the time of construction of the beach ridge (see Section 3.1.2) (Tamura, 2012). An aeolian cap is not present in all the ridges at Red Beach. Furthermore, the aeolian facies at Red Beach is unique due to the presence of pisoliths within the unit (see Section 4.4.2). Therefore, the standard literature on the use of the aeolian/beach boundary as a fixed sea level indicator may not apply. Instead, as described in Section 6.1.5 above, the unconformity between the beach ridge sediments and the underlying intertidal mudflat sediments is used as a fixed sea level indicator in this study. Geoscience Australia (2015c) define the elevation range of intertidal mudflats as being between MLWS to MHWS. The intertidal mudflat does not reach MHWS at Red Beach, where a sandy foreshore, partially inundated during MHW, is deposited over the intertidal mudflat (see Section 4.1.1). The intertidal mudflat is only visible between approximately MSL and MLW. However, the precise elevation of the transition from sandy to muddy sediments within the intertidal zone was not measured in field. Therefore, to be

conservative with the estimation, the elevation range identified by Geoscience Australia (2015c) is applied. At Albatross Bay, MLWS is at -0.88 m AHD, while MHWS is at +0.84 m AHD.

The sediments within the beach ridge unconformity deposited at Red Beach was collected +0.72 m above PMSL. Therefore, if these sediments were deposited at MLWS, relative sea level would have been +1.6 m above PMSL at the time of deposition (the upper limit of the indicative range of this sea level proxy). However, if these sediments were deposited at MHWS, relative sea level would have been -0.12 m below PMSL at the time of deposition (the lower limit of the indicative range of this sea level proxy; Figure 6.16). Accordingly, the indicative range of the beach ridge unconformity deposit at Red Beach is  $0.74 \pm 0.86$  m. The SLIP for this unconformity is represented with one reference point as shown in Figure 6.15.

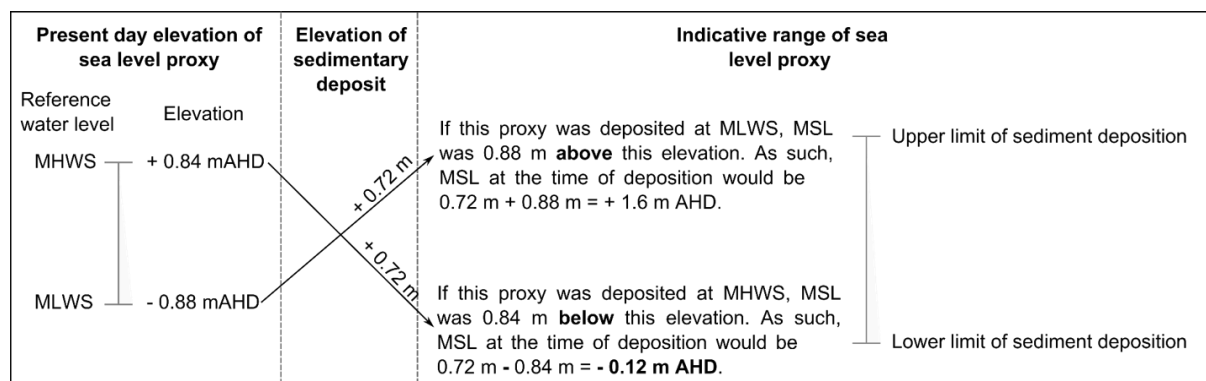


Figure 6.16: The calculation of the indicative meaning and range of the beach ridge unconformity at Red Beach.

#### 6.4.2.3 Indicative meaning for relict supratidal mudflat at Kwamter

The relict supratidal mudflat, below the beach ridge, was deposited at the distal margin of the estuarine floodplain at Kwamter during a rising sea level (see Section 6.2.3). As the supratidal mudflat forms at a definable relationship to sea level, it is a fixed sea level indicator, although this sea level proxy has a broad relation to the intertidal zone (Murray-Wallace and Woodroffe, 2014), compared with the previously discussed proxies that have a narrower elevation range. Modern supratidal mudflats are generally found above MHWS and infrequently inundated by king tides (Geoscience Australia, 2015d), which would therefore equate to the upper limit of sediment deposition. At Albatross Bay, MHWS is approximately +0.84 m AHD, while the king tide elevation is at approximately +1.35 m AHD (see Section

1.4.1). The surface of the modern supratidal mudflat at Kwamter is at an elevation of approximately +0.5 m AHD (see Section 4.2.1, Figure 4.22). As a conservative estimate, it is proposed that the modern supratidal mudflats at Albatross Bay formed at elevations of between +0.5 m AHD and +1.35 m AHD.

The relict supratidal mudflat sediment deposited at Kwamter was collected +1.47 m above PMSL. Therefore, if this supratidal mudflat sediment was deposited at the same elevation as the modern supratidal mudflat, relative sea level would have been +0.97 m above PMSL at the time of deposition (the upper limit of the indicative range of this sea level proxy). However, if the supratidal mudflat sediment was deposited by king tides, relative sea level would have been +0.12 m above PMSL at the time of deposition (the lower limit of the indicative range of this sea level proxy; Figure 6.17). Accordingly, the indicative range of the supratidal mudflat deposit at Kwamter is  $0.55 \pm 0.43$  m.

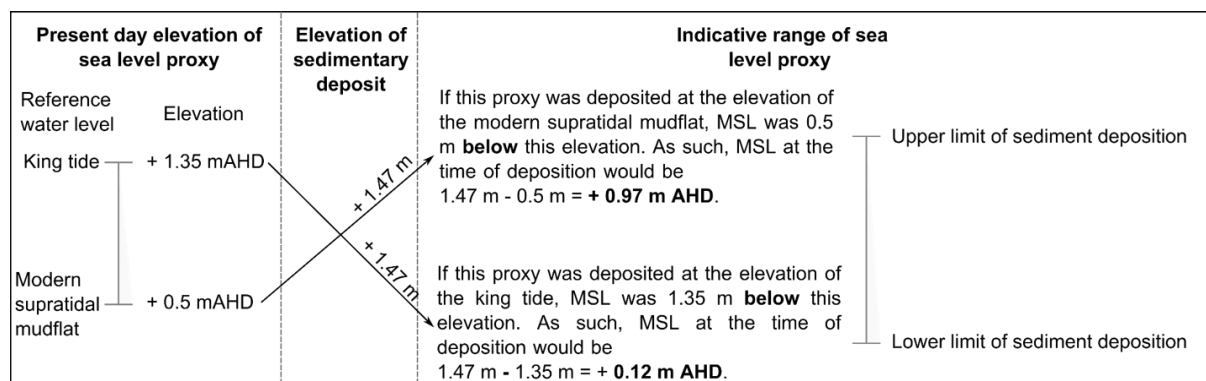


**Figure 6.17: The calculation of the indicative meaning and range of the relict supratidal mudflat at Kwamter.**

There are no ages available for the formation of the relict supratidal mudflat. However, it likely formed during the mid-Holocene sea level rise and is younger than the mangrove deposit at depth below the proximal margin of the modern mudflat, but older than the beach ridge. Since formation of the relict supratidal mudflat is bracketed by the radiocarbon age for the mangrove sediments ( $6445 \pm 45$  years BP) and the age obtained for the base of the beach ridge ( $3392 \pm 263$  years ago), rather than a single reference point for this sea level proxy, a broad sea level envelope across this age range is proposed (Figure 6.18).

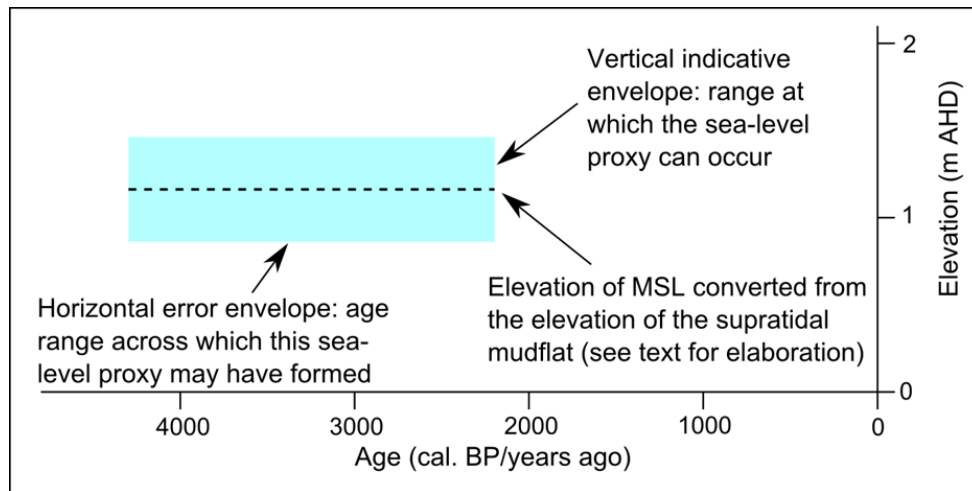


**Figure 6.18:** Example of how the sea level envelope for the relict supratidal mudflat is illustrated on the sea level curve.

#### 6.4.3 The sea level curve

The sea level curve constructed from the SLIPS described above is presented in Figure 6.19. At  $6445 \pm 45$  cal. years BP, relative sea level was approximately -1.7 m below PMSL and rising. Sometime before 5,000 years BP, sea level reached PMSL. It continued to rise at the same rate, reaching up to approximately +1 m above PMSL by approximately 4,000 years BP. Relative sea level then either remained at this highstand, or if the relative sea level did change, it either rose or fell gradually rather than rapidly. At approximately 500 years ago, the pace of sea level fall increased, falling relatively rapidly to PMSL.

In Figure 6.20 and Figure 6.21, the SLIPs and the hypothesized sea level curve from Albatross Bay are superimposed on a compilation of SLIPs and sea level envelopes from northern Australia (Figure 2.9) and eastern Australia (Figure 2.14). The sea level curve from Albatross Bay corresponds well to sea level reconstructions from northern Australia and eastern Australia, indicating that the broad sea level changes from the mid-Holocene to present are due to regional factors, such as equatorial ocean syphoning (see Section 2.1.1) (Mitrovica and Peltier, 1991; Mitrovica and Milne, 2002; Woodroffe and Horton, 2005). Variations in the timing and magnitude of the mid-Holocene highstand and subsequent sea level fall are likely due to differences in the local environmental factors (climate and oceanography), along with hydro-isostatic loading and continental levering (see Section 2.1).

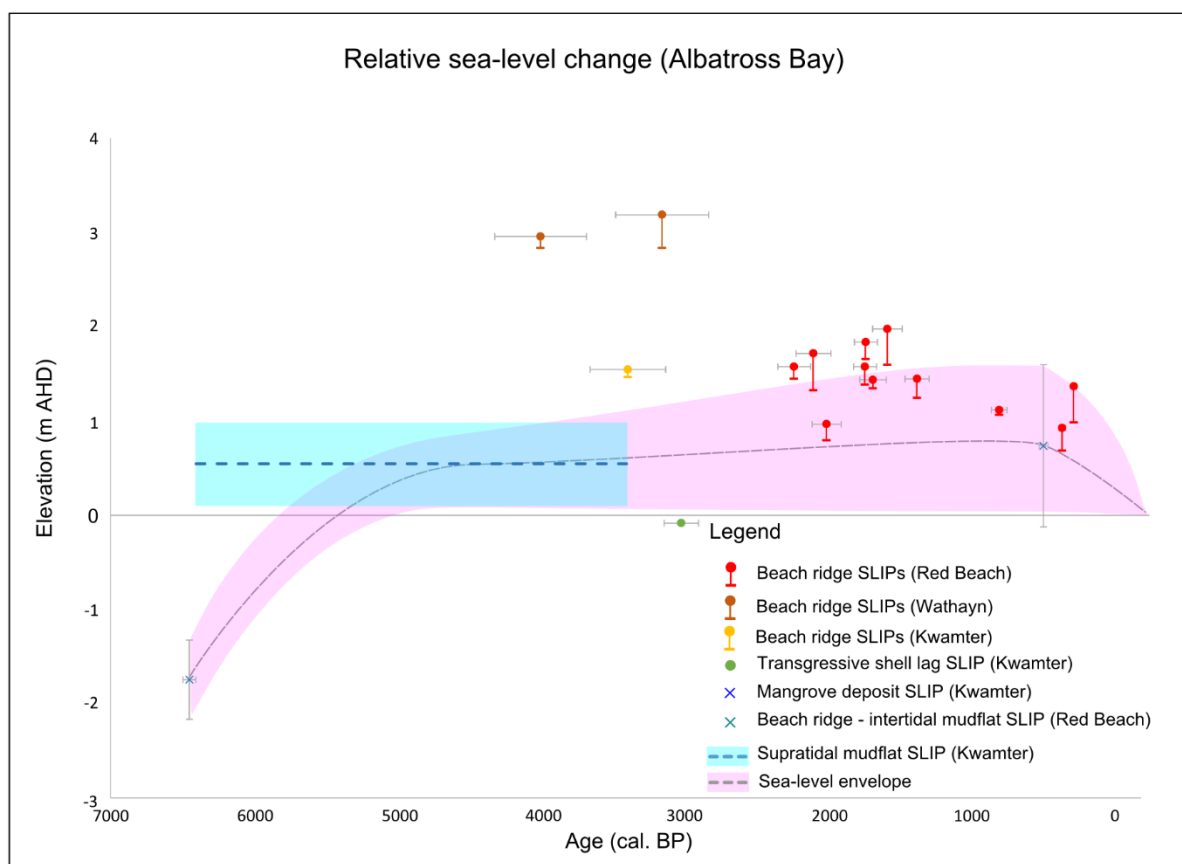


**Figure 6.19: Holocene sea level index points (SLIPs) from Albatross Bay.**

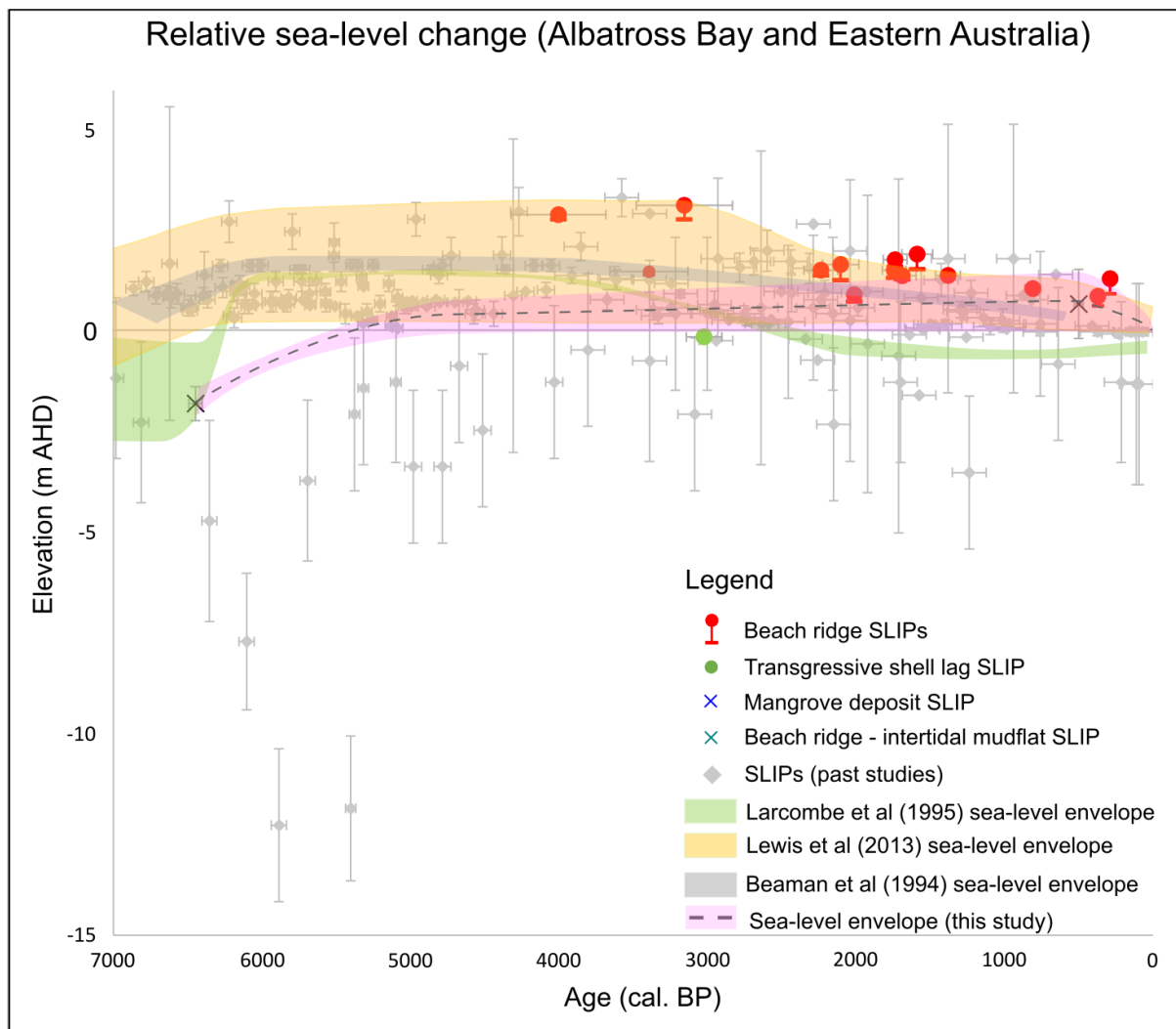


**Figure 6.20: Comparison of Holocene sea level data from Albatross Bay and SLIPs from previous studies around the eastern Queensland coast. Sea level envelopes compiled by various authors are also included, as indicated in the key.**



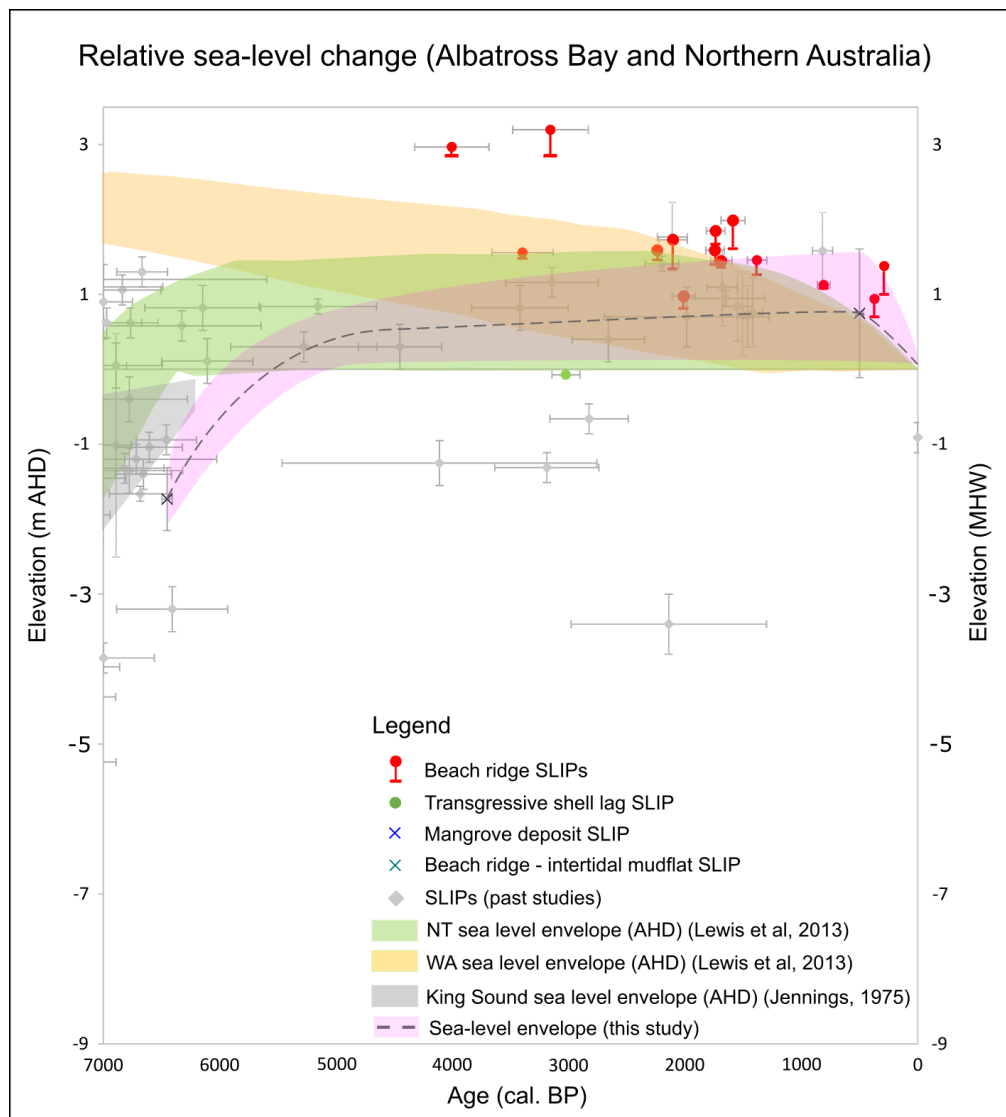


**Figure 6.21: Comparison of Holocene sea level data from Albatross Bay with SLIPs from previous studies from northern Australia. Sea level envelopes compiled by various authors are also included, as indicated in the key. Note that a few data points are referenced to MHW (to the right of the graph), while most of the SLIPs, including those from this study, are referenced to m AHD (to the left of the graph). For exact details on which SLIPs are referenced to MHW, see Figure 2.16**

#### 6.4.4 Limitations of this study

The main point of discrepancy between this research and the established literature on mid to late Holocene relative sea level change within the GoC is the intertidal mangrove deposit beneath the supratidal mudflat at Kwamter. This intertidal mangrove deposit, found -1.32 m below PMSL indicates that relative sea level was  $-1.74 \pm 0.42$  m below PMSL approximately 6,400 years BP. However, at Karumba, Christmas Creek and Edward River, Rhodes (1980) suggests that by approximately 6,500 years BP, relative sea level was already between to +0.8 to +2.4 m above PMSL. Similarly along the McArthur River delta, Woodroffe and Chappell (1993) found that relative sea level reached PMSL by approximately 7,000 years BP, rising to

+1.5 ± 0.5m above present by approximately 4,000 years BP. On the Sir Edward Pellew Group of islands, Chappell *et al.* (1982) found evidence that relative sea level was approximately +1.6 m above PMSL around 5,500 years BP, while at the Mitchell River delta, Nanson *et al.* (2013) state that the delta prograded from approximately 5,700 years BP in response to a relative sea level fall of 1.5 m (see Section 2.4).

There are several possible explanations for this discrepancy. The radiocarbon date obtained for this mangrove unit of 6,445 ± 45 years BP may be inaccurate. This radiocarbon date was obtained by extracting organic carbon from bulk sediments and, while care was taken to avoid contamination of the sample, older or younger carbon may have been mixed into the sample through bioturbation by plants or animals (see Section 5.2.1). This mangrove unit may have been contaminated by younger sediment and was therefore actually deposited prior to 6,400 years BP, when relative sea level was -1.74 ± 0.42 m below PMSL, and by 6,400 years BP, sea level was above PMSL. Apart from issues with dating, this intertidal mangrove sediment (sub-facies C1) may instead be an intertidal mudflat sediment (sub-facies C2) or even a subtidal mudflat sediment. The main distinguishing characteristics between sub-facies C1 and sub-facies C2 is that sub-facies C1 has a higher organic carbon content, a lower carbonate content and a lower proportion of sand (see Section 4.4.3). However, these differences can be subtle. If the intertidal mangrove deposit at Kwamter is instead an intertidal or subtidal mudflat deposit, relative sea level could have been close to or above PMSL 6,400 years ago, more in line with other sea level studies within the GoC. Therefore, as this intertidal mangrove fixed SLIP is the single SLIP that is at odds with other sea level studies from the GoC, it should be read with caution. Further investigation has been suggested in Section 7.2 that would help either validate or correct the interpretation in this study.

Apart from the intertidal mangrove deposit, the other SLIPs employed in this study are beach ridges, the supratidal mudflat at Kwamter, the unconformity between the beach ridge sediments and underlying intertidal mudflat at Red Beach and the shell layer at Kwamter. While the beach ridges, supratidal mudflat and the sedimentary unconformity can all be observed in the modern environment of Albatross Bay, the shell layer cannot and is open to alternate interpretations. As well as a transgressive shell lag concentration, shell concentrations can be event concentrations, hiatal concentrations and composite concentrations (Kidwell, 1991). Composite concentrations are shell concentrations formed from multiple event concentrations and are characterised as having a thickness comparable to or greater than surrounding sedimentary units. This is not the case with the Kwamter shell deposit.

Hiatal shell concentrations form during periods of low sedimentation and low shell input where there was either (1) a low amount of sediment reaching the location, (2) any sediment that reached the location was transported away without being deposited or (3) any sediment that was deposited was subsequently eroded (Kidwell, 1991). The Kwamter shell concentration was formed during a period of low sedimentation rate (see Section 6.1.3) and may be a hiatal shell concentration. However, this is unlikely as the Kwamter shell concentration is a relatively “thick” layer (approximately 20 cm in KMF2), which would require a far more substantial amount of time to accumulate than approximately 2,200 years (the shell concentration was radiocarbon dated to approximately 3,000 years BP, while the supratidal mudflat above it formed approximately 800 years ago). Even if the Kwamter shell concentration was a hiatal shell concentration, this would not change its indicative meaning as a directional SLIP – sea level would have to be above this shell concentration at the time of deposition.

The shell layer at Kwamter may also be an event concentration, formed by storm reworking. Event concentrations are hard to identify as they “...show great variation in geometry, sedimentology, and taphonomy, depending on factors such as inherited topography, shell source, whether the concentration is basically hydraulic or biogenic in origin, and the extent of later overprinting...” (Kidwell, 1991, p. 226). While a tropical cyclone may have led to the formation of this shell layer, it is unlikely to be the cause of the formation of the Kwamter shell concentration because multiple tropical cyclones have made landfall at Kwamter, but only one shell layer has been uncovered in the 6,500-year sedimentary record.

In addition to possible errors of interpretation of sedimentary units, described above, the overall preservation of the sedimentary record across Albatross Bay should also be considered, particularly because Albatross Bay lies within Australia’s cyclone belt. Tropical cyclones may lead to erosion of sediment, and, within a beach ridge plain, this may lead to a bias in the beach ridge record where highest ridges have the greatest preservation potential. However, no evidence of significant erosion was observed within the sedimentary records at all three field sites. In addition, as discussed in Section 6.1.2, there does not appear to be any significant age gaps in beach ridge formation at Red Beach, with the ridges approximately 100 to 300 years apart. In any case, even if there were gaps in the sedimentary record within the three field sites, this would not affect the sea level envelope constructed, which is based on the depositional environment, age and elevation of the sea level proxies that are present.

## 6.5 Synthesis: a record of Holocene sea level change in Albatross Bay

The sea level proxies examined at Albatross Bay contribute a record of shoreline evolution and sea level change from the mid-Holocene through to the present. Notwithstanding the limitations of the study (Section 6.4.4), as discussed in Section 6.2.3 and illustrated in Figure 6.19, relative sea level at  $6445 \pm 45$  cal. years BP was approximately -1.7 m below PMSL. Mangroves were present at Kwamter, the timing of which corresponds to the “big swamp” phase of extensive mangrove habitats across the northern margin of Australia described by Woodroffe *et al.* (1989, p. 737). Sea level was rising, reaching PMSL prior to approximately 5,000 years BP (Figure 6.19). Growth of the mangroves at Kwamter was able to keep pace with this sea level rise to PMSL, as evidenced by intertidal mangrove sediments still present in the sedimentary record at approximately -0.2 m AHD (Figure 6.6). As sea level continued to rise, however, the environment at Kwamter became unsuitable for mangroves, and the intertidal mangrove sediments were replaced by intertidal mudflat sediments (see Sections 4.4.4 and 6.2.3 and Figure 6.6).

Sometime between 5,500 years BP and 3,400 years BP, a supratidal mudflat formed inland at Kwamter, where the relict beach ridge now stands. The elevation of the relict supratidal mudflat sediments at Kwamter (+0.55 m AHD) indicates that, at some time during this time period (5,000 years BP to 3,400 years BP), MSL was approximately  $+0.55 \pm 0.43$  m AHD (see Sections 6.2.3 and 6.4.2.3 and Figure 6.19).

Beach ridge formation above the relict supratidal mudflat at Kwamter began prior to  $3392 \pm 263$  years ago (Section 6.2.3 and Figure 6.6). Beach ridge construction also commenced at Wathayn prior to  $4000 \pm 319$  years ago, associated with this same rise in sea level (Section 6.3.3 and Figure 6.10). The beach ridges at Kwamter and Wathayn were formed over a considerable period, as evidenced by a second OSL date of  $3153 \pm 324$  years ago from higher up in the beach ridge at Wathayn, and built upwards rather than outwards, most likely due to either or both a reduced sediment supply, possibly linked to the commencement and intensification of ENSO cycles, and restricted sedimentary accommodation space (Sections 6.3.3 and 6.3.2). MSL during this period of beach ridge activity at Kwamter and Wathayn (between approximately 3,000 and 4,000 years ago) would have been below the elevation of the base of the Kwamter beach ridge (i.e., below 1.52 m AHD; see Section 6.4.1 and Figure 6.19). A transgressive shell lag was also deposited at Kwamter at  $3020 \pm 120$  years BP (Figure

6.6), concurrent with beach ridge formation at Kwamter and Wathayn. This nearshore deposit provides further evidence of sea levels higher than PMSL at multiple locations around Albatross Bay during the mid to late Holocene (see Section 6.4.2.3).

After reaching the mid-Holocene highstand of approximately +1 m AHD 4,000 years ago, relative sea level either remained at this or began change (rise or fall) very gradually (Figure 6.19). MSL was still approximately +0.5 to +1 m AHD 2,200 years ago when coastal progradation commenced at Red Beach (see Section 6.1.5 and Figure 6.19). Effective precipitation increased in the Weipa region after approximately 2,200 years BP (Stevenson *et al.*, 2015a; Proske *et al.*, 2017), possibly resulting in an increased sediment supply from the rivers draining into Albatross Bay. While the increased sediment supply would have been a significant contributor to the commencement of coastal progradation at Red Beach at the mouth of the Mission River (see Section 6.1.3), the increased sediment supply within the Embley River estuary rapidly filled up the available accommodation space, causing this river channel to infill. No additional beach ridges formed at Wathayn or Kwamter. Instead, a mangrove-dominated environment developed seaward of the Kwamter beach ridge (see Section 6.2.3). Further siltation, possibly linked to a further increase in sediment supply into Albatross Bay at approximately 1,350 years BP (Table 6.3), led to the development of a supratidal mudflat at Wathayn and Kwamter, with the supratidal mudflat at Kwamter established by approximately 880 years ago (see Sections 6.2.3 and 6.3.3).

In contrast to Kwamter and Wathayn, the increased sediment supply and gradual sea level change after 2,200 years BP led to the development of a beach ridge plain at Red Beach. Between approximately 2,200 years ago and 1,700 years ago, coastal progradation at Red Beach was rapid, with the shoreline prograding at a rate of 0.84 m/yr (see Section 6.1.1). Six beach ridges (the inland beach ridge set) were constructed at Red Beach over this period, with the beach ridges forming between 6 years (RR11 to RR10) and 366 years (RR12 to RR11) apart (Figure 6.3). As described in Section 6.1.1, these beach ridges are Type 2 ridges, interpreted as having been formed by a combination of fair-weather swash processes and aeolian deposition. Tropical cyclone events, if they occurred, were not obvious contributors to ridge building during this period (see Section 6.1.3). MSL either remained at +0.5 to +1 m AHD, or changed very gradually until approximately 500 years ago (Figure 6.19).

A change in the morphology, sedimentology and coastal progradation rates within the Red Beach beach ridges occurred after 1,700 years ago, indicating a significant change in the

drivers of beach ridge building and shoreline progradation at Red Beach, namely a change in relative sea level, a change in sediment supply and/or a change in storminess (see Section 6.1.1). From 1,700 years ago to present, seven beach ridges (the seaward beach ridge set) were constructed, forming between 82 years (RR2 to RR1) and 572 (RR5 to RR4) years apart (Figure 6.3). These beach ridges are dominated by Type 1 ridges, built by a combination of fair-weather swash processes, low frequency, high magnitude tropical cyclone-induced storm surge events, and aeolian deposition (see Section 6.1.3). Coastal progradation during this time period also slowed to 0.13 m/yr (see Section 6.1.1).

The transition from the inland beach ridge set to the seaward beach ridge set at Red Beach is linked to a period of strengthened La Niña conditions between approximately 1,500 to 1,000 years ago. Strengthened La Niña conditions could have resulted in an increase in effective precipitation, and thus an increase in sediment supply (see Section 6.1.4). The sedimentary record from Big Willum Swamp on the Weipa Plateau reflects this increase in sediment supply (Table 6.3) (Stevenson *et al.*, 2015a; Proske *et al.*, 2017). Along with an increase in effective precipitation, this period of strengthened La Niña conditions likely resulted in an increase in the frequency of tropical cyclones that made landfall around Albatross Bay (see Section 6.1.4). In a review of tropical cyclone activity across Australia over the mid- to late-Holocene, Nott and Forsyth (2012) indicated that within the GoC, tropical cyclones switched from a period of inactivity to a period of activity after 1,800 years BP (i.e., tropical cyclones were active between 1,800 and 1,000 years BP). This record of tropical cyclone activity in the GoC matches with the sediment record from the seaward beach ridge set at Red Beach, with Type 1 ridges forming from  $1585 \pm 103$  years ago to present (see Section 6.1.4). The period of strengthened La Niña conditions and increase in sediment supply after 1,340 years BP is not, however, reflected in the rate of coastal progradation at Red Beach, which instead slowed to 0.13 m/yr between 286 and 1585 years ago. The slow-down in coastal progradation at Red Beach is likely a result of the erosion of the shoreline during tropical cyclone events (see Section 6.1.4).

Along with an increased sediment supply and the initiation of tropical cyclone activity within Albatross Bay from 1,700 years ago, relative sea level also began to fall more rapidly after approximately 500 years ago, to PMSL. This fall in relative sea level is reflected in the beach ridge record at Red Beach (see Sections 6.1.5 and 6.4.1), in particular the unconformity between beach ridge RR3 and the underlying intertidal mudflat (see Section 6.4.2.2). Relative

sea level was approximately +0.7 m AHD approximately 500 years ago (the beach ridge – intertidal mudflat SLIP) and continued to fall to PMSL (Figure 6.19).

## Chapter 7

### Summary and Conclusions

Attempts to construct a global eustatic sea level curve for the period of Earth history since the Last Glacial Maximum (LGM), 20 – 22 ka, have proved futile due to regional variability in tectonic, isostatic, climatic, tidal regime and oceanographic processes that influence sea level histories (Kidson, 1982; Walling and Jacovides, 1983; Pirazzoli, 1991b). The focus of sea level research therefore shifted to local and regional sea level reconstructions that would, in turn, contribute to a better understanding of past global sea level changes. There is similar regional variability in the records of Holocene sea level change across Australia, and a need for more local records to refine the sea level history of northeastern Australia in particular (Chappell *et al.*, 1982; Thom and Roy, 1983; Lambeck and Nakada, 1990; Larcombe *et al.*, 1995; Lewis *et al.*, 2013). Albatross Bay, on the northeastern coastline of the Gulf of Carpentaria (GoC) in far north Queensland, Australia, was chosen for the research reported in this thesis because, not only would it satisfy such a need but it is also the location for ongoing archaeological research on anthropogenic shell mounds with a history of formation going back at least 4,000 years (Holdaway *et al.*, 2017). A high-resolution palaeoenvironmental reconstruction of the region and, in particular, a record of Holocene sea level change are missing components that currently limit archaeological research (Morrison, 2010, 2013; Shiner *et al.*, 2013).

The aim of the research reported in this thesis, therefore, was to construct a high-resolution Holocene sea level curve for Albatross Bay by investigating the geomorphological, sedimentological and chronological evidence for relative sea level change at this location during the last 6-7,000 years. This record demonstrates that, contrary to other records from the GoC, relative sea level at Albatross Bay was approximately -1.7 m below PMSL, and rising, at approximately 6,500 years BP. Sea level reached PMSL prior to 5,000 years BP and continued to rise to a highstand of approximately +1 m above PMSL by approximately 4,000 years BP, before falling to PMSL. The outcomes of this research improve our understanding of sea level change in the past, contributing a new sea level record where data is currently lacking. This record contributes to archaeological research on human-environment interactions in the coastal regions of northern Australia.

To address this aim, the research focused on the following five objectives:



1. Investigate the environment around Albatross Bay in far north Queensland, Australia, and document the geomorphological and sedimentological evidence for Holocene sea level change (i.e., sea level proxies);
2. Establish a chronology for the response of the coastal environment to Holocene sea level change;
3. Combine the geomorphological, sedimentological and chronological evidence to establish a high resolution record of Holocene sea level change in Albatross Bay;
4. Convert this record into sea level index points (SLIPs) to construct a Holocene sea level curve for Albatross Bay;
5. Place this new sea level curve within the context of existing knowledge of Holocene sea level change in northeastern Australia.

In this chapter, I draw together the various components of the research, summarise the key findings from each objective (Table 7.1) and highlight the contributions my research makes to new knowledge. The chapter concludes with suggestions for future lines of investigation to refine the Albatross Bay sea level curve.

## **7.1 Research objectives and outcomes**

The research objectives and key associated outcomes reported in this thesis are summarised in Table 7.1.

**Table 7.1: Summary of research objectives, key outcomes and associated chapters.**

Thesis Objective	Brief Summary of findings	Associated Chapters
Investigate the marginal marine environment around Albatross Bay in far north Queensland, Australia, and document the geomorphological and sedimentological evidence for Holocene sea level change (sea level proxies) that is present in the area.  OUTCOME: Sediment facies scheme for Albatross Bay created.	The geological and geomorphological setting of Albatross Bay was described. sea level proxies present include beach ridges, beach ridge plains and sediment stratigraphic sequences (intertidal mudflats, mangrove environments and supratidal mudflats).	Chapter 1
	Existing sea level studies from within the GoC also utilise the above identified sea level proxies, further justifying their choice in this study.	Chapter 2
	Three field locations were selected - Red Beach, Kwamter and Wathayn	Chapter 3
	Field features were surveyed and samples collected for sediment analysis.	Chapter 3
	A sedimentary facies scheme was created based on the field and laboratory data, linking the sediments to their environment of deposition.	Chapter 4
Establish a chronology for the response of the marginal marine environment to Holocene sea level change.  OUTCOME: OSL and radiocarbon chronology established for locations studied	OSL and radiocarbon techniques were used to develop a chronology of environmental change at Albatross Bay	Chapters 3 and 5
	Radiocarbon dates obtained from marine shell were found to be generally inaccurate due to the reworking of shells prior to deposition.	Chapters 5 and 6
	OSL techniques allow a direct age determination from the sediments themselves, rather than their associated material, and was the preferred dating technique in this study.	Chapters 5 and 6
Combine the geomorphological, sedimentological and chronological evidence to create a high resolution record of Holocene sea level change in Albatross Bay.  OUTCOME: In-depth discussion of Holocene relative sea level change and the response of the marginal marine environment at the three field locations	The Red Beach beach ridge plain contains a record of Holocene relative sea level change and coastal progradation over the last 2,200 years, as relative sea level fell from approximately +1 m above PMSL to PMSL. In addition to relative sea level fall, the intensification of ENSO cycles, along with the commencement of tropical cyclone activity, contributed to the formation of the Red Beach beach ridge plain.	Chapter 6
	The Kwamter beach ridge and supratidal mudflat contains a record of Holocene relative sea level rise (from -1.7 m below PMSL approximately 6,500 years ago to a maximum of +1 m above PMSL prior to approximately 4,000 years BP, before falling gradually to PMSL).	Chapter 6
	The sea level record from the Wathayn beach ridge, supratidal mudflat and mangroves supplement the sea level record from Kwamter. This beach ridge was formed concurrently with the beach ridge at Kwamter. Two OSL dates collected from within the Wathayn beach ridge indicate that these beach ridges were active for a considerable period of time prior to relative sea level fall.	Chapter 6
Convert this record of Holocene sea level change in Albatross Bay into SLIPs to construct a Holocene relative sea level curve.  OUTCOME: Albatross Bay mid- to late-Holocene relative sea level curve constructed	The Red Beach, Kwamter and Wathayn sea level proxies were converted into SLIPs. The mid- to late-Holocene sea level curve constructed indicate that relative sea level was -1.7 m below PMSL approximately 6,500 years ago. Relative sea level rose, reaching PMSL prior to 5,000 years BP. Relative sea level continued to rise past PMSL, reaching a maximum of approximately +1 m above PMSL by approximately 3,000 to 4,000 years ago. Relative sea level either remained at this highstand for an extended period of time, or gradually fell and was approximately +0.7 mAHd approximately 500 years ago before falling to PMSL.	Chapter 6
Place this new sea level curve within the context of existing knowledge of Holocene relative sea level change in north-eastern Australia  OUTCOME: Albatross Bay relative sea level curve superimposed on existing sea level records. Data generally well matched.	Sea level research across the northern coast of Australia, eastern coast of Australia, and within the GoC was reviewed. SLIPs from available literature was combined to construct Holocene sea level curves for each region	Chapter 2
	The mid to late-Holocene sea level curve at Albatross Bay fits well with sea level data across the northern and eastern coasts of Australia. However, the Albatross Bay sea level curve does not match well with the records from within the GoC of Rhodes (1980), likely because the study by Rhodes (1980) utilised radiocarbon dating of marine shell that was likely extensively reworked prior to deposition. If the palaeoshoreline features identified by Rhodes (1980) are younger than the radiocarbon dates suggest, the sea level reconstruction of Rhodes (1980) within the GoC will match well with the Albatross Bay sea level curve.	Chapter 6

### 7.1.1 Objective One: Geomorphological and sedimentological evidence of Holocene sea level change in Albatross Bay

The description of the Albatross Bay study area in Chapter 1 (Section 1.4.2) identified the sea level proxies that are present – beach ridges, beach ridge plains, and sedimentary stratigraphic sequences (intertidal mudflats, mangrove environments and supratidal mudflats). The literature review in Chapter 2 (particularly Section 2.4 focussing on the GoC) demonstrated how the sea level proxies that were identified in Chapter 1 also form the basis of existing Holocene sea level studies within the Gulf, further justifying the suitability of these sea level proxies for my study.

Chapter 3 describes the methods employed in this study. The locations of Red Beach, Kwamter and Wathayn (Figure 3.1) were selected for detailed investigation because of the presence of the selected sea level proxies, access to the locations, and previous palaeoenvironmental and archaeological research that would provide comparisons with this study. Key topographic features were surveyed in the field, their stratigraphy recorded, and samples collected for laboratory analysis and dating (Sections 3.2 and 3.3).

The coastal sedimentary environments of Albatross Bay are discussed Chapter 4. A sediment facies scheme for Albatross Bay was constructed based on field descriptions, the environmental context, and laboratory analyses of the sediments comprising the coastal environments. Four primary sedimentary facies, and a variable number of sub-facies, were identified and their environments of deposition determined (Section 4.4). The facies scheme enables reconstruction of shifts in the coastal environments around Albatross Bay in response to sea level and palaeo-environmental changes.

### 7.1.2 Objective Two: Establishing a chronology of mid- to late-Holocene sea level change

In Chapter 5 (Sections 5.1.6 and 5.2.2; Table 5.13 and 5.14), OSL and radiocarbon chronologies of mid- to late-Holocene coastal evolution are established for each field location. The factors that may affect the outcomes of the application of OSL and radiocarbon techniques to the selected samples are discussed in detail. The radiocarbon ages of shell samples collected from the beach ridge plain are consistently older than the OSL burial ages from the same beach ridge – evidence that these shells have been transported and reworked for a significant period of time prior to deposition. The OSL age determinations are therefore considered to be a more accurate representation of the actual depositional event, and provide the basis for the Holocene coastal evolution and sea level change chronology presented in Section 6.1.2, 6.2.2 and 6.3.2.

### 7.1.3 Objective Three: A high-resolution record of Holocene sea level change in Albatross Bay

In Chapter 6, the facies scheme presented in Chapter 4 is combined with the chronology established for each field location in Chapter 5 to establish a narrative of Holocene coastal evolution and sea level change for Albatross Bay (Sections 6.1, 6.2 and 6.3). Approximately 6,500 years BP, relative sea level was approximately -1.7 m below PMSL. Mangroves were present at Kwamter during this period, corresponding to the “big swamp” phase of extensive mangrove habitats across the northern margin of Australia (Woodroffe *et al.*, 1989, p. 737). Relative sea level was rising, reaching a mid-Holocene highstand of approximately +1 m above PMSL approximately 4,000 years ago, leading to the formation of the beach ridges found at Kwamter and Wathayn. The beach ridges at Kwamter and Wathayn were active for a considerable period as indicated by the two OSL dates approximately 1,000 years apart taken from within the same beach ridge at Wathayn.

It was during this relative sea level rise that the transgressive shell-lag was deposited at Kwamter. Sea level either remained at this elevation for an extended period of time before falling or began to fall very gradually. Once relative sea level fell, the beach ridges at Kwamter and Wathayn were isolated from active coastal processes. Infilling of the Embley River estuary led to the formation of a mangrove zone on the proximal side of the beach ridge at Kwamter. Continued relative sea level fall then resulted in the formation of the supratidal mudflat at Kwamter and Wathayn.

Beach ridge formation commenced at Red Beach approximately 2,200 years ago, partially influenced by an increase in effective precipitation, and thus sediment supply, into Albatross Bay at this time. Coastal progradation was rapid, with the shoreline prograding at a rate of approximately 0.84 m/yr. Between approximately 1,700 and 1,600 years ago, the palaeoenvironment at Red Beach shifted from an El Niño to a La Niña- dominant phase, resulting in the occurrence of tropical cyclones making landfall at and an increase in sediment supply into Albatross Bay. This caused a change in the morphology and sedimentology within the Red Beach beach ridge plain, along with a decrease in coastal progradation rates to approximately 0.13 m/yr. Relative sea level fall after 2,200 years ago was gradual, with the rate of relative sea level fall to PMSL increasing after approximately 500 years ago

#### 7.1.4 Objective Four: A Holocene sea level curve for Albatross Bay

The method of conversion of the Red Beach, Kwamter and Wathayn sea level proxies into SLIPs is described in Chapter 6 (see Sections 6.4.1 and 6.4.2). A mid- to late-Holocene sea level curve derived from these SLIPs for Albatross Bay is then presented (Figure 6.19). My research establishes that, at  $6445 \pm 45$  cal. years BP, relative sea level was approximately -1.7 m below PMSL and rising. Relative sea level reached PMSL prior to 5,000 years BP, and continued to rise, reaching an elevation of approximately +1 m above PMSL by around 4,000 years BP. Relative sea level then either remained at this highstand, or fell very gradually. MSL was approximately +0.7 m above PMSL at approximately 500 years BP, continuing to fall, at an increasing pace, to PMSL (Figure 6.19).

#### 7.1.5 Objective Five: The significance of the Albatross Bay sea level curve

The Albatross Bay sea level curve generally fits well with the records from the northern and eastern margins of Australia compiled in Chapter 2 (illustrated in Figures 6.20 and 6.21). The broad agreement among these datasets suggests that the mid- to late-Holocene sea level changes that occurred in Albatross Bay were regionally driven rather than locally driven. Following the post-LGM relative sea level rise to PMSL around 5,000 years ago, relative sea level surpassed PMSL reaching a mid-Holocene highstand of +1 m before falling gradually back to PMSL. This mid-Holocene highstand and subsequent relative sea level fall is attributed to geoidal changes, in a process called “equatorial ocean syphoning” (see Sections 2.1 and 6.4.3) (Mitrovica and Peltier, 1991; Woodroffe and Horton, 2005).

The new Albatross Bay sea level curve is insufficient on its own to resolve some of the bigger debates surrounding Holocene sea level change in northeastern Australia outlined in Chapter 2. These debates include whether the mid-Holocene sea level highstand occurred across the entire northeastern margin of Australia, whether the subsequent fall of relative sea level to PMSL was smooth or oscillating, and the timing of the fall. No local sea level study will be able to resolve such debates. What is required are more SLIPs from new locations, and improvement of the sea level history at previously studied locations. The mid- to late- Holocene sea level curve for Albatross Bay developed by this study contributes a new sea level record for northeastern Australia and improves our understanding of Holocene sea level change.

Because of the lack of research on Holocene sea level change within the GoC (see Section 2.4), palaeoenvironmental and archaeological research at Albatross Bay currently reference the study by Rhodes (1980) from the southern GoC for data on sea level change (see, for example,

Stone, 1992; Bailey *et al.*, 1994; Stone, 1995; Morrison, 2010; Beresford, 2011; Shiner *et al.*, 2013; Morrison, 2015). Rhodes (1980) suggests that, by 6,400 years BP, relative sea level was already approximately +1 m to +1.5 m above PMSL (see Section 2.4). In contrast, my record from the Kwamter location indicates that, at  $6445 \pm 45$  years BP, relative sea level was approximately -1.7 m below PMSL (see Section 6.2.3). This disparity between my study and the study by Rhodes (1980) could be because Rhodes (1980) used conventional radiocarbon ages from shell for his sea level reconstruction. Inaccurately older ages due to the transporting and reworking of shell prior to deposition usually result (see Section 6.1.2). These inaccuracies would be particularly pronounced at Karumba, where Rhodes (1980) obtained ages from shell from a chenier ridge plain, formed during tropical cyclone events, increasing the likelihood of the shells being reworked prior to deposition (see Section 6.2.3). Assuming that the palaeoshoreline features at Christmas Creek and Edward River, also dated by Rhodes (1980), are younger than the radiocarbon dates indicate, the maximum relative sea level elevations at these locations of between +0.8 m to +1.5 m above PMSL corresponds well with the Albatross Bay sea level reconstruction produced in this study (see Section 6.2.3).

However, the estimation of relative sea level at approximately -1.7 m below PMSL around 6,500 years ago is based on one intertidal mangrove deposit found at Kwamter. This SLIP may be inaccurate due to uncertainties around the radiocarbon date obtained or the interpretation of the sediment as an intertidal mangrove deposit (see Section 6.4.4). This intertidal mangrove fixed SLIP should therefore be read with caution. Further investigation has been suggested below (see Section 7.2) that would help either validate or correct the interpretation used in this study.

The sea level curve for Albatross Bay derived from this study provides a new sea level record for the GoC, where such data was previously lacking. It will have immediate utility for ongoing archaeological research within Albatross Bay (Holdaway *et al.*, 2017; Fanning *et al.*, 2018), providing a more accurate basis for archaeologists to examine past human-environment interactions at this culturally important location.

## **7.2 Suggestions for future research**

This section outlines how the resolution of the Holocene sea level record and mid- to late-Holocene sea level curve for Albatross Bay, established by the research reported in this thesis, can be improved. In addition, the high-resolution sedimentary stratigraphy of the beach

ridge plain at Red Beach contains a record of late-Holocene tropical cyclone activity in Albatross Bay that can contribute to reconstructions of Holocene tropical cyclone behaviour.

#### 7.2.1 The geomorphological and sedimentological record

Logistical issues limited sedimentary stratigraphic recording and sediment sample collection at both the Red Beach and Wathayn field locations. Because the pits within the beach ridges were excavated by hand, digging ceased at the maximum safe dig depth, or when the presence of a calcrete layer prevented further excavation. This issue was particularly pronounced at Red Beach, where calcrete cementation prevented the exposure of the beach ridge – intertidal mudflat unconformity in all but one beach ridge (RR3, Figure 6.3). The beach ridges at Red Beach therefore could only be used as directional sea level indicators, rather than fixed indicators, with MSL at the time of formation of each ridge being below the base of the pit (see Section 6.4.1). Deeper excavations at Red Beach and the use of ground penetrating radar would provide a more complete stratigraphy of the location. A key focus would be to obtain the precise elevation of the beach ridge – intertidal mudflat unconformity which would allow these directional SLIPs to be converted to fixed SLIPs (see Section 6.4.2.2), refining the late-Holocene sea level record from Red Beach.

At Wathayn, the instability of the pit within the beach ridge prevented exposure and sampling of the complete sedimentary record of the ridge. Extrapolation of available data indicated that there may have been as much as 0.8 m of beach ridge sediments below the base of the pit (see Section 6.3.1). Like Red Beach, further excavation of the beach ridge at Wathayn would refine this directional SLIP.

#### 7.2.2 The chronological record

While a relatively large number of age determinations were obtained for the Albatross Bay study area (18 OSL burial ages and 12 radiocarbon ages), most of these were from the Red Beach location. The mid- to late-Holocene sea level record, especially at Kwamter and Wathayn, could be improved with further dating. Suggested additional dates for Kwamter (see Section 6.2.3) include:

1. A radiocarbon age on the bulk sediments from the top of the mangrove deposit within the supratidal mudflat (pit KMF1 in Figure 6.5). This age would provide an estimation of when sea level reached PMSL at Kwamter, before rising to the mid-Holocene highstand elevation.

2. An OSL burial age for the sediments at the crest of the beach ridge (pit KR1 in Figure 6.5). This sample would provide an estimated age for the cessation of ridge building due to coastal progradation separating the beach ridge from the source of sediment.
3. An OSL burial age from the distal mangrove zone (pit KS1 in Figure 6.5). It is hypothesised that, as sea level fell in the mid- to late-Holocene and isolated the Kwamter beach ridge from active coastal processes, increased sedimentation led to infilling of the Embley River estuary and the formation of a mangrove zone on the proximal side of the beach ridge. This additional OSL date would test this hypothesis and provide an additional SLIP on the sea level curve.
4. An OSL burial age for the relict supratidal mudflat beneath the Kwamter beach ridge (pit KR1 in Figure 6.5). It is hypothesised that this feature was deposited during the mid-Holocene sea level rise, inferring that MSL was approximately +0.55 above PMSL at the time. The lack of an age for this unit means that this SLIP has a large age range – relative sea level was +0.55 m above PMSL sometime between 6,500 and 3,400 years ago (see Section 6.2.3). An additional OSL date could narrow this age range, refining the SLIP.
5. An OSL burial age from within the transgressive shell lag unit (Pit KMF1/KMF2 in Figure 6.5). The current radiocarbon age is from whole shell, which may be inaccurate due to transport and reworking of the shell prior to its final deposition in the shell lag unit. An OSL age would add confidence to the SLIP for this transgressive shell lag.

Suggested additional dates for Wathayn include:

1. An OSL burial age for the crest of the Wathayn beach ridge (pit WR1 in Figure 6.9). This date would provide insights into the isolation of the Wathayn beach ridge from active coastal processes due to coastal progradation (see Section 6.3.3)
2. An OSL burial age from the base of the Wathayn beach ridge following deeper excavation to expose the unconformity between the beach ridge and the underlying substrate (see Section 7.2.1). This age would estimate the timing of the commencement of beach ridge formation at Wathayn.
3. An OSL burial age from within the supratidal mudflat at Wathayn (see Figures 4.24 and 6.9). This supratidal mudflat is currently undated, and it is assumed that it formed concurrently with that at Kwamter, approximately 800 years ago (see Section



6.3.3). This assumption could be tested by obtaining an OSL burial age from within pit WMF3 (Figure 6.9).

Suggested additional dates for Red Beach include:

1. Only one beach ridge within the beach ridge plain at Red Beach is currently undated (ridge RR6 in Figure 6.3). An OSL burial age from the base of this ridge would complete the beach ridge chronology at Red Beach, and add an additional SLIP to the Albatross Bay sea level curve.

### 7.2.3 Additional sea level proxies

The Holocene sea level record obtained from Red Beach, at an open coastal setting at the mouth of the Mission River, was different in a number of ways to that obtained from Kwamter and Wathayn, both located in more constricted settings along the Embley River estuary. However, these different records were able to be combined to build a comprehensive picture of mid- to late-Holocene sea level change in Albatross Bay. The sedimentary records from Botchet Beach (an open coastal setting directly facing Albatross Bay) and from Urquart's Point (an open coastal setting on Pera Head, at the mouth of the Embley River) are likely to be different from those at Red Beach, Kwamter and Wathayn. Similar geochronological investigations at these locations may contribute additional data on the Holocene sea level history of Albatross Bay.

Stevenson *et al.* (2015) extracted a 1.5 m long D-section core from the mangrove zone at Wathayn West, approximately 3 km downstream from the Wathayn transect in this study. Radiocarbon dating indicates that this core represents sediment accumulation from approximately 6,900 years BP to present (Stevenson *et al.*, 2015b), which is significantly older than the mangrove D-section core retrieved in this study, which was only 50 cm deep and returned a radiocarbon age of "Modern" (see Section 6.3.2). Sedimentological analysis of this D-section core could supplement the sea level reconstruction for the Embley river obtained from this study because it contains sediments dating to the mid- to late-Holocene (see Section 3.1.3). Furthermore, mangrove deposits like those obtained in the Wathayn D-section core often preserve microfossils, such as diatoms and foraminifera, which can also be used as proxies for sea level change (see Zong and Horton, 1999; Woodroffe *et al.*, 2005; Edwards, 2007a; Gehrels, 2007; Horton *et al.*, 2007b; Jones, 2007; Zong *et al.*, 2010; Lewis *et al.*, 2013 for reviews and examples of the use of microfossils in sea-level reconstruction).

#### 7.2.4 A record of tidal changes within the GoC over the mid to late Holocene

Sea level reconstructions, including this one, are often inherently based on the assumption that wave regimes and tidal ranges have not changed significantly throughout the period of reconstruction. However, such assumptions are likely false (see Section 2.4). Palaeotidal modelling over the mid to late Holocene within the GoC will fine-tune the indicative meaning of the SLIPs used in this study and therefore the relative sea level record within Albatross Bay. Palaeotidal modelling would involve obtaining an estimate of ocean stratification within the GoC (from seafloor sediments or coupled atmosphere-ocean climate simulations) and the local bathymetry over the time period in question (Griffiths and Hill, 2015). This data will then need to be inputted into tidal models to predict how the tidal range has changed in an area over time (Griffiths and Hill, 2015).

#### 7.2.5 A record of late-Holocene tropical cyclone activity at Red Beach

The sediments within the beach ridge plain at Red Beach contain a record of tropical cyclone activity within Albatross Bay from  $1,585 \pm 103$  years ago to present (see Section 6.1.4). While not a focus of this thesis, palaeotempestology (the study of prehistoric tropical cyclone activity) is an important branch of Quaternary research. It suggests that tropical cyclone activity is not constant through time, but rather there are phases when tropical cyclone activity is enhanced, and other phases of relative quiescence (Nott, 2004). "... Recognition of such regime changes, or non-stationarity in the long-term record, is important for risk assessments of this hazard..." (Nott, 2004, p 433). The high-resolution record from the beach ridge plain at Red Beach makes this field location an ideal site for future palaeotempestology research.

## References

- Aaby, B. & Digerfeldt, G. 1986. Sampling Techniques for Lakes and Bogs. *In*: Berglund, B. E. (ed.) *Handbook of Holocene Palaeoecology and Palaeohydrology*. Great Britain: John Wiley & Sons.
- Abbott, S. T. & Carter, R. M. 2007. Sequence Stratigraphy. *In*: Elias, S. A. (ed.) *Encyclopedia of Quaternary Science*. Oxford: Elsevier.
- Adamiec, G. & Aitken, M. 1998. Dose-Rate Conversion Factors: Update. *Ancient TL*, 16, 37-49.
- Aitken, M. J. 1985. *Thermoluminescence Dating*, London, Academic Press.
- Aitken, M. J. 1998. *An Introduction to Optical Dating : The Dating of Quaternary Sediments by the Use of Photon-Stimulated Luminescence*, Oxford, Oxford University Press.
- Alappat, L., Frechen, M., Kumar, S. S., Babu, D. S. S., Ravur, R. & Tsukamoto, S. 2015. Evidence of Late Holocene Shoreline Progradation in the Coast of Kerala, South India Obtained from Osl Dating of Palaeo-Beach Ridges. *Geomorphology*, 245, 73-86.
- Angulo, R. J. & Lessa, G. C. 1997. The Brazilian Sea-Level Curves: A Critical Review with Emphasis on the Curves from the Paranaguá and Cananéia Regions. *Marine Geology*, 140, 141-166.
- Angulo, R. J., Lessa, G. C. & De Souza, M. C. 2006. A Critical Review of Mid- to Late-Holocene Sea-Level Fluctuations on the Eastern Brazilian Coastline. *Quaternary Science Reviews*, 25, 486-506.
- Anthony, E. J. 2009. Beach Plains: Formation, Evolution and Ecological Significance. *In*: Isla, F. I. & Iribarne, O. (eds.) *Coastal Zones and Estuaries, Encyclopedia of Life Support Systems*. Oxford, United Kingdom: EOLSS Publishers.
- Arnold, L. J., Roberts, R. G., Galbraith, R. F. & Delong, S. B. 2009. A Revised Burial Dose Estimation Procedure for Optical Dating of Young and Modern-Age Sediments. *Quaternary Geochronology*, 4, 306-325.
- ASTM 2014. *Standard Test Methods for Moisture, Ash and Organic Matter of Peat and Other Organic Soil*, *Astm D2974-14*, West Conshohocken, Pennsylvania, ASTM International.
- Bailey, G. 1977. Shell Mounds, Shell Middens, and Raised Beaches in the Cape York Peninsula. *Mankind*, 11, 132-143.
- Bailey, G. 1991. Hens' Eggs and Cockle Shells: Weipa Shell Mounds Reconsidered. *Archaeology in Oceania*, 26, 21-23.
- Bailey, G. 1993. Shell Mounds in 1972 and 1992: Reflections on Recent Controversies at Ballina and Weipa. *Australian Archaeology*, 1-18.
- Bailey, G., Chappell, J. & Cribb, R. 1994. The Origin of "Anadara" Shell Mounds at Weipa, North Queensland, Australia. *Archaeology in Oceania*, 29, 69-80.
- Bailey, S. D., Wintle, A. G., Duller, G. a. T. & Bristow, C. S. 2001. Sand Deposition During the Last Millennium at Aberffraw, Anglesey, North Wales as Determined by Osl Dating of Quartz. *Quaternary Science Reviews*, 20, 701-704.
- Baker, R. G. V. & Haworth, R. J. 2000a. Smooth or Oscillating Late Holocene Sea-Level Curve? Evidence from Cross-Regional Statistical Regressions of Fixed Biological Indicators. *Marine Geology*, 163, 353-365.
- Baker, R. G. V. & Haworth, R. J. 2000b. Smooth or Oscillating Late Holocene Sea-Level Curve? Evidence from the Palaeo-Zoology of Fixed Biological Indicators in East Australia and Beyond. *Marine Geology*, 163, 367-386.
- Baker, R. G. V., Haworth, R. J. & Flood, P. G. 2001. Inter-Tidal Fixed Indicators of Former Holocene Sea Levels in Australia: A Summary of Sites and a Review of Methods and Models. *Quaternary International*, 83-85, 257-273.

- Baker, R. G. V., Haworth, R. J. & Flood, P. G. 2005. An Oscillating Holocene Sea-Level? Revisiting Rottnest Island, Western Australia, and the Fairbridge Eustatic Hypothesis. *Journal of Coastal Research*, 3-14.
- Ball, D. F. 1964. Loss on Ignition as an Estimate of Organic Matter and Organic Carbon in Non-Calcareous Soils. *Journal of Soil Science*, 15, 84-92.
- Ballarini, M., Wallinga, J., Murray, A. S., Van Heteren, S., Oost, A. P., Bos, A. J. J. & Van Eijk, C. W. E. 2003. Optical Dating of Young Coastal Dunes on a Decadal Time Scale. *Quaternary Science Reviews*, 22, 1011-1017.
- Banerjee, P. K. 2000. Holocene and Late Pleistocene Relative Sea Level Fluctuations Along the East Coast of India. *Marine Geology*, 167, 243-260.
- Barkley, R., John, G., Shiner, J. & Wrigley, M. 2008. Collaboration and Innovation in the Management of Cultural Landscapes in Mining Contexts, Western Cape York, Far North Queensland. *Historic Environment*, 21, 7-15.
- Barrows, T. T., Stone, J. O., Fifield, L. K. & Cresswell, R. G. 2001. Late Pleistocene Glaciation of the Kosciuszko Massif, Snowy Mountains, Australia. *Quaternary Research*, 55, 179-189.
- Barrows, T. T., Stone, J. O., Fifield, L. K. & Cresswell, R. G. 2002. The Timing of the Last Glacial Maximum in Australia. *Quaternary Science Reviews*, 21, 159-173.
- Bateman, M. D. 2015. The Application of Luminescence Dating in Sea-Level Studies. *Handbook of Sea-Level Research*. Hoboken, NJ: John Wiley & Sons, Ltd.
- Beaman, R., Larcombe, P. & Carter, R. M. 1994. New Evidence for the Holocene Sea-Level High from the Inner Shelf, Central Great Barrier Reef, Australia. *Journal of Sedimentary Research*, 64, 881-885.
- Belperio, A. P. 1979. Negative Evidence for a Mid-Holocene High Sea Level Along the Coastal Plain of the Great Barrier Reef Province. *Marine Geology*, 32, M1-M9.
- Belperio, A. P., Harvey, N. & Bourman, R. P. 2002. Spatial and Temporal Variability in the Holocene Sea-Level Record of the South Australian Coastline. *Sedimentary Geology*, 150, 153-169.
- Bendixen, M., Clemmensen, L. B. & Kroon, A. 2013. Sandy Berm and Beach-Ridge Formation in Relation to Extreme Sea-Levels: A Danish Example in a Micro-Tidal Environment. *Marine Geology*, 344, 53-64.
- Bengtsson, L. & Enell, M. 1986. Chemical Analysis. In: Berglund, B. E. (ed.) *Handbook of Holocene Palaeoecology and Palaeohydrology*. Great Britain: John Wiley & Sons.
- Benn, D. I. & Evans, D. J. A. 1998. *Glaciers and Glaciation*, London, Arnold Publishers.
- Beresford, C. E. 2011. *Understanding Human Behavioural Change and Shell Mound Location at Albatross Bay, Cape York, Australia*. Master of Arts, University of Auckland.
- Bickel, L., Lüthgens, C., Lomax, J. & Fiebig, M. 2015. Luminescence Dating of Glaciofluvial Deposits Linked to the Penultimate Glaciation in the Eastern Alps. *Quaternary International*, 357, 110-124.
- Bird, E. 2005. Australia, Coastal Geomorphology. In: Schwartz, M. (ed.) *Encyclopedia of Coastal Science*. London: Kluwer Academic.
- Bird, E. 2008. *Coastal Geomorphology. An Introduction.*, Chichester, John Wiley & Sons Ltd.
- Bird, E. C. F. 1971. The Fringing Reefs near Yule Point, North Queensland. *Australian Geographical Studies*, 9, 107-115.
- Bird, M. I., Fifield, L. K., Chua, S. & Goh, B. 2004. Calculating Sediment Compaction for Radiocarbon Dating of Intertidal Sediments. *Radiocarbon*, 46, 421-435.
- Björck, S. 2007. Younger Dryas Oscillation, Global Evidence In: Elias, S. A. (ed.) *Encyclopedia of Quaternary Science*. Oxford: Elsevier.

- Bjørnsen, M., Clemmensen, L. B., Murray, A. & Pedersen, K. 2008. New Evidence of the Littorina Transgressions in the Kattegat: Optically Stimulated Luminescence Dating of a Beach Ridge System on Anholt, Denmark. *Boreas*, 37, 157-168.
- Blaber, S. J. M., Salini, J. P. & Brewer, D. T. 1990. *A Checklist of the Fishes of Albatross Bay and the Embley Estuary, North-Eastern Gulf of Carpentaria*. *Csiro Marine Laboratories Report No. 210*, Australia, CSIRO.
- Blasco, F., Saenger, P. & Janodet, E. 1996. Mangroves as Indicators of Coastal Change. *CATENA*, 27, 167-178.
- Bloom, A. L. 1980. Late Quaternary Sea Level Change on South Pacific Coasts: A Study in Tectonic Diversity. In: Mörner, N. A. (ed.) *Earth Rheology, Isostasy and Eustasy*. London: Wiley.
- Blott, S. J. & Pye, K. 2001. Gradistat: A Grain Size Distribution and Statistics Package for the Analysis of Unconsolidated Sediments. *Earth Surface Processes and Landforms*, 26, 1237-1248.
- Bokuniewicz, H. 2005. Ingression, Regression, and Transgression. In: Schwartz, M. L. (ed.) *Encyclopedia of Coastal Science*. Dordrecht: Springer Netherlands.
- Boyle, J. 2004. A Comparison of Two Methods for Estimating the Organic Matter Content of Sediments. *Journal of Paleolimnology*, 31, 125-127.
- Breitfuss, M., Duke, N., Knight, J. & Rogers, K. 2015. *Changes in Mangrove Areas* [Online]. Canberra: Geoscience Australia. Available: [http://www.ozcoasts.gov.au/indicators/mangrove\\_areas.jsp](http://www.ozcoasts.gov.au/indicators/mangrove_areas.jsp) [Accessed 23 Aug 2017].
- Brenchley, P. J. & Harper, D. a. T. 1998. *Palaeoecology: Ecosystems, Environments and Evolution*, London, Chapman & Hal.
- Brenninkmeyer, B. 1982. Major Beach Features. In: Schwartz, M. (ed.) *Encyclopedia of Beaches and Coastal Environments*. Stroudsburg, Pennsylvania: Hutchinson Ross Pub. Co.
- Briggs, D. 1977. *Sediments*, England, Butterworths.
- Bristow, C. S., Duller, G. a. T. & Lancaster, N. 2007. Age and Dynamics of Linear Dunes in the Namib Desert. *Geology*, 35, 555-558.
- Brockwell, S., Ó Foghlú, B., Fenner, J. N., Stevenson, J., Proske, U. & Shiner, J. 2017. New Dates for Earth Mounds at Weipa, North Queensland, Australia. *Archaeology in Oceania*, 52, 127-134.
- Brooke, B., Lee, R., Cox, M., Olley, J. & Pietsch, T. 2008. Rates of Shoreline Progradation During the Last 1700 Years at Beachmere, Southeastern Queensland, Australia, Based on Optically Stimulated Luminescence Dating of Beach Ridges. *Journal of Coastal Research*, 640-648.
- Brooke, B., Ryan, D., Radke, L., Pietsch, T., Olley, J., Douglas, G., Flood, P. & Packett, B. 2006. A 1500 Year Record of Coastal Sediment Accumulation Preserved in Beach Deposits at Keppel Bay, Queensland, Australia. Queensland: Cooperative Research Centre for Coastal Zone, Estuary and Waterway Management (Coastal CRC).
- Brooke, B. P., Pietsch, T. J., Olley, J. M., Sloss, C. R. & Cox, M. E. 2015. A Preliminary Osl Chronology for Coastal Dunes on Moreton Island, Queensland, Australia – Marginal Deposits of a Large-Scale Quaternary Shelf Sediment System. *Continental Shelf Research*, 105, 79-94.
- Bryant, E. 1992. Last Interglacial and Holocene Trends in Sea-Level Maxima around Australia: Implications for Modern Rates. *Marine Geology*, 108, 209-217.
- Burdette, K. E., Rink, W. J., López, G. I., Mallinson, D. J., Parham, P. R. & Reinhardt, E. G. 2012. Geological Investigation and Optical Dating of Quaternary Siliciclastic Sediments near Apalachicola, North-West Florida, USA. *Sedimentology*, 59, 1836-1849.

- Bureau of Meteorology. 2014. *Map 1. The Key Climate Groups* [Online]. Australian Government Bureau of Meteorology. Available: [http://www.bom.gov.au/iwk/climate\\_zones/map\\_1.shtml](http://www.bom.gov.au/iwk/climate_zones/map_1.shtml) [Accessed 5 March 2016].
- Bureau of Meteorology. 2016a. *Climate of Weipa Area* [Online]. Australian Government Bureau of Meteorology. Available: <http://www.bom.gov.au/qld/weipa/climate.shtml> [Accessed 5 May 2016].
- Bureau of Meteorology. 2016b. *Climate Statistics for Australian Locations - Summary Statistics Weipa Eastern Ave* [Online]. Australian Government Bureau of Meteorology. Available: [http://www.bom.gov.au/climate/averages/tables/cw\\_027042\\_All.shtml](http://www.bom.gov.au/climate/averages/tables/cw_027042_All.shtml) [Accessed 5 May 2016].
- Bureau of Meteorology. 2016c. *Queensland Tide Tables - Weipa (Humbug Point)* [Online]. Australian Government Bureau of Meteorology. Available: [http://www.bom.gov.au/ntc/IDO59001/IDO59001\\_2016\\_QLD\\_TP036.pdf](http://www.bom.gov.au/ntc/IDO59001/IDO59001_2016_QLD_TP036.pdf) [Accessed 8 June 2016].
- Bureau of Meteorology. 2016d. *Tropical Cyclone Faqs* [Online]. Australian Government Bureau of Meteorology. Available: <http://www.bom.gov.au/cyclone/faq/> [Accessed 5 May 2016].
- Bureau of Meteorology. 2016e. *Tropical Cyclone Information for the Australian Region* [Online]. Australian Government Bureau of Meteorology. Available: <http://www.bom.gov.au/cgi-bin/silo/cyclones.cgi?region=aus&year=1906&eyear=2006&loc=1&txtloc=&radius=50&ulat=12.39&ulon=141.50> [Accessed 1 June 2016].
- Bureau of Meteorology. 2016f. *Tropical Cyclone Mark* [Online]. Australian Government Bureau of Meteorology. Available: <http://www.bom.gov.au/cyclone/history/mark.shtml> [Accessed 1 June 2016].
- Bureau of Meteorology. 2018. *Storm Surge Preparedness and Safety* [Online]. Australian Government Bureau of Meteorology. Available: <http://www.bom.gov.au/cyclone/about/stormsurge.shtml> [Accessed 4 October 2018].
- Burne, R. V. & Graham, T. L. 1995. *Coastal Environment Geoscience of Cape York Peninsula*, Brisbane, Qld, Office of the Co-ordinator General.
- Burr, G. S. 2007. Radiocarbon Dating - Causes of Temporal Variations. In: Elias, S. A. (ed.) *Encyclopedia of Quaternary Science*. Oxford: Elsevier.
- Cameron, E. E. & Cogger, H. G. 1992. The Herpetofauna of the Weipa Region, Cape York Peninsula. *Technical Reports of the Australian Museum*, 7, 1-200.
- Carlson, A. E. 2011. Ice Sheets and Sea Level in the Earth's Past. *Nature Education Knowledge*, 3, 3.
- Carr, A. S., Bateman, M. D., Roberts, D. L., Murray-Wallace, C. V., Jacobs, Z. & Holmes, P. J. 2010. The Last Interglacial Sea-Level High Stand on the Southern Cape Coastline of South Africa. *Quaternary Research*, 73, 351-363.
- Carroll, M., Kowalewski, M., Simões, M. G. & Goodfriend, G. A. 2003. Quantitative Estimates of Time-Averaging in Terebratulid Brachiopod Shell Accumulations from a Modern Tropical Shelf. *Paleobiology*, 29, 381-402.
- Carson, M. T. & Peterson, J. A. 2011. Calcrete Formation and Implications for Buried Archaeological Deposits in the Mariana Islands, Western Pacific. *Geoarchaeology*, 26, 501-513.
- Carter, M. & Bentley, S. P. 2016. *Density. Soil Properties and Their Correlations*. Chichester, West Sussex, United Kingdom: John Wiley & Sons, Ltd.
- Carter, R. M., Johnson, D. P. & Hooper, K. G. 1993. Episodic Post-Glacial Sea-Level Rise and the Sedimentary Evolution of a Tropical Continental Embayment (Cleveland Bay,

- Great Barrier Reef Shelf, Australia). *Australian Journal of Earth Sciences*, 40, 229-255.
- Chappell, J. 1983. Evidence for Smoothly Falling Sea Level Relative to North Queensland, Australia, During the Past 6,000 Yr. *Nature*, 302, 406-408.
- Chappell, J. 1987. Late Quaternary Sea-Level Changes in the Australian Region. In: Tooley, M. J. & Shennan, I. (eds.) *Sea-Level Changes*. Oxford: Basil Blackwell Ltd.
- Chappell, J. 1993. Contrasting Holocene Sedimentary Geologies of Lower Daly River, Northern Australia, and Lower Sepik-Ramu, Papua New Guinea. *Sedimentary Geology*, 83, 339-358.
- Chappell, J., Chivas, A. R., Wallensky, E., Polach, H. A. & Aharon, P. 1983. Holocene Palaeo-Environmental Changes, Central to North Great Barrier Reef Inner Zone. *BMR Journal of Australian Geology and Geophysics*, 8, 223-235.
- Chappell, J. & Grindrod, J. F. 1984. Chenier Plain Formation in Northern Australia. In: Thom, B. G. (ed.) *Coastal Geomorphology in Australia*. Sydney: Academic Press.
- Chappell, J. & Polach, H. 1991. Post-Glacial Sea-Level Rise from a Coral Record at Huon Peninsula, Papua New Guinea. *Nature*, 349, 147-149.
- Chappell, J., Rhodes, E. G., Thom, B. G. & Wallensky, E. 1982. Hydro-Isostasy and the Sea-Level Isobase of 5500 B.P. in North Queensland, Australia. *Marine Geology*, 49, 81-90.
- Cheetham, M. D., Keene, A. F., Bush, R. T., Sullivan, L. A. & Erskine, W. D. 2008. A Comparison of Grain-Size Analysis Methods for Sand-Dominated Fluvial Sediments. *Sedimentology*, 55, 1905-1913.
- Chen, X. Y., Lintern, M. J. & Roach, I. C. 2002. *Calcrete: Characteristics, Distribution and Use in Mineral Exploration*, Western Australia, Cooperative Research Centre for Landscape Environments and Mineral Exploration.
- Chivas, A., Chappell, J., Polach, H., Pillans, B. & Flood, P. 1986. Radiocarbon Evidence for the Timing and Rate of Island Development, Beach-Rock Formation and Phosphatization at Lady Elliot Island, Queensland, Australia. *Marine Geology*, 69, 273-287.
- Chivas, A. R., García, A., Van Der Kaars, S., Couapel, M. J. J., Holt, S., Reeves, J. M., Wheeler, D. J., Switzer, A. D., Murray-Wallace, C. V., Banerjee, D., Price, D. M., Wang, S. X., Pearson, G., Edgar, N. T., Beaufort, L., De Deckker, P., Lawson, E. & Cecil, C. B. 2001. Sea-Level and Environmental Changes since the Last Interglacial in the Gulf of Carpentaria, Australia: An Overview. *Quaternary International*, 19-46.
- Choi, K. H., Choi, J.-H. & Kim, J. W. 2014. Reconstruction of Holocene Coastal Progradation on the East Coast of Korea Based on Osl Dating and Gpr Surveys of Beach-Foredune Ridges. *The Holocene*, 24, 24-34.
- Church, J. A., Clark, P. U., Cazenave, A., Gregory, J. M., Jevrejeva, S., Levermann, A., Merrifield, M. A., Milne, G. A., Nerem, R. S., Nunn, P. D., Payne, A. J., Pfeffer, W. T., Stammer, D. & Unnikrishnan, A. S. 2013. Sea Level Change. In: Stocker, T. F., Qin, D., Plattner, G.-K., Tignor, M., Allen, S. K., Boschung, J., Nauels, A., Xia, Y., Bex, V. & Midgley, P. M. (eds.) *Climate Change 2013: The Physical Science Basis. Contribution of Working Group I to the Fifth Assessment Report of the Intergovernmental Panel on Climate Change*. Cambridge, United Kingdom and New York, NY, USA: Cambridge University Press.
- Clarke, D., Mcpherson, A. & Collins, C. D. N. 2011. *Australia's Seismogenic Neotectonic Record: A Case for the Heterogeneous Intraplate Deformation*, Canberra, Geoscience Australia.



- Clemmensen, L. B., Bjørnsen, M., Murray, A. & Pedersen, K. 2007. Formation of Aeolian Dunes on Anholt, Denmark since AD 1560: A Record of Deforestation and Increased Storminess. *Sedimentary Geology*, 199, 171-187.
- Clifton, H. E. 2005. Coastal Sedimentary Facies. In: Schwartz, M. (ed.) *Encyclopedia of Coastal Science*. London: Kluwer Academic.
- Clifton, H. E. & Hunter, R. E. 1982. Coastal Sedimentary Facies. In: Schwartz, M. (ed.) *Encyclopedia of Beaches and Coastal Environments*. Stroudsburg, Pennsylvania: Hutchinson Ross Pub. Co.
- Coe, A. L., Bosence, D. W. J., Church, K. D., Flint, S. S., Howell, J. A. & Wilson, R. C. L. 2003. *The Sedimentary Record of Sea Level Change*, Cambridge, U.K., Cambridge University Press.
- Cohen, M. C. L., Filho, P. W. M. S., Lara, R. J., Behling, H. & Angulo, R. J. 2005. A Model of Holocene Mangrove Development and Relative Sea-Level Changes on the Bragança Peninsula (Northern Brazil). *Wetlands Ecology and Management*, 13, 433-443.
- Collins, L. B., Zhao, J.-X. & Freeman, H. 2006. A High-Precision Record of Mid-Late Holocene Sea-Level Events from Emergent Coral Pavements in the Houtman Abrolhos Islands, Southwest Australia. *Quaternary International*, 145-146, 78-85.
- Compton, J. S. 2001. Holocene Sea-Level Fluctuations Inferred from the Evolution of Depositional Environments of the Southern Langebaan Lagoon Salt Marsh, South Africa. *Holocene*, 11, 395-405.
- Cook, G. T. & Van Der Plicht, J. 2007. Radiocarbon Dating | Conventional Method. In: Elias, S. A. (ed.) *Encyclopedia of Quaternary Science*. Oxford: Elsevier.
- Cook, P. J. & Polach, H. A. 1973. A Chenier Sequence at Broad Sound, Queensland, and Evidence against a Holocene High Sea Level. *Marine Geology*, 14, 253-268.
- Cooper, J. a. G. 2007. Sea Level Studies | High Energy Coasts Sedimentary Indicators. In: Elias, S. A. (ed.) *Encyclopedia of Quaternary Science*. Oxford: Elsevier.
- Couapel, M. J. J. 2005. *The Gulf of Carpentaria Palaeoenvironments: Osl Dating and Nannofossil Evidence*. Doctor of Philosophy, University of Wollongong.
- Cribb, R. 1991. Getting into a Flap About Shell Mounds in Northern Australia: A Reply to Stone. *Archaeology in Oceania*, 26, 23-25.
- Crowley, G. M., Anderson, P., Kershaw, A. P. & Grindrod, J. 1990. Palynology of a Holocene Marine Transgressive Sequence, Lower Mulgrave River Valley, North-East Queensland. *Australian Journal of Ecology*, 15, 231-240.
- Cutler, K. B., Edwards, R. L., Taylor, F. W., Cheng, H., Adkins, J., Gallup, C. D., Cutler, P. M., Burr, G. S. & Bloom, A. L. 2003. Rapid Sea-Level Fall and Deep-Ocean Temperature Change since the Last Interglacial Period. *Earth and Planetary Science Letters*, 206, 253-271.
- Dackombe, R. V. & Gardiner, V. 1983. *Geomorphological Field Manual*, London, George Allen and Unwin.
- Dale, P., Knight, J., Breitfuss, M., Radke, L. & Rogers, K. 2015. *Saltmarsh and Saltflat Areas* [Online]. Canberra: Geoscience Australia. Available: [http://www.ozcoasts.gov.au/indicators/changes\\_saltmarsh\\_area.jsp](http://www.ozcoasts.gov.au/indicators/changes_saltmarsh_area.jsp) [Accessed 23 Aug 2017].
- Dashtgard, S. E., Gingras, M. K. & Butler, K. E. 2006. Sedimentology and Stratigraphy of a Transgressive, Muddy Gravel Beach: Waterside Beach, Bay of Fundy, Canada. *Sedimentology*, 53, 279-296.
- Davies, B. E. 1974. Loss-on-Ignition as an Estimate of Soil Organic Matter. *Soil Sci. Soc. Am. J.*, 38, 150-151.
- Davies, J. L. 1977. The Coast. In: Jeans, D. N. (ed.) *Australia: A Geography*. Sydney: Sydney University Press.



- De Vries, H. 1958. Variation in Concentration of Radiocarbon with Time and Location on Earth *Proceedings of the Koninklijke Nederlandse Akademie Van Wetenschappen Series B - Palaeontology Geology Physics Chemistry Anthropology*, B61, 94-102.
- Demeter, F., Shackelford, L. L., Bacon, A.-M., Durringer, P., Westaway, K., Sayavongkhamdy, T., Braga, J., Sichanthongtip, P., Khamdalavong, P., Ponche, J.-L., Wang, H., Lundstrom, C., Patole-Edoumba, E. & Karpoff, A.-M. 2012. Anatomically Modern Human in Southeast Asia (Laos) by 46 Ka. *Proceedings of the National Academy of Sciences*, 109, 14375.
- Denniston, R. F., Wyrwoll, K.-H., Polyak, V. J., Brown, J. R., Asmerom, Y., Wanamaker, A. D., Lapointe, Z., Ellerbroek, R., Barthelmes, M., Cleary, D., Cugley, J., Woods, D. & Humphreys, W. F. 2013. A Stalagmite Record of Holocene Indonesian–Australian Summer Monsoon Variability from the Australian Tropics. *Quaternary Science Reviews*, 78, 155-168.
- Department of the Environment. 2007. *Characterisation of the Marine Environment of the North Marine Region* [Online]. Darwin, Northern Territory: Marine Division, Department of the Environment, Water, Heritage and the Arts. Available: <http://www.environment.gov.au/resource/characterisation-marine-environment-north-marine-region-outcomes-expert-workshop-2-3-april> [Accessed 7 June 2016].
- Dimmock, G. M. 1957. The Soils of Flinders Island, Tasmania. In: Soils, C. D. O. (ed.). Melbourne: Melbourne : Commonwealth Scientific and Industrial Research Organization, Australia.
- Donders, T. H., Haberle, S. G., Hope, G., Wagner, F. & Visscher, H. 2007. Pollen Evidence for the Transition of the Eastern Australian Climate System from the Post-Glacial to the Present-Day Enso Mode. *Quaternary Science Reviews*, 26, 1621-1637.
- Dörschner, N., Reimann, T., Wenske, D., Lüthgens, C., Tsukamoto, S., Frechen, M. & Böse, M. 2012. Reconstruction of the Holocene Coastal Development at Fulong Beach in North-Eastern Taiwan Using Optically Stimulated Luminescence (Osl) Dating. *Quaternary International*, 263, 3-13.
- Douillet, G. A., Rasmussen, K. R., Kueppers, U., Lo Castro, D., Merrison, J. P., Iversen, J. J. & Dingwell, D. B. 2014. Saltation Threshold for Pyroclasts at Various Bedslopes: Wind Tunnel Measurements. *Journal of Volcanology and Geothermal Research*, 278-279, 14-24.
- Duller, G. a. T. 1995. Luminescence Dating Using Single Aliquots: Methods and Applications. *Radiation Measurements*, 24, 217-226.
- Duller, G. a. T. 2003. Distinguishing Quartz and Feldspar in Single Grain Luminescence Measurements. *Radiation Measurements*, 37, 161-165.
- Duller, G. a. T. 2004. Luminescence Dating of Quaternary Sediments: Recent Advances. *Journal of Quaternary Science*, 19, 183-192.
- Duller, G. a. T. 2008. *Luminescence Dating: Guidelines on Using Luminescence Dating in Archaeology*, Swindon, English Heritage.
- Duller, G. a. T. 2015. Luminescence Dating. In: Rink, W. J. & Thompson, J. W. (eds.) *Encyclopedia of Scientific Dating Methods*. Dordrecht: Springer Netherlands.
- Dyer, K. R., Christie, M. C. & Wright, E. W. 2000. The Classification of Intertidal Mudflats. *Continental Shelf Research*, 20, 1039-1060.
- Edwards, R. 2007a. Sea Levels: Resolution and Uncertainty. *Progress in Physical Geography*, 31, 621-632.
- Edwards, R. J. 2007b. Low Energy Coasts Sedimentary Indicators. In: Elias, S. A. (ed.) *Encyclopedia of Quaternary Science*. Oxford: Elsevier.
- Edyvane, K. S. 2005. Australia, Coastal Ecology. In: Schwartz, M. (ed.) *Encyclopedia of Coastal Science*. London: Kluwer Academic.

- Ehlers, J. & Gibbard, P. L. 2007. Glaciations/Overview. *In*: Elias, S. A. (ed.) *Encyclopedia of Quaternary Science*. Oxford: Elsevier.
- Ellis, M. Y. 1978. *Coastal Mapping Handbook*, Washington DC, Department of the Interior, U.S. Geological survey and U.S. Department of Commerce, National Ocean Service and Office of Coastal Zone Management, U.S. Government Printing Office.
- Ellison, J. C. 2008. Long-Term Retrospection on Mangrove Development Using Sediment Cores and Pollen Analysis: A Review. *Aquatic Botany*, 89, 93-104.
- Engel, M., May, S. M., Scheffers, A., Squire, P., Pint, A., Kelletat, D. & Brückner, H. 2014. Prograded Foredunes of Western Australia's Macro-Tidal Coast – Implications for Holocene Sea-Level Change and High-Energy Wave Impacts. *Earth Surface Processes and Landforms*, n/a-n/a.
- Fairbridge, R. W. 1961. Eustatic Changes in Sea Level. *Physics and Chemistry of the Earth*, 4, 99-185.
- Fanning, P. C., Holdaway, S. J. & Allely, K. 2018. Geoarchaeology in Action: A Sedimentological Analysis of Anthropogenic Shell Mounds from the Cape York Region of Australia. *Quaternary International*, 463, 44-56.
- Feathers, J. K. & Migliorini, E. 2001. Luminescence Dating at Katanda — a Reassessment. *Quaternary Science Reviews*, 20, 961-966.
- Fitzgerald, D. M. & Buynevich, I. V. 2009. Coastal Barriers. *In*: Isla, F. I. & Iribarne, O. (eds.) *Coastal Zones and Estuaries*. United Kingdom: EOLSS Publishers.
- Fitzsimmons, K. E., Rhodes, E. J. & Barrows, T. T. 2010. Osl Dating of Southeast Australian Quartz: A Preliminary Assessment of Luminescence Characteristics and Behaviour. *Quaternary Geochronology*, 5, 91-95.
- Flannery, T. 2005. *The Weather Makers*, London, Allen Lane-Penguin.
- Flay, S. & Nott, J. 2007. Effect of Enso on Queensland Seasonal Landfalling Tropical Cyclone Activity. *International Journal of Climatology*, 27, 1327-1334.
- Fleming, K., Johnston, P., Zwartz, D., Yokoyama, Y., Lambeck, K. & Chappell, J. 1998. Refining the Eustatic Sea-Level Curve since the Last Glacial Maximum Using Far- and Intermediate-Field Sites. *Earth and Planetary Science Letters*, 163, 327-342.
- Flemming, B. W. 2002. Geographic Distribution of Muddy Coasts. *In*: Healy, T., Wang, Y. & Healy, J.-A. (eds.) *Proceedings in Marine Science: Muddy Coasts of the World, Processes, Deposits and Function*. Amsterdam: Elsevier.
- Flessa, K. W., Cutler, A. H. & Meldahl, K. H. 1993. Time and Taphonomy: Quantitative Estimates of Time-Averaging and Stratigraphic Disorder in a Shallow Marine Habitat. *Paleobiology*, 19, 266-286.
- Flessa, K. W. & Kowalewski, M. 1994. Shell Survival and Time-Averaging in Nearshore and Shelf Environments: Estimates from the Radiocarbon Literature. *Lethaia*, 27, 153-165.
- Folk, R. L. 1954. The Distinction between Grain Size and Mineral Composition in Sedimentary-Rock Nomenclature. *Journal of Geology*, 62, 344-359.
- Folk, R. L. & Ward, W. C. 1957. Brazos River Bar: A Study in the Significance of Grain Size Parameters. *Journal of Sedimentary Petrology*, 27, 3-26.
- Forman, S. L., Spaeth, M., Marín, L., Pierson, J., Gómez, J., Bunch, F. & Valdez, A. 2006. Episodic Late Holocene Dune Movements on the Sand-Sheet Area, Great Sand Dunes National Park and Preserve, San Luis Valley, Colorado, USA. *Quaternary Research*, 66, 97-108.
- Forsyth, A. J., Nott, J. & Bateman, M. D. 2010. Beach Ridge Plain Evidence of a Variable Late-Holocene Tropical Cyclone Climate, North Queensland, Australia. *Palaeogeography, Palaeoclimatology, Palaeoecology*, 297, 707-716.

- Forsyth, A. J., Nott, J., Bateman, M. D. & Beaman, R. J. 2012. Juxtaposed Beach Ridges and Foredunes within a Ridge Plain — Wonga Beach, Northeast Australia. *Marine Geology*, 307-310, 111-116.
- Friedman, G. M. 1961. Distinction between Dune, Beach, and River Sands from Their Textural Characteristics. *Journal of Sedimentary Research*, 31, 514-529.
- Fuchs, M., Kreutzer, S., Fischer, M., Sauer, D. & Sørensen, R. 2012. Osl and Irsf Dating of Raised Beach Sand Deposits Along the Southeastern Coast of Norway. *Quaternary Geochronology*, 10, 195-200.
- Gagan, M. K. 1990. *Terrigenous Sedimentation and the Geologic Impact of Cyclone Winifred, Innisfail Area, Central Great Barrier Reef Province*. Doctor of Philosophy, James Cook University.
- Gagan, M. K., Hendy, E. J., Haberle, S. G. & Hantoro, W. S. 2004. Post-Glacial Evolution of the Indo-Pacific Warm Pool and El Niño-Southern Oscillation. *Quaternary International*, 118-119, 127-143.
- Galbraith, R. F. & Roberts, R. G. 2012. Statistical Aspects of Equivalent Dose and Error Calculation and Display in Osl Dating: An Overview and Some Recommendations. *Quaternary Geochronology*, 11, 1-27.
- Galbraith, R. F., Roberts, R. G., Laslett, G. M., Yoshida, H. & Olley, J. M. 1999. Optical Dating of Single and Multiple Grains of Quartz from Jinmium Rock Shelter, Northern Australia: Part I, Experimental Design and Statistical Models. *Archaeometry*, 41, 339-364.
- Galbraith, R. F., Roberts, R. G. & Yoshida, H. 2005. Error Variation in Osl Palaeodose Estimates from Single Aliquots of Quartz: A Factorial Experiment. *Radiation Measurements*, 39, 289-307.
- Gale, S. J. & Hoare, P. G. 1991. *Quaternary Sediments. Petrographic Methods for the Study of Unlithified Rocks.*, London, Halsted Press.
- Galloway, R. W. 1965. Late Quaternary Climates in Australia. *The Journal of Geology*, 73, 603-618.
- Gao, L., Long, H., Shen, J., Yu, G. & Yin, Y. 2016. High-Resolution Osl Dating of a Coastal Sediment Sequence from the South Yellow Sea. *Geochronometria*, 43, 143-154.
- Gao, S. 2013. Holocene Shelf-Coastal Sedimentary Systems Associated with the Changjiang River: An Overview. *Acta Oceanologica Sinica*, 32, 4-12.
- Gehrels, W. R. 2007. Microfossil Reconstructions. In: Elias, S. A. (ed.) *Encyclopedia of Quaternary Science*. Oxford: Elsevier.
- Gehrels, W. R., Callard, S. L., Moss, P. T., Marshall, W. A., Blaauw, M., Hunter, J., Milton, J. A. & Garnett, M. H. 2012. Nineteenth and Twentieth Century Sea-Level Changes in Tasmania and New Zealand. *Earth and Planetary Science Letters*, 315–316, 94-102.
- Geoscience Australia. 2015a. *Auspos - Online Gps Processing Service* [Online]. Available: <http://www.ga.gov.au/scientific-topics/positioning-navigation/geodesy/auspos> [Accessed 29 June 2015].
- Geoscience Australia. 2015b. *Australian Height Datum* [Online]. Available: <http://www.ga.gov.au/scientific-topics/positioning-navigation/geodesy/geodetic-datums/australian-height-datum-ahd> [Accessed 4 February 2016].
- Geoscience Australia. 2015c. *Ozcoasts, Australian Online Coastal Information. Estuaries - Environment Types*. [Online]. Geoscience Australia. Available: [http://www.ozcoasts.gov.au/conceptual\\_mods/sed\\_environs.jsp](http://www.ozcoasts.gov.au/conceptual_mods/sed_environs.jsp) [Accessed 24 Aug 2017].
- Geoscience Australia. 2015d. *Ozcoasts, Australian Online Coastal Information. Saltmarsh and Saltflat Areas* [Online]. Geoscience Australia. Available:

- [http://www.ozcoasts.gov.au/indicators/changes\\_saltmarsh\\_area.jsp](http://www.ozcoasts.gov.au/indicators/changes_saltmarsh_area.jsp) [Accessed 24 Aug 2017].
- Geoscience Australia. 2017. *Digital Elevation Data - Elevation Foundation Spatial Data* [Online]. Available: <http://www.ga.gov.au/scientific-topics/national-location-information/digital-elevation-data> [Accessed 21 October 2017].
- Geoscience Australia. 2018. *Auspos - Understanding the Results* [Online]. Available: <http://www.ga.gov.au/scientific-topics/positioning-navigation/geodesy/auspos/faq4> [Accessed 1 November 2018].
- Giannini, P. C. F., Sawakuchi, A. O., Martinho, C. T. & Tatum, S. H. 2007. Eolian Depositional Episodes Controlled by Late Quaternary Relative Sea Level Changes on the Imituba–Laguna Coast (Southern Brazil). *Marine Geology*, 237, 143-168.
- Gill, E. D. & Hopley, D. 1972. Holocene Sea Levels in Eastern Australia — a Discussion. *Marine Geology*, 12, 223-233.
- Glew, J. R., Smol, J. P. & Last, W. M. 2001. Sediment Core Collection and Extrusion. In: Last, W. M. & Smol, J. P. (eds.) *Tracking Environmental Change Using Lake Sediments. Volume 1: Basin Analysis, Coring and Chronological Techniques*. Dordrecht, The Netherlands: Kluwer Academic Publishers.
- Godfrey-Smith, D. I., Huntley, D. J. & Chen, W. H. 1988. Optical Dating Studies of Quartz and Feldspar Sediment Extracts. *Quaternary Science Reviews*, 7, 373-380.
- Goldsmith, V. 1985. Coastal Dunes. In: Davis Jr, R. A. (ed.) *Coastal Sedimentary Environments*. 2nd ed. New York: Springer-Verlag.
- Goodwin, I. D. 1998. Did Changes in Antarctic Ice Volume Influence Late Holocene Sea Level Lowering? *Quaternary Science Reviews*, 17, 319-332.
- Gordillo, S., Bayer, M. S., Boretto, G. & Charó, M. 2014. Taphonomy. *Mollusk Shells as Bio-Geo-Archives: Evaluating Environmental Changes During the Quaternary*. Cham: Springer International Publishing.
- Griffiths, S. D. & Hill, D. F. 2015. Tidal Modelling. In: Shennan, I., Long, A. J. & Horton, B. P. (eds.) *Handbook of Sea-Level Research*. Chichester: John Wiley & Sons, Ltd.
- Grindrod, J., Moss, P. & Van Der Kaars, S. 1999. Late Quaternary Cycles of Mangrove Development and Decline on the North Australian Continental Shelf. *Journal of Quaternary Science*, 14, 465-470.
- Grindrod, J. F. & Rhodes, E. G. 1984. Holocene Sea Level History of a Tropical Estuary: Missionary Bay, North Queensland. In: Thom, B. G. (ed.) *Coastal Geomorphology in Australia*. Sydney: Academic Press.
- Guérin, G. 2015. Luminescence Dating, Dose Rates. In: Rink, W. J. & Thompson, J. W. (eds.) *Encyclopedia of Scientific Dating Methods*. Dordrecht: Springer Netherlands.
- Harris, P. T., Heap, A. D., Marshall, J. F. & McCulloch, M. 2008. A New Coral Reef Province in the Gulf of Carpentaria, Australia: Colonisation, Growth and Submergence During the Early Holocene. *Marine Geology*, 251, 85-97.
- Harris, P. T., Heap, A. D., Wassenberg, T. & Passlow, V. 2004. Submerged Coral Reefs in the Gulf of Carpentaria, Australia. *Marine Geology*, 207, 185-191.
- Hart, E. A., Stapor, F. W., Jerez, J. E. N. & Sutherland, C. J. 2017. Progradation of a Beach Ridge Plain between 5000 and 4000 Years Bp Inferred from Luminescence Dating, Coquimbo Bay, Chile. *Journal of Coastal Research*, 33, 1065-1073.
- Hayne, M. 1992. *Late Quaternary Coastal Deposition North-West Cape York Peninsula*. Bachelor of Science (Honours), Australian National University.
- Hayne, M. & Chappell, J. 2001. Cyclone Frequency During the Last 5000 Years at Curacao Island, North Queensland, Australia. *Palaeogeography, Palaeoclimatology, Palaeoecology*, 168, 207-219.

- Hays, J. D., Imbrie, J. & Shackleton, N. J. 1976. Variations in the Earth's Orbit: Pacemaker of the Ice Ages. *Science*, 194, 1121-1132.
- Healy, T. R. 2005. Dune Ridges. In: Schwartz, M. L. (ed.) *Encyclopedia of Coastal Science*. Dordrecht: Springer Netherlands.
- Heiri, O., Lotter, A. F. & Lemcke, G. 2001. Loss on Ignition as a Method for Estimating Organic and Carbonate Content in Sediments: Reproducibility and Comparability of Results. *Journal of Paleolimnology*, 25, 101-110.
- Hendricks, R. & Hodson, A. 2015. Luminescence Dating, Shell-Rich Deposits. In: Rink, W. J. & Thompson, J. W. (eds.) *Encyclopedia of Scientific Dating Methods*. Dordrecht: Springer Netherlands.
- Hesselbo, S. P. 2008. Sequence Stratigraphy and Inferred Relative Sea-Level Change from the Onshore British Jurassic. *Proceedings of the Geologists' Association*, 119, 19-34.
- Higley, M. 2000. *Fossil Oyster Beds of the Mid-Holocene Highstand of Relative Sea Level: Gbr Shelf*. Bachelor of Science, James Cook University.
- Hillis, R. R., Sandiford, M., Reynolds, S. D. & Quigley, M. C. 2008. Present-Day Stresses, Seismicity and Neogene-to-Recent Tectonics of Australia's 'Passive' Margins: Intraplate Deformation Controlled by Plate Boundary Forces. In: Johnson, H., Dore, A. G., Gatliff, R. W., Holdsworth, R., Lundin, E. R. & Ritchie, J. D. (eds.) *The Nature and Origin of Compressive Margins*. 306 ed. London: The Geological Society.
- Hogg, A. G., Hua, Q., Blackwell, P. G., Niu, M., Buck, C. E., Guilderson, T. P., Heaton, T. J., Palmer, J. G., Reimer, P. J., Reimer, R. W., Turney, C. S. M. & Zimmerman, S. R. H. 2013. Shcal13 Southern Hemisphere Calibration, 0-50,000 Years Cal Bp. *Radiocarbon*, 55, 1889-1903.
- Holdaway, S. J., Fanning, P. C., Petchey, F., Allely, K., Shiner, J. I. & Bailey, G. 2017. Temporal Variability in Shell Mound Formation at Albatross Bay, Northern Australia. *PLOS ONE*, 12, e0183863.
- Hopley, D. 1978. Sea Level Change on the Great Barrier Reef: An Introduction. *Philosophical Transactions of the Royal Society of London. Series A, Mathematical and Physical Sciences*, 291, 159-166.
- Hopley, D. 1983. Evidence of 15,000 Years of Sea Level Change in Tropical Queensland. In: Hopley, D. (ed.) *Australian Sea Levels in the Last 15,000 Years: A Review*. Townsville, Qld.: Dept. of Geography, James Cook University of North Queensland.
- Hopley, D. 1985. *Queensland*, New York, Van Nostrand Reinhold.
- Hopley, D. 1987. *Holocene Sea-Level Changes in Australasia and the Southern Pacific*, Dordrecht, Springer Netherlands.
- Hopley, D., Smithers, S. G. & Parnell, K. 2007. *The Geomorphology of the Great Barrier Reef: Development, Diversity and Change*, Cambridge, Cambridge University Press.
- Horton, B. P. 1997. *Quantification of the Indicative Meaning of a Range of Holocene Sea-Level Index Points from Western North Sea*. Doctor of Philosophy, University of Durham.
- Horton, B. P. 2007. Sea-Levels, Late Quaternary | Mid-Latitudes In: Elias, S. A. (ed.) *Encyclopedia of Quaternary Science*. Oxford: Elsevier.
- Horton, B. P., Culver, S. J., Hardbottle, M. I. J., Larcombe, P., Milne, G., Morigi, C., Whittaker, J. E. & Woodroffe, C. D. 2007a. Reconstructing Holocene Sea-Level Change for the Central Great Barrier Reef (Australia) Using Subtidal Foraminifera. *Journal of Foraminiferal Research*, 37, 327-343.
- Horton, B. P., Gibbard, P. L., Mine, G. M., Morley, R. J., Purintavaragul, C. & Stargardt, J. M. 2005. Holocene Sea Levels and Palaeoenvironments, Malay-Thai Peninsula, Southeast Asia. *The Holocene*, 15, 1199-1213.

- Horton, B. P., Zong, Y., Hillier, C. & Engelhart, S. 2007b. Diatoms from Indonesian Mangroves and Their Suitability as Sea-Level Indicators for Tropical Environments. *Marine Micropaleontology*, 63, 155-168.
- Hua, Q. 2009. Radiocarbon: A Chronological Tool for the Recent Past. *Quaternary Geochronology*, 4, 378-390.
- Huntley, D. J., Godfrey-Smith, D. I. & Thewalt, M. L. W. 1985. Optical Dating of Sediments. *Nature*, 313, 105-107.
- Jacobs, Z. 2008. Luminescence Chronologies for Coastal and Marine Sediments. *Boreas*, 37, 508-535.
- Jacobs, Z., Duller, G. a. T. & Wintle, A. G. 2006a. Interpretation of Single Grain  $D_e$  Distributions and Calculation of  $D_e$ . *Radiation Measurements*, 41, 264-277.
- Jacobs, Z., Duller, G. a. T., Wintle, A. G. & Henshilwood, C. S. 2006b. Extending the Chronology of Deposits at Blombos Cave, South Africa, Back to 140ka Using Optical Dating of Single and Multiple Grains of Quartz. *Journal of Human Evolution*, 51, 255-273.
- Jacobs, Z. & Roberts, R. G. 2007. Advances in Optically Stimulated Luminescence Dating of Individual Grains of Quartz from Archaeological Deposits. *Evolutionary Anthropology*, 16, 210-223.
- Jacobs, Z., Wintle, A. G. & Duller, G. a. T. 2003. Optical Dating of Dune Sand from Blombos Cave, South Africa: I—Multiple Grain Data. *Journal of Human Evolution*, 44, 599-612.
- Jaensch, R. 2005. Wetland Management Profile: Saltmarsh Wetlands. Brisbane: State of Queensland, Environment Protection Agency.
- Jankowski, N. R., Jacobs, Z. & Goldberg, P. 2015. Optical Dating and Soil Micromorphology at Maccauley's Beach, New South Wales, Australia. *Earth Surface Processes and Landforms*, 40, 229-242.
- Jennings, J. N. 1975. Desert Dunes and Estuarine Fill in the Fitzroy Estuary (North-Western Australia). *CATENA*, 2, 215-262.
- Jervey, M. T. 1988. Quantitative Geological Modeling of Siliciclastic Rock Sequences and Their Seismic Expression. In: Wilgus, C. K., Hastings, B. S., Kendall, C. G. S. C., Posamentier, H. W., Ross, C. A. & Van Wagoner, J. C. (eds.) *Sea-Level Changes: An Integrated Approach*. Tulsa, Oklahoma: Society of Economic Paleontologists and Mineralogists.
- Jones, B. G., Martin, G. R. & Senapati, N. 1993. Riverine—Tidal Interactions in the Monsoonal Gilbert River Fandelta, Northern Australia. *Sedimentary Geology*, 83, 319-337.
- Jones, M. R. 1987. Surficial Sediments of the Western Gulf of Carpentaria, Australia. *Marine and Freshwater Research*, 38, 151-167.
- Jones, V. 2007. Diatom Introduction. In: Scott, A. E. (ed.) *Encyclopedia of Quaternary Science*. Oxford: Elsevier.
- Kantha, L. H. & Clayson, C. A. 2000. Coastal Dynamics and Barotropic Models. *Numerical models of oceans and oceanic processes*, 66, 493-528.
- Kato, M., Fukusawa, H. & Yasuda, Y. 2003. Varved Lacustrine Sediments of Lake Tougou-Ike, Western Japan, with Reference to Holocene Sea-Level Changes in Japan. *Quaternary International*, 105, 33-37.
- Kelsey, H. M. 2015. Geomorphological Indicators of Past Sea Levels. *Handbook of Sea-Level Research*. John Wiley & Sons, Ltd.
- Kennedy, D. M. & Woods, J. L. D. 2013. Determining Organic and Carbonate Content in Sediments. In: Switzer, A. D. & Kennedy, D. M. (eds.) *Treatise on Geomorphology Volume 14: Methods in Geomorphology* San Diego: Academic Press.



- Khan, N. S., Ashe, E., Horton, B. P., Dutton, A., Kopp, R. E., Brocard, G., Engelhart, S. E., Hill, D. F., Peltier, W. R., Vane, C. H. & Scatena, F. N. 2017. Drivers of Holocene Sea-Level Change in the Caribbean. *Quaternary Science Reviews*, 155, 13-36.
- Khan, N. S., Ashe, E., Shaw, T. A., Vacchi, M., Walker, J., Peltier, W. R., Kopp, R. E. & Horton, B. P. 2015. *Holocene Relative Sea-Level Changes from near-, Intermediate-, and Far-Field Locations*.
- Kidson, C. 1982. Sea Level Changes in the Holocene. *Quaternary Science Reviews*, 1, 121-151.
- Kidwell, S. M. 1991. The Stratigraphy of Shell Concentrations. In: Allison, P. A. & Briggs, D. E. G. (eds.) *Taphonomy: Releasing the Data Locked in the Fossil Record*. New York: Plenum Press.
- Kidwell, S. M., Fürsich, F. T. & Aigner, T. 1986. Conceptual Framework for the Analysis and Classification of Fossil Concentrations. *PALAIOS*, 1, 228-238.
- Krumbein, W. C. 1934. Size Frequency Distributions of Sediments. *Journal of Sedimentary Petrology*, 4, 65-77.
- Laborel, J. & Laborel-Deguen, F. 1996. Biological Indicators of Holocene Sea-Level and Climatic Variations on Rocky Coasts of Tropical and Subtropical Regions. *Quaternary International*, 31, 53-60.
- Laffan, S. W. 2001. *Inferring the Spatial Distribution of Regolith Properties Using Surface Measurable Features*. Doctor of Philosophy, The Australian National University.
- Lambeck, K. 2002. Sea Level Change from Mid Holocene to Recent Time: An Australian Example with Global Implications. *Ice Sheets, Sea Level and the Dynamic Earth*. American Geophysical Union.
- Lambeck, K. & Chappell, J. 2001. Sea Level Change through the Last Glacial Cycle. *Science*, 292, 679-686.
- Lambeck, K. & Nakada, M. 1990. Late Pleistocene and Holocene Sea-Level Change Along the Australian Coast. *Palaeogeography, Palaeoclimatology, Palaeoecology*, 89, 143-176.
- Lambeck, K., Woodroffe, C. D., Fabrizio, A., Anzidei, M., Gehrels, W. R., Laborel, J. & Wright, A. 2010. Paleoenvironmental Records, Geophysical Modelling, and Reconstruction of Sea Level Trends and Variability on Centennial and Longer Timescales. In: Church, J. A., Woodworth, P. L., Aarup, T. & Wilson, W. S. (eds.) *Understanding Sea-Level Rise and Variability*. Singapore: Wiley-Blackwell.
- Lambeck, K., Yokoyama, Y., Johnston, P. & Purcell, A. 2000. Global Ice Volumes at the Last Glacial Maximum and Early Lateglacial. *Earth and Planetary Science Letters*, 181, 513-527.
- Lambeck, K., Yokoyama, Y. & Purcell, T. 2002. Into and out of the Last Glacial Maximum: Sea-Level Change During Oxygen Isotope Stages 3 and 2. *Quaternary Science Reviews*, 21, 343-360.
- Larcombe, P., Carter, R. M., Dye, J., Gagan, M. K. & Johnson, D. P. 1995. New Evidence for Episodic Post-Glacial Sea-Level Rise, Central Great Barrier Reef, Australia. *Marine Geology*, 127, 1-44.
- Larsen, B. P., Holdaway, S. J., Fanning, P. C., Mackrell, T. & Shiner, J. I. 2017. Shape as an Outcome of Formation History: Terrestrial Laser Scanning of Shell Mounds from Far North Queensland, Australia. *Quaternary International*, 427, 5-12.
- Lees, B. G. & Clements, A. 1987. Climatic Implications of Chenier Dates in Northern Australia. *Radiocarbon*, 29, 311-317.
- Lees, B. G., Hayne, M. & Price, D. 1993. Marine Transgression and Dune Initiation on Western Cape York, Northern Australia. *Marine Geology*, 114, 83-89.
- Lees, B. G., Lu, Y. & Head, J. 1990. Reconnaissance Thermoluminescence Dating of Northern Australian Coastal Dune Systems. *Quaternary Research*, 34, 169-185.

- Leica Geosystems Ag 2012. *Leica Gs10/Gs15 User Manual, Version 4.1*, Heerbrugg, Switzerland, Leica Geosystems.
- Leonard, N. D., Welsh, K. J., Zhao, J.-X., Nothdurft, L. D., Webb, G. E., Major, J., Feng, Y. & Price, G. J. 2013. Mid-Holocene Sea-Level and Coral Reef Demise: U-Th Dating of Subfossil Corals in Moreton Bay, Australia. *The Holocene*, 23, 1841-1852.
- Leonard, N. D., Zhao, J.-X., Welsh, K. J., Feng, Y.-X., Smithers, S. G., Pandolfi, J. M. & Clark, T. R. 2015. *Holocene Sea Level Instability in the Southern Great Barrier Reef, Australia: High-Precision U-Th Dating of Fossil Microatolls*.
- Lepper, K. & McKeever, S. W. S. 2002. An Objective Methodology for Dose Distribution Analysis. *Radiation Protection Dosimetry*, 101, 349-352.
- Lessa, G. & Masselink, G. 2006. Evidence of a Mid-Holocene Sea Level Highstand from the Sedimentary Record of a Macrotidal Barrier and Paleoeuary System in Northwestern Australia. *Journal of Coastal Research*, 22, 100-112.
- Lessa, G. C. & Angulo, R. J. 1998. Discussion: Oscillations or Not Oscillations, That Is the Question - Reply. *Marine Geology*, 150, 189-196.
- Lewis, D. W. 1984. *Practical Sedimentology*, Pennsylvania, Hutchinson Ross Publishing Company.
- Lewis, D. W. & McConchie, D. 1994. *Analytical Sedimentology*, New York, Chapman & Hall.
- Lewis, S. E., Sloss, C. R., Murray-Wallace, C. V., Woodroffe, C. D. & Smithers, S. G. 2013. Post-Glacial Sea-Level Changes around the Australian Margin: A Review. *Quaternary Science Reviews*, 74, 115-138.
- Lewis, S. E., Wüst, R. a. J., Webster, J. M., Collins, J., Wright, S. A. & Jacobsen, G. 2015. Rapid Relative Sea-Level Fall Along North-Eastern Australia between 1200 and 800 Cal. Yr Bp: An Appraisal of the Oyster Evidence. *Marine Geology*, 370, 20-30.
- Lewis, S. E., Wüst, R. a. J., Webster, J. M. & Shields, G. A. 2008. Mid-Late Holocene Sea-Level Variability in Eastern Australia. *Terra Nova*, 20, 74-81.
- Lian, O. B. & Roberts, R. G. 2006. Dating the Quaternary: Progress in Luminescence Dating of Sediments. *Quaternary Science Reviews*, 25, 2449-2468.
- López, G. I. 2015. Walther's Law of Facies. In: Jack Rink, W. & Thompson, J. W. (eds.) *Encyclopedia of Scientific Dating Methods*. Dordrecht: Springer Netherlands.
- López, G. I. & Rink, W. J. 2007. Characteristics of the Burial Environment Related to Quartz SAR-OSL Dating at St. Vincent Island, NW Florida, USA. *Quaternary Geochronology*, 2, 65-70.
- López, G. I. & Rink, W. J. 2008. New Quartz Optical Stimulated Luminescence Ages for Beach Ridges on the St. Vincent Island Holocene Strandplain, Florida, United States. *Journal of Coastal Research*, 49-62.
- Lowe, J. J. & Walker, M. J. C. 2015. *Reconstructing Quaternary Environments*, Harlow, Essex, Addison Wesley Longman.
- Madsen, A. T., Murray, A. S. & Andersen, T. J. 2007a. Optical Dating of Dune Ridges on Rømø, a Barrier Island in the Wadden Sea, Denmark. *Journal of Coastal Research*, 23, 1259-1269.
- Madsen, A. T., Murray, A. S., Andersen, T. J. & Pejrup, M. 2007b. Optical Dating of Young Tidal Sediments in the Danish Wadden Sea. *Quaternary Geochronology*, 2, 89-94.
- Malvern Instruments 2007. *Mastersizer 2000 User Manual. Man0384, Issue 1.0, March 2007*, England, Malvern Instruments Ltd.
- Mann, M. E., Zhang, Z., Rutherford, S., Bradley, R. S., Hughes, M. K., Shindell, D., Ammann, C., Faluvegi, G. & Ni, F. 2009. Global Signatures and Dynamical Origins of the Little Ice Age and Medieval Climate Anomaly. *Science*, 326, 1256.



- Mann, T., Rovere, A., Schöne, T., Klicpera, A., Stocchi, P., Lukman, M. & Westphal, H. 2016. The Magnitude of a Mid-Holocene Sea-Level Highstand in the Strait of Makassar. *Geomorphology*, 257, 155-163.
- Markgraf, V. & Diaz, H. F. 2000. The Past Enso Record: A Synthesis. In: Diaz, H. F. & Markgraf, V. (eds.) *El Niño and the Southern Oscillation: Multiscale Variability and Global and Regional Impacts*. Cambridge: Cambridge University Press.
- Marshall, S. J. 2009. Glaciations, Quaternary. In: Gornitz, V. (ed.) *Encyclopedia of Paleoclimatology and Ancient Environments*. Dordrecht: Springer Netherlands.
- Marshall, S. J., James, T. S. & Clarke, G. K. C. 2002. North American Ice Sheet Reconstructions at the Last Glacial Maximum. *Quaternary Science Reviews*, 21, 175-192.
- Martin, L., Bittencourt, A. C. S. P., Dominguez, J. M. L., Flexor, J.-M. & Suguio, K. 1998. Oscillations or Not Oscillations, That Is the Question: Comment on Augulo, R.J. And Lessa, G.C. "The Brazilian Sea-Level Curves: A Critical Review with Emphasis on the Curves from the Paranaguá and Cananéia Regions" [Mar. Geol. 140, 141-166]. *Marine Geology*, 150, 179-187.
- Martin, L., Dominguez, J. M. L. & Bittencourt, A. C. S. P. 2003. Fluctuating Holocene Sea Levels in Eastern and Southeastern Brazil: Evidence from Multiple Fossil and Geometric Indicators. *Journal of Coastal Research*, 19, 101-124.
- Martin, L., Flexor, J.-M., Boas, G. S. V., Bittencourt, A. C. S. P. & Guimarães, M. M. M. 1979. Courbe De Variation Du Niveau Relatif De La Mer Au Cours Des 7000 Dernières Années Sur Un Secteur Homogène Du Littoral Brésilien (Nord De Salvador – Bahia). In: Suguio, K., Fairchild, T. R., Martin, L. & Flexor, J.-M. (eds.) *Proceedings of the 1978 International Symposium on Coastal Evolution in the Quaternary*. Sao Paulo: IGCP.
- Martin, L., Suguio, K. & Flexor, J.-M. 1986. Shell Middens as a Source for Additional Information in Holocene Shoreline and Sea-Level Reconstruction: Examples from the Coast of Brazil. In: Van De Plassche, O. (ed.) *Sea-Level Research: A Manual for the Collection and Evaluation of Data*. Norwich: Geo Books.
- Martin, R. E. 1999. *Taphonomy: A Process Approach*, United Kingdom, Cambridge University Press.
- Mason, C. 2016. *Nmbaqc's Best Practice Guidance. Particle Size Analysis (Psa) for Supporting Biological Analysis*. [Online]. National Marine Biological AQC Coordinating Committee. Available: [http://www.nmbaqcs.org/media/1255/psa-guidance\\_update18012016.pdf](http://www.nmbaqcs.org/media/1255/psa-guidance_update18012016.pdf) [Accessed 2 February 2017].
- Mathews, T. D. 1982. Radiocarbon Dating. In: Schwartz, M. (ed.) *Encyclopedia of Beaches and Coastal Environments*. Stroudsburg, Pennsylvania: Hutchinson Ross Pub. Co.
- Mauz, B. 2015. Luminescence, Coastal Sediments. In: Rink, W. J. & Thompson, J. W. (eds.) *Encyclopedia of Scientific Dating Methods*. Dordrecht: Springer Netherlands.
- Mauz, B., Baeteman, C., Bungenstock, F. & Plater, A. J. 2010. Optical Dating of Tidal Sediments: Potentials and Limits Inferred from the North Sea Coast. *Quaternary Geochronology*, 5, 667-678.
- Mcculloch, M. T., De Deckker, P. & Chivas, A. R. 1989. Strontium Isotope Variations in Single Ostracod Valves from the Gulf of Carpentaria, Australia: A Palaeoenvironmental Indicator. *Geochimica et Cosmochimica Acta*, 53, 1703-1710.
- Mcdonald, R. C. & Isbell, R. F. 2009. Soil Profile. In: Terrain, N. C. O. S. A. (ed.) *Australian Soil and Land Survey Field Handbook*. Collingwood, Victoris: CSIRO Publishing.
- Mcdonald, R. C., Isbell, R. F. & Speight, J. G. 2009. Land Surface. In: Terrain, N. C. O. S. A. (ed.) *Australian Soil and Land Survey Field Handbook*. Collingwood, Victoris: CSIRO Publishing.

- McLean, R. F., Stoddart, D. R., Hopley, D. & Polach, H. 1978. Sea Level Change in the Holocene on the Northern Great Barrier Reef. *Philosophical Transactions of the Royal Society of London. Series A, Mathematical and Physical Sciences*, 291, 167-186.
- Mejdahl, V. 1979. Thermoluminescence Dating: Beta-Dose Attenuation in Quartz Grains. *Archaeometry*, 21, 61-72.
- Middleton, G. V. 1973. Johannes Walther's Law of the Correlation of Facies. *Geological Society of America Bulletin*, 84, 979-988.
- Milne, G. 2008. How the Climate Drives Sea-Level Changes. *Astronomy & Geophysics*, 49, 2.24-2.28.
- Mitrovica, J. X. & Milne, G. A. 2002. On the Origin of Late Holocene Sea-Level Highstands within Equatorial Ocean Basins. *Quaternary Science Reviews*, 21, 2179-2190.
- Mitrovica, J. X. & Peltier, W. R. 1991. On Postglacial Geoid Subsidence over the Equatorial Oceans. *Journal of Geophysical Research: Solid Earth*, 96, 20053-20071.
- Mohtadi, M., Oppo, D. W., Steinke, S., Stuut, J.-B. W., De Pol-Holz, R., Hebbeln, D. & Lückge, A. 2011. Glacial to Holocene Swings of the Australian–Indonesian Monsoon. *Nature Geoscience*, 4, 540.
- Montaggioni, L. F. & Braithwaite, C. J. R. 2009. Chapter Nine: Corals and Coral Reefs as Records of Climatic Change. In: Montaggioni, L. F. & Braithwaite, C. J. R. (eds.) *Developments in Marine Geology*. Elsevier.
- Moore, A. L., Mcadoo, B. G. & Ruffman, A. 2007. Landward Fining from Multiple Sources in a Sand Sheet Deposited by the 1929 Grand Banks Tsunami, Newfoundland. *Sedimentary Geology*, 200, 336-346.
- Morrison, M. 2003. Old Boundaries and New Horizons: The Weipa Shell Mounds Reconsidered. *Archaeology in Oceania*, 38, 1-8.
- Morrison, M. 2010. *The Shell Mounds of Albatross Bay: An Archaeological Investigation of Late Holocene Production Strategies near Weipa, North Eastern Australia*. Doctor of Philosophy, Flinders University.
- Morrison, M. 2013. Niche Production Strategies and Shell Matrix Site Variability at Albatross Bay, Cape York Peninsula. *Archaeology in Oceania*, 48, 78-91.
- Morrison, M. 2014. Chronological Trends in Late Holocene Shell Mound Construction across Northern Australia: Insights from Albatross Bay, Cape York Peninsula. *Australian Archaeology*, 79, 1-13.
- Morrison, M. 2015. Late Holocene Aboriginal Shellfish Production Strategies in Northern Australia: Insights from Prunung (Red Beach), Weipa, Cape York Peninsula. *Queensland Archaeological Research*, 18, 1-27.
- Morton, R. A., Gelfenbaum, G. & Jaffe, B. E. 2007. Physical Criteria for Distinguishing Sandy Tsunami and Storm Deposits Using Modern Examples. *Sedimentary Geology*, 200, 184-207.
- Moss, P., Mackenzie, L., Ulm, S., Sloss, C., Rosendahl, D., Petherick, L., Steinberger, L., Wallis, L., Heijnis, H., Petchey, F. & Jacobsen, G. 2015. Environmental Context for Late Holocene Human Occupation of the South Wellesley Archipelago, Gulf of Carpentaria, Northern Australia. *Quaternary International*, 385, 136-144.
- Murray-Wallace, C. V. 2002. Pleistocene Coastal Stratigraphy, Sea-Level Highstands and Neotectonism of the Southern Australian Passive Continental Margin—a Review. *Journal of Quaternary Science*, 17, 469-489.
- Murray-Wallace, C. V. 2007a. Sea Level Studies | Eustatic Sea-Level Changes since the Last Glaciation. In: Elias, S. A. (ed.) *Encyclopedia of Quaternary Science*. Oxford: Elsevier.
- Murray-Wallace, C. V. 2007b. Sea Level Studies | Eustatic Sea-Level Changes, Glacial-Interglacial Cycles. In: Elias, S. A. (ed.) *Encyclopedia of Quaternary Science*. Oxford: Elsevier.

- Murray-Wallace, C. V., Banerjee, D., Bourman, R. P., Olley, J. M. & Brooke, B. P. 2002. Optically Stimulated Luminescence Dating of Holocene Relict Foredunes, Guichen Bay, South Australia. *Quaternary Science Reviews*, 21, 1077-1086.
- Murray-Wallace, C. V. & Woodroffe, C. D. 2014. *Quaternary Sea-Level Changes: A Global Perspective*, Cambridge, Cambridge University Press.
- Murray, A. S. & Olley, J. M. 2002. Precision and Accuracy in the Optically Stimulated Luminescence Dating of Sedimentary Quartz: A Status Review. *Geochronometria*, 21, 1-16.
- Murray, A. S. & Roberts, R. G. 1998. Measurement of the Equivalent Dose in Quartz Using a Regenerative-Dose Single-Aliquot Protocol. *Radiation Measurements*, 29, 503-515.
- Murray, A. S. & Wintle, A. G. 2000. Luminescence Dating of Quartz Using an Improved Single-Aliquot Regenerative-Dose Protocol. *Radiation Measurements*, 32, 57-73.
- Murray, A. S. & Wintle, A. G. 2003. The Single Aliquot Regenerative Dose Protocol: Potential for Improvements in Reliability. *Radiation Measurements*, 37, 377-381.
- Murray, M. R. 2002. Is Laser Particle Size Determination Possible for Carbonate-Rich Lake Sediments? *Journal of Paleolimnology*, 27, 173-183.
- Nakada, M. & Lambeck, K. 1989. Late Pleistocene and Holocene Sea-Level Change in the Australian Region and Mantle Rheology. *Geophysical Journal International*, 96, 497-517.
- Nanson, R. A., Vakarelov, B. K., Ainsworth, R. B., Williams, F. M. & Price, D. M. 2013. Evolution of a Holocene, Mixed-Process, Forced Regressive Shoreline: The Mitchell River Delta, Queensland, Australia. *Marine Geology*, 339, 22-43.
- Nathan, R. P. & Mauz, B. 2008. On the Dose-Rate Estimate of Carbonate-Rich Sediments for Trapped Charge Dating. *Radiation Measurements*, 43, 14-25.
- National Committee on Soil and Terrain 2009. *Australian Soil and Land Survey Field Handbook*, Collingwood, Victoria, CSIRO Publishing.
- Nelson, A. R. 2015. Coastal Sediments. *Handbook of Sea-Level Research*. John Wiley & Sons, Ltd.
- Nelson, D. W. & Sommers, L. E. 1982. Total Carbon, Organic Carbon, and Organic Matter. In: Page, A. L. (ed.) *Methods of Soil Analysis Part 2: Chemical and Microbiological Properties*. 2 ed. Madison, Wisconsin: American Society of Agronomy, Inc.
- Newell, N. D. & Boyd, D. W. 1955. Extraordinarily Coarse Eolian Sand of the Ica Desert, Peru. *Journal of Sedimentary Research*, 25, 226-228.
- Newman, C. J. 1996. *Land Units of the Weipa Environs*. COMALCO Aluminium Limited.
- Nian, X., Zhang, W., Wang, Z., Sun, Q., Chen, J., Chen, Z. & Hutchinson, S. M. 2018. The Chronology of a Sediment Core from Incised Valley of the Yangtze River Delta: Comparative Osl and Ams 14c Dating. *Marine Geology*, 395, 320-330.
- Nielsen, A., Murray, A. S., Pejrup, M. & Elberling, B. 2006. Optically Stimulated Luminescence Dating of a Holocene Beach Ridge Plain in Northern Jutland, Denmark. *Quaternary Geochronology*, 1, 305-312.
- Nott, J. 1996. Late Pleistocene and Holocene Sea-Level Highstands in Northern Australia. *Journal of Coastal Research*, 12, 907-910.
- Nott, J. 2010. A Theory (Involving Tropical Cyclones) on the Formation of Coarse-Grained Sand Beach Ridges in Ne Australia. In: Bishop, P. & Pillans, B. (eds.) *Australian Landscapes*. London: Geological Society Special Publications.
- Nott, J., Chague-Goff, C., Goff, J., Sloss, C. & Riggs, N. 2013. Anatomy of Sand Beach Ridges: Evidence from Severe Tropical Cyclone Yasi and Its Predecessors, Northeast Queensland, Australia. *Journal of Geophysical Research: Earth Surface*, 118, 1710-1719.

- Nott, J. & Forsyth, A. 2012. Punctuated Global Tropical Cyclone Activity over the Past 5,000 Years. *Geophysical Research Letters*, 39, n/a-n/a.
- Nott, J., Smithers, S., Walsh, K. & Rhodes, E. 2009. Sand Beach Ridges Record 6000 Year History of Extreme Tropical Cyclone Activity in Northeastern Australia. *Quaternary Science Reviews*, 28, 1511-1520.
- Nott, J. F. 2004. Palaeotempestology: The Study of Prehistoric Tropical Cyclones--a Review and Implications for Hazard Assessment. *Environment International*, 30, 433-447.
- Ócofaigh, C. & Bentley, M. J. 2007. Sea-Levels, Late Quaternary | High Latitudes In: Elias, S. A. (ed.) *Encyclopedia of Quaternary Science*. Oxford: Elsevier.
- Oertel, G. F. 2005. Coastal Lakes and Lagoons. In: Schwartz, M. L. (ed.) *Encyclopedia of Coastal Science*. Dordrecht: Springer Netherlands.
- Oliver, T. S. N. 2016. *Holocene Depositional History of Three Coastal Sand Ridge Plains, Southeastern Australia*. Doctor of Philosophy, University of Wollongong.
- Oliver, T. S. N., Dougherty, A. J., Gliganic, L. A. & Woodroffe, C. D. 2015. Towards More Robust Chronologies of Coastal Progradation: Optically Stimulated Luminescence Ages for the Coastal Plain at Moruya, South-Eastern Australia. *The Holocene*, 25, 536-546.
- Oliver, T. S. N., Thom, B. G. & Woodroffe, C. D. 2016. Formation of Beach-Ridge Plains: An Appreciation of the Contribution by Jack L. Davies. *Geographical Research*, n/a-n/a.
- Olley, J., Caitcheon, G. & Murray, A. 1998. The Distribution of Apparent Dose as Determined by Optically Stimulated Luminescence in Small Aliquots of Fluvial Quartz: Implications for Dating Young Sediments. *Quaternary Science Reviews*, 17, 1033-1040.
- Olley, J. M., Caitcheon, G. G. & Roberts, R. G. 1999. The Origin of Dose Distributions in Fluvial Sediments, and the Prospect of Dating Single Grains from Fluvial Deposits Using Optically Stimulated Luminescence. *Radiation Measurements*, 30, 207-217.
- Olley, J. M., Murray, A. & Roberts, R. G. 1996. The Effects of Disequilibria in the Uranium and Thorium Decay Chains on Burial Dose Rates in Fluvial Sediments. *Quaternary Science Reviews*, 15, 751-760.
- Olley, J. M., Pietsch, T. & Roberts, R. G. 2004. Optical Dating of Holocene Sediments from a Variety of Geomorphic Settings Using Single Grains of Quartz. *Geomorphology*, 60, 337-358.
- Olley, J. M., Roberts, R. G. & Murray, A. S. 1997. Disequilibria in the Uranium Decay Series in Sedimentary Deposits at Allen's Cave, Nullarbor Plain, Australia: Implications for Dose Rate Determinations. *Radiation Measurements*, 27, 433-443.
- Ota, Y., Chappell, J., Kelley, R., Yonekura, N., Matsumoto, E., Nishimura, T. & Head, J. 1993. Holocene Coral Reef Terraces and Coseismic Uplift of Huon Peninsula, Papua New Guinea. *Quaternary Research*, 40, 177-188.
- Otvos, E. G. 2000. Beach Ridges — Definitions and Significance. *Geomorphology*, 32, 83-108.
- Otvos, E. G. 2005. Cheniers. In: Schwartz, M. (ed.) *Encyclopedia of Coastal Science*. London: Kluwer Academic.
- Oyama, M. & Takehara, H. 1967. *Revised Standard Soil Colour Charts*, Japan, Research Council for Agriculture, Forestry and Fisheries.
- Pain, C., Gregory, L., Wilson, P. & McKenzie, N. 2011. The Physiographic Regions of Australia. Explanatory Notes. Australia: Australian Collaborative Land Evaluation Program.
- Petchey, F., Phelan, M. & White, J. P. 2004. New  $\Delta r$  Values for the Southwest Pacific Ocean. *Radiocarbon*, 46, 1005-1014.

- Petherick, L., McGowan, H. & Moss, P. 2008. Climate Variability During the Last Glacial Maximum in Eastern Australia: Evidence of Two Stadials? *Journal of Quaternary Science*, 23, 787-802.
- Pilarczyk, J. E. & Barber, D. C. 2015. Mollusca. *Handbook of Sea-Level Research*. John Wiley & Sons, Ltd.
- Pirazzoli, P. A. 1991a. Australia. *World Atlas of Holocene Sea-Level Changes*. Amsterdam: Elsevier.
- Pirazzoli, P. A. 1991b. Introduction. *World Atlas of Holocene Sea-Level Changes*. Amsterdam: Elsevier.
- Plater, A. J., Kirby, J. R., Boyle, J. F., Shaw, T. & Mills, H. 2015. Loss on Ignition and Organic Content. *Handbook of Sea-Level Research*. John Wiley & Sons, Ltd.
- Poppe, L. J., Eliason, A. H., Fredericks, J. J., Rendigs, R. R., Blackwood, D. & Polloni, C. F. 2000. Chapter 1 - Grain-Size Analysis of Marine Sediments: Methodology and Data Processing. In: Poppe, L. J. & Polloni, C. F. (eds.) *Usgs East-Coast Sediment Analysis; Procedures, Database, and Georeferenced Displays*. United States: United States Geological Survey, Coastal and Marine Geology Program, Woods Hole Field Center.
- Porat, N. & Botha, G. 2008. The Luminescence Chronology of Dune Development on the Maputaland Coastal Plain, Southeast Africa. *Quaternary Science Reviews*, 27, 1024-1046.
- Prescott, J. R. & Hutton, J. T. 1994. Cosmic Ray Contributions to Dose Rates for Luminescence and ESR Dating: Large Depths and Long-Term Time Variations. *Radiation Measurements*, 23, 497-500.
- Proske, U., Stevenson, J., Seddon, A. W. R. & Taffs, K. 2017. Holocene Diatom Records of Wetland Development near Weipa, Cape York, Australia. *Quaternary International*, 440, 42-54.
- Pye, K. & Rhodes, E. G. 1985. Holocene Development of an Episodic Transgressive Dune Barrier, Ramsay Bay, North Queensland, Australia. *Marine Geology*, 64, 189-202.
- Pye, K. & Tsoar, H. 2009. Aeolian Sand and Sand Dunes.
- Queensland Government. 2015. *Coastal Data System - Waves (Albatross Bay)* [Online]. Queensland Government. Available: <https://data.qld.gov.au/dataset/coastal-data-system-waves-albatross-bay> [Accessed 7 June 2016].
- Queensland Herbarium. 2016. *Regional Ecosystem Description Database (Redd). Version 10.0 (December 2016)* [Online]. Brisbane: Queensland Department of Science, Information Technology and Innovation. Available: <https://www.qld.gov.au/environment/plants-animals/plants/ecosystems> [Accessed 15 June 2017].
- Quigley, M. C., Clark, D. & Sandiford, M. 2010. Tectonic Geomorphology of Australia. *Geological Society, London, Special Publications*, 346, 243-265.
- Ramsey, C. B. 2009. *Bayesian Analysis of Radiocarbon Dates*.
- Rashid, T. 2014. Sea Level Research: Methods and Techniques. In: Rashid, T. (ed.) *Holocene Sea-Level Scenarios in Bangladesh*. Singapore: Springer Singapore.
- Rasmussen, S. O., Andersen, K. K., Svensson, A. M., Steffensen, J. P., Vinther, B. M., Clausen, H. B., Siggaard-Andersen, M. L., Johnsen, S. J., Larsen, L. B., Dahl-Jensen, D., Bigler, M., Röthlisberger, R., Fischer, H., Goto-Azuma, K., Hansson, M. E. & Ruth, U. 2006. A New Greenland Ice Core Chronology for the Last Glacial Termination. *Journal of Geophysical Research: Atmospheres*, 111, D06102.
- Rayment, G. E. & Lyons, D. J. 2010. *Soil Chemical Methods - Australasia*, Melbourne, CSIRO Publishing.
- Readhead, M. L. 1987. Thermoluminescence Dose Rate Data and Dating Equations for the Case of Disequilibrium in the Decay Series. *International Journal of Radiation*

*Applications and Instrumentation. Part D. Nuclear Tracks and Radiation Measurements*, 13, 197-207.

- Reeves, J. M. 2004. *The Use of Ostracoda in the Palaeoenvironmental Reconstruction of the Gulf of Carpentaria, Australia, from the Last Interglacial to Present*. Doctor of Philosophy, University of Wollongong.
- Reeves, J. M., Barrows, T. T., Cohen, T. J., Kiem, A. S., Bostock, H. C., Fitzsimmons, K. E., Jansen, J. D., Kemp, J., Krause, C., Petherick, L. & Phipps, S. J. 2013a. Climate Variability over the Last 35,000 Years Recorded in Marine and Terrestrial Archives in the Australian Region: An Oz-Intimate Compilation. *Quaternary Science Reviews*, 74, 21-34.
- Reeves, J. M., Bostock, H. C., Ayliffe, L. K., Barrows, T. T., De Deckker, P., Devriendt, L. S., Dunbar, G. B., Drysdale, R. N., Fitzsimmons, K. E., Gagan, M. K., Griffiths, M. L., Haberle, S. G., Jansen, J. D., Krause, C., Lewis, S., McGregor, H. V., Mooney, S. D., Moss, P., Nanson, G. C., Purcell, A. & Van Der Kaars, S. 2013b. Palaeoenvironmental Change in Tropical Australasia over the Last 30,000 Years – a Synthesis by the Oz-Intimate Group. *Quaternary Science Reviews*, 74, 97-114.
- Reeves, J. M., Chivas, A. R., García, A., Holt, S., Couapel, M. J. J., Jones, B. G., Cendón, D. I. & Fink, D. 2008. The Sedimentary Record of Palaeoenvironments and Sea-Level Change in the Gulf of Carpentaria, Australia, through the Last Glacial Cycle. *Quaternary International*, 183, 3-22.
- Reimann, T., Tsukamoto, S., Harff, J., Osadczuk, K. & Frechen, M. 2011. Reconstruction of Holocene Coastal Foredune Progradation Using Luminescence Dating - an Example from the Świna Barrier (Southern Baltic Sea, Nw Poland). *Geography*, 132, 1-16.
- Reimer, P. J., Bard, E., Bayliss, A., Beck, J. W., Blackwell, P. G., Bronk Ramsey, C., Buck, C. E., Cheng, H., Edwards, R. L., Friedrich, M., Grootes, P. M., Guilderson, T. P., Hafflidason, H., Hajdas, I., Hatté, C., Heaton, T. J., Hoffmann, D. L., Hogg, A. G., Hughen, K. A., Kaiser, K. F., Kromer, B., Manning, S. W., Niu, M., Reimer, R. W., Richards, D. A., Scott, E. M., Southon, J. R., Staff, R. A., Turney, C. S. M. & Van Der Plicht, J. 2013. Intcal13 and Marine13 Radiocarbon Age Calibration Curves 0-50,000 Years Cal Bp. *Radiocarbon*, 55, 1869-1887.
- Reimer, P. J. & Reimer, R. W. 2007. Radiocarbon Dating | Calibration. In: Elias, S. A. (ed.) *Encyclopedia of Quaternary Science*. Oxford: Elsevier.
- Rein, B., Lückge, A. & Sirocko, F. 2004. A Major Holocene Enso Anomaly During the Medieval Period. *Geophysical Research Letters*, 31, n/a-n/a.
- Rémillard, A. M., Buylaert, J. P., Murray, A. S., St-Onge, G., Bernatchez, P. & Hétu, B. 2015. Quartz Osl Dating of Late Holocene Beach Ridges from the Magdalen Islands (Quebec, Canada). *Quaternary Geochronology*, 30, Part B, 264-269.
- Rendell, H. M., Webster, S. E. & Sheffer, N. L. 1994. Underwater Bleaching of Signals from Sediment Grains: New Experimental Data. *Quaternary Science Reviews*, 13, 433-435.
- Rhodes, E. G. 1980. *Modes of Holocene Progradation, Gulf of Carpentaria*. Doctor of Philosophy, Australian National University.
- Rhodes, E. G. 1982. Deposition Model for a Chenier Plain, Gulf of Carpentaria, Australia. *Sedimentology*, 29, 201-221.
- Rhodes, E. G., Polach, H. A., Thom, B. G. & Wilson, S. R. 1980. Age Structure of Holocene Coastal Sediments: Gulf of Carpentaria, Australia. *Radiocarbon*, 22, 718-727.
- Rhodes, E. J. 2011. Optically Stimulated Luminescence Dating of Sediments over the Past 200,000 Years. *Annual Review of Earth and Planetary Sciences*, 39, 461-488.
- Richardson, C. A. 2001. Residual Luminescence Signals in Modern Coastal Sediments. *Quaternary Science Reviews*, 20, 887-892.

- Rink, W. J. & Forrest, B. 2005. Dating Evidence for the Accretion History of Beach Ridges on Cape Canaveral and Merritt Island, Florida, USA. *Journal of Coastal Research*, 21, 1000-1008.
- Rink, W. J. & López, G. I. 2010. Osl-Based Lateral Progradation and Aeolian Sediment Accumulation Rates for the Apalachicola Barrier Island Complex, North Gulf of Mexico, Florida. *Geomorphology*, 123, 330-342.
- Rintoul, L. & Fredericks, P. M. 1995. Infrared Microspectroscopy of Bauxitic Pisoliths. *Applied Spectroscopy*, 49, 1608-1616.
- Roberts, D. L., Bateman, M. D., Murray-Wallace, C. V., Carr, A. S. & Holmes, P. J. 2009. West Coast Dune Plumes: Climate Driven Contrasts in Dunefield Morphogenesis Along the Western and Southern South African Coasts. *Palaeogeography, Palaeoclimatology, Palaeoecology*, 271, 24-38.
- Roberts, H. M. & Plater, A. J. 2007. Reconstruction of Holocene Foreland Progradation Using Optically Stimulated Luminescence (Osl) Dating: An Example from Dungeness, Uk. *The Holocene*, 17, 495-505.
- Roberts, R., Bird, M., Olley, J., Galbraith, R., Lawson, E., Laslett, G., Yoshida, H., Jones, R., Fullagar, R., Jacobsen, G. & Hua, Q. 1998. Optical and Radiocarbon Dating at Jinmium Rock Shelter in Northern Australia. *Nature*, 393, 358.
- Roberts, R. G. & Jacobs, Z. 2015. Luminescence Dating, Single-Grain Dose Distribution. In: Rink, W. J. & Thompson, J. W. (eds.) *Encyclopedia of Scientific Dating Methods*. Dordrecht: Springer Netherlands.
- Rovere, A., Stocchi, P. & Vacchi, M. 2016. Eustatic and Relative Sea Level Changes. *Current Climate Change Reports*, 2, 221-231.
- Rowe, C. 2007. A Palynological Investigation of Holocene Vegetation Change in Torres Strait, Seasonal Tropics of Northern Australia. *Palaeogeography, Palaeoclimatology, Palaeoecology*, 251, 83-103.
- Ryzak, M. & Bieganski, A. 2011. Methodological Aspects of Determining Soil Particle-Size Distribution Using the Laser Diffraction Method. *Journal of Plant Nutrition and Soil Science*, 174, 624-633.
- Saenger, P. 2002. Adapting to the 'Mangrove Environment'. In: Saenger, P. (ed.) *Mangrove Ecology, Silviculture and Conservation*. Dordrecht: Springer Netherlands.
- Saintilan, N., Rogers, K. & Mckee, K. 2009. Salt Marsh-Mangrove Interactions in Australasia and the Americas. In: Perillo, G. M. E., Wolanski, E., Cahoon, D. R. & Brinson, M. M. (eds.) *Coastal Wetlands an Integrated Ecosystem Approach*. Amsterdam; Boston: Elsevier.
- Salehi, M. H., Beni, O. H., Harchegani, H. B., Borujeni, I. E. & Motaghian, H. R. 2011. Refining Soil Organic Matter Determination by Loss-on-Ignition. *Pedosphere*, 21, 473-482.
- Sanderson, D. C. W. 1988. Thick Source Beta Counting (Tsbc): A Rapid Method for Measuring Beta Dose-Rates. *International Journal of Radiation Applications and Instrumentation. Part D. Nuclear Tracks and Radiation Measurements*, 14, 203-207.
- Sanderson, D. C. W., Bishop, P., Stark, M., Alexander, S. & Penny, D. 2007. Luminescence Dating of Canal Sediments from Angkor Borei, Mekong Delta, Southern Cambodia. *Quaternary Geochronology*, 2, 322-329.
- Sandiford, M. 2007. The Tilting Continent: A New Constraint on the Dynamic Topographic Field from Australia. *Earth and Planetary Science Letters*, 261, 152-163.
- Sandiford, M., Wallace, M. & Coblenz, D. 2004. Origin of the in Situ Stress Field in South-Eastern Australia. *Basin Research*, 16, 325-338.
- Santisteban, J. I., Mediavilla, R., López-Pamo, E., Dabrio, C. J., Zapata, M. B. R., García, M. J. G., Castaño, S. & Martínez-Alfaro, P. E. 2004. Loss on Ignition: A Qualitative or



- Quantitative Method for Organic Matter and Carbonate Mineral Content in Sediments? *Journal of Paleolimnology*, 32, 287-299.
- Sawai, Y., Nasu, H. & Yasuda, Y. 2002. Fluctuations in Relative Sea-Level During the Past 3000 Yr in the Onnetoh Estuary, Hokkaido, Northern Japan. *Journal of Quaternary Science*, 17, 607-622.
- Scheffers, A., Engel, M., Scheffers, S., Squire, P. & Kelletat, D. 2012. Beach Ridge Systems - Archives for Holocene Coastal Events? *Progress in Physical Geography*, 36, 5-37.
- Schellmann, G. & Bruckner, H. 2005. Geochronology. In: Schwartz, M. (ed.) *Encyclopedia of Coastal Science*. London: Kluwer Academic.
- Schumacher, B. A. 2002. *Methods for the Determination of the Total Organic Carbon (Toc) in Soils and Sediments*, Washington DC, U.S. Environmental Protection Agency.
- Searle, D. J. & Woods, P. J. 1986. Detailed Documentation of a Holocene Sea-Level Record in the Perth Region, Southern Western Australia. *Quaternary Research*, 26, 299-308.
- Semeniuk, V. 1986. Holocene Climate History of Coastal Southwestern Australia Using Calcrete as an Indicator. *Palaeogeography, Palaeoclimatology, Palaeoecology*, 53, 289-308.
- Semeniuk, V. 1995. The Holocene Record of Climatic, Eustatic and Tectonic Events Along the Coastal Zone of Western Australia: A Review. *Journal of Coastal Research*, 247-259.
- Semeniuk, V. & Searle, D. J. 1985. Distribution of Calcrete in Holocene Coastal Sands in Relationship to Climate, Southwestern Australia. *Journal of Sedimentary Research*, 55, 86-95.
- Shennan, I. 2007. Sea Level Studies | Overview. In: Elias, S. A. (ed.) *Encyclopedia of Quaternary Science*. Oxford: Elsevier.
- Shennan, I. 2015. Handbook of Sea-Level Research: Framing Research Questions. *Handbook of Sea-Level Research*. Chichester: John Wiley & Sons, Ltd.
- Shennan, I., Long, A. J. & Horton, B. P. 2015. *Handbook of Sea-Level Research*, Hoboken, NJ, John Wiley & Sons, Ltd.
- Shepard, F. P. 1963. Thirty-Five Thousand Years of Sea Level. In: Stevenson, R. E. & Halmos, D. M. (eds.) *Essays in Marine Geology in Honour of K. O. Emery*. Los Angeles: University of southern California Press.
- Shepard, F. P. 1964. Sea Level Changes in the Past 6000 Years: Possible Archeological Significance. *Science*, 143, 574-576.
- Shiner, J. & Morrison, M. 2009. The Contribution of Heritage Surveys Towards Understanding the Cultural Landscape of the Weipa Bauxite Plateau. *Australian Archaeology*, 68, 52-55.
- Shiner, J. S., Fanning, P. C., Holdaway, S. J., Petchey, F., Beresford, C. E., Hoffman, E. J. & Larsen, B. 2013. Shell Mounds as the Basis for Understanding Human-Environment Interactions in Far North Queensland, Australia. *Queensland Archaeological Research*, 16, 65-91.
- Short, A. D. 2005. Carbonate Sandy Beaches. In: Schwartz, M. (ed.) *Encyclopedia of Coastal Science*. London: Kluwer Academic.
- Short, A. D. & Woodroffe, C. D. 2009. *The Coast of Australia*, Cambridge, Cambridge University Press.
- Shulmeister, J. 1992. A Holocene Pollen Record from Lowland Tropical Australia. *The Holocene*, 2, 107-116.
- Shulmeister, J. 1999. Australasian Evidence for Mid-Holocene Climate Change Implies Precessional Control of Walker Circulation in the Pacific. *Quaternary International*, 57-58, 81-91.



- Shulmeister, J. & Lees, B. G. 1992. Morphology and Chronostratigraphy of a Coastal Dunefield; Groote Eylandt, Northern Australia. *Geomorphology*, 5.
- Shulmeister, J. & Lees, B. G. 1995. Pollen Evidence from Tropical Australia for the Onset of an Enso-Dominated Climate at C. 4000 Bp. *The Holocene*, 5, 10-18.
- Siegert, M. J. & Dowdeswell, J. A. 2004. Numerical Reconstructions of the Eurasian Ice Sheet and Climate During the Late Weichselian. *Quaternary Science Reviews*, 23, 1273-1283.
- Sloss, C. R. 2005. *Holocene Sea-Level Change and the Aminostratigraphy of Wave-Dominated Barrier Estuaries on the Southeast Coast of Australia*. Doctor of Philosophy, University of Wollongong.
- Sloss, C. R., Murray-Wallace, C. V. & Jones, B. G. 2007. Holocene Sea-Level Change on the Southeast Coast of Australia: A Review. *Holocene*, 17, 999-1014.
- Sloss, C. R., Westaway, K. E., Hua, Q. & Murray-Wallace, C. V. 2013. An Introduction to Dating Techniques: A Guide for Geomorphologists. In: Shroder, J. F. (ed.) *Treatise on Geomorphology*. San Diego: Academic Press.
- Smart, J. 1976a. *Auger Drilling of Beach Ridge Complexes, Western Cape York Peninsula, 1973 - Record 1976/16*, Queensland, Bureau of Mineral Resources, Australia.
- Smart, J. 1976b. The Nature and Origin of Beach Ridges, Western Cape York Peninsula, Queensland. *Journal of Australian Geology and Geophysics*, 1, 211-218.
- Smart, J. 1977a. Late Quaternary Sea-Level Changes, Gulf of Carpentaria, Australia. *Geology*, 5, 755-759.
- Smart, J. 1977b. *Weipa Queensland, Sheet Sd/54-3 1: 250 000 Geological Series Explanatory Notes*. Canberra: Bureau of Mineral Resources.
- Specht, R. L., Salt, R. B. & Reynolds, S. T. 1977. Vegetation in the Vicinity of Weipa, North Queensland. *Proceedings of the Royal Society of Queensland*, 88, 17-38.
- Sperazza, M., Moore, J. & Hendrix, M. 2004. High-Resolution Particle Size Analysis of Naturally Occurring Very Fine-Grained Sediment through Laser Diffractometry. *Journal of Sedimentary Research*, 74, 736-743.
- Stapor Jr, F. W., Mathews, T. D. & Lindfors-Kearns, F. E. 1991. Barrier-Island Progradation and Holocene Sea-Level History in Southwest Florida. *Journal of Coastal Research*, 7, 815-838.
- State of the Environment Committee 2011. Inland Water. *Australia State of the Environment 2011: Independent Report to the Australian Government Minister for Sustainability, Environment, Water, Population and Communities*. Canberra: DSEWPoC.
- Steinke, S., Mohtadi, M., Prange, M., Varma, V., Pittauerova, D. & Fischer, H. W. 2014. Mid-to Late-Holocene Australian-Indonesian Summer Monsoon Variability. *Quaternary Science Reviews*, 93, 142-154.
- Stephens, D. G., Eason, J. E. & Pedlow, G. W. 1973. Dissolution of Shell Material with No Disruption of Primary Sedimentary Structures. *Journal of Sedimentary Petrology*, 43, 618-620.
- Stevenson, J., Brockwell, S., Rowe, C., Proske, U. & Shiner, J. 2015a. The Palaeo-Environmental History of Big Willum Swamp, Weipa: An Environmental Context for the Archaeological Record. *Australian Archaeology*, 80, 17-31.
- Stevenson, J., Proske, U., Rowe, C., Brockwell, C. & O'foghlu, B. 2015b. Environmental Change and the Archaeological Record of Weipa, Cape York Peninsula, Australia. *Poster presented at XIX INQUA Congress - Quaternary Perspectives on Climate Change, Natural Hazards and Civilization*. Nagoya, Japan, 26 July - 2 August.
- Stokes, S., Bray, H. E. & Blum, M. D. 2001. Optical Resetting in Large Drainage Basins: Tests of Zeroing Assumptions Using Single-Aliquot Procedures. *Quaternary Science Reviews*, 20, 879-885.

- Stone, T. 1989. Origins and Environmental Significance of Shell and Earth Mounds in Northern Australia. *Archaeology in Oceania*, 24, 59-64.
- Stone, T. 1991. Two Birds with One Stone: A Reply. *Archaeology in Oceania*, 26, 26-28.
- Stone, T. 1992. *Origins of the Weipa Shell Mounds*. Masters of Science, Australian National University.
- Stone, T. 1995. Shell Mound Formation in Coastal Northern Australia. *Marine Geology*, 129, 77-100.
- Stright, M. J. 2005. Archaeological Site Location, Effect of Sea-Level Change. In: Schwartz, M. (ed.) *Encyclopedia of Coastal Science*. London: Kluwer Academic.
- Stuiver, M. 1961. Variations in Radiocarbon Concentration and Sunspot Activity. *Journal of Geophysical Research*, 66, 273-276.
- Suguio, K., Martin, L., Bittencourt, A. C. S. P., Dominguez, J. M. L., Flexor, J.-M. & Azevedo, A. E. G. 1985. Flutuações Do Nível Relativo Do Mar Durante O Quaternário Superior Ao Longo Do Litoral Brasileiro E Suas Implicações Na Sedimentação Costeira. *Revista Brasileira de Geociências*, 15, 273-286.
- Suguio, K., Martin, L. & Flexor, J.-M. 1976. Les Variations Relatives Du Niveau Moyen De La Mer Au Quaternaire Recent Dans La Region De Cananéia-Iguape, São Paulo. *Boletim IG. Instituto de Geociências, USP*, 7, 113-129.
- Suguio, K., Martin, L. & Flexor, J.-M. 1988. Quaternary Sea-Levels of the Brazilian Coast: Recent Progress. *Episodes*, 11, 203-208.
- Switzer, A. D. 2013. Measuring and Analyzing Particle Size in a Geomorphic Context. In: Shroder, J. F. (ed.) *Treatise on Geomorphology*. San Diego: Academic Press.
- Switzer, A. D. & Pile, J. 2015. Grain Size Analysis. In: Shennan, I., Long, A. J. & Horton, B. P. (eds.) *Handbook of Sea-Level Research*. Chichester: John Wiley & Sons, Ltd.
- Switzer, A. D., Sloss, C. R., Jones, B. G. & Bristow, C. S. 2010. Geomorphic Evidence for Mid-Late Holocene Higher Sea Level from Southeastern Australia. *Quaternary International*, 221, 13-22.
- Tamura, T. 2012. Beach Ridges and Prograded Beach Deposits as Palaeoenvironment Records. *Earth-Science Reviews*, 114, 279-297.
- Tamura, T., Bateman, M. D., Kodama, Y., Saitoh, Y., Watanabe, K., Yamaguchi, N. & Matsumoto, D. 2011. Building of Shore-Oblique Transverse Dune Ridges Revealed by Ground-Penetrating Radar and Optical Dating over the Last 500years on Tottori Coast, Japan Sea. *Geomorphology*, 132, 153-166.
- Tamura, T., Nicholas, W. A., Oliver, T. S. N. & Brooke, B. P. 2018. Coarse-Sand Beach Ridges at Cowley Beach, North-Eastern Australia: Their Formative Processes and Potential as Records of Tropical Cyclone History. *Sedimentology*.
- Tamura, T., Saito, Y., Bateman, M. D., Nguyen, V. L., Ta, T. K. O. & Matsumoto, D. 2012. Luminescence Dating of Beach Ridges for Characterizing Multi-Decadal to Centennial Deltaic Shoreline Changes During Late Holocene, Mekong River Delta. *Marine Geology*, 326-328, 140-153.
- Taylor, G. & Eggleton, R. A. 2008. Genesis of Pisoliths and of the Weipa Bauxite Deposit, Northern Australia. *Australian Journal of Earth Sciences*, 55, S87-S103.
- Taylor, G., Eggleton, R. A., Foster, L. D. & Morgan, C. M. 2008a. Landscapes and Regolith of Weipa, Northern Australia. *Australian Journal of Earth Sciences*, 55, S3-S16.
- Taylor, G., Eggleton, R. A., Foster, L. D., Tilley, D. B., Le Gleuher, M. & Morgan, C. M. 2008b. Nature of the Weipa Bauxite Deposit, Northern Australia. *Australian Journal of Earth Sciences*, 55, S45-S70.
- Taylor, G. & Eggleton, T. "Little Balls" the Origin of the Weipa Bauxite. In: Roach, I. C., ed. CRC LEME Regional Regolith Symposia, 2004 Adelaide, Perth and Canberra.

- Cooperative Research Centre for Landscape Environments and Mineral Exploration, 350-354.
- Taylor, M. & Stone, G. W. 1996. Beach-Ridges: A Review. *Journal of Coastal Research*, 12, 612-621.
- Thom, B. G., Hails, J. R. & Martin, A. R. H. 1969. Radiocarbon Evidence against Higher Postglacial Sea Levels in Eastern Australia. *Marine Geology*, 7, 161-168.
- Thom, B. G., Hails, J. R., Martin, A. R. H. & Phipps, C. V. G. 1972. Postglacial Sea Levels in Eastern Australia—a Reply. *Marine Geology*, 12, 233-242.
- Thom, B. G. & Roy, P. S. 1983. Sea-Level Change in New South Wales over the Past 15,000 Years. In: Hopley, D. (ed.) *Australia Sea Levels in the Last 15000 Years: A Review*. Townsville, Australia: Department of Geography, James Cook University.
- Thom, B. G., Wright, L. D. & Coleman, J. M. 1975. Mangrove Ecology and Deltaic-Estuarine Geomorphology: Cambridge Gulf-Ord River, Western Australia. *Journal of Ecology*, 63, 203-232.
- Thomas, D. S. G. & Goudie, A. 2000. Facies. In: Thomas, D. S. G. & Goudie, A. (eds.) *The Dictionary of Physical Geography*. Malden, Massachusetts: Blackwell Publishing Ltd.
- Thomas, P. J., Murray, A. S., Granja, H. M. & Jain, M. 2008. Optical Dating of Late Quaternary Coastal Deposits in Northwestern Portugal. *Journal of Coastal Research*, 134-144.
- Tibby, J. 2012. The Younger Dryas: Relevant in the Australian Region? *Quaternary International*, 253, 47-54.
- Tooley, M. J. 1982. Introduction. *Proceedings of the Geologists' Association*, 93, 3-6.
- Tooth, S. 2015. Luminescence, Geomorphological Processes. In: Rink, W. J. & Thompson, J. W. (eds.) *Encyclopedia of Scientific Dating Methods*. Dordrecht: Springer Netherlands.
- Torgersen, T., Luly, J. G., De Deckker, P., Jones, M. R., Searle, D. E., Chivas, A. R. & Ullman, W. J. 1988. Late Quaternary Environments of the Carpentaria Basin, Australia. *Palaeogeography, Palaeoclimatology, Palaeoecology*, 67, 245-261.
- Townsend, K. 2016. *Melaleuca Viridiflora* [Online]. Australian Native Plant Society (Australia) (ANPSA). Available: <http://anpsa.org.au/m-vir.html> [Accessed 13 January 2018].
- Trenhaile, A. S. 2005. Beach Sediment Characteristics. In: Schwartz, M. (ed.) *Encyclopedia of Coastal Science*. London: Kluwer Academic.
- Twaddle, R. W., Sloss, C. R., Lowe, K. M., Moss, P., Mackenzie, L. L. & Ulm, S. 2017. Short-Term Late Holocene Dry Season Occupation and Sandy-Mud Flat Focused Foraging at Murdumurdu, Bentinck Island, Gulf of Carpentaria. *Queensland Archaeological Research*, 20, 9-46.
- Twidale, C. R. 2011. Is Australia a Tectonically Stable Continent? Analysis of a Myth and Suggested Morphological Evidence of Tectonism. *Progress in Physical Geography*, 35, 493-515.
- Ulm, S. 2002. Calibrating Marine Radiocarbon Dates: A Guide to Australian  $\Delta r$  Values. *AACAI Newsletter 01/2002*, 89, 10-14.
- Ulm, S. 2006. Australian Marine Reservoir Effects: A Guide to  $\Delta r$  Values. *Australian Archaeology*, 63, 57-60.
- Van Der Plicht, J. 2007. Radiocarbon Dating | Variations in Atmospheric  $^{14}\text{C}$ . In: Elias, S. A. (ed.) *Encyclopedia of Quaternary Science*. Oxford: Elsevier.
- Van Heteren, S., Huntley, D. J., Van De Plassche, O. & Lubberts, R. K. 2000. Optical Dating of Dune Sand for the Study of Sea-Level Change. *Geology*, 28, 411-414.
- Voris, H. K. 2000. Maps of Pleistocene Sea-Levels in Southeast Asia: Shorelines, River Systems and Time Durations. *Journal of Biogeography*, 27, 1153-1167.

- Walker, R. G. 1992. Facies, Facies Models and Modern Stratigraphic Concepts. In: Walker, R. G. & James, N. P. (eds.) *Facies Models: Response to Sea Level Change*. Canada: Geological Association of Canada.
- Waller, M. 2015. Techniques and Applications of Plant Macrofossil Analysis in Sea-Level Studies. *Handbook of Sea-Level Research*. John Wiley & Sons, Ltd.
- Walling, D. E. & Jacovides, J. 1983. News. *Hydrological Sciences Journal*, 28, 319-322.
- Wassmer, P. C., Gomez, C. A., Iskandasyah, T. Y. W. M., Lavigne, F. & Sartohadi, J. 2015. Contribution of Anisotropy of Magnetic Susceptibility (Ams) to Reconstruct Flooding Characteristics of a 4220 Bp Tsunami from a Thick Unconsolidated Structureless Deposit (Banda Aceh, Sumatra). *Frontiers in Earth Science*, 3.
- Wentworth, C. K. 1922. A Scale of Grade and Class Terms for Clastic Sediments. *The Journal of Geology*, 30, 377-392.
- Williams, A. N., Ulm, S., Goodwin, I. D. & Smith, M. 2010. Hunter-Gatherer Response to Late Holocene Climatic Variability in Northern and Central Australia. *Journal of Quaternary Science*, 25, 831-838.
- Williams, M., Dunkerley, D., De Deckker, P., Kershaw, P. & Chappell, J. 1998. *Quaternary Environments*, New York, Arnold.
- Wintle, A. G. 1981. Thermoluminescence Dating of Late Devensian Loesses in Southern England. *Nature*, 289, 479-480.
- Wintle, A. G. & Murray, A. S. 2006. A Review of Quartz Optically Stimulated Luminescence Characteristics and Their Relevance in Single-Aliquot Regeneration Dating Protocols. *Radiation Measurements*, 41, 369-391.
- Wolanski, E. & Chappell, J. 1996. The Response of Tropical Australian Estuaries to a Sea Level Rise. *Journal of Marine Systems*, 7, 267-279.
- Woodroffe, C. D. 1990. The Impact of Sea-Level Rise on Mangrove Shorelines. *Progress in Physical Geography: Earth and Environment*, 14, 483-520.
- Woodroffe, C. D. 1993. Late Quaternary Evolution of Coastal and Lowland Riverine Plains of Southeast Asia and Northern Australia: An Overview. *Sedimentary Geology*, 83, 163-175.
- Woodroffe, C. D. 2007. Sea Level Studies | Coral Records. In: Elias, S. A. (ed.) *Encyclopedia of Quaternary Science*. Oxford: Elsevier.
- Woodroffe, C. D., Bryant, E. A., Price, D. M. & Short, S. A. 1992. Quaternary Inheritance of Coastal Landforms, Cobourg Peninsula, Northern Territory. *Australian Geographer*, 23.
- Woodroffe, C. D. & Chappell, J. 1993. Holocene Emergence and Evolution of the McArthur River Delta, Southwestern Gulf of Carpentaria, Australia. *Sedimentary Geology*, 83, 303-317.
- Woodroffe, C. D., Chappell, J., Thom, B. G. & Wallensky, E. 1986. *Geomorphological Dynamics and Evolution of the South Alligator Tidal River and Plains, Northern Territory*, Darwin, Australian National University, North Australia Research Unit.
- Woodroffe, C. D., Chappell, J., Thom, B. G. & Wallensky, E. 1989. Depositional Model of a Macrotidal Estuary and Floodplain, South Alligator River, Northern Australia. *Sedimentology*, 36, 737-756.
- Woodroffe, C. D., Mulrennan, M. E. & Chappell, J. 1993. Estuarine Infill and Coastal Progradation, Southern Van Diemen Gulf, Northern Australia. *Sedimentary Geology*, 83, 257-275.
- Woodroffe, C. D., Thom, B. G. & Chappell, J. 1985. Development of Widespread Mangrove Swamps in Mid-Holocene Times in Northern Australia. *Nature*, 317, 711-713.

- Woodroffe, S. A. 2009a. Recognising Subtidal Foraminiferal Assemblages: Implications for Quantitative Sea-Level Reconstructions Using a Foraminifera-Based Transfer Function. *Journal of Quaternary Science*, 24, 215-223.
- Woodroffe, S. A. 2009b. Testing Models of Mid to Late Holocene Sea-Level Change, North Queensland, Australia. *Quaternary Science Reviews*, 28, 2474-2488.
- Woodroffe, S. A. & Horton, B. P. 2005. Holocene Sea-Level Changes in the Indo-Pacific. *Journal of Asian Earth Sciences*, 25, 29-43.
- Woodroffe, S. A., Horton, B. P., Larcombe, P. & Whittaker, J. E. 2005. Intertidal Mangrove Foraminifera from the Central Great Barrier Reef Shelf, Australia: Implications for Sea-Level Reconstruction. *Journal of Foraminiferal Research*, 35, 259-270.
- Woodroffe, S. A., Long, A. J., Punwong, P., Selby, K., Bryant, C. L. & Marchant, R. 2015. Radiocarbon Dating of Mangrove Sediments to Constrain Holocene Relative Sea-Level Change on Zanzibar in the Southwest Indian Ocean. *The Holocene*, 25, 820-831.
- Woodward, C. A. & Sloss, C. R. 2013. 14.11 Coring and Augering. In: Editor-in-Chief: John, F. S. (ed.) *Treatise on Geomorphology*. San Diego: Academic Press.
- Wright, L. D. 1970. The Influence of Sediment Availability on Patterns of Beach Ridge Development in the Vicinity of the Shoalhaven River Delta, N.S.W. *Australian Geographer*, 11, 336-348.
- Wright, R. V. S. 1963. Report on Archaeological Reconnaissance Work in Cape York. Canberra: Australian Institute of Aboriginal Studies.
- Wright, S. A. 2011. *Fixed Intertidal Biological Indicators and Holocene Sea-Level on the Great Barrier Reef Coast* Doctor of Philosophy, University of New England.
- Wyrwoll, K.-H., Zhu, Z., Kendrick, G., Collins, L. & Eisenhauer, A. 1995. Holocene Sea-Level Events in Western Australia: Revisiting Old Questions. *Journal of Coastal Research*, 321-326.
- Yokoyama, Y., Purcell, A., Lambeck, K. & Johnston, P. 2001. Shore-Line Reconstruction around Australia During the Last Glacial Maximum and Late Glacial Stage. *Quaternary International*, 83-85, 9-18.
- Yu, K.-F. & Zhao, J.-X. 2010. U-Series Dates of Great Barrier Reef Corals Suggest at Least +0.7 M Sea Level ~7000 Years Ago. *The Holocene*, 20, 161-168.
- Yu, K.-F., Zhao, J.-X., Done, T. & Chen, T.-G. 2009. Microatoll Record for Large Century-Scale Sea-Level Fluctuations in the Mid-Holocene. *Quaternary Research*, 71, 354-360.
- Zhao, J. & Yu, K. 2002. Timing of Holocene Sea-Level Highstands by Mass Spectrometric U-Series Ages of a Coral Reef from Leizhou Peninsula, South China Sea. *Chinese Science Bulletin*, 47, 348-352.
- Zöller, L. & Wagner, G. A. 2015. Luminescence Dating, History. In: Rink, W. J. & Thompson, J. W. (eds.) *Encyclopedia of Scientific Dating Methods*. Dordrecht: Springer Netherlands.
- Zong, Y. 2007. Sea-Levels, Late Quaternary - Tropics. In: Elias, S. A. (ed.) *Encyclopedia of Quaternary Science*. Oxford: Elsevier.
- Zong, Y. & Horton, B. P. 1999. Diatom-Based Tidal-Level Transfer Functions as an Aid in Reconstructing Quaternary History of Sea-Level Movements in the Uk. *Journal of Quaternary Science*, 14, 153-167.
- Zong, Y., Kemp, A. C., Yu, F., Lloyd, J. M., Huang, G. & Yim, W. W.-S. 2010. Diatoms from the Pearl River Estuary, China and Their Suitability as Water Salinity Indicators for Coastal Environments. *Marine Micropaleontology*, 75, 38-49.
- Zuschin, M., Stachowitsch, M. & Stanton, R. J. 2003. Patterns and Processes of Shell Fragmentation in Modern and Ancient Marine Environments. *Earth-Science Reviews*, 63, 33-82.

# Appendix A: Sediment Laboratory Data

Pit Code	Laboratory code	Depth (cm)	Sub-facies	Sample Type	Textural Group	Sediment name	Folk and Ward Method (um)				Folk and Ward Method (description)				Proportion of clay-silt-sand-gravel				Organic carbon and carbonate content (%DW)	
							Mean	Sorting	Skewness	Kurtosis	Mean	Sorting	Skewness	Kurtosis	%Clay	%Silt	%Sand	%Gravel	Organic matter	Carbonate
RB Modern Trench	RBMT DFO1	0	B3	Bimodal, Poorly Sorted	Sandy Gravel	Sandy Fine Gravel	997.85	3.79	0.40	0.66	Coarse Sand	Poorly Sorted	Very Coarse Skewed	Very Platykurtic	0.02	1.01	57.56	41.41	4.44	0.85
		10	B3	Bimodal, Poorly Sorted	Gravelly Sand	Fine Gravelly Medium Sand	677.70	3.05	0.47	1.28	Coarse Sand	Poorly Sorted	Very Coarse Skewed	Leptokurtic	0.00	0.00	80.30	19.70	3.54	1.42
		20	A2	Unimodal, Moderately Sorted	Gravel	Fine Gravel	4335.55	1.78	-0.38	1.29	Fine Gravel	Moderately Sorted	Very Fine Skewed	Leptokurtic	0.00	0.13	5.07	94.79	5.42	4.98
		30	B3	Bimodal, Poorly Sorted	Gravelly Sand	Fine Gravelly Medium Sand	804.47	3.63	0.53	0.68	Coarse Sand	Poorly Sorted	Very Coarse Skewed	Platykurtic	0.00	0.00	70.06	29.94	4.13	2.07
		40	B3	Bimodal, Poorly Sorted	Sandy Gravel	Sandy Fine Gravel	1452.24	3.59	-0.28	0.61	Very Coarse Sand	Poorly Sorted	Fine Skewed	Very Platykurtic	0.00	0.00	50.05	49.95	4.23	1.58
Pit Code	Laboratory code	Depth (cm)	Sub-facies	Sample Type	Textural Group	Sediment name	Folk and Ward Method (um)				Folk and Ward Method (description)				Proportion of clay-silt-sand-gravel				Organic carbon and carbonate content (%DW)	
							Mean	Sorting	Skewness	Kurtosis	Mean	Sorting	Skewness	Kurtosis	%Clay	%Silt	%Sand	%Gravel	Organic matter	Carbonate
RB Modern Trench	RBMT DFO3	0	B3	Bimodal, Poorly Sorted	Sandy Gravel	Sandy Fine Gravel	1145.17	3.91	0.49	0.63	Very Coarse Sand	Poorly Sorted	Very Coarse Skewed	Very Platykurtic	0.00	0.00	64.10	35.90	3.51	0.87
		10	B3	Bimodal, Poorly Sorted	Sandy Fine Gravel	Sandy Fine Gravel	966.53	3.17	0.45	0.66	Coarse Sand	Poorly Sorted	Very Coarse Skewed	Very Platykurtic	0.00	0.00	67.91	32.09	3.28	1.17
		20	B3	Bimodal, Poorly Sorted	Gravelly Sand	Fine Gravelly Medium Sand	827.11	3.25	0.38	0.79	Coarse Sand	Poorly Sorted	Very Coarse Skewed	Platykurtic	0.00	0.00	73.90	26.10	3.80	-0.12
		30	B3	Bimodal, Poorly Sorted	Sandy Gravel	Sandy Very Fine Gravel	835.00	3.48	0.34	0.68	Coarse Sand	Poorly Sorted	Very Coarse Skewed	Platykurtic	0.00	0.00	64.18	35.82	4.25	2.26
		40	B3	Bimodal, Poorly Sorted	Gravelly Sand	Very Fine Gravelly Medium Sand	764.50	3.74	0.55	0.79	Coarse Sand	Poorly Sorted	Very Coarse Skewed	Platykurtic	0.00	0.00	71.04	28.96	5.43	1.28
		50	B3	Bimodal, Poorly Sorted	Gravelly Sand	Fine Gravelly Medium Sand	431.60	2.53	0.41	2.08	Medium Sand	Poorly Sorted	Very Coarse Skewed	Very Leptokurtic	0.00	0.00	84.10	15.90	15.22	-0.03
		Organic	B1	Unimodal, Poorly Sorted	Gravelly Sand	Fine Gravelly Medium Sand	305.35	2.10	0.17	2.01	Medium Sand	Poorly Sorted	Coarse Skewed	Very Leptokurtic	0.00	0.00	91.92	8.08	3.94	0.18
Pit Code	Laboratory code	Depth (cm)	Sub-facies	Sample Type	Textural Group	Sediment name	Folk and Ward Method (um)				Folk and Ward Method (description)				Proportion of clay-silt-sand-gravel				Organic carbon and carbonate content (%DW)	
							Mean	Sorting	Skewness	Kurtosis	Mean	Sorting	Skewness	Kurtosis	%Clay	%Silt	%Sand	%Gravel	Organic matter	Carbonate
RB Modern Trench	RBMT DFO5	0	B3	Bimodal, Poorly Sorted	Gravelly Sand	Very Fine Gravelly Medium Sand	698.03	3.14	0.55	1.37	Coarse Sand	Poorly Sorted	Very Coarse Skewed	Leptokurtic	0.00	0.00	78.09	21.91	2.88	1.60
		10	B3	Bimodal, Poorly Sorted	Sandy Gravel	Sandy Fine Gravel	990.43	3.50	0.43	0.70	Coarse Sand	Poorly Sorted	Very Coarse Skewed	Platykurtic	0.00	0.00	65.97	34.03	3.35	2.15
		20	B3	Bimodal, Poorly Sorted	Gravelly Sand	Very Fine Gravelly Medium Sand	687.03	3.00	0.49	1.32	Coarse Sand	Poorly Sorted	Very Coarse Skewed	Leptokurtic	0.00	0.00	78.94	21.06	17.19	1.37
		30	B3	Bimodal, Very Poorly Sorted	Sandy Gravel	Sandy Fine Gravel	1191.57	4.04	0.30	0.68	Very Coarse Sand	Very Poorly Sorted	Very Coarse Skewed	Platykurtic	0.00	0.00	58.80	41.20	4.07	1.46
		40	B3	Bimodal, Poorly Sorted	Sandy Gravel	Sandy Fine Gravel	993.52	3.47	0.31	0.68	Coarse Sand	Poorly Sorted	Very Coarse Skewed	Platykurtic	0.00	1.52	61.86	36.62	7.45	2.36
Pit Code	Laboratory code	Depth (cm)	Sub-facies	Sample Type	Textural Group	Sediment name	Folk and Ward Method (um)				Folk and Ward Method (description)				Proportion of clay-silt-sand-gravel				Organic carbon and carbonate content (%DW)	
							Mean	Sorting	Skewness	Kurtosis	Mean	Sorting	Skewness	Kurtosis	%Clay	%Silt	%Sand	%Gravel	Organic matter	Carbonate
RR1	RB02	0	B3	Bimodal, Poorly Sorted	Sandy Gravel	Sandy Very Fine Gravel	859.11	3.43	0.28	0.67	Coarse Sand	Poorly Sorted	Coarse Skewed	Platykurtic	0.00	0.00	60.97	39.03	3.05	1.87
		10	A1	Bimodal, Poorly Sorted	Sandy Gravel	Sandy Fine Gravel	2129.92	3.65	-0.69	0.70	Very Fine Gravel	Poorly Sorted	Very Fine Skewed	Platykurtic	0.01	1.09	27.92	70.98	4.10	5.00
		20	A1	Bimodal, Poorly Sorted	Sandy Gravel	Sandy Fine Gravel	2069.32	3.78	-0.70	0.63	Very Fine Gravel	Poorly Sorted	Very Fine Skewed	Very Platykurtic	0.04	1.69	34.07	64.20	6.49	5.29
		30	B3	Bimodal, Poorly Sorted	Sandy Gravel	Sandy Very Fine Gravel	994.88	3.80	0.20	0.66	Coarse Sand	Poorly Sorted	Coarse Skewed	Very Platykurtic	0.06	2.26	54.26	43.42	4.04	2.36
		40	B3	Bimodal, Poorly Sorted	Sandy Gravel	Sandy Fine Gravel	1379.23	3.59	-0.12	0.68	Very Coarse Sand	Poorly Sorted	Fine Skewed	Platykurtic	0.01	1.60	52.80	45.59	4.97	3.98
		50	A2	Unimodal, Moderately Well Sorted	Gravel	Very Fine Gravel	3729.17	1.52	0.16	0.77	Very Fine Gravel	Moderately Well Sorted	Coarse Skewed	Platykurtic	0.00	0.00	0.00	100.00	4.04	1.97
		60	B3	Bimodal, Poorly Sorted	Sandy Gravel	Sandy Very Fine Gravel	1251.62	3.22	0.03	0.74	Very Coarse Sand	Poorly Sorted	Symmetrical	Platykurtic	0.00	1.61	56.14	42.25	4.10	2.20
		70	B3	Bimodal, Poorly Sorted	Gravelly Sand	Fine Gravelly Medium Sand	800.95	3.33	0.40	0.78	Coarse Sand	Poorly Sorted	Very Coarse Skewed	Platykurtic	0.00	0.00	73.72	26.28	3.13	1.86
		80	B3	Bimodal, Poorly Sorted	Gravelly Sand	Fine Gravelly Medium Sand	912.48	3.28	0.30	0.75	Coarse Sand	Poorly Sorted	Very Coarse Skewed	Platykurtic	0.00	0.62	69.43	29.95	3.37	1.88
		90	B3	Bimodal, Poorly Sorted	Sandy Gravel	Sandy Very Fine Gravel	912.01	3.32	0.30	0.72	Coarse Sand	Poorly Sorted	Coarse Skewed	Platykurtic	0.00	0.00	67.15	32.85	2.93	2.74
		100	B3	Bimodal, Poorly Sorted	Sandy Gravel	Sandy Fine Gravel	1762.20	3.22	-0.26	0.68	Very Coarse Sand	Poorly Sorted	Fine Skewed	Platykurtic	0.00	0.00	46.53	53.47	3.52	4.40
		110	A2	Unimodal, Poorly Sorted	Gravel	Fine Gravel	3821.30	2.17	-0.41	1.51	Very Fine Gravel	Poorly Sorted	Very Fine Skewed	Very Leptokurtic	0.00	0.59	14.55	84.87	3.33	5.10
		130	B3	Bimodal, Poorly Sorted	Sandy Gravel	Sandy Very Fine Gravel	1221.57	3.14	0.21	0.78	Very Coarse Sand	Poorly Sorted	Coarse Skewed	Platykurtic	0.00	0.90	62.51	36.59	2.99	3.45
Pit Code	Laboratory code	Depth (cm)	Sub-facies	Sample Type	Textural Group	Sediment name	Folk and Ward Method (um)				Folk and Ward Method (description)				Proportion of clay-silt-sand-gravel				Organic carbon and carbonate content (%DW)	
							Mean	Sorting	Skewness	Kurtosis	Mean	Sorting	Skewness	Kurtosis	%Clay	%Silt	%Sand	%Gravel	Organic matter	Carbonate
RS1	RB04	0	B4	Bimodal, Poorly Sorted	Gravelly Sand	Very Fine Gravelly Medium Sand	811.81	3.56	0.19	0.90	Coarse Sand	Poorly Sorted	Coarse Skewed	Platykurtic	0.12	4.65	68.27	26.96	7.20	1.08
		10	B4	Bimodal, Poorly Sorted	Sandy Gravel	Sandy Fine Gravel	1116.48	3.62	0.17	0.64	Very Coarse Sand	Poorly Sorted	Coarse Skewed	Very Platykurtic	0.03	2.25	53.70	44.02	5.23	1.24
		20	B3	Bimodal, Poorly Sorted	Sandy Gravel	Sandy Fine Gravel	975.51	3.76	0.33	0.65	Coarse Sand	Poorly Sorted	Very Coarse Skewed	Very Platykurtic	0.00	1.60	58.09	40.30	3.25	1.87
		30	B4	Bimodal, Poorly Sorted	Gravelly Sand	Fine Gravelly Medium Sand	916.43	3.22	0.31	0.76	Coarse Sand	Poorly Sorted	Very Coarse Skewed	Platykurtic	0.00	0.12	70.75	29.13	3.43	2.75
		40	B3	Bimodal, Poorly Sorted	Sandy Gravel	Sandy Fine Gravel	947.89	3.36	0.31	0.70	Coarse Sand	Poorly Sorted	Very Coarse Skewed	Platykurtic	0.00	0.69	64.99	34.32	4.90	3.24
		50	A1	Unimodal, Poorly Sorted	Sandy Gravel	Sandy Very Fine Gravel	1516.31	2.25	0.14	0.85	Very Coarse Sand	Poorly Sorted	Coarse Skewed	Platykurtic	0.00	0.17	65.31	34.52	5.89	7.56
		60	B3	Unimodal, Poorly Sorted	Gravelly Sand	Very Fine Gravelly Coarse Sand	1222.87	2.35	0.16	1.05	Very Coarse Sand	Poorly Sorted	Coarse Skewed	Mesokurtic	0.00	0.20	74.88	24.92	5.59	4.41
		71-75	B4	Bimodal, Poorly Sorted	Sandy Gravel	Sandy Fine Gravel	1000.75	3.26	0.29	0.69	Very Coarse Sand	Poorly Sorted	Coarse Skewed	Platykurtic	0.00	0.10	64.86	35.04	4.41	6.10
		80	B3	Unimodal, Poorly Sorted	Gravelly Sand	Very Fine Gravelly Medium Sand	718.16	2.77	0.23	1.03	Coarse Sand	Poorly Sorted	Coarse Skewed	Mesokurtic	0.00	0.61	82.62	16.77	2.87	2.78

Pit Code	Laboratory code	Depth (cm)	Sub-facies	Sample Type	Textural Group	Sediment name	Folk and Ward Method (um)				Folk and Ward Method (description)				Proportion of clay-silt-sand-gravel				Organic carbon and carbonate content (%DW)	
							Mean	Sorting	Skewness	Kurtosis	Mean	Sorting	Skewness	Kurtosis	%Clay	%Silt	%Sand	%Gravel	Organic matter	Carbonate
RR2	RB01	0	A1	Bimodal, Poorly Sorted	Sandy Gravel	Sandy Fine Gravel	1565.04	3.77	-0.35	0.64	Very Coarse Sand	Poorly Sorted	Very Fine Skewed	Very Platykurtic	0.07	2.69	45.39	51.85	7.02	2.77
		10	A1	Unimodal, Poorly Sorted	Sandy Gravel	Sandy Fine Gravel	2936.47	2.74	-0.61	1.42	Very Fine Gravel	Poorly Sorted	Very Fine Skewed	Leptokurtic	0.01	1.35	19.13	79.51	8.64	14.06
		20	B4	Bimodal, Poorly Sorted	Sandy Gravel	Sandy Fine Gravel	870.23	3.84	0.48	0.61	Coarse Sand	Poorly Sorted	Very Coarse Skewed	Very Platykurtic	0.00	0.74	61.80	37.46	2.66	1.23
		30	B4	Bimodal, Poorly Sorted	Sandy Gravel	Sandy Fine Gravel	1744.95	3.59	-0.38	0.63	Very Coarse Sand	Poorly Sorted	Very Fine Skewed	Very Platykurtic	0.00	1.35	43.29	55.36	4.08	3.71
		40	A1	Unimodal, Moderately Sorted	Gravel	Fine Gravel	4208.81	1.92	-0.41	1.40	Fine Gravel	Moderately Sorted	Very Fine Skewed	Leptokurtic	0.00	0.21	8.24	91.55	6.33	13.67
		50	B3	Bimodal, Poorly Sorted	Gravelly Sand	Fine Gravelly Medium Sand	811.40	3.69	0.48	0.69	Coarse Sand	Poorly Sorted	Very Coarse Skewed	Platykurtic	0.00	0.00	70.23	29.77	2.76	1.38
		60	B3	Bimodal, Poorly Sorted	Sandy Gravel	Sandy Fine Gravel	1071.14	3.90	0.16	0.59	Very Coarse Sand	Poorly Sorted	Coarse Skewed	Very Platykurtic	0.00	1.66	50.04	48.30	3.08	1.89
		70	B3	Bimodal, Poorly Sorted	Sandy Gravel	Sandy Fine Gravel	1173.23	3.69	0.16	0.66	Very Coarse Sand	Poorly Sorted	Coarse Skewed	Very Platykurtic	0.00	0.96	55.38	43.66	3.20	3.20
		80	B3	Bimodal, Poorly Sorted	Sandy Gravel	Sandy Fine Gravel	1196.31	3.31	0.16	0.74	Very Coarse Sand	Poorly Sorted	Coarse Skewed	Platykurtic	0.00	0.13	60.29	39.58	5.09	4.31
		90	B3	Bimodal, Poorly Sorted	Gravelly Sand	Very Fine Gravelly Coarse Sand	922.96	3.20	0.21	0.85	Coarse Sand	Poorly Sorted	Coarse Skewed	Platykurtic	0.00	0.59	71.81	27.60	3.94	1.06
		100	B3	Bimodal, Poorly Sorted	Sandy Gravel	Sandy Fine Gravel	1421.03	3.29	-0.06	0.73	Very Coarse Sand	Poorly Sorted	Symmetrical	Platykurtic	0.00	0.38	54.59	45.03	4.16	2.81
		110	B3	Bimodal, Poorly Sorted	Sandy Gravel	Sandy Very Fine Gravel	1335.80	3.09	-0.01	0.88	Very Coarse Sand	Poorly Sorted	Symmetrical	Platykurtic	0.00	0.49	60.68	38.82	7.02	7.69
		120	B3	Bimodal, Poorly Sorted	Sandy Gravel	Sandy Very Fine Gravel	1163.87	3.26	0.05	0.75	Very Coarse Sand	Poorly Sorted	Symmetrical	Platykurtic	0.00	0.44	59.18	40.38	4.54	3.59
		125	B3	Bimodal, Very Poorly Sorted	Sandy Gravel	Sandy Fine Gravel	951.70	4.42	0.43	0.63	Coarse Sand	Very Poorly Sorted	Very Coarse Skewed	Very Platykurtic	0.02	2.65	55.47	41.86	4.26	4.26
		125+	B3	Bimodal, Poorly Sorted	Sandy Gravel	Sandy Fine Gravel	1751.61	3.74	-0.43	0.68	Very Coarse Sand	Poorly Sorted	Very Fine Skewed	Platykurtic	0.08	1.81	37.90	60.21	5.35	6.95
RS2	RB05	0	B2	Unimodal, Poorly Sorted	Gravelly Sand	Very Fine Gravelly Coarse Sand	718.58	2.43	0.04	1.15	Coarse Sand	Poorly Sorted	Symmetrical	Leptokurtic	0.01	2.19	88.30	9.50	12.62	0.67
		10	B2	Bimodal, Very Poorly Sorted	Sandy Gravel	Sandy Fine Gravel	928.10	4.26	0.12	0.96	Coarse Sand	Very Poorly Sorted	Coarse Skewed	Mesokurtic	0.29	5.30	62.03	32.38	4.87	0.60
		20	B2	Bimodal, Very Poorly Sorted	Muddy Sandy Gravel	Coarse Silty Sandy Very Fine Gravel	929.39	4.45	-0.04	1.08	Coarse Sand	Very Poorly Sorted	Symmetrical	Mesokurtic	0.44	6.99	58.54	34.03	7.02	0.68
		30	B2	Bimodal, Poorly Sorted	Sandy Gravel	Sandy Very Fine Gravel	1237.93	3.48	-0.11	1.13	Very Coarse Sand	Poorly Sorted	Fine Skewed	Leptokurtic	0.28	4.58	57.06	38.08	7.07	0.76
		40	B3	Trimodal, Very Poorly Sorted	Muddy Sandy Gravel	Coarse Silty Sandy Very Fine Gravel	817.82	6.72	-0.27	1.31	Coarse Sand	Very Poorly Sorted	Fine Skewed	Leptokurtic	1.71	12.69	48.49	37.11	6.91	0.79
		50	B3	Bimodal, Very Poorly Sorted	Muddy Sandy Gravel	Very Coarse Silty Sandy Fine Gravel	2056.07	4.07	-0.47	1.14	Very Fine Gravel	Very Poorly Sorted	Very Fine Skewed	Leptokurtic	0.47	6.43	35.26	57.84	6.96	9.41
		60	B3	Bimodal, Poorly Sorted	Sandy Gravel	Sandy Very Fine Gravel	1530.06	3.47	-0.18	1.34	Very Coarse Sand	Poorly Sorted	Fine Skewed	Leptokurtic	0.24	5.50	53.07	41.19	6.29	8.08
		70	B3	Unimodal, Poorly Sorted	Gravelly Sand	Very Fine Gravelly Coarse Sand	875.46	2.92	0.07	1.07	Coarse Sand	Poorly Sorted	Symmetrical	Mesokurtic	0.00	1.67	77.13	21.20	4.77	4.68
		80	B3	Bimodal, Poorly Sorted	Gravelly Sand	Fine Gravelly Coarse Sand	990.32	3.08	0.09	1.38	Coarse Sand	Poorly Sorted	Symmetrical	Leptokurtic	0.33	4.17	73.49	22.00	10.49	4.88
		90	B3	Unimodal, Poorly Sorted	Gravelly Sand	Very Fine Gravelly Coarse Sand	978.98	2.02	0.10	1.16	Coarse Sand	Poorly Sorted	Coarse Skewed	Leptokurtic	0.30	3.68	82.69	13.33	5.51	6.48
		100	B3	Bimodal, Poorly Sorted	Sandy Gravel	Sandy Very Fine Gravel	1549.38	2.82	-0.12	1.09	Very Coarse Sand	Poorly Sorted	Fine Skewed	Mesokurtic	0.35	3.34	54.89	41.42	6.49	3.44
		120	B3	Bimodal, Very Poorly Sorted	Sandy Gravel	Sandy Fine Gravel	1365.66	4.44	-0.21	0.66	Very Coarse Sand	Very Poorly Sorted	Fine Skewed	Very Platykurtic	0.00	1.34	49.10	49.57	3.74	2.11
		130	B3	Bimodal, Very Poorly Sorted	Sandy Gravel	Sandy Fine Gravel	685.41	4.41	0.53	0.52	Coarse Sand	Very Poorly Sorted	Very Coarse Skewed	Very Platykurtic	0.00	0.00	61.15	38.85	4.13	5.63
		140	B3	Bimodal, Very Poorly Sorted	Sandy Gravel	Sandy Fine Gravel	564.47	4.39	0.55	0.60	Coarse Sand	Very Poorly Sorted	Very Coarse Skewed	Very Platykurtic	0.00	1.99	61.54	36.48	3.38	2.61
RS3	RB17	0	B2	Bimodal, Very Poorly Sorted	Sandy Gravel	Sandy Very Fine Gravel	991.35	4.16	-0.03	1.11	Coarse Sand	Very Poorly Sorted	Symmetrical	Leptokurtic	0.35	5.41	62.36	31.89	5.95	1.92
		10	B2	Unimodal, Very Poorly Sorted	Gravelly Muddy Sand	Very Fine Gravelly Coarse Silty Coarse Sand	941.90	4.21	-0.13	1.59	Coarse Sand	Very Poorly Sorted	Fine Skewed	Very Leptokurtic	0.66	8.21	64.85	26.29	5.06	1.99
		20	B3	Unimodal, Very Poorly Sorted	Gravelly Muddy Sand	Very Fine Gravelly Very Coarse Silty Coarse Sand	675.10	4.49	-0.23	1.57	Coarse Sand	Very Poorly Sorted	Fine Skewed	Very Leptokurtic	0.88	11.60	68.53	18.99	4.88	2.02
		30	B3	Unimodal, Poorly Sorted	Gravelly Sand	Very Fine Gravelly Coarse Sand	881.17	2.72	0.06	1.42	Coarse Sand	Poorly Sorted	Symmetrical	Leptokurtic	0.00	3.47	78.63	17.89	4.96	6.83
		40	B3	Unimodal, Poorly Sorted	Gravelly Sand	Very Fine Gravelly Coarse Sand	1196.74	2.53	0.19	1.04	Very Coarse Sand	Poorly Sorted	Coarse Skewed	Mesokurtic	0.00	1.94	71.53	26.53	4.64	8.59
		50	B3	Bimodal, Poorly Sorted	Sandy Gravel	Sandy Very Fine Gravel	1012.35	3.39	0.18	0.81	Very Coarse Sand	Poorly Sorted	Coarse Skewed	Platykurtic	0.00	2.49	64.63	32.87	3.51	7.11
		60	B3	Bimodal, Poorly Sorted	Gravelly Sand	Very Fine Gravelly Medium Sand	763.36	3.06	0.32	1.16	Coarse Sand	Poorly Sorted	Very Coarse Skewed	Leptokurtic	0.00	2.18	76.89	20.93	3.19	6.94
		70	B3	Unimodal, Poorly Sorted	Gravelly Muddy Sand	Very Fine Gravelly Coarse Silty Very Coarse Sand	1277.61	2.73	-0.43	4.17	Very Coarse Sand	Poorly Sorted	Very Fine Skewed	xtremely Leptokurtic	0.73	8.09	78.98	12.19	5.24	8.83
		80	B3	Unimodal, Poorly Sorted	Gravelly Sand	Very Fine Gravelly Coarse Sand	838.42	2.03	0.09	1.15	Coarse Sand	Poorly Sorted	Symmetrical	Leptokurtic	0.00	2.20	87.97	9.83	3.76	6.08
		90	B3	Bimodal, Poorly Sorted	Gravelly Sand	Fine Gravelly Coarse Sand	1309.33	3.17	0.10	1.14	Very Coarse Sand	Poorly Sorted	Symmetrical	Leptokurtic	0.00	2.54	69.43	28.03	4.27	5.56
		100	B3	Trimodal, Poorly Sorted	Sandy Gravel	Sandy Fine Gravel	1433.71	3.81	-0.23	1.10	Very Coarse Sand	Poorly Sorted	Fine Skewed	Mesokurtic	0.28	4.20	51.83	43.69	5.10	4.58
		110	B3	Bimodal, Poorly Sorted	Gravelly Sand	Very Fine Gravelly Very Coarse Sand	846.73	3.96	-0.21	1.14	Coarse Sand	Poorly Sorted	Fine Skewed	Leptokurtic	0.35	4.79	67.89	26.97	4.57	3.56
	RBD17	120	B3	Bimodal, Very Poorly Sorted	Muddy Sandy Gravel	Very Coarse Silty Sandy Fine Gravel	1158.11	5.90	-0.46	0.67	Very Coarse Sand	Very Poorly Sorted	Very Fine Skewed	Platykurtic	0.51	6.83	38.04	54.62	5.98	1.57
		123	C1	Unimodal, Poorly Sorted	Muddy Sand	Very Coarse Silty Fine Sand	100.92	3.03	-0.38	1.41	Very Fine Sand	Poorly Sorted	Very Fine Skewed	Leptokurtic	1.17	23.02	75.82	0.00	6.23	0.78
		130	C1	Unimodal, Poorly Sorted	Muddy Sand	Very Coarse Silty Very Fine Sand	69.62	3.31	-0.31	1.33	Very Fine Sand	Poorly Sorted	Very Fine Skewed	Leptokurtic	2.22	34.39	63.38	0.00	11.57	0.97
		140	C1	Unimodal, Poorly Sorted	Muddy Sand	Very Coarse Silty Very Fine Sand	58.37	3.96	-0.36	1.22	Very Coarse Silt	Poorly Sorted	Very Fine Skewed	Leptokurtic	2.78	37.67	59.55	0.00	9.96	1.75
		150	C2	Unimodal, Poorly Sorted	Muddy Sand	Very Coarse Silty Fine Sand	92.34	3.87	-0.42	1.41	Very Fine Sand	Poorly Sorted	Very Fine Skewed	Leptokurtic	1.96	24.70	73.35	0.00	7.59	2.34
		160	C2	Unimodal, Poorly Sorted	Muddy Sand	Very Coarse Silty Fine Sand	92.22	3.88	-0.48	1.54	Very Fine Sand	Poorly Sorted	Very Fine Skewed	Very Leptokurtic	2.13	23.11	74.76	0.00	5.17	5.34
		170	C2	Unimodal, Poorly Sorted	Muddy Sand	Very Coarse Silty Fine Sand	103.16	3.50	-0.50	1.62	Very Fine Sand	Poorly Sorted	Very Fine Skewed	Very Leptokurtic	2.10	20.73	77.17	0.00	2.63	1.91
		180	C2	Unimodal, Very Poorly Sorted	Muddy Sand	Very Coarse Silty Fine Sand	80.10	4.09	-0.50	1.26	Very Fine Sand	Very Poorly Sorted	Very Fine Skewed	Leptokurtic	3.30	27.81	68.89	0.00	2.39	5.41
		190	C2	Unimodal, Poorly Sorted	Muddy Sand	Coarse Silty Fine Sand	112.54	3.53	-0.52	1.81	Very Fine Sand	Poorly Sorted	Very Fine Skewed	Very Leptokurtic	2.23	17.80	79.96	0.00	2.35	2.22
		200	C2	Unimodal, Poorly Sorted	Muddy Sand	Coarse Silty Fine Sand	106.98	3.74	-0.54	1.78	Very Fine Sand	Poorly Sorted	Very Fine Skewed	Very Leptokurtic	2.40	18.42	79.18	0.00	2.29	7.65
		206	C2	Unimodal, Poorly Sorted	Muddy Sand	Very Coarse Silty Fine Sand	111.23	3.38	-0.50	1.78	Very Fine Sand	Poorly Sorted	Very Fine Skewed	Very Leptokurtic	2.39	17.53	80.09	0.00	2.30	2.71

Pit Code	Laboratory code	Depth (cm)	Sub-facies	Sample Type	Textural Group	Sediment name	Folk and Ward Method (um)				Folk and Ward Method (description)				Proportion of clay-silt-sand-gravel				Organic carbon and carbonate content (%DW)	
							Mean	Sorting	Skewness	Kurtosis	Mean	Sorting	Skewness	Kurtosis	%Clay	%Silt	%Sand	%Gravel	Organic matter	Carbonate
RR3	RB06	0	B3	Bimodal, Poorly Sorted	Sandy Gravel	Sandy Very Fine Gravel	1753.78	3.25	-0.28	0.83	Very Coarse Sand	Poorly Sorted	Fine Skewed	Platykurtic	0.00	2.14	45.22	52.65	13.98	0.58
		10	B4	Bimodal, Poorly Sorted	Sandy Gravel	Sandy Fine Gravel	1622.64	3.73	-0.33	0.70	Very Coarse Sand	Poorly Sorted	Very Fine Skewed	Platykurtic	0.00	2.50	45.26	52.25	6.40	10.73
		20	B4	Bimodal, Poorly Sorted	Sandy Gravel	Sandy Fine Gravel	979.61	3.95	0.22	0.66	Coarse Sand	Poorly Sorted	Coarse Skewed	Very Platykurtic	0.00	2.05	61.37	36.58	5.35	5.92
		30	B3	Bimodal, Poorly Sorted	Gravelly Sand	Fine Gravelly Coarse Sand	963.00	2.97	0.19	1.18	Coarse Sand	Poorly Sorted	Coarse Skewed	Leptokurtic	0.00	2.77	74.90	22.33	4.33	7.87
		40	B3	Bimodal, Poorly Sorted	Gravelly Sand	Fine Gravelly Coarse Sand	1123.70	2.91	0.24	0.86	Very Coarse Sand	Poorly Sorted	Coarse Skewed	Platykurtic	0.00	2.31	68.81	28.89	3.60	6.32
		50	B3	Bimodal, Poorly Sorted	Gravelly Sand	Very Fine Gravelly Coarse Sand	699.96	2.67	0.27	1.37	Coarse Sand	Poorly Sorted	Coarse Skewed	Leptokurtic	0.00	2.07	82.13	15.79	3.52	6.45
		60	B3	Bimodal, Poorly Sorted	Gravelly Sand	Fine Gravelly Coarse Sand	946.45	2.23	0.22	1.25	Coarse Sand	Poorly Sorted	Coarse Skewed	Leptokurtic	0.00	1.25	83.38	15.37	4.16	8.62
		70	B3	Unimodal, Poorly Sorted	Gravelly Sand	Very Fine Gravelly Coarse Sand	1120.27	2.29	0.21	1.08	Very Coarse Sand	Poorly Sorted	Coarse Skewed	Mesokurtic	0.00	0.66	77.72	21.62	4.61	8.53
		80	B3	Unimodal, Poorly Sorted	Gravelly Sand	Very Fine Gravelly Coarse Sand	1046.60	2.48	0.18	1.06	Very Coarse Sand	Poorly Sorted	Coarse Skewed	Mesokurtic	0.00	1.20	76.54	22.26	5.73	15.53
		90	B3	Unimodal, Moderately Sorted	Gravelly Sand	Very Fine Gravelly Coarse Sand	881.86	1.85	0.08	1.06	Coarse Sand	Moderately Sorted	Symmetrical	Mesokurtic	0.00	0.79	92.45	6.76	3.24	6.87
		100	B3	Unimodal, Moderately Sorted	Gravelly Sand	Very Fine Gravelly Coarse Sand	822.30	1.92	0.10	1.10	Coarse Sand	Moderately Sorted	Coarse Skewed	Mesokurtic	0.00	0.38	92.10	7.52	3.14	6.87
		110	B3	Unimodal, Poorly Sorted	Gravelly Sand	Very Fine Gravelly Coarse Sand	989.00	2.13	0.12	1.14	Coarse Sand	Poorly Sorted	Coarse Skewed	Leptokurtic	0.00	0.00	84.05	15.95	3.44	5.22
		120	B3	Unimodal, Poorly Sorted	Gravelly Sand	Very Fine Gravelly Coarse Sand	906.14	2.18	0.07	1.09	Coarse Sand	Poorly Sorted	Symmetrical	Mesokurtic	0.00	0.00	85.67	14.33	3.02	3.51
		130	B3	Unimodal, Poorly Sorted	Gravelly Sand	Very Fine Gravelly Coarse Sand	790.85	2.46	0.03	1.18	Coarse Sand	Poorly Sorted	Symmetrical	Leptokurtic	0.00	0.00	85.88	14.12	4.53	2.36
		140	B3	Unimodal, Poorly Sorted	Gravelly Sand	Very Fine Gravelly Coarse Sand	1151.00	2.56	-0.02	1.26	Very Coarse Sand	Poorly Sorted	Symmetrical	Leptokurtic	0.00	1.16	75.09	23.76	7.04	1.74
	RBD06	150	C1	Unimodal, Poorly Sorted	Muddy Sand	Very Coarse Silty Very Fine Sand	77.16	3.30	-0.30	1.38	Very Fine Sand	Poorly Sorted	Very Fine Skewed	Leptokurtic	2.47	30.70	66.83	0.00	3.76	0.40
		160	C1	Unimodal, Poorly Sorted	Muddy Sand	Very Coarse Silty Very Fine Sand	74.71	3.69	-0.23	1.40	Very Fine Sand	Poorly Sorted	Fine Skewed	Leptokurtic	2.01	32.51	65.48	0.00	6.50	0.96
		170	C1	Unimodal, Poorly Sorted	Muddy Sand	Very Coarse Silty Very Fine Sand	72.79	3.81	-0.33	1.28	Very Fine Sand	Poorly Sorted	Very Fine Skewed	Leptokurtic	2.41	31.59	66.00	0.00	17.69	1.81
		179	C1	Unimodal, Poorly Sorted	Muddy Sand	Very Coarse Silty Very Fine Sand	58.01	3.86	-0.31	1.16	Very Coarse Silt	Poorly Sorted	Very Fine Skewed	Leptokurtic	2.49	41.71	55.80	0.00	7.77	1.44
Pit Code	Laboratory code	Depth (cm)	Sub-facies	Sample Type	Textural Group	Sediment name	Folk and Ward Method (um)				Folk and Ward Method (description)				Proportion of clay-silt-sand-gravel				Organic carbon and carbonate content (%DW)	
							Mean	Sorting	Skewness	Kurtosis	Mean	Sorting	Skewness	Kurtosis	%Clay	%Silt	%Sand	%Gravel	Organic matter	Carbonate
RS4	RB07	0	B3	Bimodal, Poorly Sorted	Sandy Gravel	Sandy Fine Gravel	1289.09	3.45	0.03	0.82	Very Coarse Sand	Poorly Sorted	Symmetrical	Platykurtic	0.01	2.59	53.35	44.05	13.11	0.05
		10	B3	Bimodal, Poorly Sorted	Sandy Gravel	Sandy Fine Gravel	1285.08	3.38	0.22	0.87	Very Coarse Sand	Poorly Sorted	Coarse Skewed	Platykurtic	0.00	2.05	61.19	36.76	10.19	1.92
		20	B3	Trimodal, Poorly Sorted	Sandy Gravel	Sandy Fine Gravel	1574.35	3.85	0.33	0.89	Very Coarse Sand	Poorly Sorted	Very Coarse Skewed	Platykurtic	0.00	1.69	59.17	39.14	6.77	4.79
		30	B3	Unimodal, Poorly Sorted	Gravelly Sand	Very Fine Gravelly Coarse Sand	972.68	2.64	0.25	1.07	Coarse Sand	Poorly Sorted	Coarse Skewed	Mesokurtic	0.00	2.90	75.28	21.82	5.93	6.93
		40	B3	Unimodal, Poorly Sorted	Gravelly Sand	Very Fine Gravelly Coarse Sand	864.11	2.27	0.23	1.29	Coarse Sand	Poorly Sorted	Coarse Skewed	Leptokurtic	0.00	2.69	82.01	15.30	5.56	6.39
		50	B3	Unimodal, Poorly Sorted	Gravelly Sand	Very Fine Gravelly Coarse Sand	774.65	2.25	0.16	1.19	Coarse Sand	Poorly Sorted	Coarse Skewed	Leptokurtic	0.00	2.57	84.35	13.08	4.62	6.06
		60	B3	Unimodal, Poorly Sorted	Gravelly Sand	Very Fine Gravelly Coarse Sand	631.23	2.51	0.11	1.29	Coarse Sand	Poorly Sorted	Coarse Skewed	Leptokurtic	0.00	2.85	86.16	10.99	4.89	7.70
		70	B3	Unimodal, Poorly Sorted	Gravelly Sand	Very Fine Gravelly Coarse Sand	841.41	2.60	0.00	1.27	Coarse Sand	Poorly Sorted	Symmetrical	Leptokurtic	0.00	3.45	79.67	16.88	5.30	8.58
		80	B3	Unimodal, Poorly Sorted	Gravelly Sand	Very Fine Gravelly Coarse Sand	1000.35	2.32	0.16	1.25	Very Coarse Sand	Poorly Sorted	Coarse Skewed	Leptokurtic	0.00	2.18	80.28	17.54	6.41	5.74
		90	B3	Unimodal, Poorly Sorted	Gravelly Sand	Very Fine Gravelly Coarse Sand	957.17	2.83	-0.06	1.63	Coarse Sand	Poorly Sorted	Symmetrical	Very Leptokurtic	0.05	4.98	76.73	18.24	6.13	8.19
		100	B3	Unimodal, Poorly Sorted	Gravelly Sand	Very Fine Gravelly Coarse Sand	901.79	2.16	-0.07	1.48	Coarse Sand	Poorly Sorted	Symmetrical	Leptokurtic	0.00	2.65	89.69	7.66	6.53	6.49
		110	B3	Trimodal, Very Poorly Sorted	Muddy Sandy Gravel	Very Coarse Silty Sandy Very Fine Gravel	674.90	6.08	-0.31	0.89	Coarse Sand	Very Poorly Sorted	Very Fine Skewed	Platykurtic	0.95	11.98	49.14	37.93	5.77	4.23
		120	B3	Bimodal, Very Poorly Sorted	Muddy Sandy Gravel	Very Coarse Silty Sandy Very Fine Gravel	421.08	6.20	0.42	0.66	Medium Sand	Very Poorly Sorted	Very Coarse Skewed	Very Platykurtic	0.77	8.52	46.70	44.00	2.21	0.12
		130	C2	Unimodal, Poorly Sorted	Slightly Gravelly Muddy Sand	Slightly Very Fine Gravelly Very Coarse Silty Very Fine Sand	93.12	2.86	-0.36	1.78	Very Fine Sand	Poorly Sorted	Very Fine Skewed	Very Leptokurtic	3.46	31.35	63.84	1.34	3.02	0.00
		140	C2	Unimodal, Poorly Sorted	Slightly Gravelly Sand	Slightly Very Fine Gravelly Fine Sand	149.89	2.16	-0.24	1.52	Fine Sand	Poorly Sorted	Fine Skewed	Very Leptokurtic	0.22	12.09	84.24	3.45	3.86	0.20
Pit Code	Laboratory code	Depth (cm)	Sub-facies	Sample Type	Textural Group	Sediment name	Folk and Ward Method (um)				Folk and Ward Method (description)				Proportion of clay-silt-sand-gravel				Organic carbon and carbonate content (%DW)	
							Mean	Sorting	Skewness	Kurtosis	Mean	Sorting	Skewness	Kurtosis	%Clay	%Silt	%Sand	%Gravel	Organic matter	Carbonate
RR4	RB08	0	B3	Unimodal, Poorly Sorted	Gravelly Sand	Very Fine Gravelly Coarse Sand	947.59	2.91	0.13	1.14	Coarse Sand	Poorly Sorted	Coarse Skewed	Leptokurtic	0.02	2.14	74.49	23.35	11.29	5.31
		10	B3	Unimodal, Poorly Sorted	Gravelly Sand	Very Fine Gravelly Coarse Sand	1005.15	2.08	0.19	1.06	Very Coarse Sand	Poorly Sorted	Coarse Skewed	Mesokurtic	0.00	0.07	82.87	17.06	6.18	10.94
		20	B3	Unimodal, Moderately Sorted	Gravelly Sand	Very Fine Gravelly Very Coarse Sand	1078.90	1.97	-0.04	1.12	Very Coarse Sand	Moderately Sorted	Symmetrical	Leptokurtic	0.00	2.05	82.60	15.35	7.09	12.33
		30	A1	Bimodal, Poorly Sorted	Muddy Sandy Gravel	Very Coarse Silty Sandy Very Fine Gravel	1605.88	3.66	-0.51	1.34	Very Coarse Sand	Poorly Sorted	Very Fine Skewed	Leptokurtic	0.33	5.96	37.08	56.62	6.07	22.89
		40	B4	Bimodal, Poorly Sorted	Gravelly Sand	Very Fine Gravelly Coarse Sand	662.41	2.95	-0.06	0.86	Coarse Sand	Poorly Sorted	Symmetrical	Platykurtic	0.00	1.71	82.64	15.65	4.06	7.28
		50	A1/B3	Unimodal, Poorly Sorted	Sandy Gravel	Sandy Very Fine Gravel	1493.66	2.86	-0.09	0.98	Very Coarse Sand	Poorly Sorted	Symmetrical	Mesokurtic	0.00	0.63	58.57	40.80	4.96	9.12
		60	cemented/B3	Unimodal, Moderately Sorted	Gravelly Sand	Very Fine Gravelly Coarse Sand	894.58	1.96	0.22	1.23	Coarse Sand	Moderately Sorted	Coarse Skewed	Leptokurtic	0.00	0.00	90.41	9.59	3.58	8.03
		70	cemented/B3	Unimodal, Poorly Sorted	Gravelly Sand	Very Fine Gravelly Coarse Sand	836.36	2.55	0.12	1.10	Coarse Sand	Poorly Sorted	Coarse Skewed	Mesokurtic	0.00	0.40	82.04	17.55	2.56	5.01
		80	cemented/B3	Unimodal, Poorly Sorted	Gravelly Sand	Very Fine Gravelly Coarse Sand	707.73	2.90	0.23	1.09	Coarse Sand	Poorly Sorted	Coarse Skewed	Mesokurtic	0.00	0.33	82.13	17.54	11.67	4.79
		84-88	B3	Bimodal, Poorly Sorted	Sandy Gravel	Sandy Fine Gravel	952.91	3.77	0.25	0.78	Coarse Sand	Poorly Sorted	Coarse Skewed	Platykurtic	0.16	3.04	65.54	31.26	3.84	9.66
		90	cemented/B3	Bimodal, Poorly Sorted	Gravelly Sand	Very Fine Gravelly Medium Sand	468.39	2.36	0.32	1.48	Medium Sand	Poorly Sorted	Very Coarse Skewed	Leptokurtic	0.00	1.66	84.64	13.69	2.05	4.10
		100	cemented/B3	Unimodal, Poorly Sorted	Gravelly Sand	Fine Gravelly Medium Sand	415.44	2.23	0.33	1.86	Medium Sand	Poorly Sorted	Very Coarse Skewed	Very Leptokurtic	0.00	0.00	90.57	9.43	1.56	3.03
		110	cemented/B3	Bimodal, Poorly Sorted	Gravelly Sand	Fine Gravelly Coarse Sand	706.79	2.64	0.23	1.21	Coarse Sand	Poorly Sorted	Coarse Skewed	Leptokurtic	0.00	0.00	85.27	14.73	2.84	8.02
		120	cemented/B3	Bimodal, Poorly Sorted	Gravelly Sand	Very Fine Gravelly Medium Sand	523.25	2.57	0.27	1.15	Coarse Sand	Poorly Sorted	Coarse Skewed	Leptokurtic	0.00	0.50	87.23	12.27	3.01	4.86



Pit Code	Laboratory code	Depth (cm)	Sub-facies	Sample Type	Textural Group	Sediment name	Folk and Ward Method (um)				Folk and Ward Method (description)				Proportion of clay-silt-sand-gravel				Organic carbon and carbonate content (%DW)	
							Mean	Sorting	Skewness	Kurtosis	Mean	Sorting	Skewness	Kurtosis	%Clay	%Silt	%Sand	%Gravel	Organic matter	Carbonate
RS5	RB09	0	B2	Unimodal, Poorly Sorted	Gravelly Sand	Very Fine Gravelly Medium Sand	363.39	2.72	-0.11	2.30	Medium Sand	Poorly Sorted	Fine Skewed	Very Leptokurtic	0.52	7.28	87.05	5.15	4.48	0.57
		10	B2	Bimodal, Very Poorly Sorted	Sandy Gravel	Sandy Fine Gravel	742.61	4.71	0.18	0.96	Coarse Sand	Very Poorly Sorted	Coarse Skewed	Mesokurtic	0.59	6.18	61.02	32.22	3.51	0.97
		20	B2	Bimodal, Very Poorly Sorted	Gravelly Muddy Sand	Very Fine Gravelly Very Coarse Silty Medium Sand	653.83	4.43	0.11	1.16	Coarse Sand	Very Poorly Sorted	Coarse Skewed	Leptokurtic	0.52	7.78	67.15	24.56	4.31	0.20
		30	B3	Bimodal, Poorly Sorted	Gravelly Sand	Very Fine Gravelly Medium Sand	367.82	2.36	0.24	1.84	Medium Sand	Poorly Sorted	Coarse Skewed	Very Leptokurtic	0.01	4.37	84.42	11.21	2.46	1.77
		40	B2	Unimodal, Poorly Sorted	Gravelly Sand	Very Fine Gravelly Medium Sand	344.92	2.33	0.23	1.99	Medium Sand	Poorly Sorted	Coarse Skewed	Very Leptokurtic	0.01	4.52	84.39	11.09	1.94	1.16
		50	B3	Bimodal, Poorly Sorted	Gravelly Sand	Fine Gravelly Medium Sand	418.19	2.57	0.33	1.94	Medium Sand	Poorly Sorted	Very Coarse Skewed	Very Leptokurtic	0.01	4.43	81.13	14.43	2.88	5.18
		60	B3	Unimodal, Poorly Sorted	Gravelly Sand	Fine Gravelly Medium Sand	409.42	2.78	0.11	2.13	Medium Sand	Poorly Sorted	Coarse Skewed	Very Leptokurtic	0.04	5.47	84.30	10.19	2.26	5.50
		70	B3	Bimodal, Poorly Sorted	Gravelly Sand	Very Fine Gravelly Medium Sand	579.26	3.85	0.16	1.62	Coarse Sand	Poorly Sorted	Coarse Skewed	Very Leptokurtic	0.29	7.21	70.55	21.96	3.05	10.48
		71-75	B3, cemented	Bimodal, Very Poorly Sorted	Muddy Sandy Gravel	Very Coarse Silty Sandy Very Fine Gravel	715.61	4.87	0.23	1.00	Coarse Sand	Very Poorly Sorted	Coarse Skewed	Mesokurtic	0.21	8.10	57.42	34.27	2.18	5.54
		80	B3	Bimodal, Poorly Sorted	Gravelly Sand	Fine Gravelly Medium Sand	605.40	3.51	0.50	1.49	Coarse Sand	Poorly Sorted	Very Coarse Skewed	Leptokurtic	0.00	2.66	76.02	21.33	1.39	5.65
		90	B4	Bimodal, Poorly Sorted	Gravelly Sand	Very Fine Gravelly Medium Sand	571.76	3.24	0.49	1.41	Coarse Sand	Poorly Sorted	Very Coarse Skewed	Leptokurtic	0.00	0.00	80.00	20.00	2.75	4.13
		100	B3	Bimodal, Poorly Sorted	Sandy Gravel	Sandy Fine Gravel	808.67	3.93	0.56	0.73	Coarse Sand	Poorly Sorted	Very Coarse Skewed	Platykurtic	0.00	0.00	69.93	30.07	3.53	6.60
RR5	RB10	0	B3	Bimodal, Very Poorly Sorted	Muddy Sandy Gravel	Very Coarse Silty Sandy Fine Gravel	788.70	8.20	-0.20	0.71	Coarse Sand	Very Poorly Sorted	Fine Skewed	Platykurtic	1.22	13.59	29.81	55.38	15.98	1.00
		10	B3	Bimodal, Very Poorly Sorted	Muddy Sandy Gravel	Very Coarse Silty Sandy Fine Gravel	486.80	7.56	0.12	0.65	Medium Sand	Very Poorly Sorted	Coarse Skewed	Very Platykurtic	0.90	17.55	38.78	42.78	7.90	14.02
		20	A2	Trimodal, Very Poorly Sorted	Muddy Sandy Gravel	Very Coarse Silty Sandy Fine Gravel	1098.95	8.65	-0.81	0.69	Very Coarse Sand	Very Poorly Sorted	Very Fine Skewed	Platykurtic	1.13	18.46	20.98	59.44	6.01	19.84
		30	A2	Unimodal, Poorly Sorted	Gravel	Fine Gravel	4385.55	2.38	-0.51	2.53	Fine Gravel	Poorly Sorted	Very Fine Skewed	Very Leptokurtic	0.26	3.50	1.69	94.54	5.81	21.85
		40	A1	Unimodal, Poorly Sorted	Gravel	Fine Gravel	4712.48	2.80	-0.49	3.72	Fine Gravel	Poorly Sorted	Very Fine Skewed	extremely Leptokurtic	0.58	4.55	0.81	94.05	6.57	22.71
		50	A2	Unimodal, Poorly Sorted	Gravel	Fine Gravel	4212.30	2.98	-0.55	2.96	Fine Gravel	Poorly Sorted	Very Fine Skewed	Very Leptokurtic	0.70	5.88	3.82	89.61	6.90	15.60
		54	B3	Bimodal, Poorly Sorted	Sandy Gravel	Sandy Fine Gravel	878.88	3.84	0.47	0.64	Coarse Sand	Poorly Sorted	Very Coarse Skewed	Very Platykurtic	0.14	4.24	54.64	40.98	4.10	6.34
		60	A2	Bimodal, Poorly Sorted	Sandy Gravel	Sandy Fine Gravel	2482.47	2.89	-0.34	1.03	Very Fine Gravel	Poorly Sorted	Very Fine Skewed	Mesokurtic	0.13	2.16	28.51	69.19	6.94	17.99
		62	A1	Unimodal, Poorly Sorted	Gravel	Fine Gravel	3352.67	2.86	-0.53	1.61	Very Fine Gravel	Poorly Sorted	Very Fine Skewed	Very Leptokurtic	0.13	1.36	16.52	81.98	4.73	11.93
		70	B3	Bimodal, Poorly Sorted	Sandy Gravel	Sandy Fine Gravel	1050.44	3.50	0.27	0.62	Very Coarse Sand	Poorly Sorted	Coarse Skewed	Very Platykurtic	0.00	1.41	55.35	43.24	2.71	4.06
		80	B3	Bimodal, Poorly Sorted	Sandy Gravel	Sandy Fine Gravel	1207.44	3.37	0.21	0.64	Very Coarse Sand	Poorly Sorted	Coarse Skewed	Very Platykurtic	0.00	1.27	57.21	41.52	3.49	5.98
		90	A2	Bimodal, Poorly Sorted	Sandy Gravel	Sandy Fine Gravel	2176.21	3.27	-0.56	1.48	Very Fine Gravel	Poorly Sorted	Very Fine Skewed	Leptokurtic	0.02	1.76	19.28	78.93	4.06	11.30
		100	B3	Bimodal, Poorly Sorted	Sandy Gravel	Sandy Fine Gravel	1035.57	3.52	0.42	0.58	Very Coarse Sand	Poorly Sorted	Very Coarse Skewed	Very Platykurtic	0.00	0.00	59.61	40.39	3.41	5.40
		110	B3	Bimodal, Poorly Sorted	Gravelly Sand	Very Fine Gravelly Medium Sand	688.40	3.02	0.55	1.38	Coarse Sand	Poorly Sorted	Very Coarse Skewed	Leptokurtic	0.00	0.00	78.93	21.07	2.17	2.37
		120	B3	Bimodal, Poorly Sorted	Sandy Gravel	Sandy Fine Gravel	956.84	3.35	0.54	0.56	Coarse Sand	Poorly Sorted	Very Coarse Skewed	Very Platykurtic	0.00	0.00	63.39	36.61	2.60	4.20
		130	B3	Bimodal, Poorly Sorted	Sandy Gravel	Sandy Fine Gravel	958.28	3.81	0.64	0.66	Coarse Sand	Poorly Sorted	Very Coarse Skewed	Very Platykurtic	0.00	0.00	66.01	33.99	2.26	3.54
		140	B3	Bimodal, Poorly Sorted	Sandy Gravel	Sandy Fine Gravel	935.64	3.60	0.50	0.65	Coarse Sand	Poorly Sorted	Very Coarse Skewed	Very Platykurtic	0.00	0.00	64.73	35.27	2.16	5.21
		144	cemented B3	Unimodal, Poorly Sorted	Gravelly Sand	Fine Gravelly Medium Sand	444.29	2.00	0.36	1.66	Medium Sand	Poorly Sorted	Very Coarse Skewed	Very Leptokurtic	0.00	0.00	93.68	6.32	2.45	5.37
Pit Code	Laboratory code	Depth (cm)	Sub-facies	Sample Type	Textural Group	Sediment name	Folk and Ward Method (um)				Folk and Ward Method (description)				Proportion of clay-silt-sand-gravel				Organic carbon and carbonate content (%DW)	
							Mean	Sorting	Skewness	Kurtosis	Mean	Sorting	Skewness	Kurtosis	%Clay	%Silt	%Sand	%Gravel	Organic matter	Carbonate
RS6	RB11	0	B2	Bimodal, Very Poorly Sorted	Gravelly Muddy Sand	Fine Gravelly Very Coarse Silty Medium Sand	459.52	7.08	0.09	0.92	Medium Sand	Very Poorly Sorted	Symmetrical	Mesokurtic	0.92	15.89	55.80	27.39	7.36	0.00
		10	B2	Bimodal, Very Poorly Sorted	Muddy Sandy Gravel	Very Coarse Silty Sandy Fine Gravel	1576.93	6.08	-0.55	0.78	Very Coarse Sand	Very Poorly Sorted	Very Fine Skewed	Platykurtic	0.47	7.62	31.45	60.47	5.64	0.00
		20	B2	Bimodal, Very Poorly Sorted	Muddy Sandy Gravel	Very Coarse Silty Sandy Fine Gravel	1951.48	5.48	-0.63	0.86	Very Coarse Sand	Very Poorly Sorted	Very Fine Skewed	Platykurtic	0.66	6.20	23.76	69.38	4.63	0.10
		30	B2	Bimodal, Very Poorly Sorted	Muddy Sandy Gravel	Very Coarse Silty Sandy Fine Gravel	1669.32	5.30	-0.43	0.79	Very Coarse Sand	Very Poorly Sorted	Very Fine Skewed	Platykurtic	0.43	5.39	37.41	56.76	3.60	0.39
		40	B2	Bimodal, Very Poorly Sorted	Sandy Gravel	Sandy Fine Gravel	1670.54	4.22	-0.37	0.64	Very Coarse Sand	Very Poorly Sorted	Very Fine Skewed	Very Platykurtic	0.30	3.34	41.29	55.07	3.05	0.10
		50	B2	Bimodal, Poorly Sorted	Sandy Gravel	Sandy Fine Gravel	2149.66	3.92	-0.58	0.61	Very Fine Gravel	Poorly Sorted	Very Fine Skewed	Very Platykurtic	0.12	1.59	32.54	65.74	2.36	-0.20
		60	B2	Bimodal, Poorly Sorted	Sandy Gravel	Sandy Fine Gravel	1109.45	3.71	0.23	0.59	Very Fine Gravel	Poorly Sorted	Coarse Skewed	Very Platykurtic	0.00	0.82	51.43	47.75	2.40	-0.20
		70	B2	Bimodal, Poorly Sorted	Sandy Gravel	Sandy Fine Gravel	1557.46	3.75	-0.37	0.60	Very Coarse Sand	Poorly Sorted	Very Fine Skewed	Very Platykurtic	0.02	1.52	44.60	53.86	2.75	0.00
		80	B3	Bimodal, Very Poorly Sorted	Sandy Gravel	Sandy Fine Gravel	1021.55	4.00	0.41	0.63	Very Coarse Sand	Very Poorly Sorted	Very Coarse Skewed	Very Platykurtic	0.00	0.40	57.07	42.53	2.56	2.86
		90	B3	Bimodal, Poorly Sorted	Sandy Gravel	Sandy Fine Gravel	973.55	3.78	0.34	0.64	Coarse Sand	Poorly Sorted	Very Coarse Skewed	Very Platykurtic	0.00	1.55	53.56	44.89	3.17	6.05
		100*	cemented B3	Unimodal, Well Sorted	Gravel	Fine Gravel	5114.89	1.40	-0.22	1.12	Fine Gravel	Well Sorted	Fine Skewed	Leptokurtic	0.00	0.00	0.00	100.00	6.11	10.34
RR6	RB13	0	B2	Bimodal, Poorly Sorted	Gravelly Sand	Fine Gravelly Medium Sand	768.66	3.78	0.55	0.81	Coarse Sand	Poorly Sorted	Very Coarse Skewed	Platykurtic	0.01	3.54	70.30	26.14	7.18	0.60
		10	B2	Bimodal, Very Poorly Sorted	Sandy Gravel	Sandy Fine Gravel	1526.25	4.06	-0.38	0.61	Very Coarse Sand	Very Poorly Sorted	Very Fine Skewed	Very Platykurtic	0.10	3.82	43.15	52.94	6.03	0.29
		20	B2	Bimodal, Very Poorly Sorted	Muddy Sandy Gravel	Very Coarse Silty Sandy Fine Gravel	1498.08	4.38	-0.42	0.68	Very Coarse Sand	Very Poorly Sorted	Very Fine Skewed	Platykurtic	0.15	4.70	41.03	54.12	5.76	0.30
		30	B3	Bimodal, Very Poorly Sorted	Sandy Gravel	Sandy Fine Gravel	848.69	4.07	0.55	0.66	Coarse Sand	Very Poorly Sorted	Very Coarse Skewed	Very Platykurtic	0.00	3.06	64.52	32.42	3.97	15.18
		40	B3	Bimodal, Poorly Sorted	Sandy Gravel	Sandy Very Fine Gravel	1931.26	3.23	-0.42	0.72	Very Coarse Sand	Poorly Sorted	Very Fine Skewed	Platykurtic	0.00	0.71	33.95	65.34	6.84	12.02
		50	B3	Unimodal, Moderately Sorted	Slightly Gravelly Sand	Slightly Fine Gravelly Medium Sand	405.03	1.64	0.14	1.31	Medium Sand	Moderately Sorted	Coarse Skewed	Leptokurtic	0.00	0.00	96.23	3.77	2.22	7.43
		60	B3	Unimodal, Poorly Sorted	Gravelly Sand	Fine Gravelly Medium Sand	414.51	2.04	0.38	2.35	Medium Sand	Poorly Sorted	Very Coarse Skewed	Very Leptokurtic	0.00	0.00	91.66	8.34	2.19	3.62
		70	B3	Bimodal, Very Poorly Sorted	Gravelly Sand	Fine Gravelly Medium Sand	817.97	4.31	0.63	0.89	Coarse Sand	Very Poorly Sorted	Very Coarse Skewed	Platykurtic	0.00	0.00	71.97	28.03	2.18	3.86
		80	B3	Bimodal, Very Poorly Sorted	Sandy Gravel	Sandy Fine Gravel	938.00	4.26	0.58	0.66	Coarse Sand	Very Poorly Sorted	Very Coarse Skewed	Very Platykurtic	0.00	0.00	62.48	37.52	2.37	2.37
		90	B3	Bimodal, Poorly Sorted	Sandy Gravel	Sandy Fine Gravel	875.27	3.93	0.50	0.60	Coarse Sand	Poorly Sorted	Very Coarse Skewed	Very Platykurtic	0.00	0.00	57.25	42.75	2.55	2.65
		100	cemented B3	Bimodal, Poorly Sorted	Sandy Gravel	Sandy Fine Gravel	1038.31	3.79	0.24	0.59	Very Coarse Sand	Poorly Sorted	Coarse Skewed	Very Platykurtic	0.00	0.00	53.32	46.68	3.08	3.75

Pit Code	Laboratory code	Depth (cm)	Sub-facies	Sample Type	Textural Group	Sediment name	Folk and Ward Method (um)				Folk and Ward Method (description)				Proportion of clay-silt-sand-gravel				Organic carbon and carbonate content (%DW)	
							Mean	Sorting	Skewness	Kurtosis	Mean	Sorting	Skewness	Kurtosis	%Clay	%Silt	%Sand	%Gravel	Organic matter	Carbonate
RS7	RB14	0	D1	Bimodal, Very Poorly Sorted	Slightly Gravelly Sandy Mud	Slightly Very Fine Gravelly Very Fine Sandy Medium Silt	17.18	5.92	0.22	1.03	Coarse Silt	Very Poorly Sorted	Coarse Skewed	Mesokurtic	10.90	74.47	14.10	0.53	14.60	0.89
		10	D1	Unimodal, Very Poorly Sorted	Slightly Gravelly Sandy Mud	Slightly Very Fine Gravelly Very Fine Sandy Coarse Silt	20.53	4.42	-0.03	0.92	Coarse Silt	Very Poorly Sorted	Symmetrical	Mesokurtic	10.01	77.50	11.79	0.71	5.62	0.38
		20	D1	Trimodal, Extremely Poorly Sorted	Gravelly Mud	Very Fine Gravelly Medium Silt	34.47	18.34	0.63	1.21	Very Coarse Silt	Extremely Poorly Sorted	Very Coarse Skewed	Leptokurtic	16.79	61.07	5.46	16.68	8.07	1.75
		30	D1	Bimodal, Very Poorly Sorted	Slightly Gravelly Mud	Slightly Very Fine Gravelly Medium Silt	7.76	4.77	0.41	1.26	Fine Silt	Very Poorly Sorted	Very Coarse Skewed	Leptokurtic	20.10	70.46	5.31	4.12	9.58	2.00
		56	D2	Trimodal, Very Poorly Sorted	Gravelly Mud	Very Fine Gravelly Medium Silt	20.86	10.41	0.48	1.35	Coarse Silt	Very Poorly Sorted	Very Coarse Skewed	Leptokurtic	13.85	66.73	5.11	14.30	10.38	1.44
		70	D2	Trimodal, Very Poorly Sorted	Muddy Sandy Gravel	Coarse Silty Sandy Very Fine Gravel	317.64	15.04	-0.29	0.72	Medium Sand	Very Poorly Sorted	Fine Skewed	Platykurtic	4.11	22.82	31.18	41.89	6.72	0.75
Pit Code	Laboratory code	Depth (cm)	Sub-facies	Sample Type	Textural Group	Sediment name	Folk and Ward Method (um)				Folk and Ward Method (description)				Proportion of clay-silt-sand-gravel				Organic carbon and carbonate content (%DW)	
							Mean	Sorting	Skewness	Kurtosis	Mean	Sorting	Skewness	Kurtosis	%Clay	%Silt	%Sand	%Gravel	Organic matter	Carbonate
RR7	RB12	0	B2	Bimodal, Very Poorly Sorted	Muddy Gravel	Very Coarse Silty Fine Gravel	964.49	9.71	-0.74	0.72	Coarse Sand	Very Poorly Sorted	Very Fine Skewed	Platykurtic	1.57	19.73	10.70	68.00	29.41	0.99
		10	B2	Unimodal, Very Poorly Sorted	Muddy Gravel	Very Coarse Silty Fine Gravel	1249.50	7.28	-0.76	0.95	Very Coarse Sand	Very Poorly Sorted	Very Fine Skewed	Mesokurtic	0.90	13.79	8.03	77.28	12.36	0.70
		20	A2	Unimodal, Very Poorly Sorted	Muddy Sandy Gravel	Very Coarse Silty Sandy Fine Gravel	1994.24	5.91	-0.67	2.50	Very Coarse Sand	Very Poorly Sorted	Very Fine Skewed	Very Leptokurtic	0.81	8.99	8.55	81.66	13.45	6.03
		20-23	A2	Unimodal, Poorly Sorted	Gravel	Fine Gravel	4625.54	2.98	-0.46	2.94	Fine Gravel	Poorly Sorted	Very Fine Skewed	Very Leptokurtic	1.45	22.70	18.74	57.11	11.18	5.49
		23-26	B3	Trimodal, Very Poorly Sorted	Muddy Sandy Gravel	Very Coarse Silty Sandy Fine Gravel	808.60	9.15	-0.61	0.66	Coarse Sand	Very Poorly Sorted	Very Fine Skewed	Very Platykurtic	0.32	4.82	2.93	91.92	7.98	19.94
		26-30	A2	Unimodal, Very Poorly Sorted	Gravel	Fine Gravel	2406.93	4.73	-0.68	2.96	Very Fine Gravel	Very Poorly Sorted	Very Fine Skewed	Very Leptokurtic	1.32	11.40	2.85	84.43	9.63	17.58
		30	A2	Bimodal, Very Poorly Sorted	Muddy Sandy Gravel	Very Coarse Silty Sandy Fine Gravel	2394.52	5.35	-0.80	2.10	Very Fine Gravel	Very Poorly Sorted	Very Fine Skewed	Very Leptokurtic	0.48	7.17	13.45	78.91	6.38	16.65
		35	A2	Unimodal, Very Poorly Sorted	Muddy Gravel	Very Coarse Silty Very Fine Gravel	961.34	8.26	-0.73	3.65	Coarse Sand	Very Poorly Sorted	Very Fine Skewed	xtremely Leptokur	1.54	15.59	4.48	78.39	8.15	18.84
		40	A2	Unimodal, Very Poorly Sorted	Muddy Gravel	Coarse Silty Fine Gravel	956.66	10.33	-0.78	1.20	Coarse Sand	Very Poorly Sorted	Very Fine Skewed	Leptokurtic	1.89	17.08	8.33	72.71	7.52	16.42
		50	A2	Unimodal, Poorly Sorted	Gravel	Fine Gravel	5010.14	2.83	-0.52	4.90	Fine Gravel	Poorly Sorted	Very Fine Skewed	xtremely Leptokur	0.53	5.73	0.35	93.39	7.77	22.25
		60	A2	Unimodal, Very Poorly Sorted	Gravel	Fine Gravel	2689.77	5.18	-0.66	2.60	Very Fine Gravel	Very Poorly Sorted	Very Fine Skewed	Very Leptokurtic	0.60	8.08	8.10	83.22	5.93	21.44
		70	B3	Bimodal, Poorly Sorted	Sandy Gravel	Sandy Fine Gravel	827.41	3.60	0.53	0.67	Coarse Sand	Poorly Sorted	Very Coarse Skewed	Very Platykurtic	0.00	2.36	62.72	34.91	2.07	5.22
		80	cemented B3	Bimodal, Poorly Sorted	Gravelly Sand	Fine Gravelly Medium Sand	700.68	3.63	0.62	2.33	Coarse Sand	Poorly Sorted	Very Coarse Skewed	Very Leptokurtic	0.00	0.00	80.76	19.24	1.84	2.90
Pit Code	Laboratory code	Depth (cm)	Sub-facies	Sample Type	Textural Group	Sediment name	Folk and Ward Method (um)				Folk and Ward Method (description)				Proportion of clay-silt-sand-gravel				Organic carbon and carbonate content (%DW)	
							Mean	Sorting	Skewness	Kurtosis	Mean	Sorting	Skewness	Kurtosis	%Clay	%Silt	%Sand	%Gravel	Organic matter	Carbonate
RS8	RB15	0	D1	Trimodal, Very Poorly Sorted	Slightly Gravelly Sandy Mud	Slightly Very Fine Gravelly Fine Sandy Coarse Silt	37.10	6.17	0.09	1.02	Very Coarse Silt	Very Poorly Sorted	Symmetrical	Mesokurtic	6.20	65.47	23.08	5.25	5.45	1.70
		10	D2	Trimodal, Very Poorly Sorted	Gravelly Mud	Very Fine Gravelly Coarse Silt	110.50	14.48	0.11	0.84	Very Fine Sand	Very Poorly Sorted	Coarse Skewed	Platykurtic	6.72	43.91	28.78	20.59	5.86	1.81
		20	D2	Trimodal, Extremely Poorly Sorted	Gravelly Mud	Fine Gravelly Coarse Silt	163.34	16.16	0.09	0.86	Fine Sand	Extremely Poorly Sorted	Symmetrical	Platykurtic	5.59	41.24	27.00	26.17	4.59	2.02
		30	B2	Unimodal, Very Poorly Sorted	Muddy Gravel	Coarse Silty Fine Gravel	876.00	12.86	-0.81	0.84	Coarse Sand	Very Poorly Sorted	Very Fine Skewed	Platykurtic	2.92	18.76	11.00	67.33	5.73	2.17
		38	B2	Trimodal, Extremely Poorly Sorted	Muddy Sandy Gravel	Coarse Silty Sandy Fine Gravel	316.80	16.19	-0.19	0.69	Medium Sand	Extremely Poorly Sorted	Fine Skewed	Platykurtic	4.20	24.76	30.31	40.72	4.70	2.27
		60	B2	Trimodal, Very Poorly Sorted	Muddy Sandy Gravel	Coarse Silty Sandy Fine Gravel	396.88	11.59	-0.21	0.95	Medium Sand	Very Poorly Sorted	Fine Skewed	Mesokurtic	2.55	18.85	36.58	42.02	5.54	2.39
		70	B2	Trimodal, Very Poorly Sorted	Gravelly Muddy Sand	Fine Gravelly Coarse Silty Medium Sand	312.02	11.88	-0.13	1.02	Medium Sand	Very Poorly Sorted	Fine Skewed	Mesokurtic	2.76	21.00	46.47	29.77	4.69	1.96
		80	B2	Trimodal, Very Poorly Sorted	Muddy Gravel	Coarse Silty Fine Gravel	508.57	14.00	-0.61	0.69	Coarse Sand	Very Poorly Sorted	Very Fine Skewed	Platykurtic	3.78	24.58	21.06	50.58	6.36	2.52
		90	D2	Trimodal, Very Poorly Sorted	Gravelly Muddy Sand	Very Fine Gravelly Coarse Silty Medium Sand	233.03	13.32	-0.16	0.72	Fine Sand	Very Poorly Sorted	Fine Skewed	Platykurtic	3.98	28.45	39.42	28.15	4.47	2.14
Pit Code	Laboratory code	Depth (cm)	Sub-facies	Sample Type	Textural Group	Sediment name	Folk and Ward Method (um)				Folk and Ward Method (description)				Proportion of clay-silt-sand-gravel				Organic carbon and carbonate content (%DW)	
							Mean	Sorting	Skewness	Kurtosis	Mean	Sorting	Skewness	Kurtosis	%Clay	%Silt	%Sand	%Gravel	Organic matter	Carbonate
RR8	RB03	0	B1	Unimodal, Poorly Sorted	Gravelly Sand	Fine Gravelly Medium Sand	364.32	2.20	0.15	1.33	Medium Sand	Poorly Sorted	Coarse Skewed	Leptokurtic	0.00	3.04	91.69	5.28	6.45	0.98
		10	B2	Bimodal, Poorly Sorted	Gravelly Sand	Fine Gravelly Medium Sand	493.81	3.61	0.34	1.56	Medium Sand	Poorly Sorted	Very Coarse Skewed	Very Leptokurtic	0.15	4.15	79.18	16.52	3.56	0.79
		20	B2	Bimodal, Very Poorly Sorted	Gravelly Sand	Fine Gravelly Medium Sand	705.62	4.33	0.38	0.72	Coarse Sand	Very Poorly Sorted	Very Coarse Skewed	Platykurtic	0.33	3.74	65.38	30.55	3.27	1.23
		30	B2	Bimodal, Very Poorly Sorted	Sandy Gravel	Sandy Fine Gravel	793.37	4.60	0.38	0.65	Coarse Sand	Very Poorly Sorted	Very Coarse Skewed	Very Platykurtic	0.30	3.51	58.66	37.54	1.74	0.87
		40	B2	Bimodal, Very Poorly Sorted	Sandy Gravel	Sandy Medium Gravel	771.00	4.73	0.48	0.73	Coarse Sand	Very Poorly Sorted	Very Coarse Skewed	Platykurtic	0.10	2.86	65.49	31.55	1.98	0.69
		50	B2	Bimodal, Poorly Sorted	Gravelly Sand	Fine Gravelly Medium Sand	711.48	3.92	0.51	0.78	Coarse Sand	Poorly Sorted	Very Coarse Skewed	Platykurtic	0.00	1.99	71.99	26.02	1.89	0.99
		60	cemented B3	Unimodal, Poorly Sorted	Gravelly Sand	Fine Gravelly Medium Sand	420.43	2.58	0.30	1.51	Medium Sand	Poorly Sorted	Coarse Skewed	Very Leptokurtic	0.00	0.81	86.51	12.68	2.20	7.90
		70	cemented B3	Unimodal, Poorly Sorted	Gravelly Sand	Fine Gravelly Medium Sand	432.81	2.38	0.26	1.47	Medium Sand	Poorly Sorted	Coarse Skewed	Leptokurtic	0.00	0.58	90.25	9.17	2.85	6.88
		80	cemented B3	Trimodal, Very Poorly Sorted	Gravelly Sand	Very Fine Gravelly Medium Sand	804.88	4.10	0.47	0.81	Coarse Sand	Very Poorly Sorted	Very Coarse Skewed	Platykurtic	0.00	0.55	70.34	29.11	2.09	7.36
		90	cemented B3	Bimodal, Poorly Sorted	Gravelly Sand	Fine Gravelly Medium Sand	569.79	3.66	0.48	1.37	Coarse Sand	Poorly Sorted	Very Coarse Skewed	Leptokurtic	0.00	3.22	76.58	20.19	2.06	6.58
		100	B3	Bimodal, Very Poorly Sorted	Sandy Gravel	Sandy Fine Gravel	958.75	4.49	0.37	0.63	Coarse Sand	Very Poorly Sorted	Very Coarse Skewed	Very Platykurtic	0.00	1.15	60.25	38.60	1.67	9.44

Pit Code	Laboratory code	Depth (cm)	Sub-facies	Sample Type	Textural Group	Sediment name	Folk and Ward Method (um)				Folk and Ward Method (description)				Proportion of clay-silt-sand-gravel				Organic carbon and carbonate content (%DW)	
							Mean	Sorting	Skewness	Kurtosis	Mean	Sorting	Skewness	Kurtosis	%Clay	%Silt	%Sand	%Gravel	Organic matter	Carbonate
RS9	RB16	0	D1	Polymodal, Very Poorly Sorted	Gravelly Mud	Fine Gravelly Coarse Silt	50.36	10.69	0.13	0.81	Very Coarse Silt	Very Poorly Sorted	Coarse Skewed	Platykurtic	9.27	47.62	36.43	6.69	7.57	1.36
		10	D1	Trimodal, Very Poorly Sorted	Slightly Gravelly Sandy Mud	Slightly Fine Gravelly Medium Sandy Coarse Silt	57.23	6.51	-0.02	0.89	Very Coarse Silt	Very Poorly Sorted	Symmetrical	Platykurtic	5.54	49.59	39.93	4.94	5.69	1.80
		20	D2	Trimodal, Very Poorly Sorted	Muddy Gravel	Coarse Silty Very Fine Gravel	287.87	15.44	-0.06	0.75	Medium Sand	Very Poorly Sorted	Symmetrical	Platykurtic	4.31	31.90	30.00	33.78	4.07	1.19
		30	D2	Trimodal, Very Poorly Sorted	Gravelly Mud	Very Fine Gravelly Coarse Silt	52.91	9.82	0.09	0.88	Very Coarse Silt	Very Poorly Sorted	Symmetrical	Platykurtic	8.07	44.92	35.42	11.60	3.03	1.17
		40	D2	Trimodal, Very Poorly Sorted	Muddy Sandy Gravel	Coarse Silty Sandy Fine Gravel	270.30	13.94	-0.19	0.74	Medium Sand	Very Poorly Sorted	Fine Skewed	Platykurtic	3.86	23.15	41.08	31.91	4.68	1.53
		50	B1	Unimodal, Very Poorly Sorted	Slightly Gravelly Muddy Sand	Slightly Very Fine Gravelly Coarse Silty Medium Sand	133.86	4.74	-0.66	1.99	Fine Sand	Very Poorly Sorted	Very Fine Skewed	Very Leptokurtic	2.39	20.27	76.26	1.08	2.07	0.69
		60	B2	Polymodal, Very Poorly Sorted	Muddy Sandy Gravel	Coarse Silty Sandy Very Fine Gravel	461.45	11.57	-0.07	1.10	Medium Sand	Very Poorly Sorted	Symmetrical	Mesokurtic	2.10	15.28	43.56	39.07	3.88	0.95
		70	B2	Bimodal, Very Poorly Sorted	Muddy Sandy Gravel	Medium Silty Sandy Fine Gravel	838.45	6.89	-0.02	1.03	Coarse Sand	Very Poorly Sorted	Symmetrical	Mesokurtic	1.48	10.94	46.10	41.47	3.00	1.16
		80	B2	Bimodal, Very Poorly Sorted	Muddy Sandy Gravel	Medium Silty Sandy Fine Gravel	987.10	6.89	0.01	1.01	Coarse Sand	Very Poorly Sorted	Symmetrical	Mesokurtic	1.43	7.88	43.95	46.75	4.24	1.16
		90	B2	Bimodal, Very Poorly Sorted	Gravelly Sand	Very Fine Gravelly Medium Sand	734.92	4.72	0.29	1.08	Coarse Sand	Very Poorly Sorted	Coarse Skewed	Mesokurtic	0.63	5.63	65.63	28.11	2.16	1.13
100	cemented B3	Trimodal, Very Poorly Sorted	Muddy Sandy Gravel	Coarse Silty Sandy Fine Gravel	515.01	10.25	-0.01	0.96	Coarse Sand	Very Poorly Sorted	Symmetrical	Mesokurtic	2.12	14.60	47.20	36.08	2.79	2.60		

Pit Code	Laboratory code	Depth (cm)	Sub-facies	Sample Type	Textural Group	Sediment name	Folk and Ward Method (um)				Folk and Ward Method (description)				Proportion of clay-silt-sand-gravel				Organic carbon and carbonate content (%DW)	
							Mean	Sorting	Skewness	Kurtosis	Mean	Sorting	Skewness	Kurtosis	%Clay	%Silt	%Sand	%Gravel	Organic matter	Carbonate
RR9	RB21	0	B2	Unimodal, Poorly Sorted	Gravelly Sand	Fine Gravelly Medium Sand	303.85	2.38	0.22	2.02	Medium Sand	Poorly Sorted	Coarse Skewed	Very Leptokurtic	0.04	3.00	85.63	11.34	4.97	0.29
		10	B2	Unimodal, Poorly Sorted	Gravelly Sand	Medium Gravelly Medium Sand	288.99	2.33	0.19	1.95	Medium Sand	Poorly Sorted	Coarse Skewed	Very Leptokurtic	0.26	4.05	86.22	9.48	3.17	2.28
		20	B2	Unimodal, Poorly Sorted	Gravelly Sand	Very Fine Gravelly Medium Sand	277.91	2.10	0.04	1.66	Medium Sand	Poorly Sorted	Symmetrical	Very Leptokurtic	0.17	4.59	90.08	5.16	11.37	0.30
		30	B2	Bimodal, Very Poorly Sorted	Gravelly Sand	Fine Gravelly Medium Sand	641.47	4.35	0.56	1.43	Coarse Sand	Very Poorly Sorted	Very Coarse Skewed	Leptokurtic	0.13	3.60	72.88	23.39	2.37	0.20
		40	B2	Bimodal, Very Poorly Sorted	Sandy Gravel	Sandy Fine Gravel	674.90	4.21	0.52	0.64	Coarse Sand	Very Poorly Sorted	Very Coarse Skewed	Very Platykurtic	0.08	2.83	66.00	31.09	2.47	0.20
		50	B2	Bimodal, Very Poorly Sorted	Sandy Gravel	Sandy Fine Gravel	786.23	4.53	0.49	0.60	Coarse Sand	Very Poorly Sorted	Very Coarse Skewed	Very Platykurtic	0.04	2.10	57.00	40.85	2.96	0.30
		60	B2	Bimodal, Very Poorly Sorted	Sandy Gravel	Sandy Fine Gravel	791.03	4.07	0.38	0.60	Coarse Sand	Very Poorly Sorted	Very Coarse Skewed	Very Platykurtic	0.00	0.72	53.50	45.78	4.36	0.39
		70	B2	Bimodal, Very Poorly Sorted	Sandy Gravel	Sandy Fine Gravel	642.03	4.38	0.54	0.63	Coarse Sand	Very Poorly Sorted	Very Coarse Skewed	Very Platykurtic	0.00	0.63	68.18	31.19	1.68	0.30
		80	B2	Bimodal, Poorly Sorted	Gravelly Sand	Fine Gravelly Medium Sand	555.10	3.85	0.52	1.16	Coarse Sand	Poorly Sorted	Very Coarse Skewed	Leptokurtic	0.01	2.04	75.39	22.57	3.17	0.00
		90	B2	Bimodal, Poorly Sorted	Gravelly Sand	Fine Gravelly Medium Sand	533.50	3.74	0.53	1.59	Coarse Sand	Poorly Sorted	Very Coarse Skewed	Very Leptokurtic	0.00	1.36	78.69	19.95	1.88	0.10
		100	cemented B3	Bimodal, Poorly Sorted	Sandy Gravel	Sandy Fine Gravel	1562.41	3.95	-0.34	0.61	Very Coarse Sand	Poorly Sorted	Very Fine Skewed	Very Platykurtic	0.00	0.46	46.88	52.66	19.64	7.04
		110	cemented B2	Bimodal, Very Poorly Sorted	Gravelly Sand	Very Fine Gravelly Fine Sand	576.22	4.09	0.52	0.67	Coarse Sand	Very Poorly Sorted	Very Coarse Skewed	Platykurtic	0.00	1.77	70.30	27.93	2.99	5.18
		120	cemented B2	Trimodal, Very Poorly Sorted	Sandy Gravel	Sandy Coarse Gravel	1606.19	7.26	0.13	0.71	Very Coarse Sand	Very Poorly Sorted	Coarse Skewed	Platykurtic	0.21	1.84	48.29	49.66	3.07	7.33

Pit Code	Laboratory code	Depth (cm)	Sub-facies	Sample Type	Textural Group	Sediment name	Folk and Ward Method (um)				Folk and Ward Method (description)				Proportion of clay-silt-sand-gravel				Organic carbon and carbonate content (%DW)	
							Mean	Sorting	Skewness	Kurtosis	Mean	Sorting	Skewness	Kurtosis	%Clay	%Silt	%Sand	%Gravel	Organic matter	Carbonate
RR10	RB25	0	B1	Unimodal, Moderately Sorted	Slightly Gravelly Sand	Slightly Very Fine Gravelly Medium Sand	315.32	1.76	-0.06	1.14	Medium Sand	Moderately Sorted	Symmetrical	Leptokurtic	0.01	3.72	94.69	1.58	4.60	0.49
		10	B1	Unimodal, Poorly Sorted	Slightly Gravelly Sand	Slightly Very Fine Gravelly Medium Sand	330.43	2.00	-0.11	1.46	Medium Sand	Poorly Sorted	Fine Skewed	Leptokurtic	0.15	4.78	90.97	4.10	4.05	0.39
		20	B2	Bimodal, Poorly Sorted	Gravelly Sand	Fine Gravelly Medium Sand	513.69	3.33	0.44	1.62	Coarse Sand	Poorly Sorted	Very Coarse Skewed	Very Leptokurtic	0.25	4.28	78.91	16.56	2.82	0.19
		30	B2	Bimodal, Poorly Sorted	Gravelly Sand	Fine Gravelly Medium Sand	550.52	3.49	0.46	1.35	Coarse Sand	Poorly Sorted	Very Coarse Skewed	Leptokurtic	0.11	3.57	76.59	19.73	2.54	0.38
		40	B2	Bimodal, Very Poorly Sorted	Sandy Gravel	Sandy Fine Gravel	696.16	4.06	0.46	0.65	Coarse Sand	Very Poorly Sorted	Very Coarse Skewed	Very Platykurtic	0.07	2.58	62.96	34.39	0.80	0.50
		50	B2	Bimodal, Very Poorly Sorted	Sandy Gravel	Sandy Fine Gravel	780.03	4.26	0.40	0.58	Coarse Sand	Very Poorly Sorted	Very Coarse Skewed	Very Platykurtic	0.16	2.51	52.90	44.44	4.39	0.67
		60	B2	Bimodal, Very Poorly Sorted	Sandy Gravel	Sandy Fine Gravel	987.55	4.30	0.13	0.58	Coarse Sand	Very Poorly Sorted	Coarse Skewed	Very Platykurtic	0.04	1.76	49.32	48.88	4.05	0.69
		70	B2	Bimodal, Very Poorly Sorted	Sandy Gravel	Sandy Very Fine Gravel	776.34	4.16	0.39	0.63	Coarse Sand	Very Poorly Sorted	Very Coarse Skewed	Very Platykurtic	0.02	1.61	57.87	40.49	4.39	0.49
		80	B2	Bimodal, Very Poorly Sorted	Sandy Gravel	Sandy Fine Gravel	663.88	4.15	0.42	0.63	Coarse Sand	Very Poorly Sorted	Very Coarse Skewed	Very Platykurtic	0.02	1.73	64.78	33.47	2.29	0.10
		90	B2	Trimodal, Very Poorly Sorted	Sandy Gravel	Sandy Fine Gravel	668.01	4.84	0.51	0.69	Coarse Sand	Very Poorly Sorted	Very Coarse Skewed	Platykurtic	0.15	2.43	62.82	34.60	2.48	0.20
		95	B2	Bimodal, Poorly Sorted	Gravelly Sand	Fine Gravelly Fine Sand	317.42	2.96	0.38	1.78	Medium Sand	Poorly Sorted	Very Coarse Skewed	Very Leptokurtic	0.31	3.41	80.91	15.36	2.24	0.29
		100	B3	Bimodal, Very Poorly Sorted	Gravelly Sand	Fine Gravelly Medium Sand	661.21	4.13	0.49	0.70	Coarse Sand	Very Poorly Sorted	Very Coarse Skewed	Platykurtic	0.00	1.91	70.54	27.55	2.83	6.53
		110	cemented B3	Unimodal, Moderately Sorted	Sand	Moderately Sorted Medium Sand	281.42	1.73	-0.04	0.94	Medium Sand	Moderately Sorted	Symmetrical	Mesokurtic	0.00	3.05	96.95	0.00	1.79	5.28
		120	cemented B3	Unimodal, Moderately Sorted	Sand	Moderately Sorted Medium Sand	372.30	1.83	-0.04	1.07	Medium Sand	Moderately Sorted	Symmetrical	Mesokurtic	0.07	3.46	96.48	0.00	2.78	8.74

Pit Code	Laboratory code	Depth (cm)	Sub-facies	Sample Type	Textural Group	Sediment name	Folk and Ward Method (um)				Folk and Ward Method (description)				Proportion of clay-silt-sand-gravel				Organic carbon and carbonate content (%DW)	
							Mean	Sorting	Skewness	Kurtosis	Mean	Sorting	Skewness	Kurtosis	%Clay	%Silt	%Sand	%Gravel	Organic matter	Carbonate
RR11	RB18	0	B1	Unimodal, Moderately Sorted	Slightly Gravelly Sand	Slightly Very Fine Gravelly Medium Sand	358.88	1.71	0.01	1.35	Medium Sand	Moderately Sorted	Symmetrical	Leptokurtic	0.00	2.68	94.73	2.60	3.86	0.10
		10	B1	Unimodal, Moderately Sorted	Slightly Gravelly Sand	Slightly Very Fine Gravelly Medium Sand	354.24	1.79	-0.02	1.28	Medium Sand	Moderately Sorted	Symmetrical	Leptokurtic	0.05	3.78	94.05	2.13	3.67	0.10
		20	B1	Unimodal, Poorly Sorted	Gravelly Sand	Very Fine Gravelly Medium Sand	347.12	2.07	0.15	1.94	Medium Sand	Poorly Sorted	Coarse Skewed	Very Leptokurtic	0.17	4.04	90.08	5.72	3.17	0.00
		30	B2	Unimodal, Poorly Sorted	Gravelly Sand	Very Fine Gravelly Medium Sand	346.61	2.22	0.20	1.88	Medium Sand	Poorly Sorted	Coarse Skewed	Very Leptokurtic	0.10	3.38	89.46	7.06	2.55	0.00
		40	B2	Unimodal, Poorly Sorted	Gravelly Sand	Very Fine Gravelly Medium Sand	367.32	2.39	0.26	1.90	Medium Sand	Poorly Sorted	Coarse Skewed	Very Leptokurtic	0.10	3.13	86.24	10.53	2.77	0.30
		50	B2	Bimodal, Very Poorly Sorted	Gravelly Sand	Fine Gravelly Medium Sand	685.18	4.06	0.53	0.81	Coarse Sand	Very Poorly Sorted	Very Coarse Skewed	Platykurtic	0.04	2.64	71.44	25.88	2.27	0.30
		60	B2	Bimodal, Very Poorly Sorted	Sandy Gravel	Sandy Fine Gravel	1503.66	4.06	-0.39	0.60	Very Coarse Sand	Very Poorly Sorted	Very Fine Skewed	Very Platykurtic	0.05	1.78	44.24	53.93	1.98	0.40
		70	B2	Bimodal, Very Poorly Sorted	Sandy Gravel	Sandy Fine Gravel	951.26	4.02	0.20	0.60	Coarse Sand	Very Poorly Sorted	Coarse Skewed	Very Platykurtic	0.06	1.96	52.29	45.69	3.02	0.29
		80	B2	Bimodal, Very Poorly Sorted	Sandy Gravel	Sandy Fine Gravel	986.10	4.07	0.18	0.61	Coarse Sand	Very Poorly Sorted	Coarse Skewed	Very Platykurtic	0.03	1.64	53.27	45.07	2.91	0.19
		90	B2	Bimodal, Poorly Sorted	Gravelly Sand	Very Fine Gravelly Medium Sand	527.00	3.33	0.44	1.27	Coarse Sand	Poorly Sorted	Very Coarse Skewed	Leptokurtic	0.14	2.22	79.48	18.16	1.87	0.10
		100	B2	Bimodal, Very Poorly Sorted	Sandy Gravel	Sandy Fine Gravel	718.29	4.09	0.42	0.61	Coarse Sand	Very Poorly Sorted	Very Coarse Skewed	Very Platykurtic	0.03	1.87	59.50	38.59	1.89	0.10
		110	cementid B4	Bimodal, Very Poorly Sorted	Sandy Gravel	Sandy Fine Gravel	1476.18	4.28	-0.35	0.59	Very Coarse Sand	Very Poorly Sorted	Very Fine Skewed	Very Platykurtic	0.00	0.61	46.51	52.88	1.88	2.77

Pit Code	Laboratory code	Depth (cm)	Sub-facies	Sample Type	Textural Group	Sediment name	Folk and Ward Method (um)				Folk and Ward Method (description)				Proportion of clay-silt-sand-gravel				Organic carbon and carbonate content (%DW)	
							Mean	Sorting	Skewness	Kurtosis	Mean	Sorting	Skewness	Kurtosis	%Clay	%Silt	%Sand	%Gravel	Organic matter	Carbonate
RR12	RB20	0	B2	Unimodal, Poorly Sorted	Gravelly Sand	Fine Gravelly Medium Sand	358.42	2.59	0.30	1.69	Medium Sand	Poorly Sorted	Coarse Skewed	Very Leptokurtic	0.24	3.37	84.09	12.31	7.18	0.78
		10	B2	Bimodal, Poorly Sorted	Gravelly Sand	Fine Gravelly Medium Sand	486.98	3.78	0.37	1.78	Medium Sand	Poorly Sorted	Very Coarse Skewed	Very Leptokurtic	0.38	4.50	77.73	17.39	3.42	3.12
		20	B2	Bimodal, Poorly Sorted	Gravelly Sand	Very Fine Gravelly Medium Sand	533.35	3.88	0.31	1.16	Coarse Sand	Poorly Sorted	Very Coarse Skewed	Leptokurtic	0.34	4.63	74.16	20.88	2.67	0.69
		30	B2	Bimodal, Very Poorly Sorted	Gravelly Sand	Fine Gravelly Medium Sand	557.02	4.28	0.32	1.29	Coarse Sand	Very Poorly Sorted	Very Coarse Skewed	Leptokurtic	0.45	4.89	71.61	23.06	2.79	0.67
		40	B2	Bimodal, Very Poorly Sorted	Sandy Gravel	Sandy Fine Gravel	853.36	4.39	0.27	0.62	Coarse Sand	Very Poorly Sorted	Coarse Skewed	Very Platykurtic	0.25	3.44	54.28	42.04	2.95	0.95
		50	cemented B3	Bimodal, Poorly Sorted	Sandy Gravel	Sandy Fine Gravel	2360.09	3.47	-0.44	0.85	Very Fine Gravel	Poorly Sorted	Very Fine Skewed	Platykurtic	0.00	0.57	32.55	66.88	2.57	22.11
		60	cemented B3	Unimodal, Poorly Sorted	Gravel	Fine Gravel	5162.13	2.55	-0.37	2.58	Fine Gravel	Poorly Sorted	Very Fine Skewed	Very Leptokurtic	0.01	0.41	11.52	88.06	1.19	32.44
		70	cemented B3	Bimodal, Poorly Sorted	Sandy Gravel	Sandy Fine Gravel	1845.37	3.68	-0.52	0.66	Very Coarse Sand	Poorly Sorted	Very Fine Skewed	Very Platykurtic	0.00	0.67	38.06	61.26	3.75	16.90
		80	B3	Bimodal, Very Poorly Sorted	Sandy Gravel	Sandy Fine Gravel	1487.93	4.29	-0.47	0.61	Very Coarse Sand	Very Poorly Sorted	Very Fine Skewed	Very Platykurtic	0.02	1.38	38.45	60.15	5.71	10.74
		90	cemented B3	Bimodal, Poorly Sorted	Gravelly Sand	Fine Gravelly Medium Sand	355.34	2.59	0.32	1.69	Medium Sand	Poorly Sorted	Very Coarse Skewed	Very Leptokurtic	0.00	2.82	84.62	12.56	2.40	1.20
		100	cemented B3	Bimodal, Very Poorly Sorted	Sandy Gravel	Sandy Fine Gravel	893.14	4.70	0.43	0.62	Coarse Sand	Very Poorly Sorted	Very Coarse Skewed	Very Platykurtic	0.08	2.53	53.71	43.68	8.70	6.00
		110	cemented B3	Bimodal, Very Poorly Sorted	Gravelly Sand	Fine Gravelly Medium Sand	394.39	4.07	0.16	2.01	Medium Sand	Very Poorly Sorted	Coarse Skewed	Very Leptokurtic	0.66	7.92	75.89	15.54	2.57	6.62
		112-116	cemented B3	Unimodal, Poorly Sorted	Sand	Poorly Sorted Medium Sand	273.57	2.33	-0.24	1.60	Medium Sand	Poorly Sorted	Fine Skewed	Very Leptokurtic	0.52	7.11	92.37	0.00	1.28	5.51
		120	cemented B3	Unimodal, Moderately Well Sorted	Sand	Moderately Well Sorted Medium Sand	269.79	1.53	-0.16	0.77	Medium Sand	Moderately Well Sorted	Fine Skewed	Platykurtic	0.00	0.00	100.00	0.00	0.89	1.19
RR13	RB19	0	B1	Unimodal, Moderately Sorted	Slightly Gravelly Sand	Slightly Fine Gravelly Medium Sand	309.80	1.70	-0.05	1.31	Medium Sand	Moderately Sorted	Symmetrical	Leptokurtic	0.00	1.82	94.26	3.93	6.04	0.38
		10	B2	Unimodal, Poorly Sorted	Gravelly Sand	Medium Gravelly Medium Sand	351.87	2.51	0.30	2.55	Medium Sand	Poorly Sorted	Coarse Skewed	Very Leptokurtic	0.00	2.98	85.86	11.17	2.86	0.20
		20	B2	Unimodal, Poorly Sorted	Gravelly Sand	Fine Gravelly Medium Sand	323.01	2.30	0.22	2.26	Medium Sand	Poorly Sorted	Coarse Skewed	Very Leptokurtic	0.00	2.54	85.75	11.71	2.07	0.39
		30	B2	Bimodal, Very Poorly Sorted	Gravelly Sand	Fine Gravelly Medium Sand	759.27	4.57	0.58	0.73	Coarse Sand	Very Poorly Sorted	Very Coarse Skewed	Platykurtic	0.00	2.07	69.35	28.58	2.05	0.39
		40	B2	Bimodal, Very Poorly Sorted	Sandy Gravel	Sandy Fine Gravel	859.06	4.12	0.48	0.58	Coarse Sand	Very Poorly Sorted	Very Coarse Skewed	Very Platykurtic	0.01	1.86	54.10	44.03	2.87	0.69
		50	B3	Bimodal, Very Poorly Sorted	Sandy Gravel	Sandy Fine Gravel	764.72	4.05	0.53	0.70	Coarse Sand	Very Poorly Sorted	Very Coarse Skewed	Platykurtic	0.00	2.02	66.04	31.93	2.54	0.29
		58-62	B3	Bimodal, Poorly Sorted	Gravelly Sand	Very Fine Gravelly Medium Sand	652.07	3.14	0.49	1.17	Coarse Sand	Poorly Sorted	Very Coarse Skewed	Leptokurtic	0.00	0.00	76.27	23.73	2.89	8.16
		60	B3	Bimodal, Poorly Sorted	Sandy Gravel	Sandy Fine Gravel	823.32	3.96	0.53	0.65	Coarse Sand	Poorly Sorted	Very Coarse Skewed	Very Platykurtic	0.00	0.00	66.76	33.24	3.62	0.59
		70	B2	Bimodal, Poorly Sorted	Sandy Gravel	Sandy Fine Gravel	752.90	3.95	0.53	0.73	Coarse Sand	Poorly Sorted	Very Coarse Skewed	Platykurtic	0.04	2.07	67.38	30.51	2.83	0.39
		80	B2	Bimodal, Poorly Sorted	Gravelly Sand	Very Fine Gravelly Medium Sand	711.93	3.55	0.48	0.80	Coarse Sand	Poorly Sorted	Very Coarse Skewed	Platykurtic	0.00	2.00	72.55	25.45	2.95	0.59
		90	B2	Bimodal, Poorly Sorted	Sandy Gravel	Sandy Very Fine Gravel	881.75	3.66	0.32	0.66	Coarse Sand	Poorly Sorted	Very Coarse Skewed	Very Platykurtic	0.06	1.92	57.01	41.01	2.93	0.49
		100	B2	Bimodal, Poorly Sorted	Gravelly Sand	Fine Gravelly Medium Sand	400.05	2.51	0.35	2.07	Medium Sand	Poorly Sorted	Very Coarse Skewed	Very Leptokurtic	0.00	0.18	86.14	13.68	1.49	0.40
		110	B3	Bimodal, Poorly Sorted	Gravelly Sand	Fine Gravelly Medium Sand	590.66	3.21	0.49	1.49	Coarse Sand	Poorly Sorted	Very Coarse Skewed	Leptokurtic	0.00	0.00	81.93	18.07	2.61	5.22
		120	B3	Bimodal, Poorly Sorted	Gravelly Sand	Very Fine Gravelly Medium Sand	726.16	3.35	0.31	0.74	Coarse Sand	Poorly Sorted	Very Coarse Skewed	Platykurtic	0.00	1.56	70.51	27.93	3.64	7.09
RS10	RB27	130	B3	Bimodal, Poorly Sorted	Gravelly Sand	Very Fine Gravelly Medium Sand	763.48	3.42	0.25	0.74	Coarse Sand	Poorly Sorted	Coarse Skewed	Platykurtic	0.00	1.23	69.67	29.11	2.37	7.50
		136	B3	Bimodal, Poorly Sorted	Sandy Gravel	Sandy Fine Gravel	993.72	3.80	0.25	0.63	Coarse Sand	Poorly Sorted	Coarse Skewed	Very Platykurtic	0.00	0.55	60.73	38.72	2.29	6.98
		0	D2	Trimodal, Very Poorly Sorted	Gravelly Muddy Sand	Medium Gravelly Coarse Silty Medium Sand	154.14	7.10	-0.25	1.42	Fine Sand	Very Poorly Sorted	Fine Skewed	Leptokurtic	1.70	26.51	60.39	11.40	16.35	1.28
		10	D2	Trimodal, Very Poorly Sorted	Gravelly Muddy Sand	Fine Gravelly Very Coarse Silty Medium Sand	175.94	5.54	-0.23	1.26	Fine Sand	Very Poorly Sorted	Fine Skewed	Leptokurtic	1.29	26.79	59.46	12.45	9.40	1.27
		20	D2	Trimodal, Very Poorly Sorted	Gravelly Muddy Sand	Very Fine Gravelly Very Coarse Silty Medium Sand	188.89	4.88	-0.27	1.86	Fine Sand	Very Poorly Sorted	Fine Skewed	Very Leptokurtic	1.16	21.55	66.70	10.59	7.67	1.08
		30	B2	Bimodal, Very Poorly Sorted	Gravelly Muddy Sand	Fine Gravelly Coarse Silty Medium Sand	620.13	6.03	0.20	1.05	Coarse Sand	Very Poorly Sorted	Coarse Skewed	Mesokurtic	1.67	7.35	62.79	28.18	3.61	1.17
		40	B2	Bimodal, Very Poorly Sorted	Sandy Gravel	Sandy Fine Gravel	1824.16	4.45	-0.43	0.64	Very Coarse Sand	Very Poorly Sorted	Very Fine Skewed	Very Platykurtic	0.35	2.49	38.30	58.86	2.68	0.60
		50	B2	Bimodal, Very Poorly Sorted	Sandy Gravel	Sandy Fine Gravel	2155.38	4.04	-0.39	0.65	Very Fine Gravel	Very Poorly Sorted	Very Fine Skewed	Very Platykurtic	0.08	1.28	38.30	60.33	2.64	0.78
		60	B1	Unimodal, Moderately Sorted	Gravelly Sand	Fine Gravelly Medium Sand	373.96	2.00	0.22	1.84	Medium Sand	Moderately Sorted	Coarse Skewed	Very Leptokurtic	0.00	0.45	94.14	5.40	1.75	0.58
		70	B2	Bimodal, Poorly Sorted	Sandy Gravel	Sandy Fine Gravel	1862.79	3.30	-0.46	0.62	Very Coarse Sand	Poorly Sorted	Very Fine Skewed	Very Platykurtic	0.27	1.63	33.38	64.71	4.11	1.27
		73	B2	Bimodal, Poorly Sorted	Sandy Gravel	Sandy Fine Gravel	885.57	3.77	0.44	0.65	Coarse Sand	Poorly Sorted	Very Coarse Skewed	Very Platykurtic	0.15	2.02	62.47	35.36	2.97	0.89
		80	B2	Bimodal, Poorly Sorted	Sandy Gravel	Sandy Fine Gravel	2080.65	3.68	-0.37	0.65	Very Fine Gravel	Poorly Sorted	Very Fine Skewed	Very Platykurtic	0.11	1.42	39.65	58.83	2.66	0.69
		90	B2	Bimodal, Poorly Sorted	Sandy Gravel	Sandy Fine Gravel	2069.47	3.68	-0.33	0.70	Very Fine Gravel	Poorly Sorted	Very Fine Skewed	Platykurtic	0.07	1.05	39.01	59.87	3.16	0.89
		100	B2	Bimodal, Very Poorly Sorted	Gravelly Sand	Fine Gravelly Medium Sand	776.65	4.07	0.34	0.73	Coarse Sand	Very Poorly Sorted	Very Coarse Skewed	Platykurtic	0.24	2.45	67.54	29.78	3.28	1.00
		105	B2	Bimodal, Very Poorly Sorted	Sandy Gravel	Sandy Fine Gravel	2061.59	4.75	-0.27	0.78	Very Fine Gravel	Very Poorly Sorted	Fine Skewed	Platykurtic	0.28	2.08	38.15	59.48	3.19	1.16
		110	B2	Bimodal, Very Poorly Sorted	Sandy Gravel	Sandy Fine Gravel	895.01	5.08	0.18	0.78	Coarse Sand	Very Poorly Sorted	Coarse Skewed	Platykurtic	0.48	4.46	56.75	38.31	2.74	0.76
		120	B2	Bimodal, Very Poorly Sorted	Sandy Gravel	Sandy Fine Gravel	1994.69	4.32	-0.28	0.71	Very Coarse Sand	Very Poorly Sorted	Fine Skewed	Platykurtic	0.24	1.29	42.36	56.10	3.09	0.80
		130	B2	Bimodal, Very Poorly Sorted	Sandy Gravel	Sandy Fine Gravel	693.02	5.53	0.16	0.90	Coarse Sand	Very Poorly Sorted	Coarse Skewed	Platykurtic	0.89	5.43	60.86	32.82	2.90	1.10
		140	B2	Bimodal, Very Poorly Sorted	Muddy Sandy Gravel	Coarse Silty Sandy Fine Gravel	777.10	6.01	0.17	0.87	Coarse Sand	Very Poorly Sorted	Coarse Skewed	Platykurtic	0.73	6.10	54.77	38.39	2.68	0.89
		150	B2	Bimodal, Very Poorly Sorted	Muddy Sandy Gravel	Coarse Silty Sandy Fine Gravel	893.42	5.67	-0.02	0.77	Coarse Sand	Very Poorly Sorted	Symmetrical	Platykurtic	0.68	5.41	48.74	45.16	2.66	0.59



Pit Code	Laboratory code	Depth (cm)	Sub-facies	Sample Type	Textural Group	Sediment name	Folk and Ward Method (um)				Folk and Ward Method (description)				Proportion of clay-silt-sand-gravel				Organic carbon and carbonate content (%DW)	
							Mean	Sorting	Skewness	Kurtosis	Mean	Sorting	Skewness	Kurtosis	%Clay	%Silt	%Sand	%Gravel	Organic matter	Carbonate
KMF4	KW05	0	C4	Bimodal, Very Poorly Sorted	Slightly Gravelly Sandy Mud	Slightly Very Fine Gravelly Fine Sandy Medium Silt	14.13	5.35	0.33	0.85	Medium Silt	Very Poorly Sorted	Very Coarse Skewed	Platykurtic	12.03	67.97	18.96	1.03	15.88	3.14
		10	C4	Bimodal, Very Poorly Sorted	Slightly Gravelly Sandy Mud	Slightly Very Fine Gravelly Fine Sandy Medium Silt	12.94	5.40	0.42	0.82	Medium Silt	Very Poorly Sorted	Very Coarse Skewed	Platykurtic	13.82	66.17	19.34	0.66	8.88	1.80
		20	C4	Bimodal, Poorly Sorted	Slightly Gravelly Mud	Slightly Very Fine Gravelly Fine Silt	6.91	3.47	0.49	0.96	Fine Silt	Poorly Sorted	Very Coarse Skewed	Mesokurtic	19.14	70.94	9.07	0.86	8.07	2.40
		30	C4	Trimodal, Very Poorly Sorted	Gravelly Mud	Very Fine Gravelly Fine Silt	14.97	8.58	0.54	0.87	Medium Silt	Very Poorly Sorted	Very Coarse Skewed	Platykurtic	15.65	58.63	18.73	6.99	11.68	1.80
		40	C4	Bimodal, Very Poorly Sorted	Slightly Gravelly Sandy Mud	Slightly Very Fine Gravelly Fine Sandy Medium Silt	26.91	7.18	0.21	0.64	Coarse Silt	Very Poorly Sorted	Coarse Skewed	Very Platykurtic	8.85	50.31	39.41	1.43	4.09	1.60
		50	C4	Trimodal, Very Poorly Sorted	Slightly Gravelly Sandy Mud	Slightly Very Fine Gravelly Medium Sandy Medium Silt	41.85	8.94	-0.04	0.63	Very Coarse Silt	Very Poorly Sorted	Symmetrical	Very Platykurtic	9.08	41.54	46.01	3.37	4.03	1.41

Pit Code	Laboratory code	Depth (cm)	Sub-facies	Sample Type	Textural Group	Sediment name	Folk and Ward Method (um)				Folk and Ward Method (description)				Proportion of clay-silt-sand-gravel				Organic carbon and carbonate content (%DW)	
							Mean	Sorting	Skewness	Kurtosis	Mean	Sorting	Skewness	Kurtosis	%Clay	%Silt	%Sand	%Gravel	Organic matter	Carbonate
KH1	KW04	0	C4	Unimodal, Poorly Sorted	Slightly Gravelly Mud	Slightly Very Fine Gravelly Coarse Silt	10.60	3.76	0.12	0.87	Medium Silt	Poorly Sorted	Coarse Skewed	Platykurtic	12.00	77.79	8.27	1.94	30.65	3.05
		10	C4	Unimodal, Poorly Sorted	Slightly Gravelly Mud	Slightly Very Fine Gravelly Fine Silt	6.94	3.09	0.43	0.79	Fine Silt	Poorly Sorted	Very Coarse Skewed	Platykurtic	19.41	72.92	7.31	0.36	11.88	2.63
		20	C4	Trimodal, Very Poorly Sorted	Slightly Gravelly Sandy Mud	Slightly Very Fine Gravelly Fine Sandy Medium Silt	15.24	6.00	0.40	0.75	Medium Silt	Very Poorly Sorted	Very Coarse Skewed	Platykurtic	12.84	63.34	20.72	3.10	7.11	1.48
		30	C4	Bimodal, Very Poorly Sorted	Slightly Gravelly Sandy Mud	Slightly Very Fine Gravelly Fine Sandy Medium Silt	14.03	5.55	0.41	0.83	Medium Silt	Very Poorly Sorted	Very Coarse Skewed	Platykurtic	12.36	65.55	20.58	1.52	5.79	1.25
		40	C4	Bimodal, Very Poorly Sorted	Slightly Gravelly Sandy Mud	Slightly Very Fine Gravelly Fine Sandy Medium Silt	19.87	6.46	0.33	0.62	Coarse Silt	Very Poorly Sorted	Very Coarse Skewed	Very Platykurtic	8.78	56.68	31.54	2.00	5.09	1.10
		50	C4	Bimodal, Very Poorly Sorted	Slightly Gravelly Sandy Mud	Slightly Very Fine Gravelly Fine Sandy Medium Silt	26.25	6.20	0.14	0.68	Coarse Silt	Very Poorly Sorted	Coarse Skewed	Platykurtic	7.88	53.34	37.47	1.31	4.20	1.05
		60	C4	Bimodal, Very Poorly Sorted	Slightly Gravelly Sandy Mud	Slightly Very Fine Gravelly Fine Sandy Medium Silt	27.92	6.06	0.09	0.70	Coarse Silt	Very Poorly Sorted	Symmetrical	Platykurtic	7.57	51.39	39.52	1.52	4.97	1.27

Pit Code	Laboratory code	Depth (cm)	Sub-facies	Sample Type	Textural Group	Sediment name	Folk and Ward Method (um)				Folk and Ward Method (description)				Proportion of clay-silt-sand-gravel				Organic carbon and carbonate content (%DW)	
							Mean	Sorting	Skewness	Kurtosis	Mean	Sorting	Skewness	Kurtosis	%Clay	%Silt	%Sand	%Gravel	Organic matter	Carbonate
KS1	KW09	0	C1	Unimodal, Poorly Sorted	Sandy Mud	Very Fine Sandy Coarse Silt	16.79	3.36	-0.18	0.96	Coarse Silt	Poorly Sorted	Fine Skewed	Mesokurtic	7.51	80.92	11.57	0.00	38.04	2.04
		10	C1	Unimodal, Poorly Sorted	Mud	Coarse Silt	10.76	3.11	-0.11	0.69	Medium Silt	Poorly Sorted	Fine Skewed	Platykurtic	12.44	82.64	4.92	0.00	18.41	1.99
		20	C1	Unimodal, Poorly Sorted	Mud	Medium Silt	8.00	2.93	0.02	0.63	Medium Silt	Poorly Sorted	Symmetrical	Very Platykurtic	15.86	81.32	2.82	0.00	11.49	2.16
		30	C1	Unimodal, Poorly Sorted	Mud	Coarse Silt	10.02	3.19	-0.04	0.69	Medium Silt	Poorly Sorted	Symmetrical	Platykurtic	13.38	80.88	5.74	0.00	10.18	2.17
		40	C1	Unimodal, Poorly Sorted	Mud	Coarse Silt	9.61	3.07	-0.04	0.70	Medium Silt	Poorly Sorted	Symmetrical	Platykurtic	12.92	81.74	5.34	0.00	9.60	1.68
		50	C1	Unimodal, Poorly Sorted	Mud	Coarse Silt	9.94	3.37	0.02	0.72	Medium Silt	Poorly Sorted	Symmetrical	Platykurtic	13.94	78.56	7.49	0.00	9.07	1.78

Pit Code	Laboratory code	Depth (cm)	Sub-facies	Sample Type	Textural Group	Sediment name	Folk and Ward Method (um)				Folk and Ward Method (description)				Proportion of clay-silt-sand-gravel				Organic carbon and carbonate content (%DW)	
							Mean	Sorting	Skewness	Kurtosis	Mean	Sorting	Skewness	Kurtosis	%Clay	%Silt	%Sand	%Gravel	Organic matter	Carbonate
KR1	KW07	0	B5	Unimodal, Poorly Sorted	Gravelly Sand	Very Fine Gravelly Coarse Sand	826.23	2.01	-0.03	1.07	Coarse Sand	Poorly Sorted	Symmetrical	Mesokurtic	0.00	2.10	90.85	7.04	3.55	0.00
		10	B5	Unimodal, Moderately Sorted	Gravelly Sand	Very Fine Gravelly Coarse Sand	861.97	1.92	-0.04	1.01	Coarse Sand	Moderately Sorted	Symmetrical	Mesokurtic	0.00	1.37	92.34	6.29	2.14	0.00
		20	B5	Unimodal, Poorly Sorted	Gravelly Sand	Very Fine Gravelly Coarse Sand	791.29	2.10	-0.04	1.11	Coarse Sand	Poorly Sorted	Symmetrical	Mesokurtic	0.08	2.31	90.01	7.60	2.23	0.00
		30	B5	Unimodal, Poorly Sorted	Gravelly Sand	Very Fine Gravelly Coarse Sand	724.84	2.28	-0.05	1.11	Coarse Sand	Poorly Sorted	Symmetrical	Leptokurtic	0.19	2.24	89.55	8.01	1.20	0.00
		40	B5	Unimodal, Poorly Sorted	Gravelly Sand	Very Fine Gravelly Coarse Sand	748.98	2.44	-0.04	1.10	Coarse Sand	Poorly Sorted	Symmetrical	Mesokurtic	0.05	2.07	86.10	11.78	0.88	0.00
		50	B5	Unimodal, Poorly Sorted	Gravelly Sand	Very Fine Gravelly Coarse Sand	683.67	2.30	-0.13	1.14	Coarse Sand	Poorly Sorted	Fine Skewed	Leptokurtic	0.08	2.38	91.70	5.84	1.15	0.00
		60	B5	Unimodal, Poorly Sorted	Gravelly Sand	Very Fine Gravelly Coarse Sand	721.61	2.24	-0.05	1.15	Coarse Sand	Poorly Sorted	Symmetrical	Leptokurtic	0.08	1.76	90.71	7.46	1.16	0.00
		70	B5	Unimodal, Poorly Sorted	Gravelly Sand	Very Fine Gravelly Coarse Sand	704.18	2.18	-0.08	1.20	Coarse Sand	Poorly Sorted	Symmetrical	Leptokurtic	0.11	2.39	91.55	5.95	0.75	0.00
		80	B5	Unimodal, Poorly Sorted	Gravelly Sand	Very Fine Gravelly Coarse Sand	774.21	2.17	-0.01	1.11	Coarse Sand	Poorly Sorted	Symmetrical	Leptokurtic	0.00	0.59	90.29	9.12	0.68	0.00
		90	B5	Unimodal, Poorly Sorted	Gravelly Sand	Very Fine Gravelly Coarse Sand	679.98	2.52	-0.16	1.19	Coarse Sand	Poorly Sorted	Fine Skewed	Leptokurtic	0.13	2.48	90.04	7.36	0.39	0.00
		100	B5	Unimodal, Poorly Sorted	Slightly Gravelly Sand	Slightly Very Fine Gravelly Coarse Sand	463.85	3.10	-0.25	1.10	Medium Sand	Poorly Sorted	Fine Skewed	Mesokurtic	0.70	4.93	89.54	4.83	0.91	0.00
		110	C4	Bimodal, Very Poorly Sorted	Gravelly Mud	Very Fine Gravelly Medium Silt	10.43	6.73	0.43	1.34	Medium Silt	Very Poorly Sorted	Very Coarse Skewed	Leptokurtic	16.50	67.46	4.16	11.88	7.46	1.53

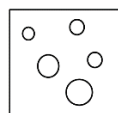
  

Pit Code	Laboratory code	Depth (cm)	Sub-facies	Sample Type	Textural Group	Sediment name	Folk and Ward Method (um)				Folk and Ward Method (description)				Proportion of clay-silt-sand-gravel				Organic carbon and carbonate content (%DW)	
							Mean	Sorting	Skewness	Kurtosis	Mean	Sorting	Skewness	Kurtosis	%Clay	%Silt	%Sand	%Gravel	Organic matter	Carbonate
KS2	KW08	0	C1	Unimodal, Poorly Sorted	Sandy Mud	Very Fine Sandy Coarse Silt	18.25	3.61	-0.15	1.00	Coarse Silt	Poorly Sorted	Fine Skewed	Mesokurtic	6.12	78.20	15.68	0.00	24.10	1.60
		5	C1	Unimodal, Poorly Sorted	Mud	Coarse Silt	12.97	3.34	-0.08	0.88	Medium Silt	Poorly Sorted	Symmetrical	Platykurtic	9.32	82.38	8.30	0.00	10.10	2.00
		15	C1	Unimodal, Poorly Sorted	Mud	Medium Silt	7.94	2.83	0.01	0.63	Medium Silt	Poorly Sorted	Symmetrical	Very Platykurtic	14.86	83.24	1.90	0.00	10.43	1.29

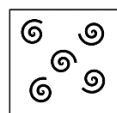
Pit Code	Laboratory code	Depth (cm)	Sub-facies	Sample Type	Textural Group	Sediment name	Folk and Ward Method (um)				Folk and Ward Method (description)				Proportion of clay-silt-sand-gravel				Organic carbon and carbonate content (%DW)	
							Mean	Sorting	Skewness	Kurtosis	Mean	Sorting	Skewness	Kurtosis	%Clay	%Silt	%Sand	%Gravel	Organic matter	Carbonate
WR1	WHA01	0	B5	Unimodal, Poorly Sorted	Slightly Gravelly Sand	Slightly Very Fine Gravelly Medium Sand	365.38	2.36	-0.28	1.72	Medium Sand	Poorly Sorted	Fine Skewed	Very Leptokurtic	0.58	7.09	91.36	0.96	3.97	0.21
		10	B5	Unimodal, Poorly Sorted	Slightly Gravelly Muddy Sand	Slightly Very Fine Gravelly Very Coarse Silty Medium Sand	323.63	2.82	-0.36	1.87	Medium Sand	Poorly Sorted	Very Fine Skewed	Very Leptokurtic	1.04	9.81	87.55	1.60	3.84	0.29
		20	B5	Unimodal, Poorly Sorted	Slightly Gravelly Muddy Sand	Slightly Very Fine Gravelly Very Coarse Silty Medium Sand	333.58	2.79	-0.36	2.01	Medium Sand	Poorly Sorted	Very Fine Skewed	Very Leptokurtic	1.13	9.54	88.37	0.97	2.66	0.26
		30	B5	Unimodal, Poorly Sorted	Slightly Gravelly Muddy Sand	Slightly Very Fine Gravelly Very Coarse Silty Medium Sand	325.04	2.98	-0.37	1.93	Medium Sand	Poorly Sorted	Very Fine Skewed	Very Leptokurtic	1.26	11.37	84.86	2.50	2.62	0.32
		40	B5	Unimodal, Poorly Sorted	Slightly Gravelly Muddy Sand	Slightly Very Fine Gravelly Very Coarse Silty Medium Sand	326.16	3.17	-0.32	2.16	Medium Sand	Poorly Sorted	Very Fine Skewed	Very Leptokurtic	1.33	11.94	81.92	4.81	2.49	0.31
		50	B5	Unimodal, Poorly Sorted	Slightly Gravelly Muddy Sand	Slightly Very Fine Gravelly Very Coarse Silty Medium Sand	327.76	2.64	-0.34	2.14	Medium Sand	Poorly Sorted	Very Fine Skewed	Very Leptokurtic	0.94	9.61	88.95	0.50	2.24	0.29
		60	B5	Unimodal, Poorly Sorted	Slightly Gravelly Sand	Slightly Very Fine Gravelly Medium Sand	341.00	2.48	-0.30	2.10	Medium Sand	Poorly Sorted	Very Fine Skewed	Very Leptokurtic	0.78	7.47	91.43	0.32	1.71	0.17
		70	B5	Unimodal, Poorly Sorted	Slightly Gravelly Sand	Slightly Very Fine Gravelly Medium Sand	315.11	2.43	-0.28	1.46	Medium Sand	Poorly Sorted	Fine Skewed	Leptokurtic	0.84	6.78	91.97	0.41	1.25	0.11
		80	B5	Unimodal, Poorly Sorted	Slightly Gravelly Sand	Slightly Very Fine Gravelly Medium Sand	266.57	2.86	-0.29	1.27	Medium Sand	Poorly Sorted	Fine Skewed	Leptokurtic	1.09	8.43	89.07	1.41	1.37	0.09
		90	B5	Unimodal, Poorly Sorted	Slightly Gravelly Muddy Sand	Slightly Very Fine Gravelly Very Coarse Silty Medium Sand	264.48	3.41	-0.28	1.50	Medium Sand	Poorly Sorted	Fine Skewed	Leptokurtic	1.44	9.55	85.40	3.61	1.44	0.13
Pit Code	Laboratory code	Depth (cm)	Sub-facies	Sample Type	Textural Group	Sediment name	Folk and Ward Method (um)				Folk and Ward Method (description)				Proportion of clay-silt-sand-gravel				Organic carbon and carbonate content (%DW)	
							Mean	Sorting	Skewness	Kurtosis	Mean	Sorting	Skewness	Kurtosis	%Clay	%Silt	%Sand	%Gravel	Organic matter	Carbonate
WS1	WHA02	0	B5	Unimodal, Poorly Sorted	Slightly Gravelly Muddy Sand	Slightly Very Fine Gravelly Very Coarse Silty Medium Sand	224.90	3.96	-0.41	1.35	Fine Sand	Poorly Sorted	Very Fine Skewed	Leptokurtic	1.80	15.20	82.76	0.25	8.93	0.58
		10	B5	Bimodal, Very Poorly Sorted	Muddy Sand	Very Coarse Silty Medium Sand	113.73	5.00	-0.34	0.97	Very Fine Sand	Very Poorly Sorted	Very Fine Skewed	Mesokurtic	2.75	31.97	65.27	0.00	6.89	0.69
		20	B5	Unimodal, Very Poorly Sorted	Muddy Sand	Very Coarse Silty Medium Sand	154.98	5.48	-0.44	1.09	Fine Sand	Very Poorly Sorted	Very Fine Skewed	Mesokurtic	3.06	23.48	73.46	0.00	5.27	0.63
		30	B5	Bimodal, Very Poorly Sorted	Slightly Gravelly Muddy Sand	Slightly Very Fine Gravelly Coarse Silty Medium Sand	143.33	5.27	-0.46	1.08	Fine Sand	Very Poorly Sorted	Very Fine Skewed	Mesokurtic	2.91	23.69	73.00	0.40	4.15	0.57
		40	B5	Bimodal, Very Poorly Sorted	Slightly Gravelly Muddy Sand	Slightly Very Fine Gravelly Coarse Silty Medium Sand	185.75	6.40	-0.45	1.38	Fine Sand	Very Poorly Sorted	Very Fine Skewed	Leptokurtic	3.20	18.66	74.36	3.78	3.15	0.51
		50	B6	Trimodal, Very Poorly Sorted	Gravelly Muddy Sand	Fine Gravelly Coarse Silty Medium Sand	213.28	11.93	-0.24	1.03	Fine Sand	Very Poorly Sorted	Fine Skewed	Mesokurtic	4.45	23.60	54.38	17.58	4.28	0.70
		60	B6	Trimodal, Extremely Poorly Sorted	Muddy Sandy Gravel	Coarse Silty Sandy Medium Gravel	509.13	16.49	-0.21	0.96	Coarse Sand	Extremely Poorly Sorted	Fine Skewed	Mesokurtic	3.64	17.44	44.82	34.09	4.59	0.78
		70	B6	Trimodal, Very Poorly Sorted	Muddy Sandy Gravel	Medium Silty Sandy Medium Gravel	547.25	15.25	-0.31	1.18	Coarse Sand	Very Poorly Sorted	Very Fine Skewed	Leptokurtic	3.76	14.93	41.29	40.02	4.89	0.80
Pit Code	Laboratory code	Depth (cm)	Sub-facies	Sample Type	Textural Group	Sediment name	Folk and Ward Method (um)				Folk and Ward Method (description)				Proportion of clay-silt-sand-gravel				Organic carbon and carbonate content (%DW)	
							Mean	Sorting	Skewness	Kurtosis	Mean	Sorting	Skewness	Kurtosis	%Clay	%Silt	%Sand	%Gravel	Organic matter	Carbonate
WMF3	WHA03	0	C4	Bimodal, Very Poorly Sorted	Sandy Mud	Fine Sandy Medium Silt	17.06	5.34	0.16	0.69	Coarse Silt	Very Poorly Sorted	Coarse Skewed	Platykurtic	12.70	61.91	25.39	0.00	20.75	1.79
		10	C4	Bimodal, Very Poorly Sorted	Slightly Gravelly Sandy Mud	Slightly Very Fine Gravelly Fine Sandy Medium Silt	10.36	4.37	0.24	0.82	Medium Silt	Very Poorly Sorted	Coarse Skewed	Platykurtic	16.16	69.26	14.36	0.23	13.20	2.13
		20	C4	Unimodal, Poorly Sorted	Slightly Gravelly Mud	Slightly Very Fine Gravelly Fine Silt	5.66	2.99	0.57	1.04	Fine Silt	Poorly Sorted	Very Coarse Skewed	Mesokurtic	23.44	67.07	6.36	3.12	9.61	2.06
		30	C5	Trimodal, Very Poorly Sorted	Slightly Gravelly Sandy Mud	Slightly Very Fine Gravelly Fine Sandy Medium Silt	29.27	9.27	0.27	0.70	Coarse Silt	Very Poorly Sorted	Coarse Skewed	Platykurtic	11.34	50.14	34.27	4.25	6.92	1.46
Pit Code	Laboratory code	Depth (cm)	Sub-facies	Sample Type	Textural Group	Sediment name	Folk and Ward Method (um)				Folk and Ward Method (description)				Proportion of clay-silt-sand-gravel				Organic carbon and carbonate content (%DW)	
							Mean	Sorting	Skewness	Kurtosis	Mean	Sorting	Skewness	Kurtosis	%Clay	%Silt	%Sand	%Gravel	Organic matter	Carbonate
WMF2	WHA04	0	C1	Unimodal, Poorly Sorted	Sandy Mud	Medium Sandy Fine Silt	6.46	3.28	0.60	0.98	Fine Silt	Poorly Sorted	Very Coarse Skewed	Mesokurtic	22.37	67.56	10.07	0.00	11.51	2.50
		10	C1	Unimodal, Very Poorly Sorted	Sandy Mud	Very Fine Sandy Fine Silt	8.21	4.11	0.45	0.95	Medium Silt	Very Poorly Sorted	Very Coarse Skewed	Mesokurtic	18.12	69.09	12.79	0.00	10.68	2.30
		20	C4	Polymodal, Very Poorly Sorted	Gravelly Mud	Fine Gravelly Fine Silt	12.89	7.75	0.61	1.20	Medium Silt	Very Poorly Sorted	Very Coarse Skewed	Leptokurtic	18.50	62.23	13.69	5.57	9.89	2.31
		30	C4	Bimodal, Very Poorly Sorted	Slightly Gravelly Sandy Mud	Slightly Very Fine Gravelly Medium Sandy Medium Silt	16.27	7.32	0.44	0.82	Coarse Silt	Very Poorly Sorted	Very Coarse Skewed	Platykurtic	15.71	60.51	23.29	0.49	8.57	2.40
		40	C5	Bimodal, Very Poorly Sorted	Slightly Gravelly Sandy Mud	Slightly Very Fine Gravelly Medium Sandy Medium Silt	22.84	6.86	0.28	0.79	Coarse Silt	Very Poorly Sorted	Coarse Skewed	Platykurtic	9.76	62.67	27.13	0.45	8.16	1.98
		50	C5	Trimodal, Very Poorly Sorted	Gravelly Mud	Medium Gravelly Medium Silt	40.20	13.13	0.34	0.93	Very Coarse Silt	Very Poorly Sorted	Very Coarse Skewed	Mesokurtic	8.59	51.56	28.78	11.08	7.93	1.99
Pit Code	Laboratory code	Depth (cm)	Sub-facies	Sample Type	Textural Group	Sediment name	Folk and Ward Method (um)				Folk and Ward Method (description)				Proportion of clay-silt-sand-gravel				Organic carbon and carbonate content (%DW)	
							Mean	Sorting	Skewness	Kurtosis	Mean	Sorting	Skewness	Kurtosis	%Clay	%Silt	%Sand	%Gravel	Organic matter	Carbonate
WMF1	WHA05	0	C1	Unimodal, Poorly Sorted	Mud	Fine Silt	5.47	2.23	0.52	0.61	Fine Silt	Poorly Sorted	Very Coarse Skewed	Very Platykurtic	23.07	74.56	2.37	0.00	22.27	2.84
		10	C1	Unimodal, Poorly Sorted	Mud	Fine Silt	5.43	2.29	0.53	0.66	Fine Silt	Poorly Sorted	Very Coarse Skewed	Very Platykurtic	22.83	73.79	3.38	0.00	14.78	2.63
		20	C1	Unimodal, Poorly Sorted	Mud	Fine Silt	5.13	2.13	0.52	0.64	Fine Silt	Poorly Sorted	Very Coarse Skewed	Very Platykurtic	21.96	75.15	2.89	0.00	14.29	2.75
		30	C1	Bimodal, Poorly Sorted	Mud	Fine Silt	6.04	2.80	0.40	0.84	Fine Silt	Poorly Sorted	Very Coarse Skewed	Platykurtic	18.50	74.87	6.62	0.00	11.85	2.65
		40	C1	Bimodal, Very Poorly Sorted	Slightly Gravelly Sandy Mud	Slightly Very Fine Gravelly Very Fine Sandy Medium Silt	9.47	4.18	0.38	0.82	Medium Silt	Very Poorly Sorted	Very Coarse Skewed	Platykurtic	15.76	68.94	15.17	0.13	11.93	2.30
		50	C1	Bimodal, Very Poorly Sorted	Sandy Mud	Very Fine Sandy Medium Silt	16.81	5.29	0.25	0.64	Coarse Silt	Very Poorly Sorted	Coarse Skewed	Very Platykurtic	10.34	59.70	29.95	0.00	6.81	1.88
		60	C1	Bimodal, Very Poorly Sorted	Sandy Mud	Fine Sandy Medium Silt	18.42	4.90	0.16	0.69	Coarse Silt	Very Poorly Sorted	Coarse Skewed	Platykurtic	8.91	62.35	28.74	0.00	6.57	2.05
		70	C1	Bimodal, Very Poorly Sorted	Sandy Mud	Very Fine Sandy Medium Silt	16.85	5.01	0.19	0.65	Coarse Silt	Very Poorly Sorted	Coarse Skewed	Very Platykurtic	10.76	60.33	28.92	0.00	11.91	2.11
		80	C1	Bimodal, Very Poorly Sorted	Sandy Mud	Very Fine Sandy Medium Silt	17.56	4.81	0.15	0.70	Coarse Silt	Very Poorly Sorted	Coarse Skewed	Platykurtic	9.65	63.47	26.88	0.00	6.57	2.20
Pit Code	Laboratory code	Depth (cm)	Sub-facies	Sample Type	Textural Group	Sediment name	Folk and Ward Method (um)				Folk and Ward Method (description)				Proportion of clay-silt-sand-gravel				Organic carbon and carbonate content (%DW)	
							Mean	Sorting	Skewness	Kurtosis	Mean	Sorting	Skewness	Kurtosis	%Clay	%Silt	%Sand	%Gravel	Organic matter	Carbonate
W11	WHA D06	0	C1	Unimodal, Very Poorly Sorted	Sandy Mud	Very Fine Sandy Very Coarse Silt	19.25	4.30	-0.05	1.01	Coarse Silt	Very Poorly Sorted	Symmetrical	Mesokurtic	5.02	74.51	20.47	0.00	28.77	3.01
		10	C1	Bimodal, Very Poorly Sorted	Sandy Mud	Very Fine Sandy Very Coarse Silt	33.74	6.44	0.00	1.06	Very Coarse Silt	Very Poorly Sorted	Symmetrical	Mesokurtic	5.20	57.84	36.96	0.00	18.27	2.44
		20	C1	Unimodal, Very Poorly Sorted	Sandy Mud	Very Fine Sandy Very Coarse Silt	29.92	5.34	-0.11	0.93	Coarse Silt	Very Poorly Sorted	Fine Skewed	Mesokurtic	5.76	57.11	37.13	0.00	13.56	2.22
		30	C1	Unimodal, Very Poorly Sorted	Sandy Mud	Very Fine Sandy Very Coarse Silt	26.21	5.25	-0.05	0.85	Coarse Silt	Very Poorly Sorted	Symmetrical	Platykurtic	6.64	59.45	33.91	0.00	13.10	2.07
		40	C1	Unimodal, Very Poorly Sorted	Sandy Mud	Very Fine Sandy Very Coarse Silt	33.57	5.55	-0.11	0.96	Very Coarse Silt	Very Poorly Sorted	Fine Skewed	Mesokurtic	6.67	53.45	39.99	0.00	11.97	2.30
		48	C1	Unimodal, Very Poorly Sorted	Sandy Mud	Very Fine Sandy Very Coarse Silt	29.25	5.07	-0.12	0.88	Coarse Silt	Very Poorly Sorted	Fine Skewed	Platykurtic	6.54	56.89	36.57	0.00	14.02	3.17

## Appendix B: Sedimentary Logs

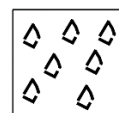
### Sediment logs legend



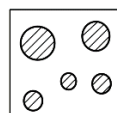
Pisoliths



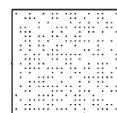
Whole shell



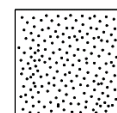
Shell hash and  
shell fragments



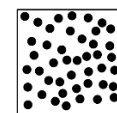
Quartz  
granules



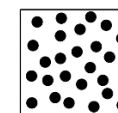
Fine sand



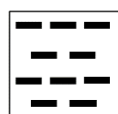
Medium  
sand



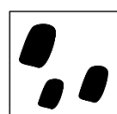
Coarse  
sand



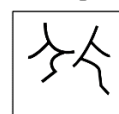
Very coarse  
sand



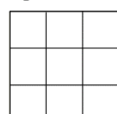
Silt



Gravel  
clasts



Developed  
root system



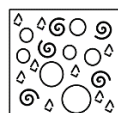
Interbedded  
layers



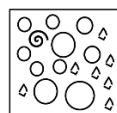
Patchy CaCO<sub>3</sub>  
cementation



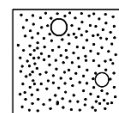
CaCO<sub>3</sub>  
cementation



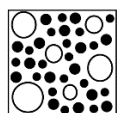
A1: Pisoliths with  
common whole  
shell and abundant  
shell fragments  
(clast-supported)



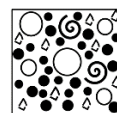
A2: Pisoliths with  
few whole shell and  
abundant shell  
fragments (clast-  
supported)



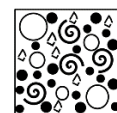
B1: Medium  
sand with few  
pisoliths



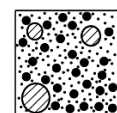
B2: Coarse to  
very coarse  
sand with  
many pisoliths



B3: Coarse to very  
coarse sand with many  
pisoliths, very few to  
few whole shell, many  
shell fragments



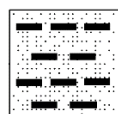
B4: Coarse to very coarse  
sand with many pisoliths,  
common to many whole  
shell and many shell  
fragments



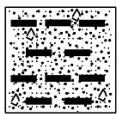
B5: Medium to  
coarse sand with  
very few to few  
quartz granules



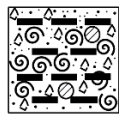
B6: Silty  
coarse sand with  
common to  
many gravel  
clasts



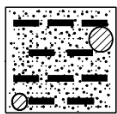
C1: Sandy silt



C2: Sandy silt  
with few shell  
hash



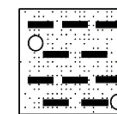
C3: Abundant whole  
and fragmented shell  
in a sandy silt matrix  
with few quartz  
granules (clast-  
supported)



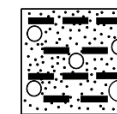
C4: Sandy silt  
with very few to  
few quartz  
granules



C5: Sandy silt  
with few gravel  
clasts



D1: Sandy silt  
with few  
pisoliths



D2: Sandy silt  
with common  
pisoliths



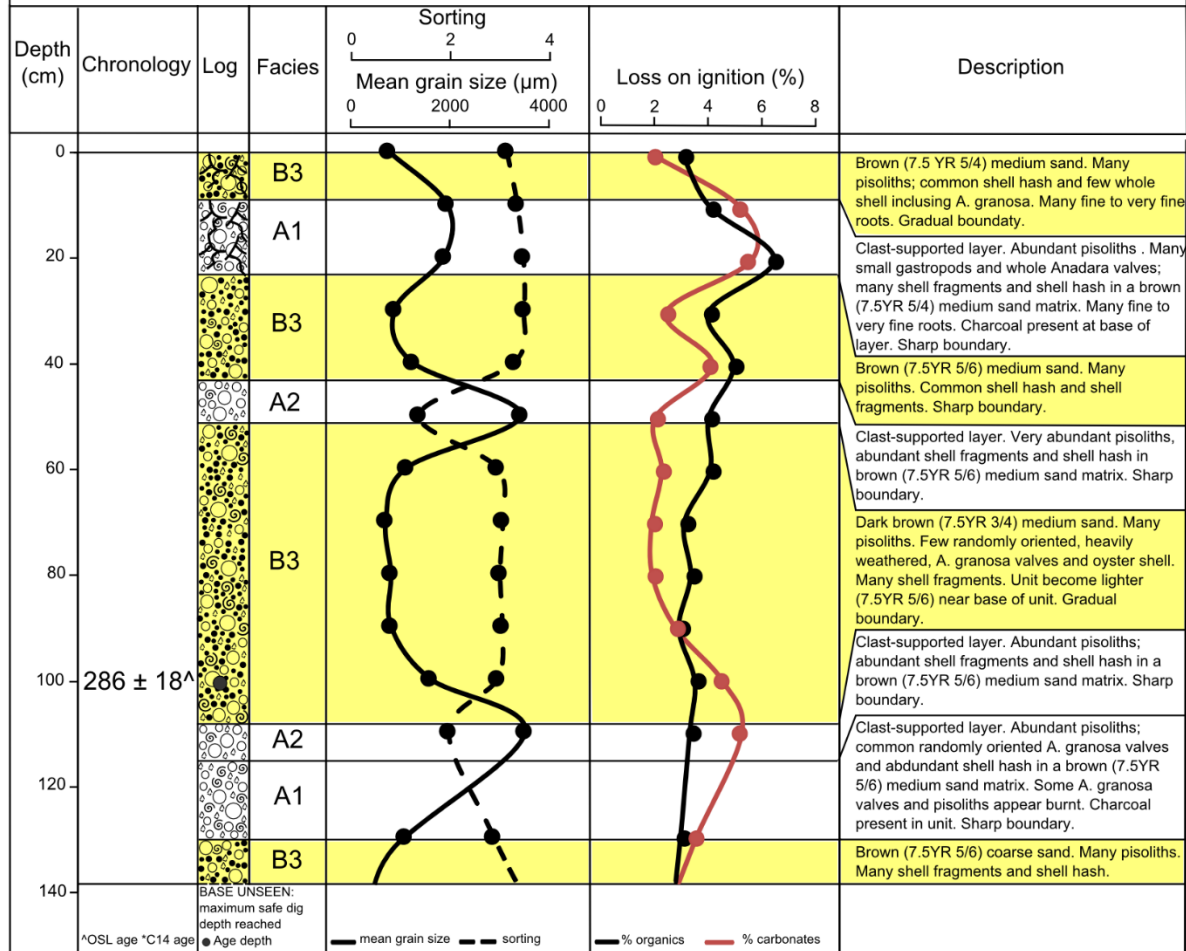
Location: Red Beach

UTM coordinates: E 595194.3321 N 8608559.992

Pit Location: Crest of beach ridge 1 (RR1)

Surface elevation: 2.37 m AHD

Pit Code: RB02

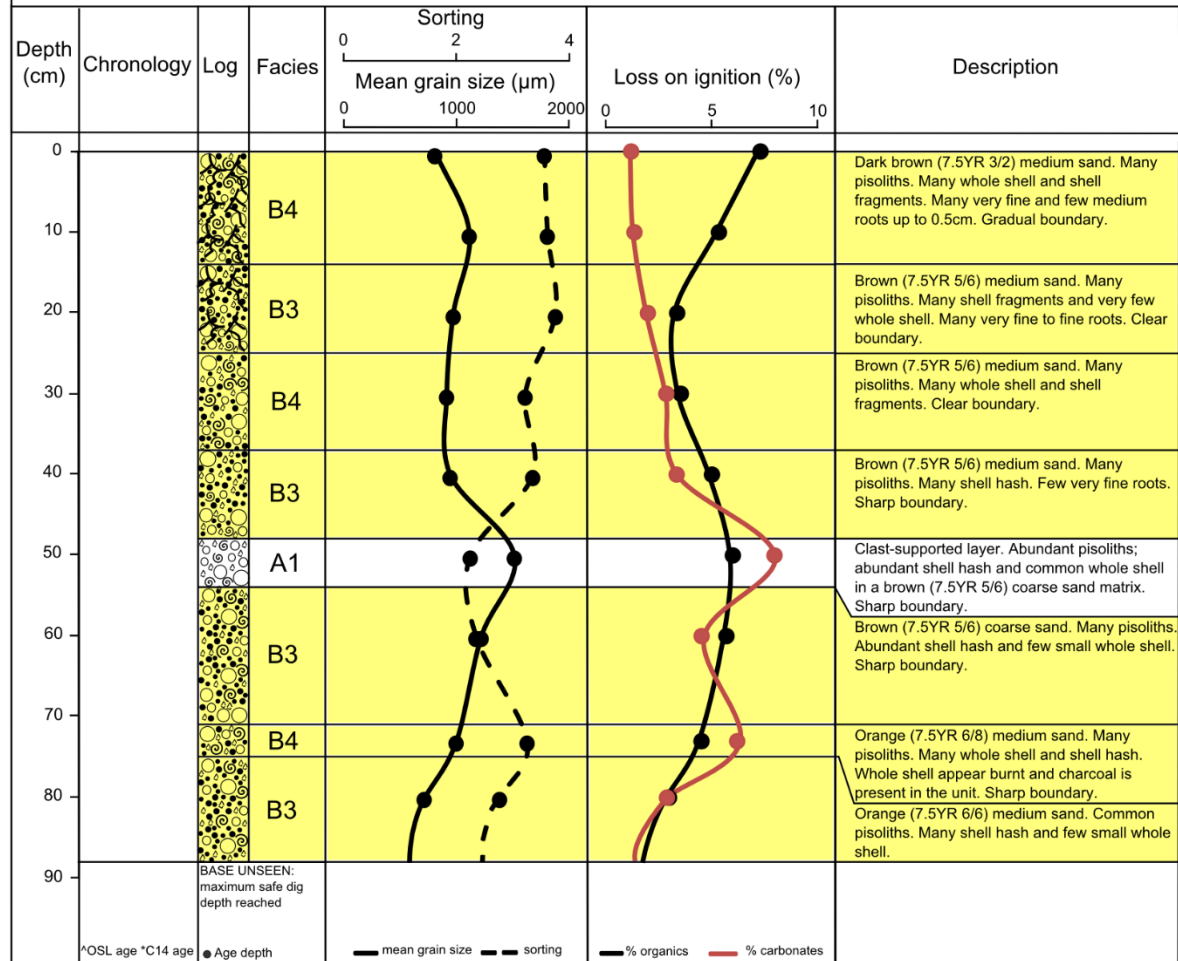


Location: Red Beach

UTM coordinates: E 595174.9934 N 8608563.137

Pit Location: Swale between beach ridge 1 and beach ridge 2 (RS1) Surface elevation: 1.80 m AHD

Pit Code: RB04



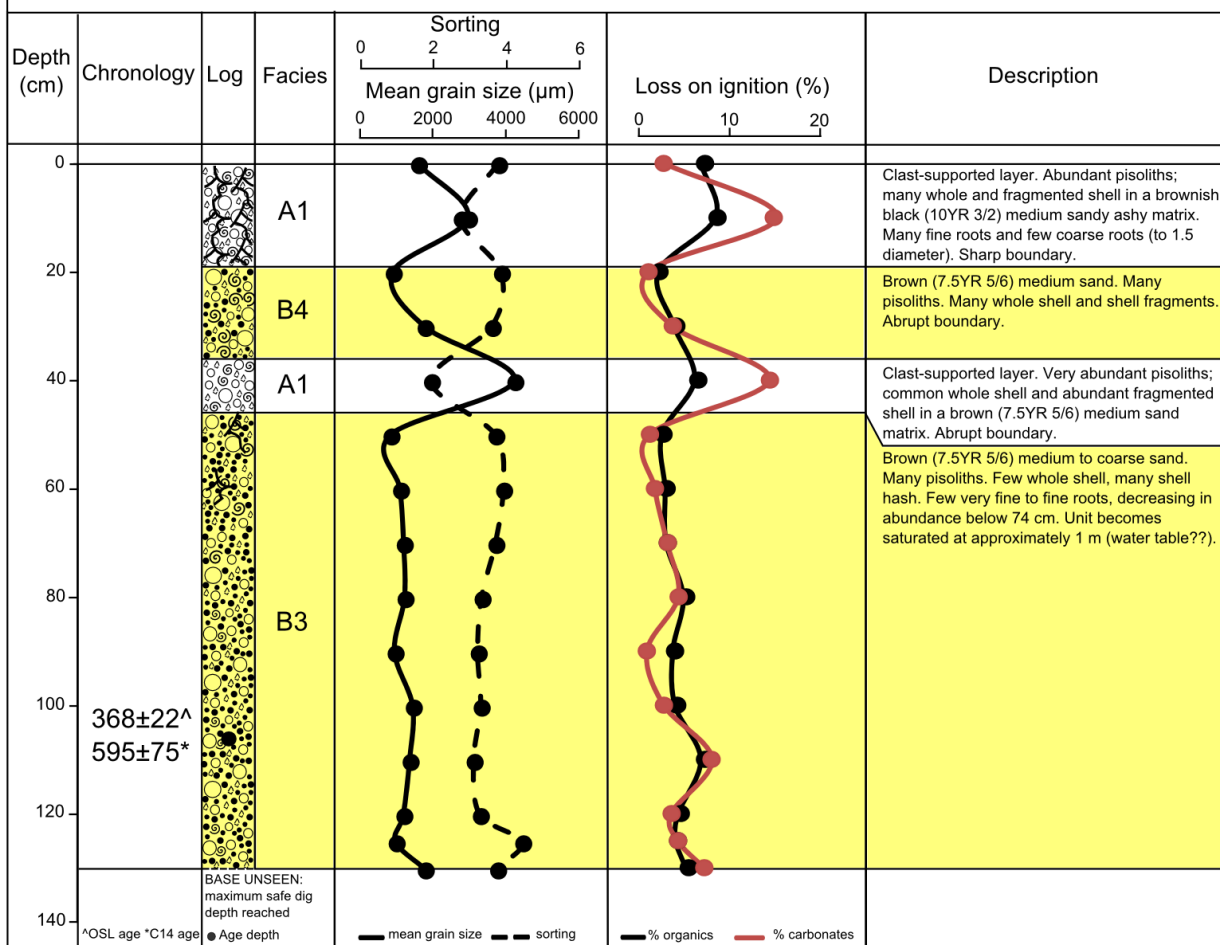
Location: Red Beach

UTM coordinates: E 595171.1147 N 8608563.894

Pit Location: Crest of beach ridge 2 (RR2)

Surface elevation: 1.99m AHD

Pit Code: RB01

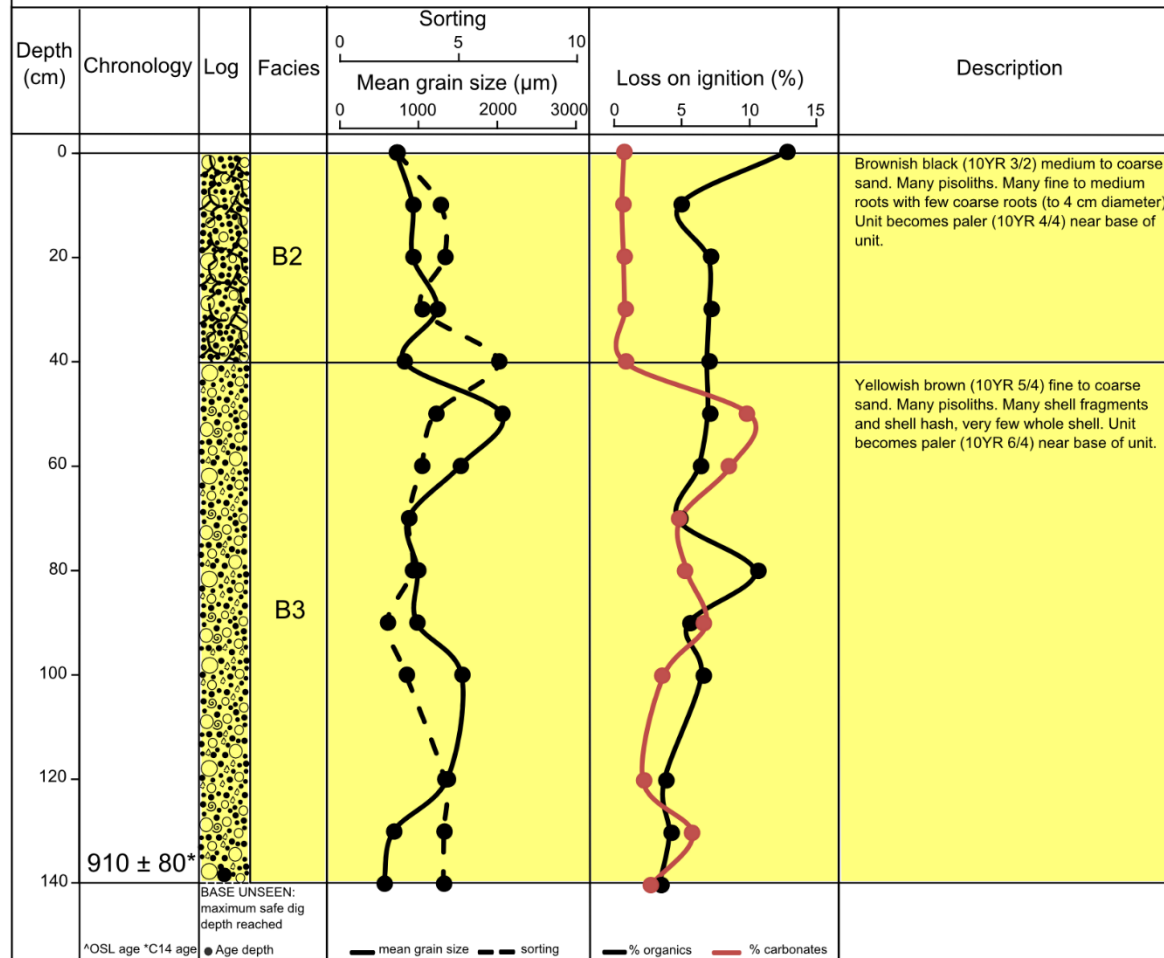


Location: Red Beach

UTM coordinates: E 595153.1557 N 8608566.034

Pit Location: Swale between beach ridge 2 and beach ridge 3 (RS2) Surface elevation: 1.53 m AHD

Pit Code: RB05



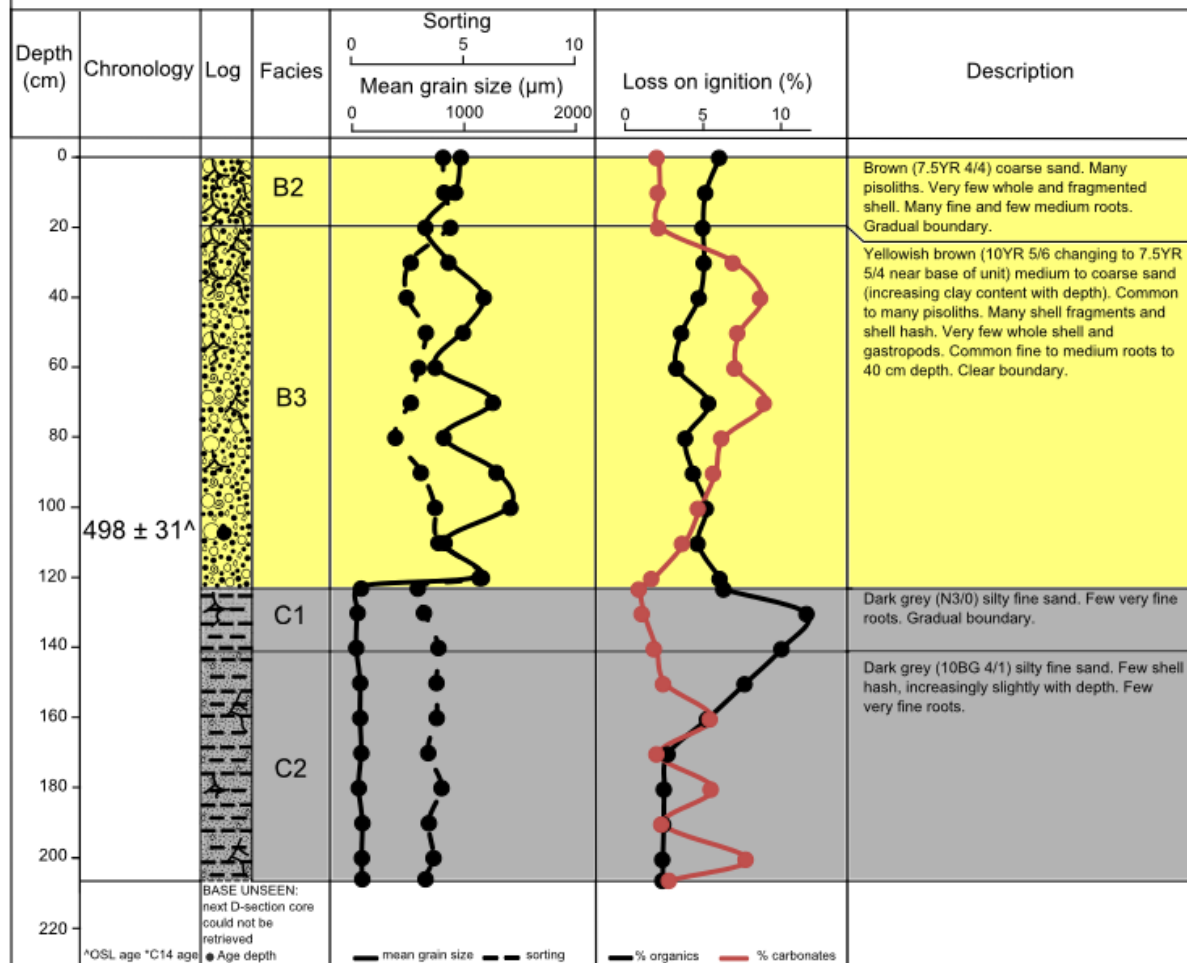
Location: Red Beach

UTM coordinates: E 595148.8877 N 8608566.476

Pit Location: Proximal flank of beach ridge 3 (RS3)

Surface elevation: 1.96 m AHD

Pit Code: RB17



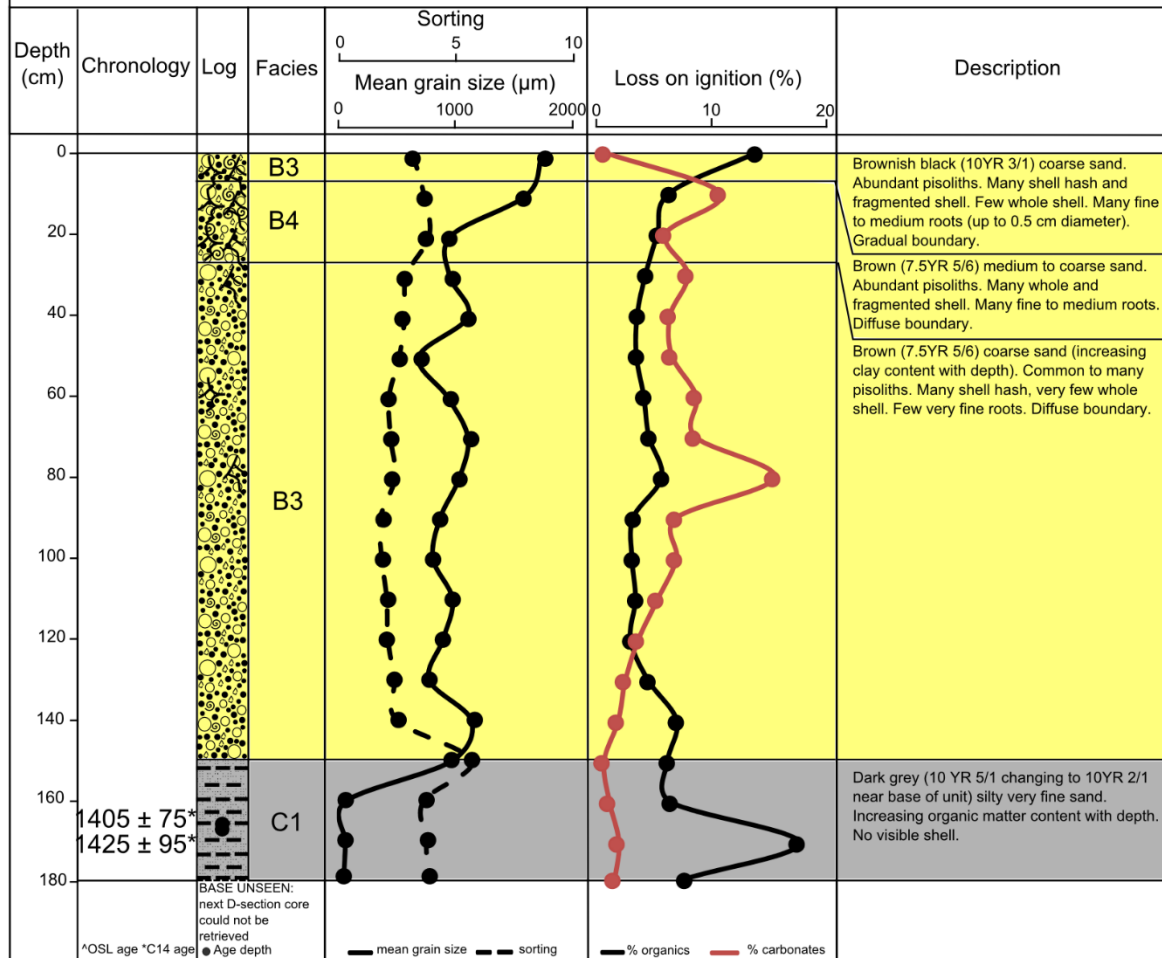
Location: Red Beach

UTM coordinates: E 595145.0251 N 8608567.358

Pit Location: Crest of beach ridge 3 (RR3)

Surface elevation: 2.21 m AHD

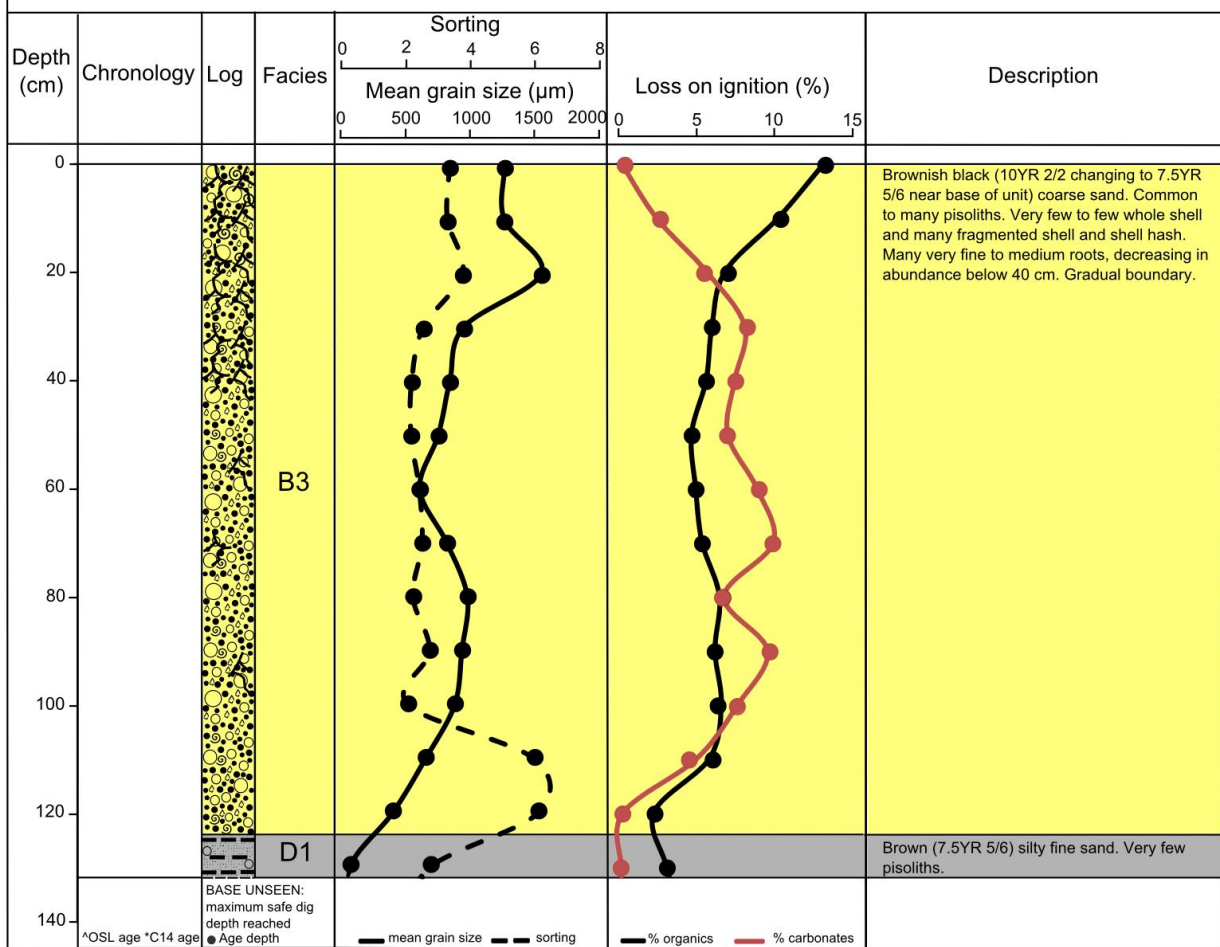
Pit Code: RB06



UTM coordinates: E 595138.7368 N 8608568.088

Pit Location: Swale between beach ridge 3 and beach ridge 4 (RS4)      Surface elevation: 2.04 m AHD

Pit Code: RB07



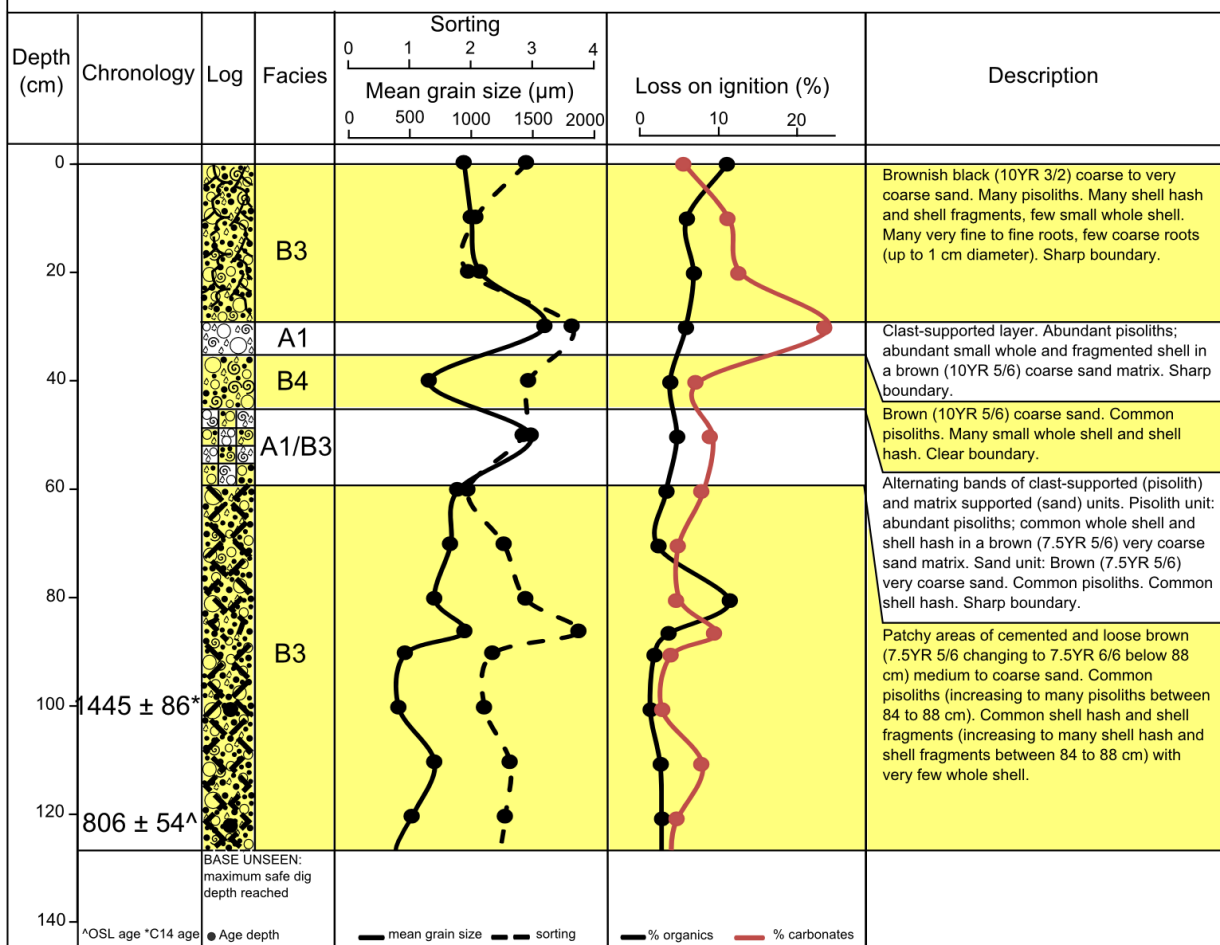
Location: Red Beach

UTM coordinates: E 595131.7323 N 8608568.384

Pit Location: Crest of beach ridge 4 (RR4)

Surface elevation: 2.33 m AHD

Pit Code: RB08





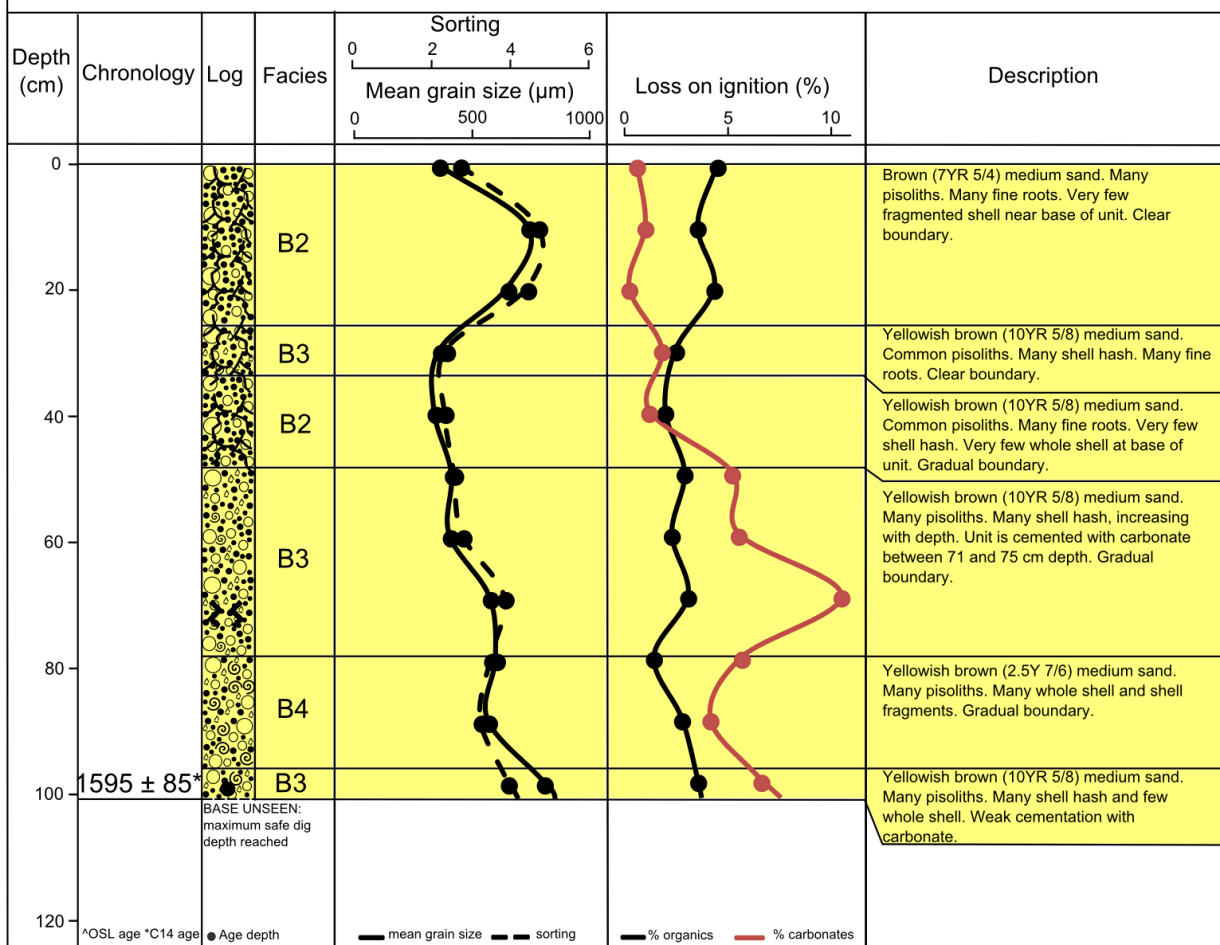
Location: Red Beach

UTM coordinates: E 595123.4966 N 8608568.818

Pit Location: Swale between beach ridge 4 and beach ridge 5 (RS5)

Surface elevation: 2.27 m AHD

Pit Code: RB09



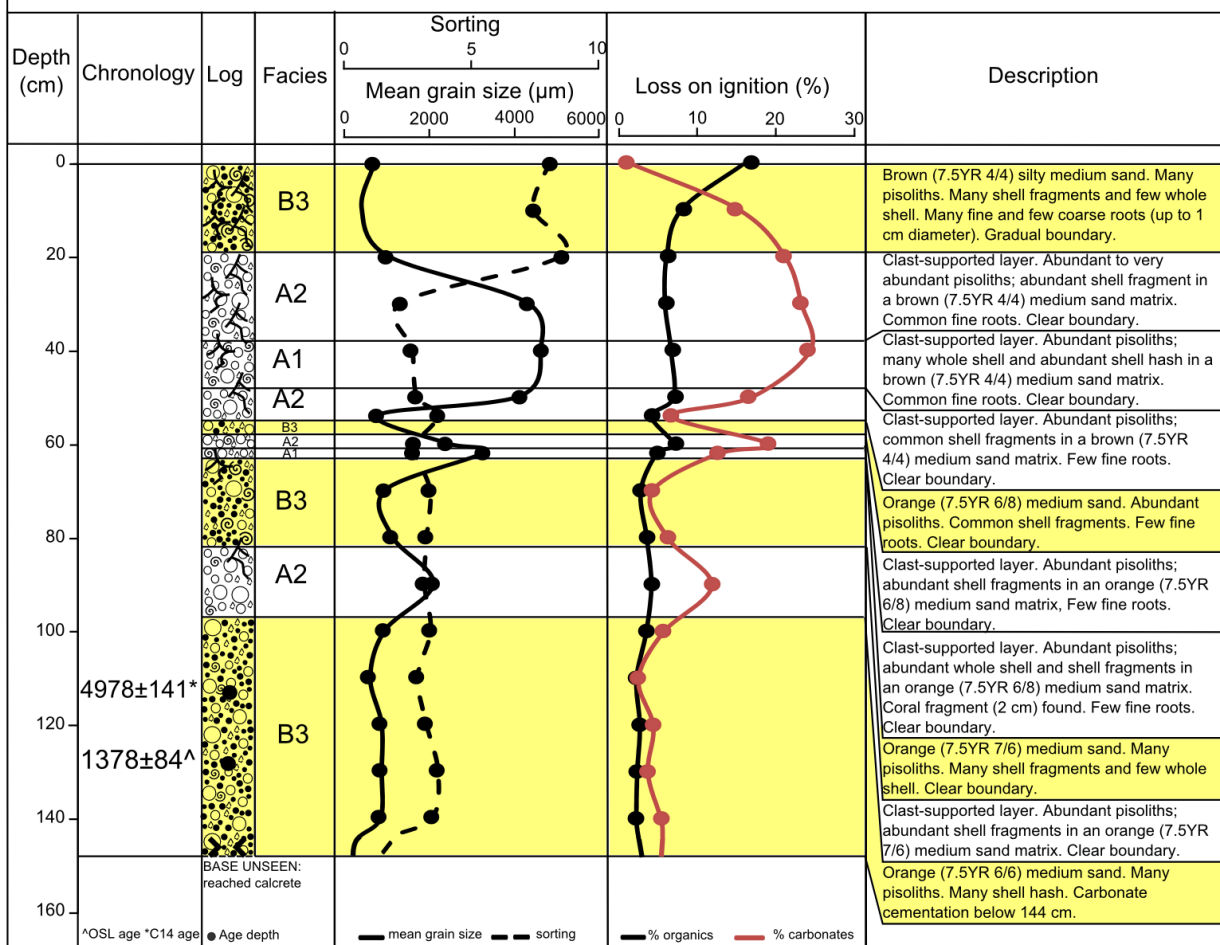
Location: Red Beach

UTM coordinates: E 595093.0226 N 8608571.045

Pit Location: Crest of beach ridge 5 (RR5)

Surface elevation: 2.73 m AHD

Pit Code: RB10



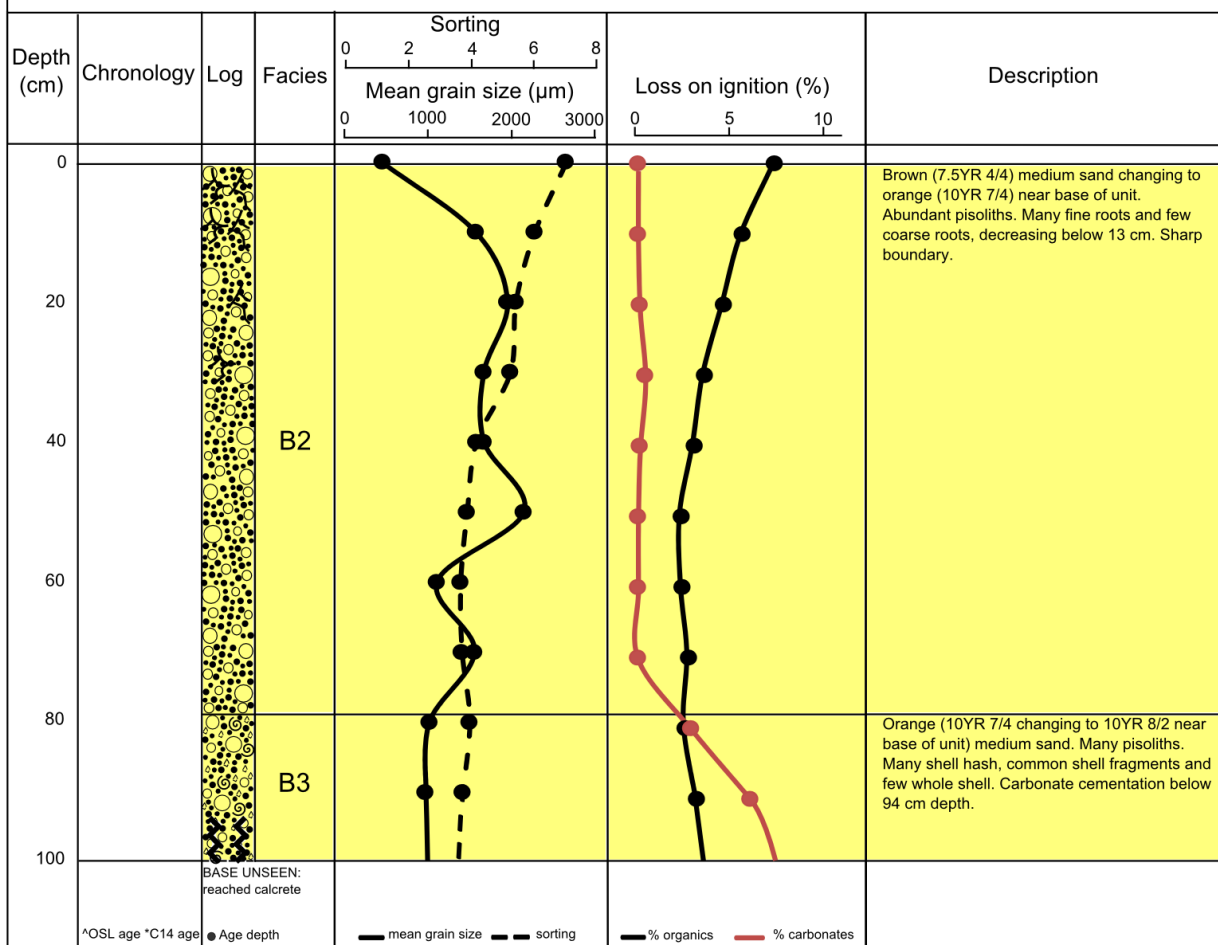
Location: Red Beach

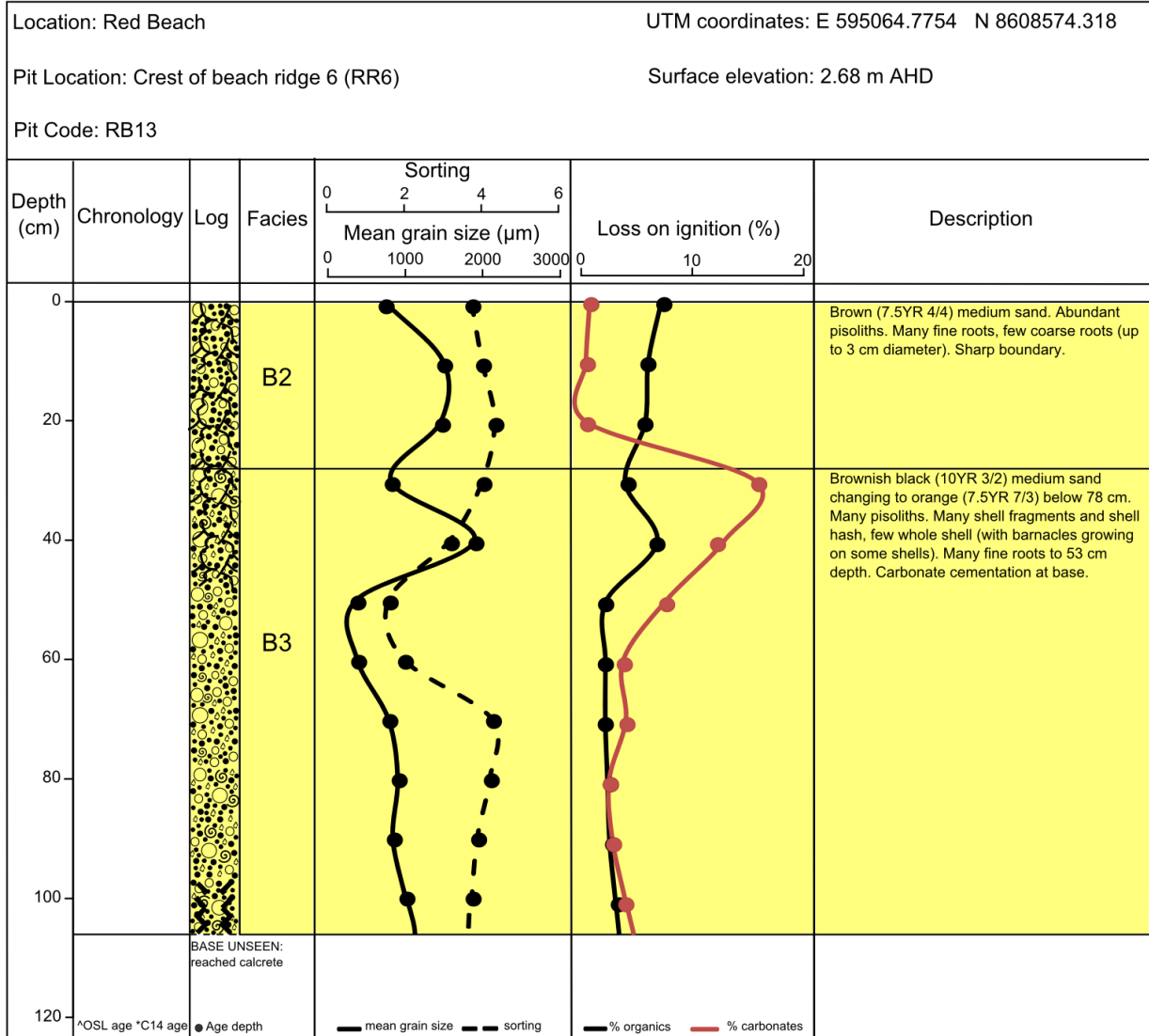
UTM coordinates: E 595084.7887 N 8608572.398

Pit Location: Swale between beach ridge 5 and beach ridge 6 (RS6)

Surface elevation: 2.50 m AHD

Pit Code: RB11





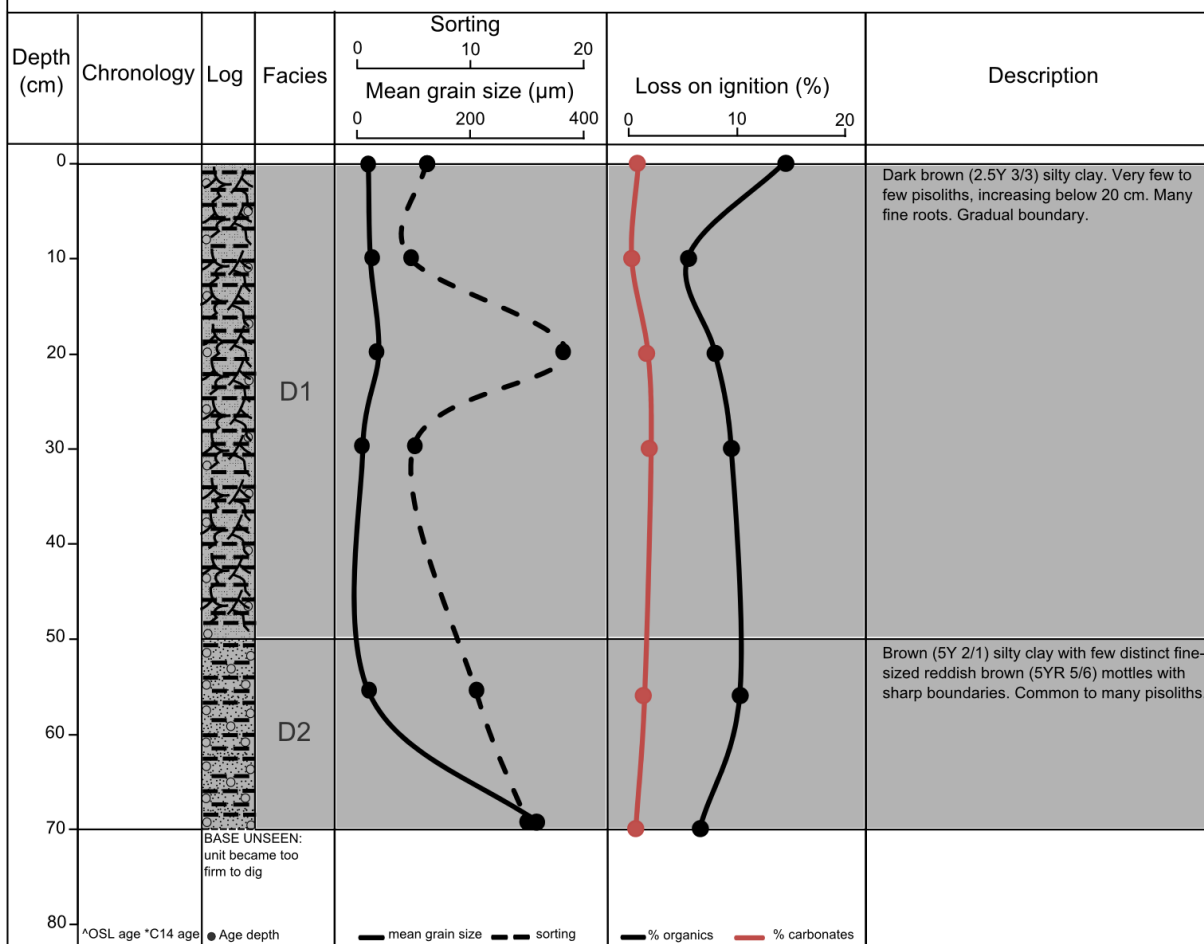
Location: Red Beach

UTM coordinates: E 595042.6492 N 8608577.16

Pit Location: Swale between beach ridge 6 and beach ridge 7 (RS7)

Surface elevation: 2.11 m AHD

Pit Code: RB14



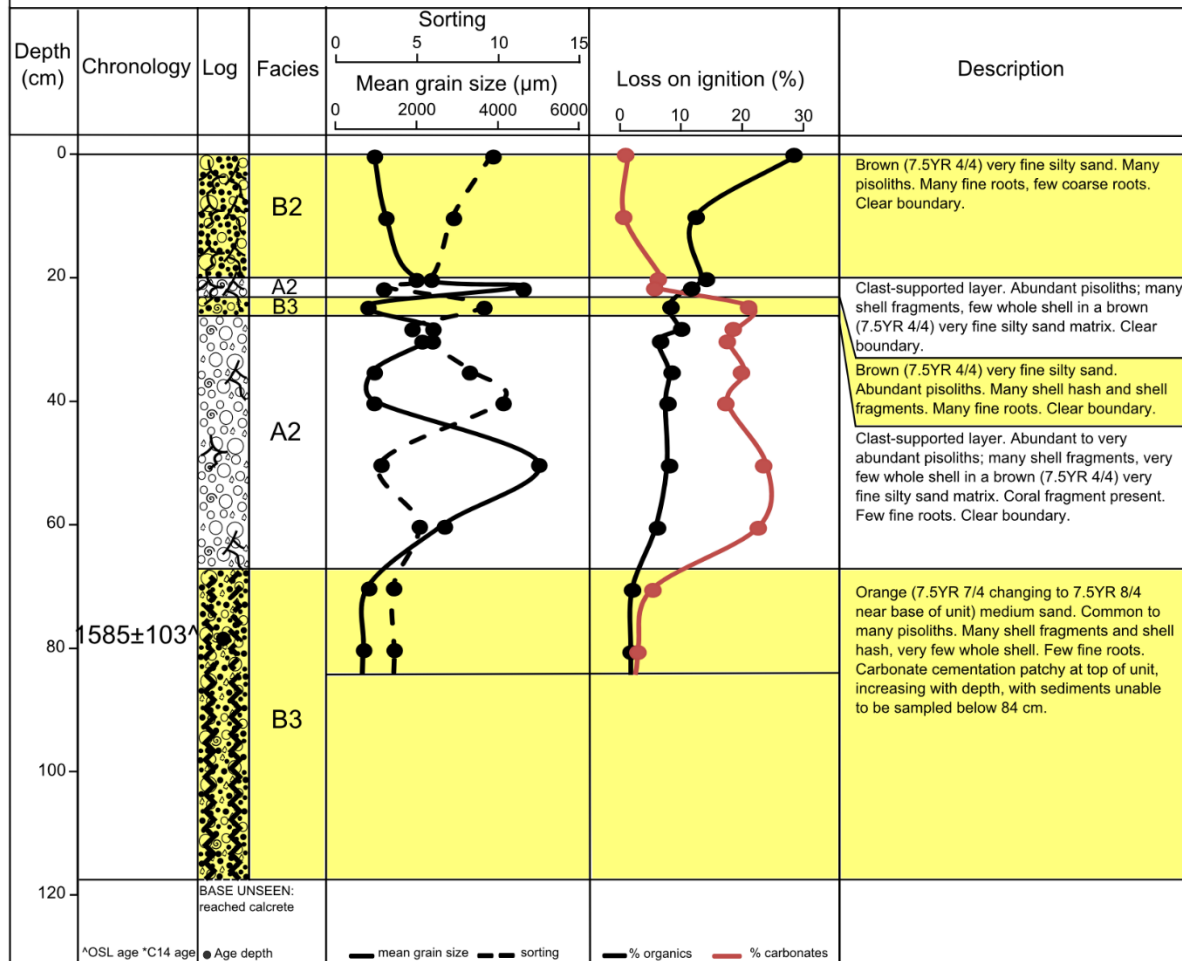
Location: Red Beach

UTM coordinates: E 595026.337 N 8608578.91

Pit Location: Crest of beach ridge 7 (RR7)

Surface elevation: 2.77 m AHD

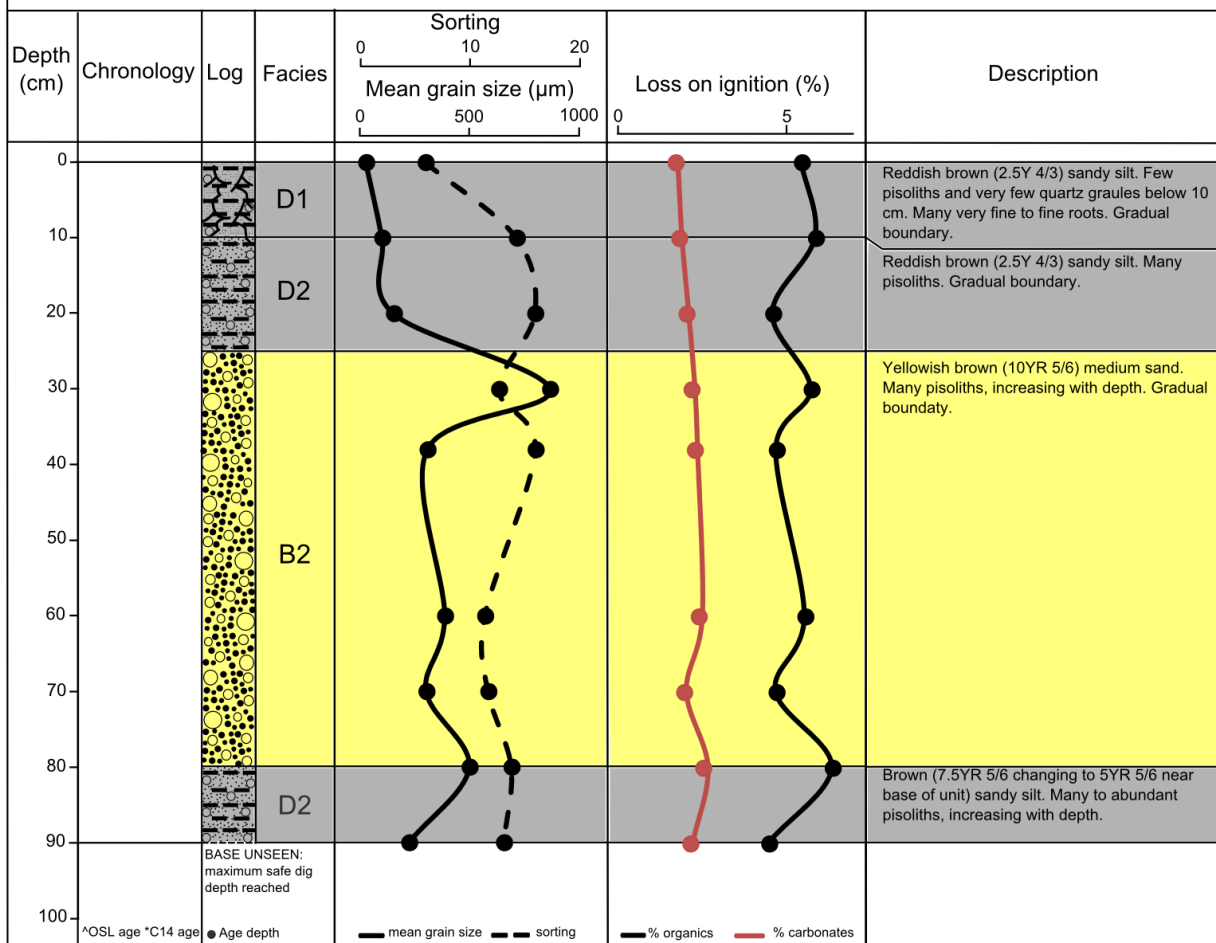
Pit Code: RB12

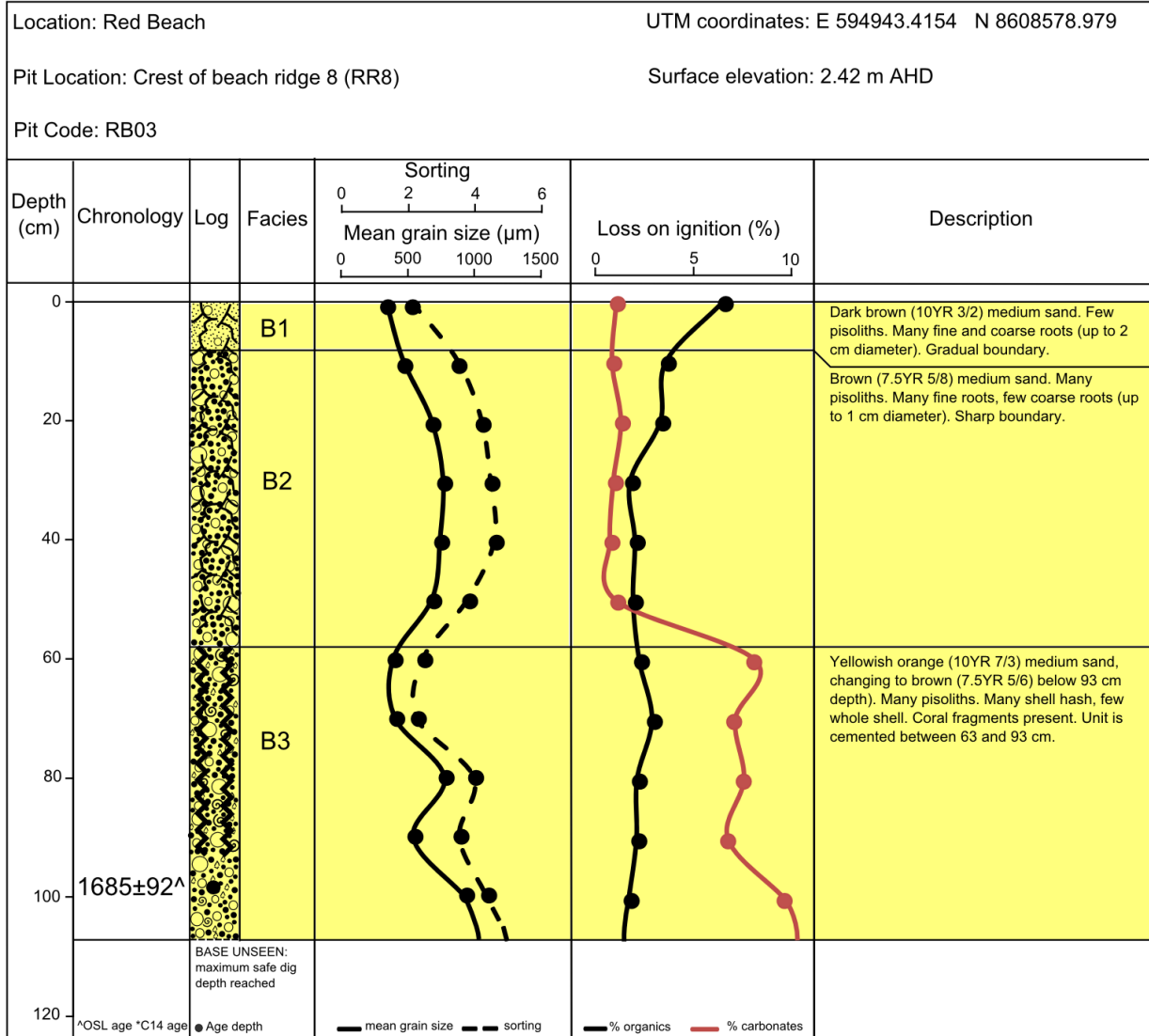


Location: Red Beach UTM coordinates: E 594991.061 N 8608582.558

Pit Location: Swale between beach ridge 7 and beach ridge 8 (RS8) Surface elevation: 2.12 m AHD

Pit Code: RB15





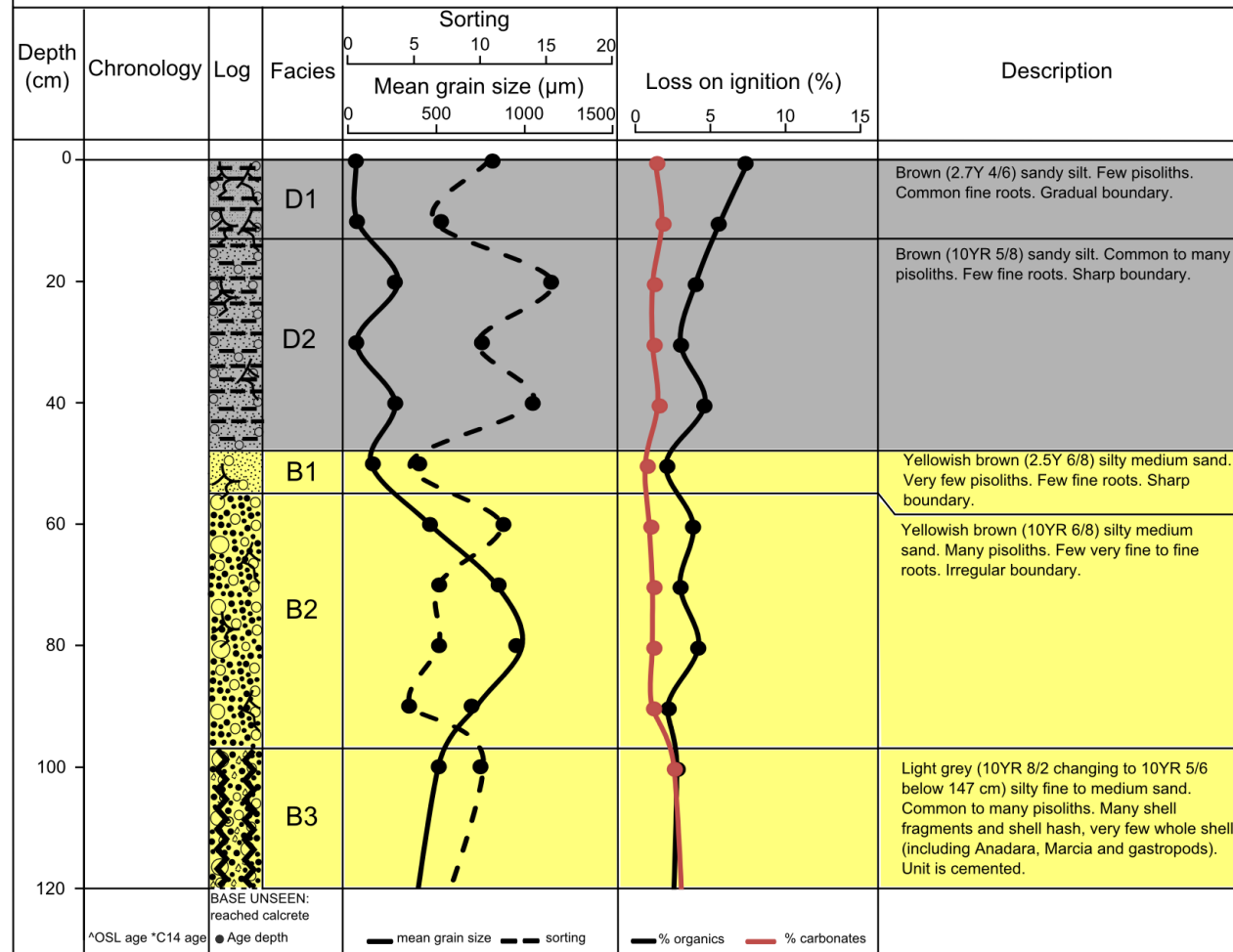


Location: Red Beach

UTM coordinates: E 594916.6305 N 8608576.047

Pit Location: Swale between beach ridge 8 and beach ridge 9 (RS9) Surface elevation: 2.01 m AHD

Pit Code: RB16



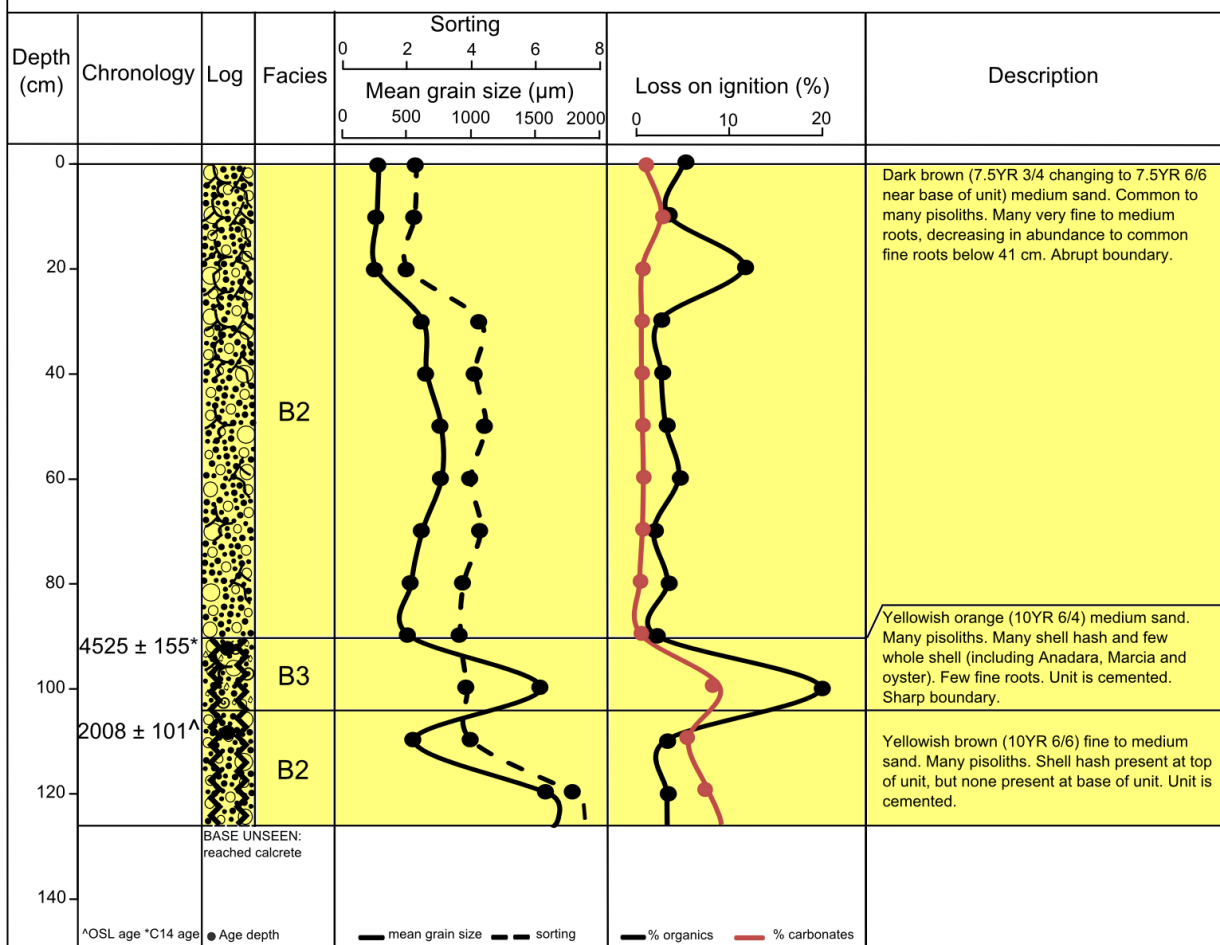
Location: Red Beach

UTM coordinates: E 594861.5084 N 8608580.512

Pit Location: Crest of beach ridge 9 (RR9)

Surface elevation: 2.06m AHD

Pit Code: RB21



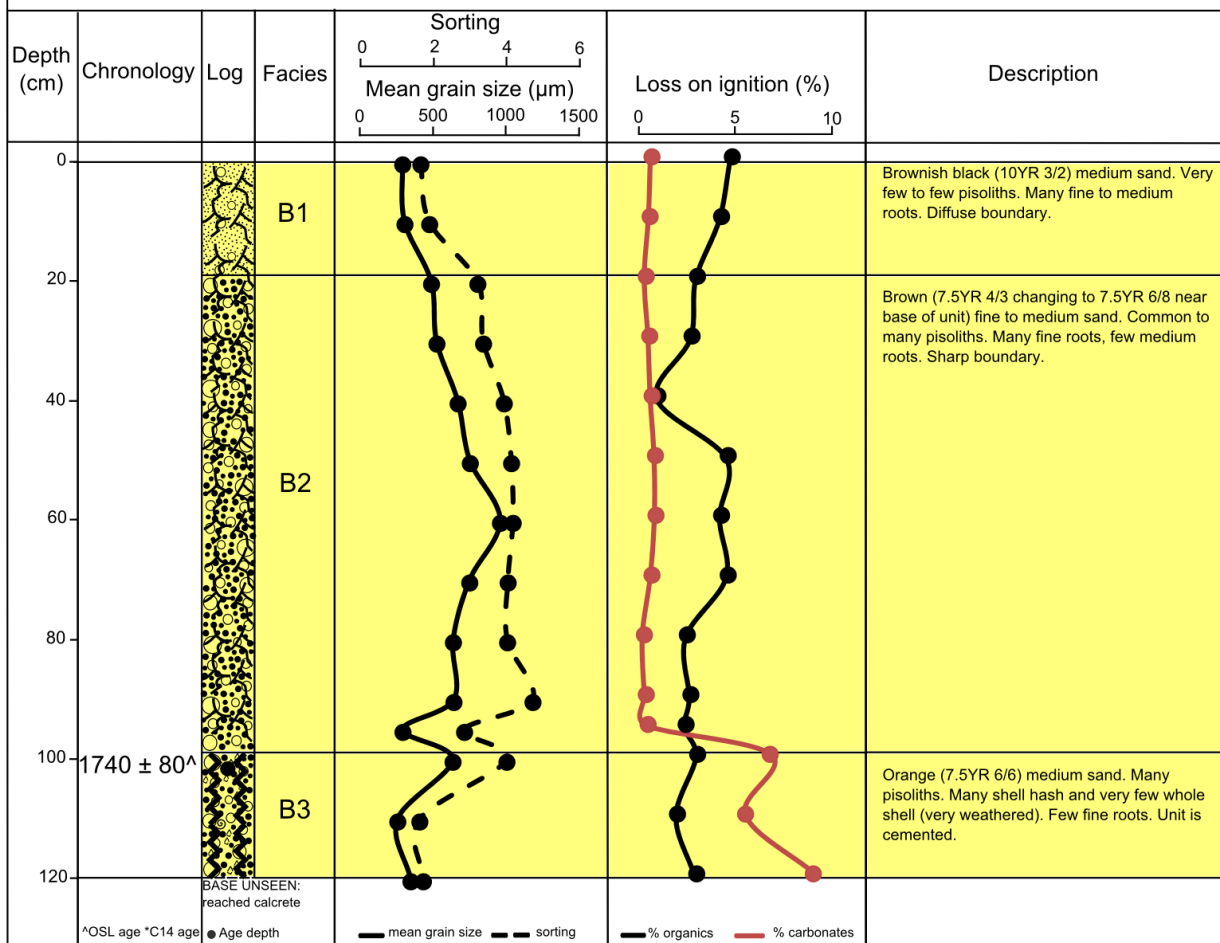
Location: Red Beach

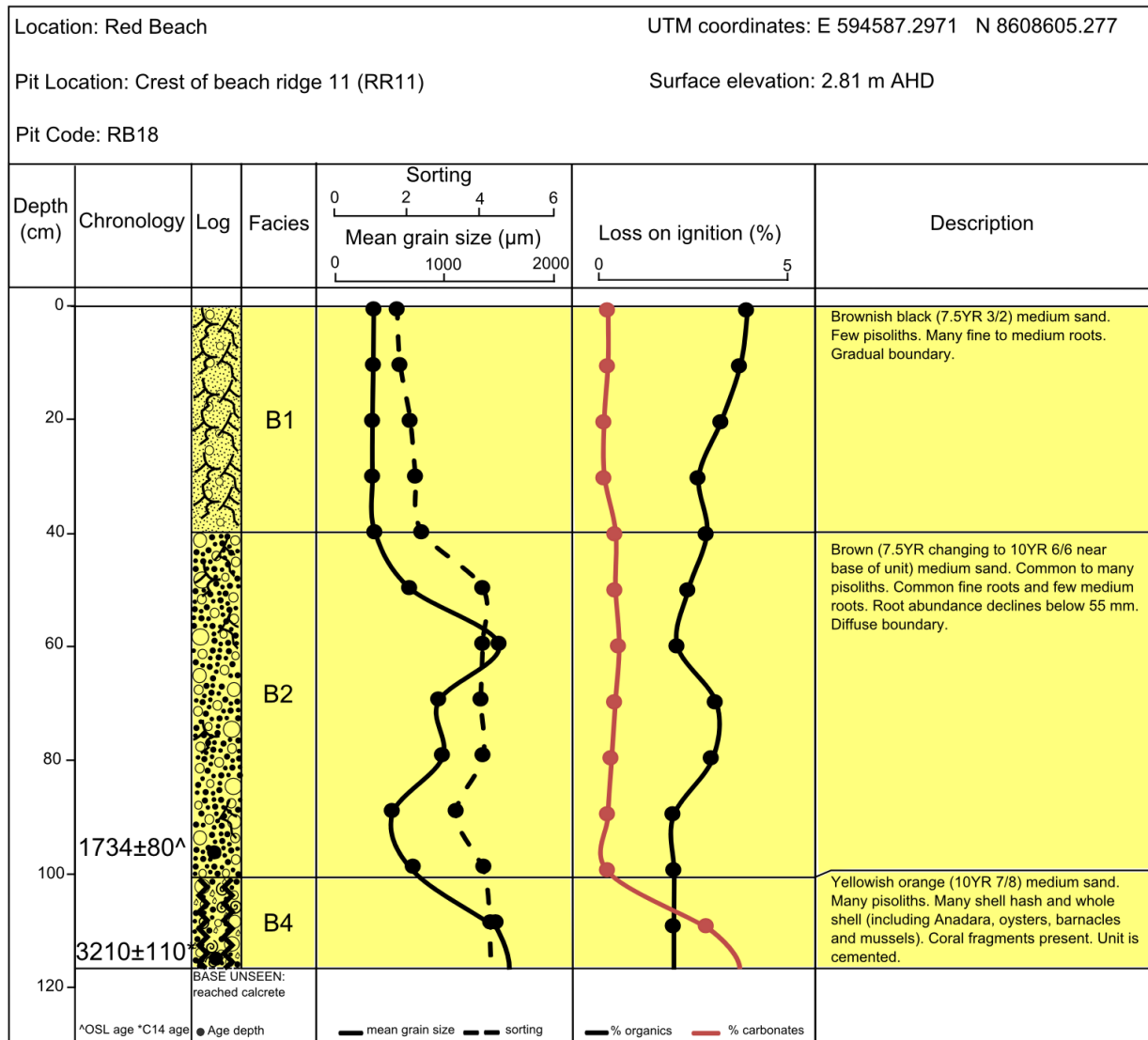
UTM coordinates: E 594674.145 N 8608597.795

Pit Location: Crest of beach ridge 10 (RR10)

Surface elevation: 2.59 m AHD

Pit Code: RB25





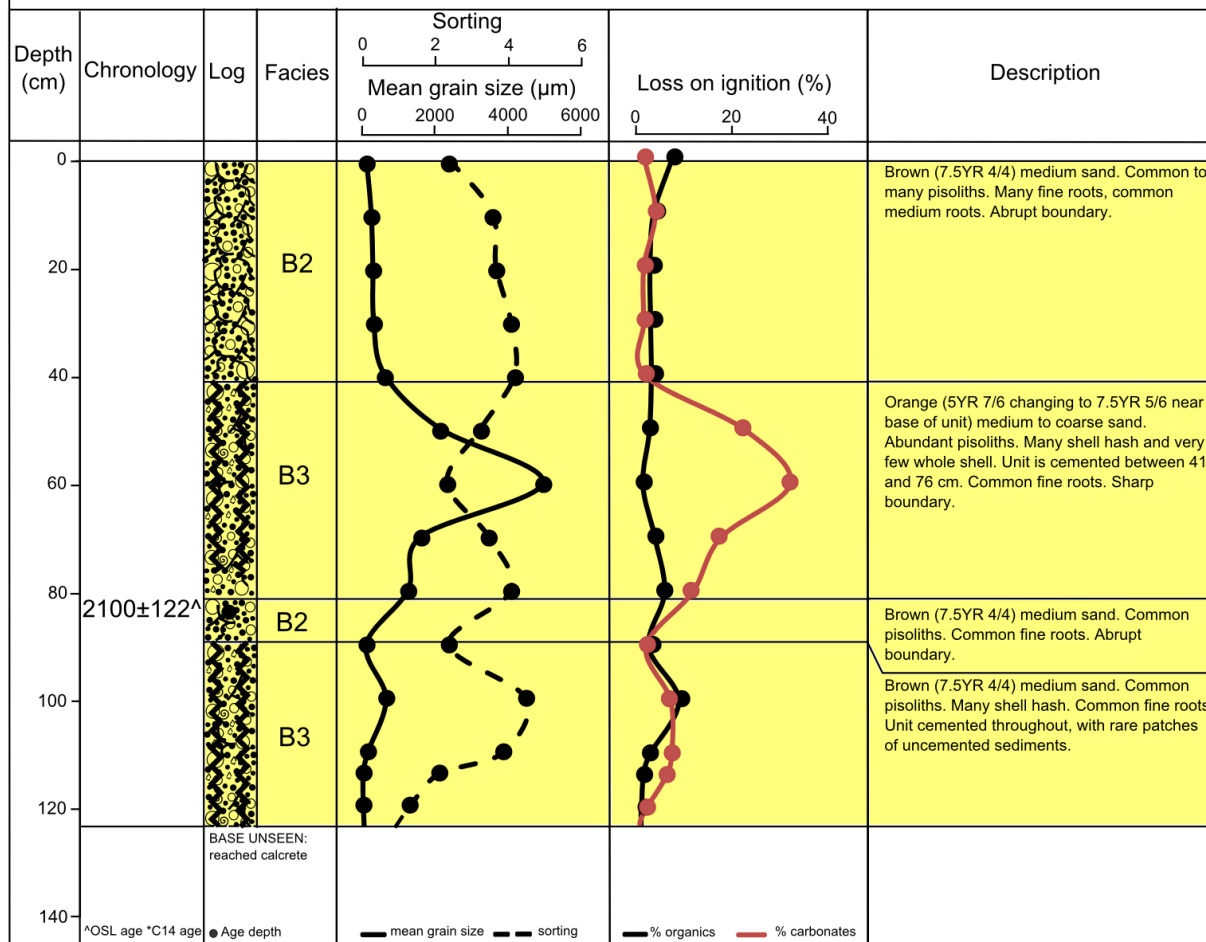
Location: Red Beach

UTM coordinates: E 593540.3258 N 8608607.882

Pit Location: Crest of beach ridge 12 (RR12)

Surface elevation: 2.56 m AHD

Pit Code: RB20



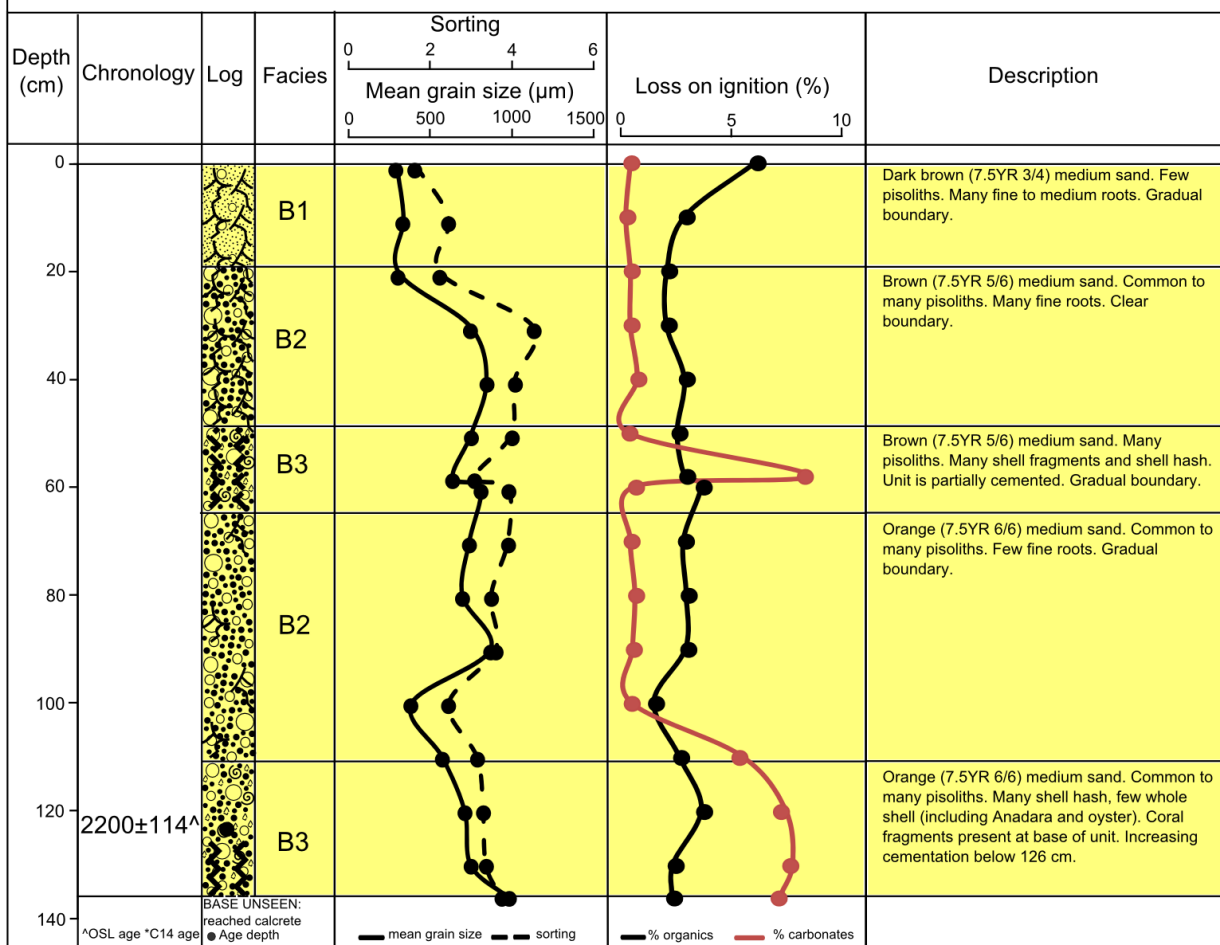
Location: Red Beach

UTM coordinates: E 594491.3462 N 8608613.654

Pit Location: Crest of beach ridge 13 (RR13)

Surface elevation: 2.81 m AHD

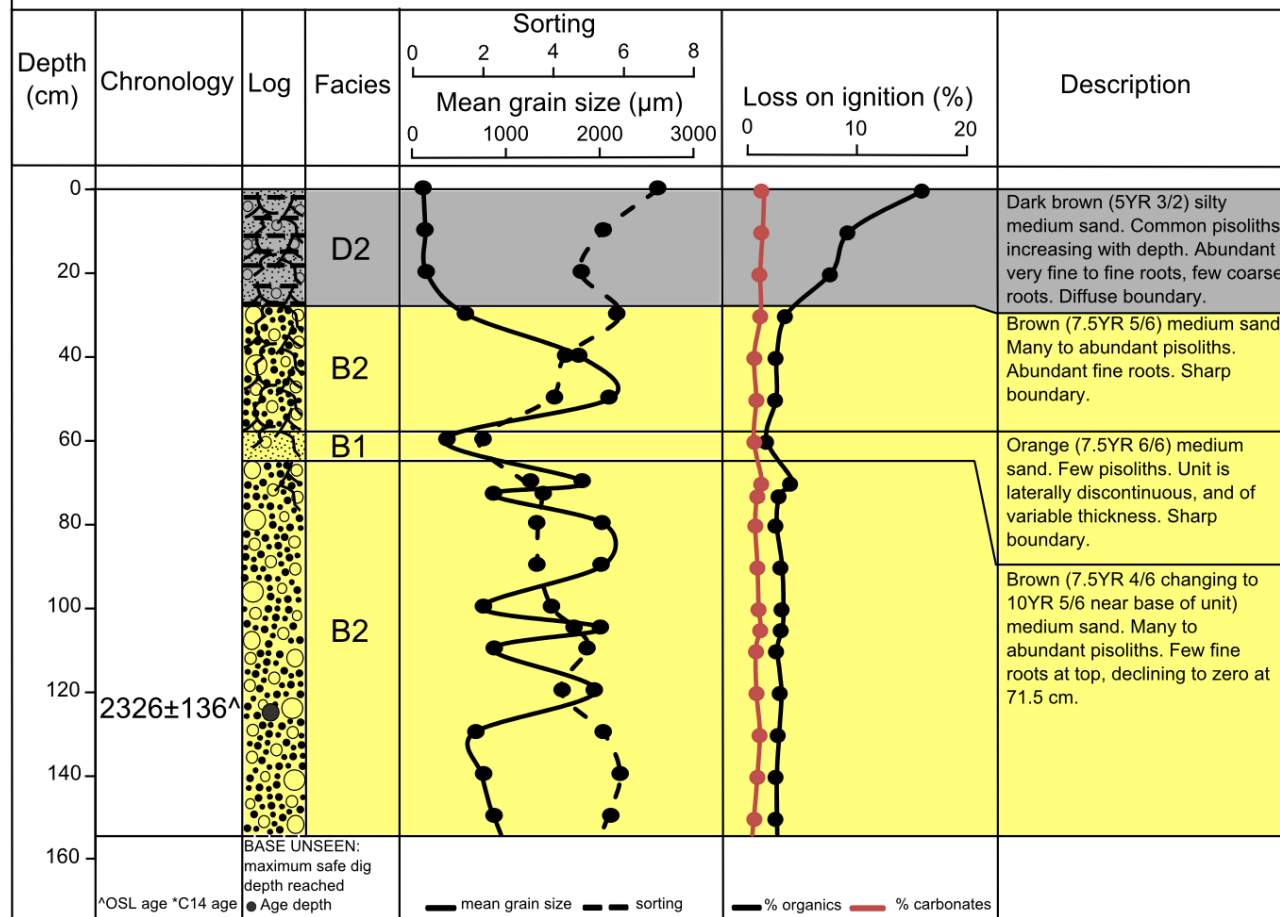
Pit Code: RB19

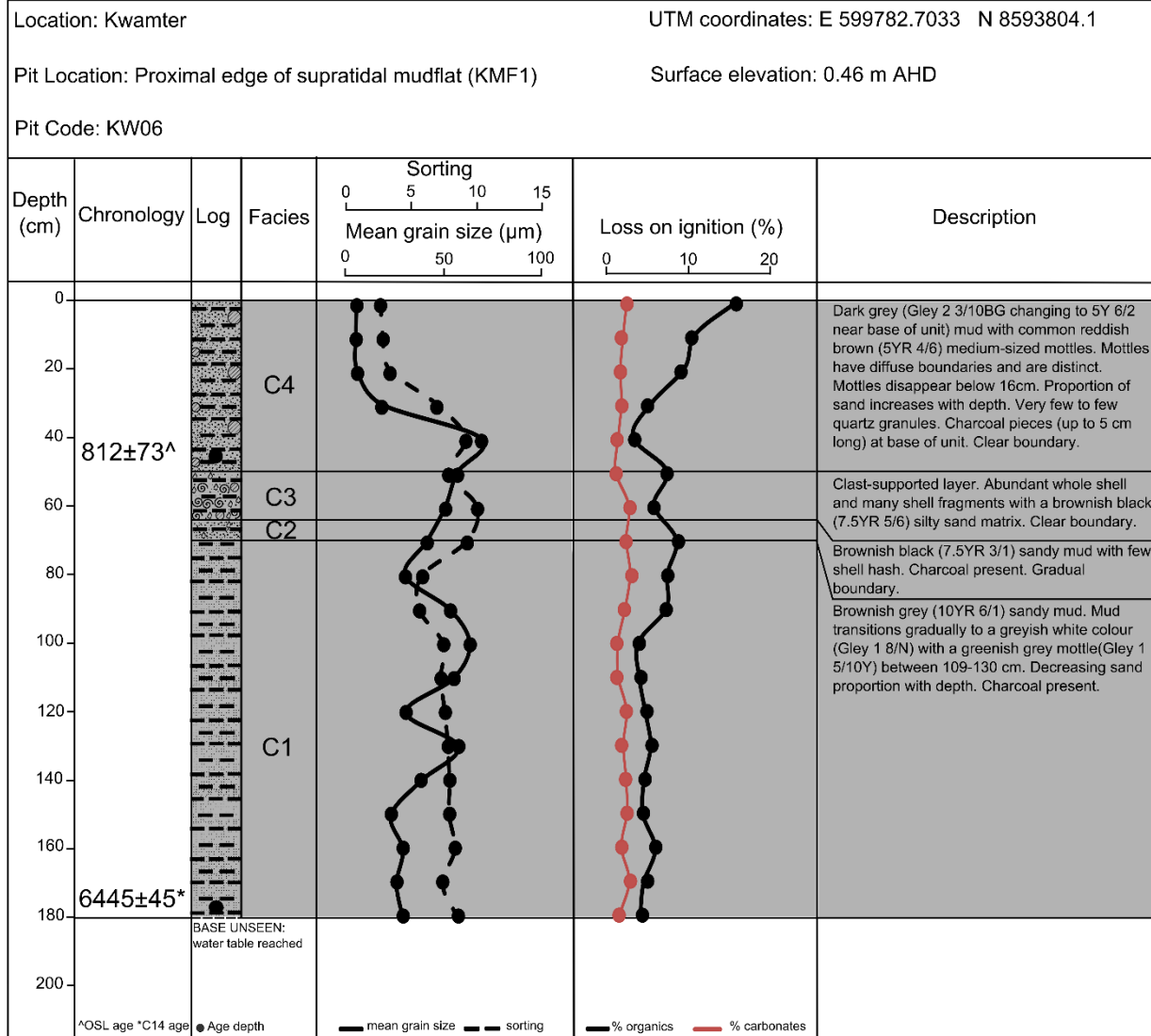


Location: Red Beach UTM coordinates: E 594398.2002 N 8608621.533

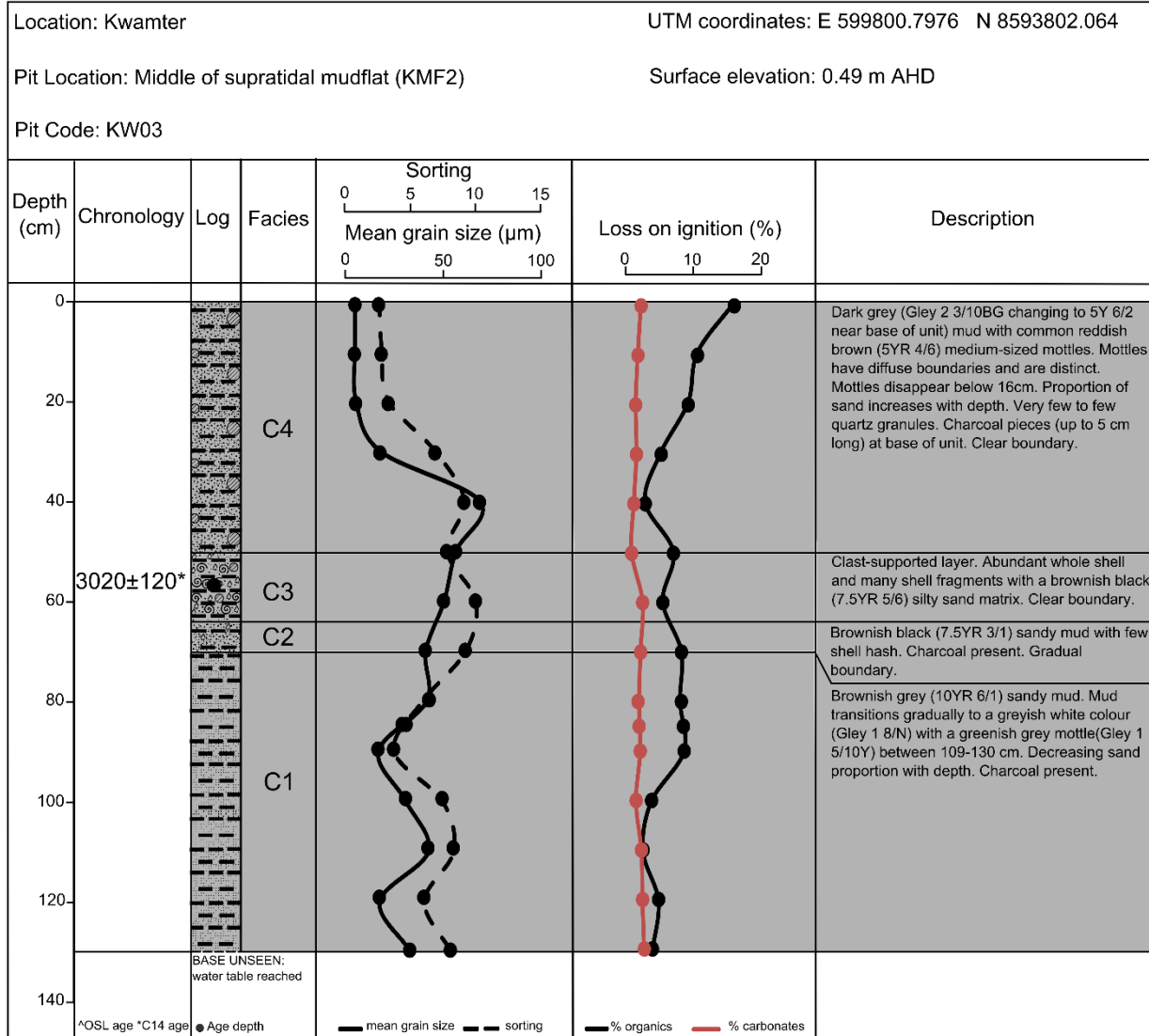
Core Location: Swale between beach ridge 13 and bauxite plateau (RS10) Surface elevation: 2.24 m AHD

Core Code: RB27





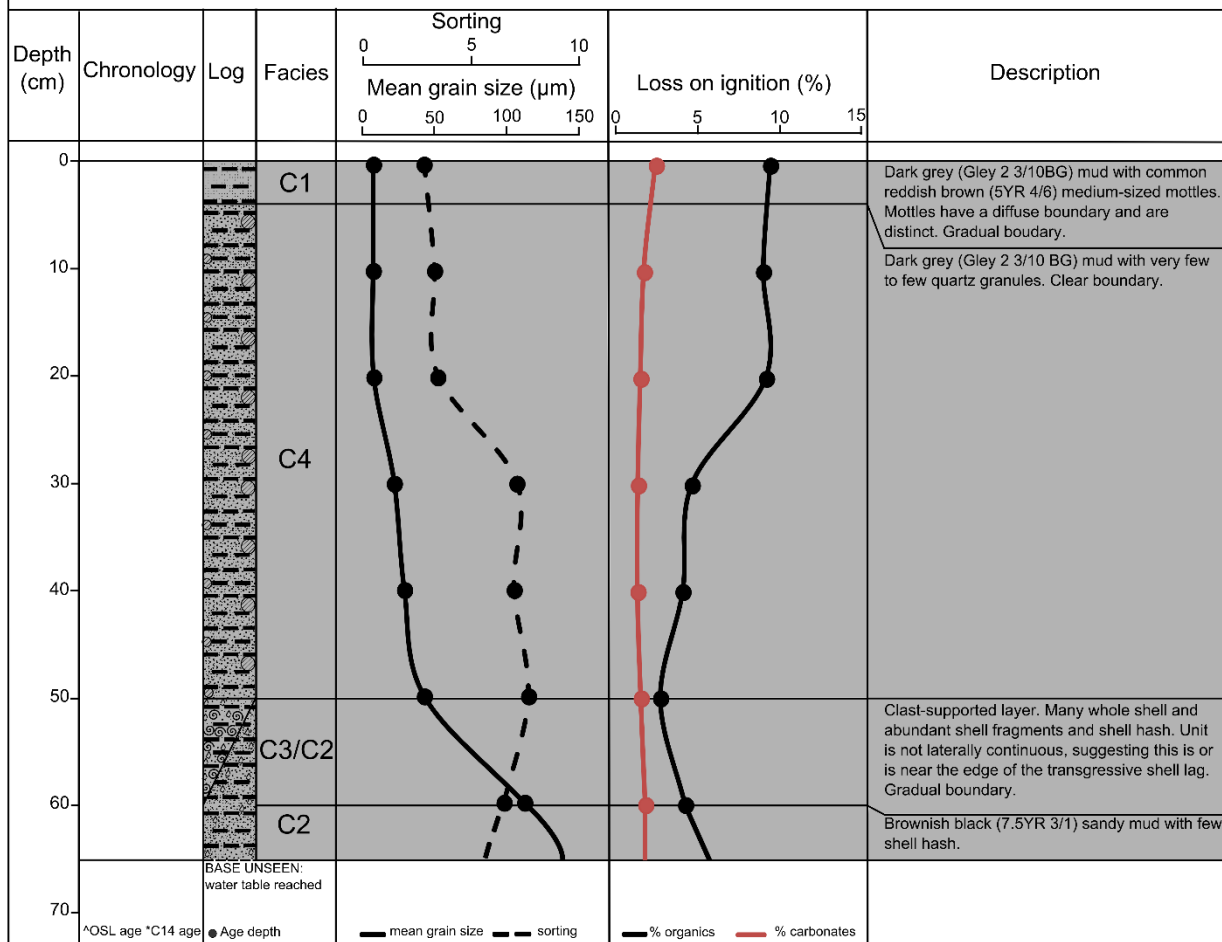


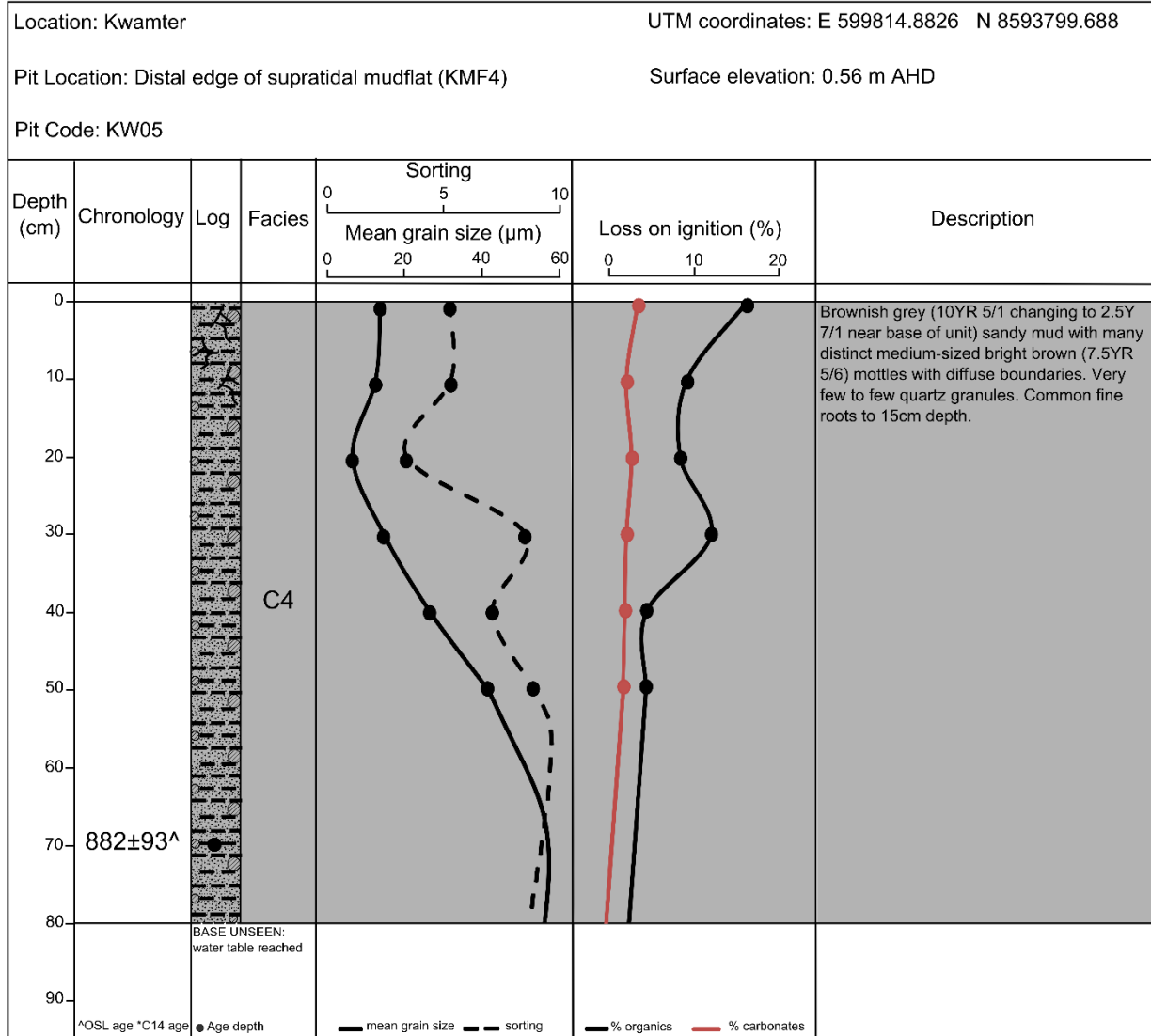


Location: Kwamter UTM coordinates: E 599808.2071 N 8593800.397

Pit Location: Distal edge of supratidal mudflat (KMF3) Surface elevation: 0.52 m AHD

Pit Code: KW10





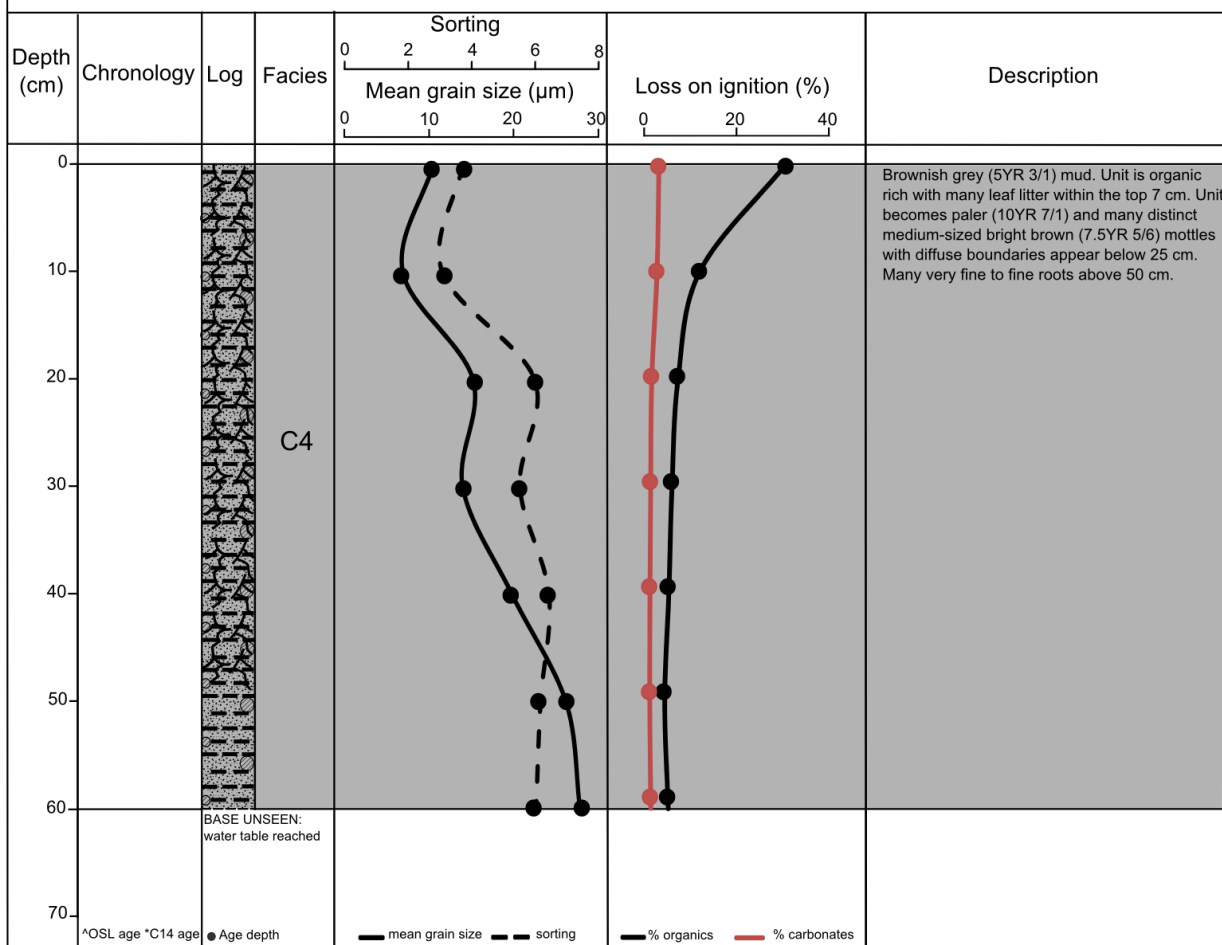
Location: Kwamter

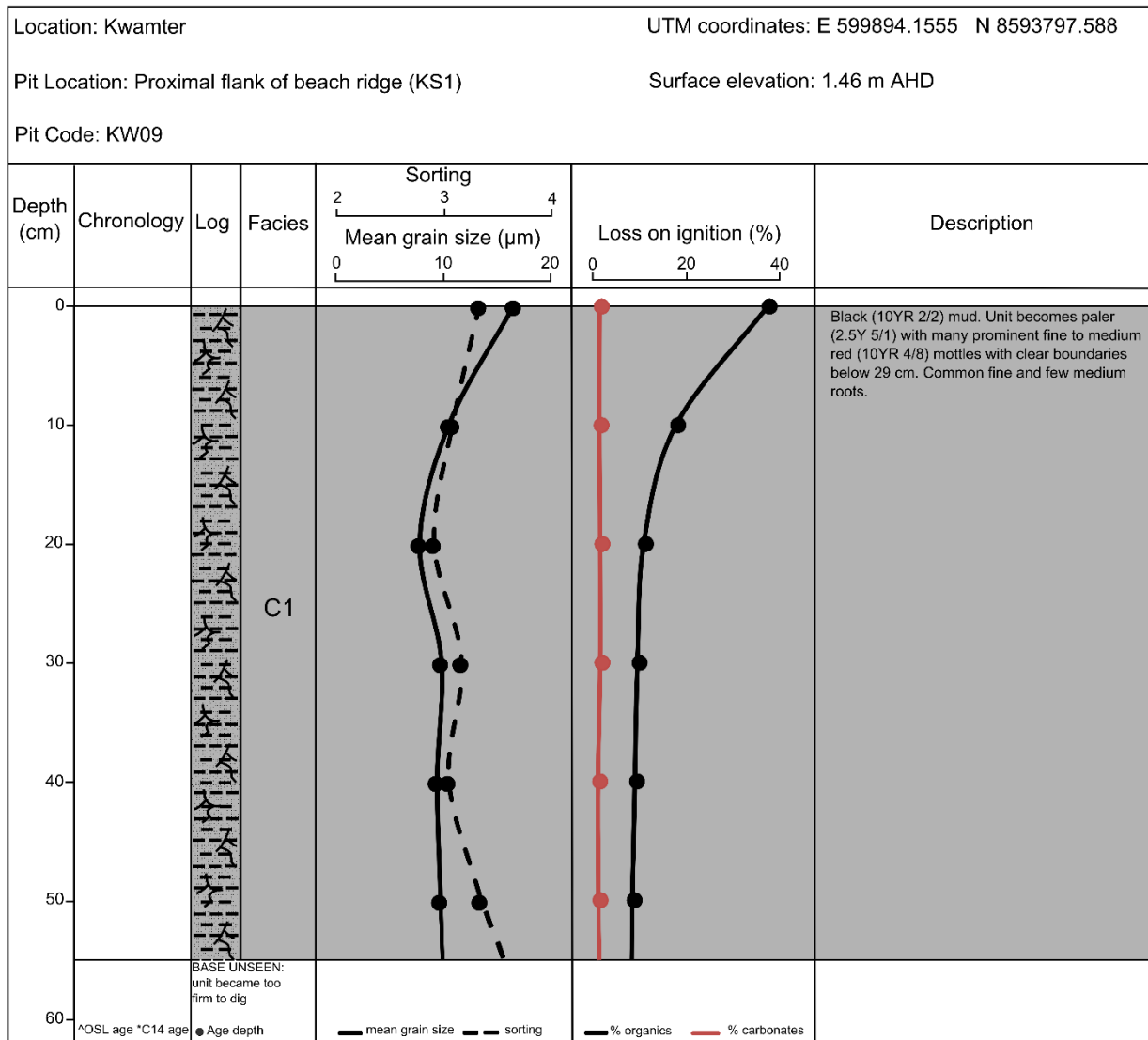
UTM coordinates: E 599837.8668 N 8593796.209

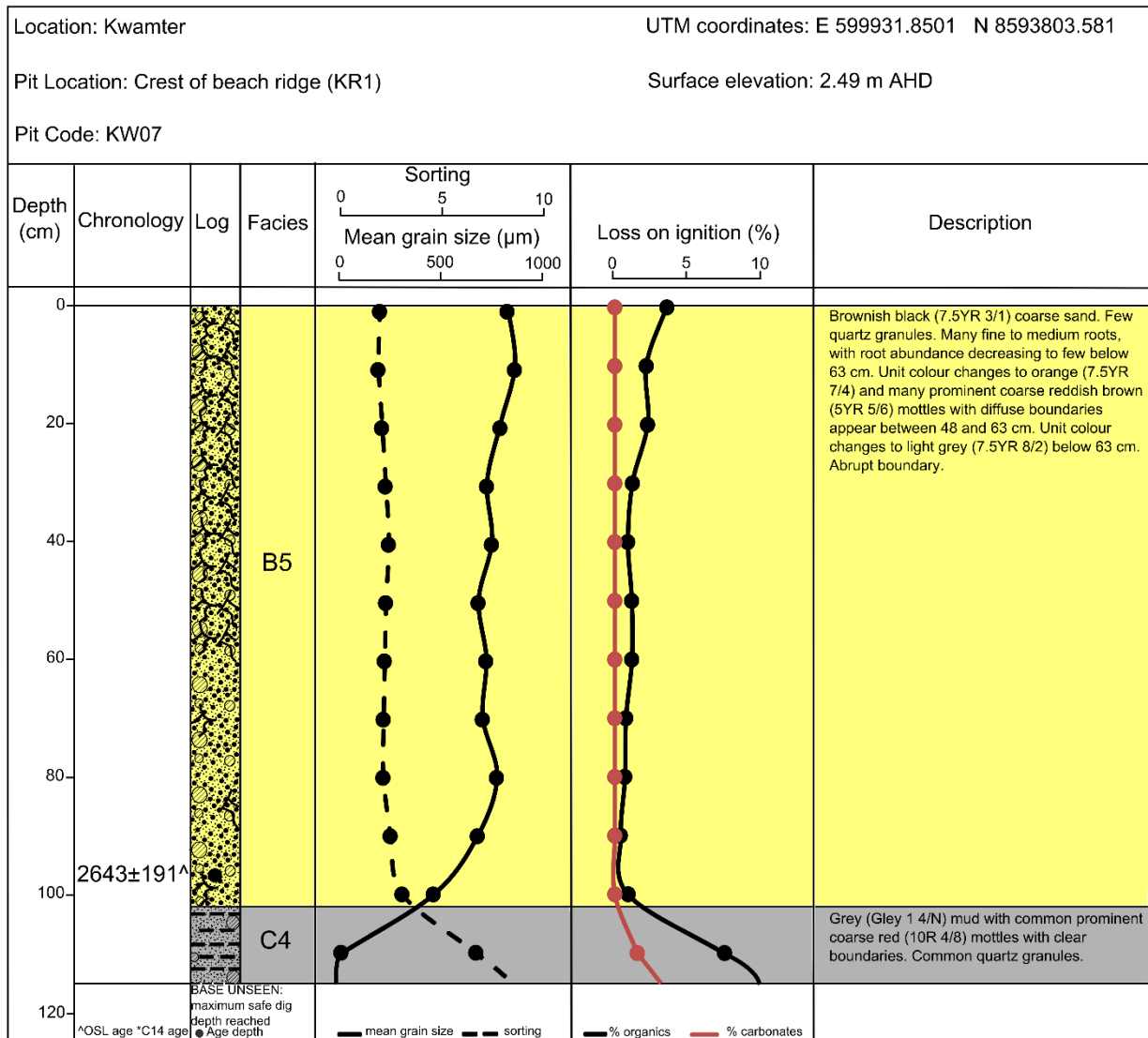
Pit Location: Middle of mangrove fringe (K11)

Surface elevation: 0.71 m AHD

Pit Code: KW04



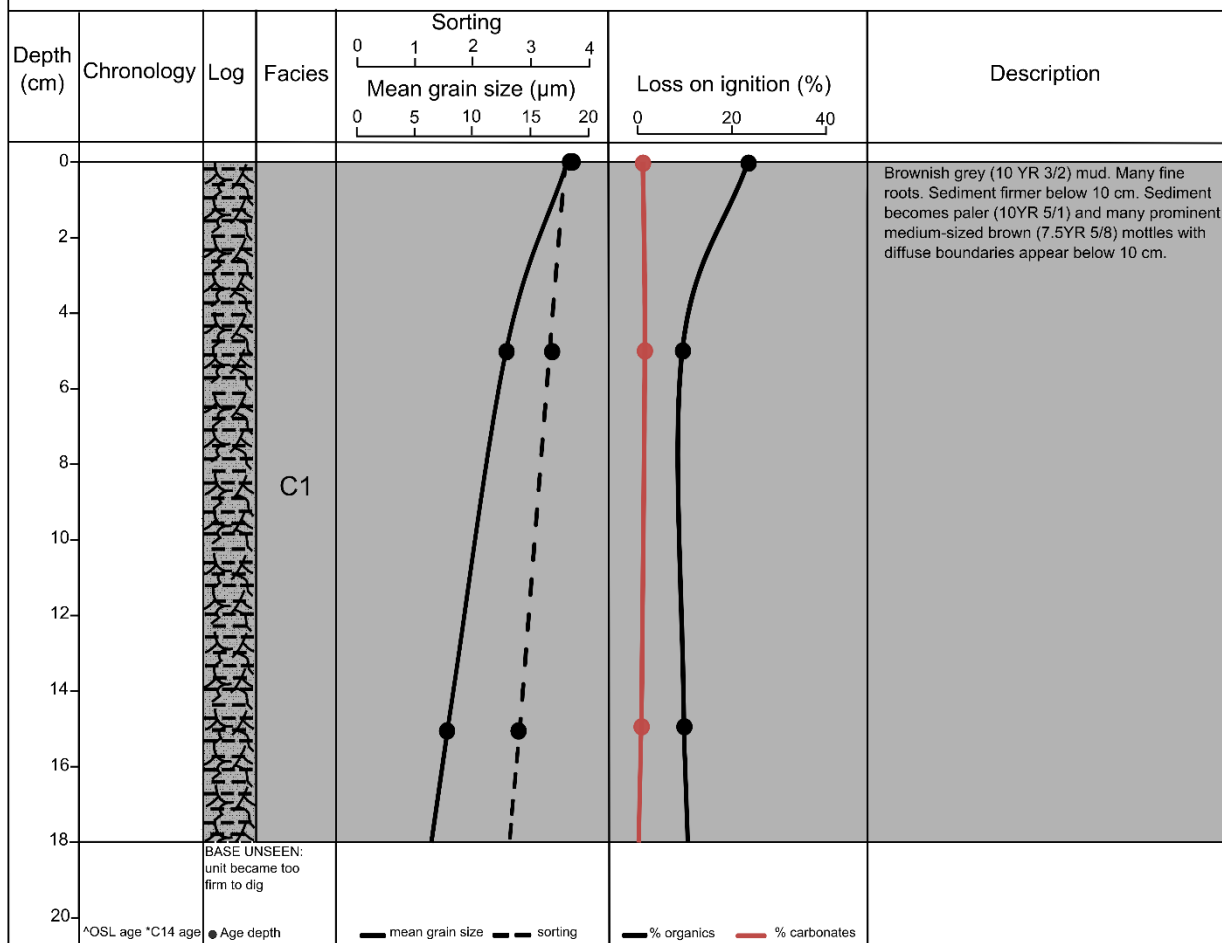




Location: Kwamter UTM coordinates: E 599974.357 N 8593809.751

Pit Location: Swale behind beach ridge (KS2) Surface elevation: 1.82 m AHD

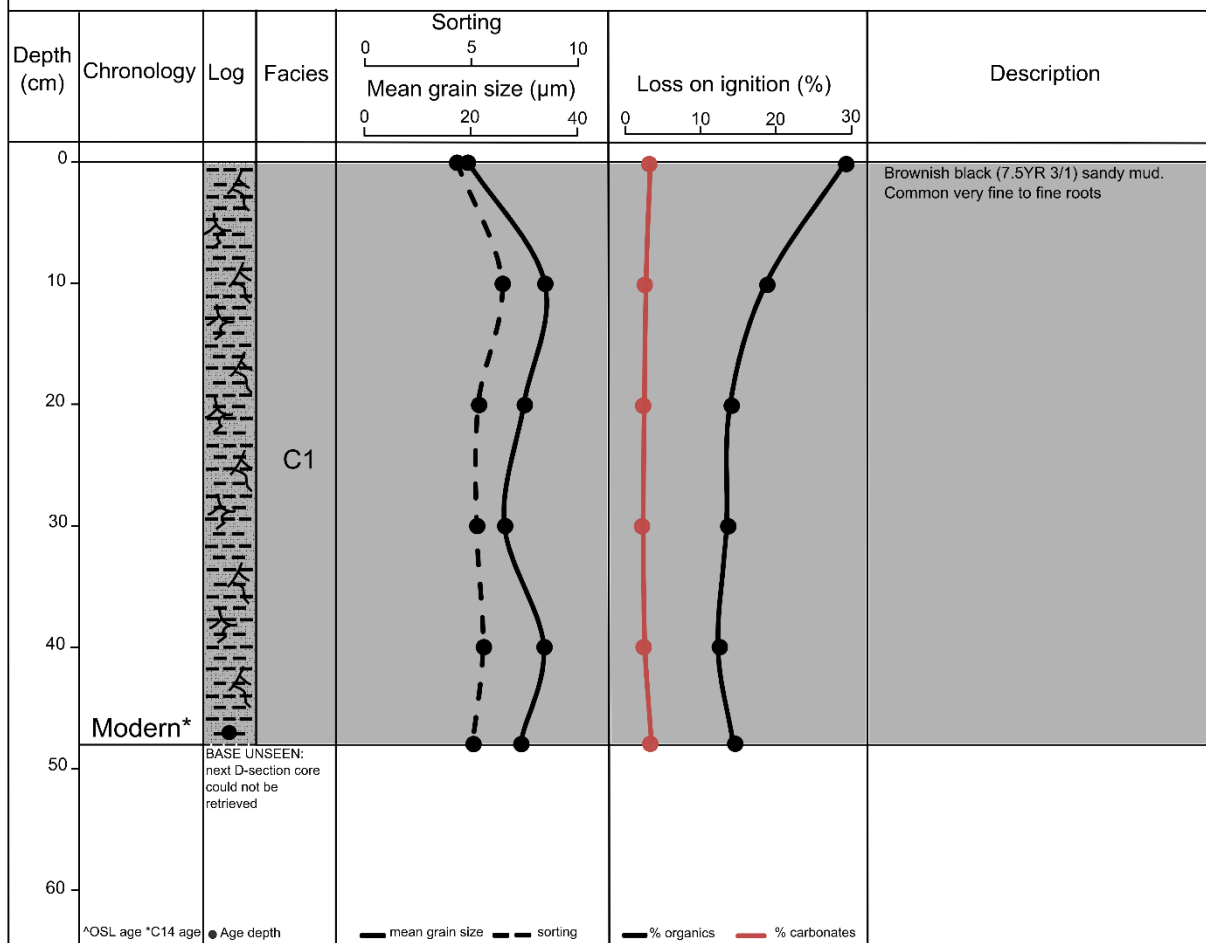
Pit Code: KW08



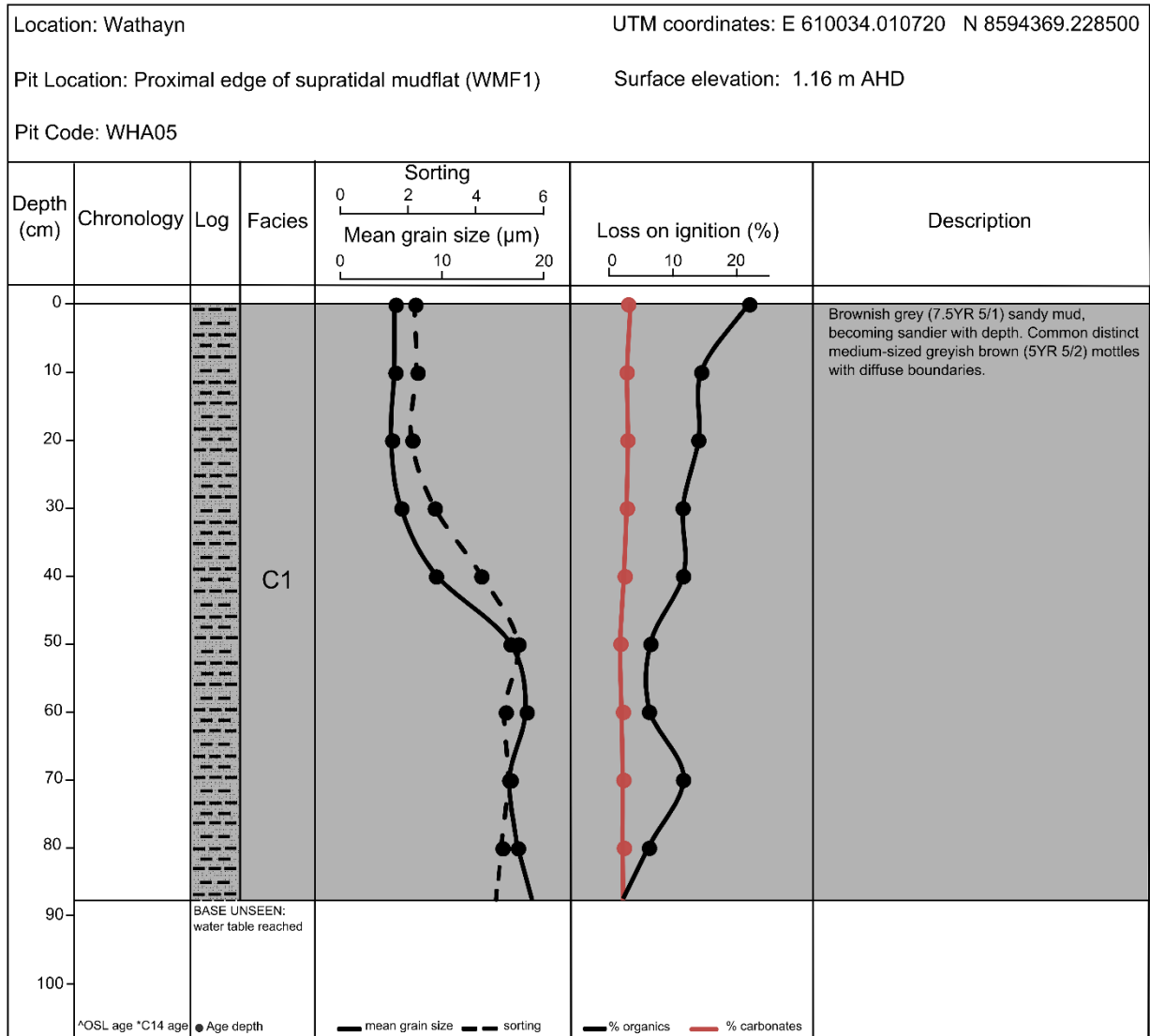
UTM coordinates: E 610027.1809 N 8594274.447

Surface elevation: 1.00 m AHD

Pit Code: WHAD06



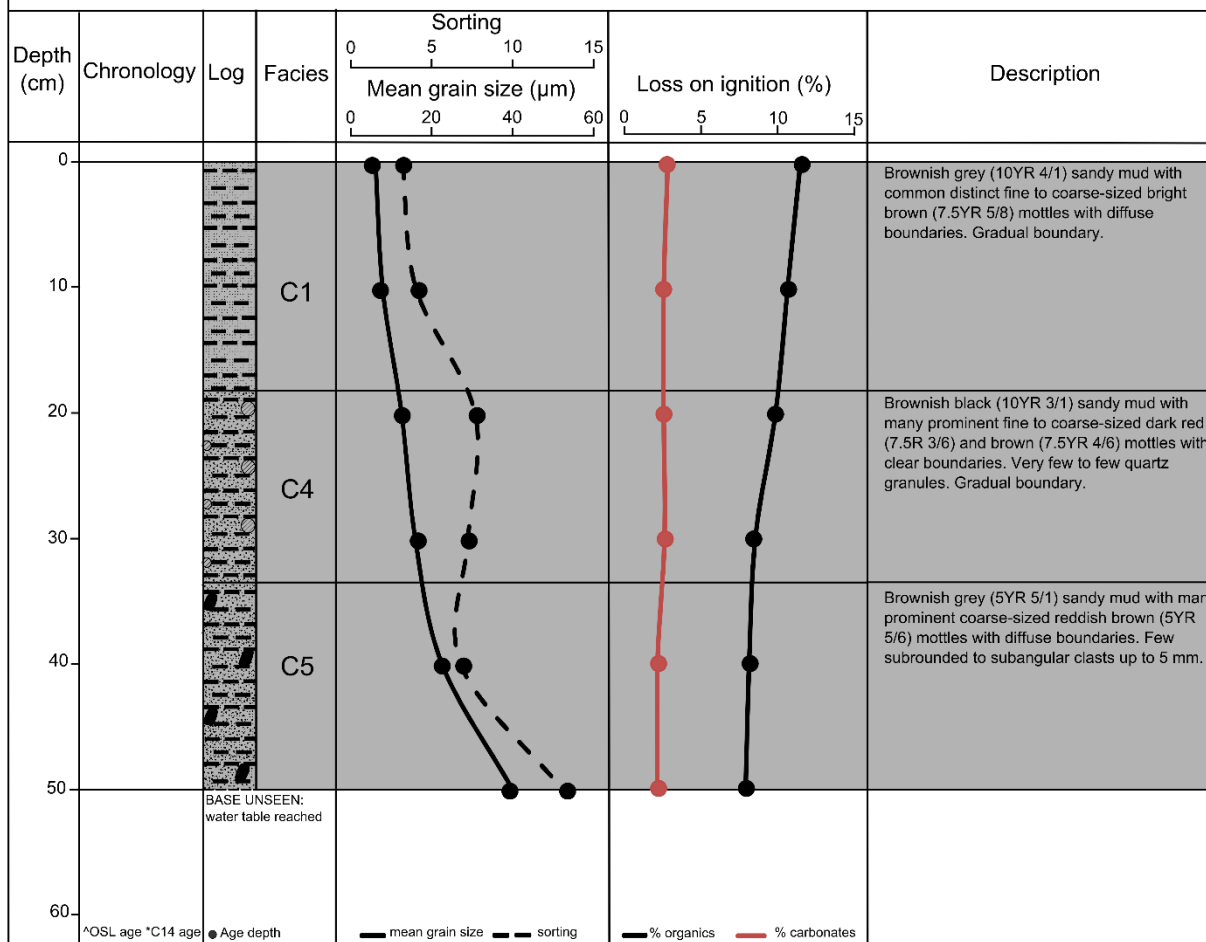


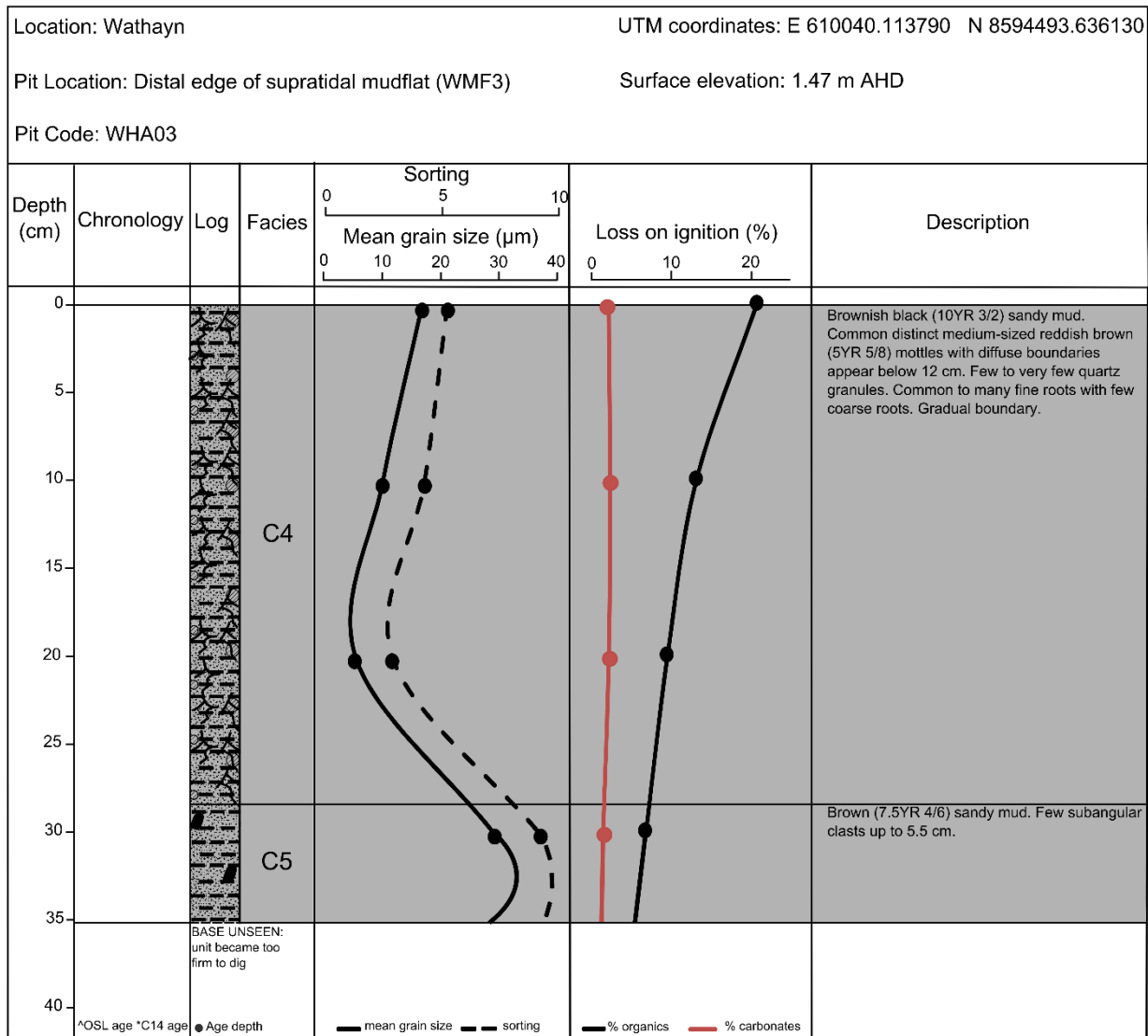


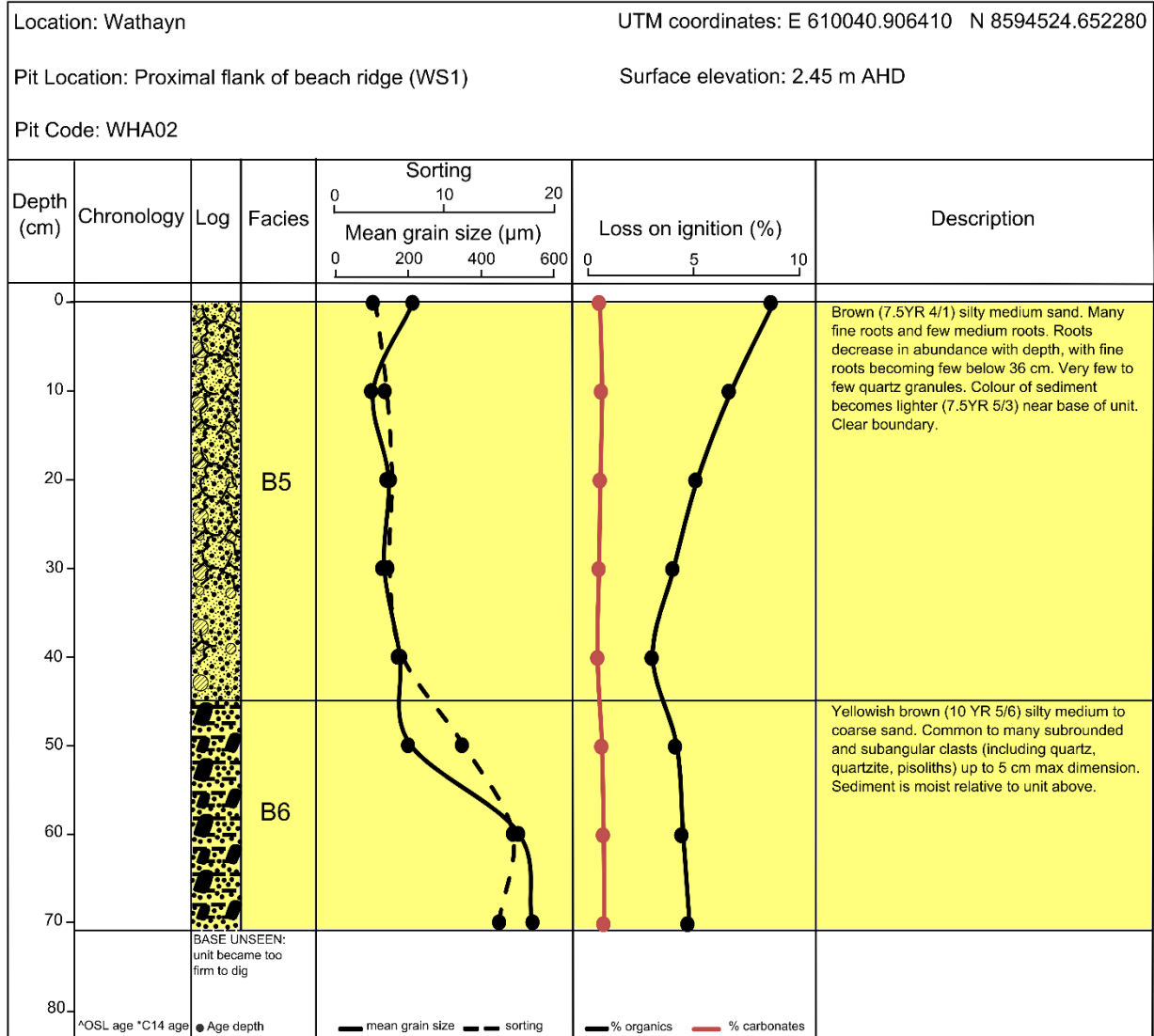
Location: Wathayn UTM coordinates: E 610039.666870 N 8594446.150630

Pit Location: Middle of supratidal mudflat (WMF2) Surface elevation: 1.18 m AHD

Pit Code: WHA04



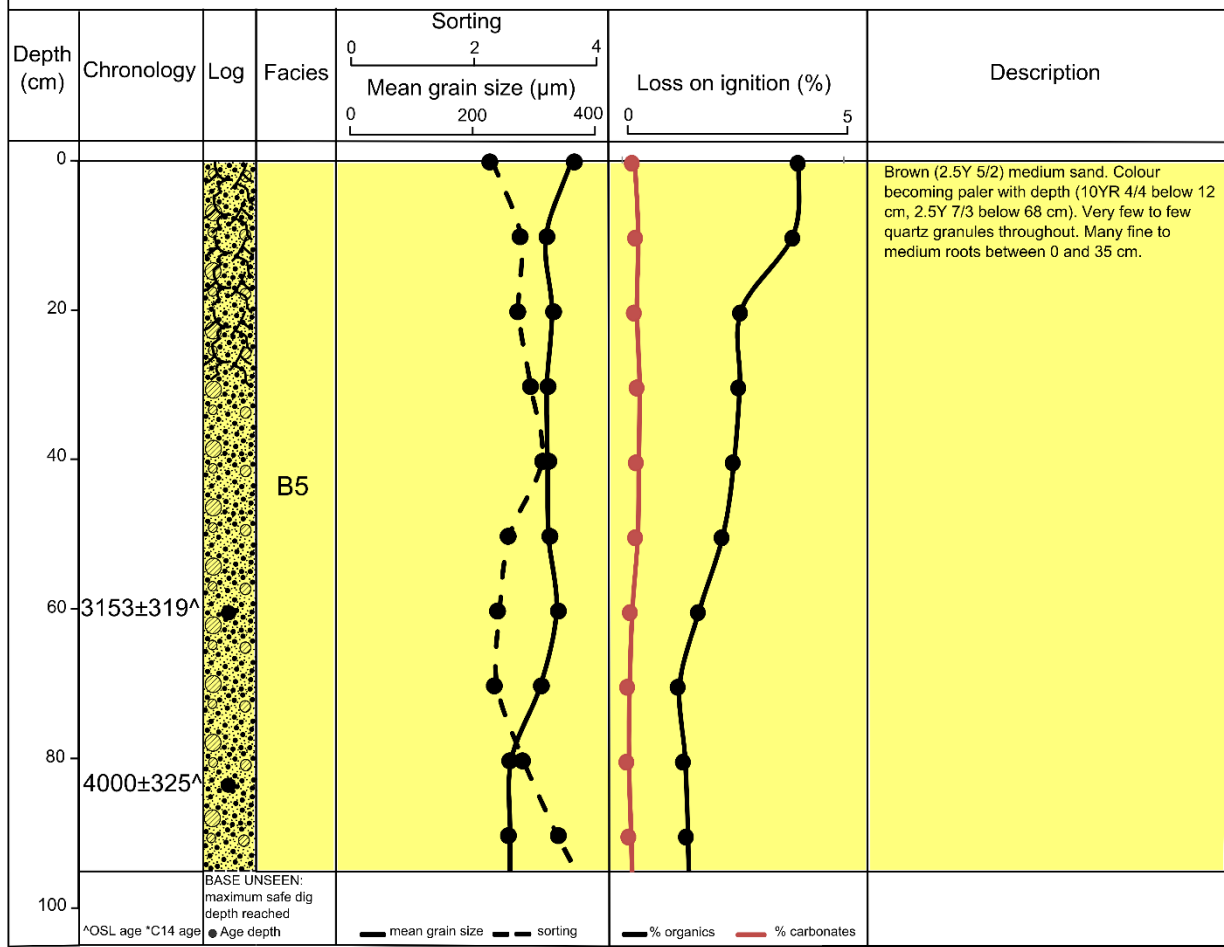




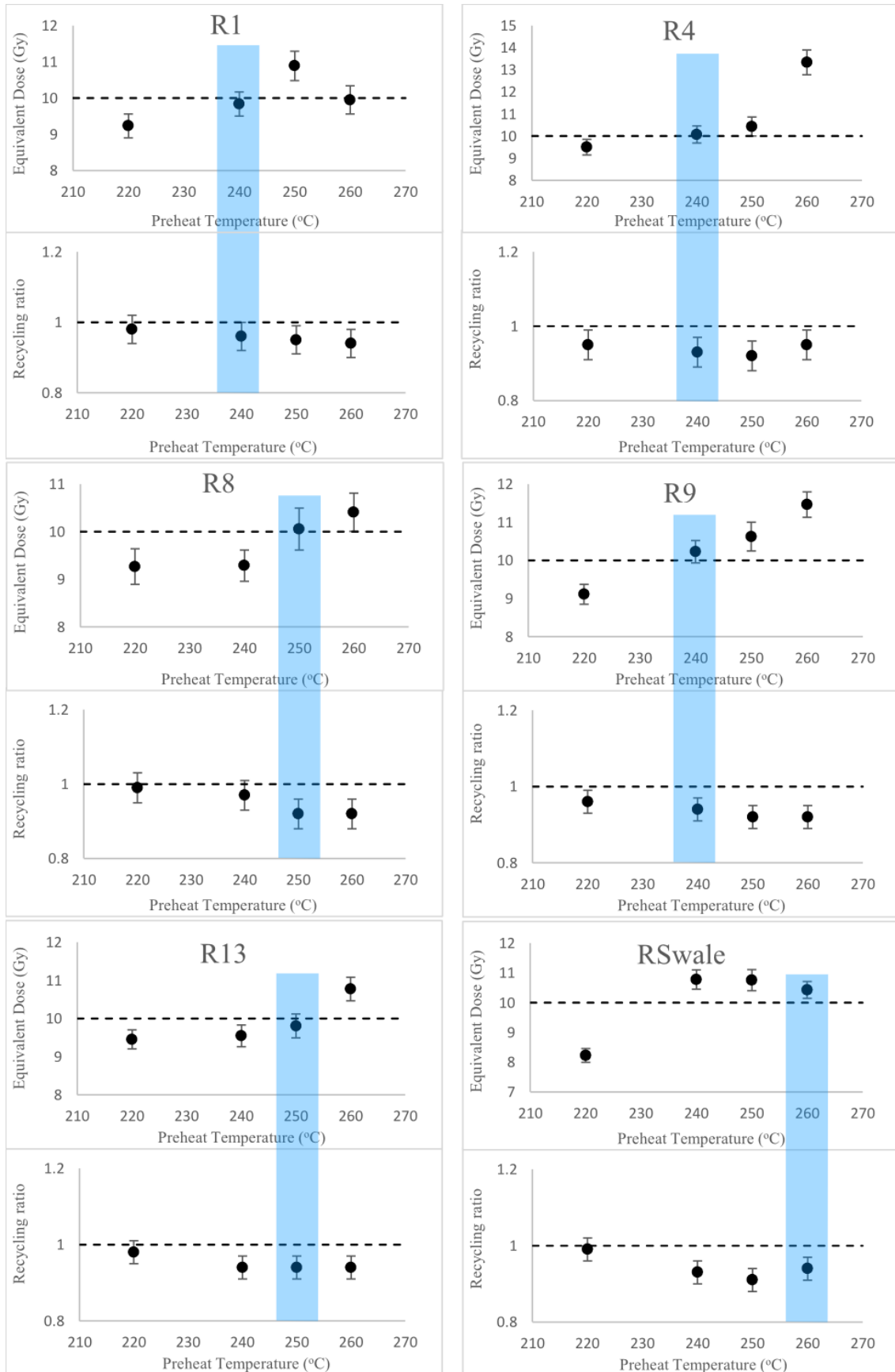
Location: Wathayn UTM coordinates: E 610040.133330 N 8594548.235200

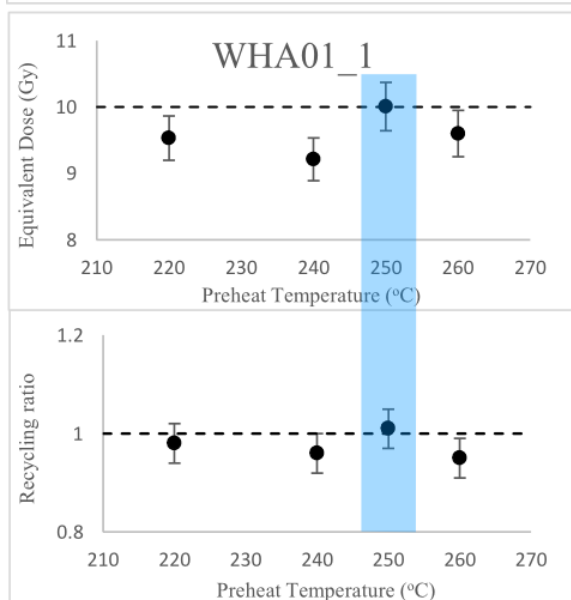
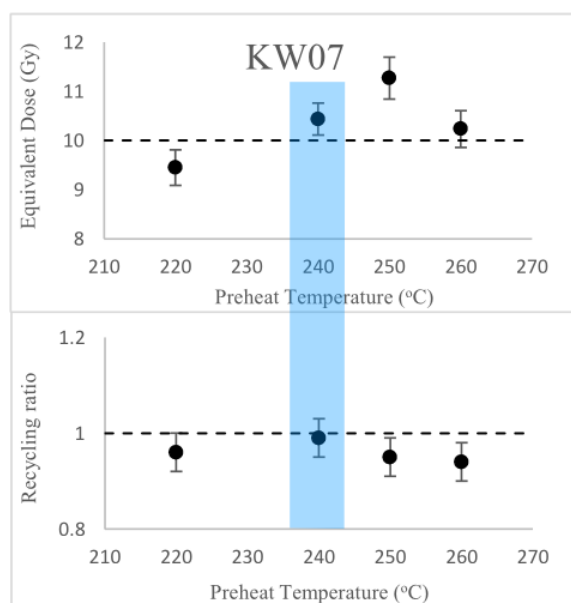
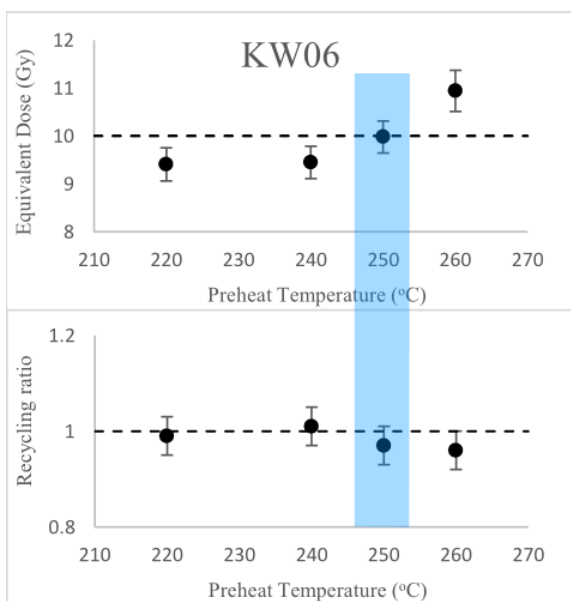
Pit Location: Crest of beach ridge (WR1) Surface elevation: 3.79 m AHD

Pit Code: WHA01



## Appendix C: OSL Preheat Test Results





## Appendix D: OSL Dose Recovery Results

